SOFT X-RAYS AND EXTREME ULTRAVIOLET RADIATION

This self-contained, comprehensive book describes the fundamental properties of soft x-rays and extreme ultraviolet (EUV) radiation and discusses their applications in a wide variety of fields, including EUV lithography for semiconductor chip manufacture and soft x-ray biomicroscopy.

The author begins by presenting the relevant basic principles such as radiation and scattering, wave propagation, diffraction, and coherence. He then goes on to examine a broad range of phenomena and applications. Each chapter begins with a simple summary of key results and concepts, followed by an introduction with little or no mathematics so as to be accessible to the widest possible audience. This is followed by a detailed mathematical development of the theoretical structure of the subject in question. The topics covered include EUV lithography, biomicroscopy, spectromicroscopy, EUV astronomy, synchrotron radiation, and soft x-ray lasers.

The author also provides a great deal of useful reference material such as electron binding energies, characteristic emission lines, and photoabsorption cross-sections. The book will be of great interest to graduate students and researchers in engineering, physics, chemistry, and the life sciences. It will also appeal to practicing engineers involved in semiconductor fabrication and materials science.

David Attwood is the Director of the Center for X-Ray Optics at the Lawrence Berkeley National Laboratory. He is also a Professor in Residence in both the Department of Electrical Engineering and Computer Science and the Graduate Group in Applied Science and Technology at the University of California, Berkeley. He is a Fellow of the Optical Society of America and has published over 100 scientific articles.

SOFT X-RAYS AND EXTREME ULTRAVIOLET RADIATION

Principles and Applications

DAVID ATTWOOD

UNIVERSITY OF CALIFORNIA, BERKELEY
AND
LAWRENCE BERKELEY
NATIONAL LABORATORY

CAMBRIDGE
UNIVERSITY PRESS

CAMBRIDGE UNIVERSITY PRESS
Cambridge, New York, Melbourne, Madrid, Cape Town, Singapore, São Paulo

Cambridge University Press
The Edinburgh Building, Cambridge CB2 2RU, UK

Published in the United States of America by Cambridge University Press, New York

www.cambridge.org
Information on this title: www.cambridge.org/9780521652148

First published 1999
This digitally printed first paperback version (with amendments) 2007

A catalogue record for this publication is available from the British Library

Library of Congress Cataloguing in Publication data

Attwood. David T.
Soft x-rays and extreme ultraviolet radiation : principles and applications / David Attwood.
p. cm.
Includes bibliographical references.
ISBN 0-521-65214-6 (hbk.)
1. Grenz rays. 2. Ultraviolet radiation. I. Title.
QC482.G68A88 1999
539.7′222 – dc21 99-21078
CIP

ISBN-13 978-0-521-65214-8 hardback
ISBN-10 0-521-65214-6 hardback

ISBN-13 978-0-521-02997-1 paperback
ISBN-10 0-521-02997-X paperback

The colour figures referred to in this publication have been replaced with black and white images for this digital reprinting. At the time of going to press the original images were available in colour for download from http://www.cambridge.org/9780521029971

To Professors Stanley Goldstein
and Nathan Marcuvitz

Contents

Preface

This book is intended to provide an introduction to the physics and applications of soft x-rays and extreme ultraviolet (EUV) radiation. These short wavelengths are located within the electromagnetic spectrum between the ultraviolet, which we commonly associate with sunburn, and harder x-rays, which we often associate with medical and dental imaging. The soft x-ray/EUV region of the spectrum has been slow to develop because of the myriad atomic resonances and concomitant short absorption lengths in all materials, typically of order one micrometer or less. This spectral region, however, offers great opportunities for both science and technology. Here the wavelengths are considerably shorter than visible or ultraviolet radiation, thus permitting one to see smaller features in microscopy, and to write finer patterns in lithography. Furthermore, optical techniques such as high spatial resolution lenses and high reflectivity mirrors have been developed that enable these applications to a degree not possible at still shorter wavelengths. Photon energies in the soft x-ray/EUV spectral region are well matched to primary resonances of essentially all elements. While this leads to very short absorption lengths, typically one micrometer or less, it provides a very accurate means for elemental and chemical speciation, which is essential, for instance, in the surface and environmental sciences. Interestingly, water is relatively transparent in the spectral region below the oxygen absorption edge, providing a natural contrast mechanism for imaging carbon-containing material in the spectral window extending from 284 to 543 eV. This provides interesting new opportunities for both the life and the environmental sciences.

Exploitation of this region of the spectrum is relatively recent. Indeed the names and spectral limits of soft x-rays and extreme ultraviolet radiation are not yet uniformly accepted. We have chosen here to follow the lead of astronomers, the lithography community, and much of the synchrotron and plasma physics communities in taking extreme ultraviolet as extending from photon energies of about 30 eV to 250 eV (wavelengths from about 40 nm to 5 nm) and soft x-rays as extending from about 250 eV (just below the carbon K edge) to several thousand eV (wavelengths from 5 nm to about 0.3 nm). The overlaps with ultraviolet radiation on the low photon energy side and with x-rays on the high photon energy side of the spectrum are not well defined. For comparison, green light has a photon energy in the vicinity of 2.3 eV and a wavelength of 530 nm. Recent developments involve advances in both science and technology, moving forward in a symbiotic relationship. Of particular importance is the development of nanofabrication techniques by the electronics industry. These provide well-defined structures with feature sizes similar to the wavelengths of interest here. The development of thin film multilayer coating capabilities by the materials science community has also been of great importance.

This book is intended for use by graduate students and researchers from physics, chemistry, engineering, and the life sciences. It is an outgrowth of classes I have taught during the past 14 years at the University of California at Berkeley. Typically the students in these classes were from the Ph.D. programs in Applied Science and Technology, Electrical Engineering and Computer Science, Physics, Chemistry, Materials Science, Nuclear Engineering, and Bioengineering. In some cases there were undergraduate students. This diversity of academic backgrounds has led to a text well suited for interdisciplinary pursuits. The text is intended to be comprehensive, covering basic knowledge of electromagnetic theory, sources, optics, and applications. It is designed to bring readers from these backgrounds to a common understanding with reviews of relevant atomic physics and electromagnetic theory in the first chapters. The remaining chapters develop understanding of multilayer coated optics with applications to materials science and EUV astronomy; synchrotron and undulator radiation; laser-produced plasmas; EUV and soft-x-ray lasers; coherence at short wavelengths; zone plate lenses and other diffractive structures with applications to biomicroscopy, materials microscopy and inspection of nanostructure patterns; and, finally, a chapter on the application of EUV and soft x-ray lithography to future high-volume production of sub-100 nm feature size electronic devices.

While the book is comprehensive in nature, it is meant to be accessible to the widest possible audience. Each chapter begins with a short summary of the important points in the material, illustrations that capture the main subject matter, and a few selected equations to whet the academic appetite. Most chapters have introductory sections designed for readers new to the field that include heuristic arguments and illustrations meant to clarify basic concepts. Each chapter also contains a mathematical development of equations for graduate students and specialists with particular interest in the chapter subject matter. To follow these mathematical developments, an undergraduate training in vector calculus and Fourier transforms is required. Descriptions of current applications in the physical and life sciences are incorporated. While there is a rigorous mathematical development, it is possible to absorb important concepts in the introductory material and then skip directly to the applications. Homework problems, which may be found at the website http://www.coe.berkeley.edu/AST/sxreuv, are designed to strengthen understanding of the material, to familiarize the reader with units and magnitudes, and to illustrate application of various formulas to current applications.

Over 600 references are provided to serve as an entry point to current research and applications. To facilitate use as a reference work many of the more important equations are boxed. In some cases the equations are repeated in numerical form, with common units, for more convenient use in a handbook fashion. Reference appendicies include tables of electron binding energies, characteristic emission lines, tables and graphs of real and imaginary scattering factors for many elements, graphs of calculated photo-absorption cross-sections, updated physical constants, and a convenient list of vector and mathematical relations. The International System of Units (SI) is also summarized, with lists of derived units and conversion factors commonly used in this field.

Berkeley, California
June 1999

Acknowledgments

It is my pleasure to acknowledge the sustained efforts, over several years, of Rudolf (Bob) Barton and Linda Geniesse. Bob typed and edited several versions of the text, carefully setting all the equations and showing great patience as I constantly revised the text and references. Linda, my wife, was responsible for all of the figures and created all of the original artwork, which I believe will benefit readers. She too showed patience far beyond reasonable expectations as we fine-tuned the artwork many times over for maximum clarity.

This book is a direct descendant of notes used at UC Berkeley in classes taught in thirteen of the past fourteen years. As such its content, method of presentation, and level of detail have been greatly influenced by Cal students. Their probing questions, discussions in class, occasional puzzled looks, contributions to homeworks, critical advice, and suggestions at semesters end have affected every paragraph of this book. I greatly appreciate their contributions. In particular I wish to acknowledge specific contributions by Kostas Adam, Junwei Bao, H. Raul Beguiristain, Kevin Bowers, Matt Brukman, Chang Chang, Gregory Denbeaux (Duke University), Eric DeVries, Daniel Finkenthal, Andrea Franke, Qian Fu, Ernie Glover, Kenneth Goldberg, Susanna Gordon, Joseph Heanue, Ronald Haff (UC Davis), John Heck, W.R. (Tony) Huff, Nasif Iskander, Ishtak Karim, Chih-wei Lai, Luke Lee, Sang Hun Lee, Yanwei Liu, Martin Magnuson (Uppsala University), Edward Moler, Vladimir Nikitin, Khanh Nguyen, Tai Nguyen, Tom Pistor, Nen-Wen Pu, Richard Schenker, Robert Socha, Regina Soufli, Alan Sullivan, Edita Tejnil, Akira Villar, Max Wei, Yan Wu, and Andrew Zenk.

The book has also benefited substantially from colleagues near and far. In preparing lectures I have sought advice and clarification from members of the Center for X-Ray Optics at Lawrence Berkeley National Laboratory. James Underwood provided original material and helpful insights on many occasions, Eric Gullikson modified many tables and graphs for use in the text, and Kwang-Je Kim, now at Argonne National Laboratory and the University of Chicago, patiently tutored me on the subject of synchrotron radiation. Werner Meyer-Ilse, Stanley Mrowka, Erik Anderson, Jeffrey Bokor (also of UC Berkeley), Patrick Naulleau, and Kenneth Goldberg each made contributions in their areas of expertise. Several of them also read particular chapters of the text and provided critical feedback. Michael Lieberman of UC Berkeley also read several early chapters and provided feedback. Portions of Chapters 2 and 6 follow lectures by Nathan Marcuvitz, then at New York University.

From a greater distance many other colleagues helped to improve the text by reading specific chapters and suggesting a wide range of improvements, corrections, and additions. For this I am grateful to Ingolf Lindau (Stanford and Lund Universities), Bernd Crasemann (University of Oregon), Joseph Nordgren (Uppsala University), David Windt (Lucent

Technologies), Claude Montcalm (LLNL), Eric Ziegler (ESRF), Alexandre Vinogradov (Lebedev Physical Institute), Albert Hofmann (CERN), R. Paul Drake (University of Michigan), R. Kauffman (LLNL), Andrei Shikanov (Lebedev Physical Institute), Luiz DaSilva (LLNL), Syzmon Suckewer (Princeton University), Jorge Rocca (Colorado State University), Emil Wolf (University of Rochester), Günter Schmahl (Göttingen University), Janos Kirz (SUNY, Stony Brook), Alexei Popov (Instit. Terr. Magn. Iono. Rad. Prop., Troitsk), Franco Cerrina (University of Wisconsin), Donald Sweeney (LLNL), Richard Stulen (Sandia), Hiroo Kinoshita (Himeji University), Victor Pol (Motorola), David Williamson (SVGL), and Frits Zernike.

Finally I am grateful to those who contributed to the atmosphere of support for research and teaching in Berkeley. These include Louis Ianiello, Iran Thomas, William Oosterhuis, and Jerry Smith at the Department of Energy's Office of Basic Energy Sciences; Howard Schlossberg at the Air Force Office of Scientific Research, who supported student research activities in our group over many years; David Patterson, who heads DARPA's Advanced Lithography Program; and the Intel, Motorola, and Advanced Micro Devices Corporations. A special note of gratitude goes to John Carruthers of Intel for his continual support of these activities and of this book in particular. Daniel Chemla is warmly acknowledged for his support and encouragement, without which it would not have been possible to maintain a vibrant research group while teaching, advising, and writing a lengthy text.

Berkeley, California
June 1999

Chapter 1

INTRODUCTION

1.1 THE SOFT X-RAY AND EXTREME ULTRAVIOLET REGIONS OF THE ELECTROMAGNETIC SPECTRUM

One of the last regions of the electromagnetic spectrum to be developed is that between ultraviolet and x-ray radiation, generally shown as a dark region in charts of the spectrum. It is a region where there are a large number of atomic resonances, leading to absorption of radiation in very short distances, typically measured in nanometers (nm) or micrometers (microns, μm), in all materials. This has historically inhibited the pursuit and exploration of the region. On the other hand, these same resonances provide mechanisms for both elemental (C, N, O, etc.) and chemical (Si, SiO_2, $TiSi_2$) identification, creating opportunities for advances in both science and technology. Furthermore, because the wavelengths are relatively short, it becomes possible both to see smaller structures as in microscopy, and to write smaller patterns as in lithography. To exploit these opportunities requires advances in relevant technologies, for instance in materials science and nanofabrication. These in turn lead to new scientific understandings, perhaps through surface science, chemistry, and physics, providing feedback to the enabling technologies. Development of the extreme ultraviolet and soft x-ray spectral regions is presently in a period of rapid growth and interchange among science and technology.

Figure 1.1 shows that portion of the electromagnetic spectrum extending from the infrared to the x-ray region, with wavelengths across the top and photon energies along the bottom. Major spectral regions shown are the infrared (IR), which we associate with molecular resonances and heat; the visible region from red to violet, which we associate with color and vision; the ultraviolet (UV), which we associate with sunburn and ionizing radiation; the regions of extreme ultraviolet (EUV) and soft x-rays (SXR), which are the subject of this book; and finally hard x-rays, which we associate with medical and dental x-rays and with the scientific analysis of crystals, materials, and biological samples through the use of diffractive and other techniques.

The extreme ultraviolet is taken here as extending from photon energies of about 30 eV to about 250 eV, with corresponding wavelengths in vacuum extending from about 5 nm to 40 nm.* The soft x-ray region is taken as extending from about 250 eV (just below the carbon

*It is common to express photon energies in this spectral region in electron volts (eV) or thousands of electron volts (keV), where the photon energy is $\hbar\omega$, $\hbar$ is Planck's constant divided by 2π, and $\omega = 2\pi f$

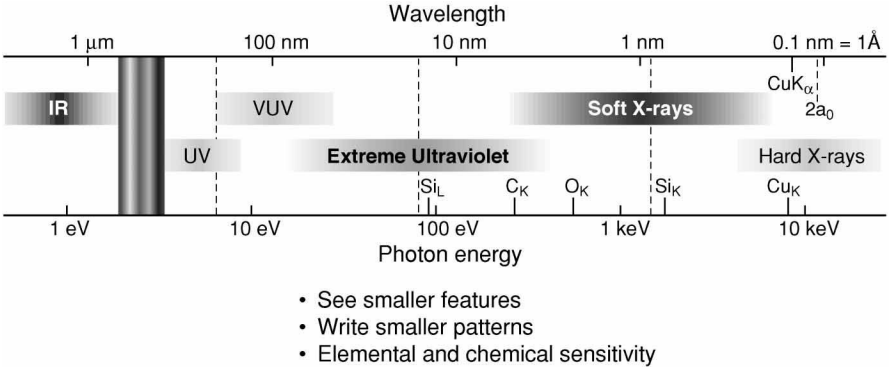

FIGURE 1.1 (see Colorplate I). The electromagnetic spectrum as it extends from the infrared (IR) to the x-ray regions. Visible light is shown with red (650 nm), green (530 nm), and blue (470 nm) wavelengths. At shorter wavelengths are ultraviolet (UV) radiation, extreme ultraviolet radiation (EUV), soft x-rays (SXR), and hard x-rays. Shown for reference are the silicon L-absorption edge at 99.2 eV (12.5 nm wavelength), the carbon K-absorption edge at 284 eV (4.37 nm), the oxygen K-absorption edge at 543 eV (2.28 nm), the silicon K-absorption edge at 1.84 keV (0.674 nm), the copper K-absorption edge at 8.98 keV (0.138 nm), the copper K_α-emission line at 0.154 nm or 1.54 Å (8.05 keV), and twice the Bohr radius at $2a_0 = 1.06$ Å, the diameter of the $n = 1$ orbit in Bohr's model of the hydrogen atom, but more generally a dimension within which resides most of the charge for all atoms. Vertical dashed lines correspond to the transmission limits of common window materials used to isolate vacuum. Shown are approximate transmission limits for common thicknesses of fused silica (pure SiO_2) at 200 nm, a thin film of silicon nitride (~100 nm thick Si_3N_4) at 15 nm, and an 8 μm thick beryllium foil at a wavelength of about 1 nm.

K-edge) to several keV, as shown in Figure 1.1. These spectral regions are characterized by the presence of the primary atomic resonances and absorption edges of most low and intermediate Z elements, where Z is the atomic number (the number of protons in the nucleus). The primary atomic absorption edges[†] for selected elements are given in Table 1.1, along with $1/e$ absorption lengths at photon energies of 100 eV and 1 keV. The K- and L-absorption edges, associated with the removal of a core electron by photoabsorption from the most tightly bound atomic states (orbitals of principal quantum numbers $n = 1$ and $n = 2$, respectively), are described later in this chapter. The K-absorption edges of carbon (C_K), oxygen, silicon, and copper are shown in Figure 1.1, as is the L-absorption edge of silicon (Si_L), just below 100 eV.

We see in Table 1.1 that many of these absorption edges lie in the combined soft-x-ray and extreme ultraviolet spectral region. What differentiates these regions from neighboring spectral regions is the high degree of absorption in all materials. At lower photon energies, in the visible and ultraviolet, and at higher photon energies, in the hard x-ray region, many materials become transparent and it is not necessary to utilize vacuum isolation techniques in general. For example, Figure 1.1 shows dashed vertical lines at the locations of common window materials that can hold vacuum over square centimeter areas while still transmitting radiation in the indicated regions. In the UV, fused silica, a form of pure SiO_2, is transmissive to wavelengths as short as 200 nm, in millimeter thickness. For shorter wavelengths one quickly enters the vacuum ultraviolet (VUV), where air and all materials are absorbing. Shown just

is the radian frequency. Wavelengths (λ) are commonly expressed in nanometers (1 nm $= 10^{-9}$ m) and angstroms (1 Å $= 10^{-10}$ m). See Appendix A for the values of physical constants and conversion factors.

[†]Standard reference data for this spectral region are given in Refs. 1–4.

TABLE 1.1. K- and L_3-absorption edges for selected elements. Also given are $1/e$ absorption depths at photon energies of 100 eV and 1 keV. Energies are given to the nearest electron volt. They are measured from the vacuum level for gases (N_2, O_2), relative to the Fermi level for metals, and relative to the top of the valence band for semiconductors. Wavelengths are given to three significant figures. These K- and L-edge values can vary somewhat with the chemical environment of the atom. Values here are taken from Williams.[1] Absorption lengths are obtained from Henke, Gullikson, and Davis.[3]

						l_{abs}	
Element	**Z**	**K_{abs}-edge (eV)**	**L_{abs}-edge (eV)**	**λ_{K-abs} (nm)**	**λ_{L-abs} (nm)**	100 eV (nm)	1 keV (μm)
Be	4	112	—	11.1	—	730	9.0
C	6	284	—	4.36	—	190	2.1
N	7	410	—	3.02	—	—	—
O	8	543	—	2.28	—	—	—
H_2O						160	2.3
Al	13	1,560	73	0.795	17.1	34	3.1
Si	14	1,839	99	0.674	12.5	63	2.7
S	16	2,472	163	0.502	7.63	330	1.9
Ca	20	4,039	346	0.307	3.58	290	1.3
Ti	22	4,966	454	0.250	2.73	65	0.38
V	23	5,465	512	0.227	2.42	46	0.26
Cr	24	5,989	574	0.207	2.16	31	0.19
Fe	26	7,112	707	0.174	1.75	22	0.14
Ni	28	8,333	853	0.149	1.45	16	0.11
Cu	29	8,979	933	0.138	1.33	18	0.10
Se	34	12,658	1,434	0.0979	0.865	63	0.96
Mo	42	20,000	2,520	0.0620	0.492	200	0.19
Sn	50	29,200	3,929	0.0425	0.316	17	0.17
Xe	54	34,561	4,782	0.0359	0.259	—	—
W	74	69,525	10,207	0.0178	0.121	28	0.13
Au	79	80,725	11,919	0.0154	0.104	28	0.10

below 1 nm wavelength is the transmission limit of a thin ($\simeq 8\ \mu$m)beryllium foil that transmits photons of energy greater than about 1.5 keV. For many years these two materials defined the limits of available window materials. More recently thin films ($\sim$100 nm) such as silicon nitride (stoichiometrically Si_3N_4) have extended transmissive windows to photon energies just under 100 eV, as shown in Figure 1.1.

While this plenitude of atomic resonances and efficient photoabsorption has made the EUV and soft x-ray regions more difficult to access, it also provides a very sensitive tool for elemental and chemical identification, thus creating many scientific and technological opportunities. These opportunities are enhanced in this spectral region in that the wavelengths are short, but not so short as to preclude the development of high resolution optical techniques, thus permitting direct image formation and spatially resolved spectroscopies, to spatial resolutions measured in tens of nanometers. The relative transparency of water and its natural contrast with other elements further add to these opportunities, for instance for spectroscopy in the life and environmental sciences.

In the paragraphs that follow we will briefly review the basic processes of absorption, scattering, and photoemission; atomic energy levels and allowed transitions; and associated

absorption edges and characteristic emission lines. We note two interesting features associated with wavelengths in the EUV/soft-x-ray spectral region. In general the wavelengths are large compared to the Bohr radius, $\lambda \gg a_0$, where a_0 is the radius of the first ($n = 1$) stationary electron orbit in the Bohr model of hydrogen.[‡] More significantly here, the diameter $2a_0 = 1.06$ Å typically encompasses most of the electronic charge in multi-electron atoms,[¶] so that to a large degree the treatment of scattering simplifies as the various electrons experience a rather uniform phase variation, an assumption that would not hold at shorter x-ray wavelengths. Furthermore, because the wavelengths are long on the atomic scale, much greater than the Compton wavelength[4,5] ($\lambda \gg \lambda_C = h/mc = 0.0243$ Å), momentum transfer from the photon can be ignored during scattering, i.e., the photon momentum $\hbar k \ll \hbar k_C$, where $k = 2\pi/\lambda$ is the wavenumber, again simplifying the analysis of scattering in this spectral region.

Finally, we close this section with some numerical relationships[7] in units[8] convenient for work in this spectral region. Based on the dispersion relation in vacuum, $f\lambda = c$ or $\omega = kc$, where c is the velocity of light[§] in vacuum and $\omega = 2\pi f$, the product of photon energy $\hbar\omega$ and wavelength λ is given by (see Appendix A for values of physical constants)

$$\boxed{\hbar\omega \cdot \lambda = hc = 1239.842 \text{ eV nm}} \tag{1.1}$$

The number of photons required for one joule of energy, with wavelength given in nanometers (nm), is

$$\boxed{1 \text{ joule} \Rightarrow 5.034 \times 10^{15} \lambda[\text{nm}] \text{ photons}} \tag{1.2a}$$

or in terms of power

$$\boxed{1 \text{ watt} \Rightarrow 5.034 \times 10^{15} \lambda[\text{nm}] \, \frac{\text{photons}}{\text{s}}} \tag{1.2b}$$

where 1 nm = 10 Å. Thus for a wavelength $\lambda = 1$ nm, a power of one watt corresponds to a photon flux of 5.034×10^{15} photons/s, each photon having an energy $E \simeq 1240$ eV.

[‡]Numerically $a_0 = 4\pi\epsilon_0\hbar^2/me^2 = 0.529$ Å, where m is the electron rest mass, e the electron charge, ϵ_0 the permittivity of free space, and $\hbar$ Planck's constant divided by 2π. See Eisberg and Resnick, Ref. 5, for a discussion of Bohr's model of the hydrogen atom (Chapter 4) through a discussion of wave mechanics for the multi-electron atom (Chapter 10). Also see Tipler, Ref. 6, for a somewhat more introductory presentation.

[¶]In multi-electron atoms the inner shells typically have very small radii, of order a_0/Z, as they experience nearly the full Coulomb attraction of the higher-Z nucleus, with little shielding by the outer electrons. A few outer electrons typically orbit with a radius na_0. See Eisberg and Resnick, Ref. 5.

[§]The phase velocity of EUV and soft x-ray radiation is derived from Maxwell's equations in Chapters 2 and 3, for propagation in vacuum and materials.

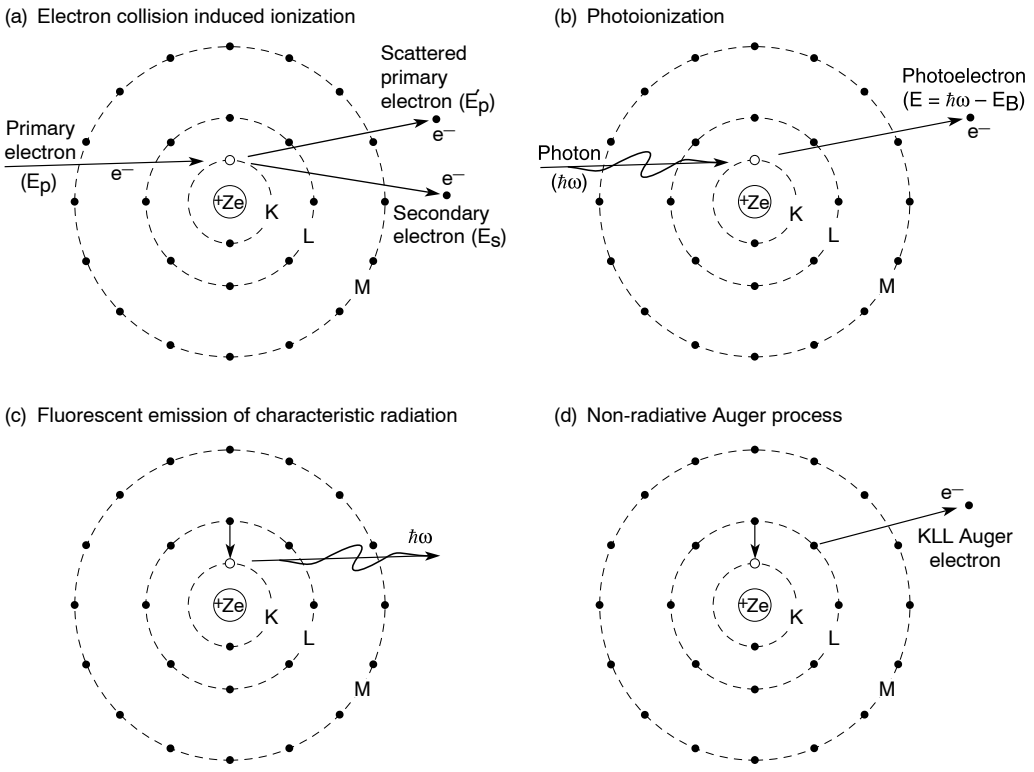

FIGURE 1.2. (a) An incident *primary electron* of sufficiently high energy E_p is scattered by an atom as it knocks free a core electron from the K-shell. The primary electron now travels in a new direction, with a reduced energy E'_p. The lost energy is used to overcome the binding energy of the previously bound electron, and to impart kinetic energy to what is now referred to as a *secondary electron*. The core vacancy (K-shell in this case) can then be filled by a higher-lying L- or M-shell electron. (b) An incident photon of sufficient energy $\hbar\omega$ is absorbed by the atom with the emission of a *photoelectron* of kinetic energy equal to the photon energy minus the binding energy. Again a vacancy is created, eventually to be filled by an outer electron. (c) An atom with a core vacancy readjusts as a higher-lying electron makes a transition to the vacancy, with the emission of a photon of characteristic energy (fluorescent radiation). (d) The atom adjusts to the core vacancy through the non-radiative Auger process in which one electron makes a transition to the core vacancy, while a second electron of characteristic energy is emitted. The second electron is not necessarily emitted from the same shell.

1.2 BASIC ABSORPTION AND EMISSION PROCESSES

In this section we briefly review the basic processes through which radiation interacts with matter. In Figure 1.2 we show simplified models of the atom, with point electrons in orbit around a nucleus of positive charge $+Ze$. In x-ray notation the electron orbits are labeled K, L, and M, corresponding to principal quantum numbers $n = 1$, 2, and 3, respectively. A more accurate model of the atom is discussed in the next section, but that shown in Figure 1.2 suffices for these introductory comments.

Shown in Figure 1.2(a) is a primary electron incident on a multi-electron atom, with sufficient energy to remove a core electron in a close encounter. Common nomenclature refers to the incident electron as a *primary* electron, shown as *scattered* (redirected) off at some new

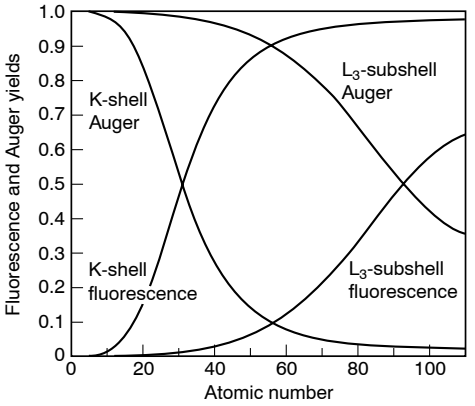

FIGURE 1.3. Fluorescence and Auger yields for the K-shell and the L_3-subshell as a function of atomic number Z. The Auger yields include all non-radiative contributions. (Following M. Krause,[9] Oak Ridge National Laboratory.)

angle, and in this case with reduced energy (E'_p), where the lost energy is used to overcome the binding energy needed to remove the core electron, now free and referred to as a *secondary* electron, and to supply kinetic energy to the electron (E_s). The core vacancy can then be filled by an electron from a higher-lying orbit, pulled by the strong nuclear potential, with the emission of a photon of characteristic energy equal to the difference between the two shells. In Figure 1.2(b), a related process, photoionization, is shown in which a photon of sufficient energy is absorbed by the atom, transferring the energy to an emitted *photoelectron* with a kinetic energy equal to that of the incident photon, minus the binding energy of an electron in the particular shell. As an L-shell electron is bound to the atom with less energy than a K-shell electron, it will emerge with greater kinetic energy. Electron binding energies for hydrogen through uranium are given in Appendix B, Table B.1.

In both of these ionization processes [(a) and (b)] the atom is left with a core vacancy. The atom can rearrange itself for minimal total energy by the transition of a higher-lying electron, pulled by the strong nuclear potential, to the vacancy by one of two competing processes.

In (c) the atom is shown rearranging in a process of fluorescence, in which the electron transition is accompanied by the emission of a photon of characteristic energy equal to the difference between that of the initial and final atomic states. Characteristic emission energies are given in Appendix B, Table B.2. In a competing effect (d) the atom rearranges through the emission of a second *Auger* (pronounced ō −′zhā), electron, again of characteristic energy. The emitted Auger electron is labeled with three capital letters, the first representing the shell of the original vacancy, the second representing the shell from which the vacancy is filled, and the third representing the shell from which the Auger electron is ejected. In the competition between fluorescent emission and the Auger process, the probability tends to favor fluorescence for high Z atoms, as shown in Figure 1.3, and the Auger process for low Z atoms.[9] Auger electron energies[10] for lithium through uranium are given in Appendix B, Table B.3. As the Auger electrons have a fixed characteristic energy, they are used extensively for elemental characterization in surface and interface analysis.

The study of atoms, molecules, and surfaces by the measurement of photoelectron kinetic energies, as a function of incident photon energy, is known as photoemission spectroscopy. This process is widely used for the elemental identification and analysis of chemical bonding for atoms at or near surfaces. As generally employed, photons of fixed energy illuminate a surface or thin film, providing the necessary energy to lift bound electrons into the continuum, as shown in Figure 1.4. With well-known electron binding energies (Appendix B, Table B.1) the observed kinetic energies can be used to identify the elements present. As the binding energies of core electrons are affected by the orbital parameters of the outer electrons (chemical

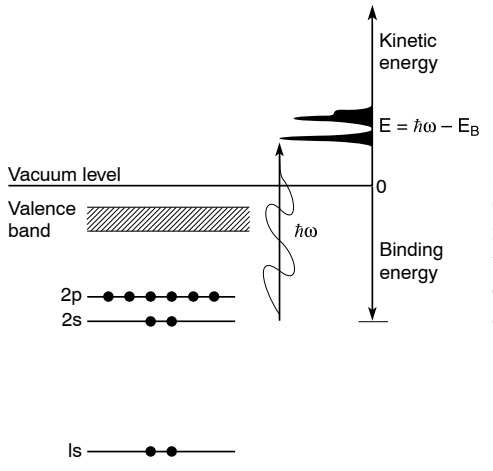

FIGURE 1.4. The process of photoemission in which an absorbed photon transfers its energy to a bound electron near the material–vacuum interface, resulting in a transition to a free electron state in the continuum with kinetic energy (E) equal to that of the incident photon ($\hbar\omega$) minus the binding energy (E_B).

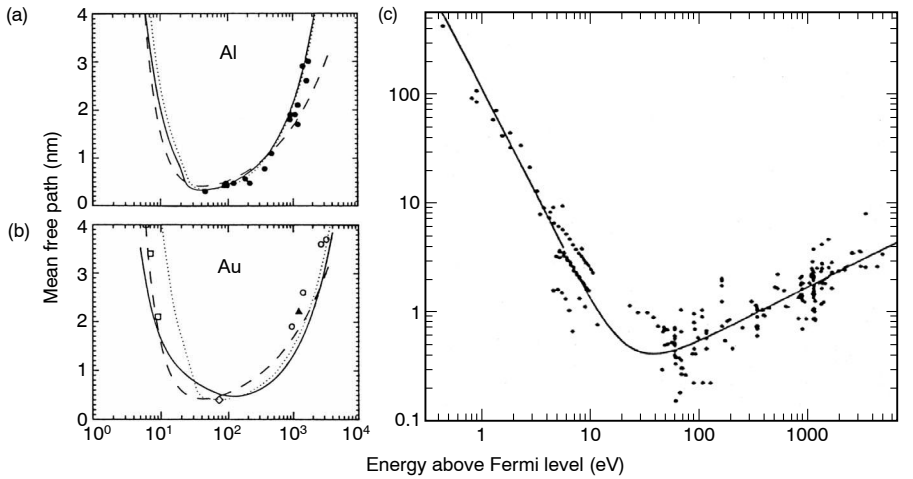

FIGURE 1.5. Electron mean free path, as a function of electron energy, for (a) aluminum, (b) gold, and (c) a combination of many materials. The data in (a) and (b) is from Penn,[18] while that in (c) is from Seah and Dench.[19] The various curves reflect efforts to develop a universal model that describes inelastic scattering of electrons in a solid.

bonding in molecules, valence and conduction bonds in solids), photoemission also provides a powerful tool for the study of chemical states.[11–17] As L-shell energies are more sensitive to the bonding of outer electrons than are the energies of the more tightly bound and shielded K-shell electrons, the L-shell electrons are more commonly used in photoemission studies.

If the emitted photoelectron travels any distance in a material, it is likely to lose energy quickly through interactions with other electrons (individual collisions or collective motion). Figure 1.5 shows typical electron range data, as a function of electron energy, in aluminum and gold,[18] as well as a *universal curve* for many materials.[19, 20] With incident photon energies characteristic of the EUV/soft-x-ray spectral region, it is clear that photoelectron ranges will be extremely short, of order 1 nm, so that these techniques are clearly limited to surface science.

When observing the emission spectrum from a solid material bombarded by electrons it is typical to observe both characteristic line emission and continuum emission. This latter

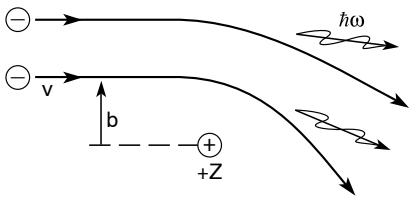

FIGURE 1.6. Bremsstrahlung radiation occurs predominantly when an incident electron is accelerated as it passes a nucleus, causing it to radiate. A broad continuum of radiation results when a large number of electrons interact randomly with nuclei at various distances of closest approach, b, resulting in wide variations in experienced acceleration and collision time.

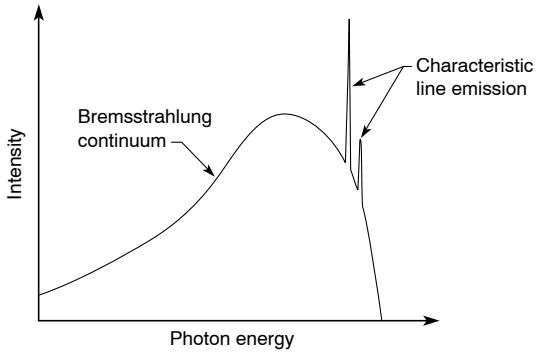

FIGURE 1.7. Continuum radiation and narrow line emission from a solid target with incident electrons, as might be observed from the anode of an electrical discharge tube.

process is called *bremsstrahlung*, from the German word for "braking radiation." Figure 1.6 shows a simple diagram of the process, in which electrons of a given velocity v, or energy E, approach an electron or nucleus at various distances of closest approach, b (the *impact parameter*), experiencing a wide range of accelerations (depending on the closeness of the interaction) and thus emitting photons across a wide range of energies. With a large number of incident electrons and a wide variety of impact parameters, a rather broad continuum of radiation is produced. Where photoemission occurs due to direct impact with bound electrons, as described earlier in Figure 1.2(a), characteristic line emission is also observed. Both phenomena are illustrated, as they might typically be observed,[21] in Figure 1.7. The nature and nomenclature of the characteristic line emissions are discussed in the following section.

Historically, the process of photoabsorption [Figure 1.2(b)] has been observed macroscopically by passing radiation through thin foils and observing the resultant decrease in intensity as a function of thickness.[22] As shown in Figure 1.8, one observes that with incremental increases in thickness, Δx, there is an an incremental decrease in transmitted intensity I, relative to the incident intensity I_0, such that

$$\frac{\Delta I}{I_0} = -\rho\mu\,\Delta x$$

where ρ is the mass density and μ is an energy- and material-dependent absorption coefficient. Writing this in the differential limit ($\Delta x \rightarrow dx,\ \Delta I \rightarrow dI$), the equation integrates to a

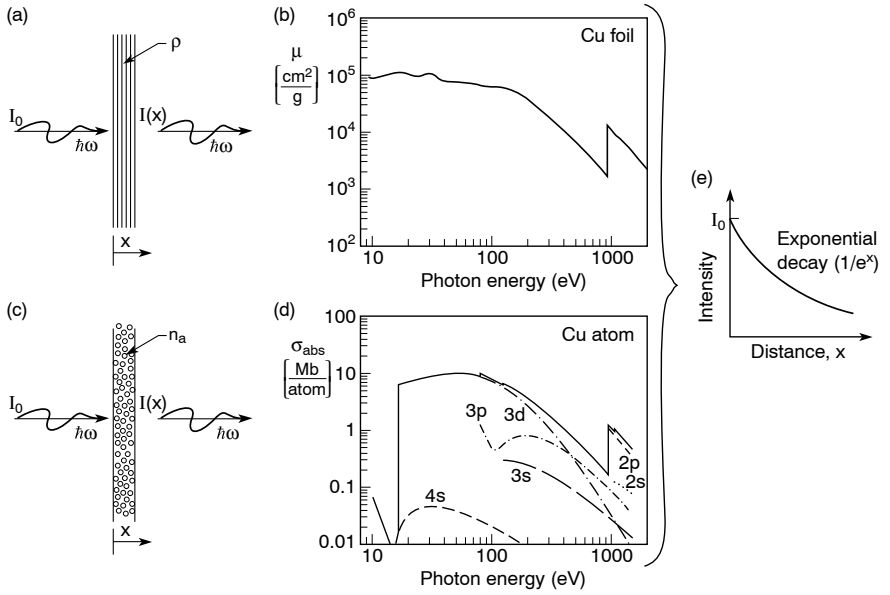

FIGURE 1.8. (a) Photoabsorption as observed with thin foils of increasing thickness x at fixed photon energy, with (b) an example of the (mass) absorption coefficient μ for copper (from Henke, Gullikson, and Davis[3]). The same process is described on an atomic level in (c), with the photoabsorption cross-section (photoionization) for a copper atom in (d) (from Yeh and Lindau[4]). Exponential attenuation of the radiation is shown in (e). Differences observed in comparing (b) and (d) are due to solid state effects in metallic copper foils, most noticably for copper in the absence of the atomic 3d edge just above 10 eV photon energy.

logarithmic dependence $\ln(I/I_0) = -\rho\mu x$, or in exponential form

$$\frac{I}{I_0} = e^{-\rho\mu x} \tag{1.3a}$$

where $\mu = \mu(E,\ Z),\ E = \hbar\omega$ is the photon energy, Z represents the elemental dependence, and μ has the somewhat unfortunate, but historical, name *mass absorption coefficient*. Standard values of μ are given in Appendix C for representative materials. This same expression can be written in terms of an atomic density n_a and a cross-section for photoabsorption, σ_{abs}, as

$$\frac{I}{I_0} = e^{-n_a\sigma_{\text{abs}}x} \tag{1.3b}$$

where σ_{abs} depends on both element (Z) and photon energy. Curves of σ_{abs}, also referred to as the photoionization cross-section, are given in Appendix C for representative elements, and more completely in Ref. 4. The development of Eqs. (1.3a) and (1.3b), which represent macroscopic and microscopic descriptions of the same process, is given in Chapter 3,

Section 3.2, where it is shown that $\mu = \sigma_{abs}/Am_u$, where A is the number of atomic mass units and m_u is an atomic mass unit (approximately the mass of a proton or neutron), as given in Appendix A. There are some differences in the two sets of data, as the thin foil absorption coefficients μ are experimentally derived and thus involve atoms in a particular solid material or molecular form. The cross-sections σ_{abs} are calculated for single isolated atoms. The latter have the benefit that they include separately identifiable contributions of the various atomic subshells,[4] as seen here in Figure 1.8(d).

While Figure 1.8(b) and (d) are macroscopic and microscopic manifestations of the same physical processes, some differences are notable. At low photon energies solid state effects in the metallic copper foil [Figure 1.8(b)] are important, and as a result the sharp 3d edge of the isolated copper atom [Figure 1.8(d)] just above 10 eV is not observed. Such data are of great interest to atomic and solid state researchers. Examples of the measured and calculated curves are given in Appendix C. A variety of techniques are employed to study atomic positions within solids and on surfaces, based on details of the absorption and emission processes in the presence of near-neighbor atoms. Examples of the literature are given in Refs. 11–17.

1.3 ATOMIC ENERGY LEVELS AND ALLOWED TRANSITIONS

The modern understanding of atomic energy levels, and allowed transitions between these levels, began with the Bohr–Rutherford model of the atom[5, 6] consisting of a small positive nucleus of charge $+Ze$, surrounded by electrons of charge $-e$ orbiting at relatively large radii, of order 1 Å. Based on Rutherford's experiments (1911) with the scattering of α-particles,[‖] which demonstrated the existence of a very small nucleus of positive charge, Planck's concept (1900) of radiation from quantized oscillators, and extensive spectroscopic data showing that atoms emit characteristic narrow lines with frequencies (or wavelengths) in specific numerical sequences, Bohr (1913) proposed the first partially successful quantum model of the atom. By equating the Coulomb force due to the positive nucleus, $Ze^2/4\pi\epsilon_0 r^2$, to the centripetal force mv^2/r for quantized circular orbits of angular momentum $mvr = n\hbar$ ($n = 1, 2, 3, \ldots$), Bohr found stationary electron orbits, for the single electron atom, of energy E_n and radius r_n, where

$$E_n = -\frac{mZ^2e^4}{32\pi^2\epsilon_0^2\hbar^2}\frac{1}{n^2} \tag{1.4}$$

and

$$r_n = \frac{4\pi\epsilon_0\hbar^2}{mZe^2}\cdot n^2 \tag{1.5}$$

where e and m are the electron charge and mass, respectively, Ze is the nuclear charge, ϵ_0 is the permittivity of free space, and $\hbar$ is Planck's constant divided by 2π.

[‖] The α-particle derives its name from early studies of the radioactive decay of heavy elements. It consists of two protons and two neutrons, but no electrons, and thus is essentially a bare helium nucleus, ^{4}He. As a radioactive decay product it is typically emitted with an energy of 5–9 MeV (Ref. 4). The other particles observed through trajectory variations in a magnetic field were β-particles (electrons, opposite curvature of trajectory to α-particles) and γ-rays (photons, no deflection).

The Bohr model, despite continuous acceleration of the electron, permits radiation only when the electron makes a transition from one stationary state (n_i) to another (n_f), with characteristic energies

$$\hbar\omega = E_i - E_f = \frac{mZ^2e^4}{32\pi^2\epsilon_0^2\hbar^2}\left(\frac{1}{n_f^2} - \frac{1}{n_i^2}\right) \tag{1.6}$$

– characteristic in that there is a Z^2 dependence specific to the particular element radiating, and because of the numerical sequence involving the possible combinations of n_i and n_f. The constant $me^4/32\pi^2\epsilon_0^2\hbar^2 = hcR_\infty = 13.606$ eV, known historically as the Rydberg constant from earlier studies of hydrogen spectra, gives the ionization potential** of the ground state ($n_i = 1,\ n_f = \infty$) of the hydrogen atom ($Z = 1$). The value of the first Bohr radius of the hydrogen atom, $r_1 \equiv a_0$, is a common scale of atomic radii; from Eq. (1.5)

$$a_0 = \frac{4\pi\epsilon_0\hbar^2}{me^2} = 0.529\ \text{Å} \tag{1.7}$$

In terms of the Rydberg constant and first Bohr radius, the characteristic emission lines of a single electron atom of nuclear charge Z are

$$\hbar\omega = (13.606\ \text{eV})Z^2\left(\frac{1}{n_f^2} - \frac{1}{n_i^2}\right) \tag{1.8}$$

and the radii are

$$r_n = \frac{a_0 n^2}{Z} \tag{1.9}$$

A great success of the Bohr model was its ability to accurately match the well-known optical spectra of hydrogen, known as the Balmer series (1885), corresponding to $n_f = 2$ and $n_i = 3, 4, 5, \ldots$, and also to give an accurate theoretical value for the experimentally known (1890) Rydberg constant. This was soon extended to the then unknown Lyman series, largely in the ultraviolet, with $n_f = 1,\ n_i = 2, 3, 4, \ldots$; the Paschen series with $n_f = 3$, $n_i = 4, 5, 6, \ldots$; the Brackett and Pfund series with $n_f = 4$ and $n = 5$, respectively, both in the infrared. Sommerfeld (1916) extended the success of the Bohr atom by introducing elliptical orbits and a second, azimuthal quantum number characterizing the ellipticity of the orbits. Additionally, taking account of the relativistic nature of the electron motion ($v/c \sim 10^{-2}$ in the hydrogen atom), Sommerfeld showed that quantized elliptical orbits introduce energetic fine structure in the spectra, as was observed experimentally.

**The energy required to remove an electron from an atom.

These successes, however, raised questions about the model and the very nature of the physics. Among the specifics, not all predicted emission lines were observed, suggesting that among the possible quantum states, only some transitions were permitted. Indeed, the model said nothing regarding transition rates or line intensities. More generally, the model was perplexing in that it was based on continuous electron acceleration within the permitted orbits, but without radiation and thus loss of energy – clearly in conflict with classical radiation physics. Collectively, elements contributing to the above model are now known as "the old quantum theory." Following a decade of intense creativity,[††] in the period from 1925 to 1930, Schrödinger, Heisenberg, Dirac and others developed a new quantum theory based on wave mechanics, in which the particles are described in terms of a probabilistic wave function $\Psi(\mathbf{r}, t)$. In combination with the introduction of electron spin, the new quantum mechanics provides a procedure for accurately predicting and matching experimental observations regarding properties of the atoms.

The quantum mechanical description[5, 6, 23–26] of a particle's motion is in terms of a wave function $\Psi(\mathbf{r}, t)$, which obeys Schrödinger's wave equation

$$-\frac{\hbar^2}{2m}\nabla^2\Psi(\mathbf{r}, t) + V(\mathbf{r}, t)\Psi(\mathbf{r}, t) = i\hbar\frac{\partial\Psi(\mathbf{r}, t)}{\partial t} \tag{1.10}$$

where m is the particle mass, $V(\mathbf{r})$ is the potential energy, and ∇ is the vector gradient. Particle energy and momentum are associated with the operators

$$E \rightarrow i\hbar\frac{\partial}{\partial t} \tag{1.11}$$

and

$$\mathbf{p} \rightarrow -i\hbar\nabla \tag{1.12}$$

respectively. In wave mechanics, the probability of finding a particle within coordinates $d\mathbf{r}$ is

$$P(\mathbf{r}, t)d\mathbf{r} = \Psi^*(\mathbf{r}, t)\,\Psi(\mathbf{r}, t)\,d\mathbf{r} \tag{1.13}$$

where Ψ^* is the complex conjugate of Ψ, and $d\mathbf{r}$ is shorthand notation for the scalar volume around the position $\mathbf{r}$, for instance $d\mathbf{r} = dx\,dy\,dz$ in rectangular coordinates. The function $\Psi(\mathbf{r}, t)$ is normalized to unity, so that

$$\iiint\limits_{\substack{\text{all}\\ \text{space}}} |\Psi(\mathbf{r}, t)|^2\,d\mathbf{r} = 1 \tag{1.14}$$

Furthermore, expectation values for quantities such as the position vector, energy, and momentum are given by integrals of the following form: For the expectation value of vector position,

$$\bar{\mathbf{r}} = \iiint \mathbf{r}P(\mathbf{r}, t)\,d\mathbf{r} = \iiint \Psi^*(\mathbf{r}, t)\mathbf{r}\,\Psi(\mathbf{r}, t)\,d\mathbf{r} \tag{1.15}$$

which is a probabilistic average position where the particle can be expected to be found at a

[††]For a review see the texts by Tipler (Ref. 6) and by Eisberg and Resnick (Ref. 5), for example.

time t. For the expectation value of energy,

$$\bar{E} = \iiint \Psi^*(\mathbf{r}, t)\, E\, \Psi(\mathbf{r}, t)\, d\mathbf{r} = i\hbar \iiint \Psi^*(\mathbf{r}, t)\, \frac{\partial \Psi(\mathbf{r}, t)}{\partial t}\, d\mathbf{r} \tag{1.16}$$

and for the expectation value of momentum,

$$\bar{\mathbf{p}} = \iiint \Psi^*(\mathbf{r}, t)\, \mathbf{p}(\mathbf{r}, t)\, \Psi(\mathbf{r}, t)\, d\mathbf{r} = -i\hbar \iiint \Psi^*(\mathbf{r}, t)\, \nabla \Psi(\mathbf{r}, t)\, d\mathbf{r} \tag{1.17}$$

where Eqs. (1.11) and (1.12) have been used.

Solution of Schrödinger's equation for the one-electron atom assumes a time dependence

$$\Psi(\mathbf{r}, t) = \Psi(\mathbf{r}) e^{-iEt/\hbar} \tag{1.18}$$

in a Coulomb potential

$$V(\mathbf{r}) = \frac{-Ze^2}{4\pi\epsilon_0 r} \tag{1.19}$$

with separable functions in spherical coordinates

$$\Psi(\mathbf{r}) = \Psi(r, \theta, \phi) = R(r)\Theta(\theta)\Phi(\phi) \tag{1.20}$$

where θ is measured from the z-axis. Requiring that these functions be finite, continuous, singlevalued and normalizable introduces three quantum numbers, $n,\ l$, and m_l, one for each coordinate. For negative energy these correspond to bound electrons in orbits of discrete, quantized energy. For positive energy the states are continuous and the electron is free. Here n is the principal quantum number, associated with the radial coordinate, and having allowed integer values $n = 1, 2, 3, \ldots$ The orbital quantum number l associated with the θ-coordinate is related to the angular momentum by $L = \sqrt{l(l+1)}\hbar$, and is constrained to the integer values $l = 0, 1, 2, \ldots, n-1$. The magnetic quantum number m_l, associated with continuity of the wave function in the angle ϕ, is related to the z-component of angular momentum by $L_z = m_l\hbar$, and is constrained to the integer values $m_l = -l,\ -l+1, \ldots, 0, 1, \ldots, l$.

The quantum mechanical description is completed with the introduction of a fourth quantum number, m_s, associated with the intrinsic electron angular momentum or spin, s. With s having a value of $\frac{1}{2}$, the quantum number m_s can have values of $\pm\frac{1}{2}$. This admits the Pauli exclusion principle, that no two electrons can have an identical set of quantum numbers. Electron spin additionally allows a spin–orbit coupling that energetically matches the fine structure observed in emission lines.

The enumerated constraints on allowable quantum numbers $n,\ l,\ m_l$, and m_s, along with the exclusion principle, dictate limits on the number of electrons in each shell. For instance, the first shell, with $n = 1$, can hold only two electrons, with quantum numbers $l = 0,\ m_l = 0,\ m_s = \pm\frac{1}{2}$. The second shell, with $n = 2$, can hold eight electrons, two in the $l = 0$ subshell, and six in the $l = 1$ subshell, with $m_l = 0,\ \pm1$ and $m_s = \pm\frac{1}{2}$. The third shell, with $n = 3$, can hold 18, with quantum number combinations $l = 0,\ m_l = 0,\ m_s = \pm\frac{1}{2}$; $l = 1,\ m_l = 0,\ \pm1$, and $m_s = \pm\frac{1}{2}$; and $l = 2,\ m_l = 0,\ \pm1,\ \pm2$, and $m_s = \pm\frac{1}{2}$; etc. In spectroscopic notation the electron configuration according to n and l, for an atom such as argon ($Z = 18$), would be written as $1s^2\ 2s^2\ 2p^6\ 3s^2\ 3p^6$, where s refers to an $l = 0$ subshell and p refers to $l = 1$ (d refers to $l = 2$, f refers to $l = 3$, etc.), and where the historical use of s predates the later use of s for spin.

With the constraints on the quantum numbers $n,\ l,\ m_l$, the Schrödinger equation provides a set of wavefunctions, Ψ_{n,l,m_l}, with which to describe the atom. For instance, the probability

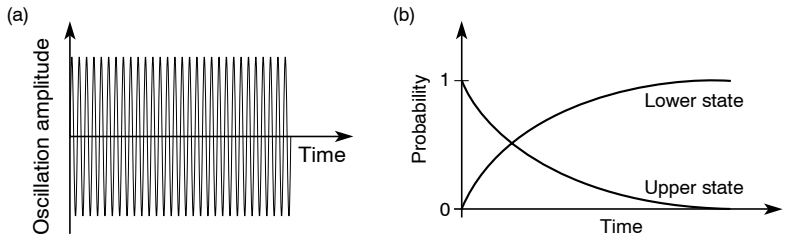

FIGURE 1.9. (a) Radiative decay from an upper state Ψ_i to a lower state Ψ_f involves a mixed atomic state in which the atom oscillates between the two at a frequency $\omega_{if} = (E_i - E_f)/\hbar$, (b) with the probability of finding the atom in the upper state slowly decaying to zero in a transition lifetime equal to many millions of cycles. (Following Liboff[31].)

of finding an electron within coordinates $d\mathbf{r}$ at a vector position $\mathbf{r}$, in a state described by Ψ_{n,l,m_l}, is given by Eq. (1.13) to be $|\Psi_{n,l,m_l}|^2\, d\mathbf{r}$. The expectation value of vector coordinates for this particular state ("orbit") of the atom is given by Eq. (1.15) to be

$$\bar{\mathbf{r}}_{n,l,m_l} = \iiint \Psi^*_{n,l,m_l}\, \mathbf{r}\, \Psi_{n,l,m_l}\, d\mathbf{r}$$

That is, the coordinates are only known probabilistically, in contrast with the Bohr model, where there were well-defined orbital coordinates. Interestingly, for the hydrogen atom, the expectation values of energy are equal to those of the Bohr atom [Eq. (1.4)], with a correction due to spin–orbit coupling. The explicit coordinate dependence of the hydrogen atom wavefunctions, and their energies including spin–orbit fine structure, are described in the literature.[5, 27, 28]

The probability of a transition between two stationary states of the atom, which we abbreviate here as Ψ_i and Ψ_f for initial and final states, is proportional to the square of the quantum mechanical dipole matrix element[29–31]

$$-e\bar{\mathbf{r}}_{if} = -e \int \Psi^*_i \mathbf{r} \Psi_f\, d\mathbf{r} \tag{1.21}$$

During a transition from the higher energy stationary state Ψ_i to the lower energy stationary state Ψ_f, the average position of the electron oscillates between the two states at a frequency equal to the difference in energies $\omega_{if} = (E_i - E_f)/\hbar$, as shown in Figure 1.9. Quantum mechanically the atom is in a mixed state in which the probability of finding the atom in the upper state gradually diminishes from unity to zero, while the probability of finding it in the lower state increases during this same transition period, or *lifetime*, from zero to unity. During the transition period the electron typically executes millions of oscillations. This provides a quantum mechanical description of the spontaneous emission of radiation that occurs after an atom is excited to a higher energy level by photoabsorption (the inverse process) or collision with an electron. The line width of the resultant emission depends on the time duration (lifetime) of the transition, as the latter affects the number of oscillations corresponding to the emitted photon or wavetrain. The longer the wavetrain, the better defined the wavelength and hence the narrower the line width.

The transition probability depends on the integral matrix element given by Eq. (1.21). The integral has a classical counterpart[23] in the current density $\mathbf{J} = -en\mathbf{v}$, whose time derivative is used to calculate radiation in Maxwell's equations, a subject we return to in Chapter 2. Here the particle *density* is given by $\Psi^*\Psi$, the charge density by $-e\Psi^*\Psi$, and the velocity $\mathbf{v}$ by $d\mathbf{r}/dt \rightarrow -i\omega_{if}\mathbf{r}$, so that a time derivative of the classical current is analogous to that of the

quantum mechanical *dipole moment* as given in Eq. (1.21). Transitions from an initial state Ψ_i to a final state Ψ_f occur quantum mechanically when the two wave functions yield a finite oscillation amplitude $\bar{\mathbf{r}}(t)$ as given by the matrix element in Eq. (1.21). If the wavefunctions $\Psi_i,\ \Psi_f$ are such that the integral is zero, there is no oscillation leading to a transition, and the transition is said to be *not allowed*. Examining the integral, one notes that $\mathbf{r}$ is an odd function of the coordinates (replacing r by $-r$ changes the sign of the integrand), requiring that the initial and final wavefunctions be of opposite parity (one even, one odd in the coordinates of integration) for a non-zero integral. The parity of the wavefunctions is found to alternate with increasing quantum number l, leading to *selection rules* for allowed transitions in the hydrogen or single electron atom[5, 6, 23–31]:

$$\Delta l = \pm 1 \tag{1.22}$$

Furthermore, the total angular momentum quantum number, j, determined by the vector sum of orbital and spin angular momentum, must satisfy

$$\Delta j = 0,\ \pm 1 \tag{1.23}$$

where j can take the values $l + s,\ l - s$, or s when $l = 0$. The special case of a transition between $j = 0$ states is not allowed. Note that in order to conserve angular momentum in the allowed transitions, the emitted photon must carry away a quantum ($\hbar$) of angular momentum.[5, 29] These allowed transitions lead to the strong characteristic spectral emission lines observed experimentally. Furthermore, the atomic transition probabilities[23, 29, 30] between any two states can be computed on the basis of matrix elements of the form given in Eq. (1.21).

Selection rules for transitions involving multi-electron atoms follow similar rules when the quantum numbers are assigned to a core level vacancy, as occurs in the photoemission process described earlier in Figure 1.2. Figures 1.10 and 1.11 illustrate the energy levels and several prominent transitions for the multi-electron atom. Figure 1.10 introduces the x-ray nomenclature[22] wherein the $n = 1$ state is referred to as the K-shell, $n = 2$ as the L-shell, $n = 3$ as the M-shell, etc. Emission lines terminating in the ground state ($n = 1$) are referred to as K-shell emissions, shown here as K_α, K_β, etc. The energy required to lift a K-shell electron to a free state of zero binding energy is referred to as the K-absorption edge $E_{K,abs}$. Excess energy beyond this value goes to kinetic energy of the liberated electron. Similar notation is shown for the L-shell emissions.

Figure 1.10 is useful for an introduction. It is simplified, however, in that it does not show shell substructure, and that it implies a systematic labeling of sequential emission lines within a given series by ordered Greek subscripts α, β, etc. In fact the lines have historical designations of limited value today. Figure 1.11 shows a more accurate version[28] of the energy levels and some well-known transitions (on a logarithmic scale) for the copper atom ($Z = 29$). Values of the quantum numbers $n,\ l$, and total angular momentum j are given for each subshell, along with the subshell designations and spectroscopic notation. Specific values of the various energy levels and a few well-known transition energies are given for the specific example of a copper atom. Note the substantial energy fine structure due to spin–orbit coupling in the various angular momentum states.[5, 27, 28] Note also that the 29 copper electrons are written in spectroscopic notation as $1s^2\ 2s^2\ 2p^6\ 3s^2\ 3p^6\ 3d^{10}\ 4s^1$, thus consisting of closed K-, L-, and M-shells, plus a single valance or conduction electron. Tabulated values of binding energies[1] and prominent emission lines[2] for elements through uranium ($Z = 92$) are given in Appendix B.

Of great interest to us in later chapters is the spatial distribution of charge in multi-electron atoms, as we will be calculating the scattering of electromagnetic radiation and are interested in the appropriateness of assuming that the wavelength λ is large compared to atomic

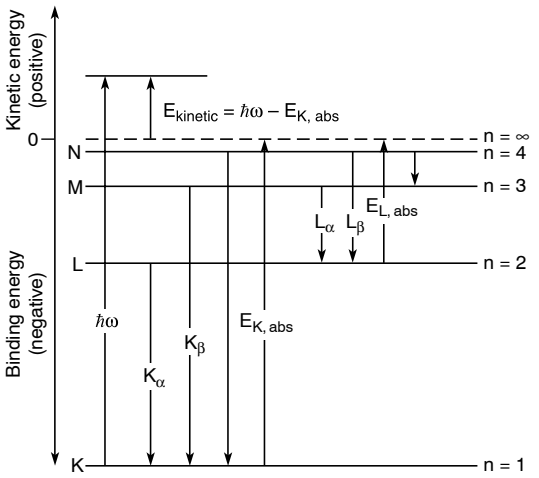

FIGURE 1.10. Energy levels for a multi-electron atom, showing the K-shell ($n = 1$), L-shell ($n = 2$), M-shell ($n = 3$), and N-shell ($n = 4$), with transitions that provide characteristic narrow line emission at well-defined photon energies. Examples shown include K_α ($n = 2$ to $n = 1$), K_β ($n = 3$ to $n = 1$), L_α ($n = 3$ to $n = 2$), etc. Also shown are the absorbtion edge energies, such as $E_{K,abs}$, the energy required to take an electron from the K-shell ($n = 1$) to the continuum limit ($n = \infty$). For an incident photon of energy $\hbar\omega > E_{K,abs}$, a K-shell electron can be lifted beyond the continuum limit to a state of positive kinetic energy, as shown. An L-shell electron would acquire a greater kinetic energy. The binding energies are not drawn to scale. Subscript labeling of the emission lines is less systematic than implied here, as discussed in the text. (Following Compton and Allison.[22])

radii for extreme ultraviolet and soft x-ray radiation. Toward that end, the probabilistic radial charge distribution density for filled quantum states of the argon atom ($1s^2\ 2s^2\ 2p^6\ 3s^2\ 3p^6$) is shown in Figure 1.12. Due to the strong nuclear attraction ($Z = 18$), the K-shell electrons (1s; $n = 1,\ l = 0$) are pulled into a region of small radius, with highest probable radial coordinate much smaller than the hydrogenic Bohr radius a_0. The 2s and 2p L-shells ($n = 2,\ l = 0$ and $n = 2,\ l = 1$, respectively) have their charge distribution largely within a radius less than a_0, while only the M-shell 3s and 3p have significant probability of being located in the radial interval from a_0 to $3a_0$. Thus in EUV and soft-x-ray scattering calculations, with wavelengths of order 1 nm or longer (about $20a_0$), a reasonable approximation is that all electrons see approximately the same phase and scatter collectively (in phase) in all directions. This approximation cannot be made for shorter x-ray wavelengths where $\lambda \sim a_0$, at least not for the outer valence levels. Note that the valence electrons at radii beyond a_0 are those responsible for chemical bonding, and to first order set the apparent size of an atom, as in a molecule, crystal, or other solid.[32] This compact binding of the inner electrons explains the relatively small variation of volume occupied by atoms of widely different atomic number (Z) in solids and molecules: in the higher Z elements the additional electrons are largely confined to tight orbits nearer to the highly charged nucleus, with outer *valence* electrons having radial charge distributions, or equivalent mean radii, not too different from their lower Z cousins. For instance, in diamond the carbon atoms are separated by only 1.5 Å. For comparison, the hydrogen $n = 1$ mean diameter ($2a_0$) is 1.1 Å. For the face-centered cubic silicon crystal ($Z = 14$), adjacent silicon nuclei are separated by about 2.4 Å, and for common salt (NaCl) the separation distance between closest Na and Cl nuclei is about 2.8 Å.[27, 32] Indeed, for gold ($Z = 79$) with an atomic mass of 197 and a mass density of 19.3 g/cm^3, the atom to

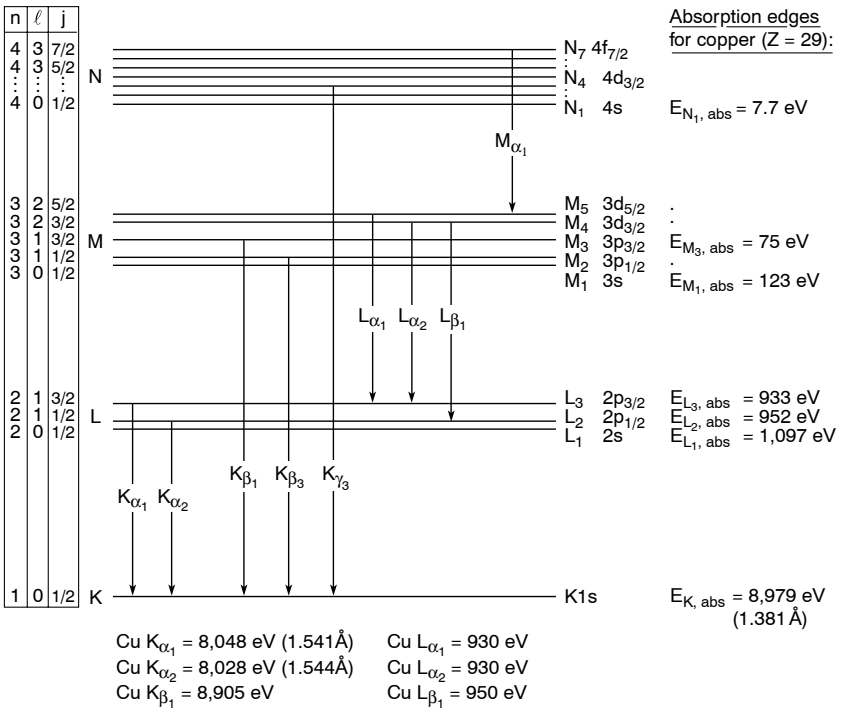

FIGURE 1.11. Energy level diagram for copper ($Z = 29$) showing transitions allowed by the selection rules $\Delta l = \pm 1$ and $\Delta j = 0, \pm 1$, where n is the principal quantum number, l is the quantum number for orbital angular momentum, and j is the quantum number for total angular momentum (orbital plus spin). In x-ray notation the K-shell corresponds to $n = 1$, the L-shell to $n = 2$, etc. Absorption edge nomenclature is shown to the right. Following spectroscopic notation, angular momentum quantum numbers $l = 0, 1, 2, 3$ are represented by the letters s, p, d, and f, respectively. Sample energies (and wavelengths) are shown for various absorption edges and allowed transitions. Note that the energy levels are not to scale, but are approximately logarithmic.

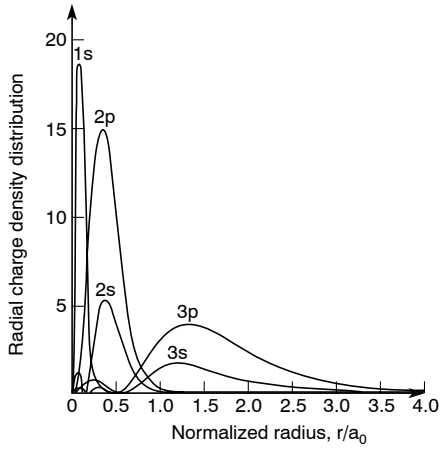

FIGURE 1.12. The probabilistic radial distribution of charge density in the argon atom, in units of electrons per unit radius ($e/\text{Å}$), as a function of normalized radius r/a_0, where a_0 is the Bohr radius as given in Eq. (7). This is essentially the probability of finding an electron in the region between two concentric spheres of radius r and $r + \Delta r$. Probabilities are shown for the 1s K-shell ($n = 1,\ l = 0$), the 2s and 2p L-shells ($n = 2,\ l = 0$ and $n = 2,\ l = 1$), and the 3s and 3p M-shells. Note that much of the electronic charge is pulled close to the high Z nucleus. (From *Quantum Physics of Atoms, Molecules, Solids, Nuclei, and Particles*, 2nd ed., by R. Eisberg and R. Resnick[5]; reprinted by permission of John Wiley & Sons, Inc.)

TABLE 1.2. Key to the periodic table of the elements. See back inside cover of book for full periodic table.

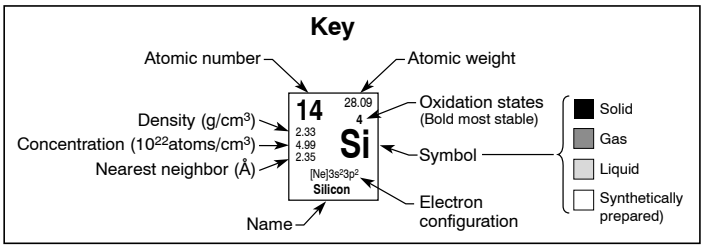

References: International Tables for X-ray Crystallography (Ref. 44) and J.R. De Laeter and K.G. Heumann (Ref. 46, 1991).

atom separation is only 2.9 Å. There is strikingly little difference in the separation distances between gold, or other high Z atoms, and low Z atoms in their natural states.

A periodic table of the elements, including atomic number, atomic mass, common mass density, atomic density, atomic separation distance, and spectroscopic notation of electron structure, can be found on the inside of the back cover. The key to the periodic table of the elements is given in Table 1.2. The atomic density is obtained from the relation $n_a = \rho N_A/A$, where ρ is the mass density, N_A is Avogadro's number (see Appendix A), and A is the atomic weight of the atom, as given in the periodic chart, expressed in atomic mass units (amu).

1.4 SCATTERING, DIFFRACTION, AND REFRACTION OF ELECTROMAGNETIC RADIATION

This text assumes a familiarity with Maxwell's equations, which describe the propagation of electromagnetic radiation. A wide range of literature is available that discusses the development of these equations.[33–38] In Chapters 2, 3, 4, 8, and 9 we will consider various aspects of wave propagation, scattering, diffraction, and refraction of radiation, with particular emphasis on application to the soft x-ray and extreme ultraviolet regions of the spectrum. In general we will use these words in the following senses.

Scattering is a process by which incident radiation[‡‡] is redirected over a very wide angular pattern, perhaps even 4π sr, generally by disordered systems or rough surfaces, as shown in Figure 1.13(a) and (b). The angular pattern of scattering is related to the spatial periodicities of the scattering object through the Fourier transform of their charge density correlation function. A point particle, for example, scatters radiation equally in all directions. The subject of scattering from free and bound electrons is discussed in Chapter 2. The term "scattering" is used in the same sense when discussing particles, as when high energy electrons are scattered by individual nuclei.

Diffraction is generally used to describe the process whereby incident radiation is redirected into relatively well-defined directions by ordered arrays of scatterers. The diffraction patterns result from positive interference in certain directions. Examples include the diffraction of x-rays by a crystal in which the position of the atoms, in a periodic array, provide well-defined planes from which the radiation appears to reflect at well-defined angles, as

[‡‡]In this section we use "incident radiation" to mean nearly monochromatic radiation propagating in a well-defined direction.

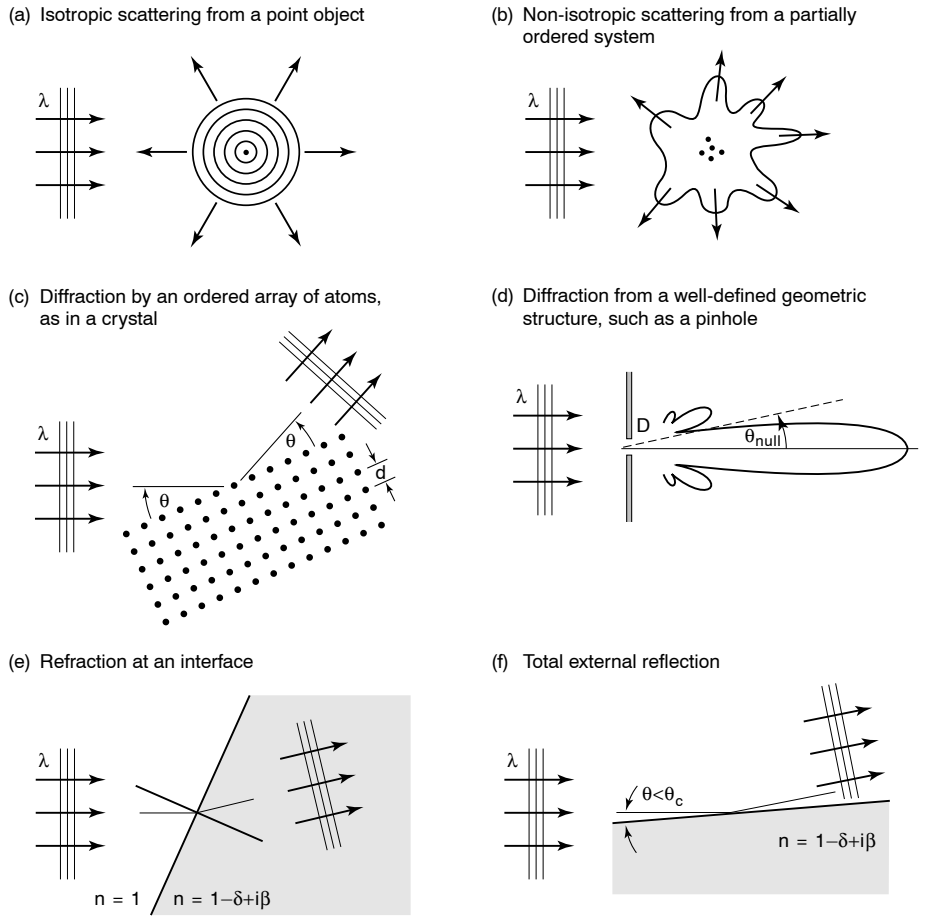

FIGURE 1.13. Scattering, diffraction, and refraction of electromagnetic radiation.

described by Bragg's law (1913) [see Chapter 4]:[22, 27, 28, 32, 41, 42]

$$m\lambda = 2d \sin\theta \tag{1.24}$$

where d is the spatial periodicity, λ is the wavelength, m is an integer, and θ is measured from the reflecting plane, as shown in Figure 1.13(c). In fact, the atomic positions in a crystal always describe many such planes, so that diffraction (positive interference) occurs in several directions. While the diffraction of x-rays by crystals is not discussed further in this text, diffraction from one-dimensional ordered systems, known in the EUV and soft-x-ray community as multilayer mirrors, is described in Chapter 4. These structures may be amorphous or partially ordered within the individual layers but well ordered in the stack direction, leading to very strong positive interference in directions described by the Bragg condition, Eq. (24). This leads to very high reflectance for appropriate choices of material, wavelength (photon energy), and angle. Readers interested in the important subject of x-ray diffraction by crystals are referred to Refs. 27, 28, 32, and 41–43.

"Diffraction" is also used to describe the situation in which incident radiation is redirected in some well-defined pattern, as when visible light or shorter wavelength radiation is diffracted by a small circular aperture (a pinhole), causing a divergence of the radiation with bright and dark angular interference rings, as shown in Figure 1.13(d). This is known as an Airy pattern (1835); the first dark null in the diffraction pattern occurs at a half angle (see Chapter 9, Section 9.3)

$$\theta_{\text{null}} = \frac{1.22\lambda}{d} \tag{1.25}$$

where θ is measured from the axis of symmetry through the center of the pinhole, and d is the pinhole diameter. Similar characteristic angular patterns occur when radiation is diffracted from other well-defined objects, such as a knife edge or a sphere.

Finally, *refraction* is the turning of radiation at an interface of materials of dissimilar refractive index n, generally written in the EUV/soft x-ray region as[‡‡]

$$n = 1 - \delta + i\beta \tag{1.26}$$

where in this spectral region both δ and β are generally small compared to unity, as is discussed in Chapter 3. Refractive turning at an interface occurs as the incident wave excites radiation among atoms at the surface of the second material. This launches a new wave through interference of radiation from the various atoms, in a manner that ensures continuity of the field quantities at the boundary. The process is sketched in Figure 1.13(e). Finally, Figure 1.13(f) shows an example of reflection peculiar to this spectral region. With a refractive index less than unity it is possible to have *total external reflection* in which most of the incident energy is redirected by the surface. There is little absorption even in the case of an otherwise absorptive material ($\beta \leq \delta$). Total external reflection occurs as long as the glancing angle of incidence θ is less than a critical angle $\theta_c \simeq \sqrt{2\delta}$, as described[22] first by Compton in 1922. This subject is described further in Chapter 3.

The development of electromagnetic theory with special emphasis on the application to EUV and soft x-ray wavelengths, based on Maxwell's equations, begins in Chapter 2. The wave equation in vacuum is obtained, Poynting's theorem and expressions for radiated power are developed, and scattering cross-sections are introduced. The cross-sections for scattering

[‡‡]The choice of $\pm i\beta$ in Eq. (1.26) depends on the mathematical form by which waves are represented, and must be consistent with wave decay in the presence of absorption. Early x-ray workers such as Compton[22] employed a plane wave representation equivalent to $\exp[i(\omega t - kr)]$, where ω is the radian frequency, $k = 2\pi/\lambda$, and the refractive index n is defined by the dispersion relation $\omega = kc/n$, or equivalently $f\lambda = c/n$. Written in this form, n has a *negative* imaginary component in the presence of absorption; thus for x-rays $n = 1 - \delta - i\beta$. This form continues to dominate common usage in the x-ray community. However, in the broader community of modern electrodynamics and optical sciences (Sommerfeld,[39] Born and Wolf,[37] Fowles,[40] Jackson,[36] and Spiller[45]) plane wave representations are more commonly written in the form $\exp[-i(\omega t - kr)]$, where the imaginary component of refractive index is *positive* in the presence of absorption, as in Eq. (1.26). For this text the more modern approach has been adopted; however, its adaptation to the older one should cause the reader little inconvenience. Algebraic demonstration of the above is given in Chapter 3, Section 3.2.

of radiation by free and bound electrons are obtained. These results are extended to scattering by multi-electron atoms and to atomic scattering factors, within certain approximations generally applicable in the EUV and soft x-ray regions of the spectrum.

In Chapter 3 Maxwell's equations are applied to the propagation of short wavelength radiation in a medium of uniform density, developing expressions for the complex refractive index, phase variation, and attenuation. Also discussed are reflection and refraction at arbitrary angle of incidence, total external reflectance and normal incidence reflection as special cases, Brewster's angle, and topics such as the Kramers–Kronig relations among the real and imaginary parts of the atomic scattering factors.

In Chapter 4 the subject of multilayer interference coatings is discussed, with applications to a variety of activities, including multilayer curved mirrors for focusing EUV, soft x-ray, and x-ray radiation. The applications discussed in Chapter 4 include photoemission microscopy, polarization control, astronomy, plasma diagnostics, and industrial lithography.

In Chapters 8 and 9 the topics of coherence and diffraction are discussed. In Chapter 9 the use of Fresnel zone plates as diffractive lenses is discussed, with application to soft x-ray microscopy at high spatial resolution – well beyond that of visible light microscopy – in the physical and life sciences.

REFERENCES

1. A compilation by G.P. Williams of Brookhaven National Laboratory, "Electron Binding Energies," in *X-Ray Data Booklet* (Lawrence Berkeley National Laboratory Pub-490 Rev.2, 1999), based largely on values given by J.A. Bearden and A.F. Barr, "Reevaluation of X-Ray Atomic Energy Levels," *Rev. Mod. Phys. 39*, 125 (1967); M. Cardona and L. Ley, Editors, *Photoemission in Solids I: General Principles* (Springer, Berlin, 1978); and J.C. Fuggle and N. Mårtensson, "Core-Level Binding Energies in Metals," *J. Electron. Spectrosc. Relat. Phenom. 21*, 275 (1980).
2. A compliation by J.B. Kortright, "Characteristic X-Ray Energies," in *X-Ray Data Booklet* (Lawrence Berkeley National Laboratory Pub. 490 Rev. 2, 1999), based on values given by J.A. Bearden, "X-Ray Wavelengths," *Rev. Mod. Phys. 39*, 78 (1967).
3. B.L. Henke, E.M. Gullikson, and J.C. Davis, "X-Ray Interactions: Photoabsorption, Scattering, Transmission, and Reflection at $E = 50$–$30{,}000$ eV, $Z = 1$–92," *Atomic Data and Nucl. Data Tables 54*, 181 (1993). Current updates maintained by E.M. Gullikson at http://www-cxro.lbl.gov/
4. J.-J. Yeh and I. Lindau, "Atomic Subshell Photoionization Cross Sections and Asymmetry Parameters: $1 \leq Z \leq 103$," *Atomic Data and Nucl. Data Tables 32*, 1–155 (1985); J.-J. Yeh, *Atomic Calculation of Photoionization Cross-Sections and Asymmetry Parameters* (Gordon and Breach, Langhorne, PA, 1993); I. Lindau, "Photoemission Cross Sections," Chapter 1, p. 3, in *Synchrotron Radiation Research: Advances in Surface and Interface Science*, Vol. 2 (Plenum, New York, 1992), R.Z. Bachrach, Editor.
5. R. Eisberg and R. Resnick, *Quantum Physics of Atoms, Molecules, Solids, Nuclei, and Particles* (Wiley, New York, 1985), Second Edition.
6. P.A. Tipler, *Modern Physics* (Worth, New York, 1978).
7. Numerical values of fundamental physical constants are obtained from E.R. Cohen and B.N. Taylor, "The Fundamental Physical Constants," *Phys. Today*, p. BG9 (August 1995).
8. Use of metric units (SI) follows R.A. Nelson, "Guide for Metric Practice," *Phys. Today*, p. BG15 (August 1995).
9. M.O. Krause, "Atomic Radiative and Radiationless Yields for K and L Shells," *J. Phys. Chem. Ref. Data 8*, 307 (1979); M.O. Krause and J.H. Oliver, "Natural Widths of Atomic K and L Levels, K_α X-Ray Lines and Several KLL Auger Lines," *J. Phys. Chem. Ref. Data 8*, 329 (1979); M.O. Krause, "Average L-Shell Fluorescence, Auger, and Electron Yields," *Phys. Rev. A 22*, 1958 (1980).
10. J.F. Moulder, W.F. Stickle, P.E. Sobol, and K.D. Bomben, *Handbook of X-Ray Photoelectron Spectroscopy* (Physical Electronics, Eden Prairie, MN, 1995).

11. D.E. Eastman and F.J. Himpsel, "Ultraviolet Radiation – An Incisive and Versatile Tool," *Physics Today*, p. 64 (May 1981).
12. C.S. Fadley, "Basic Concepts of X-Ray Photoelectron Spectroscopy," pp. 1–156 in *Electron Spectroscopy, Theory, Techniques and Applications* (Pergamon Press, Oxford, 1978), C.R. Brundle and A.D. Baker, Editors; C.S. Fadley et al., "Surface, Interface and Nanostructure Characterization with Photoelectron Diffraction and Photoelectron and X-ray Holography," *J. Surface Anal. 3*, 334 (1997); C.S. Fadley and P.M. Len, "Holography with X-rays," *Nature 380*, 27 (1996); A. Kay, E. Arenholz, S. Mun, F.J. Garcia de Abajo, C.S. Fadley, R. Denecke, Z. Hussain, and M.A. Van Hove, "Multiatom Resonant Photoemission: A Method for Determining Near-Neighbor Atomic Identities and Bonding," *Science 281*, 679 (1998); G. Faigel and M. Tegze, "X-ray Holography," *Rep. Progr. Phys. 62*, 355 (1999).
13. P.Y. Yu and M. Cardona, *Fundamentals of Semiconductors: Physics and Materials Properties* (Springer, Berlin, 1996), Chapter 8, "Photoelectron Spectroscopy."
14. S. Hüfner, *Photoelectron Spectoscopy: Principles and Application* (Springer, Berlin, 1996).
15. V. Schmidt, *Electron Spectroscopy of Atoms Using Synchrotron Radiation* (Cambridge Univ. Press, 1997).
16. W. Eberhardt, Editor, *Applications of Synchrotron Radiation: High Resolution Studies of Molecular Adsorbates on Surfaces* (Springer-Verlag, Berlin, 1995).
17. C.R. Brundle, C.A. Evans, and S. Wilson, *Encylopedia of Materials Characterization* (Butterworth-Heinemann, London, 1992); J. Stöhr, *NEXAFS Spectroscopy* (Springer-Verlag, Berlin, 1992).
18. D.R. Penn, "Electron Mean-Free-Path Calculations Using a Model Dielectric Function," *Phys. Rev. B 35*, 482 (1987).
19. M.P. Seah and W.A. Dench, "Quantitative Electron Spectroscopy of Surfaces: A Standard Data Base for Electron Inelastic Mean Free Paths in Solids," *Surface and Interface Anal. 1*, 2 (1979).
20. C.J. Powell, "Attenuation Lengths of Low-Energy Electrons in Solids," *Surface Sci. 44*, 29 (1974); C.J. Powell and M.P. Seah, "Precision, Accuracy, and Uncertainty in Quantitative Surface Analysis by Auger-Electron Spectroscopy and X-Ray Photoelectron Spectroscopy," *J. Vac. Sci. Technol. A 8*, 735 (March/April 1990).
21. For example, see data for Mo ($Z = 42$) in the *Handbuch der Physik: Röntgenstrahlen*, Encyclopedia of Physics: X-Rays, Vol. XXX, (Springer-Verlag, Berlin, 1957), S. Flügge, Editor, pp. 10, 338.
22. A.H. Compton and S.K. Allison, *X-Rays in Theory and Experiment* (Van Nostrand, New York, 1935), Second Edition.
23. L.I. Schiff, *Quantum Mechanics* (McGraw-Hill, New York, 1968), Third Edition.
24. A. Messiah, *Quantum Mechanics* (Wiley, New York, 1961).
25. J.L. Powell and B. Crasemann, *Quantum Mechanics* (Addison-Wesley, Reading, MA, 1961).
26. D.I. Blokhintsev, *Principles of Quantum Mechanics* (Allyn and Bacon, Boston, 1964).
27. R.B. Leighton, *Principles of Modern Physics* (McGraw-Hill, New York, 1959).
28. F.K. Richtmyer, E.H. Kennard, and T. Lauritsen, *Introduction to Modern Physics* (McGraw-Hill, New York, 1955).
29. A. Corney, *Atomic and Laser Spectroscopy* (Clarendon, Oxford, 1977).
30. R. Louden, *The Quantum Theory of Light* (Clarendon Press, Oxford, 1983), Second Edition.
31. R.L. Liboff, *Introductory Quantum Mechanics* (Addison-Wesley, Reading, MA, 1998), Third Edition, Section 10.7.
32. C. Kittel, *Introduction to Solid State Physics* (Wiley, New York, 1976), Fifth Edition.
33. G.S. Smith, *Classical Electromagnetic Radiation* (Cambridge Univ. Press, 1997).
34. J.A. Stratton, *Electromagnetic Theory* (McGraw-Hill, New York, 1941).
35. S. Ramo, J. Whinnery, and T. Van Duzer, *Fields and Waves in Communications Electronics* (Wiley, New York, 1984).
36. J.D. Jackson, *Classical Electrodynamics* (Wiley, New York, 1998), Third Edition.
37. M. Born and E. Wolf, *Principles of Optics* (Cambridge Univ. Press, New York, 1999), Seventh Edition.
38. E. Hecht, *Optics* (Addison-Wesley, Reading, MA, 1998), Third Edition.

39. A. Sommerfeld, *Optics* (Academic Press, New York, 1964); A. Sommerfeld, *Electrodynamics* (Academic Press, New York, 1964).
40. G.R. Fowles, *Introduction to Modern Optics* (Dover, New York, 1975), Second Edition.
41. R.W. James, *The Optical Principles of the Diffraction of X-Rays* (Ox Bow Press, Woodbridge, CT., 1982).
42. J. Helliwell, *Macromolecular Crystallography with Synchrotron Radiation* (Cambridge Univ. Press, New York, 1992); S.W. Lovesey and S.P. Collins, *X-ray Scattering and Absorption by Magnetic Materials* (Oxford Univ. Press, 1996); J.R. Helliwell and P.M. Rentzepis, Editors, *Time-Resolved Diffraction* (Oxford Univ. Press, 1997).
43. B.D. Cullity, *Elements of X-Ray Diffraction* (Addison-Wesley, Reading, MA, 1978), Second Edition.
44. *International Tables for X-Ray Crystallography, Vol. III*, International Union of Crystallography (Reidel, London, 1983), C.H. MacGillavry, G.D. Rieck, and K. Lonsdale, Editors.
45. E. Spiller, *Soft X-Ray Optics* (SPIE, Bellingham, WA, 1994).
46. J.R. DeLaeter and K.G. Heumann, "Atomic Weights of the Elements 1989," *J. Phys. Chem. Ref. Data 20*, 1313 (1991).

HOMEWORK PROBLEMS

Homework problems for each chapter will be found at the website:
http://www.coe.berkeley.edu/AST/sxreuv

Chapter 2

RADIATION AND SCATTERING AT EUV AND SOFT X-RAY WAVELENGTHS

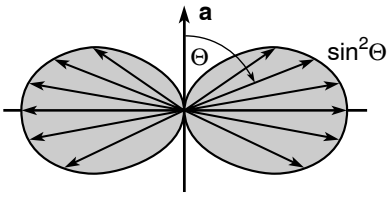

$$\frac{dP}{d\Omega} = \frac{e^2|\mathbf{a}|^2 \sin^2\Theta}{16\pi^2\epsilon_0 c^3} \tag{2.34}$$

$$r_e = \frac{e^2}{4\pi\epsilon_0 mc^2} \tag{2.44}$$

$$\sigma_e = \frac{8\pi}{3} r_e^2 \tag{2.45}$$

$$\sigma = \frac{8\pi}{3} r_e^2 \frac{\omega^4}{(\omega^2 - \omega_s^2)^2 + (\gamma\omega)^2} \tag{2.51}$$

$$f(\Delta\mathbf{k}, \omega) = \sum_{s=1}^{Z} \frac{\omega^2 e^{-i\Delta\mathbf{k}\cdot\Delta\mathbf{r}_s}}{\omega^2 - \omega_s^2 + i\gamma\omega} \tag{2.66}$$

$$f^0(\omega) = \sum_{s=1}^{Z} \frac{\omega^2}{\omega^2 - \omega_s^2 + i\gamma\omega} \tag{2.72}$$

In this chapter basics of electromagnetic theory are reviewed. Beginning with Maxwell's equations, the wave equation is developed and used to solve several problems of interest at short wavelengths. Poynting's theorem regarding the flow of electromagnetic energy is used to solve the power radiated by an accelerated electron. The concept of a scattering cross-section is introduced and applied to the scattering of radiation by free and bound electrons. A semiclassical model is used in the latter case. Scattering by a multi-electron atom is described in terms of a complex atomic scattering factor. Tabulated scattering factors, which are available in the literature for use in special circumstances, are described.

2.1 MAXWELL'S EQUATIONS AND THE WAVE EQUATION

In this chapter we will consider radiation and scattering by accelerated charges. We will use these results to study scattering cross-sections and interesting phenomena at visible, EUV, and

soft x-ray wavelengths. In later chapters we will examine their relation to the refractive index (propagation effects) and the properties of undulator radiation.

Our study begins with *Maxwell's equations*,[1–5] written in a form appropriate to the use of MKS units:*

$$\nabla \times \mathbf{H} = \frac{\partial \mathbf{D}}{\partial t} + \mathbf{J} \qquad \text{(Ampere's law)} \tag{2.1}$$

$$\nabla \times \mathbf{E} = -\frac{\partial \mathbf{B}}{\partial t} \qquad \text{(Faraday's law)} \tag{2.2}$$

$$\nabla \cdot \mathbf{B} = 0 \tag{2.3}$$

$$\nabla \cdot \mathbf{D} = \rho \qquad \text{(Coulomb's law)} \tag{2.4}$$

where **E** is the electric field vector, **H** is the magnetic field vector, **D** is the electric displacement, **B** is the magnetic density or magnetic induction, **J** is the current density, ρ is the charge density, ϵ_0 is the permittivity (dielectric constant) of free space, and μ_0 is the magnetic permeability. If the above are considered to describe fields in free space (vacuum), the constitutive relations take the form

$$\mathbf{D} = \epsilon_0 \mathbf{E} \tag{2.5}$$

$$\mathbf{B} = \mu_0 \mathbf{H} \tag{2.6}$$

where now the charge density ρ and current density **J** must be described in a self-consistent manner, i.e., where the fields affect the particles and the particles contribute to the fields. Note that, as is common in the literature, we have used ρ for both charge and mass density (Chapter 1). The reader will recognize the difference by the context.

As described by James Maxwell in 1865, these equations can be combined to form a vector wave equation describing the propagation of electromagnetic waves, as later demonstrated by Heinrich Hertz in 1888. The mathematical description covers electromagnetic phenomena extending from very long wavelengths, to radiowaves, microwaves, infrared, visible, ultraviolet, and x-rays and beyond. The *vector wave equation* can be obtained from Maxwell's equations by taking $\nabla \times$ [Eq. (2.2)] and using the vector identity† $\nabla \times \nabla \times \mathbf{A} = \nabla(\nabla \cdot \mathbf{A}) - \nabla^2 \mathbf{A}$ to obtain

$$\nabla \times (\nabla \times \mathbf{E}) = \nabla \times \left(-\frac{\partial \mathbf{B}}{\partial t} \right)$$

$$\nabla(\nabla \cdot \mathbf{E}) - \nabla^2 \mathbf{E} = -\mu_0 \frac{\partial}{\partial t}(\nabla \times \mathbf{H})$$

*See Appendix A, Units and Physical Constants.

†See Appendix D, Mathematical and Vector Relations.

$$\nabla\left(\frac{\rho}{\epsilon_0}\right) - \nabla^2\mathbf{E} = -\mu_0\frac{\partial}{\partial t}\left(\frac{\partial D}{\partial t} + \mathbf{J}\right)$$

$$\nabla\left(\frac{\rho}{\epsilon_0}\right) - \nabla^2\mathbf{E} = -\epsilon_0\mu_0\frac{\partial}{\partial t}\left(\frac{\partial \mathbf{E}}{\partial t} + \frac{\mathbf{J}}{\epsilon_0}\right)$$

Rearranging terms, we obtain

$$\epsilon_0\mu_0\frac{\partial^2\mathbf{E}}{\partial t^2} - \nabla^2\mathbf{E} = -\mu_0\frac{\partial \mathbf{J}}{\partial t} - \frac{1}{\epsilon_0}\nabla\rho$$

which when properly grouped is recognized as the vector wave equation:

$$\left(\frac{\partial^2}{\partial t^2} - c^2\nabla^2\right)\mathbf{E}(\mathbf{r}, t) = -\frac{1}{\epsilon_0}\left[\frac{\partial \mathbf{J}(\mathbf{r}, t)}{\partial t} + c^2\nabla\rho(\mathbf{r}, t)\right] \tag{2.7}$$

where

$$c \equiv \frac{1}{\sqrt{\epsilon_0\mu_0}} \tag{2.8}$$

is identified as the phase velocity of an electromagnetic wave in vacuum, often referred to as the "speed of light in vacuum." Note that this is an inhomogeneous partial differential equation. The driving terms on the right-hand side of the equation can be linear or non-linear, leading to a wealth of interesting phenomena.

The wave equation (2.7) will serve as our point of departure in considering radiation, scattering, and refractive index in situations including free and bound electrons, single atoms, and various distributions of atoms. In this chapter we will treat the scattering of x-rays by individual electrons and atoms through appropriate representations of the induced source terms on the right side of the wave equation. We will obtain several interesting results, including expressions for the well-known Thomson and Rayleigh scattering cross-sections for free and bound electrons, as well as atomic scattering cross-sections for multi-electron atoms. We will employ very simple models of the atom, but will observe that the basic results are identical in form to those obtained with more sophisticated quantum mechanical models. In Chapter 3 we will treat wave propagation phenomena in relatively uniform media containing many atoms. There we will find it convenient to bring the uniformly distributed source terms to the left side of the wave equation, where the combined terms will lead to a modified phase velocity and thus the introduction of a refractive index. This will lead to several practical results, including equations governing the total external reflection of x-rays. We will also discuss how refractive indices and complex scattering cross-sections are determined and tabulated in practice.

Before proceeding to these topics, we note that an expression for conservation of charge, the so-called equation of charge continuity, is easily developed and will be useful later. This follows by taking $\nabla\cdot$ [Eq. (2.1)] and noting the vector identity $\nabla\cdot\nabla\times\mathbf{A} \equiv 0$. We have

$$\nabla\cdot\nabla\times\mathbf{H} = \frac{\partial}{\partial t}\nabla\cdot\mathbf{D} + \nabla\cdot\mathbf{J}$$

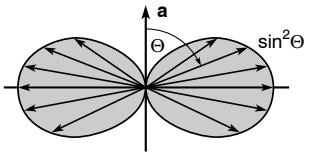

FIGURE 2.1. As observed at a great distance, fields radiated by an accelerated charge propagate over a broad angular range, but not in the direction of acceleration.

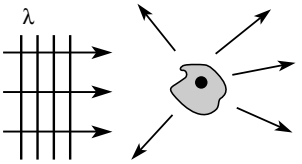

FIGURE 2.2. Irregularly shaped objects and isolated charges, including free electrons and electrons bound to isolated atoms, scatter radiation in many directions.

where the left hand side is identically 0, and on the right-hand side $\nabla \cdot \mathbf{D} = \rho$. This gives the equation for conservation of charge:

$$\nabla \cdot \mathbf{J} + \frac{\partial \rho}{\partial t} = 0 \tag{2.9}$$

What we would like to accomplish in this chapter is a solution to Eq. (2.7) for $\mathbf{E}(\mathbf{r}, t)$ in the presence of source terms – for instance, radiated fields due to accelerated free and bound electrons (Figure 2.1), or the *scattered* fields caused by such oscillating charges in the presence of incident (x-ray) radiation. The latter is a process whereby well-directed energy, propagating in a given direction, is widely redirected by non-uniformly distributed charges or by irregularly shaped objects (Figure 2.2).

One can write the current density $\mathbf{J}(r, t)$ as

$$\mathbf{J}(\mathbf{r}, t) = qn(\mathbf{r}, t)\mathbf{v}(\mathbf{r}, t) \tag{2.10}$$

a product of charge density and velocity, both as functions of space and time. Note that the product $n\mathbf{v}$ raises the possibility of non-linear terms entering via particle motions into the otherwise linear electromagnetic fields. This interesting phenomenon, which we touch on in later chapters, occurs in media (plasmas, fluids, solids) in which both n and $\mathbf{v}$ vary, giving rise to beat frequencies, sum and difference frequencies, and such phenomena as harmonic generation. In this chapter we concern ourselves with isolated charges, both free and bound, for which Eq. (2.10) can be written in a somewhat different form convenient to this simple case. We will consider this shortly.

2.2 CALCULATING SCATTERED FIELDS

First we outline the approach to be taken in solving the wave equation (2.7) for $\mathbf{E}(\mathbf{r}, t)$ in the presence of a source term. Then we calculate the radiated power and its angular dependence. Treating the bracketed quantity on the left side of Eq. (2.7) as an operator, we can imagine solving for $\mathbf{E}(\mathbf{r}, t)$ in terms of arbitrary sources, with a formal solution of the form

$$\mathbf{E}(\mathbf{r}, t) = \int_{\text{volume}} [\text{Green's function}][\text{source terms}]\, d\mathbf{r} \tag{2.11}$$

where the field $\mathbf{E}$ is described mathematically in terms of the response to a distribution of sources – embodied in the so-called *Green's function* – integrated over the full volume.

This is not convenient to do with Eq. (2.7) in the form of a vector partial differential equation. But it can be accomplished[6, 7] without too much difficulty by introducing space-time transformations of $\mathbf{E}(r, t)$ that algebraize the partial differential operators, ∇ and $\partial/\partial t$. Working then with transform amplitudes $\mathbf{E}(\mathbf{k}, \omega)$, abbreviated $\mathbf{E}_{k\omega}$, the differential operators become algebraic multipliers, the inversions required in Eq. (2.11) become simple, and the integration proceeds using standard techniques. Note that the vector field transform amplitudes $\mathbf{E}_{k\omega}$ are a generalization of the Fourier coefficients utilized in one dimensional (scalar) problems. Using this technique to solve for $\mathbf{E}(\mathbf{r}, t)$, the remaining fields, including $\mathbf{H}(\mathbf{r}, t)$ etc., can be determined from transforms of Eqs. (2.1)–(2.6).

In order to simplify both the space (∇) and time ($\partial/\partial t$) operators, we introduce the *Fourier–Laplace transform*

$$\mathbf{E}(\mathbf{r}, t) = \int_{\mathbf{k}} \int_{\omega} \mathbf{E}_{k\omega} e^{-i(\omega t - \mathbf{k}\cdot\mathbf{r})} \frac{d\omega\, d\mathbf{k}}{(2\pi)^4} \tag{2.12a}$$

and its inverse

$$\mathbf{E}_{k\omega} = \int_{\mathbf{r}} \int_{t} \mathbf{E}(\mathbf{r}, t) e^{i(\omega t - \mathbf{k}\cdot\mathbf{r})}\, d\mathbf{r}\, dt \tag{2.12b}$$

where the symbols $d\mathbf{k}$ and $d\mathbf{r}$ are shorthand notation for scalar volume elements. These abbreviations correspond in rectangular coordinates to $d\mathbf{r} = dx\, dy\, dz$ and $d\mathbf{k} = dk_x\, dk_y\, dk_z$. We also understand that the Fourier–Laplace amplitudes $\mathbf{E}_{k\omega}$ are shorthand notation for $\mathbf{E}(\mathbf{k}, \omega)$, as they are vector field amplitudes and are functions of the wave vector $\mathbf{k}$ and frequency ω. We assume that the frequency has a small imaginary component such that the amplitude $\mathbf{E}_{k\omega}$, defined by the integral in Eq. (2.12b), is finite for real fields $\mathbf{E}(\mathbf{r}, t)$. Thus with $\omega = \omega_r + i\omega_i$, where ω_i is small but positive, the integrand in Eq. (2.12b) goes to zero as $t \to \infty$.

Representing all field quantities in a similar manner, i.e.,

$$\mathbf{J}(\mathbf{r}, t) = \int_{\mathbf{k}} \int_{\omega} \mathbf{J}_{k\omega} e^{-i(\omega t - \mathbf{k}\cdot\mathbf{r})} \frac{d\omega\, d\mathbf{k}}{(2\pi)^4} \tag{2.13a}$$

$$\mathbf{J}_{k\omega} = \int_{\mathbf{r}} \int_{t} \mathbf{J}(\mathbf{r}, t) e^{i(\omega t - \mathbf{k}\cdot\mathbf{r})}\, d\mathbf{r}\, dt \tag{2.13b}$$

$$\rho(\mathbf{r}, t) = \int_{\mathbf{k}} \int_{\omega} \rho_{k\omega} e^{-i(\omega t - \mathbf{k}\cdot\mathbf{r})} \frac{d\omega\, d\mathbf{k}}{(2\pi)^4} \tag{2.14a}$$

$$\rho_{k\omega} = \int_{\mathbf{r}} \int_{t} \rho(\mathbf{r}, t) e^{i(\omega t - \mathbf{k}\cdot\mathbf{r})} d\mathbf{r}\, dt \tag{2.14b}$$

etc., we can appreciate the algebrized nature of the operators. For instance, if we consider the time derivative, $\partial/\partial t$, acting on $\rho(\mathbf{r}, t)$, we have

$$\frac{\partial \rho(\mathbf{r}, t)}{\partial t} = \frac{\partial}{\partial t} \int_{\mathbf{k}} \int_{\omega} \left[\rho_{k\omega} e^{-i(\omega t - \mathbf{k}\cdot\mathbf{r})}\right] \frac{d\omega\, d\mathbf{k}}{(2\pi)^4}$$

Note that $\partial/\partial t$ passes through the integrals (to first order, $\mathbf{k}$ and ω are not functions of time). Since $\rho_{k\omega}$ is also not a function of time (to first order), the time derivative acts only on the

exponent, giving

$$\frac{\partial \rho(\mathbf{r}, t)}{\partial t} = \int_{\mathbf{k}} \int_{\omega} (-i\omega) \rho_{k\omega} e^{-i(\omega t - \mathbf{k}\cdot\mathbf{r})} \frac{d\omega\, d\mathbf{k}}{(2\pi)^4}$$

Thus the time differential operator $\partial/\partial t$ results in an algebraic multiplier $(-i\omega)$ when acting on $\rho(\mathbf{r},\ t)$, i.e., when operating in $\mathbf{k},\ \omega$-space. Similarily the gradient operator, taken component by component in some coordinate space, becomes

$$\nabla \rho(\mathbf{r}, t) = \nabla \int_{\mathbf{k}} \int_{\omega} \left[\rho_{k\omega} e^{-i(\omega t - \mathbf{k}\cdot\mathbf{r})} \right] \frac{d\omega\, d\mathbf{k}}{(2\pi)^4}$$

Although the algebraization may be evident to the reader at this point, it is easily illustrated by introducing rectangular coordinates, such that the $\mathbf{k}\cdot\mathbf{r}$ term in the exponent becomes $k_x x + k_y y + k_z z$, the gradient becomes $\nabla = \mathbf{x}_0\, \partial/\partial x + \mathbf{y}_0\, \partial/\partial y + \mathbf{z}_0\, \partial/\partial z$, and $\mathbf{k} = \mathbf{x}_0 k_x + \mathbf{y}_0 k_y + \mathbf{z}_0 k_z$, where $\mathbf{x}_0, \mathbf{y}_0, \mathbf{z}_0$ are unit vectors. Since the components $\partial/\partial x,\ \partial/\partial y,\ \partial/\partial z$ act only on the exponent, the expression for $\nabla\rho(\mathbf{r}, t)$ becomes

$$\nabla \rho(\mathbf{r}, t) = \int_{\mathbf{k}} \int_{\omega} (i\mathbf{x}_0 k_x + i\mathbf{y}_0 k_y + i\mathbf{z}_0 k_z) \left[\rho_{k\omega} e^{-i(\omega t - \mathbf{k}\cdot\mathbf{r})} \right] \frac{d\omega\, d\mathbf{k}}{(2\pi)^4}$$

or

$$\nabla \rho(\mathbf{r}, t) = \int_{\mathbf{k}} \int_{\omega} i\mathbf{k} \rho_{k\omega} e^{-i(\omega t - \mathbf{k}\cdot\mathbf{r})} \frac{d\omega\, d\mathbf{k}}{(2\pi)^4}$$

so that the ∇ operator is replaced by a multiplicative factor $i\mathbf{k}$ in $\mathbf{k}, \omega$-space. Finally, if we consider the operator $\nabla^2 \equiv \nabla \cdot \nabla = \partial^2/\partial x^2 + \partial^2/\partial y^2 + \partial^2/\partial z^2$, we can readily demonstrate that

$$\nabla^2 \mathbf{E}(\mathbf{r}, t) = \int_{\mathbf{k}} \int_{\omega} (i\mathbf{k})^2 \mathbf{E}_{k\omega} e^{-i(\omega t - \mathbf{k}\cdot\mathbf{r})} \frac{d\omega\, d\mathbf{k}}{(2\pi)^4}$$

where now it can be seen that $\nabla^2 = \nabla \cdot \nabla$ algebrizes to $i\mathbf{k} \cdot i\mathbf{k} = -k^2$ in $\mathbf{k}, \omega$-space.

The vector wave equation (2.7) can now be algebrized itself into a very convenient form in terms of the Fourier–Laplace amplitudes:

$$\int_{\mathbf{k}} \int_{\omega} (-i\omega)^2 \mathbf{E}_{k\omega} e^{-i(\omega t - \mathbf{k}\cdot\mathbf{r})} \frac{d\omega\, d\mathbf{k}}{(2\pi)^4} - c^2 \int_{\mathbf{k}} \int_{\omega} (-k^2) \mathbf{E}_{k\omega} e^{-i(\omega t - \mathbf{k}\cdot\mathbf{r})} \frac{d\omega\, d\mathbf{k}}{(2\pi)^4}$$

$$= -\frac{1}{\epsilon_0} \left[\int_{\mathbf{k}} \int_{\omega} (-i\omega) \mathbf{J}_{k\omega} e^{-i(\omega t - \mathbf{k}\cdot\mathbf{r})} \frac{d\omega\, d\mathbf{k}}{(2\pi)^4} + c^2 \int_{\mathbf{k}} \int_{\omega} i\mathbf{k} \rho_{k\omega} e^{-i(\omega t - \mathbf{k}\cdot\mathbf{r})} \frac{d\omega\, d\mathbf{k}}{(2\pi)^4} \right]$$

where we note that every term includes the same $\mathbf{k}, \omega$-integration, which can therefore be removed, and further, that each term contains an exponential factor $-i(\omega t - \mathbf{k}\cdot\mathbf{r})$, which can also be removed, leaving

$$(-i\omega)^2 \mathbf{E}_{k\omega} - c^2(-k^2)\mathbf{E}_{k\omega} = -\frac{1}{\epsilon_0}[(-i\omega)\mathbf{J}_{k\omega} + c^2(i\mathbf{k})\rho_{k\omega}]$$

In operator form, the wave equation in $\mathbf{k}, \omega$-space is

$$(\omega^2 - k^2 c^2)\mathbf{E}_{k\omega} = \frac{1}{\epsilon_0}[(-i\omega)\mathbf{J}_{k\omega} + ic^2\mathbf{k}\rho_{k\omega}] \tag{2.15}$$

which, if inverted, can be solved for $\mathbf{E}_{k\omega}$:

$$\mathbf{E}_{k\omega} = \frac{(-i\omega)\mathbf{J}_{k\omega} + ic^2\mathbf{k}\rho_{k\omega}}{\epsilon_0(\omega^2 - k^2c^2)} \tag{2.16}$$

This shows the source terms in the numerator, and poles at $\omega = \pm kc$ representing the system response in terms of incoming and outgoing waves. Our task now is to set models for the sources in a given problem, $\mathbf{J}(\mathbf{r}, t)$ and $\rho(\mathbf{r}, t)$, obtain their transforms $\mathbf{J}_{k\omega}$ and $\rho_{k\omega}$, determine a solution for $\mathbf{E}_{k\omega}$ from Eq. (2.16), and then return to the inverse transform [Eq. (6.12a)] to calculate the radiated field $\mathbf{E}(r, t)$ through the required $d\omega\, d\mathbf{k}$ integrations [Eq. (6.12a)].

Making the same substitutions as above in the equation for charge conservation [Eq. (2.9)],

$$\nabla \cdot \mathbf{J} + \frac{\partial \rho}{\partial t} = 0$$

permits similar simplification of it. Upon use of similar transforms and operations this becomes

$$i\mathbf{k} \cdot \mathbf{J}_{k\omega} - i\omega\rho_{k\omega} = 0$$

so that

$$\rho_{k\omega} = \frac{\mathbf{k} \cdot \mathbf{J}_{k\omega}}{\omega}$$

Thus the expression for the radiated fields $\mathbf{E}_{k\omega}$ [Eq. (16)] can be written as

$$\mathbf{E}_{k\omega} = -\frac{i\omega}{\epsilon_0}\left[\frac{\mathbf{J}_{k\omega} - (c^2/\omega^2)\mathbf{k}(\mathbf{k} \cdot \mathbf{J}_{k\omega})}{\omega^2 - k^2c^2}\right]$$

or

$$\mathbf{E}_{k\omega} = -\frac{i\omega}{\epsilon_0}\left[\frac{\mathbf{J}_{k\omega} - \mathbf{k}_0(\mathbf{k}_0 \cdot \mathbf{J}_{k\omega})}{\omega^2 - k^2c^2}\right] \tag{2.17}$$

Here we have written the wave propagaton vector as $\mathbf{k} = \mathbf{k}_0 k$. The unit vector $\mathbf{k}_0$ is in the propagation direction, and $k = 2\pi/\lambda$ is the scalar wavenumber. The equation $\omega = kc$ (equivalent to $f\lambda = c$) is most readily appreciated from Eq. (2.17) as the required condition for finite field amplitude $\mathbf{E}_{k,\omega}$ even in the absence of sources. In other words, $\omega = kc$ satisfies the homogeneous (vacuum) case where the right-hand side of Eq. (2.15) is zero. These are the so-called resonances or natural modes of the system. The condition $\omega = kc$ is often referred to as a dispersion relation; we will discuss it further in Chapter 3.

We can simplify Eq. (2.17) for $\mathbf{E}_{k\omega}$ by introducing a coordinate system oriented around the wave propagation direction $\mathbf{k}_0$, as shown in Figure 2.3. For instance, we can decompose the vector $\mathbf{J}_{k\omega}$ into components along and transverse to the propagation direction $\mathbf{k}_0$:

$$\mathbf{J}_{k\omega} = \mathbf{J}_{T_{k\omega}} + J_{L_{k\omega}}\mathbf{k}_0$$

If we do so, it is evident that with $\mathbf{k} = k\mathbf{k}_0$ the numerator in the bracketed factor in Eq. (2.17) becomes

$$\mathbf{J}_{k\omega} - \underbrace{\mathbf{k}_0(\mathbf{k}_0 \cdot \mathbf{J}_{k\omega})}_{\mathbf{k}_0 \text{ portion}} = \mathbf{J}_{T_{k\omega}}$$

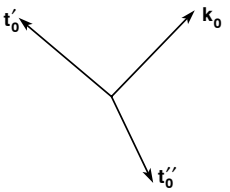

FIGURE 2.3. (a) A vector coordinate system useful for decomposing vector fields into components parallel and transverse to the wave propagation direction. Polar coordinates in this k-space are k, θ, ϕ, where θ is the polar angle measured from $\mathbf{k}_0$ and ϕ lies in the transverse plane (t_0', t_0''). The unit vectors are related by $\mathbf{k}_0 \times \mathbf{t}_0' = \mathbf{t}_0''$.

where $\mathbf{J}_{Tk\omega}$ is the component of the vector $\mathbf{J}_{k\omega}$ *transverse* to $\mathbf{k}_0$. Note that $\mathbf{k}_0 \cdot \mathbf{J}_{k\omega}$ is the scalar component of $\mathbf{J}_{k\omega}$ in the $\mathbf{k}_0$-direction, and thus $\mathbf{k}_0(\mathbf{k}_0 \cdot \mathbf{J}_{k\omega})$ is the vector component of $\mathbf{J}_{k\omega}$ in the $\mathbf{k}_0$-direction, i.e., the longitudinal vector component. Thus, when it is subtracted from $\mathbf{J}_{k,\omega}$, only the transverse vector portion remains. The solution for $\mathbf{E}_{k\omega}$, Eq. (2.17), then becomes

$$\mathbf{E}_{k\omega} = \frac{-i\omega}{\epsilon_0} \cdot \frac{\mathbf{J}_{T_{k\omega}}}{\omega^2 - k^2c^2} \tag{2.18}$$

Having a formal solution (2.18) to $\mathbf{E}_{k\omega}$ in terms of the source, we can now return to the Fourier–Laplace transform relations, specifically Eq. (2.12a), to find the space and time dependent field $\mathbf{E}(\mathbf{r}, t)$:

$$\mathbf{E}(\mathbf{r}, t) = \int_{\mathbf{k}} \int_{\omega} \mathbf{E}_{k\omega} e^{-i(\omega t - \mathbf{k}\cdot\mathbf{r})} \frac{d\omega\, d\mathbf{k}}{(2\pi)^4}$$

With Eq. (2.18) we can express the radiated electric field $\mathbf{E}(\mathbf{r},\ t)$ in terms of the transverse component of current density as

$$\mathbf{E}(\mathbf{r}, t) = \int_{\mathbf{k}} \int_{\omega} \left(-\frac{i\omega}{\epsilon_0}\right) \frac{\mathbf{J}_{T_{k\omega}} e^{-i(\omega t - \mathbf{k}\cdot\mathbf{r})}}{(\omega^2 - k^2c^2)} \frac{d\omega\, d\mathbf{k}}{(2\pi)^4} \tag{2.19}$$

which is the form of a Green's function integration, albeit in k, ω-space. The question now is: what is $\mathbf{J}_{T_{k\omega}}$? This will depend on the specific problem of interest.

Let us start by considering a *point radiator* that is small compared to the radiating wavelength, and could be an oscillating free or bound electron. If this radiating particle is sufficiently small, we can represent its density $n(\mathbf{r})$ as a Dirac delta function[‡] such that the current density, $J(\mathbf{r},\ t)$ [Eq. (2.10)], given by

$$\mathbf{J}(\mathbf{r}, t) = qn(\mathbf{r}, t)\mathbf{v}(\mathbf{r}, t)$$

can be written for an electron as

$$\mathbf{J}(\mathbf{r}, t) = -e\delta(\mathbf{r})\mathbf{v}(t) \tag{2.20}$$

In rectangular coordinates $\delta(\mathbf{r})$ is shorthand notation for the product $\delta(x)\delta(y)\delta(z)$, where the delta function has the properties

$$\delta(x) = \begin{cases} 0 & \text{for } x \neq 0 \\ \infty & \text{for } x = 0 \end{cases}$$

[‡]See Appendix D.

The normalization condition of the delta function is

$$\int_{-\infty}^{\infty} \delta(x)\, dx = 1$$

The delta function has the additional property that

$$\delta(x-a) = \begin{cases} 0 & \text{for } x \neq a \\ \infty & \text{for } x = a \end{cases}$$

with the normalization condition

$$\int_{-\infty}^{\infty} \delta(x-a)\, dx = 1$$

This leads to the so-called *sifting property*

$$\int_{-\infty}^{\infty} f(x)\delta(x-a)\, dx = f(a)$$

The transformed current density $\mathbf{J}_{k\omega}$ for a point source radiator can now be determined for use in Eq. (2.19) by utilizing Eq. (2.13b):

$$\mathbf{J}_{k\omega} = \iint \mathbf{J}(\mathbf{r}, t) e^{i(\omega t - \mathbf{k}\cdot\mathbf{r})}\, d\mathbf{r}\, dt$$

Using Eq. (2.20) for the current density of a point source, one has

$$\mathbf{J}_{k\omega} = \int_{\mathbf{r}} \int_{t} [-e\delta(\mathbf{r})\mathbf{v}(t)] e^{i(\omega t - \mathbf{k}\cdot\mathbf{r})}\, d\mathbf{r}\, dt$$

$$\mathbf{J}_{k\omega} = -e \underbrace{\int_{t} \mathbf{v}(t) e^{i\omega t}\, dt}_{\mathbf{v}(\omega)}$$

$$\mathbf{J}_{k\omega} = -e\mathbf{v}(\omega)$$

This has a transverse component

$$\mathbf{J}_{T_{k\omega}} = -e\mathbf{v}_T(\omega) \tag{2.21}$$

where $\mathbf{v}_T$ is the velocity component transverse to the propagation direction $\mathbf{k}_0$.

To determine the electric field, as given in Eq. (2.19), one must then perform the integration

$$\mathbf{E}(\mathbf{r}, t) = \frac{ie}{\epsilon_0} \int_{\mathbf{k}} \int_{\omega} \frac{\omega \mathbf{v}_T(\omega) e^{-i(\omega t - \mathbf{k}\cdot\mathbf{r})}}{\omega^2 - k^2 c^2} \frac{d\omega\, d\mathbf{k}}{(2\pi)^4} \tag{2.22}$$

The **k**-space integration is accomplished by introducing spherical coordinates oriented around the propagation vector $\mathbf{k}_0$, with differential volume element (a scalar quantity), for instance, as in Figure 2.3,

$$d\mathbf{k} = k^2 \underbrace{\sin\theta\, d\theta\, d\phi}_{d\Omega}\, dk \tag{2.23}$$

where θ is measured from $\mathbf{k}_0$, and where $0 \leq k \leq \infty$, $0 \leq \theta \leq \pi$, and $0 \leq \phi \leq 2\pi$. In these coordinates, for a vector $\mathbf{r}$ at a polar angle θ to $\mathbf{k}$, the phase term that occurs in the exponent of Eq. (2.22) becomes

$$\mathbf{k} \cdot \mathbf{r} = kr \cos\theta$$

The angular integrations of Eq. (2.22) in polar coordinates are straightforward. This leaves the k- and ω-integrations. The k-integration can be performed in the complex k-plane using the Cauchy integral formula.[8] The integrand is seen to have two poles, at $k = \pm\omega/c$, representing incoming and outgoing waves. Assuming that the poles each have a small lossy component representing wave decay, the integration path can be closed in the upper half plane with a semicircle of infinite radius, which makes no contribution to the integral. The closed path then encloses a single pole, slightly displaced from the real axis, and the k-integral is readily evaluated. Details of the integration are given in Appendix E. The result of the k-integration is

$$\mathbf{E}(\mathbf{r}, t) = \frac{e}{4\pi\epsilon_0 c^2 r} \int_{-\infty}^{\infty} (-i\omega)\mathbf{v}_T(\omega) e^{-i\omega(t-r/c)} \frac{d\omega}{2\pi} \tag{2.24}$$

which leaves only the ω-integration to be completed. The quantity $-i\omega$ in the integrand is recognized as equivalent to the differential operator d/dt, which can then be taken outside the integral, leaving the transform of $\mathbf{v}_T(\omega)$. The result for the radiated electric field due to an oscillating point electron is then

$$\mathbf{E}(\mathbf{r}, t) = \frac{e}{4\pi\epsilon_0 c^2 r} \frac{d\mathbf{v}_T\,(t - r/c)}{dt}$$

Recognizing this as the transverse component of acceleration, the electric field associated with the radiated wave can be written as

$$\boxed{\mathbf{E}(\mathbf{r}, t) = \frac{e\mathbf{a}_T\,(t - r/c)}{4\pi\epsilon_0 c^2 r}} \tag{2.25}$$

That is, the radiated electric field $\mathbf{E}(\mathbf{r}, t)$ is due to the component of electron acceleration transverse to the propagation direction, observed at a *retarded time* $t - r/c$, that is, after traveling a distance r to the observer at the speed of light, c. The dependence on only the transverse component of acceleration introduces angular effects into radiation and scattering problems, to be addressed in a following section.

2.3 RADIATED POWER AND POYNTING'S THEOREM

Radiated power, or more specifically power per unit area, is described in electromagnetic theory by the so-called *Poynting vector* [1–5]

$$\boxed{\mathbf{S} = \mathbf{E}(\mathbf{r}, t) \times \mathbf{H}(\mathbf{r}, t)} \tag{2.26}$$

which gives the magnitude and direction of energy flow or power per unit area. This can be obtained directly from Maxwell's equations. We will derive it, and then calculate the power radiated by an accelerated electron, using the radiated electric field $\mathbf{E}(\mathbf{r}, t)$ given by Eq. (2.25).

To obtain Poynting's theorem for $\mathbf{S}$, we begin with Maxwell's equations (2.1–2.6), and form the difference of $\mathbf{H} \cdot$ [Eq. (2.2)] $- \mathbf{E} \cdot$ [Eq. (2.1)] to obtain

$$\mathbf{H} \cdot (\nabla \times \mathbf{E}) - \mathbf{E} \cdot (\nabla \times \mathbf{H}) = -\mathbf{H} \cdot \frac{\partial \mathbf{B}}{\partial t} - \mathbf{E} \cdot \frac{\partial \mathbf{D}}{\partial t} - \mathbf{E} \cdot \mathbf{J}$$

Recalling the vector identity $\nabla \cdot (\mathbf{A} \times \mathbf{B}) = \mathbf{B} \cdot (\nabla \times \mathbf{A}) - \mathbf{A} \cdot (\nabla \times \mathbf{B})$, and using Eqs. (2.5) and (2.6) for $\mathbf{B}$ and $\mathbf{D}$, this becomes

$$\nabla \cdot (\mathbf{E} \times \mathbf{H}) = -\mu_0 \mathbf{H} \cdot \frac{\partial \mathbf{H}}{\partial t} - \epsilon_0 \mathbf{E} \cdot \frac{\partial \mathbf{E}}{\partial t} - \mathbf{E} \cdot \mathbf{J}$$

or

$$\nabla \cdot \underbrace{(\mathbf{E} \times \mathbf{H})}_{\mathbf{S}} = -\frac{\partial}{\partial t}\left(\frac{\mu_0 H^2}{2}\right) - \frac{\partial}{\partial t}\left(\frac{\epsilon_0 E^2}{2}\right) - \mathbf{E} \cdot \mathbf{J} \tag{2.27}$$

Equation (2.27) is the differential form of Poynting's theorem. The time derivative terms on the right side of the equation represent the rate of change of energy per unit volume (energy density) stored in the magnetic and electric fields, respectively. The rightmost term represents the rate of energy dissipation per unit volume associated with the current density $\mathbf{J}$. Identification of $\mathbf{S} = \mathbf{E} \times \mathbf{H}$ on the left is thus suggestive, as this would represent the net flow of energy into or out of a controlled volume. Certain ambiguities[3, 4] in this interpretation can be removed by integrating (27) over a closed volume, e.g.,

$$\iiint_{\text{vol.}} \nabla \cdot (\mathbf{E} \times \mathbf{H})\, dV = -\frac{\partial}{\partial t} \iiint_{\text{vol.}} \left(\frac{\mu_0 H^2}{2} + \frac{\epsilon_0 E^2}{2}\right) dV - \iiint_{\text{vol.}} (\mathbf{E} \cdot \mathbf{J})\, dV$$

which by Gauss's divergence theorem[¶] for a vector quantity $\mathbf{B}$,

$$\iiint_{\text{vol.}} (\nabla \cdot \mathbf{B})\, dV = \iint_{\text{surface}} \mathbf{B} \cdot d\mathbf{A}$$

becomes the *integral form of Poynting's theorem:*

$$\iint_{\text{surface}} \underbrace{(\mathbf{E} \times \mathbf{H})}_{\mathbf{S}} \cdot d\mathbf{A} = -\frac{\partial}{\partial t} \iiint_{\text{vol.}} \underbrace{\left(\frac{\mu_0 H^2}{2} + \frac{\epsilon_0 E^2}{2}\right)}_{\text{stored energy density}} dV - \iiint_{\text{vol.}} \underbrace{(\mathbf{E} \cdot \mathbf{J})}_{\text{energy dissipation}}\, dV \tag{2.28}$$

[¶]See Appendix D.

where $\mathbf{S}(\mathbf{r}, t) = \mathbf{E}(\mathbf{r}, t) \times \mathbf{H}(\mathbf{r}, t)$, the Poynting vector, represents the vector flow of energy per unit area in the direction orthogonal to $\mathbf{E}$ and $\mathbf{H}$, which we shall see shortly is the propagation direction $\mathbf{k}_0$ for plane waves. The units of $\mathbf{S}$ are those of energy per unit time and per unit area. The magnitude of $\mathbf{S}$ is often referred to as the intensity, I, typically with units of watts per square centimeter.

To complete the calculation of radiated power we must form the vector product $\mathbf{E} \times \mathbf{H}$, wherein to this point we have only calculated $\mathbf{E}$ [Eq. (2.25)]. To obtain $\mathbf{H}(\mathbf{r}, t)$ knowing $\mathbf{E}(\mathbf{r}, t)$ we return to Eq. (2.2):

$$\nabla \times \mathbf{E}(\mathbf{r}, t) = -\frac{\partial \mathbf{B}(\mathbf{r}, t)}{\partial t}$$

By Eq. (2.6),

$$\mathbf{B} = \mu_0 \mathbf{H}$$

which gives

$$\nabla \times \mathbf{E} = -\mu_0 \frac{\partial \mathbf{H}}{\partial t}$$

Recalling the algebraic equivalents of ∇ and $\partial/\partial t$ for fields transformed to a $\mathbf{k}$, ω plane wave presentation, this takes the form

$$i\mathbf{k} \times \mathbf{E}_{k\omega} = +i\omega\mu_0 \mathbf{H}_{k\omega}$$

Thus in $\mathbf{k}$, ω-space

$$\mathbf{H}_{k\omega} = \sqrt{\frac{\epsilon_0}{\mu_0}} \mathbf{k}_0 \times \mathbf{E}_{k\omega}$$

where we have used the fact that for waves propagating in free space $\omega = kc$ and $c = 1/\sqrt{\epsilon_0 \mu_0}$. Now it is possible to replace both $\mathbf{E}_{k\omega}$ and $\mathbf{H}_{\mathbf{k}\omega}$ by their inverse transforms, as in Eq. (2.12b). Noting that the rotation operator $\mathbf{k}_0 \times$ passes through the $d\mathbf{r}\, dt$ integrals on both sides of the resulting equation, one obtains an equation of identical form in $\mathbf{r}, t$-space. That is, for plane waves propagating in free space the electric and magnetic fields are related by

$$\boxed{\mathbf{H}(\mathbf{r}, t) = \sqrt{\frac{\epsilon_0}{\mu_0}} \mathbf{k}_0 \times \mathbf{E}(\mathbf{r}, t)} \tag{2.29}$$

For example, the magnetic field associated with radiation from an accelerated charge, with $\mathbf{E}(\mathbf{r}, t)$ given by Eq. (2.25), is

$$\mathbf{H}(\mathbf{r}, t) = \frac{e}{4\pi cr} \mathbf{k}_0 \times \mathbf{a}_T \left(t - \frac{r}{c}\right) \tag{2.30}$$

which we note is both transverse to the propagation direction $\mathbf{k}_0$ and, by Eq. (2.29), transverse to $\mathbf{E}$.

The radiated power per unit area can be determined from Eqs. (2.26, 2.29), and consideration of Poynting's vector, where for a plane wave in vacuum

$$\mathbf{S} = \mathbf{E} \times \mathbf{H} = \mathbf{E}(\mathbf{r}, t) \times \left[\sqrt{\frac{\epsilon_0}{\mu_0}} \mathbf{k}_0 \times \mathbf{E}(\mathbf{r}, t) \right]$$

Noting the vector identity $\mathbf{A} \times (\mathbf{B} \times \mathbf{C}) = (\mathbf{A} \cdot \mathbf{C})\mathbf{B} - (\mathbf{A} \cdot \mathbf{B})\mathbf{C}$, and that for a transverse wave $\mathbf{k}_0 \cdot \mathbf{E} = 0$, we have

$$\boxed{\mathbf{S}(\mathbf{r}, t) = \sqrt{\frac{\epsilon_0}{\mu_0}} |\mathbf{E}|^2 \mathbf{k}_0} \tag{2.31}$$

The quantity $\sqrt{\mu_0/\epsilon_0}$ is often referred to as the "impedance of free space," Z_0.

For the accelerated point charge with radiated electric field given by Eq. (2.25), Eq. (2.31) gives *the instantaneous power per unit area*, radiated in the direction $\mathbf{k}_0$:

$$\mathbf{S}(\mathbf{r}, t) = \frac{e^2 |\mathbf{a}_T|^2}{16\pi^2 \epsilon_0 c^3 r^2} \mathbf{k}_0 \tag{2.32}$$

which decreases as the distance squared and is proportional to the square of the vector acceleration in a direction orthogonal to $\mathbf{k}_0$, i.e., to $|\mathbf{a}_T|^2$. Referring to the vector coordinates for propagation described in Figure 2.4, the acceleration $\mathbf{a}$ at angle Θ to the propagation (observation) direction $\mathbf{k}_0$ has a transverse component of magnitude

$$|\mathbf{a}_T| = |\mathbf{a}| \sin \Theta$$

Thus from Eq. (2.32) the *instantaneous power per unit area radiated by an accelerated electron* becomes

$$\mathbf{S}(\mathbf{r}, t) = \frac{e^2 |\mathbf{a}|^2 \sin^2 \Theta}{16\pi^2 \epsilon_0 c^3 r^2} \mathbf{k}_0 \tag{2.33}$$

again showing the r^2 decrease with distance, the dependence on a^2, and the well-known[1–5, 9] $\sin^2 \Theta$ angular pattern of *dipole radiation,* as observed in the far field when the oscillation amplitude is small compared to the wavelength, e.g., in the point source approximation. The resultant radiation pattern, sketched in Figure 2.5, displays a $\sin^2 \Theta$ toroidal pattern, with maximum radiation intensity orthogonal to the acceleration direction, and zero radiation in the direction of acceleration. The power per unit solid angle is obtained by noting that $\mathbf{S} = (dP/dA)\mathbf{k}_0$, and that the differential elements of area and solid angle are related by $dA = r^2 \, d\Omega$, so that it follows from Eq. (2.33) that

$$\boxed{\frac{dP}{d\Omega} = \frac{e^2 |\mathbf{a}|^2 \sin^2 \Theta}{16\pi^2 \epsilon_0 c^3}} \tag{2.34}$$

in an outgoing $\mathbf{k}_0$-direction.

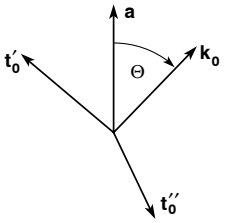

FIGURE 2.4. Vector coordinates for acceleration **a** and propagation (observation) direction $\mathbf{k}_0$, separated by an angle Θ measured from the acceleration direction **a**. Note that the vector components of the acceleration are $a_L = \mathbf{k}_0 \cdot \mathbf{a} = a\cos\Theta$, and $\mathbf{a}_T = -\mathbf{k}_0 \times (\mathbf{k}_0 \times \mathbf{a})$, where $|\mathbf{a}_T| = a\sin\Theta$.

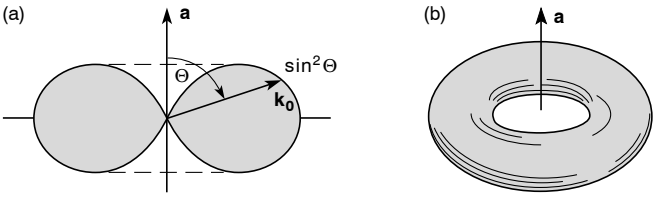

FIGURE 2.5. (a) The $\sin^2\Theta$ radiation pattern of a small accelerated charge, and (b) its three-dimensional toroidal appearance.

The total power radiated, P, is determined by integrating $\mathbf{S}$ over the area of a distant sphere:

$$P = \iint_{\text{area}} \mathbf{S} \cdot d\mathbf{A} = \iint_{\substack{\text{solid}\\ \text{angle}}} \mathbf{S} \cdot (r^2\, d\Omega\, \mathbf{k}_0) \tag{2.35}$$

where for $0 \le \Theta \le \pi$ and $0 \le \phi \le 2\pi$ we have $d\Omega = \sin\Theta\, d\Theta\, d\phi$; thus

$$P = \iint \left[\frac{e^2|\mathbf{a}|^2 \sin^2\Theta}{16\pi^2\epsilon_0 c^3 r^2}\, \mathbf{k}_0 \right] \cdot r^2 \sin\Theta\, d\Theta\, d\phi\, \mathbf{k}_0$$

$$P = \frac{e^2|\mathbf{a}|^2}{16\pi^2\epsilon_0 c^3} \int_0^{2\pi} \underbrace{\int_0^{\pi} \sin^3\Theta\, d\Theta}_{\int_0^{\pi}(1-\cos^2\Theta)\sin\Theta\, d\Theta = \frac{4}{3}}\, d\phi$$

Thus the *total power radiated* by an oscillating electron of acceleration a is

$$\boxed{P = \frac{8\pi}{3}\left(\frac{e^2|\mathbf{a}|^2}{16\pi^2\epsilon_0 c^3}\right)} \tag{2.36}$$

For sinusoidal fields we are often interested in the time-averaged power $\bar{P}$ and the time-averaged power per unit area, $\bar{\mathbf{S}}$. To form appropriate expressions it is necessary to take the product of real field quantities. For sinusoidal fields we have found it convenient to write the various vectors **E**, **H**, **a**, etc., in the form

$$\mathbf{E}(\mathbf{r}, t) = \mathbf{E}_0 e^{-i(\omega t - \mathbf{k}\cdot\mathbf{r})}$$

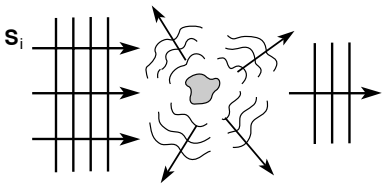

FIGURE 2.6. Scattering of incident radiation into many directions, leaving a less intense wave in the forward direction.

where the amplitude $\mathbf{E}_0$ itself may include a complex phase factor $e^{i\phi}$. For such fields one can show by algebraic substitution [3, 4] that the time-averaged real power per unit area flowing in a particular direction is

$$\bar{\mathbf{S}} = \tfrac{1}{2}\,\mathrm{Re}(\mathbf{E} \times \mathbf{H}^*) \tag{2.37}$$

where Re refers to the real part, the asterisk refers to complex conjugation, and the factor $\frac{1}{2}$ arises from averaging a $\sin^2 \omega t$ or $\cos^2 \omega t$ product term over a full cycle.[3] In calculations of average power and intensity we will thus encounter quantities such as $\mathbf{E}_0 \cdot \mathbf{E}_0^*$, and $\mathbf{a} \cdot \mathbf{a}^*$, which we will abbreviate as $|\mathbf{E}_0|^2$ and $|\mathbf{a}|^2$, etc. Following these procedures, the average power radiated by an oscillating electron, $\bar{P}$, will be half that given by Eq. (2.36), and the average power per unit solid angle will be half that given by Eq. (2.34), when the field amplitudes **a** and **E** are expressed in terms of their peak values.

2.4 SCATTERING CROSS SECTIONS

We are now in a position to calculate the power radiated by free and bound electrons experiencing an acceleration $\mathbf{a}(\mathbf{r}, t)$. An interesting problem is that of an oscillating electron, free or bound, accelerated by an incident electromagnetic field. As this process redirects radiation to a wide range of angles (Figure 2.6), it is generally referred to as *scattering*. A measure of the scattering power of an electron is given by its equivalent *scattering cross-section* σ, that is, its effective area for redirecting incident radiation. This cross-section is defined as the average power radiated divided by the average incident power per unit area, $|\bar{\mathbf{S}}_i|$, that is,

$$\sigma \equiv \frac{\bar{P}_{\text{scatt.}}}{|\bar{\mathbf{S}}_i|} \tag{2.38}$$

where $\bar{\mathbf{P}}_{\text{scatt.}}$ is the average power scattered to all directions when an incident wave of electric field $\mathbf{E}_i(\mathbf{r}, t)$ excites an electron to acceleration $\mathbf{a}(\mathbf{r}, t)$. By Eqs. (2.37) and (2.31) the average power per unit area carried by the incident electromagnetic wave is given by

$$\bar{\mathbf{S}}_i = \frac{1}{2}\sqrt{\frac{\epsilon_0}{\mu_0}}\,|\mathbf{E}_i|^2\,\mathbf{k}_0 \tag{2.39}$$

2.5 SCATTERING BY A FREE ELECTRON

For a free electron the incident field causes an oscillatory motion described by Newton's second equation of motion, $\mathbf{F} = m\mathbf{a}$, where $\mathbf{F}$ is the Lorentz force on the electron; thus

$$m\mathbf{a} = -e[\mathbf{E}_i + \mathbf{v} \times \mathbf{B}_i] \tag{2.40}$$

From Eq. (2.29), $\mathbf{H} = \sqrt{\epsilon_0/\mu_0}\,\mathbf{k}_0 \times \mathbf{E}(\mathbf{r}, t)$ for an incident plane electromagnetic wave in vacuum, so that with $\mathbf{B} = \mu_0\mathbf{H}$,

$$\mathbf{B}_i(\mathbf{r}, t) = \frac{\mathbf{k}_0 \times \mathbf{E}_i(\mathbf{r}, t)}{c} \tag{2.41}$$

We see from the above that the term $\mathbf{v} \times \mathbf{B}_i(\mathbf{r}, t)$ in Eq. (2.40) is of order v/c compared to $\mathbf{E}_i(\mathbf{r}, t)$, and therefore negligible for non-relativistic oscillation velocities. The instantaneous acceleration of a free electron driven by a passing (incident) electromagnetic wave is then

$$\mathbf{a}(\mathbf{r}, t) = -\frac{e}{m}\mathbf{E}_i(\mathbf{r}, t) \tag{2.42}$$

The scattered electric field, given by Eq. (2.25), depends only on the transverse component of acceleration, which as seen in Figure 2.4 has scalar amplitude

$$a_T = a \sin\Theta = -\frac{e}{m}E_i \sin\Theta$$

From Eq. (2.25) the scalar electric field, scattered to an angle Θ with respect to the polarization direction of the incident electric field, can thus be expressed as

$$E(\mathbf{r}, t) = -\frac{e^2 E_i \sin\Theta}{4\pi\epsilon_0 m c^2 r}\, e^{-i\omega(t - r/c)}$$

Introducing the classical electron radius, r_e, the electric field scattered by a free electron can be written more compactly as

$$\boxed{E(\mathbf{r}, t) = -\frac{r_e E_i \sin\Theta}{r} e^{-i\omega(t - r/c)}} \tag{2.43}$$

where

$$\boxed{r_e = \frac{e^2}{4\pi\epsilon_0 m c^2}} \tag{2.44}$$

is defined[1] by equating the electrostatic energy of a uniform sphere of radius r and charge e, $e^2/4\pi\epsilon_0 r$, to its rest energy mc^2. In a later section we will calculate the scattered field due to a many-electron atom and will compare it with that for a single free electron, Eq. (2.43). In this way we will introduce an *atomic scattering factor*, a multiplying factor that compares the electric field scattered by a multi-electron atom with that scattered by a single free electron.

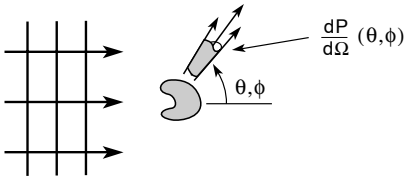

FIGURE 2.7. Angle-dependent scattering can be described in terms of a differential scattering cross-section that takes account of variations in power per unit solid angle.

The average power scattered by an oscillating electron is obtained by combining Eqs. (2.36) and (2.42):

$$\bar{P}_{\text{scatt.}} = \frac{1}{2}\frac{8\pi}{3}\frac{e^2\left(\frac{e^2}{m^2}|\mathbf{E}_i|^2\right)}{16\pi^2\epsilon_0 c^3}$$

where the factor $\frac{1}{2}$ appears due to time averaging the squared sinusoidal fields. The scattering cross-section given by Eq. (2.38) is then

$$\sigma = \frac{\bar{P}_{\text{scatt.}}}{|\bar{\mathbf{S}}|} = \frac{\frac{4\pi}{3}\left(\frac{e^4|\mathbf{E}_i|^2}{16\pi^2\epsilon_0 m^2 c^3}\right)}{\frac{1}{2}\sqrt{\frac{\epsilon_0}{\mu_0}}|\mathbf{E}_i|^2}$$

where we have used Eq. (2.39) for the time averaged Poynting vector of the incident wave. Again using the classical electron radius r_e, the scattering cross-section for a free electron can be expressed as

$$\boxed{\sigma_e = \frac{8\pi}{3}r_e^2} \tag{2.45}$$

where the subscript e denotes the fact that this is the scattering cross-section for a single electron. This result was first obtained by J.J. Thomson,[§] and is referred to as the *Thomson cross-section*[1] for scattering of electromagnetic waves by a free electron. Note that for a free (unbound) electron, Eq. (2.45) has no frequency (wavelength) dependence, thus indicating that the scattering cross-section is the same across the electromagnetic spectrum, from microwaves to visible light to x-rays. Limitations for very short wavelength x-rays and gamma rays, where the momentum of the incident photon is sufficient to cause recoil, are discussed in the literature.[10] Note that numerically

$$r_e = 2.82 \times 10^{-13}\ \text{cm} \tag{2.46a}$$

$$\sigma_e = 6.65 \times 10^{-25}\ \text{cm}^2 \tag{2.46b}$$

[§]See J.J. Thomson, *Conduction of Electricity Through Gases* (Cambridge Univ. Press, 1906), Second Edition, p. 325. The "corpuscles" (see his p. 197 as well) are what we now call electrons. In the Third Edition (1933, with G.P. Thomson) the classical theory of scattering is presented in the manner followed by modern texts.

A differential scattering cross-section per unit solid angle (Figure 2.7) can be obtained by the same procedures. Using Eq. (2.34), with a factor $\frac{1}{2}$ for average power in terms of peak acceleration, and normalizing to $|\bar{\mathbf{S}}_i| = \frac{1}{2}\sqrt{\epsilon_0/\mu_0}E_i^2$, the differential scattering cross-section is defined as

$$\frac{d\sigma_e}{d\Omega} \equiv \frac{1}{|\mathbf{S}_i|}\frac{d\bar{P}}{d\Omega} = \frac{\dfrac{e^2a^2\sin^2\Theta}{32\pi^2\epsilon_0c^3}}{\dfrac{1}{2}\sqrt{\dfrac{\epsilon_0}{\mu_0}}|\mathbf{E}_i^2|}$$

Again using Eq. (2.42), we now obtain the *differential Thomson scattering cross-section for a free electron*:

$$\boxed{\frac{d\sigma_e}{d\Omega} = r_e^2\sin^2\Theta} \tag{2.47}$$

In addition to Thomson's early efforts to identify the nature of the electron, knowledge of the free-electron cross-section is widely used for other purposes. In modern studies of plasma physics, as in fusion research, Thomson scattering of laser light is widely used as a diagnostic of free electron density and of temperature (both electron and ion), and to determine the presence of various plasma waves.[11]

2.6 SCATTERING BY BOUND ELECTRONS

A number of interesting phenomena can be explained on the basis of scattering by bound electrons. Topics of interest here include the scattering of x-rays by multi-electron atoms, the refractive index at x-ray wavelengths, and phenomena such as total external reflection of x-rays at glancing incidence to a material surface, as well as the more common scattering of visible sunlight in the atmosphere, which leads to the appearance of a blue sky and a red sunset. While the scattering is accurately described by quantum mechanical techniques,[12–16] much can be learned from a simple semi-classical model in which the atom is represented by a massive positively charged $(+Ze)$ nucleus surrounded by several (Z) electrons held at discrete binding energies. In this model the relatively massive nucleus does not respond dynamically to the high frequency incident fields, but the electrons are caused to oscillate at the frequency ω imposed by the electric field $\mathbf{E}_i$ of a passing electromagnetic wave. The various electrons, being bound by differing restoring forces, respond differently to the impressed fields. The response depends on the resonant frequencies ω_s of the bound electrons and, more specifically, on the closeness of the driving (incident wave) frequency to the resonances, that is, on $\omega - \omega_s$. A discussion of this semi-classical model and its relation to more rigorous quantum mechanical models is found in Refs. 1 and 12 through 17.

To proceed we require an equation of motion for each of the bound electrons so that we may determine its acceleration $\mathbf{a}$ in the presence of an incident field – and from that determine the reradiated power in much the same manner as we did previously for free electrons. Thus we must determine an appropriate formulation of Newton's second law of motion ($\mathbf{F} = m\mathbf{a}$) for each of the bound electrons. In the semi-classical model we treat the multi-electron atom as a collection of harmonic oscillators, each with its own set of resonances, $\hbar\omega_s$, which we can associate with known transitions between stationary states of the atom. We note, before

proceeding to the semi-classical equation of motion, that in a proper quantum mechanical model, the presence of a time dependent external electric field perturbs the atomic system so that there is a time dependent probability of finding the atom in various stationary states ψ_n – perhaps upper and lower states – oscillating continuously between the two at the impressed frequency and thus giving the sense of a time-dependent oscillation of charge distribution within the atom.

In the semi-classical model each bound electron is forced to execute simple harmonic motion by the impressed electric field while in the presence of the restoring central force field of the massive, positively charged nucleus. The equation of motion can then be written as follows:[‖]

$$m\frac{d^2\mathbf{x}}{dt^2} + m\gamma\frac{d\mathbf{x}}{dt} + m\omega_s^2\mathbf{x} = -e(\mathbf{E}_i + \underbrace{\mathbf{v}\times\mathbf{B}_i}_{\simeq 0}) \tag{2.48}$$

where the first term is the acceleration ($m\mathbf{a}$), the second term is a dissipative force term that accounts for energy loss (we assume $\gamma/\omega \ll 1$), and the third term is due to the restoring force for an oscillator of resonant frequency ω_s; where $-e(\mathbf{E}_i + \mathbf{v}\times\mathbf{B}_i)$ is the Lorentz force exerted by the incident fields; and where, as before, the $\mathbf{v}\times\mathbf{B}_i$ term is small for non-relativistic oscillation velocities $\mathbf{v}$. With oscillations impressed by an incident electric field of the form

$$\mathbf{E} = \mathbf{E}_i e^{-i\omega t}$$

we anticipate that the displacement $\mathbf{x}$, velocity, and acceleration will all have the same $e^{-i\omega t}$ time dependence. The time derivative in all terms can then be replaced by $-i\omega$, so that the equation of motion (2.48) becomes

$$m(-i\omega)^2\mathbf{x} + m\gamma(-i\omega)\mathbf{x} + m\omega_s^2\mathbf{x} = -e\mathbf{E}_i$$

where we have suppressed the explicit $e^{-i\omega t}$ factor that appears in each term. Combining factors, we see that the harmonic displacement is given by

$$\mathbf{x} = \frac{1}{\omega^2 - \omega_s^2 + i\gamma\omega}\frac{e\mathbf{E}_i}{m} \tag{2.49}$$

and thus the acceleration is

$$\mathbf{a} = \frac{-\omega^2}{\omega^2 - \omega_s^2 + i\gamma\omega}\frac{e\mathbf{E}_i}{m} \tag{2.50}$$

Following the procedures used earlier for the free electron [Eqs. (2.38), (2.39), and (2.44)], we obtain the semi-classical *scattering cross-section for a bound electron* of resonant frequency ω_s:

$$\sigma = \frac{8\pi}{3}r_e^2\frac{\omega^4}{\left(\omega^2 - \omega_s^2\right)^2 + (\gamma\omega)^2} \tag{2.51}$$

[‖] J.D. Jackson, Ref. 1, p. 309.

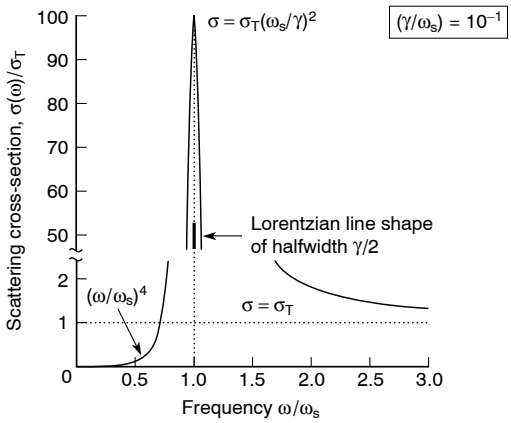

FIGURE 2.8. The semi-classical scattering cross-section, Eq. (2.51), for a bound electron of resonant energy $\hbar\omega_s$ and an assumed damping factor $\gamma/\omega_s = 0.1$.

where we note that the scattering cross-section for bound electrons displays a strong frequency dependence, especially near the resonance.

This is substantially different from the free electron cross-section, which is frequency independent. The form of the bound electron cross-section is illustrated in Figure 2.8. This semi-classical result shows a strong resonance at $\omega \simeq \omega_s$, with a peak cross-section very large compared to the free electron result. Near resonance the line shape approximates that of a Lorentzian of half width at half maximum $\gamma/2$. For very large frequencies the cross-section approaches Thomson's result [Eq. (2.45)] for the free electron. In this very high frequency limit, where $\omega^2 \gg \omega_s^2$, the bound electrons scatter as though they were free. In this case the oscillations forced by the incident radiation are too rapid to be affected by the natural response of the resonant system. For incident frequencies well below the resonant frequency, such that $\omega^2 \ll \omega_s^2$ and $\gamma \ll \omega_s$, the cross-section takes on a form first described by Lord Rayleigh:[18]

$$\sigma_R = \frac{8\pi}{3} r_e^2 \left(\frac{\omega}{\omega_s}\right)^4 = \frac{8\pi}{3} r_e^2 \left(\frac{\lambda_s}{\lambda}\right)^4 \tag{2.52}$$

which has a very strong (λ^{-4}) wavelength dependence.

Rayleigh first used this result in 1899 to explain the blue color of the sky. The photon energies ($\hbar\omega$) of visible light extend from about 1.8 eV (7000 Å) for red to about 2.3 eV (5300 Å) for green and about 3.3 eV (3800 Å) for blue light. The bound electrons of atmospheric oxygen and nitrogen, with UV resonances at 8.6 eV and 8.2 eV (1520 Å), respectively, cause very strong scattering at the shorter visible light wavelengths. Indeed, the λ^{-4} wavelength dependence of the scattering cross-section gives a factor of about 2^4, or 16 times more scattering for blue light than for red. This explains both the blue appearance of the sky when looking overhead, and the residual red appearance of the setting sun – the latter being observed in direct viewing after the light has propagated over a long path in which the blue, green, etc. have been preferentially scattered to the other directions, as illustrated in Figure 2.9. For a quantum mechanical description of resonant scattering, including lifetime and Doppler (motion) effects, refer to Loudon, Ref. 12, pp. 314–318 and 70–78.

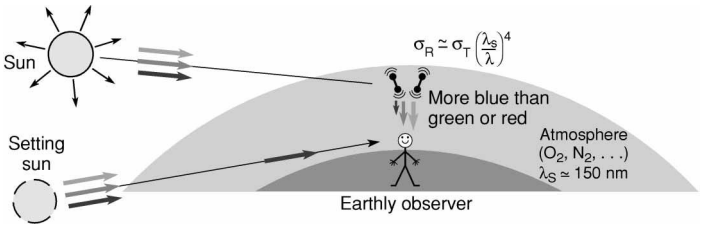

FIGURE 2.9 (see Colorplate II). Looking upward, the earthly observer at night sees only blackness or the occasional star. However during daylight, indirect light is scattered toward the observer when looking overhead. This scattering is caused by non-uniformities in the atmospheric density of O_2 and N_2, and appears blue because of the strong wavelength dependence of bound electron scattering. Upon direct viewing of the sun, particularly at sunset, the light path is long and passes through the most dense portion of the atmosphere. As much of the residual light reaching the observer at sunset is greatly depleted in blue and green, the sun appears red, as do any clouds off which this reddish light reflects. Very fine atmospheric dust, such as volcanic ash, causes a similar effect.

2.7 SCATTERING BY A MULTI-ELECTRON ATOM

In this section we turn to the subject of scattering by an atom that contains many electrons. We again use a semi-classical model of point electrons, each with its own resonant frequency, excited by a continuous electromagnetic wave. Because we do not wish to make the assumption that the wavelength is long compared to atomic dimensions – which is often not true for x-rays – we permit each of the electrons to have separate coordinates. Although this is a very simple atomic model, it gives valuable insights into the angular and wavelength limitations of various scattering formulae.

In this semi-classical model we can write the electron distribution function within the atom as

$$n(\mathbf{r}, t) = \sum_{s=1}^{Z} \delta[\mathbf{r} - \Delta\mathbf{r}_s(t)] \tag{2.53}$$

where $\mathbf{r}$ is the coordinate of the nucleus, $\Delta\mathbf{r}$ is the vector displacement from the nucleus, and Z is the total number of electrons held by the atom. The total current density can be written as

$$\mathbf{J}(\mathbf{r}, t) = -e \sum_{s=1}^{Z} \delta[\mathbf{r} - \Delta\mathbf{r}_s(t)]\mathbf{v}_s(t) \tag{2.54}$$

where for the purposes of scattering calculations $\mathbf{v}_s(t)$ will be dominated by the incident field. The assumption that $\mathbf{v}_s$ is dominated by the incident field, ignoring the effect of waves scattered by neighboring electrons, is referred to as the *Born approximation*.

To make use of our radiated power and scattering cross-section formulae we follow the procedures developed earlier, first calculating the $\mathbf{k}, \omega$ transform of $\mathbf{J}(\mathbf{r}, t)$ [see Eq. (2.13b)]:

$$\mathbf{J}_{k\omega} = \int_{\mathbf{r}} \int_{t} \mathbf{J}(\mathbf{r}, t) e^{i(\omega t - \mathbf{k}\cdot\mathbf{r})}\, d\mathbf{r}\, dt$$

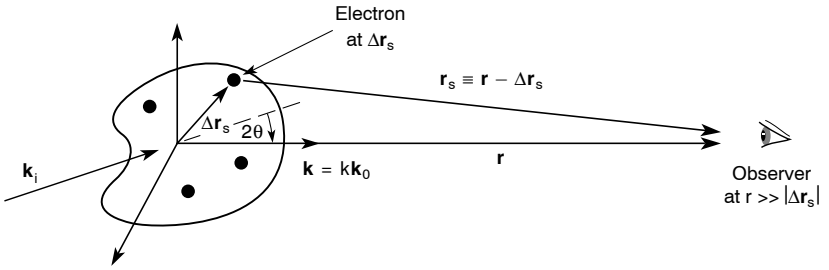

FIGURE 2.10. Scattering diagram for radiation incident on a many-electron atom, semi-classically described as a collection of quantized point electrons surrounding a nucleus of charge $+Ze$ at $\mathbf{r} = 0$.

which with Eq. (2.54) becomes

$$\mathbf{J}_{k\omega} = -e \sum_{s=1}^{Z} \iint \delta(\mathbf{r} - \Delta\mathbf{r}_s)\mathbf{v}_s(t) e^{i(\omega t - \mathbf{k}\cdot\mathbf{r})}\, d\mathbf{r}\, dt$$

$$\mathbf{J}_{k\omega} = -e \sum_{s=1}^{Z} e^{-i\mathbf{k}\cdot\Delta\mathbf{r}_s} \underbrace{\int \mathbf{v}_s(t) e^{i\omega t}\, dt}_{\mathbf{v}_s(\omega)}$$

where we have assumed that the time dependence of $\Delta\mathbf{r}_s(t)$ due to positional variation of the electrons is on a slower time scale than ω^{-1} and thus separable to first order from the integration. Recognizing the time integral as the Laplace transform $\mathbf{v}_s(\omega)$, we have

$$\mathbf{J}_{k\omega} = -e \sum_{s=1}^{Z} e^{-i\mathbf{k}\cdot\Delta\mathbf{r}_s} \mathbf{v}_s(\omega) \tag{2.55}$$

Continuing to follow our earlier procedures, the electric field scattered by the Z electrons of the atom is given by Eq. (2.19):

$$\mathbf{E}(\mathbf{r}, t) = \int_{\mathbf{k}} \int_{\omega} \frac{-i\omega}{\epsilon_0} \frac{\mathbf{J}_{T_{k\omega}} e^{-i(\omega t - \mathbf{k}\cdot\mathbf{r})}}{\omega^2 - k^2c^2} \frac{d\mathbf{k}\, d\omega}{(2\pi)^4}$$

$$\mathbf{E}(\mathbf{r}, t) = -\frac{e}{\epsilon_0} \sum_{s=1}^{Z} \int_{\mathbf{k}} \int_{\omega} \frac{(-i\omega) e^{-i\mathbf{k}\cdot\Delta\mathbf{r}_s} \mathbf{v}_{T,s}(\omega) e^{-i(\omega t - \mathbf{k}\cdot\mathbf{r})}}{\omega^2 - k^2c^2} \frac{d\mathbf{k}\, d\omega}{(2\pi)^4}$$

$$\mathbf{E}(\mathbf{r}, t) = -\frac{e}{\epsilon_0} \sum_{s=1}^{Z} \int_{\mathbf{k}} \int_{\omega} \frac{(-i\omega) e^{i\mathbf{k}\cdot(\mathbf{r} - \Delta\mathbf{r}_s)} \mathbf{v}_{T,s}(\omega) e^{-i\omega t}}{(\omega - kc)(\omega + kc)} \frac{d\mathbf{k}\, d\omega}{(2\pi)^4}$$

where $\mathbf{v}_{T,s}(\omega)$ is the component of $\mathbf{v}_s(\omega)$ transverse to the direction of propagation (observation) $\mathbf{k}$. The quantity $\mathbf{r} - \Delta\mathbf{r}_s$ in the exponent is identified as the vector distance from the particular s-electron ($\Delta\mathbf{r}_s$) to the observation point ($\mathbf{r}$), as illustrated in Figure 2.10.

Shown in Figure 2.10 are the various point electrons at their positions $\Delta\mathbf{r}_s$ (measured from the nucleus at $\mathbf{r} = 0$), an incident wavevector $\mathbf{k}_i$, and the scattered wavevector $\mathbf{k}$ propagating toward the observer at $\mathbf{r}$. Note that the scattered wavevector $\mathbf{k}_0$ is at angle 2θ (lowercase) to the incident wavevector $\mathbf{k}_i$, and that this *scattering angle* is different from Θ (uppercase),

which is the angle between E_i (not shown) and $\mathbf{k}$. Note also that the diagram defines the vector position of each electron as seen by the observer,

$$\mathbf{r}_s \equiv \mathbf{r} - \Delta\mathbf{r}_s \tag{2.56}$$

With this definition the expression for $\mathbf{E}(\mathbf{r}, t)$ becomes

$$\mathbf{E}(\mathbf{r}, t) = -\frac{e}{\epsilon_0}\sum_{s=1}^{Z}\int_{\mathbf{k}}\int_{\omega}\frac{(-i\omega)e^{i\mathbf{k}\cdot\mathbf{r}_s}\mathbf{v}_{T,s}(\omega)e^{-i\omega t}}{(\omega - kc)(\omega + kc)}\frac{d\mathbf{k}\,d\omega}{(2\pi)^4}$$

where now $\mathbf{r}_s$ is the vector distance to the point at which radiated fields are detected. Proceeding as before with the $d\mathbf{k}\,d\omega$ integrals, which led to Eq. (2.25), we find for the multi-electron atom that

$$\mathbf{E}(\mathbf{r}, t) = \frac{e}{4\pi\epsilon_0 c^2}\sum_{s=1}^{Z}\frac{1}{|\mathbf{r}_s|}\frac{d}{dt}\mathbf{v}_{T,s}\underbrace{\left(t - \frac{|\mathbf{r}_s|}{c}\right)}_{t'_s}$$

where there now appears a retarded time of observation $t'_s = t - |\mathbf{r}_s|/c$ appropriate to each electron. Defining the scalar magnitude of observer distance to the sth electron as

$$r_s \equiv |\mathbf{r}_s|$$

the expression for the electric field scattered from a multi-electron atom becomes

$$\mathbf{E}(\mathbf{r}, t) = \frac{e}{4\pi\epsilon_0 c^2}\sum_{s=1}^{Z}\frac{\mathbf{a}_{T,s}\,(t - r_s/c)}{r_s} \tag{2.57}$$

which is an evident extension of the earlier result for a single electron [Eq. (2.25)].

Using expressions for the transverse acceleration of each bound electron, $\mathbf{a}_{T,s}$, in terms of the incident field $\mathbf{E}_i$ which excites it to oscillation, we can calculate the scattered power and cross-section. We can write the equation of motion for each of these electrons as

$$m\frac{d^2\mathbf{x}_s}{dt^2} + m\gamma\frac{d\mathbf{x}_s}{dt} + m\omega_s^2\mathbf{x}_s = -e(\mathbf{E}_i + \underbrace{\mathbf{v}_s \times \mathbf{B}}_{\simeq 0}) \tag{2.58}$$

where in this case we must be careful to keep the spatial dependence of the incoming wave in order to account for the differing phase seen by each electron. To do so we rewrite the electric field as

$$\mathbf{E}_i(\mathbf{r}, t) \rightarrow \mathbf{E}_i e^{-i(\omega t - \mathbf{k}_i\cdot\Delta\mathbf{r}_s)} \tag{2.59}$$

where we explicitly label the incoming (incident) wavevector as $\mathbf{k}_i$. Combining Eqs. (2.58) and (2.59), we proceed as before to a solution of the equation of motion (at position $\Delta\mathbf{r}_s$) for the oscillatory motion of a bound electron in the presence of an incident electromagnetic field:

$$\mathbf{x}_s(t) = \frac{1}{\omega^2 - \omega_s^2 + i\gamma\omega}\frac{e}{m}\,\mathbf{E}_i\,e^{-i(\omega t - \mathbf{k}_i\cdot\Delta\mathbf{r}_s)} \tag{2.60}$$

and

$$\mathbf{a}_s(t) = \frac{-\omega^2}{\omega^2 - \omega_s^2 + i\gamma\omega}\,\frac{e}{m}\,\mathbf{E}_i\, e^{-i(\omega t - \mathbf{k}_i\cdot\Delta\mathbf{r}_s)} \tag{2.61}$$

The electric field scattered by a multi-electron atom to a distant observer can now be obtained by combining Eqs. (2.57) and (2.61), defining the transverse component of acceleration as was done previously for the single electron case, and introducing the classical electron radius [Eq. (2.44)], so that in terms of field amplitudes

$$E(\mathbf{r}, t) = \frac{-e^2}{4\pi\epsilon_0 mc^2}\sum_{s=1}^{Z}\frac{\omega^2 E_i \sin\Theta}{\omega^2 - \omega_s^2 + i\gamma\omega}\,\frac{1}{r_s}\,e^{-i[\omega(t - r_s/c) - \mathbf{k}_i\cdot\Delta\mathbf{r}_s]}$$

where $\mathbf{r}_s \equiv \mathbf{r} - \Delta\mathbf{r}_s$ and $r_s = |\mathbf{r}_s|$. For $r \gg \Delta r_s$ we can write to good approximation (see the boxed note below)

$$r_s \simeq r - \mathbf{k}_0\cdot\Delta\mathbf{r}_s \tag{2.62}$$

Note on the relative phase terms *for a multi-electron atom:* If $\mathbf{r}_s = \mathbf{r} - \Delta\mathbf{r}_s$ then

$$\mathbf{r}_s\cdot\mathbf{r}_s = (\mathbf{r} - \Delta\mathbf{r}_s)\cdot(\mathbf{r} - \Delta\mathbf{r}_s) = \mathbf{r}\cdot\mathbf{r} + \Delta\mathbf{r}_s\cdot\Delta\mathbf{r}_s - 2\mathbf{r}\cdot\Delta\mathbf{r}_s$$

$$r_s^2 = r^2 + \Delta r_s^2 - 2\mathbf{r}\cdot\Delta\mathbf{r}_s$$

For $r \gg \Delta r_s$,

$$r_s^2 \simeq r^2 - 2\mathbf{r}\cdot\Delta\mathbf{r}_s = r^2\left(1 - \frac{2\mathbf{r}\cdot\Delta\mathbf{r}_s}{r^2}\right)$$

$$r_s \simeq r\left(1 - \frac{\mathbf{r}\cdot\Delta\mathbf{r}_s}{r^2}\right)$$

and for $\mathbf{r}$ in the $\mathbf{k}_0$-direction (see Figure 2.10)

$$\frac{\mathbf{r}}{r} \equiv \mathbf{r}_0 = \mathbf{k}_0$$

Thus for $r \gg \Delta r_s$

$$r_s \simeq r - \mathbf{k}_0\cdot\Delta\mathbf{r}_s$$

as given in Eq. (2.62).

We can simplify the expression for $\mathbf{E}(\mathbf{r}, t)$ by approximating r_s by r in the slowly varying amplitude term, while retaining it in the rapidly varying phase term. The electric field is then

$$E(r, t) = -r_e\sum_{s=1}^{Z}\frac{\omega^2 E_i \sin\Theta}{\omega^2 - \omega_s^2 + i\gamma\omega}\,\frac{1}{r}\exp\left\{-i\left[\omega\left(t - \frac{r}{c}\right) + \omega\left(\frac{\mathbf{k}_0\cdot\Delta\mathbf{r}_s}{c}\right) - \mathbf{k}_i\cdot\Delta\mathbf{r}_s\right]\right\}$$

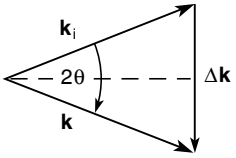

FIGURE 2.11. A vector scattering diagram for incident wave vector $\mathbf{k}_i$ and scattered wave vector $\mathbf{k}$. If both waves are at the same frequency (stationary scatterer), the vector diagram is isosceles.

Noting that $\omega/c = k$ and that $k\mathbf{k}_0 = \mathbf{k}$, the phase term can be written more compactly as

$$E(\mathbf{r}, t) = -r_e \sum_{s=1}^{Z} \frac{\omega^2 E_i \sin\Theta}{\omega^2 - \omega_s^2 + i\gamma\omega} \frac{1}{r} \exp\left\{ -i\left[\omega\left(t - \frac{r}{c}\right) + \underbrace{(\mathbf{k} - \mathbf{k}_i)}_{\Delta\mathbf{k}} \cdot \Delta\mathbf{r}_s\right]\right\}$$

where we have introduced the quantity $\Delta\mathbf{k}$ defined by

$$\Delta\mathbf{k} = \mathbf{k} - \mathbf{k}_i \tag{2.63}$$

where $\Delta\mathbf{k}$ is the vector periodicity associated with the inhomogeneity of the medium that results in a wave of propagation vector $\mathbf{k}_i$ being scattered into a direction characterized by the scattered wavevector $\mathbf{k}$. This *density fluctuation wave vector*, denoted here by $\Delta\mathbf{k}$, is a quantity one encounters generally in the study of scattering processes, including the scattering of light or x-rays from crystals, plasma waves, and a host of other non-uniform density distributions.

Since both $\mathbf{k}$ and $\mathbf{k}_i$ propagate in vacuum, the magnitudes of the wave vectors satisfy $|\mathbf{k}| = |\mathbf{k}_i| = \omega/c$, so that the scattering diagram, illustrated in Figure 2.11, is isosceles with

$$|\Delta\mathbf{k}| = 2k_i \sin\theta \tag{2.64}$$

With simple identifications this will be recognized as the Bragg equation, $\lambda = 2d\sin\theta$, where $k_i = 2\pi/\lambda$ and for a crystal the periodicity is $\Delta k = 2\pi/d$. A powerful insight into this simple equation (2.64) is that electron density distributions of periodicity d scatter radiation of wavelength λ through an angle 2θ, and can thus provide a Fourier analysis technique useful in many fields of study.

Using the definition $\Delta\mathbf{k}$ in the expression for $\mathbf{E}(\mathbf{r}, t)$, we have

$$E(\mathbf{r}, t) = -\frac{r_e}{r} \underbrace{\left[\sum_{s=1}^{Z} \frac{\omega^2 e^{-i\Delta\mathbf{k}\cdot\Delta\mathbf{r}_s}}{\omega^2 - \omega_s^2 + i\gamma\omega}\right]}_{f(\Delta\mathbf{k}, \omega)} E_i \sin\Theta\, e^{-i\omega(t - r/c)} \tag{2.65}$$

where the quantity $f(\Delta\mathbf{k}, \omega)$ is the *complex atomic scattering factor*

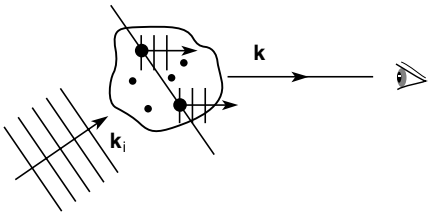

FIGURE 2.12. Scattering diagram for a multi-electron atom. Note that the two electrons shown as large dots see the same incident phase, but are of different phase to the observer.

$$f(\Delta\mathbf{k}, \omega) = \sum_{s=1}^{Z} \frac{\omega^2 e^{-i\Delta\mathbf{k}\cdot\Delta\mathbf{r}_s}}{\omega^2 - \omega_s^2 + i\gamma\omega} \tag{2.66}$$

a function of the incident wave frequency ω, the various resonance frequencies ω_s of the bound electrons, and the phase terms due to their various positions within the atom, $\Delta k \cdot \Delta\mathbf{r}_s$. The atomic scattering factor describes the electric field amplitude of the scattered wave relative to that scattered by a free electron:

$$E(\mathbf{r}, t) = -\frac{r_e f(\Delta\mathbf{k}, \omega) E_i \sin\Theta}{r} e^{-i\omega(t-r/c)} \tag{2.67}$$

where for the referenced (single) free electron, Eq. (2.43), ω_s, γ, and Δr_s are zero, so that $f(\Delta\mathbf{k}, \omega)$ is unity. Note that the expression $\Delta\mathbf{k} \cdot \Delta\mathbf{r}_s$ gives the phase variation of the scattered fields, due to differing electron positions, as seen by the observer. Thus that product contains both the different incident phases seen by the various electrons and the phase variations due to the different path lengths to the observer (see Figure 2.12).

Having determined $\mathbf{E}(\mathbf{r}, t)$ for the semi-classical multi-electron atom, we can now calculate the *differential and total scattering cross-sections* following the procedures used earlier in this chapter for the free electron, obtaining

$$\frac{d\sigma(\omega)}{d\Omega} = r_e^2 |f|^2 \sin^2\Theta \tag{2.68}$$

$$\sigma(\omega) = \frac{8\pi}{3} |f|^2 r_e^2 \tag{2.69}$$

where the complex atomic scattering factor (2.66) is

$$f(\Delta\mathbf{k}, \omega) = \sum_{s=1}^{Z} \frac{\omega^2 e^{-i\Delta\mathbf{k}\cdot\Delta\mathbf{r}_s}}{\left(\omega^2 - \omega_s^2 + i\gamma\omega\right)}$$

and where the cross-sections (2.68) and (2.69) now display not only the various resonances and a damping term, but also explicit phase terms $e^{-i\phi_s}$ allowing for the discrete positions of the various electrons in the semi-classical atom – factors that are significant when λ is less than or similar to the atomic radius. In general the $\Delta\mathbf{k} \cdot \Delta\mathbf{r}_s$ phase terms do not simplify, and treatment of the complex atomic scattering factor is problematical. However, in two special situations $f(\Delta\mathbf{k}, \omega)$ does simplify. To understand these two special cases we reconsider the

vector scattering diagram of Figure 2.12. We recall Eq. (2.64):

$$|\Delta\mathbf{k}| = 2k_i \sin\theta$$

where $k_i = 2\pi/\lambda$, so that

$$\Delta k = \frac{4\pi}{\lambda} \sin\theta$$

With the charge distribution within the atom largely contained within dimensions of the order of the Bohr radius,** traditionally written as a_0, the phase term in Eq. (2.66) for the complex atomic scattering function is bounded by

$$|\Delta\mathbf{k} \cdot \Delta\mathbf{r}_s| \leq \frac{4\pi a_0}{\lambda} \sin\theta \tag{2.70}$$

where the inequality results from the nature of the vector dot product. The phase expression in (2.70) clearly simplifies in two special cases:

$$|\Delta\mathbf{k} \cdot \Delta\mathbf{r}_s| \to 0 \quad \text{for } a_0/\lambda \ll 1 \qquad \text{(long wavelength limit)} \tag{2.71}$$

$$|\Delta\mathbf{k} \cdot \Delta\mathbf{r}_s| \to 0 \quad \text{for } \theta \ll 1 \qquad \text{(forward scattering)} \tag{2.72}$$

In each of these two cases the atomic scattering factor $f(\Delta\mathbf{k}, \omega)$ reduces to

$$f^0(\omega) = \sum_{s=1}^{Z} \frac{\omega^2}{\omega^2 - \omega_s^2 + i\gamma\omega} \tag{2.72}$$

where we denote these special cases by the superscript zero.

It is convenient at this point to introduce the concept of *oscillator strengths*, g_s, which in the simple semi-classical model are integers that indicate the number of electrons associated with a given resonance frequency ω_s. In such a model one could associate two electrons with a K-shell resonance, six with an L-shell resonance, etc. Spectroscopists have long taken this model a step further, introducing fractional oscillator strengths to accommodate known probabilities for transition to various higher-lying energy states for each atom. Thus we take the sum of oscillator strengths as equal to the total number of electrons:

$$\sum_s g_s = Z \tag{2.73}$$

A shortcoming of the semi-classical model, among others, is that while it gives the proper form of scattering cross-sections and refractive index, it does not provide a basis for calculating oscillator strengths. In the quantum mechanical description[12–15] these oscillator strengths†† arise naturally as non-integer *transition probabilities*, g_{kn}, between stationary states ψ_k and ψ_n of the atom, leading to an expression similar to Eq. (2.73) when summed over final states

**For example see Chapter 1, Figure 1.12. Note that the Bohr radius for the ground state of the hydrogen atom ($n = 1$) is $a_0 = 4\pi\epsilon_0\hbar^2/me^2 = 0.529$ Å.

††In the literature the symbol f is commonly used to represent both scattering factor and oscillator strength. To avoid confusion we use g to represent oscillator strength in this chapter and in Chapter 3. In Chapter 7, where the scattering factor does not occur, we use f for oscillator strength.

n from an initial state k:

$$\sum_n g_{kn} = Z \tag{2.74}$$

Equation (2.74) is known[14,15,19] as the Thomas–Reiche–Kuhn sum rule. It was deduced before wave mechanics was introduced to provide the modern understanding of quantum mechanics.

Introducing the oscillator strengths, we can rewrite the atomic scattering cross-sections (2.72) for the special cases of *long wavelength* ($\lambda \gg a_0$) or *small angles* ($\theta \ll \lambda/a_0$) as

$$\boxed{\frac{d\sigma(\omega)}{d\Omega} = r_e^2 |f^0(\omega)|^2 \sin^2 \Theta} \tag{2.75}$$

and

$$\boxed{\sigma(\omega) = \frac{8\pi}{3} r_e^2 |f^0(\omega)|^2} \tag{2.76}$$

where now

$$\boxed{f^0(\omega) = \sum_s \frac{g_s \omega^2}{\omega^2 - \omega_s^2 + i\gamma\omega}} \tag{2.77}$$

where again $\sum_s g_s = Z$. Although based on a very simple semi-classical model, Eqs. (2.75–2.77) give a solution for the scattering of radiation by a multi-electon atom, which, except for the different interpretations of oscillator strengths, is identical within the limitations discussed to that derived by modern quantum mechanical techniques. These limitations require that either the wavelength be large compared to atomic dimensions [Eq. (2.71a)] or that the scattering be in the forward direction [Eq. (2.71b)], and also that the photon energy be not too close to an atomic resonance, as that case requires an understanding of lifetimes (damping rates γ), which is not addressed by the semi-classical model.[20]

An interesting limit of scattering involves low-Z atoms and relatively long wavelength soft x-rays and extreme ultraviolet radiation, for which λ/a_0 is much greater than unity. Such scattering played a role in the development of early atomic theory[19] in that it gave evidence of the number of electrons bound to the atom. In this very special case one can simultaneously satisfy the conditions that $\omega^2 \gg \omega_s^2$ and $\lambda/a_0 \gg 1$, so that the atomic scattering factor $f(\Delta\mathbf{k}, \omega)$ reduces to[‡‡]

$$f(\Delta\mathbf{k}, \omega) \rightarrow f^0(\omega) \rightarrow \sum_s g_s = Z \tag{2.78a}$$

[‡‡]For high-Z atoms some orbits bring electrons very close to the nucleus, at highly relativistic velocities, thus increasing their mass and decreasing their scattering strength from that of a free electron. Corrections of order $(Z\alpha)^2$, where α is the fine structure constant, are discussed in the literature.[22]

and thus

$$\frac{d\sigma(\omega)}{d\Omega} \simeq Z^2 r_e^2 \sin^2\Theta = Z^2 \frac{d\sigma_T}{d\Omega} \tag{2.78b}$$

and

$$\sigma(\omega) \simeq \frac{8\pi}{3} r_e^2 Z^2 = Z^2 \sigma_e \tag{2.78c}$$

Thus, for example, a carbon atom ($Z = 6$) scatters 4 Å wavelength radiation about 36 times more than that of a single free electron. In this case we say that the six electrons are scattering *coherently* in all directions, that is, the scattered electric fields from all atomic electrons add in phase at all distant points of observation. In the case of carbon at 4 Å wavelength, the photon energy is $\hbar\omega \simeq 3$ keV, well above the binding energy of the most tightly held electrons, the K-shell electrons, for which the binding energy is about 284 eV (Ref. 21). This is indeed much less than the photon energy (3 keV), and λ is much greater than the Bohr radius, $a_0 \simeq 0.5$ Å.

For both scattering and refractive index (the latter to be considered in the next chapter) we will want to determine the real and imaginary parts of $f^0(\omega)$, which we will write as[23]¶¶

$$f^0(\omega) = f_1^0(\omega) - i f_2^0(\omega) \tag{2.79}$$

where the sign of the imaginary portion is chosen to be consistent with our use of $e^{-i\omega t}$ time dependence. In general these are not calculable for the many electron atom. We will see in Chapter 3 that there is a very close relation between forward scattering ($\theta = 0$), where we can use the f^0 approximation, and refractive index. Indeed, we will determine that the refractive index $n(\omega)$ can be written as[19]

$$n(\omega) = 1 - \delta + i\beta = 1 - \frac{n_a r_e \lambda^2}{2\pi}\left(f_1^0 - i f_2^0\right) \tag{2.80}$$

relating the complex atomic scattering factor for forward scattering ($\theta = 0$) to both phase velocity variation, through f_1^0, and wave amplitude decay due to absorption, through the imaginary component f_2^0. We will address the experimental determination of f_1^0 and f_2^0 in the next chapter. At this point we simply note that these quantities are tabulated,[21] and attach as an example the data for carbon as Figure 2.13. Note that for the special case of low-Z atoms (such as carbon), the approximation $\lambda \gg a_0$ combined with $\hbar\omega \gg \hbar\omega_s$ does work well. In the case of carbon cited above, the tabulated data gives $f_1^0 \simeq 6.1$, which is very close to the value of Z. The tabulated value $f_2^0 \simeq 0.071$ shows that absorption is relatively weak well above the binding energy. Note, however, that in general f_1^0 and f_2^0 are very strong functions of photon energy, particularly near absorption edges. In the limit of very high photon energy the binding energies become relatively unimportant and all electrons scatter as though they were free. In this limit f_1^0 goes to Z, and f_2^0 goes to zero. Discussions of the oscillator strength sum rules for intermediate energies are given by Soufli[24] and Wooten.[17] Note too that the tabulations are for $f^0(\omega)$, not $f(\Delta\mathbf{k}, \omega)$, and thus do not address angular effects at short wavelengths. Nonetheless, the data is very useful for refractive index and long wavelength (soft x-ray) scattering where these specialized approximations are valid.

¶¶Note that at high frequencies, such that $\omega^2 \gg \omega_s^2$, Eq. (2.77) goes to the limit $f^0(\omega) \simeq \sum_s g_s = Z$. For this reason some authors[14] write $f_1^0(\omega)$ as a decrement from the total electronic charge, $Z + \Delta f_1^0(\omega)$.

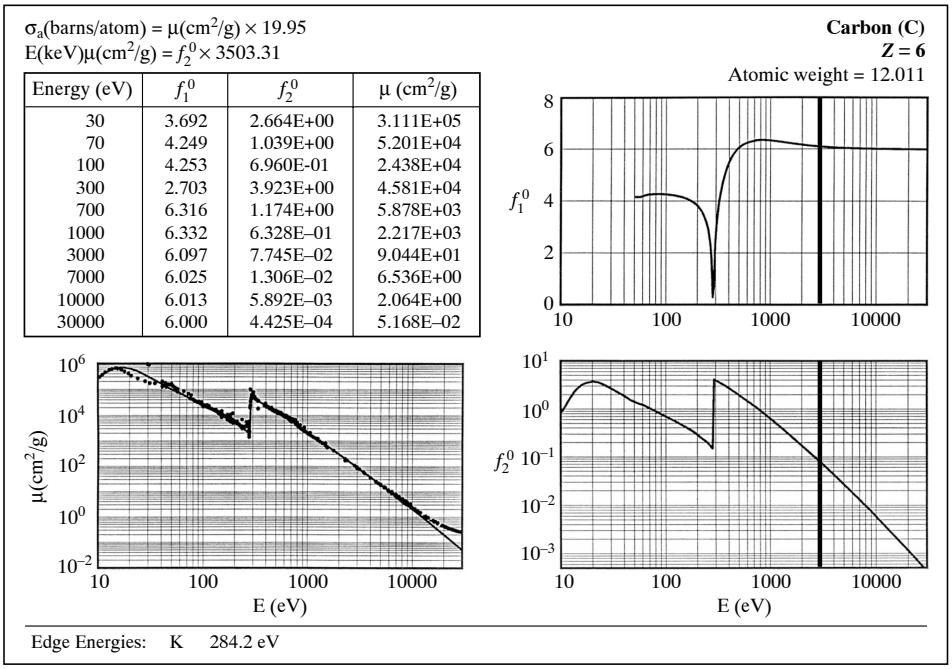

FIGURE 2.13. Tabulated real (f_1^0) and imaginary (f_2^0) parts of the atomic scattering factor for the carbon atom in the limit (superscript zero) of long wavelength or small scattering angle. Note that the sign of f_2^0 is consistent with the mathematical representation of forward wave propagation as $\exp[-i(\omega t - \mathbf{k}\cdot\mathbf{r})]$. Data is from Henke, Gullikson, and Davis[21]; also see E. Gullikson.[23]

REFERENCES

1. J.D. Jackson, *Classical Electrodynamics* (Wiley, New York, 1998), Third Edition.
2. S. Ramo, J. Whinnery, and T. Van Duzer, *Fields and Waves in Communication Electronics* (Wiley, New York, 1984), Chapter 3.
3. J.A. Stratton, *Electromagnetic Theory* (McGraw Hill, New York, 1941), pp. 135–137.
4. M. Born and E. Wolf, *Principles of Optics* (Cambridge Univ. Press, 1999), Seventh Edition.
5. G.S. Smith, *Classical Electromagnetic Radiation* (Cambridge Univ. Press, 1997).
6. Following N. Marcuvitz, *Notes on Plasma Turbulence,* unpublished (New York University, 1969).
7. P.C. Clemmow, *The Plane Wave Spectrum Representation of Electromagnetic Fields* (Pergamon, Oxford, 1966).
8. E. Kreyszig, *Advanced Engineering Mathematics* (Wiley, New York, 1993), Seventh Edition, p. 770.
9. R Leighton, *Principles of Modern Physics* (McGraw-Hill, New York, 1959), p. 410.
10. W. Heitler, *The Quantum Theory of Radiation* (Clarendon Press, Oxford, 1954).
11. D. Evans and J. Katzenstein, *Rpts. Progress Phys. (London) 32*, 207 (April 1969).
12. R. Loudon, *The Quantum Theory of Light* (Oxford Univ. Press, London, 1983), Second Edition.
13. D.I. Blokhintsev, *Quantum Mechanics* (Gordon and Breach, New York, 1964).
14. R.W. James, *The Optical Principles of the Diffraction of X-Rays* (Bell, London, 1962), Chapter IV.
15. R.L. Liboff, *Introductory Quantum Mechanics* (Addison-Wesley, Reading, MA, 1998), Third Edition, Section 13.9; also see J.C. Slater, *The Quantum Theory of Matter* (McGraw Hill, New York, 1968), Second Edition, Chapter 14.
16. R. Eisberg and R. Resnick, *Quantum Physics of Atoms, Molecules, Solids, Nuclei and Particles* (Wiley, New York, 1985).

17. F. Wooten, *Optical Properties of Solids* (Academic Press, New York, 1972), Chapter 3.
18. Lord Rayleigh, *Phil. Mag. (London) XLVII*, 375–384 (1899); *Scientific Papers, Vol. IV* (Dover, New York, 1964), p. 397.
19. A.H. Compton and S.K. Allison, *X-Rays in Theory and Practice* (Van Nostrand, New York, 1935), Second Edition.
20. See J.C. Slater, Ref. 15, pp. 276–280, comparing the semi-classical and quantum mechanical interpretations. References 12–14 have similar discussions.
21. B.L. Henke, E.M. Gullikson, and J.C. Davis, "X-Ray Interactions: Photoabsorption, Scattering, Transmission and Reflection," *Atomic and Nuclear Data 54*, 181–342 (1993).
22. L. Kissel and R.H. Pratt, "Rayleigh Scattering: Elastic Photon Scattering by Bound Electrons," p. 465 in *Atomic Inner Shell Physics* (Plenum, New York, 1985), B. Crasemann, Editor.
23. E.M. Gullikson, "Optical Properties of Materials," Chapter 13, pp. 257–270, in *Vacuum Ultraviolet Spectroscopy I* (Academic Press, New York, 1998), J.A.R. Samson and D.L. Ederer, Editors.
24. R. Soufli, "Optical Constants of Materials in the EUV/Soft X-Ray Region for Multilayer Mirror Applications," Ph.D. thesis, Department of Electrical Engineering and Computer Science, University of California at Berkeley (1997).

HOMEWORK PROBLEMS

Homework problems for each chapter will be found at the website:
http://www.coe.berkeley.edu/AST/sxreuv

Chapter 3

WAVE PROPAGATION AND REFRACTIVE INDEX AT EUV AND SOFT X-RAY WAVELENGTHS

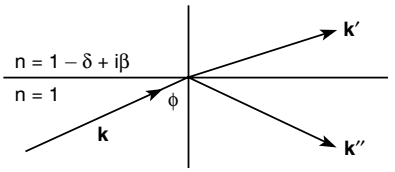

$$n(\omega) = 1 - \frac{n_a r_e \lambda^2}{2\pi}\left(f_1^0 - i f_2^0\right) \quad (3.9)$$

$$n(\omega) = 1 - \delta + i\beta \quad (3.12)$$

$$l_{\text{abs}} = \frac{\lambda}{4\pi\beta} \quad (3.22)$$

$$\sigma_{\text{abs.}} = 2 r_e \lambda f_2^0(\omega) \quad (3.28)$$

$$\Delta\phi = \left(\frac{2\pi\delta}{\lambda}\right)\Delta r \quad (3.29)$$

$$\theta_c = \sqrt{2\delta} \quad (3.41)$$

$$R_{s,\perp} \simeq \frac{\delta^2 + \beta^2}{4} \quad (3.50)$$

$$\phi_B \simeq \frac{\pi}{4} - \frac{\delta}{2} \quad (3.60)$$

In this chapter wave propagation in a medium of uniform atomic density is considered. Expressions for the induced motion of bound atomic electrons are used in combination with the wave equation to obtain the complex refractive index for EUV and soft x-ray propagation. This is then expressed in terms of the atomic scattering factors of Chapter 2. Phase velocity, absorption, reflection, and refraction are then considered. Results such as the total external reflection of x-rays at glancing incidence from the surface of a lossy material, the weak normal incidence reflection of x-rays, Brewster's angle, and Kramers–Kronig relations are obtained.

3.1 THE WAVE EQUATION AND REFRACTIVE INDEX

Here we consider the subjects of electromagnetic wave propagation, reflection, and refraction,[1–5] with particular emphasis on application to the EUV and soft x-ray regions of the spectrum. Here the wavelengths are very short, approaching atomic dimensions, and the photon energies are comparable to the binding energies of atomic electrons. Whereas in the previous chapter we considered scattering from a single atom, in this chapter we consider the effect of many atoms, each containing many electrons. We can imagine that in general this could be a very complicated problem; however, if we restrict ourselves to propagation in the forward direction, the problem simplifies significantly, leading to relatively simple expressions for the refractive index, related to those obtained in the previous chapter. Indeed, it is the sum of forward-scattered radiation from all atoms that interferes with the incident wave to produce a modified propagating wave, compared to that in vacuum. As the scattering process involves both elastic (lossless) and inelastic (dissipative) processes, the resultant refractive index is in general a complex quantity, describing not only a modified phase velocity, compared to that in vacuum (c), but also a wave amplitude that decays as it propagates.

Our point of departure for the study of refractive index is the vector wave equation [Chapter 2, Eq. (2.7)]

$$\left(\frac{\partial^2}{\partial t^2} - c^2\,\nabla^2\right)\mathbf{E}(\mathbf{r},t) = \frac{-1}{\epsilon_0}\left[\frac{\partial \mathbf{J}(\mathbf{r},t)}{\partial t} + c^2\nabla\rho(\mathbf{r},t)\right]$$

which, as seen in Chapter 2, follows directly from Maxwell's equations with the identification that [Eq. (2.8)]

$$c \equiv \frac{1}{\sqrt{\mu_0\epsilon_0}}$$

is the phase velocity for propagation in vacuum. For the propagation of transverse waves (**E** perpendicular to **k**) the $\nabla\rho$ term does not contribute, nor does the longitudinal component of **J**, i.e., the component of **J** in the direction of propagation [see the arguments in Chapter 2 leading to Eqs. (2.16) and (2.18)]. Thus for transverse electromagnetic waves of the form $\exp[-i(\omega t - \mathbf{k}\cdot\mathbf{r})]$, propagating in the vector **k**-direction, we need consider only field components transverse to **k**,

$$\left(\frac{\partial^2}{\partial t^2} - c^2\nabla^2\right)\mathbf{E}_{\mathrm{T}}(\mathbf{r},t) = -\frac{1}{\epsilon_0}\frac{\partial \mathbf{J}_{\mathrm{T}}(\mathbf{r},t)}{\partial t} \tag{3.1}$$

where the subscript T denotes a direction transverse to **k**, as illustrated previously in the vector coordinate system shown in Figure 2.3. The two possible transverse coordinates correspond to the two possible states of polarization. Equation (3.1) is recognized as the inverse Fourier–Laplace transform of Eq. (2.18), the transverse wave equation in **k**, ω-space.

To determine $\mathbf{J}_{\mathrm{T}}$ for the many-atom situation we must sum the contributions of all electrons. We recall from Chapter 2 that a passing electromagnetic wave of frequency ω induces an oscillatory electron motion of the same frequency, with an amplitude of oscillation given by [Eq. (2.49)]

$$\mathbf{x}(\mathbf{r},t) = \frac{e}{m}\frac{1}{\left(\omega^2 - \omega_s^2\right) + i\gamma\omega}\mathbf{E}(\mathbf{r},t)$$

where in the semi-classical model of the atom ω_s is the electron's natural frequency of oscillation, γ is a dissipative factor, and $\mathbf{E}(\mathbf{r}, t)$ is the electric field of the passing wave. For small amplitude oscillations, the oscillation velocity is thus

$$\mathbf{v}(\mathbf{r}, t) = \frac{e}{m} \frac{1}{\left(\omega^2 - \omega_s^2\right) + i\gamma\omega} \frac{\partial \mathbf{E}(\mathbf{r}, t)}{\partial t} \tag{3.2}$$

The total current density $\mathbf{J}(\mathbf{r}, t)$ must sum the contributions of all such bound electrons within an atom, and sum over all atoms. Were we interested in the scattering to all angles within this many atom system, we would have the formidable problem of describing not only the positions of all electrons within the atom, as was considered in Chapter 2, but also the relative positions of all atoms. However, in this chapter we restrict our interests to propagation only in the forward direction ($\theta = 0$), which as we saw in the previous chapter leads to a significant simplification. Indeed, we found that in the forward direction the positions of the individual electrons are irrelevant [Eq. (2.67)], as the forward-scattered radiation has the same phase, with respect to the incident radiation, for all electrons of like resonant frequency, independent of their positions. It is the interaction of these forward-scattered waves with the incident wave that contributes to modified propagation characteristics that we refer to as the refractive index – both the modified phase velocity and the amplitude decay.

As the electron positions do not affect forward propagation, we can simplify the current density expression for these purposes by introducing an expression with subscript zero, $J_0(\mathbf{r}, t)$, referring to the special case of forward scattering ($\theta = 0$) where now all similar atoms contribute identically, and the summation is only over like resonances, that is,

$$\mathbf{J}_0(\mathbf{r}, t) = -en_a \sum_s g_s \mathbf{v}_s(\mathbf{r}, t) \tag{3.3}$$

where n_a is the average density of atoms, and where the oscillator strengths for the various resonances sum to the total number of electrons per atom,* i.e., [Eq. (2.73)]

$$\sum_s g_s = Z$$

where Z is the number of electrons per atom. Combining Eqs. (3.2) and (3.3), the total current density $\mathbf{J}_0$ contributing to propagation in the forward direction is

$$\mathbf{J}_0(\mathbf{r}, t) = -\frac{e^2 n_a}{m} \sum_s \frac{g_s}{\left(\omega^2 - \omega_s^2\right) + i\gamma\omega} \frac{\partial \mathbf{E}(\mathbf{r}, t)}{\partial t} \tag{3.4}$$

Substituting this into the transverse wave equation (3.1), one has

$$\left(\frac{\partial^2}{\partial t^2} - c^2 \nabla^2\right) \mathbf{E}_\mathrm{T}(\mathbf{r}, t) = \frac{e^2 n_a}{\epsilon_0 m} \sum_s \frac{g_s}{\left(\omega^2 - \omega_s^2\right) + i\gamma\omega} \frac{\partial^2 \mathbf{E}_\mathrm{T}(\mathbf{r}, t)}{\partial t^2}$$

*As in Chapter 2, we use g_s for the oscillator strength to avoid confusion with the use of f for the scattering factor. In Chapter 7, Extreme Ultraviolet and Soft X-ray Lasers, the oscillator strength is represented by the more traditional f_{lu}.

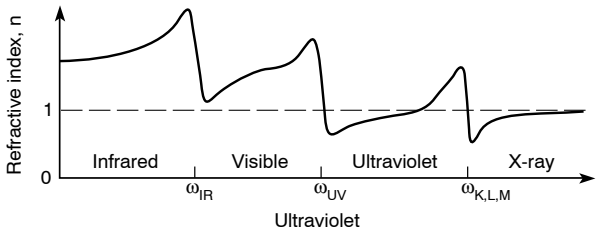

FIGURE 3.1. A sketch of refractive index showing the strong variations near IR, UV, and x-ray resonances (ω_s), and the general tendency toward unity for very short wavelengths where the frequencies are higher than all atomic resonances. Only the real part of the refractive index is shown here.

Combining terms with similar differential operators, one has

$$\left[\left(1 - \frac{e^2 n_a}{\epsilon_0 m}\sum_s \frac{g_s}{\left(\omega^2 - \omega_s^2\right) + i\gamma\omega}\right)\frac{\partial^2}{\partial t^2} - c^2\,\nabla^2\right]\mathbf{E}_{\mathrm{T}}(\mathbf{r}, t) = 0 \tag{3.5}$$

which can be rewritten in the standard form of the wave equation as

$$\left[\frac{\partial^2}{\partial t^2} - \frac{c^2}{n^2(\omega)}\nabla^2\right]\mathbf{E}_{\mathrm{T}}(\mathbf{r}, t) = 0 \tag{3.6}$$

where the frequency dependent refractive index $n(\omega)$ is identified as

$$n(\omega) \equiv \left[1 - \frac{e^2 n_a}{\epsilon_0 m}\sum_s \frac{g_s}{\left(\omega^2 - \omega_s^2\right) + i\gamma\omega}\right]^{1/2} \tag{3.7}$$

Note that we have used n for both the refractive index $n(\omega)$ and the number density n_a (atoms or electrons per unit volume), as is also common. The reader will have to be alert to these differences, generally differentiated by subscripts or indicated independent variables.

Note that as it appears in Eq. (3.7) the refractive index $n(\omega)$ has a strong frequency dependence, particularly near the resonant frequencies ω_s, and is thus said to be *dispersive*. That is, waves of different frequencies propagate at different phase velocities and thus tend to separate (disperse). It is a simple matter to show that for EUV/SXR radiation ω^2 is very large compared to the quantity $e^2 n_a/\epsilon_0 m$, so that to a high degree of accuracy the index of refraction can be written as

$$n(\omega) = 1 - \frac{1}{2}\frac{e^2 n_a}{\epsilon_0 m}\sum_s \frac{g_s}{\left(\omega^2 - \omega_s^2\right) + i\gamma\omega} \tag{3.8}$$

This equation predicts both positive and negative dispersion, depending on whether the frequency ω is less or greater than ω_s. This sign convention follows experience with visible light, where the resonances, ω_s are generally in the ultraviolet region for common glass lenses and prisms. Among early researchers this led to what became known as *normal dispersion*. Radiation for which $\omega > \omega_s$ was considered "anomalous." Figure 3.1 illustrates a generic refractive index across the electromagnetic spectrum with resonances in the infrared (IR), in the ultraviolet (UV), and the x-ray region.

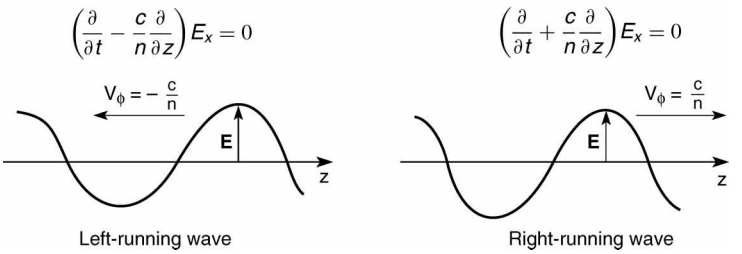

FIGURE 3.2. Left- and right-propagating waves.

Note that Eq. (3.8) can be rewritten in somewhat simpler form in terms of the classical electron radius [Eq. (2.44)]

$$r_e = \frac{e^2}{4\pi\epsilon_0 mc^2}$$

and the complex atomic scattering factor ($\theta = 0$, superscript zero) [Eq. (2.77)]

$$f^0(\omega) = \sum_s \frac{g_s\omega^2}{\omega^2 - \omega_s^2 + i\gamma\omega}$$

which can be written in terms of its complex components [Eq. (2.79)]

$$f^0(\omega) = f_1^0(\omega) - if_2^0(\omega)$$

Making these substitutions, the refractive index [Eq. (3.8)] can be rewritten as

$$\boxed{n(\omega) = 1 - \frac{n_a r_e \lambda^2}{2\pi}\left[f_1^0(\omega) - if_2^0(\omega)\right]} \tag{3.9}$$

where λ is the wavelength in vacuum. Note that this relationship shows explicitly the link between forward scattering and refractive index. In a later section we will discuss the experimental and computational determinations of $f_1^0(\omega)$ and $f_2^0(\omega)$ and their utilization in various x-ray experiments.

Some further comments can be made on the role of the refractive index as embodied in the wave equation (3.6), which can be factored into the product of two operators, viz.,

$$\left(\frac{\partial}{\partial t} - \frac{c}{n(\omega)}\nabla\right)\left(\frac{\partial}{\partial t} + \frac{c}{n(\omega)}\nabla\right)\mathbf{E}_{\mathrm{T}}(\mathbf{r}, t) = 0 \tag{3.10}$$

When either factor is zero the equation can be satisfied for non-zero electric field. These two conditions correspond to left and right propagating waves, as illustrated in Figure 3.2:

Note from Eq. (3.10) that for a wave propagating in a medium of uniform atomic density the phase velocity (the speed with which crests of fixed phase move) is not equal to c as in vacuum, but rather is modified to a value

$$\mathrm{v}_\phi = \frac{c}{n(\omega)} \tag{3.11}$$

That this is so can be seen by examining Eq. (3.10) for the case of fixed amplitude, for instance traveling with fixed phase at the peak amplitude of the wave. This requires that one of the brackets, which correspond to left- and right-propagating waves, contribute as a zero multiplier. For the right-running one-dimensional wave illustrated in Figure 3.2, with space–time dependence $E = E_0 \exp[-i(\omega t - kz)]$, setting the operator to zero gives the condition

$$-i\left(\omega - \frac{ck}{n}\right) = 0$$

or

$$\frac{\omega}{k} = \frac{c}{n}$$

which we recognize as a *phase velocity* v_ϕ different from the vacuum value c, in a medium of refractive index n. Thus for visible light, with $\omega < \omega_s$, the refractive index is greater than unity, typically 1.5 or so for common glass, which corresponds to a relatively low phase velocity, less than c. Typical phenomena affected by low phase velocity propagation of visible wavelengths include reflection and refractive turning at tilted interfaces, focusing by lenses, dispersive separation of wavelengths by prisms, and total internal reflection, as in a prism or a fish tank. For EUV/SXR radiation, where ω is greater than ω_s for many of the atomic electrons, the refractive index is less than unity, but only slightly so, indicating that x-rays propagate in materials at phase velocities somewhat greater than in vacuum (c). This gives rise to the interesting and important phenomenon of *total external reflection* of x-rays, whereby reflection occurs with little absorption at glancing incidence from material interfaces. Note that although the phase velocity can be greater than c for x-rays, the group velocity, which represents energy flow, is less than c. For further discussion of phase and group velocities, see Refs. 1–3.

As the refractive index for EUV and soft x-ray radiation deviates only a small amount from unity, it is common[6] to write it in the following form:

$$\boxed{n(\omega) = 1 - \delta + i\beta} \tag{3.12}$$

where the choice of a positive sign for the β term is consistent with the form of exponential wave description used throughout these notes,[†] $\exp[-i(\omega t - \mathbf{k}\cdot\mathbf{r})]$. As we shall see shortly, this choice of sign for the imaginary term leads to an appropriate decay of wave intensity in a lossy medium.

[†]See the footnote following Eq. (1.26) in Chapter 1. The consistency of this choice is clarified in the algebra leading to Eq. (3.17) in Section 3.2 below. For assumed waves of the form $\exp[+i(\omega t - \mathbf{k}\cdot\mathbf{r})]$ the proper choice for wave decay in a passive lossy medium would be $n(\omega) = 1 - \delta - i\beta$.

Comparing Eqs. (9) and (12), we observe that

$$\delta = \frac{n_a r_e \lambda^2}{2\pi} f_1^0(\omega) \tag{3.13a}$$

$$\beta = \frac{n_a r_e \lambda^2}{2\pi} f_2^0(\omega) \tag{3.13b}$$

That these are small quantities can be verified by a simple example. We consider carbon with mass density $\rho = 2.26$ g/cm^3, and thus atomic density 1.13×10^{23} atoms/cm^3 (see the periodic chart, Chapter 1, Table 1.2). For carbon at a wavelength of 4 Å, $f_1^0 = 6.09$ and $f_2^0 = 0.071$, as we saw in the tabulated example at the end of Chapter 2 (Figure 2.13). Thus with $r_e = 2.82 \times 10^{-13}$ cm [Eqs. (2.44) and (2.46)], we have $\delta = 4.90 \times 10^{-5}$ and $\beta = 5.71 \times 10^{-7}$, indeed much less than unity. For longer wavelengths or higher Z (atomic number on the periodic chart) materials, the values of δ and β will be larger, but still much less than unity. The strongest dependence is on λ^2, while f_2^0 scales slowly with Z, somewhat less than linearly. Thus even for a high Z element such as gold, at soft x-ray wavelengths δ and β will have values of order 10^{-2}, still far less than unity. Values of $f_1^0(\omega)$ and $f_2^0(\omega)$ have been tabulated by Henke, Gullikson, and Davis[7] for all elements from hydrogen to uranium ($Z = 92$), and for photon energies extending from 50 eV to 30 keV (from 10 eV for f_2^0), by techniques we will return to at the end of this chapter. See Appendix C for representative values for several common elements.

3.2 PHASE VARIATION AND ABSORPTION OF PROPAGATING WAVES

Having convenient relations, Eqs. (3.12) and (3.13), for the refractive index, it is now convenient to consider phase variation and absorption during wave propagation at EUV/SXR wavelengths. In Chapter 1 we considered absorption and transmission by thin foils in terms of a so-called[‡] mass-dependent absorption coefficient, $\mu(\lambda)$. We now inquire as to how the absorption coefficient μ relates to the refractive index that appears in the propagation of short-wavelength electromagnetic radiation. We can answer this by considering a plane wave of the form

$$\mathbf{E}(\mathbf{r}, t) = \mathbf{E}_0 e^{-i(\omega t - \mathbf{k}\cdot\mathbf{r})} \tag{3.14}$$

propagating in some material with an initial amplitude $\mathbf{E}_0$ and having a complex dispersion relation given by

$$\frac{\omega}{k} = \frac{c}{n} = \frac{c}{1 - \delta + i\beta} \tag{3.15}$$

[‡]The choice of name is not the best, as it is photons that are absorbed. The name is meant to differentiate this absorption coefficient from that defined in terms of an atomic density, that is, in terms of n_a rather than ρ.

Solving for k, we obtain

$$k = \frac{\omega}{c}(1 - \delta + i\beta) \tag{3.16}$$

Substituting this into Eq. (3.14), in the propagation direction defined by $\mathbf{k} \cdot \mathbf{r} = kr$ one has

$$\mathbf{E}(\mathbf{r}, t) = \mathbf{E}_0 e^{-i[\omega t - (\omega/c)(1-\delta+i\beta)r]}$$

or

$$\mathbf{E}(\mathbf{r}, t) = \underbrace{\mathbf{E}_0 e^{-i\omega(t-r/c)}}_{\text{vacuum propagation}} \underbrace{e^{-i(2\pi\delta/\lambda)r}}_{\phi\text{-shift}} \underbrace{e^{-(2\pi\beta/\lambda)r}}_{\text{decay}} \tag{3.17}$$

where the first exponential factor represents the phase advance had the wave been propagating in vacuum, the second factor (containing $2\pi\delta r/\lambda$) represents the modified phase shift due to the medium, and the factor containing $2\pi\beta r/\lambda$ represents decay of the wave amplitude.

To compute the intensity of the wave whose electric field is given by Eq. (3.17), we must first determine the associated magnetic field and take the cross product of $\mathbf{E}$ and $\mathbf{H}$ to obtain the Poynting vector $\mathbf{S}$. We follow the same general procedure as was used in Chapter 2 for a plane electromagnetic wave in vacuum, but now use the refractive index appropriate to propagation in a uniform, isotropic material. For a plane wave in any medium, we found in Chapter 2 [above Eq. (2.29)] that the field components are given by

$$i\mathbf{k} \times \mathbf{E}_{k\omega} = i\omega\mu_0 \mathbf{H}_{k\omega}$$

while for a material of refractive index n, according to Eq. (3.15),

$$\frac{\omega}{k} = \frac{c}{n}$$

Thus with $\mathbf{k} = k\mathbf{k}_0$, where $\mathbf{k}_0$ is a unit vector in the direction of propagation, the field components are related by

$$ik\mathbf{k}_0 \times \mathbf{E}_{k\omega} = i(kc/n)\mu_0 \mathbf{H}_{k\omega}$$

or

$$\mathbf{H}_{k\omega} = \frac{n}{c\mu_0}\mathbf{k}_0 \times \mathbf{E}_{k\omega}$$

With $c \equiv 1/\sqrt{\epsilon_0\mu_0}$ and refractive index n varying slowly with frequency, the transformed fields in real space are given by

$$\mathbf{H}(\mathbf{r}, t) = n\sqrt{\frac{\epsilon_0}{\mu_0}}\mathbf{k}_0 \times \mathbf{E}(\mathbf{r}, t) \tag{3.18}$$

which is similar in form to Eq. (2.29), but more general in that Eq. (3.18) includes the effect of the refractive index n.

The scalar average intensity of a plane electromagnetic wave, $\bar{I}$, in units of power per unit area, is given for sinusoidal fields by the magnitude of the Poynting vector averaged over one period (as denoted by the bar). Following the discussion in Chapter 2 [Eq. (2.37)], the

average intensity[1, 3] is

$$\bar{I} = |\bar{\mathbf{S}}| = \tfrac{1}{2}|\mathrm{Re}(\mathbf{E} \times \mathbf{H}^*)| \tag{3.19}$$

which for a plane wave in a medium of complex refractive index n, with use of Eq. (3.18), is given by

$$\bar{I} = \frac{1}{2}\mathrm{Re}(n)\sqrt{\frac{\epsilon_0}{\mu_0}}|\mathbf{E}|^2 \tag{3.20}$$

where in Eqs. (3.19) and (3.20) the field values are those at the peak of the cycle. Thus for the plane wave described by the electric field of Eq. (3.17), the average intensity is given by

$$\bar{I} = \frac{1}{2}\mathrm{Re}(n)\sqrt{\frac{\epsilon_0}{\mu_0}}|\mathbf{E}_0|^2 e^{-2(2\pi\beta/\lambda)r}$$

which can be written completely in terms of the intensity $\bar{I}_0$ at some reference plane in the material (for instance just on the material side of an interface with vacuum), as

$$\bar{I} = \bar{I}_0 e^{-(4\pi\beta/\lambda)r} \tag{3.21}$$

that is, the wave decays with distance r into the material, with an exponential decay length

$$\boxed{l_{\mathrm{abs}} = \frac{\lambda}{4\pi\beta}} \tag{3.22}$$

where we recall that β is the absorptive portion of the complex refractive index, as seen in Eq. (3.12). Referring back to Eq. (3.13b), we can write the absorption length in terms of the imaginary portion of the complex atomic scattering coefficient, $f_2^0(\omega)$, as

$$\boxed{l_{\mathrm{abs}} = \frac{1}{2n_a r_e \lambda f_2^0(\omega)}} \tag{3.23}$$

In Chapter 1 we considered experimentally observed absorption in thin foils, writing

$$\frac{\bar{I}}{\bar{I}_0} = e^{-\rho\mu r} \tag{3.24}$$

where ρ is the mass density,[¶] μ is the absorption coefficient, and r is the foil thickness. Comparing Eqs. (3.21) to (3.24) shows that macroscopic (μ) and atomic (f_2^0) absorption

[¶]Again we have the inconvenience of a letter, ρ in this case, being commonly used for two different quantities: mass density here, and charge density in Maxwell's equations [Eqs. (2.1)–(2.4)]. The reader will recognize the proper meaning by its usage.

factors are related by

$$\rho\mu = 2n_a r_e \lambda f_2^0(\omega)$$

Since the mass density ρ is related to the atomic density n_a by

$$\rho = m_a n_a = A m_u n_a \tag{3.25}$$

where m_a is the atomic mass, m_u is the atomic mass unit,[§] and A is the number of atomic mass units (as given in the periodic chart, Table 1.2), the macroscopic-to-atomic relationship can be written as

$$\boxed{\mu = \frac{2r_e\lambda}{Am_u} f_2^0(\omega)} \tag{3.26}$$

Thus we have a relationship between the macroscopically observed absorption of x-rays by thin foils, $\mu(\omega)$, and the absorptive portion of the atomic scattering factor for a single atom, f_2^0.

For some applications the absorption of radiation by thin films is expressed in terms of an atomic cross-section for absorption, σ_{abs}, through a relation similar to Eq. (3.24), but in terms of the atomic density n_a rather than the mass density ρ [see Eq. (1.3)]. In this case one expresses the absorption as

$$\frac{\bar{I}}{\bar{I}_0} = e^{-n_a \sigma_{\text{abs}} r} \tag{3.27}$$

so that a comparison with Eqs. (3.21–3.23) gives an expression between the atomic absorption cross-section and β or f_2^0, viz.,

$$\boxed{\sigma_{\text{abs}} = 2r_e\lambda f_2^0(\omega)} \tag{3.28a}$$

or equivalently

$$\boxed{\sigma_{\text{abs}} = Am_u\mu(\omega)} \tag{3.28b}$$

An example showing the photon energy dependence of μ and σ_{abs} for copper atoms is given in Chapter 1, Figure 1.8.

Returning to Eq. (3.17), we note that we have written the electric field in terms of an initial value $\mathbf{E}_0$ multiplied by factors involving δ and β that take account of phase shifting

[§]The atomic mass unit is given in Appendix A as $m_u = 1.66054 \times 10^{-24}$ g. Note that numerically m_u is equal to the reciprocal of Avogadro's number N_{A} (Appendix A), so that the mass of one mole is $m = Am_u N_{\text{A}} = A$, the atomic weight expressed in grams.

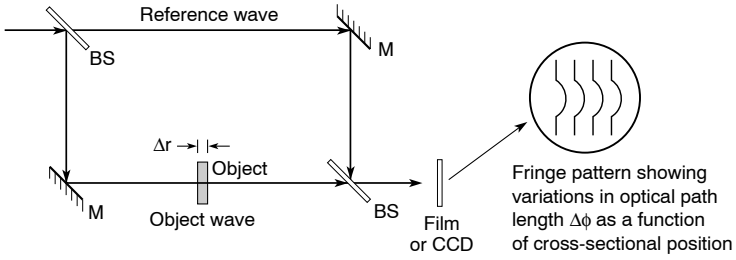

FIGURE 3.3. A Mach–Zehnder interferometer for measuring phase shift.

and absorption in the medium. We see from Eq. (3.17) that the phase of the wave is shifted because of its propagation through the medium of atoms (n_a), and that the relative phase shift $\Delta\phi$, compared to propagation in vacuum, is given by

$$\Delta\phi = \left(\frac{2\pi\delta}{\lambda}\right)\Delta r \tag{3.29}$$

where Δr is the thickness or propagation distance. We will see in later chapters that this phase shift plays an important role in diffractive optics, multilayer mirrors, interferometry, and many other subjects.

The measurement of phase shift in a material is most directly accomplished with the use of an interferometer, an instrument in which a wavefront is dissected into parts, one of which is propagated through the object and one of which is propagated through a reference path, typically vacuum or air. The two waves are then recombined to form an interference pattern where differences in optical path ($\Delta\phi$) are manifested as localized shifts of the fringe pattern.[‖] Interferometry is a widely used technique[1, 8] at visible and longer wavelengths, with many variations based on available optics, parameters of interest, and coherence properties of the radiation.

To introduce the general concept, Figure 3.3 illustrates an interferometer introduced in the 1880s by Mach and Zehnder to study airflow patterns with incoherent visible light. Knowing the material thickness Δr and measuring the phase shift $\Delta\phi$, one can deduce δ, the real part of the refractive index, through use of Eq. (3.29), and thus for our purposes find f_1^0 as a function of probe wavelength or photon energy. Note that the beamsplitters (BS) and mirrors must (M) be optically flat to a fraction of a wavelength across the aperture of the beam. This is particularly challenging at x-ray wavelengths. Nonetheless, through the clever use of cut monolithic crystals, Bonse and Hart[9] have introduced the use of interferometric techniques at x-ray wavelengths.

Interferometry at soft x-ray and EUV wavelengths is more challenging because of the higher degree of absorption at these wavelengths. Soft x-ray interferometry is, however, becoming a reality as various techniques are investigated that provide the requisite splitting into sufficiently flat wavefronts. An example of an EUV interferometer is given near the end of

[‖]The phrase *fringe pattern* refers to the alternating bright and dark bands caused by the positive and negative interference of two waves.

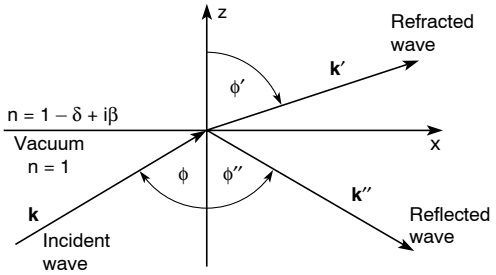

FIGURE 3.4. Interface geometry for incident, reflected, and refracted waves. The *plane of incidence* is defined as containing the incident wave vector k and the surface normal z_0.

Chapter 8. Note that in the interferometer illustrated in Figure 3.3, the two wavefronts are recombined in a manner that maintains their original spatial orientation, thus requiring minimal coherence properties** for the formation of a high-contrast fringe pattern.

3.3 REFLECTION AND REFRACTION AT AN INTERFACE

To consider the phenomena of reflection and refraction we introduce Figure 3.4, which illustrates the incident, reflected, and refracted waves at a material interface. Note that all angles are measured from the surface normal (z-axis), and that propagation effects such as phase velocity and attenuation are contained in $\mathbf{k}$, the vector propagation constant, through the complex refractive index, e.g., as in Eq. (3.16):

$$k = |\mathbf{k}| = \frac{\omega}{c}(1 - \delta + i\beta)$$

where we assume that ω is real and that all waves have the same time dependence, $e^{-i\omega t}$, because they are driven by the incident wave. We consider a plane wave incident from the vacuum side and write the incident wave as

$$\mathbf{E} = \mathbf{E}_0 e^{-i(\omega t - \mathbf{k}\cdot\mathbf{r})} \tag{3.30a}$$

the *refracted wave* as

$$\mathbf{E}' = \mathbf{E}'_0 e^{-i(\omega t - \mathbf{k}'\cdot\mathbf{r})} \tag{3.30b}$$

and the *reflected wave* as

$$\mathbf{E}'' = \mathbf{E}''_0 e^{-i(\omega t - \mathbf{k}''\cdot\mathbf{r})} \tag{3.30c}$$

where the subscript zero denotes the vector field amplitudes at the interface position $\mathbf{r} = 0$. Because the incident and reflected waves propagate in the same medium (vacuum), they experience the same refractive index ($n = 1$). Thus for the same oscillating frequency (ω),

**The subjects of spatial and temporal coherence are discussed in Chapter 8.

from Eq. (3.16), one can write

$$|\mathbf{k}| = \mathbf{k}''| = \frac{\omega}{c} \tag{3.31}$$

At the interface ($z = 0$) where these three waves meet, the fields must obey certain boundary conditions[1–5] in order to satisfy Maxwell's equations:

Condition 1: Field components of **E** and **H** parallel to the interface must be continuous. For the geometry shown in Figure 3.4, where $\mathbf{z}_0$ is a unit vector normal to the interface, the boundary conditions in the absence of surface currents are

$$\mathbf{z}_0 \times (\mathbf{E}_0 + \mathbf{E}_0'') = \mathbf{z}_0 \times \mathbf{E}_0' \tag{3.32a}$$

and

$$\mathbf{z}_0 \times (\mathbf{H}_0 + \mathbf{H}_0'') = \mathbf{z}_0 \times \mathbf{H}_0' \tag{3.32b}$$

Condition 2: Field components of **D** and **B** normal (perpendicular) to the interface must be continuous. For the geometry in Figure 3.4 the boundary conditions in the absence of surface charge are

$$\mathbf{z}_0 \cdot (\mathbf{D}_0 + \mathbf{D}_0'') = \mathbf{z}_0 \cdot \mathbf{D}_0' \tag{3.32c}$$

and

$$\mathbf{z}_0 \cdot (\mathbf{B}_0 + \mathbf{B}_0'') = \mathbf{z}_0 \cdot \mathbf{B}_0' \tag{3.32d}$$

We consider the incident wave vector **k** to lie in the x, z-plane, and refer to this as the *plane of incidence*, as it contains both **k** and the surface normal $\mathbf{z}_0$. At this point we make no assumption as to the polarization of the incident wave, that is, to the direction of **E** with respect to this plane. If the parallel field components are to be continuous everywhere along the interface as required by Eqs. (3.32a) and (3.32b), then the phase and amplitude variations for all waves must be identical along the interface. This requires that the x-direction components of the wavevectors in Eqs. (3.30a–c) satisfy the condition

$$(\mathbf{k} \cdot \mathbf{x}_0 = \mathbf{k}' \cdot \mathbf{x}_0 = \mathbf{k}_0'' \cdot \mathbf{x}_0) \qquad \text{at } z = 0 \tag{3.33}$$

Since **k** has no y-component by our orientation of axes, neither can $\mathbf{k}'$ or $\mathbf{k}''$. Thus all three vectors must lie in the plane of incidence defined by **k** and the surface normal direction $\mathbf{z}_0$. If the phase and amplitude factors are to match along the interface in the x-direction, all waves must have equal k_x components. In this way one ensures that the boundary condition is met everywhere along the interface if it is met at any one point. Following this argument Eq. (3.33) requires that

$$k_x = k_x' = k_x'' \tag{3.34a}$$

or in terms of the angles shown in Figure 3.5,

$$k \sin\phi = k' \sin\phi' = k'' \sin\phi'' \tag{3.34b}$$

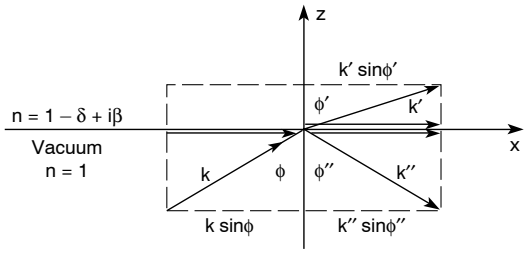

FIGURE 3.5. Parallel components of the wave vectors.

Since k and k'' propagate in vacuum, they are real and equal in magnitude as observed in Eq. (3.31); thus from (34b) we can write

$$\sin\phi = \sin\phi'' \tag{3.35a}$$

or

$$\boxed{\phi = \phi''} \tag{3.35b}$$

which states that *the angle of incidence equals the angle of reflection.* Considering the refracted wave $\mathbf{k}'$, Eq. (3.34b) permits us to write

$$k\sin\phi = k'\sin\phi' \tag{3.36}$$

Since both waves must oscillate at the same frequency (ω), we can write, by using Eq. (3.15), that

$$\omega = kc = k'c/n$$

or

$$k' = kn = \frac{\omega}{c}(1 - \delta + i\beta) \tag{3.37}$$

indicating that the propagation vector in the medium is complex, representing both phase variation and amplitude decay as the wave propagates, as seen previously in Eqs. (3.16) and (3.17). Equation (3.36) can now be rewritten as *Snell's law:*

$$\boxed{\sin\phi' = \frac{\sin\phi}{n}} \tag{3.38}$$

which formally describes the refractive turning of a wave entering a uniform, isotropic medium of complex refractive index n. The fact that n is complex implies that $\sin\phi'$ is also complex for real incidence angle ϕ. Thus both the wavevector k' and the turning angle ϕ', in the medium, have real and imaginary components, giving a somewhat more complicated representation of refraction and propagation.

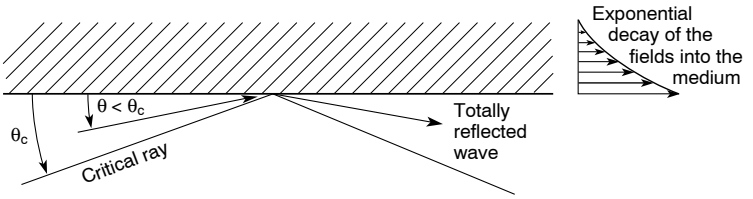

FIGURE 3.6. Glancing incidence radiation and total external reflection.

Snell's law (3.38) is valid over a wide range of wavelengths and photon energies. It is widely used in lens designs at visible wavelengths, and to describe such interesting phenomena as total internal reflection of visible light within the denser medium at water–air and glass–air interfaces. We will use Snell's law here to describe the near-total reflection of short wavelength radiation at glancing incidence to a material surface.

3.4 TOTAL EXTERNAL REFLECTION OF SOFT X-RAYS AND EUV RADIATION

For most angles of incidence the reflection coefficient for soft x-rays and extreme ultraviolet radiation is very small, as we will see in a following section of this chapter. This is due to the fact that the refractive index is very close to unity so that there is little change of field amplitudes across the interface. However, there is an important exception for radiation incident at a glancing angle to the material surface, far from the surface normal. We will see that in this case, radiation of any polarization experiences near total reflection. This *total external reflection* is widely used in experiments involving radiation transport, deflection, focusing, and filtering. Like its visible light counterpart total internal reflection (commonly observed in fish tanks and used for turning visible laser beams within glass prisms where the refractive index is greater than unity), the x-ray effect can be understood in large measure on the basis of Snell's law, Eq. (3.38). Snell's law indicates that visible light will be bent towards the surface normal ($\phi' < \phi$) when entering a medium of greater refractive index (n typically greater than 1.5 for glass or water at visible wavelengths). For EUV and x-rays, however, with the real part of the refractive index slightly less than unity, Snell's law indicates that the radiation is refracted in a direction slightly further from the surface normal. Inspection of Eq. (3.38) shows that for n slightly less than unity, $\sin\phi'$ is slightly larger than $\sin\phi$. Thus for near-glancing incidence (ϕ near $\pi/2$) the refraction angle ϕ' can equal $\pi/2$, indicating that to first order the refracted wave does not penetrate into the material, but rather propagates along the interface. In short order we will investigate the dependence of these fields on the parameters of the problem: the wavelength λ, incidence angle ϕ, and refractive index components δ and β. First, however, we consider the simplified problem with β approaching zero, which permits us to understand the basic phenomenon of total external reflection and quantify the critical angle with minimal mathematical complexity. The general effect is illustrated in Figure 3.6.

Considering Snell's law for a refractive index of $n \simeq 1 - \delta$, where for the moment we assume that β approaches zero, one has

$$\sin\phi' = \frac{\sin\phi}{1-\delta} \tag{3.39}$$

Thus the refracted wave is at an angle ϕ', somewhat further from the surface normal than ϕ

because of the $1 - \delta$ factor. As ϕ approaches $\pi/2$ it is evident that $\sin\phi'$ approaches unity somewhat faster. The limiting condition occurs at a *critical angle of incidence*, $\phi = \phi_c$, where $\phi' = \pi/2$, so that $\sin\phi' = 1$ and from Eq. (3.39)

$$\sin\phi_c = 1 - \delta \tag{3.40}$$

This is the condition for total external reflection; the incident x-rays do not penetrate the medium, but rather propagate along the interface at an angle $\phi' = \pi/2$. The angle for which this condition is just met is given by Eq. (3.40). Since $\delta \ll 1$ for x-rays, the phenomenon occurs only for glancing angles where ϕ is near 90°. Thus it is convenient to introduce the complimentary angle θ, measured from the interface as shown in Figure 3.6, where

$$\theta + \phi = 90^\circ$$

The critical angle condition (3.40) then becomes

$$\sin(90^\circ - \theta_c) = 1 - \delta$$

or

$$\cos\theta_c = 1 - \delta$$

Since $\delta \ll 1$ for x-rays, $\cos\theta_c$ is near unity, θ_c is very small, and we may make the small angle approximation

$$1 - \frac{\theta_c^2}{2} + \cdots = 1 - \delta$$

which has the solution

$$\boxed{\theta_c = \sqrt{2\delta}} \tag{3.41}$$

as the *critical angle for total external reflection of x-rays and extreme ultraviolet radiation*, a result first obtained by Compton[6] in 1922.

Since the real part of the refractive index can be written as [Eq. (3.13a)]

$$\delta = \frac{n_a r_e \lambda^2 f_1^0(\lambda)}{2\pi}$$

we have, to first order,

$$\theta_c = \sqrt{2\delta} = \sqrt{\frac{n_a r_e \lambda^2 f_1^0(\lambda)}{\pi}} \tag{3.42a}$$

Because the atomic density n_a, in atoms per unit volume, varies only slowly among the natural elements, the major functional dependencies of the critical angle are

$$\theta_c \propto \lambda\sqrt{Z} \tag{3.42b}$$

where we have used the fact that to first order f_1^0 is approximated by Z, although as we have seen f_1^0 is also a complicated function of wavelength (photon energy) for each element.

To obtain a conveniently large critical angle, Eq. (3.42) suggests use of a relatively long wavelength and a higher Z material. We will see that other factors enter, such as the absorption β, specific absorption edges available with differing materials, and the availability of certain elements in convenient form for laboratory use. We will return to this subject, with illustrations for a variety of materials, later in this chapter.

As a specific example of the critical angle for total external reflection we consider a carbon mirror with incident radiation of 0.4 nm wavelength. We have previously observed, in the paragraph below Eq. (3.13), that for this case $\delta = 4.90 \times 10^{-5}$, and thus $\theta_c = \sqrt{2\delta} \simeq 10^{-2}$ rad, or about 0.6° from the surface. At longer wavelengths one finds larger critical angles, as indicated in Eq. (3.42). For instance, at a wavelength of 1.04 nm one finds from the tables (see Appendix C) that $\delta = 3.4 \times 10^{-4}$, so that θ_c increases to about 2.6×10^{-2} rad, or about 1.5°. Use of a higher Z material, such as nickel or gold (coating), increases the critical angle further. Note that not only are these angles small, and perhaps inconvenient, but as a consequence the possible collection solid angles for use in experiments such as plasma diagnostics and EUV/x-ray astronomy are quite limited.

The above model of total external reflection is incomplete in that it does not include the effect of finite β. Since a portion of the field extends into the lossy medium, even if only in an evanescent manner, losses are incurred and total reflection is not achieved. In the following section we calculate the reflection coefficients for radiation incident on an interface at arbitrary angle of incidence for finite δ and β. In a later section we investigate further the nature of field penetration near the critical angle for finite β.

3.5 REFLECTION COEFFICIENTS AT AN INTERFACE

Returning to Figure 3.4, which shows the geometry of incident, reflected, and refracted waves at an interface, we use the various wave amplitudes given in Eqs. (3.30) and the boundary conditions [Eq. (3.32)] to determine the field amplitudes in both regions, and from these determine the reflectivity. Incident radiation of any polarization (linear, circular, elliptical) can be described in terms of two orthogonal polarizations with appropriate amplitudes and phase angle between the two. For the purpose of analysis, it is convenient to decompose incident radiation into two geometries, one with the incident electric field $\mathbf{E}$ perpendicular to the plane of incidence (containing $\mathbf{k}$ and $\mathbf{z}_0$), and one with $\mathbf{E}$ parallel to that plane. These orientations are often referred to as s and p polarizations, respectively, following the German words for perpendicular (*senkrecht*) and parallel (*parallele*). Any incident wave, polarized or not, can be represented in terms of these two polarizations. We can determine the refracted and reflected wave amplitudes at the interface, $\mathbf{E}_0'$ and $\mathbf{E}_0''$, by applying the boundary conditions given by Eqs. (32a) and (32b). We treat the two possible field orientations separately.

3.5.1 E_0 Perpendicular to the Plane of Incidence

For the case of the incident electric field polarized perpendicular to the plane of incidence, in the y-direction for our choice of axes (see Figure 3.7), application of Eq. (3.32a) is relatively simple. The scalar field amplitudes at the interface (subscript zero) must satisfy the condition

$$E_0 + E_0'' = E_0' \tag{3.43}$$

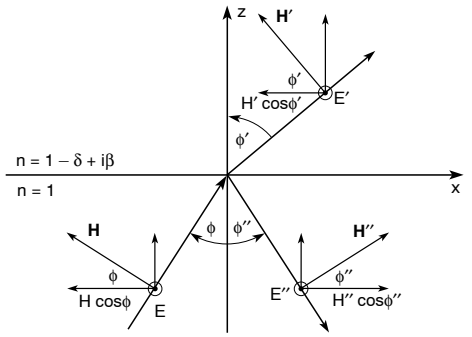

FIGURE 3.7. Field components for perpendicular (s) polarization, where **E** is polarized in the y-direction (into the paper as shown here), perpendicular to the x, z plane of incidence.

while continuity of the magnetic field [Eq. 3.32b], upon inspection of Figure 3.7, requires that at the interface

$$H_0 \cos\phi - H_0'' \cos\phi = H_0' \cos\phi' \tag{3.44}$$

Equations (3.43) and (3.44) can be combined to solve for the fields by recalling that for plane waves propagating in a medium of refractive index n, **E** and **H** are related by Eq. (3.18):

$$\mathbf{H}(\mathbf{r}, t) = n\sqrt{\frac{\epsilon_0}{\mu_0}}\mathbf{k}_0 \times \mathbf{E}(\mathbf{r}, t)$$

or, more conveniently, the amplitudes are related by

$$H = n\sqrt{\frac{\epsilon_0}{\mu_0}}E$$

where the field orientations are described by Eq. (3.18) with $\mathbf{E}_0 = E_0\mathbf{y}_0$, $\mathbf{E}_0' = E_0'\mathbf{y}_0$, and $\mathbf{E}_0'' = E_0''\mathbf{y}_0$. Equation (3.44) can now be expressed, after eliminating magnetic fields, as

$$\sqrt{\frac{\epsilon_0}{\mu_0}}E_0 \cos\phi - \sqrt{\frac{\epsilon_0}{\mu_0}}E_0'' \cos\phi = n\sqrt{\frac{\epsilon_0}{\mu_0}}E_0' \cos\phi'$$

or

$$(E_0 - E_0'')\cos\phi = nE_0' \cos\phi' \tag{3.45}$$

From Snell's law [Eq. (3.38)] we know the relation between ϕ and ϕ':

$$\sin\phi' = \frac{\sin\phi}{n}$$

Thus we have three equations [(3.38), (3.43), and (3.45)] in five unknowns (E_0, E_0', E_0'', ϕ, and ϕ'), which can be solved by treating two (E_0 and ϕ) as independent variables describing the incident radiation. We can now solve for the refracted and reflected field amplitudes, E_0' and E_0'', in terms of the incident wave parameters E_0 and ϕ.

Combining Eqs. (3.43) and (3.45), we have

$$(E_0 - E_0'')\cos\phi = n(E_0 + E_0'')\cos\phi'$$

Combining terms according to incident and reflected fields, one has

$$(\cos\phi - n\cos\phi')E_0 = (\cos\phi + n\cos\phi')E_0''$$

so that the ratio of field amplitudes is

$$\frac{E_0''}{E_0} = \frac{\cos\phi - n\cos\phi'}{\cos\phi + n\cos\phi'}$$

From Snell's law,

$$\cos\phi' = \sqrt{1 - \sin^2\phi'} = \sqrt{1 - \frac{\sin^2\phi}{n^2}}$$

or

$$n\cos\phi' = \sqrt{n^2 - \sin^2\phi}$$

The ratio of field amplitudes is then

$$\frac{E_0''}{E_0} = \frac{\cos\phi - \sqrt{n^2 - \sin^2\phi}}{\cos\phi + \sqrt{n^2 - \sin^2\phi}} \tag{3.46}$$

The refracted field E_0' can then be determined from Eq. (3.43):

$$\frac{E_0'}{E_0} = 1 + \frac{E_0''}{E_0} = 1 + \frac{\cos\phi - \sqrt{n^2 - \sin^2\phi}}{\cos\phi + \sqrt{n^2 - \sin^2\phi}}$$

or

$$\frac{E_0'}{E_0} = \frac{2\cos\phi}{\cos\phi + \sqrt{n^2 - \sin^2\phi}} \tag{3.47}$$

Thus we have the refracted and reflected field amplitudes for the case of perpendicular polarization. The reflectivity R, defined as the ratio of reflected to incident intensity (at the surface), is determined, with the use of Eq. (3.19), to be

$$R = \frac{\bar{I}''}{\bar{I}_0} = \frac{|\bar{\mathbf{S}}''|}{|\bar{\mathbf{S}}|} = \frac{\frac{1}{2}\mathrm{Re}(\mathbf{E}_0'' \times \mathbf{H}_0''^*)}{\frac{1}{2}\mathrm{Re}(\mathbf{E}_0 \times \mathbf{H}_0^*)} \tag{3.48}$$

With $n = 1$ for both incident and reflected waves,

$$R = \frac{|E_0''|^2}{|E_0|^2}$$

which with Eq. (3.46) becomes, for the case of perpendicular (s) polarization,

$$\boxed{R_s = \frac{\left|\cos\phi - \sqrt{n^2 - \sin^2\phi}\right|^2}{\left|\cos\phi + \sqrt{n^2 - \sin^2\phi}\right|^2}} \tag{3.49}$$

where n is complex. Knowing the values of δ and β as functions of photon energy, one can now calculate the reflectivity, at an arbitrary angle of incidence, for s-polarized radiation. Alternatively, angle-dependent reflectivity can be used to experimentally determine values of δ and β, that is, determine the refractive index at short wavelengths. Soufli and Gullikson[10] have used this technique, with tunable synchrotron radiation and specially prepared (smooth, unoxidized) surfaces, to measure the optical constants (δ and β) of silicon in the photon energy range from 50 eV to 180 eV, extending above and below the L-edges.

Two cases of particular interest are normal incidence reflection ($\phi = 0$) and glancing incidence reflection ($\phi \geq \phi_c,\ \theta \leq \theta_c$). For normal incidence ($\phi = 0$) one has

$$R_{s,\perp} = \frac{|1-n|^2}{|1+n|^2} = \frac{(1-n)(1-n^*)}{(1+n)(1+n^*)}$$

For $n = 1 - \delta + i\beta$

$$R_{s,\perp} = \frac{(\delta - i\beta)(\delta + i\beta)}{(2-\delta+i\beta)(2-\delta-i\beta)} = \frac{\delta^2+\beta^2}{(2-\delta)^2+\beta^2}$$

which for $\delta \ll 1$ and $\beta \ll 1$ gives the *reflectivity for x-rays and EUV radiation at normal incidence* ($\phi = 0$) as

$$\boxed{R_{s,\perp} \simeq \frac{\delta^2+\beta^2}{4}} \tag{3.50}$$

which shows that the reflection is indeed very small for x-rays incident normally on a single interface. Similar results follow from Eq. (3.49) for all angles except those at glancing incidence.

The case of glancing incidence at or below the critical angle ($\theta \geq \theta_c$) can also be considered by examining Eq. (3.49). Using the definitions

$$\theta = 90^\circ - \phi \leq \theta_c$$

where

$$\theta_c = \sqrt{2\delta} \ll 1$$

and where for glancing incidence

$$\cos\phi = \sin\theta \simeq \theta$$

we have to a high degree of accuracy

$$\sin^2\phi = 1 - \cos^2\phi = 1 - \sin^2\theta \simeq 1 - \theta^2$$

Noting further that for $n = 1 - \delta + i\beta$

$$n^2 = (1-\delta)^2 + 2i\beta(1-\delta) - \beta^2$$

we see that the reflectivity [Eq. (3.49)] for glancing incidence of perpendicularly polarized

x-rays can be written to a good approximation as

$$R_{s,\theta} = \frac{\left|\theta - \sqrt{(1-\delta)^2 - \beta^2 + 2i\beta(1-\delta) - (1-\theta^2)}\right|^2}{\left|\theta + \sqrt{(1-\delta)^2 - \beta^2 + 2i\beta(1-\delta) - (1-\theta^2)}\right|^2} \qquad (\theta \ll 1)$$

Dropping second order terms of order δ^2, β^2, $\delta\beta$,

$$R_{s,\theta} = \frac{\left|\theta - \sqrt{\theta^2 - 2\delta + 2i\beta}\right|^2}{\left|\theta + \sqrt{\theta^2 - 2\delta + 2i\beta}\right|^2}$$

Recalling that $\theta_c = \sqrt{2\delta}$,

$$\boxed{R_{s,\theta} = \frac{\left|\theta - \sqrt{\left(\theta^2 - \theta_c^2\right) + 2i\beta}\right|^2}{\left|\theta + \sqrt{\left(\theta^2 - \theta_c^2\right) + 2i\beta}\right|^2} \qquad (\theta \ll 1)}$$

Absolute values can be taken to obtain a purely real coefficient of reflection by first expressing the square root of the complex quantity in terms of a sum of real and imaginary components. This is accomplished by introducing the quantity $\sqrt{a + ib}$ such that

$$R_{s,\theta} = \frac{\left|\theta - \sqrt{a + ib}\right|^2}{\left|\theta + \sqrt{a + ib}\right|^2} \tag{3.51a}$$

where

$$a = \theta^2 - \theta_c^2 \tag{3.51b}$$

$$b = 2\beta \tag{3.51c}$$

and from Appendix D

$$\sqrt{a + ib} = \frac{1}{\sqrt{2}}\left[\sqrt{(a^2 + b^2)^{1/2} + a} + i\sqrt{(a^2 + b^2)^{1/2} - a}\right] = A + iB \tag{3.51d}$$

so that complex conjugates are readily identified and the reflectivity for glancing incidence can be written relatively simply, following Compton and Allison,[6] and Parratt,[11] as

$$R_{s,\theta} = \left|\frac{\theta - (A + iB)}{\theta + (A + iB)}\right|^2 = \frac{(\theta - A)^2 + B^2}{(\theta + A)^2 + B^2} \tag{3.52a}$$

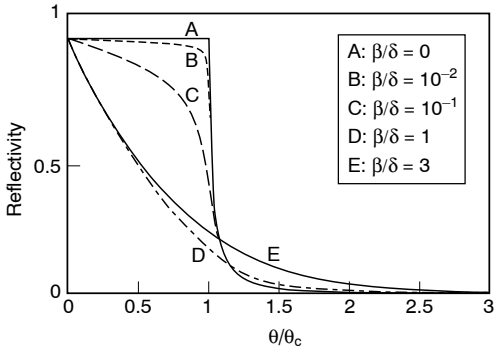

FIGURE 3.8. Reflectivity curves from Eq. (3.52) as a function of the parameter β/δ for radiation incident from vacuum upon an idealized material interface. Finite absorption (β) causes a rounding of the otherwise sharp angular dependence of reflectance at the critical angle. These results apply to both perpendicular (s) and parallel (p) polarization.

where now

$$A = \sqrt{\frac{(a^2 + b^2)^{1/2} + a}{2}} \tag{3.52b}$$

$$B = \sqrt{\frac{(a^2 + b^2)^{1/2} - a}{2}} \tag{3.52c}$$

and where

$$a = \theta^2 - \theta_c^2 = \theta^2 - 2\delta \tag{3.52d}$$

$$b = 2\beta \tag{3.52e}$$

which, although convenient in form, reveals a somewhat complicated dependence of the reflection coefficient on θ, δ, and β near glancing incidence. Numerical solutions are shown in Figure 3.8 for various values of the parameter β/δ. Analytic expressions are readily obtained for two special cases. Just at the critical angle $\theta = \theta_c$, one has $a = 0$ and one obtains

$$\boxed{R_{s,\theta_c} = \frac{1 - \dfrac{\sqrt{2\delta\beta}}{\delta + \beta}}{1 + \dfrac{\sqrt{2\delta\beta}}{\delta + \beta}}} \tag{3.53}$$

which is unity for $\beta/\delta = 0$, 0.20 for $\beta/\delta = \frac{1}{2}$, and 0.17 for $\beta/\delta = 1$. For $\theta = 0$, Eq. (3.52a) is unity for all values of δ and β.

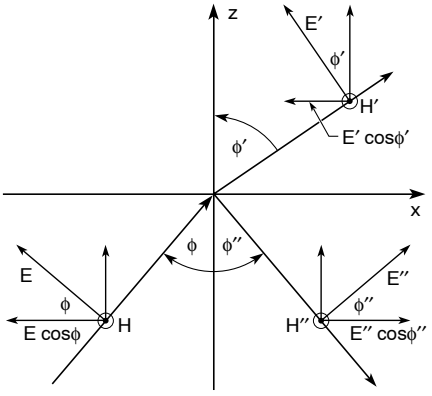

FIGURE 3.9. Field components for parallel (p) polarization, where **E** lies in the x, z-plane of incidence.

3.5.2 E_0 Parallel to the Plane of Incidence

The second decomposition of incident polarization is that in which the electric field vector lies in the x, z-plane of incidence, as shown in Figure 3.9, and is referred to as parallel (p) polarization (in both English and German). Applying the boundary conditions as in the previous case, one now obtains

$$\frac{E_0''}{E_0} = \frac{n\cos\phi - \cos\phi'}{n\cos\phi + \cos\phi'}$$

Noting that

$$\cos\phi' = \sqrt{1 - \sin^2\phi'} = \sqrt{1 - \frac{\sin^2\phi}{n^2}}$$

this becomes

$$\frac{E_0''}{E_0} = \frac{n\cos\phi - \frac{1}{n}\sqrt{n^2 - \sin^2\phi}}{n\cos\phi + \frac{1}{n}\sqrt{n^2 - \sin^2\phi}}$$

or

$$\frac{E_0''}{E_0} = \frac{n^2\cos\phi - \sqrt{n^2 - \sin^2\phi}}{n^2\cos\phi + \sqrt{n^2 - \sin^2\phi}} \tag{3.54}$$

for the reflected field amplitude. The refracted electric field is then determined from the boundary condition

$$nE_0' = E_0 + E_0''$$

to be

$$\frac{E_0'}{E_0} = \frac{1}{n}\left[1 + \frac{n^2\cos\phi - \sqrt{n^2 - \sin^2\phi}}{n^2\cos\phi + \sqrt{n^2 - \sin^2\phi}}\right]$$

or

$$\frac{E_0'}{E_0} = \frac{2n\cos\phi}{n^2\cos\phi + \sqrt{n^2 - \sin^2\phi}} \tag{3.55}$$

which we note are similar in form, but slightly different than the equations for reflected and refracted fields in the case of perpendicular polarization [Eqs. (3.46) and (3.47)]. The reflectivity for parallel polarization is determined from Eq. (3.54) to be

$$R_p = \left|\frac{E_0''}{E_0}\right|^2 = \frac{\left|n^2\cos\phi - \sqrt{n^2 - \sin^2\phi}\right|^2}{\left|n^2\cos\phi + \sqrt{n^2 - \sin^2\phi}\right|^2} \tag{3.56}$$

which we note is different than Eq. (3.49) for the case of perpendicular polarization.

It is interesting that in several important special cases both polarizations give the same result. For normal incidence, Eq. (3.56) for p-polarization reduces to

$$R_{p,\perp} = \frac{(n-1)(n^*-1)}{(n+1)(n^*+1)} \simeq \frac{\delta^2 + \beta^2}{4} \tag{3.57}$$

which is identical to Eq. (3.50) for s-polarization at $\phi = 0$, as it should be, since the two polarizations are physically indistinguishable at normal incidence. For glancing incidence Eq. (3.56) also reduces to the same result obtained previously for perpendicular polarization, given as Eq. (3.52) and plotted in Figure 3.8.

While Figure 3.8 is very instructive, showing the effect of finite β on the shape of an idealized critical angle reflection ($\beta = 0$), more practical results can also be obtained through the use of Eq. (3.52) for real materials at various photon energies. For instance, in laboratory studies it is often interesting to know what is the reflectivity vs. photon energy for a given mirror material at various angles of incidence near the critical angle. To calculate such curves one must know the values of δ and β for the material of interest, across the photon energies of interest, and use them in Eq. (3.52) for the incident angles relevant to the experiment. Values of δ and β are tabulated by Henke et al.[7]; examples are given in Appendix C for selected materials. The resultant reflectivity curves are interesting in that they relate to real materials and include the effects of absorption edges, which can be used to enhance angular cutoffs at a given photon energy, and also can include the effects of oxidation and other multi-element effects. Figure 3.10 illustrates glancing incidence reflection curves for carbon, aluminum, aluminum oxide, and gold. Results for other materials are given in Ref. 7.

As the reflectivity curves show, mirrors at glancing incidence do not reflect well at higher photon energies, and thus can be used as *low pass filters*. This contrasts with thin transmitting foils, which are highly absorptive at low photon energies and thus serve as *high pass filters*. In combination, a mirror–filter pair can provide a moderate resolution *notch filter*, which blocks low and high energy photons, but passes a central pass band of relative spectral bandwidth $E/\Delta E$ of 3–5, depending on the degree to which absorption edges can be used to enhance the sharpness of reflection or transmission curves. Figure 3.11 illustrates the idea of a notch filter based on an idealized mirror whose cutoff angle is matched to the K-absorption edge of a transmission filter. Such mirror–filter pairs are quite convenient to use, and are often utilized in imaging and transport applications involving broadband sources of radiation.

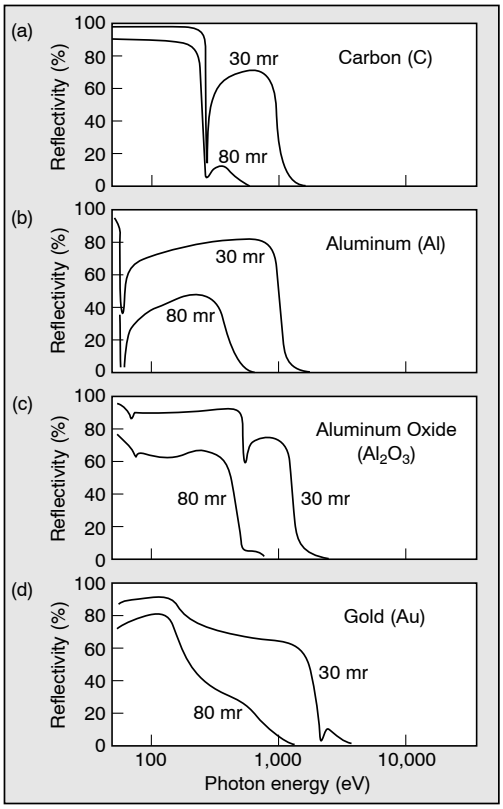

FIGURE 3.10. Glancing incidence reflectivity vs. photon energy for incidence angles (θ) of 30 mrad and 80 mrad, for materials of (a) carbon, (b) aluminum, (c) aluminum oxide, and (d) gold. The results follow from Eq. (3.52), for both parallel and perpendicular polarization, as a function of θ. Values of δ and β are from the tabulations of Henke, Gullikson, and Davis.[7] Note how the combination of cutoff angle and absorption edge can be used to enhance the sharpness of the reflectivity curve, which is useful when the material is used as a low pass filter. Recall that 1 mrad $= 0.0573^\circ = 3.44$ arcmin (see Appendix A).

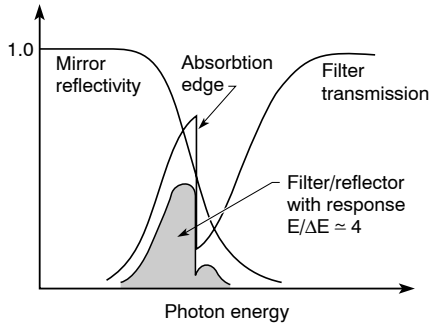

FIGURE 3.11. A moderate resolution spectral bandpass, or *notch filter*, is constructed by sequential reflection from an idealized mirror of glancing incidence, and transmission through a foil whose absorption edge is matched to the decline in mirror reflectivity.

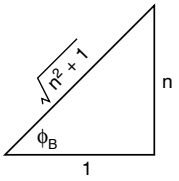

FIGURE 3.12. A diagram for understanding Brewster's angle.

Another, more specialized option for spectral filtering involves the failure of total external reflectance in the vicinity of certain absorption edges. For EUV radiation there is strong anomalous dispersion near the $L_{2,3}$-edges of the third period elements, such as Al and Si, which results in a sign reversal of f_1^0, and thus δ. This results in a sharp transmission window, making it possible to exploit the effect to create very narrow spectral bandwidth filters.[12]

3.6 BREWSTER'S ANGLE

An effect unique to parallel polarization occurs at an angle for which the numerator of Eq. (3.56) is zero, or at least reaches a minimum. At visible light wavelengths, where β/δ is extremely small, this phenomenon has important applications and is known as Brewster's angle, or the polarizing angle (see Refs. 1, 4, and 5). For instance, visible light laser rods often have their ends cut at Brewster's angle to minimize intracavity reflective losses and to provide a mechanism for polarization selection. At EUV and x-ray wavelengths, where reflectivities are already very small at relevant angles (near 45°, as we shall see shortly), the effect is less dramatic but still very useful in polarization sensitive applications. Furthermore, the effect is reduced by absorptive losses (β), which are more important in this region of the spectrum. The minimum in reflectivity occurs when the numerator in Eq. (3.56) satisfies the condition

$$n^2 \cos\phi_B = \sqrt{n^2 - \sin^2\phi_B} \tag{3.58}$$

Squaring both sides, collecting like terms involving ϕ_B, and factoring, one has

$$n^2(n^2 - 1) = (n^4 - 1)\sin^2\phi_B$$

or

$$\sin\phi_B = \frac{n}{\sqrt{n^2 + 1}}$$

This permits us to construct the diagram in Figure 3.12, from which we see that the condition for a minimum in the reflection coefficient, for parallel polarized radiation, occurs at an angle given by

$$\tan\phi_B = n \tag{3.59}$$

For visible light where glass typically has a refractive index $n = 1.5$, Brewster's angle is about 56° from the surface normal.

Since n is complex, Eq. (3.59) does not yield a real angle ϕ_B for which $R_p(\phi)$ would be zero; rather, a minimum is achieved. From Eq. (3.56) we expand the reflectivity $R_p(\phi)$ in the

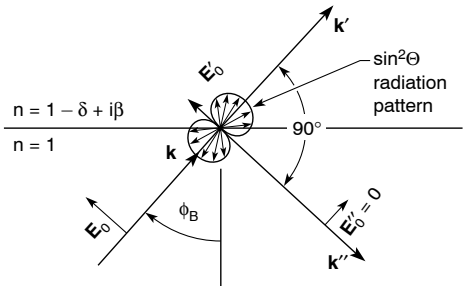

FIGURE 3.13. The special angle ϕ_B that results in minimal or no refracted wave for parallel polarization because the refracted wave is oriented so as to excite no reflected field components.

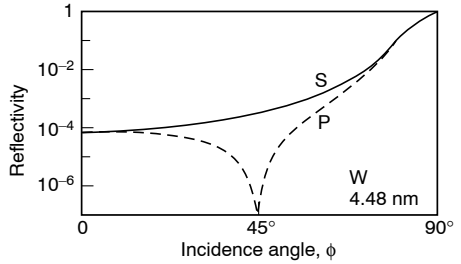

FIGURE 3.14. Reflectivity versus angle for parallel (dashed line) and perpendicular polarized radiation (solid line) incident on a tungsten surface at a wavelength of 4.48 nm (from Underwood[13]).

small parameters δ and β, then find the minimum by setting the derivative with respect to ϕ to zero. Doing this, we find that the Brewster minimum occurs at a real angle of incidence given by

$$\tan \phi_B = 1 - \delta$$

which for $\delta \ll 1$ corresponds to an angle of incidence ϕ_B slightly less than 45° from the surface normal. Taking a Taylor expansion of $\tan \phi_B$ about $\pi/4$, one finds that Brewster's angle, or, if one prefers, the polarizing angle, is given by

$$\phi_B \simeq \frac{\pi}{4} - \frac{\delta}{2} \tag{3.60}$$

This result has an interesting physical interpretation. At Brewster's angle the refracted wave is turned in just such a manner that the refracted wave vector $\mathbf{k}'$ is at a right angle to the reflected wave vector $\mathbf{k}''$, as illustrated in Figure 3.13. Note that with parallel polarization the refracted electric field $\mathbf{E}'$ is then coaligned with the reflected wave vector $\mathbf{k}''$ – a condition in which it cannot generate a reflected wave. In this situation the atoms at the interface respond to the impressed field $\mathbf{E}'_0$, oscillating in a direction parallel to $\mathbf{k}''$, each radiating a $\sin^2 \theta$ pattern which is zero in the reflected direction and thus producing no reflected field component $\mathbf{E}''_0$. Figure 3.14 shows an example of reflection coefficients for both parallel and perpendicular polarized radiation incident on a tungsten surface at a wavelength of 4.48 nm.[13] Note the sharp reflectivity dip at an incidence angle just below 45° for parallel polarization (dashed line).

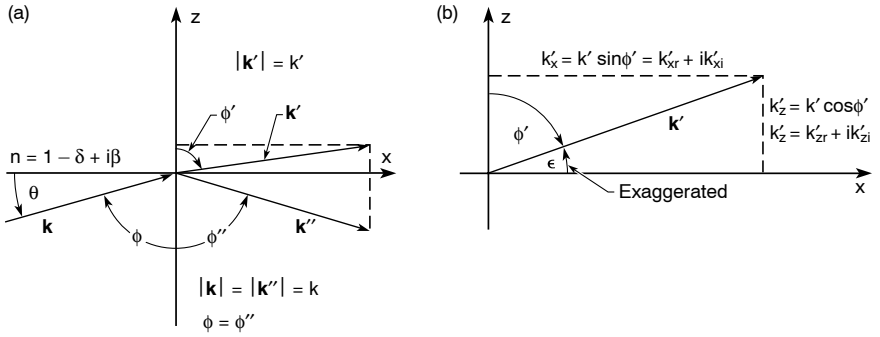

FIGURE 3.15. (a) Wave vectors for radiation incident on a lossy medium near the critical angle. (b) Real and imaginary components of the refracted wave vector for a complex angle ϕ'. The very small angle ϵ is exaggerated for clarity of the vector components.

3.7 FIELD PENETRATION INTO A LOSSY MEDIUM NEAR THE CRITICAL ANGLE

In an earlier section we considered the nature of the refracted wave incident upon a lossless medium ($\beta = 0$) at glancing incidence. It was determined that for angles of incidence θ less than a critical angle $\theta_c = \sqrt{2\delta}$, the refracted wave propagated along the interface, with no energy flow into the material. However, in the preceding section where we considered reflectivity from a material with finite δ and β, we found that even at glancing incidence finite values of β have a significant effect on reflectivity, as seen in Eq. (3.52) and Figure 3.8. These results raise questions as to the nature of the wave at the interface, the penetration depth of the fields, and the flow of power across the interface when finite losses are considered. Because of finite absorptive losses in the medium, there must now be some energy flow into the medium, even for $\theta < \theta_c$. This is different from the idealized case ($\beta = 0$) considered earlier, in which the refracted wave was found to propagate at a real angle $\phi' = \pi/2$, just along and parallel to the surface. Now with finite β, we must permit the refracted wave vector $\mathbf{k}'$ to have a finite real component $\mathbf{k}'_{zr}$ into the medium, as illustrated in Figure 3.15. Thus we expect that even for $\theta < \theta_c$, ϕ' will have a solution slightly less than $\pi/2$.

We start our analysis, as we did for the ideal case ($\beta = 0$), with Snell's law [Eq. (3.38)], but now for a complex refractive index

$$\sin\phi' = \frac{\sin\phi}{n}$$

where

$$n = 1 - \delta + i\beta$$

Since n is complex, ϕ' will be complex for real angle of incidence ϕ. Since δ and β are very small for x-rays, we may write

$$\sin\phi' = (1 + \delta - i\beta)\sin\phi \tag{3.61}$$

and assume

$$\phi' = \phi'_r - i\phi'_i \tag{3.62}$$

where we have taken a negative imaginary component for consistency with the sign of β in Eq. (3.61). Upon inspection of Figure 3.15 we see that the propagation vector $\mathbf{k}'$ in the medium has components

$$k'_x = k' \sin\phi'$$

and

$$k'_z = k' \cos\phi'$$

where from Eq. (3.37)

$$k' = \frac{\omega}{c}(1 - \delta + i\beta)$$

so that

$$k'_x = \frac{\omega}{c}(1 - \delta + i\beta)\sin\phi' \tag{3.63a}$$

and

$$k'_z = \frac{\omega}{c}(1 - \delta + i\beta)\cos\phi' \tag{3.63b}$$

Recognizing that k'_x and k'_z are in general complex, we may rewrite the above in terms of real and imaginary components

$$k'_{xr} + ik'_{xi} = \frac{\omega}{c}(1 - \delta + i\beta)\sin\phi' \tag{3.64a}$$

and

$$k'_{zr} + ik'_{zi} = \frac{\omega}{c}(1 - \delta + i\beta)\cos\phi' \tag{3.64b}$$

For a complex angle $\phi' = \phi'_r - i\phi'_i$, as in Eq. (3.62), one has the trigonometric identities (see Appendix A)

$$\sin\phi' = \sin\phi'_r \cosh\phi'_i - i\cos\phi'_r \sinh\phi'_i \tag{3.65a}$$

and

$$\cos\phi' = \cos\phi'_r \cosh\phi'_i + i\sin\phi'_r \sinh\phi'_i \tag{3.65b}$$

The real and imaginary parts of the wave vector components can now be identified by combining Eqs. (3.64) and (3.65), viz.,

$$k'_{xr} + ik'_{xi} = \frac{\omega}{c}(1 - \delta + i\beta)[\sin\phi'_r \cosh\phi'_i - i\cos\phi'_r \sinh\phi'_i] \tag{3.66a}$$

and

$$k'_{zr} + ik'_{zi} = \frac{\omega}{c}(1 - \delta + i\beta)[\cos\phi'_r \cosh\phi'_i + i\sin\phi'_r \sinh\phi'_i] \tag{3.66b}$$

For $\beta \ll 1$, so that $\phi'_i \ll 1$, one can make the approximations

$$\sinh\phi'_i \simeq \phi'_i \tag{3.67a}$$

and

$$\cosh \phi_i' \simeq 1 + \frac{\phi_i'^2}{2} \tag{3.67b}$$

For angles ϕ near the critical angle we can again take the approximation

$$\sin \phi = \cos \theta \simeq 1 - \frac{\theta^2}{2} \tag{3.67c}$$

For angles near critical, with a refracted wave propagating very close to the interface of a lossy medium, we can take the solution for ϕ' in which the real part is very close to but slightly less than $\pi/2$, such that

$$\boxed{\phi_r' = \frac{\pi}{2} - \epsilon, \qquad \epsilon \ll 1} \tag{3.68}$$

This permits the refracted wave to propagate very close to the interface, but with a small real component of k_z' so that energy can propagate across the interface and thus maintain steady state fields in the presence of finite absorptive losses. In this limit we can make the additional approximations

$$\sin \phi_r' = \cos \epsilon \simeq 1 - \frac{\epsilon^2}{2} \tag{3.69a}$$

and

$$\cos \phi_r' = \sin \epsilon \simeq \epsilon \tag{3.69b}$$

Collecting these various angular approximations [Eqs. (3.67), (3.68), and (3.69)], the expressions for real and imaginary wave vector components in the lossy medium [Eqs. (3.66a) and (3.66b)] become

$$k_{xr}' + ik_{xi}' = \frac{\omega}{c}(1 - \delta + i\beta)\left[\left(1 - \frac{\epsilon^2}{2}\right)\left(1 + \frac{\phi_i'^2}{2}\right) - i\epsilon\phi_i'\right] \tag{3.70a}$$

and

$$k_{zr}' + ik_{zi}' = \frac{\omega}{c}(1 - \delta + i\beta)\left[\epsilon\left(1 + \frac{\phi_i'^2}{2}\right) + i\left(1 - \frac{\epsilon^2}{2}\right)\phi_i'\right] \tag{3.70b}$$

Thus for k_x', along the interface,

$$k_{xr}' = \frac{\omega}{c}(1 - \delta)\left(1 - \frac{\epsilon^2}{2}\right)\left(1 + \frac{\phi_i'^2}{2}\right) + \frac{\omega}{c}\beta\epsilon\phi_i' \tag{3.71a}$$

and

$$k_{xi}' = \frac{\omega}{c}\beta\left(1 - \frac{\epsilon^2}{2}\right)\left(1 + \frac{\phi_i'^2}{2}\right) - \frac{\omega}{c}(1 - \delta)\epsilon\phi_i' \tag{3.71b}$$

and for k'_z, in a direction perpendicular to the interface,

$$k'_{zr} = \frac{\omega}{c}(1-\delta)\epsilon\left(1+\frac{\phi_i'^2}{2}\right) - \frac{\omega}{c}\beta\left(1-\frac{\epsilon^2}{2}\right)\phi'_i \tag{3.72a}$$

and

$$k'_{zi} = \frac{\omega}{c}\beta\epsilon\left(1+\frac{\phi_i'^2}{2}\right) + \frac{\omega}{c}(1-\delta)\left(1-\frac{\epsilon^2}{2}\right)\phi'_i \tag{3.72b}$$

If we now apply the boundary condition that $k'_x = k_x$, ensuring continuous transverse field components along the interface [Eq. (34a)], then we must set $k'_{xr} = k_{xr} = (\omega/c)(1-\theta^2/2)$ in Eq. (3.71a) and $k'_{xi} = 0$ in Eq. (3.71b). From the latter we obtain

$$\beta\left(1-\frac{\epsilon^2}{2}\right)\left(1+\frac{\phi_i'^2}{2}\right) = (1-\delta)\epsilon\phi'_i$$

Dropping second order terms ϵ^2 and $\phi_i'^2$ as being small, and noting that $\delta \ll 1$, we have to first order

$$\phi'_i \simeq \frac{\beta}{\epsilon} \tag{3.73}$$

while the condition on k'_{xr} gives

$$\frac{\omega}{c}\left(1-\frac{\theta^2}{2}\right) \simeq \frac{\omega}{c}(1-\delta)\left(1-\frac{\epsilon^2}{2}\right)\left(1+\frac{\phi_i'^2}{2}\right) + \frac{\omega}{c}\beta\epsilon\phi'_i$$

$$\left(1-\frac{\theta^2}{2}\right) \simeq (1-\delta)\left(1-\frac{\epsilon^2}{2}\right)\left(1+\frac{\beta^2}{2\epsilon^2}\right) + \beta^2$$

Thus to first order, with $\beta^2 \ll \delta$,

$$\left(1+\delta-\frac{\theta^2}{2}\right) \simeq \left(1-\frac{\epsilon^2}{2}\right)\left(1+\frac{\beta^2}{2\epsilon^2}\right)$$

$$\delta - \frac{\theta^2}{2} \simeq -\frac{\epsilon^2}{2} + \frac{\beta^2}{2\epsilon^2}$$

which we can write in quadratic form

$$\epsilon^4 - (\theta^2 - 2\delta)\epsilon^2 - \beta^2 = 0 \tag{3.74}$$

which has solution for the (real) angular decrement ϵ (from $\pi/2$)

$$\boxed{\epsilon^2 = \frac{\sqrt{(\theta^2-2\delta)^2+4\beta^2} + (\theta^2-2\delta)}{2}} \tag{3.75}$$

and where we have taken the positive square root to ensure a real solution for the angle ϵ.

Thus general solutions for the complex refraction angle ϕ', at glancing incidence, are obtained from Eqs. (68) and (73) to be

$$\phi'_r = \frac{\pi}{2} - \epsilon = \frac{\pi}{2} - \left[\frac{\sqrt{(\theta^2 - 2\delta)^2 + 4\beta^2} + (\theta^2 - 2\delta)}{2}\right]^{1/2} \tag{3.76a}$$

$$\phi'_i = \frac{\beta}{\epsilon} = \frac{\sqrt{2}\beta}{\left[\sqrt{(\theta^2 - 2\delta)^2 + 4\beta^2} + (\theta^2 - 2\delta)\right]^{1/2}} \tag{3.76b}$$

from which we can now determine the various wave vector components, from Eqs. (3.71) and (3.72), for the refracted wave in a lossy medium near the critical angle. Note that, with these same approximations that θ^2, δ, and β are all much less than unity, the wave vector components in the medium, Eqs. (3.71) and (3.72), now reduce to

$$k'_{xr} \simeq \frac{\omega}{c}\left(1 - \frac{\theta^2}{2}\right) \tag{3.77a}$$

$$k'_{xi} = 0 \tag{3.77b}$$

$$k'_{zr} \simeq \frac{\omega}{c}\epsilon \tag{3.77c}$$

$$k'_{zi} \simeq \frac{\omega}{c}\frac{\beta}{\epsilon} \tag{3.77d}$$

The first two are set by the boundary conditions. The third, Eq. (3.77c), simply says that the real wave vector, related to power flow, propagates at an angle ϵ, slightly non-parallel to the interface. Lastly, Eq. (3.77d) shows that field decay into the medium is proportional to β/ϵ, which must be carefully analyzed for the various angles of interest.

Two cases of special interest offer insights into the nature of wave propagation, the resultant fields, and their relation to energy loss in a lossy medium near the critical angle of incidence. The special cases are those of extreme glancing incidence, such that $\theta \ll \theta_c$, and incidence just at the critical angle $\theta = \theta_c$. Combining Eqs. (3.76) and (3.77), we have the following:

(1) *Glancing incidence*, $\theta^2 \ll \theta_c^2$, $\epsilon = \beta/(\theta_c^2 - \theta^2)^{1/2} \to \beta/\sqrt{2\delta}$:

$$\phi'_r \simeq \frac{\pi}{2} - \frac{\beta}{\left(\theta_c^2 - \theta^2\right)^{1/2}} \to \frac{\pi}{2} - \frac{\beta}{\sqrt{2\delta}} \tag{3.78a}$$

$$\phi'_i \simeq \left(\theta_c^2 - \theta^2\right)^{1/2} \to \sqrt{2\delta} \tag{3.78b}$$

$$k'_{xr} \simeq \frac{\omega}{c}\left(1 - \frac{\theta^2}{2}\right) \tag{3.78c}$$

$$k'_{xi} = 0 \tag{3.78d}$$

$$k'_{zr} \simeq \frac{\omega}{c}\frac{\beta}{\left(\theta_c^2-\theta^2\right)^{1/2}} \rightarrow \frac{\omega\beta}{c\sqrt{2\delta}} \tag{3.78e}$$

$$k'_{zi} \simeq \frac{\omega}{c}\sqrt{\theta_c^2-\theta^2} \rightarrow \frac{\omega}{c}\sqrt{2\delta} \tag{3.78f}$$

where the arrows indicate limiting values as θ goes to zero.

(2) *Critical angle,* $\theta = \theta_c$, $\epsilon_c \simeq \beta^{1/2}$:

$$\phi'_r \simeq \frac{\pi}{2} - \beta^{1/2} \tag{3.79a}$$

$$\phi'_i \simeq \beta^{1/2} \tag{3.79b}$$

$$k'_{xr} \simeq \frac{\omega}{c}\left(1-\frac{\theta^2}{2}\right) = \frac{\omega}{c}(1-\delta) \tag{3.79c}$$

$$k'_{xi} = 0 \tag{3.79d}$$

$$k'_{zr} \simeq \frac{\omega}{c}\beta^{1/2} \tag{3.79e}$$

$$k'_{zi} \simeq \frac{\omega}{c}\beta^{1/2} \tag{3.79f}$$

In both special cases above, the solutions indicate an evanescent wave propagating very nearly parallel to the interface, with field amplitudes decaying with distance z into the material. The small angle ϵ by which the wave vector is non-parallel to the interface is zero only in the lossless limit, β equal to zero. It is interesting to note the differing field penetrations in the two cases, and relate these to reflectance curves previously seen in Figure 3.8. According to Eq. (3.78), at glancing incidence *the fields decay with an exponential dependence*

$$e^{-k'_{zi}z} \simeq \exp\left[-\left(\frac{\omega}{c}\sqrt{\theta_c^2-\theta^2}\right)z\right] \rightarrow e^{-(2\pi\sqrt{2\delta}/\lambda)z} \tag{3.80a}$$

i.e., with a field penetration depth for θ near zero,

$$\boxed{z_0 \simeq \frac{\lambda}{2\sqrt{2}}\pi\delta^{1/2} \qquad (\theta \ll \theta_c)} \tag{3.80b}$$

This is to be compared with the case just at the critical angle, where according to Eq. (3.79)

$$e^{-k'_{zi}z} \simeq \exp\left[-\left(\frac{\omega}{c}\beta^{1/2}\right)z\right] = e^{-(2\pi\beta^{1/2}/\lambda)z} \tag{3.81a}$$

with a field penetration depth at the critical angle

$$z_c \simeq \frac{\lambda}{2\pi\beta^{1/2}} \qquad (\theta = \theta_c) \tag{3.81b}$$

Thus for $\beta < \delta$, the penetration depth at the critical angle will be greater than for incidence angles closer to the surface, leading to greater absorption of the wave and thus less reflectivity at the critical angle, as was seen in Figure 3.8. In an earlier section we calculated that for carbon at a wavelength of 0.4 nm $\delta = 4.90 \times 10^{-5}$ and $\beta = 5.71 \times 10^{-7}$. Thus for a carbon mirror the critical angle is 9.9 mrad (0.57°) at 0.4 nm wavelength, and according to Eqs. (3.80b) and (3.81b) the penetration depth at near-zero glancing angle is 16λ, or 6.4 nm, and extends to 210 λ, or 84.0 nm, at the critical angle. In both cases energy propagates across the interface, as indicated by the finite values of k'_{zr}, which we note goes to zero as β goes to zero.

The nature of energy flow into the lossy medium can be seen explicitly by considering the z-directed portion of the Poynting vector, $\bar{S}_z$, which we can deduce by taking the cross product of the appropriate fields. For convenience we consider the case of incident radiation with the electric field polarized in the y-direction. In addition to the primary component of magnetic field associated with the refracted plane wave calculated for a lossless medium far from the critical angle ($\theta \gg \theta_c$), we also expect a second-order magnetic field due to the non-uniform nature of the wave. This non-uniformity has contributions both due to absorption and due to the evanescent decay for incidence angles θ less than the critical angle. For this non-uniform wave, characterized by an evanescent electric field $E'_y(x, z)\mathbf{y}_0$ in the medium, we can calculate the magnetic fields from Faraday's law, Eq. (2.2) in Chapter 2:

$$-\frac{\partial \mathbf{B}'}{\partial t} = \nabla \times \mathbf{E}'$$

or in terms of vector components

$$-\frac{\partial \mathbf{B}'}{\partial t} = \left(\frac{\partial}{\partial x}\mathbf{x}_0 + \frac{\partial}{\partial y}\mathbf{y}_0 + \frac{\partial}{\partial z}\mathbf{z}_0\right) \times E'_y(x, z)\mathbf{y}_0$$

or

$$-\frac{\partial \mathbf{B}'}{\partial t} = \underbrace{\frac{\partial E'_y}{\partial x}}_{B'_z}\mathbf{z}_0 - \underbrace{\frac{\partial E'_y}{\partial z}}_{B'_x}\mathbf{x}_0 \tag{3.82}$$

In Eq. (3.82), above the first term on the right of the equality is B'_z, the first order magnetic field associated with a uniform plane wave propagating in the x-direction. The second term on the right is B'_x, which includes the second order magnetic fields due to absorption and below-critical evanescence, each of which give z-dependent variations, and also includes the z-direction component of plane wave propagation. Thus the second-order magnetic field, B'_x, which will cross with E'_y to give power flow in the z-direction (across the interface), corresponds to the $\mathbf{x}_0$-components of Eq. (3.82), viz.,

$$-\frac{\partial B'_x}{\partial t} = -\frac{\partial E'_y}{\partial z}$$

The time dependence for all fields is the same; thus $\partial/\partial t = -i\omega$. Furthermore, from Eq. (3.77) the z-dependence of $E'_y(x,z)$ is given by

$$E'_y(z) = E'_y(0)e^{i\omega\epsilon z/c}e^{-\omega\beta z/\epsilon c}$$

so that

$$B'_x(x,z) = -\frac{1}{i\omega}\left(\frac{i\omega\epsilon}{c} - \frac{\omega\beta}{\epsilon c}\right)E'_y(x,z)$$

$$B'_x(x,z) = -\left(\frac{\epsilon}{c} + i\frac{\beta}{\epsilon c}\right)E'_y(x,z)$$

For non-magnetic materials, where $\mu = \mu_0$, the magnetic field vector is

$$H'_x(x,z)\mathbf{x}_0 = -\sqrt{\frac{\epsilon_0}{\mu_0}}\left(\epsilon + i\frac{\beta}{\epsilon}\right)E'_y(x,z)\mathbf{x}_0 \tag{3.83}$$

where ϵ is the angle measured from the interface. With the magnitude of the average Poynting vector given by Eq. (3.19), the time-averaged power per unit area crossing the interface is given by

$$|\tilde{\mathbf{S}}| = \tfrac{1}{2}\mathrm{Re}(\mathbf{E}\times\mathbf{H}^*)$$

with z-component

$$\tilde{S}'_z\mathbf{z}_0 = \tfrac{1}{2}\mathrm{Re}(E'_y\mathbf{y}_0 \times H'^*_x\mathbf{x}_0)$$

so that

$$\tilde{S}'_z = -\frac{1}{2}\mathrm{Re}\left[(E'_y)\left(-\sqrt{\frac{\epsilon_0}{\mu_0}}\right)\left(\epsilon - i\frac{\beta}{\epsilon}\right)E'_y\right]$$

$$\boxed{\tilde{S}'_z = \frac{1}{2}\sqrt{\frac{\epsilon_0}{\mu_0}}\epsilon|E'_y|^2} \tag{3.84}$$

where the angle ϵ is given in Eq. (3.75). We see that the power flowing across the interface is directly proportional to ϵ, which has a complicated dependence on θ, δ, and β, but which goes to zero as β goes to zero. Tracing this term back through the mathematics, we observe that it is due to the non-parallelism of the refracted wave with respect to the surface, which arises because of the finite absorptivity β. The second term [for instance the $i\beta/\epsilon$ term in Eq. (3.83)], which is due to the evanescent nature of the fields, even when β is zero (β/ϵ is not zero in this limit), does not contribute to power flow across the interface, as is seen in the mathematical progression from Eq. (3.83) to (3.84). This term gives a measure of the stored energy in the evanescent fields.

In summary, we observe that in the case of a lossy medium, with an angle of incidence θ less than the critical angle, the refracted wave is non-uniform, that is, the field amplitudes are

no longer constant in planes transverse to the propagation direction. The wave now propagates at a slight angle (ϵ) to the interface, with second order fields out of the plane. That is, the refracted wave is neither uniform nor plane. Power flows across the interface for non-zero absorptivity β. Details of the evanescent field decay, and power flow, depend on both δ and β, and of course the angle of incidence ϕ (or θ).

3.8 DETERMINATION OF δ AND β: THE KRAMERS–KRONIG RELATIONS

In principle δ and β can be determined for all materials through measurements of absorption and phase shift, as discussed in the text leading to Eqs. (3.22) and (3.29). This is in fact how β is determined. However, determining δ proves to be more problematic, particularly for soft x-rays, because interferometry is not sufficiently advanced. Rather, the general approach is to return to Eqs. (3.13a) and (3.13b), where δ and β are expressed in terms of real and imaginary parts of the complex atomic scattering factor, i.e.,

$$\delta = \frac{n_a r_e \lambda^2}{2\pi} f_1^0(\omega)$$

$$\beta = \frac{n_a r_e \lambda^2}{2\pi} f_2^0(\omega)$$

where from Eq. (2.79) the complex atomic scattering factor

$$f^0(\omega) = f_1^0(\omega) - i f_2^0(\omega)$$

is the ratio of the electric field strength scattered by an atom to that of a single free electron. Recall that the subscript zero refers to the limiting cases of either long wavelength or forward scattering [Eqs. (2.70)–(2.72)], the latter having a direct relation to the refractive index.

The determination of $f_2^0(\omega)$ is accomplished by measuring the absorption of radiation through thin foils (or gases) of an element of interest (C, O, . . . , Ni, . . . , Au, . . .) for a broad range of photon energies ($\hbar\omega$). This can be done using broadly tunable synchrotron radiation (discussed in Chapter 5) and a suitable monochromator. From these measurements the macroscopic mass absorption coefficient $\mu(\omega)$ can be determined, as described in Chapter 1, and here in Eq. (3.24). The imaginary part of the atomic scattering factor is then determined from Eq. (3.26), viz.,

$$f_2^0(\omega) = \frac{A m_u}{2 r_e \lambda} \mu(\omega)$$

– a macroscopic-to-microscopic relationship, where for the element in question A is the number of atomic mass units, m_u is the atomic mass unit, r_e is the classical electron radius, λ is the wavelength in vacuum, and μ is the photon energy dependent mass absorption coefficient.

The real part of the atomic scattering factor, $f_1^0(\omega)$, is then determined through mathematical relationships between f_1^0 and f_2^0, generally referred to as *Kramers–Kronig relations,*[14–17] first derived in 1927. For a broad class of physical problems – including damped electrical circuits, scattering, and refractive index – these relate the real and imaginary parts of the physical "response" to a "stimulus" in linear, stable, causal systems. If the system is causal, there is no response ($\mathbf{E}_{\text{scatt}}$) until there is a cause ($\mathbf{E}_{\text{inc}}$). The scattering of radiation is just such a problem. For the problem of interest here, we shall show in this section that the real and

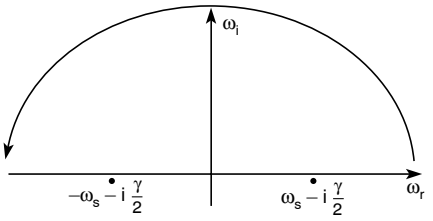

FIGURE 3.16. Representing $f^0(\omega)$ in the complex ω-plane. For $\gamma \ll \omega_s$ the function $f^0(\omega)$ has poles at $\pm\omega_s - i(\gamma/2)$ in the lower half plane, and is analytic in the upper half plane.

imaginary parts of the complex atomic scattering factor are related by

$$f_1^0(\omega) = Z - \frac{2}{\pi}\mathcal{P}_C \int_0^\infty \frac{u f_2^0(u)}{u^2 - \omega^2}\, du \tag{3.85a}$$

and

$$f_2^0 = \frac{2\omega}{\pi}\mathcal{P}_C \int_0^\infty \frac{f_1^0(u) - Z}{u^2 - \omega^2}\, du \tag{3.85b}$$

where f_1^0 is written as having a first order term Z, the number of electrons per atom, and a departure therefrom due to the degree of binding, as discussed in Chapter 2. $\mathcal{P}_C$ indicates taking only the non-divergent Cauchy principal part of the integral. As shown in Appendix D, $\mathcal{P}_C(1/x)$ is defined by *Cauchy's principal value theorem:*

$$\lim_{\epsilon \to 0} \frac{1}{x \mp i\epsilon} = \mathcal{P}_C\,(1/x) \pm i\pi\delta(x) \tag{3.86}$$

where the principal value $\mathcal{P}_C(1/x)$ refers to a function that behaves like $1/x$ everywhere except at $x = 0$, with the discontinuous behavior separated out and described by the Dirac delta function, $\delta(x)$, which is described in Appendix D.

The significance of Eqs. (3.85a) and (3.85b) is that a knowledge of either the real or the imaginary part of the response function $f^0(\omega)$ across the full spectrum of frequencies is sufficient to determine the other. Thus if one can determine $f_2^0(\omega)$ through absorption measurements, across a sufficiently broad range of frequencies, that the integral converges, one can determine $f_1^0(\omega)$. In other words, measurement of β across a sufficiently broad photon energy range allows one to determine $f_1^0(\omega)$, and thus the real part of the refractive index decrement $\delta(\omega)$, by use of Eq. (3.85a). This is in fact the procedure used by Henke and his colleagues[5] to deduce the values of f_1^0 and f_2^0 for all elements from hydrogen ($Z = 1$) to uranium ($Z = 92$), for photon energies extending from the extreme ultraviolet to the hard x-ray region of the spectrum. Experimental confirmations of these tables is of great interest, being pursued with several new types of interferometers, and with glancing incidence technologies based on best fits of Eq. (3.52) to reflections from very clean, homogeneous, and very flat surfaces.

To derive the Kramers–Kronig relations [Eqs. (3.85a) and (3.85b)] we begin with the expression for the atomic scattering factor [Eq. (2.77)]

$$f^0(\omega) = \sum_s \frac{g_s \omega^2}{\omega^2 - \omega_s^2 + i\gamma\omega}$$

where the oscillator strengths g_s in this semi-classical model sum to the total number of

atomic electrons, Z, and where for small γ the poles lie in the lower half plane (LHP) at $\omega = \pm\omega_s - i\gamma/2$ (see Figure 3.16). Multiplying the numerator and denominator of $f^0(\omega)$ by the complex conjugate of the scattering factor, we obtain the real and imaginary parts

$$f_1^0(\omega) = \sum_s \frac{g_s\omega^2\left(\omega^2 - \omega_s^2\right)}{\left(\omega^2 - \omega_s^2\right)^2 + \gamma^2\omega^2} \tag{3.87a}$$

and

$$f_2^0(\omega) = \sum_s \frac{g_s\gamma\omega^3}{\left(\omega^2 - \omega_s^2\right)^2 + \gamma^2\omega^2} \tag{3.87b}$$

where again

$$f^0(\omega) = f_1^0(\omega) - if_2^0(\omega)$$

Using the Cauchy residue theorem[18] (Appendix D), we can represent the complex function $f^0(\omega)$, which has poles only in the lower half plane, in terms of a function $f(u)$ which is analytic in the upper half plane (UHP), viz.,

$$f^0(\omega) = \frac{1}{2\pi i}\oint \frac{f^0(u)}{u - \omega}\,du \tag{3.88a}$$

More conveniently, for a function that has a limiting value Z as ω approaches infinity, we can write this as

$$f^0(\omega) - Z = \frac{1}{2\pi i}\oint \frac{f^0(u) - Z}{u - \omega}\,du \tag{3.88b}$$

Recalling the normalization condition for g_s from Eq. (2.73), we can write

$$f^0(\omega) - Z = \sum_s \frac{g_s\omega^2}{\omega^2 - \omega_s^2 + i\gamma\omega} - \sum_s \frac{g_s\left(\omega^2 - \omega_s^2 + i\gamma\omega\right)}{\omega^2 - \omega_s^2 + i\gamma\omega}$$

or

$$f^0(\omega) - Z = \sum_s \frac{g_s\left(\omega_s^2 - i\gamma\omega\right)}{\omega^2 - \omega_s^2 + i\gamma\omega}$$

This sum goes to zero as ω approaches infinity, and thus does not contribute to the integral in Eq. (3.88b) along the semicircle of infinite radius in the UHP. Thus only the integral along the real axis remains, which can be written as

$$f^0(\omega) - Z = \frac{1}{2\pi i}\int_{-\infty}^{+\infty} \frac{f^0(u) - Z}{u - \omega}\,du$$

Using the principal value theorem, Eq. (3.86), this can be rewritten as

$$f^0(\omega) - Z = \frac{1}{2\pi i}\int_{-\infty}^{\infty}\left[\mathcal{P}_{\mathrm{C}}\left(\frac{1}{u - \omega}\right) + \pi i\delta(u - \omega)\right]\left[f^0(u) - Z\right]du$$

or

$$f^0(\omega) - Z = \frac{1}{2\pi i}\mathcal{P}_C \int_{-\infty}^{\infty} \frac{f^0(u) - Z}{u - \omega}\, du + \frac{1}{2}[f^0(\omega) - Z]$$

Combining like terms,

$$f^0(\omega) - Z = \frac{1}{\pi i}\mathcal{P}_C \int_{-\infty}^{\infty} \frac{f^0(u) - Z}{u - \omega}\, du$$

Recalling that $f^0(\omega) = f_1^0(\omega) - i f_2^0(\omega)$, we can equate real and imaginary components to obtain

$$f_1^0(\omega) - Z = -\frac{1}{\pi}\mathcal{P}_C \int_{-\infty}^{\infty} \frac{f_2^0(u)}{u - \omega}\, du \tag{3.89a}$$

and

$$f_2^0(\omega) = \frac{1}{\pi}\mathcal{P}_C \int_{-\infty}^{\infty} \frac{f_1^0(u) - Z}{u - \omega}\, du \tag{3.89b}$$

where the integration is along the real axis, from minus infinity to plus infinity. To rewrite these equations in terms of only positive frequencies, we divide Eq. (3.89a) into two parts as follows:

$$f_1^0(\omega) - Z = -\frac{1}{\pi}\left[\mathcal{P}_C \int_{-\infty}^{0} \frac{f_2^0(u)}{u - \omega}\, du + \mathcal{P}_C \int_{0}^{\infty} \frac{f_2^0(u)}{u - \omega}\, du\right]$$

Replacing u by $-u$ in the first integral, and noting from Eq. (3.87b) that $f_2^0(-u) = -f_2^0(u)$ and that in general reversing the limits of integration causes a sign change, the integration can be rewritten in terms of positive frequencies only as

$$f_1^0(\omega) - Z = -\frac{1}{\pi}\mathcal{P}_C \int_{0}^{\infty} \left[\frac{1}{u + \omega} + \frac{1}{u - \omega}\right] f_2^0(u)\, du$$

or more concisely as

$$\boxed{f_1^0(\omega) - Z = -\frac{2}{\pi}\mathcal{P}_C \int_{0}^{\infty} \frac{u f_2^0(u)}{u^2 - \omega^2}\, du} \tag{3.85a}$$

which gives a solution for $f_1^0(\omega)$, and thus δ, at some specific frequency ω in terms of an integral of $f_2^0(\omega)$, or equivalently β, over all real positive frequencies – a result we stated without proof at the beginning of this section. In similar fashion we can separate Eq. (3.89b) into integrals from minus infinity to zero and from zero to infinity, make the substitution $-u$ for u in the first integral, and observe that in this case according to Eq. (3.87a) we have $f_1^0(-u) = f_1^0(u)$, and that

$$\frac{1}{u - \omega} - \frac{1}{u + \omega} = \frac{u + \omega}{u^2 - \omega^2} - \frac{u - \omega}{u^2 - \omega^2} = \frac{2\omega}{u^2 - \omega^2}$$

With these substitutions Eq. (3.89b) becomes

$$f_2^0(\omega) = \frac{2\omega}{\pi}\mathcal{P}_C \int_0^\infty \frac{f_1^0(u) - Z}{u^2 - \omega^2}\, du \tag{3.85b}$$

showing that f_2^0, and thus β, could in complementary fashion be obtained by an integration of $f_1^0(u)$, if it were δ that was more easily measured. Equations (3.85a) and (3.85b), the Kramers–Kronig relations,[13–16] provide the desired integral relationship between the real and imaginary parts of the atomic scattering factor, f_1^0 and f_2^0, or equivalently between δ and β. Since it is easier to determine β for a wide range of photon energies (frequencies) through absorption measurements, this provides a technique for numerically determining values of $\delta(\omega)$.

Henke and his colleagues[5] have compiled absorption data (f_2^0) for all elements from hydrogen to uranium, for photon energies extending from 10 eV to 30 keV, and from this data have computed and tabulated values of f_1^0 from 50 eV to 30 keV. Sample tabulations of f_1^0 and f_2^0 are given for some common elements in Appendix C. Recall that we have used the superscript zero to emphasize the simplification of the atomic scattering factor [see Eqs. (2.70)–(2.77)] when the exponent $\delta\mathbf{k}\cdot\delta\mathbf{r}_s$ goes to zero, i.e., in either the long wavelength or the forward scattering limit. As a consequence the reader must make the identifications of f_1^0 and f_2^0 here, with f_1 and f_2 in Ref. 5. Furthermore, the sign on f_2^0 is negative because of our choice regarding $e^{-i\omega t}$, as discussed earlier in this chapter.

3.9 APPLICATIONS TO GLANCING INCIDENCE OPTICS

We have seen in the preceding chapters that it is possible to reflect EUV, soft x-ray, and x-ray radiation using glancing (or grazing) incidence techniques. The critical angle for such reflections was found to be [Eq. (3.41)] $\theta_c = \sqrt{2\delta}$, where δ scales to first order as $\lambda\sqrt{Z}$, as described in Eq. (3.42). For example, a nickel mirror ($Z = 28$) has a critical angle of about 10 mrad (0.57°) for a photon energy of 6 keV, while a carbon mirror ($Z = 6$) has a critical angle of about 250 mrad (14°) for a photon energy of 100 eV. Absorption edges can be used to sharpen the reflectivity curves for particular applications, as has been illustrated here in Figure 3.10. Further examples of reflection curves for common mirror materials are given by Henke et al.[7] Glancing incidence optics are widely used to transport and moderately filter short wavelength radiation in applications such as plasma diagnostics, astronomy, synchrotron radiation beamlines, and laser research.

Imaging is possible with glancing incidence optics, as illustrated in Figure 3.17. As originally suggested by Kirkpatrick and Baez,[19] a pair of spherical mirrors, placed orthogonal to each other at glancing incidence, can be used to form an image of an emitting or backlighted object. The first mirror provides strong focusing in the horizontal direction, while the second mirror provides strong focusing in the vertical direction. The combination provides a real image with properly adjusted focal lengths (mirror curvatures).[20] In principle this is similar to forming a real visible light image with a pair of orthogonal refractive cylindrical lenses. In the EUV–x-ray case the incident radiation is far from the surface normal – a situation that

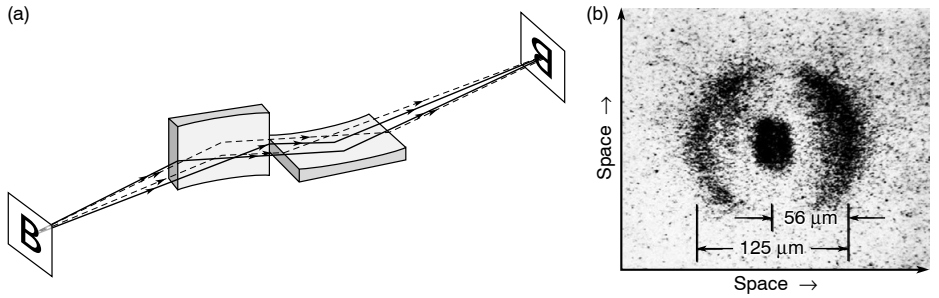

FIGURE 3.17. (a) Principle of the Kirkpatrick–Baez mirror system. The rays shown solid are the tangential rays for the first mirror and are strongly focused by it, but weakly focused by the second mirror, for which they are sagittal rays. The opposite is true for the dashed rays. (Following Underwood.[20, 21]) (b) An image of a compressed and heated laser-fusion fuel capsule, as observed at about 2 keV photon energy, using a glancing incidence Kirkpatrick–Baez microscope.[26]

introduces strong aberrations in the image, as we know from visible light experience.[††] In the Kirkpatrick–Baez microscope, astigmatism from the first mirror, which would result in more of a line focus, is compensated by that from the second mirror. A discussion of other image forming glancing incidence mirror systems, including Wolter's combinations of conic sections, is given in the review article by Underwood.[21] A discussion of common aberrations in visible light optical systems is given in the text by Hecht.[5] A discussion of aberrations in images formed with glancing incidence optics is given by Underwood.[21] Applications to EUV and soft x-ray astronomy are discussed in the texts of Charles and Seward,[22] and that of Golub and Pasachoff.[23] The use of glancing incidence optics in the design of synchrotron beamlines and monochromaters is discussed in articles by Namioka, Koike, Padmore, Howells, McKinney, and Underwood in the two-volume edition Vacuum Ultraviolet Spectroscopy edited by Samson and Ederer.[24] The use of glancing incidence optics in the design of synchrotron radiation beamlines is also described in the text by Peatman.[25]

3.10 ENHANCED REFLECTIVITY FROM PERIODIC STRUCTURES

In this chapter we have shown that, except at glancing incidence, the reflection of x-rays from a single surface is very small. In Chapter 4 on Multilayer Interference Coatings we will see that in fact large reflectivities can be obtained from a periodic structure in which the weak reflected fields add constructively at certain angles, producing a Bragg effect, even where the alternating material layers are amorphous (non-crystalline, without order) within the plane. At glancing incidence these coatings provide a Bragg peak at an angle several times larger than θ_c and thus permit increased numerical aperture, increased collection solid angle, and reduced aberrations (closer to the surface normal). For mirrors at normal incidence ($\phi = 0$),

[††]Recall the childhood use of a visible light spherical lens to burn a leaf using focused light from the sun. If the lens is held so that the incoming radiation is normal to the lens surface (parallel to the optic axis), the smallest focal spot is obtained, causing the leaf to burn. If the lens is tilted so that the incident radiation is at an angle far from the surface normal, the focal spot becomes highly aberrated, resulting in a large and distorted focal region, not sufficiently intense to burn the leaf.

constructive interference requires that each material layer (in a bi-layer periodic structure) have a thickness of approximately $\lambda/4$. With typical atomic diameters of about 2.5 Å (see the periodic chart in Chapter 1, Table 1.2), this would in principle permit normal incidence reflection at 10 Å (1 nm) wavelength. In practice the formation of amorphous layers with stable interfaces, particularly on curved substrates, requires more like 10 atomic planes per layer. As a result high normal incidence reflectivity is most likely achieved at wavelengths of order 10 nm in the EUV. The pursuit of high normal incidence reflectivity in the soft x-ray spectral region is of great interest and a very active area of research. Such multilayer mirrors, as they are often called, significantly extend the scientific and technical opportunities addressable with short wavelength radiation. The subject is discussed further in Chapter 4.

REFERENCES

1. M. Born and E. Wolf, *Principles of Optics* (Cambridge Univ. Press, 1999), Seventh Edition, Chapter VII.
2. J.D. Jackson, *Classical Electrodynamics* (Wiley, New York, 1998), Third Edition. See the discussion in Section 7.8 regarding group velocity in the vicinity of atomic resonances.
3. J.A. Stratton, *Electromagnetic Theory* (McGraw-Hill, New York, 1941).
4. G.R. Fowles, *Introduction to Modern Optics* (Dover, New York, 1989).
5. E. Hecht, *Optics* (Addison-Wesley, Reading, 1998), Third Edition.
6. A.H. Compton and S.K. Allison, *X-Rays in Theory and Practice* (Van Nostrand, New York, 1935).
7. B.L. Henke, E.M. Gullikson, and J.C. Davis, *Atomic and Nuclear Data Tables 54*, 181–342 (1993).
8. M. Francon, *Optical Interferometry* (Academic, New York, 1966).
9. U. Bonse and M. Hart, "An X-Ray Interferometer," *Appl. Phys. Lett. 6*, 155 (1965).
10. R. Soufli and E.M. Gullikson, "Reflectance Measurements on Clean Surfaces for the Determination of Optical Constants of Silicon in the Extreme Ultraviolet-Soft X-Ray Region," *Appl. Optics 36*, 5499 (1997); R. Soufli, "Optical Constants of Materials in the EUV/Soft X-Ray Region for Multilayer Mirror Applications," Ph.D. thesis, Department of Electrical Engineering and Computer Sciences, University of California at Berkeley (1997).
11. L.G. Parratt, "Surface Studies of Solids by Total Reflection of X-Rays," *Phys. Rev. 95*, 359 (1954).
12. D.Y. Smith and J.H. Barkyoumb, "Sign Reversal of the Atomic Scattering Factor and Grazing Incidence Transmission at X-Ray Absorption Edges," *Phys. Rev. B 41*, 11529 (1990).
13. J.H. Underwood, *Optics News 12*, 20 (Opt. Soc. Am., Washington, DC, March 1996).
14. L.D. Landau and E.M. Lifshitz, *Electrodynamics of Continuous Media* (Addison-Wesley, New York, 1960), pp. 256–261.
15. J.E. Marsden and M.J. Hoffman *Basic Complex Analysis* (Freeman, New York, 1973), Second Edition, p. 548.
16. F. Wooten, *Optical Properties of Solids* (Academic, New York, 1972).
17. R.W. Ditchburn, *Light* (Blackie, London, 1963), Second Edition, Appendix XIX.
18. E. Kreyszig, *Advanced Engineering Mathematics* (Wiley, New York, 1993), Seventh Edition, p. 770.
19. P. Kirkpatrick and A.V. Baez, "Formation of Optical Images by X-Rays," *J. Opt. Soc. Amer. 38*, 766 (1948); P. Kirkpatrick, "The X-Ray Microscope," *Sci. Am. 180*, 44 (1949).
20. J.H. Underwood, "Imaging Properties and Aberrations of Spherical Optics and Nonspherical Optics," p. 145 in *Vacuum Ultraviolet Spectroscopy I* (Academic, New York, 1998), J.A.R Samson and D.L. Ederer, Editors.
21. J.H. Underwood, "X-Ray Optics," *Amer. Sci. 66*, 476 (1978); J.H. Underwood and D.T. Attwood, "The Renaissance of X-Ray Optics," *Phys. Today*, p. 44 (April 1984).
22. P.A. Charles and F.D. Seward, *Exploring the X-Ray Universe*; also see the web site http://asc.harvard.edu/AXAF-description.html
23. L. Golub and J.M. Pasachoff, *The Solar Corona* (Cambridge Univ. Press, New York 1997).

24. J.A.R. Samson and D.L. Ederer, *Vacuum Ultraviolet Spectroscopy, Vols. I and II* (Academic, New York, 1998).
25. W.B. Peatman, *Gratings, Mirrors and Slits: Beamline Desisgn for Soft X-Ray Synchrotron Radiation Sources* (Gordon and Breach, Amsterdam, 1997).
26. F. Seward, J. Dent, M. Boyle, L. Koppel, T. Harper, P. Stoering, and A. Toor, "Calibrated Four-Color X-Ray Microscope for Laser Plasma Diagnostics," *Rev. Sci. Instr. 47*, 464 (1976).

HOMEWORK PROBLEMS

Homework problems for each chapter will be found at the website:
http://www.coe.berkeley.edu/AST/sxreuv

Chapter 4

MULTILAYER INTERFERENCE COATINGS

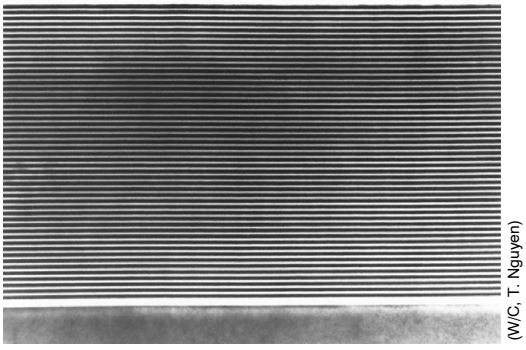

(W/C, T. Nguyen)

$$m\lambda = 2d \sin\theta$$

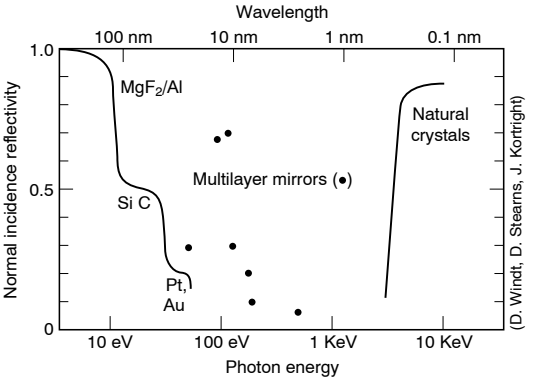

Multilayer interference coatings, often referred to as multilayer mirrors, are formed by depositing alternating layers of two materials of differing refractive index that form long-term stable interfaces. Typically the two materials are of alternating high and low atomic number (Z) in order to maximize the difference in electron density. The coatings permit the achievement of high normal incidence reflectivity, within a modest spectral bandwidth, at EUV wavelengths. They also offer new opportunities for glancing incidence reflectivity at soft x-ray and x-ray wavelengths. The coatings are largely amorphous (or to some degree polycrystalline) within individual layers, and reflection conforms to Bragg's law for a periodicity d equal to the thickness of one bilayer pair, typically measured in tens of atomic monolayers. Multilayer coatings have the great advantage of being adaptable to curved surfaces, enabling their use as reflective optics in EUV and soft x-ray microscopes, telescopes, and other applications.

4.1 INTRODUCTION

High reflectivity at normal incidence* can be achieved at EUV, and to some extent soft x-ray, wavelengths through the use of multilayer interference coatings, sometimes called reflection

*$\mathbf{k}$-vector perpendicular to the surface.

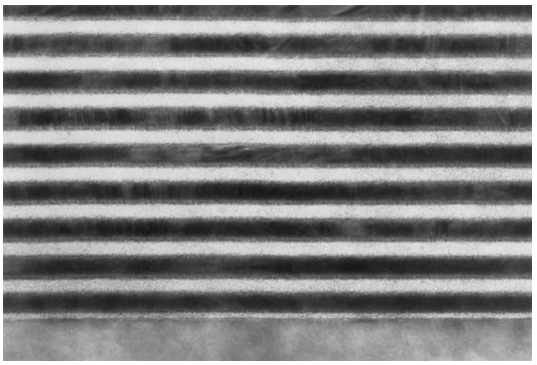

FIGURE 4.1. Side view of a multilayer interference coating, obtained by transmission electron microscopy (TEM) of a thinned section. In this example there are 20 layer pairs of molybdenum (dark) and silicon (light), which were sputtered onto a silicon substrate. The d-spacing, the thickness of one layer pair of Mo and Si, is 9.0 nm. The materials are largely amorphous, but some nanocrystalline substructure is discernible. Note also the interference transition layers due to the (asymmetric) interdiffusion of Mo into the Si layer and of Si into the Mo layer. (From T. Nguyen, Ph.D. thesis.[10])

coatings or multilayer mirrors.[1–6] The coatings, largely amorphous or polycrystalline in nature, consist of alternating high and low Z materials, with a periodicity (one layer pair) $d = \lambda/2$ for normal incidence illumination at wavelength λ. A side view of such a coating is shown in Figure 4.1. Normal incidence reflectivities of approximately 70% have been achieved[7–9] in the EUV with Mo/Si and Mo/Be, just below the absorption edges of the low Z materials at 99 eV (Si) and 111 eV (Be). The spectral bandpass for these mirrors is of order $1/N$, where N is the number of layer pairs, typically between 30 and 50 for high reflectivity. For normal incidence reflection, individual layers are each about $\lambda/4$ thick. Thus for soft x-rays each layer is only a few atoms thick. Lack of interface perfection on this spatial scale, due principally to roughness and interdiffusion, greatly reduces collective interference and thus sharply diminishes achievable normal-incidence reflectivity at these shorter wavelengths. Off-normal incidence, however, is still possible and very useful, following the traditional Bragg's law dependence $d = \lambda/(2\sin\theta)$, where θ is measured from the surface. Applications of multilayer mirror techniques to surface science (photoemission microscopy), astronomy, lithography, plasma diagnostics, polarimetry, and materials microprobing are described in this chapter.

4.2 CONSTRUCTIVE INTERFERENCE OF SCATTERED RADIATION

In a medium of uniform refractive index, of infinite extent, there is no scattering. Scattering arises from variations in refractive index, within a material or at its boundary with another material (or vacuum). We have considered the scattering from isolated free and atomically bound electrons. With a large number of such scattering centers (electrons, atoms) per unit wavelength, the scattering in any direction is canceled by interference with that from another scattering center, a distance $\lambda/2$ away, along the direction of observation. Residual scattering occurs only because of fluctuations from the mean. The sky would not be blue – or any other color – if it were not for density fluctuations in the atmosphere that redirect light away from its initial path. For short wavelengths this requires further consideration, but basically one

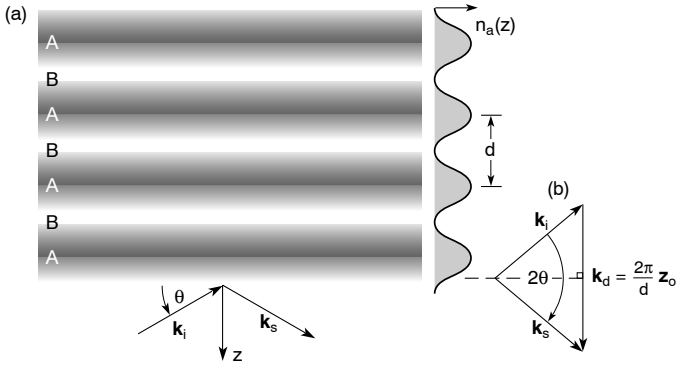

FIGURE 4.2. (a) Scattering of incident radiation, of wave vector $\mathbf{k}_\mathrm{i}$ by a one-dimensional sinusoidal density distribution of scattering centers (atoms or electrons) characterized by density $n_a(z)$ and periodicity d. (b) The associated density wave vector, $\mathbf{k}_d = (2\pi/d)\mathbf{z}_0$, points in the z-direction, where $\mathbf{z}_0$ is a unit vector. The scattered wave vector $\mathbf{k}_\mathrm{s}$ is obtained by adding wave vectors as described in Eq. (4.5).

observes scattering only to the degree that there are departures from the average density along a given line of sight. This occurs at an interface (for example, between a material and vacuum or between two materials) because the density of scatterers is different. In such cases one can apply the techniques described in Chapter 3 and solve for the resultant reflection in terms of changes in the refractive index at the interface – essentially uncompensated changes in scattering density or strength.

We begin the study of multilayer mirrors by considering first the scattering of radiation by a one-dimensional sinusoidal density profile $n_a(z)$, uniform across the $x,\ y$-plane, as shown in Figure 4.2. Considering Maxwell's equations, scattered fields are generated by induced bound electron currents that can be described for long wavelengths ($\lambda > a_0$) in terms of a complex atomic scattering factor $f^0(\omega)$, as seen earlier in Chapter 2, Eq. (2.66). The induced current can then be written as

$$\mathbf{J}(\mathbf{r},\ t) = -ef^0(\omega)n_a(\mathbf{r},\ t)\mathbf{v}(\mathbf{r},\ t) \tag{4.1}$$

where $-e$ is the electron charge, n_a is the density in atoms per unit volume, $\mathbf{v}$ is the oscillatory velocity that would be experienced by a single free electron (dominated by the electric field $\mathbf{E}_i$ of the incident field), and $f^0(\omega)$ is the frequency dependent factor that takes account of the multiplicity of bound electrons held by each atom. Performing a space–time Fourier transform, or simply representing the three waves (incident, scattered, and density) in terms of amplitudes and exponential factors, one obtains an expression for the induced current that drives the scattering process,

$$\mathbf{J}_\mathrm{scatt}e^{-i(\omega_\mathrm{s}t-\mathbf{k}_\mathrm{s}\cdot\mathbf{r})} = -ef^0(\omega_\mathrm{i})n_a e^{-i(\omega_\mathrm{d}t-\mathbf{k}_\mathrm{d}\cdot\mathbf{r})}\frac{-e\mathbf{E}_\mathrm{i}}{-i\omega_\mathrm{i}m}e^{-i(\omega_\mathrm{i}t-\mathbf{k}_\mathrm{i}\cdot\mathbf{r})} \tag{4.2}$$

where the subscript d denotes a density wave, and where the oscillating velocity $\mathbf{v}$ is related to the incident electric field by the equation of motion $m\,d\mathbf{v}/dt = -e\mathbf{E}_\mathrm{i}$, as in Chapter 2. Matching amplitudes and phase for all $\mathbf{r},\ t$, one has the general scattering relationships

$$\mathbf{J}_\mathrm{s} = \frac{ie^2n_a f^0(\omega_\mathrm{i})}{\omega_\mathrm{i}m}\mathbf{E}_\mathrm{i} \tag{4.3}$$

$$\omega_\mathrm{s} = \omega_\mathrm{i} + \omega_\mathrm{d} \tag{4.4a}$$

and

$$\mathbf{k}_s = \mathbf{k}_i + \mathbf{k}_d \tag{4.4b}$$

Equations (4.4a) and (4.5a), multiplied by $\hbar$, provide familiar expressions for conservation of energy and momentum in the scattering process, i.e.,

$$\hbar\omega_s = \hbar\omega_i + \hbar\omega_d \tag{4.5a}$$

$$\hbar\mathbf{k}_s = \hbar\mathbf{k}_i + \hbar\mathbf{k}_d \tag{4.5b}$$

These general scattering relations can be applied to a wide variety of phenomena, including Raman and Brillouin scattering, which we will consider in Chapter 6 for the case of propagating plasma waves. Here we are interested in the stationary density distribution of atoms, as illustrated in Figure 4.2. In this case the density "wave" does not move, so that ω_d is zero and $\omega_s = \omega_i$. In this case the magnitudes of the incident and scattered wave vectors must be equal, $|\mathbf{k}_s| = |\mathbf{k}_i| = 2\pi/\lambda$, so that the scattering diagram representing Eq. (4.5) must be isosceles, as shown in Figure 4.2(b). Taking $\sin\theta$ in one half of the isosceles triangle, one obtains

$$\sin\theta = \frac{k_d/2}{k_i}$$

or

$$\lambda = 2d\sin\theta \tag{4.6a}$$

which we recognize as the first order ($m = 1$) of Bragg's law – a rather general relationship for scattering or diffraction from periodic structures, including crystal planes and plasma waves. If the density distribution $n_a(z)$ is not a simple sinusoid, it can be Fourier decomposed into harmonic components of period d/m. In an angular (θ) scan of incident wave vector $k_i = 2\pi/\lambda$, the various Fourier components will generate successive scattering peaks, corresponding to wavenumbers $k_{d/m} = 2\pi/(d/m)$, yielding the more general form of Bragg's law[†]

$$m\lambda = 2d\sin\theta \tag{4.6b}$$

where $m = 1,\ 2,\ 3, \ldots$. At this point the terminology used to describe this process generally changes from use of the word "scattering" to "diffraction," or even "reflection," implying that the observed scattering has coalesced into a rather well-defined angular pattern, characteristic of the orderliness of the scattering medium.

[†]Correcting for refraction in the multilayer mirror, this becomes

$$m\lambda = 2d\sin\theta\sqrt{1 - \frac{2\bar{\delta}}{\sin^2\theta}} = 2d\sin\theta\sqrt{1 - \frac{4\bar{\delta}d^2}{m^2\lambda^2}}$$

where $\bar{\delta}$ is the bilayer weighted real part of the refractive index.

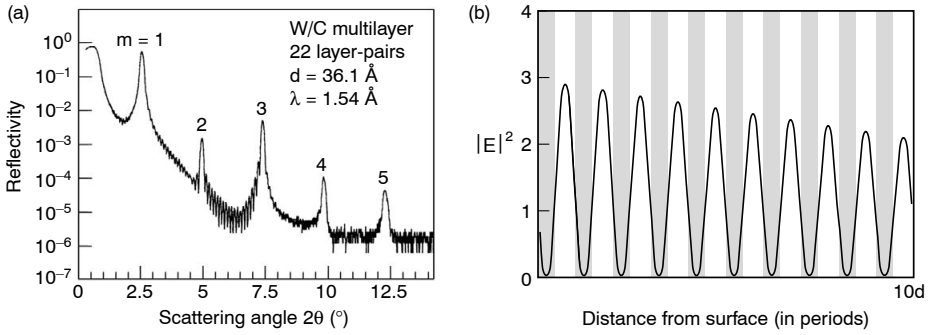

FIGURE 4.3. (a) Measured angular scan (2θ) of reflectivity for a tungsten–carbon multilayer at $\lambda = 1.54$ Å (Cu K_α). The mirror consists of 22 W–C bilayer pairs of 36.1 Å period. In addition to total external reflection at small angles, one observes a strong first order ($m = 1$) Bragg peak at about 2.5°, and less intense peaks corresponding to $m = 2,\ 3,\ 4$, and 5. (Courtesy of Y. Wu and J. Underwood.) (b) The calculated interference pattern of electric fields associated with the incident and reflected waves within the multilayer. Fields are calculated at the Bragg angle for which the interference nulls are centered within the more absorptive material, thus maximizing reflectivity. (Courtesy of J. Underwood, Lawrence Berkeley National Laboratory.)

In the fabrication and testing of multilayer mirrors, a common method for measuring d-spacing, and inferring interface sharpness, is to perform an angle dependent reflectivity scan with short wavelength radiation, typically Cu K_α at 1.54 Å. An example of such data is shown in Figure 4.3(a), for a tungsten–carbon multilayer mirror of 36.1 Å period, where several Bragg peaks are evident. The amplitudes of the peaks can be understood in terms of a spatial Fourier transform of the multilayer density distribution, or more accurately, the scattering strength $n_a f(\omega)$ as in Eq. (4.3). For example, if we examine Figure 4.2, where the density $n(z)$ is sinusoidal, we expect to see only a single Bragg peak ($m = 1$) in an angular scan. However, if $n(z)$ were a symmetric step function we would expect to see a series of Bragg peaks corresponding to $m = 1,\ 3,\ 5, \ldots$, with peak intensities declining as $1/(m\pi)^2$. If the interfaces were not so sharp, being somewhat rounded, we would expect the higher order peaks to vanish and intermediate orders to diminish in amplitude. If the density function were asymmetric, due to unequal thicknesses of high and low Z materials, we would expect the even orders ($m = 2,\ 4, \ldots$) to appear. Thus a large number of higher order Bragg peaks indicates a sharp interface, while the presence of even orders indicates an asymmetry within the bilayer. In Figure 4.3(a) Bragg peaks to $m = 5$ are quite clear. However, the intensities decline more rapidly than $1/(m\pi)^2$, indicating that the density profile is less pronounced than a square wave, which is not surprising when one considers the finite number of atomic monolayers contributing to each layer pair (about seven per layer in this case – see Table 1.4).

The appearance of even orders in Figure 4.3(a) indicates that the multilayer coating is somewhat asymmetric. In fact this coating was designed to have the tungsten layers somewhat thinner than the carbon layers, which has the effect of decreasing absorption and thus enhancing diffraction to the first order.[11, 12] In designing multilayer coatings an important parameter is the ratio of high Z material thickness to bilayer period, represented here by the Greek letter Γ, i.e.,

$$\Gamma = \frac{\Delta t_{\mathrm{H}}}{\Delta t_{\mathrm{H}} + \Delta t_{\mathrm{L}}} = \frac{\Delta t_{\mathrm{H}}}{d} \tag{4.7}$$

where Δt_H is the thickness of the high Z material and Δt_L is the thickness of the low Z material. In a manner somewhat analogous to the Borrmann effect[13] in crystals, the incident and reflected fields interfere to form a standing wave within the multilayer stack, as shown in Figure 4.3(b). This calculation of $|E|^2$ within the multilayer corresponds to incident radiation at the Bragg angle. In this case the inward- and outward-propagating waves interfere in such a way that the resultant field minima (nulls) are centered within the high Z absorbing layers. This has the effect of decreasing absorption and thus increasing reflectance at the Bragg condition.‡ Each period of the interference pattern corresponds to one period of the multilayer. For angles of incidence off the Bragg peak the interference pattern shifts within the multilayer, moving the null away from the position of minimum absorption, thus causing the reflectivity to drop.

In general it is best if the low Z material acts simply as a "spacer," with as little absorption as possible. In fact, the optical constants of the low Z material, δ_L and β_L [as in Eq. (3.12)], should be as small as possible to provide the greatest refractive index contrast at the interfaces. In that limit, or an approximation to that limit, the high Z layers provide both the scattering and absorption. The tradeoff then is to obtain sufficiently strong scattering, to first approximation through refractive index contrast at the interfaces, while minimizing the absorption by reducing the thickness of the high Z layer. Vinogradov and Zeldovich have studied this and find, for normal incidence, an optimized value Γ_{opt} given by

$$\tan(\pi\Gamma_{opt}) = \pi\left[\Gamma_{opt} + \frac{\beta_L}{\beta_H - \beta_L}\right] \tag{4.8}$$

where β_L and β_H are the absorptive components of refractive index for the low Z (L) and high Z (H) materials. For the W–C multilayer in Figure 4.3, at 1.54 Å wavelength, using values of β derived from the tables of Henke et al.[14] [see Eqs. (3.12) and (3.13)], Eq. (4.8) indicates that the optimum value is $\Gamma_{opt} \simeq 0.1$. For the specific case considered here, with $d = 36.1$ Å, the ideal thickness of the tungsten layers would be about 3.6 Å, or about 1.5 monolayers (see Table 1.4). This of course is not very realistic, considering current experience with achievable interface definition. Factors such as interface roughness (typically several monolayers), compound formation (tungsten carbide, molybdenum silicide, etc.), cross-interface interpenetration, crystallite formation, etc., limit the minimum layer thickness to at least several monolayers. For such practical reasons, typically achieved values of Γ are more generally in the region of 0.3 to 0.5 for small d-spacing coatings. For further discussion, see the text by Spiller.[1]

4.3 COMPUTATIONAL MODEL FOR CALCULATING REFLECTION FROM A MULTILAYER MIRROR

In the limit where material interfaces are well defined, it is possible to use the optical techniques developed in Chapter 3, Section 3.5, where reflection and refraction at well-defined interfaces

‡The interference in atomic crystals, which gives rise to very high reflectance at x-ray wavelengths and phenomena such as the Borrmann effect (important to x-ray interferometry), has the additional advantage that the absorbing atomic states are tightly confined to a region at the null (near-zero field). In such crystals the separation of atomic planes is set by the relatively non-absorbing valence electrons, while the more absorbing K-shell orbitals are very tightly confined to regions near the respective nuclei (see Figure 1.12). As a result, with properly controlled illumination (low angular divergence), the incident and reflected fields in atomic crystals primarily scatter off the more numerous outer electrons and experience little absorption.

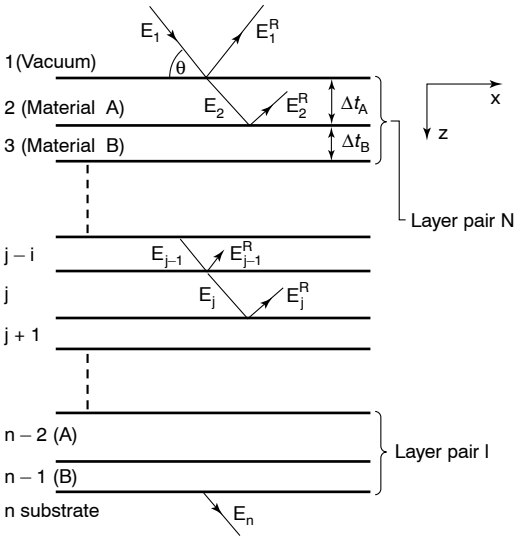

FIGURE 4.4. Computational model for calculating multilayer reflectivity, shown here as N bilayer pairs of two materials, A and B, of thickness Δt_A and Δt_B, where the multilayer period is $d = \Delta t_A + \Delta t_B$. (From Underwood.[4])

are calculated in terms of increments in refractive index. In fact, finite transition zones can be addressed using these same techniques. Following Underwood,[4] Figure 4.4 illustrates the method for calculating multilayer reflection.

The calculation is performed for incident radiation at an angle θ from the surface, applying the boundary conditions that tangential components of **E** and **H** must be continuous at each interface, as employed earlier in Chapter 3 for a single interface. Each material is characterized by a refractive index, described in Eqs. (3.12) and (3.13) as

$$n = 1 - \delta + i\beta = 1 - \frac{n_a r_e \lambda^2}{2\pi}\left(f_1^0 - i f_2^0\right) \tag{4.9}$$

where n_a is the density in atoms per unit volume, r_e is the classical electron radius, λ is the wavelength, and f_1^0, f_2^0 are the real and imaginary components of the complex atomic scattering function.[14] Calculations of reflected and refracted waves are then performed at each interface and summed. The calculations are done separately for perpendicular (s) and parallel (p) polarization. Examples of calculated reflectance are shown in Figures 4.5 and 4.6.

Figure 4.5 shows reflectivity as a function of glancing incidence angle θ, for a soft x-ray W–C multilayer mirror at 8.34 Å wavelength.[15] The multilayer coating in this calculation has 100 layer pairs, with $d = 22.5$ Å and $\Gamma = \frac{1}{3}$. High reflectivity due to total external reflection is predicted for $\theta < 2^\circ$. The calculation also predicts a strong, first order Bragg peak at a glancing incidence angle just under 11°, with a reflectivity of about 70%. The angular bandpass is about 1.5%, indicating that the spectral bandpass, for a given incidence angle, would also be about 1.5%. This proves useful in various applications where modest but well-defined spectral selectivity is desired, such as plasma diagnostics, EUV/soft x-ray astronomy, EUV/soft x-ray laser line isolation, and others. Measured values are typically somewhat less due to interface roughness, interpenetration of the two materials, and compound formation, although these have a much stronger effect on higher orders.[4]

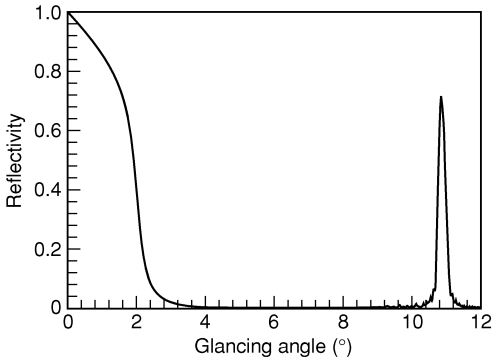

FIGURE 4.5. Computed reflectivity versus glancing incidence angle for a tungsten–carbon multilayer mirror of 100 bilayers, with periodicity $d = 22.5$ Å, $\Gamma = \frac{1}{3}$, at a wavelength of 8.34 Å. The angle θ is measured from the surface. Total external reflectance is shown below 2°, and a strong first order ($m = 1$) Bragg peak is seen at just under 11°. (From Underwood,[15] LBNL.)

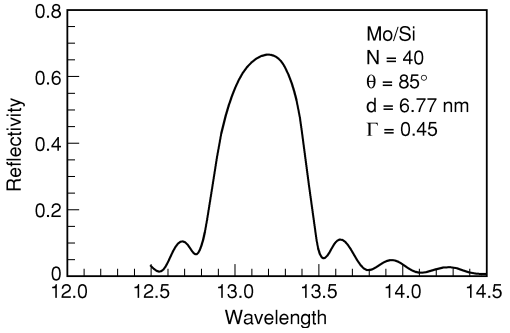

FIGURE 4.6. Measured reflectivity versus wavelength for a molybdenum–silicon (Mo/Si) mirror consisting of 40 layer pairs, with a d-spacing of 6.77 nm and $\Gamma = 0.45$. Peak reflectivity is 66.5% at 13.2 nm wavelength. The mirror was coated by C. Montcalm of Lawrence Livermore National Laboratory,[9] and measured by Underwood and Gullikson of Lawrence Berkeley National Laboratory.[16]

Figure 4.6 shows reflectivity versus wavelength for a Mo/Si multilayer at $\theta = 85°$, i.e., 5° from normal incidence. The multilayer has a d-spacing of 6.77 nm and a Γ-value of 0.45 as measured with Cu K_α radiation and atomic resolution transmission electron microscopy (TEM). The measured peak reflectivity is 66.5% at 13.2 nm wavelength. Based on best available refractive index data,[17] and with an assumption of perfectly sharp interfaces, the theoretical reflectivity would be 74%. The difference is quite likely due to interface roughness, interpenetration and molybdenum silicide formation at the interfaces, etc. Indeed, even small variations in refractive index, due to density variations in the layering process, and improved values of the scattering factors at these wavelengths can account for differences of order 2%.[18]

To account for the differences between experimental results and idealized (perfect interfaces) calculations, researchers sometimes invoke a Debye–Waller factor[1] in the reflection coefficients that is meant to represent in some fashion the diffuse nature of the interface. Originally introduced to take account of thermal motion of atoms in a crystalline lattice, it is used in multilayer characterization as a catch-all factor representing the spatial scale of interface broadening and roughness, generally in the form of a Gaussian distribution of rms value σ, to either side of the ideal interface.[1] To account for the observed difference between

experimental and observed reflectivity of the Mo–Si mirror considered in Figure 4.6, it is necessary to invoke an interface parameter $\sigma = 6.5$ Å rms, which could represent two or three atom roughness, or random interpenetration, to either side of the ideal interface location.

It is worth noting that although both roughness and (uniform) interdiffusion reduce reflectivity, only roughness generates non-specular scattering. Toward that end substantial efforts are presently underway to measure scattering[1, 19–21] from multilayer structures, and to model it in terms of spectral density distributions with various layer to layer and lateral distribution functions. With a better understanding of interface parameters, this may lead to new techniques for controlling the growth of interface non-uniformities. This is done in conjunction with other valued diagnostic tools such as TEM, atomic force microscopy (AFM), and visible light profilometry. This combination of techniques provides the primary basis for the deterministic assessment of Debye–Waller coefficients mentioned above.

Before closing this section we note that somewhat higher EUV reflectivities have been achieved with Mo/Be coatings.[8, 9] In such coatings the Be provides a less absorptive spacer material than Si, permitting the achievement of reflectivity in excess of 70% at a wavelength of 11.3 nm (110 eV), just below the K-absorption edge of Be at 111.5 eV.

As pointed out in the introduction, normal incidence reflection requires nominal $\lambda/4$ thicknesses for each layer. Thus for soft x-rays, with wavelengths of just a few nanometers, each layer would be of order 1 nm thick, which corresponds to only a few atomic monolayers. To be more specific, a normal incidence multilayer mirror designed to operate just below the oxygen K-edge at 543 eV (2.28 nm wavelength in vacuum) would require individual layers of about 0.6 nm, corresponding to only two or three atomic monolayers. Clearly this is very difficult to achieve in non-crystalline material combinations. As a consequence it has not been possible to date to achieve high normal incidence reflectivity at soft x-ray wavelengths. This is illustrated in the reflectivity data presented in the frontispiece of this chapter, which shows sample experimental values reported in the recent literature. Several groups have reported values of order 5% near the nitrogen K-edge.

Finally, we note that during high thermal loading, multilayer mirrors can be heated to high temperatures, potentially leading to degradation of otherwise stable interfaces. Toward this end Ziegler,[23] Takenaka et al.,[24] and others have studied multilayer mirrors at high x-ray intensity, and countermeasures such as interleaved barrier layers.

4.4 MULTILAYER FABRICATION

Multilayer interference coatings for short wavelength applications have been successfully fabricated using evaporation,[1] sputtering,[2, 25–27] epitaxial growth,[28] and laser-plasma deposition techniques.[29] For applications involving curved surfaces, especially where uniformity or d-spacing control is of interest, sputtering is particularly attractive and widely used. Figure 4.7 shows the basic sputtering technique and geometry.

Blank mirror substrates are placed face down over holes in a circular table that rotates above sputtering targets for the two desired materials, labeled here as "high Z" and "low Z." In this manner a bilayer pair is deposited with each revolution of the table. In addition to table rotation, the substrates are also rotated, at higher angular speed, in localized planetary motions so as to improve coating uniformity. Shadow masks[25–27] are often employed to further improve uniformity or control specified d-space variation, as shown schematically in Figure 4.7(a).

The magnetron sputtering process described here involves a plasma discharge maintained just above the desired target materials. The discharge is maintained between the grounded rotation table (anode) and the negative target (cathode) housings, with most of the voltage drop very close to the target. A magnetron structure, shown in Figure 4.7(b), provides magnetic

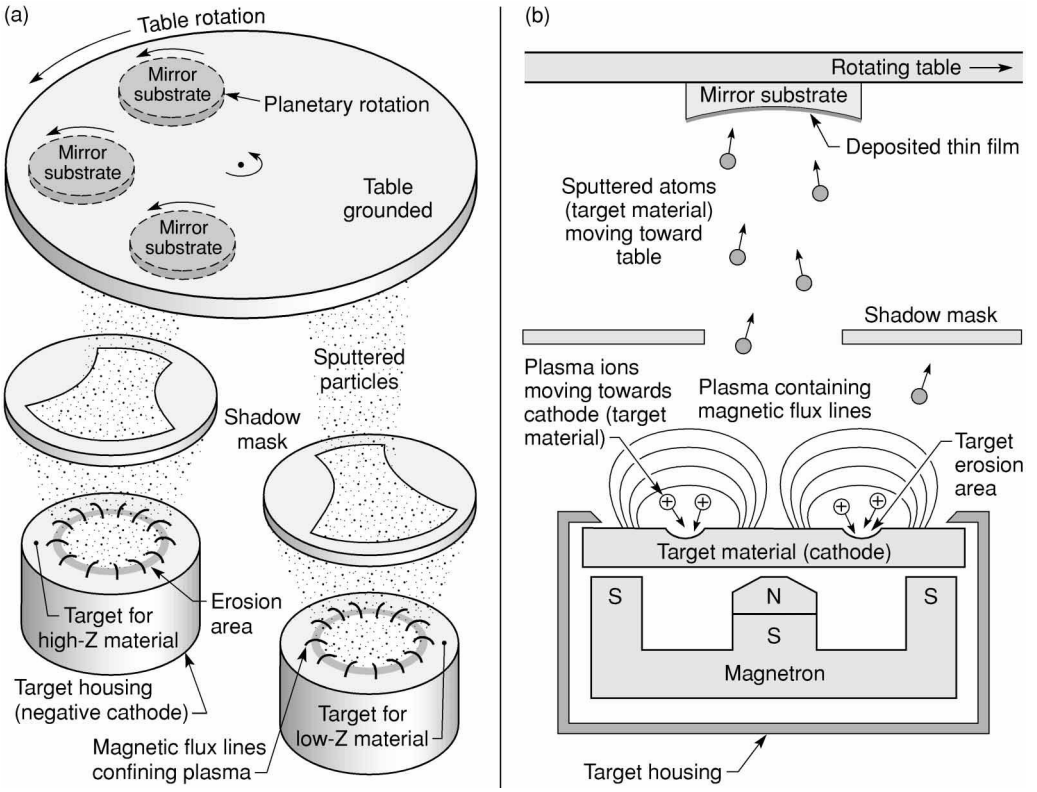

FIGURE 4.7. Magnetron sputtering is illustrated for two materials, one high Z and one low Z. Positive argon ions from a magnetically confined plasma are attracted to the negative cathode, where they sputter away (knock free) neutral atoms of the desired material. These neutral atoms move freely, some reaching the mirror substrates passing above. Shadow masks and planetary rotations are used to improve uniformity and control desired d-space variation. The magnetron sputtering source is shown in (b). (Courtesy of J. Bowers and J. Underwood, Lawrence Berkeley National Laboratory.)

flux lines that tend to hold the plasma in the vicinity of the target material. Typically the plasma is formed in a low pressure argon gas. Argon ions are attracted to the negative target housing, colliding and knocking free desired atoms for the coating process. These uncharged atoms then freely move away in all directions, perhaps restricted by a shadow mask, many of them reaching the substrate passing above and adhering as a sputtered thin film. The table rotation speed is set to provide a single layer of the desired thickness on each pass. Stable control of the plasma properties through gas pressure and well regulated voltages make this a very reproducible process. Nonetheless, the use of witness plates with Cu K_α measurements of d-spacing is usual. In some cases, in situ x-ray monitoring is also employed. Often it is desirable to employ a third material as a *capping layer*, at the end of the process, to control oxidation upon eventual exposure to air.[30] In some cases an adhesion or sacrificial separation layer is employed between the substrate and multilayer coating.

4.5 APPLICATIONS OF MULTILAYER COATED OPTICS

A great advantage of multilayer interference coatings is that they can be applied to curved substrates for use in imaging applications, such as microscopes and telescopes. This is not

possible with purely crystalline structures. Furthermore, they provide a modest well-defined spectral bandpass, with a relatively high throughput, which finds many additional applications. In this section we give illustrative examples from surface science, astronomy, plasma physics, industrial lithography, polarization sensitive materials science, and materials microprobing for chemical analysis, impurity detection, and microdiffraction.

4.5.1 Soft X-ray and Extreme Ultraviolet Photoemission Microscopy for Surface Science

As modern materials science and nanofabrication techniques permit the advance of structures to ever smaller dimensions, surface and interface properties become ever more important. Prime examples in which small structures are technologically and economically important are the semiconductor electronics and magnetic recording industries, where typical feature sizes are well below 1 μm and will soon be as small as 100-nm. In such situations there is great interest in analytic tools that can measure surface composition, including elemental concentrations and chemical bonding, on a sub-100-nm spatial scale. Toward this end, a very valuable tool is the photoemission microscope, which combines high spectral and spatial resolution, and permits the study of heterogeneous surfaces.

A photoemission microscope employing multilayer coated optics is shown in Figure 4.8. Photons of specified energy are focused onto a sample, in this case by a multilayer coated optical system known as a Schwarzschild objective,[31, 32] causing the emission of photoelectrons, which reveal the elemental composition and chemical bonding among elements at the surface. The basic photoemission process is described in Chapter 1, Section 1.2, with further applications in Chapter 9, Section 9.9. For the microscope illustrated in Figure 4.8, undulator radiation, tuned and monochromatized to provide the desired photon energy, illuminates a 2 μm diameter pinhole that is imaged at 20:1 demagnification to a nominal 100 nm spot size on the surface to be investigated. Emitted photoelectrons are then drawn off the surface by a suitable potential and analyzed using an electron energy spectrometer.

The Schwarzschild reflecting microscope is shown in profile in Figure 4.8(b). The two spherical surfaces are multilayer coated to provide peak reflectivity matched to the photon energy selected by the undulator and monochromator. The microscope has been operated with Mo–Si coatings for photoemission at 91.8 eV (13.5 nm wavelength), and also with Ru–B_4C coatings[27] for photoemission at 130 eV (9.54 nm wavelength). For Ru–B_4C the number of effective layer pairs is greater ($\simeq$70), thus narrowing the Bragg peak and requiring graded d-spacing across the high curvature primary mirror.

A secondary electron photoemission micrograph of a 435 nm thick $Al_xGa_{1-x}N$ film is shown in Figure 4.8(c). The sample was grown on a sapphire substrate, with $x = 0.23$, using metal–organic chemical vapor deposition (MOCVD). Secondary electrons of 5 eV kinetic energy were collected with a cylindrical mirror analyzer (CMA) electron spectrometer, as the sample was illuminated with 130 eV photons from an undulator at the Advanced Light Source in Berkeley (see Chapter 5). The sample field size in Figure 4.8(c) is 30 μm $\times$ 60 μm. The photoemission image indicates morphological inhomogeneities with a mean grain size of about 2 μm, in agreement with atomic force microscope (AFM) results. Further results obtained with this microscope are presented in Chapter 9, Figure 9.39.

4.5.2 Extreme Ultraviolet and Soft X-ray Astronomy

Until the emergence of multilayer coatings, EUV, soft x-ray, and x-ray astronomy were limited to glancing-incidence optics characterized by limited collection angle ($\theta \leq \theta_c$; see Chapter 3, Sections 3.4 and 3.9) and broad spectral bandpass ($E/\Delta E \sim 3$ or so). With multilayer

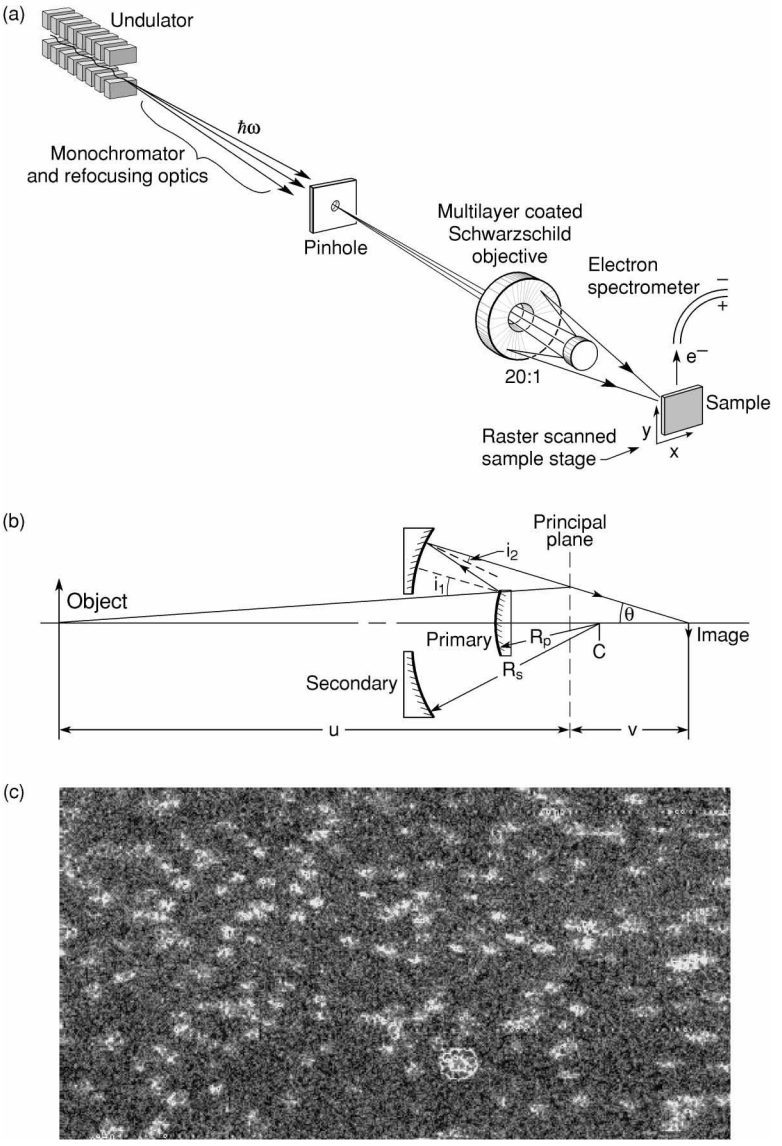

FIGURE 4.8 (see Colorplate III). (a) The photoemission microscope of Cerrina, Underwood, and colleagues,[32] employing a multilayer coated Schwarzschild objective to focus monochromatic undulator radiation to a nominal 100 nm spot size. Photoelectron energy distributions are measured as a function of position as the sample position $(x,\ y)$ is raster scanned. (b) Details of the Schwarzschild optics are shown. The object is a pinhole demagnified $(u/v = 20)$ to a reduced focal spot size. (c) A secondary electron photoemission micrograph of an AlGaN thin film. The incident photon energy is 126 eV, and the collected secondary electrons have a kinetic energy of 5 eV. Lateral inhomogeneities show a mean grain size of about 2 μm in this 30 μm $\times$ 60 μm image. (Courtesy of G.F. Lorusso, and F. Cerrina, University of Wisconsin, Madison.) Further results obtained with this photoemission microscope are described in Chapter 9, Section 9.9.

coatings large collection solid angle optics are possible at EUV wavelengths, with improved angular resolution and well-defined spectral bandpass of width $E/\Delta E \sim N$, where N is the number of layer pairs.[33] At soft x-ray wavelengths normal incidence optics are not generally an option, but improved spectral bandpass is available, and the increased angle of incidence ($\theta_{\text{Bragg}} > \theta_c$) reduces off axis aberrations in image forming studies.

The use of multilayer coated normal incidence optics to obtain high resolution astronomical images is clearly illustrated in Figure 4.9(a). This shows an image of the solar corona obtained at nominal 17.3-nm wavelength (71.7 eV). The image was obtained by Walker, Barbee, Hoover, and Lindblom[35] using a rocket-launched Cassegrain telescope with Mo/Si-coated optics, as shown in Figure 4.9(b). The primary optic is a concave spherical mirror with a diameter of 6.4 cm and a radius of curvature of 1.2 m. The secondary mirror is a 2.5 cm diameter convex sphere of radius 0.5 m. Both employ superpolished substrates, for maximum reflectivity and minimal nonspecular scattering. The Mo–Si multilayer coating has a d-spacing of 8.55 nm and $\Gamma = 0.43$, achieving a peak reflectivity of 35% at 17.2 nm with a spectral bandpass $\lambda/\Delta\lambda$ of about 13. The bandpass is further narrowed by use of an aluminum L-edge filter (72.5 eV, 17.1 nm) to $\lambda/\Delta\lambda \simeq 40$, extending from 17.1 nm to 17.5 nm. This spectral band is dominated by line emission from highly ionized iron (Fe^{+8} and Fe^{+9}, eight and nine times ionized, respectively), which is present in the coronal plasma in regions where the temperature is of order 100 eV (1.2×10^6 K).

In Figure 4.9(a) the authors identify several areas of particularly intense emission, including areas of known activity (lower right), magnetically confined coronal loops at the solar limb, and relatively quiescent north and south (upper left and lower right) coronal holes where long polar plumes of escaping plasma emerge along radial magnetic field lines to contribute to the solar wind. Also seen are lower temperature filaments and prominences (upper left). With the relatively large collection solid angle, and well-defined spectral bandpass, these multilayer coated optics clearly provide new opportunities for the study of more distant matter in the universe.

Figure 4.10 shows further detail of solar activity obtained with the NASA TRACE[¶] telescope.[36] The instrument employs a 30 cm diameter Cassegrain telescope with an angular resolution of 1 arcsec. The optics are coated in quadrants to provide three EUV passbands and one UV passband. The three EUV channels employ Mo_2C/Si multilayer coatings with respective spectral peaks at 17.3 nm, 19.5 nm, and 28.4 nm. Images are read out with a 1024×1024 CCD array in which one pixel corresponds to 0.5 arcsec. The image in Figure 4.10, obtained at 17.3 nm wavelength, shows fine loop detail at the solar limb. This spectral band is dominated by Fe^{+8} and Fe^{+9} emissions, characteristic of a solar region with a temperature of order 100 eV. Typical exposure times are several seconds, permitting continuous time coverage and thus a powerful new tool for studies of coronal dynamics.[36]

4.5.3 Extreme Ultraviolet Lithography

Lithography is a process for printing or copying a pattern from a flat surface, originally a stone, in some cases using inks or other treatments to enhance image transfer. In today's semiconductor industry lithography is used to copy patterns for manufacturing nanoelectronic processors and memory devices for modern computing systems. These computer chips, as they are called, contain millions of transistors, with feature sizes as small as 250 nm, across square centimeter

[¶]Transition Region and Coronal Explorer (TRACE).

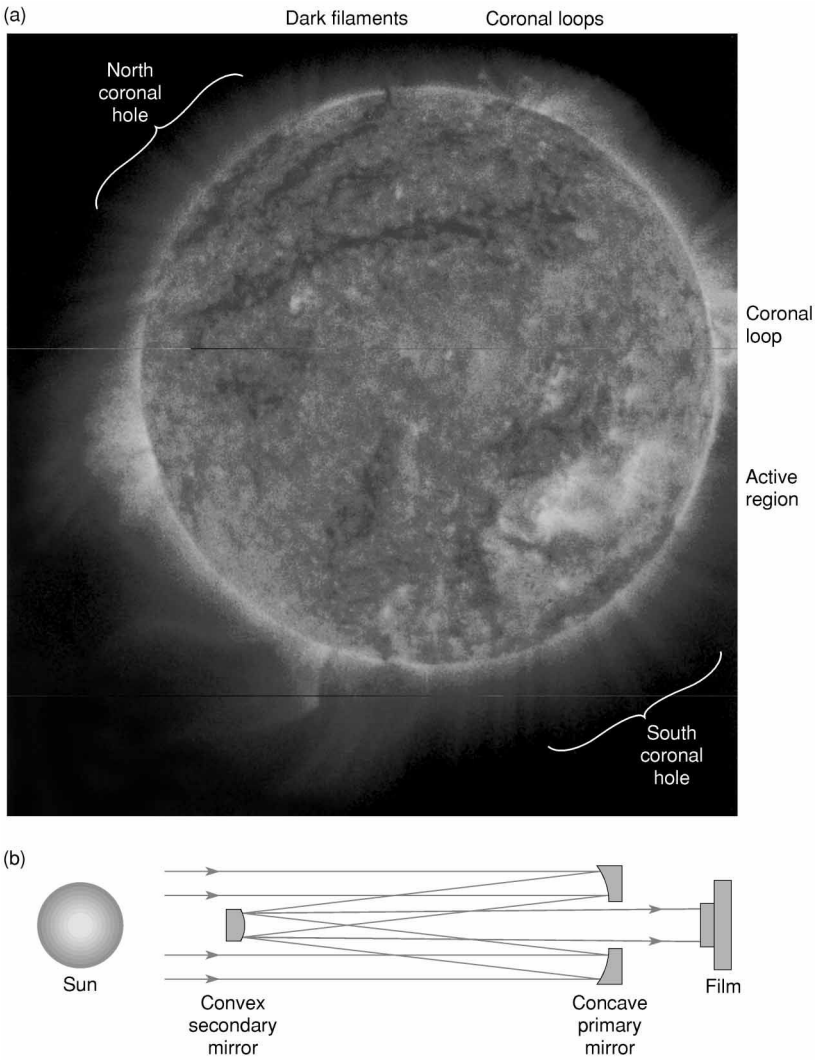

FIGURE 4.9 (see Colorplate IV). (a) EUV image of the sun obtained with a rocket launched Cassegrain telescope employing multilayer coated normal incidence optics. (b) The telescope employs Mo/Si-coated spherical optics that, in combination with an aluminum L-edge filter, provide a 17.1 nm to 17.5 nm spectral bandpass. It achieves an angular resolution of about 1.2 arcsec (5.8 μrad). (Courtesy of A.B.C. Walker, T.W. Barbee, R.B. Hoover, and J.F. Lindblom; Stanford, LLNL, and NASA.)

dimensions. The most critical layers are printed with nominally four times ($4\times$) reduction cameras, known as "optical steppers," using 248-nm wavelength KrF laser radiation as the deep ultraviolet (DUV) source. Critical dimensions for use in high volume manufacturing are anticipated to decrease on a schedule of $\sqrt{2}$ reductions every two or three years, to 100 nm in the year 2006, and to 50 nm in the year 2012.[37] There are several competing technologies that can potentially provide these capabilities, some of which are described in Chapter 10. Among them are continuations of DUV techniques using 193 nm ArF lasers, soft x-ray proximity

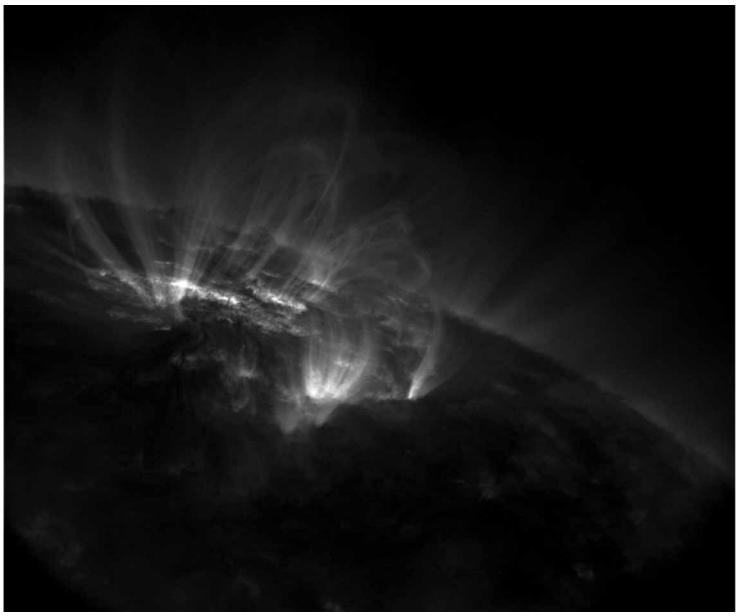

FIGURE 4.10 (see Colorplate V). An EUV image of the solar corona showing arcsecond details of loops near the solar limb. (Courtesy of L. Golub, A. Title, C. Wolfson, B. Handy, T.W. Barbee; Harvard-Smithsonian Center for Astrophysics, Lockheed Martin, LLNL, and NASA.)

printing at nominally 1 nm wavelength, electron beam writing techniques, ion beam writing, and extreme ultraviolet lithography based on multilayer coated reflective optics. The last is of particular interest in this chapter.

Concisely, the advantages of EUV are the continuation of optical techniques at a significantly reduced wavelength (11–13 nm versus 193–248 nm), permitting the achievement of small feature size (100 nm or smaller) with modest numerical aperture and large depth of focus. To print large (square centimeter) field sizes with a modest number of curved surfaces, limited by finite reflectivities and thus system throughput, requires the use of high precision aspheric optics, at technically challenging specifications. That notwithstanding, the dominant enabling technology for this approach to lithography is the ability of Mo/Si and Mo/Be multilayers, first perfected by Barbee,[7] to achieve reflectivities of order 70%. Figure 4.11(a) shows schematically the basic elements of EUV lithography.

In this example, nominal 13 nm radiation, from a laser produced plasma (Chapter 6) or a synchrotron radiation source (Chapter 5), illuminates a multilayer coated reflective mask that is overcoated with an absorber pattern. Multilayer coated reduction optics are then used to replicate the pattern at nominal 4:1 reduction on a suitable wafer. In practice a four or five bounce imaging system would be used for pattern reduction, and further condenser optics would be used between the source and mask for proper illumination. Further discussion and references are given in Chapter 10. A pattern of both 80 nm and 90 nm wide lines printed at a 1 : 2 pitch within a small field of view with a developmental EUV microstepper camera[38] is shown in Figure 4.11(b). The camera uses a 10 : 1 reduction Schwarzschild system, similar to that seen in Figure 4.8(b). Cameras based on aspheric optics, designed to print over a 26 mm $\times$ 56 mm field, are presently under development.

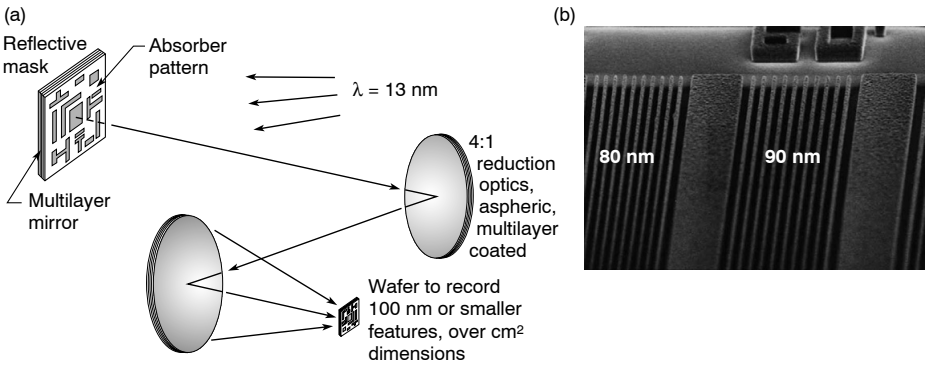

FIGURE 4.11. (a) Extreme ultraviolet (EUV) lithography is illustrated schematically, showing multilayer coated reflective optics used to image a mask pattern at a nominal 4 : 1 reduction at the wafer. With wavelengths in the range of 11–14 nm, features of order 100 nm can be printed with relatively low numerical aperture and large depth of focus. (b) A pattern showing both 80 nm and 90 nm lines (1 : 2 pitch) printed with a developmental EUV microstepper camera using Mo–Si-coated 10 : 1 Schwarzschild optics. Companion images showing line widths down to 50 nm are shown in Chapter 10, Figure 10.10 (Courtesy of J.E. Goldsmith, C.F Cardinale, C.C. Henderson, R.H. Stulen, and colleagues, Sandia National Laboratories.)

4.5.4 Plasma Diagnostics

Multilayer coated mirrors provide many opportunities and are widely used for the diagnostics of hot plasmas that radiate at wavelengths from the EUV to x-ray regions of the spectrum. As in astronomy, the well-defined spectral bandpass makes them ideal for many studies of energy transport and temperature where only moderate spectral resolution ($\lambda/\Delta\lambda \simeq 10$–$30$) suffices. Again as in astronomy, they are very convenient for clearly isolating certain spectral lines, for instance in the development of EUV and soft x-ray lasers, where one lasing line may be isolated from others (see Chapter 7). As their top surfaces are generally reflective for visible light as well, they are conveniently combined with a wide range of detectors in imaging, spectroscopic, and transport experiments.

An early application of multilayer mirrors to plasma diagnostics is outlined in Figure 4.12(a). Of interest here is the transport of energy into a layered laser-plasma target,[39] with characteristic emissions of the various layers to be separated through the use of matching multilayer mirrors, and recorded with a single 15 ps time resolved streak camera. Discussion of the emission from laser produced plasmas, including the diagnostic use of streak cameras, is presented in Chapter 6. For example, using a glass (SiO_2) target with overlayers of CF and CH, one would expect to see delayed emissions of characteristic line emissions from He-like fluorine ($1s2p \rightarrow 1s^2$ at 737 eV) and H-like oxygen ($2p \rightarrow 1s$ at 653 eV), as well as several narrow channels that sample the broad continuum of emission at energies of 102 eV, 267 eV, and 943 eV, as delivered energy burns through the target and "lights up" the various lines. For each multilayer bandpass, a matching thin film absorber is used to block top surface reflections of long wavelength visible, IR, and UV radiation. For the transport studies proposed in Figure 4.12(a), the multilayer channels fielded[39, 40] were as follows: V/C with $d = 14.3$ nm at 25° incidence angle for the 102 eV channel, Ti/C with $d = 5.5$ nm at 25° for the 267 eV channel, W/C with $d = 2.1$ nm at 27.1° for the 653 eV channel, W/C with $d = 2.1$ nm at 23.8° for the 737 eV channel, and W/C with $d = 1.5$ nm at 25° incidence angle

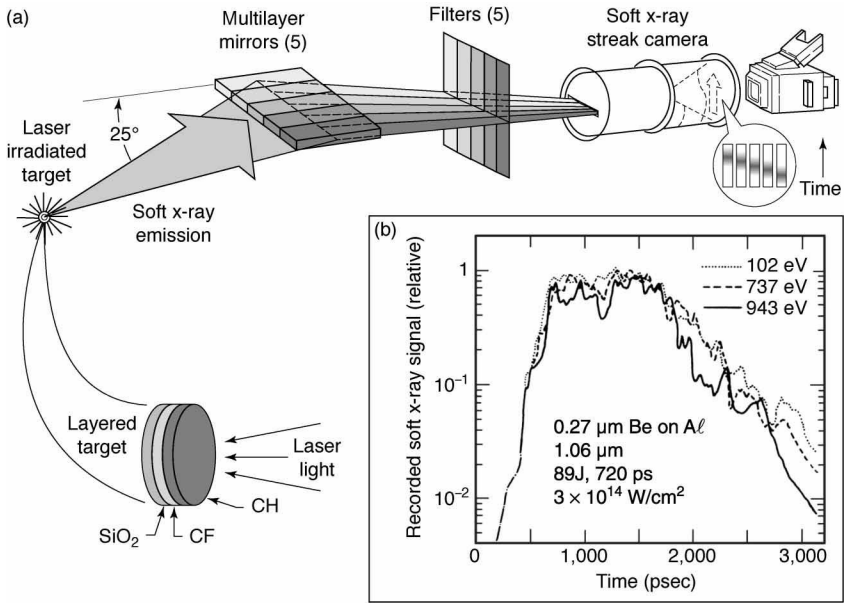

FIGURE 4.12. (a) Time resolved soft x-ray emission, in five well-defined spectral windows defined by multilayer mirrors, for use in thermal transport studies of laser irradiated targets. (b) Sample data for a laser irradiated Be on Al target, showing three channels. (Courtesy of G. Stradling.)

for the 943 eV channel. Sample data[40] for emission from a non-optimized Be on Al target are shown in Figure 4.12(b), for an 89 J, 720 ps duration (FWHM), 1.06 μm laser pulse at an incident intensity of 3×10^{14} W/cm^2. Further discussion of hot dense plasmas and their emission characteristics is presented in Chapter 6.

4.5.5 Polarization Studies of Magnetic Materials

It has been known since the time of Michael Faraday (1845) that the presence of magnetic fields can alter the propagation properties of light in certain materials. Magneto-optical effects refer to various changes in the polarization vector, taken here as the wave's electric field vector **E**, as radiation interacts with magnetic materials. These effects include rotation of a linearly polarized electric field vector, as in the Faraday and Kerr effects, and the differential absorption (or scattering) of left and right circularly polarized radiation, known as circular dichroism.[42, 43] For visible and ultraviolet light these effects involve valence electrons in molecules, loosely bound valence and conduction electrons in solids, and free electrons in plasmas. However, in the EUV and soft x-ray regions, these interactions involve more tightly bound core (K- and L-shell) electrons, and thus provide a mechanism for providing element specific information.

Multilayer mirrors provide a powerful tool for controlling and measuring the polarization properties of radiation at these short wavelengths, based on reflection properties near 45° incidence angle.[44–47]. As seen earlier in Chapter 3, Section 3.6, there is an angle at which p-polarized radiation (electric field vector **E** lying in the plane of incidence) is not reflected at an interface, or is minimally reflected in the case of a lossy material ($\beta \neq 0$). At this same angle the s-polarization can have a relatively large reflection. For a single interface this angle is

known as Brewster's angle, and for short wavelength radiation it is very close to $\pi/4$ radians. As seen in Chapter 3, Eq. (3.60), Brewster's angle for EUV/soft x-ray radiation incident from vacuum onto a material of refractive index $n = 1 - \delta + i\beta$ is given by

$$\phi_B \simeq \frac{\pi}{4} - \frac{\delta}{2}$$

where ϕ_B is measured from the surface normal.

For multilayer mirrors the reflection process is somewhat different because the radiation interacts sequentially with two alternating materials. As a consequence the radiation experiences small refractive turnings toward and away from the surface normal, in response to small positive and negative changes in refractive index. At each interface, however, the result is similar in that for p-polarized radiation a minimal reflection occurs at each sequential interface, preserving the essence and advantage of Brewster's angle. Thus with multilayer mirrors designed for use at Brewster's angle the difference in reflectivities can be very great, approaching unity for s-polarized radiation at the Bragg peak, and orders of magnitude less for p-polarized radiation.[45] Kortright and his colleagues[48–50] have pursued the application of multilayer mirrors to the study of magnetic materials utilizing several of these magneto-optical techniques. For example, the use of a polarizing multilayer mirror to analyze Faraday rotation of linearly polarized soft x-rays, after passing through magnetized iron (Fe), is illustrated in Figure 4.13(a).

In this example linearly polarized undulator radiation (see Chapter 5) passes though an Fe/Cr sandwiched material[§] magnetized by a static axial magnetic field ($\mathbf{H}_0$) of 3 kOe. The radiation is then reflected off a W/B_4C multilayer mirror (polarization analyzer) at Brewster's angle ($\simeq 45^\circ$), into a detector. The multilayer mirror is laterally graded (tapered), as shown in Figure 4.13(b), so that with translation it can be used over a range of photon energies. In the case cited here, the nominal d-spacing is only 1.23 nm, for use at photon energies from 680 eV to 740 eV at 45° incidence angle. With such a short d-spacing the maximum achieved reflectivity for s-polarized radiation was only about 1%. However the p-to-s polarized extinction ratio was 3×10^{-4}.

The multilayer mirror can be rotated about the axis of symmetry (the coaligned axes of the applied static magnetic field $\mathbf{H}_0$ and the wave propagation vector direction $\mathbf{k}$) to measure the new direction of polarization after traversing the medium. Rotating the mirror with no sample present results in a sinusoidal reference signal, with maximum amplitude when the linearly polarized undulator radiation intersects the mirror as s-polarization, and minimal amplitude when that same undulator radiation intersects the mirror as p-polarization (90° rotation difference). With the sample in place the wave vector $\mathbf{E}$ rotates some amount due to the Faraday effect, causing the measured sinusoidal signal (as the mirror is rotated 360°) to exhibit a phase shift. The sense of rotation is reversed if the axial magnetic field direction is reversed. As shown in Figure 4.13(d), data is then obtained as a function of photon energy, in this case across the Fe L_2 and L_3 edges at 720 eV and 707 eV, respectively. The measured maximum rotation of 4.8°, for a total Fe thickness of 80 nm, corresponds to a Faraday rotation constant of 6.0×10^4 deg/mm, about twice that of visible light, and 1000 times greater than with 7.1 keV x-rays. The rotation angle can then be used to determine the magnetization of the material.[42, 43]

[§]Actually in the form of an Fe/Cr multilayer structure consisting of 40 bilayers of 2.0 nm Fe and 1.9 nm Cr on a 100 nm thick silicon nitride membrane.

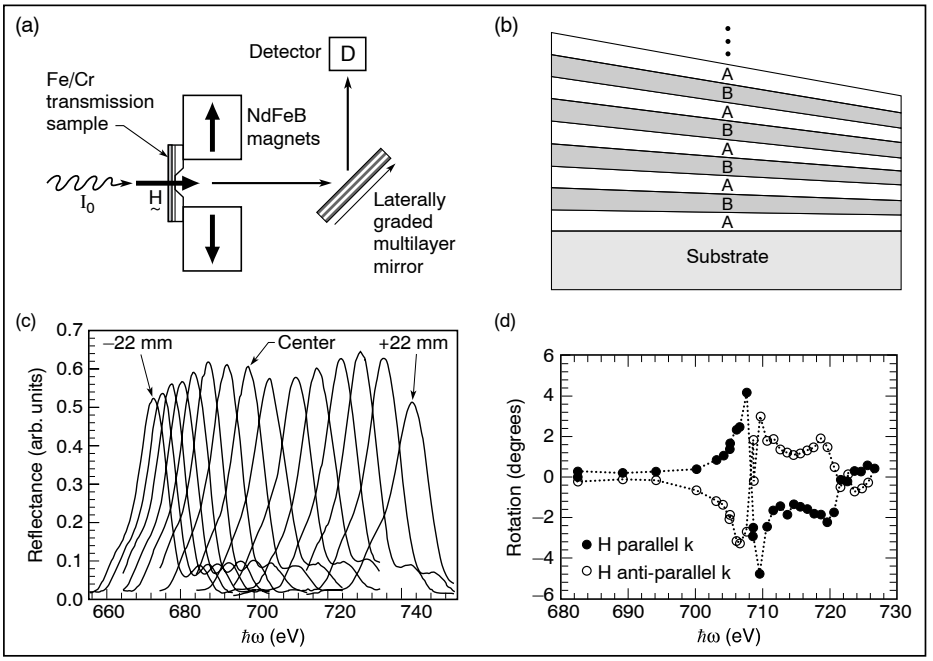

FIGURE 4.13. (a) Technique for measuring Faraday rotation at soft x-ray wavelengths using a multilayer mirror polarization analyzer at Brewster's angle ($\simeq 45^\circ$ in this region). (b) Use of a laterally graded multilayer permits the measurement at a range of wavelengths. (c) Multilayer reflectivity versus photon energy, at 45° angle of incidence, as the mirror is translated to expose regions of varied d-spacing and thus varied photon energy at the Bragg peak. (d) Recorded Faraday rotation angle for an Fe/Cr sample as a function of photon energy, crossing the Fe L-edges at 707 eV and 720 eV. (Courtesy of J.B. Kortright, M. Rice, LBNL, and R. Carr, Stanford University.)

The resonant behavior observed in Figure 4.13(c) suggests that this technique is extendable to element specific applications in multicomponent magnetic films containing other transition metals such as V, Cr, Mn, Co, and Ni. Kortright and Rice[49] have used the soft x-ray Kerr effect to observe hysteresis in Fe and Cr. Magnetic circular dichroism (MCD) for the conversion of linearly polarized soft x-rays to an elliptically polarized state is also discussed in the literature.[50]

4.5.6 The X-Ray Microprobe

For x-rays of photon energy 6–20 keV it is not possible to make normal incidence multilayer mirrors. Nonetheless, they are quite useful in applications of coated optics, in part because of the well-defined but not overly narrow spectral bandpass, and in part because the Bragg angle can be several times larger than the critical angle for total external reflection. The latter offers the potential for increased collection solid angle in some applications and reduced off-axis aberrations in others.

Figure 4.14 shows a pair of crossed, multilayer coated optics, used to focus 8–12 keV x-rays to a nominal 1 μm diameter spot size.[51] In the Kirkpatrick–Baez (KB) configuration one mirror provides the horizontal focus while the other provides the vertical focus. In this

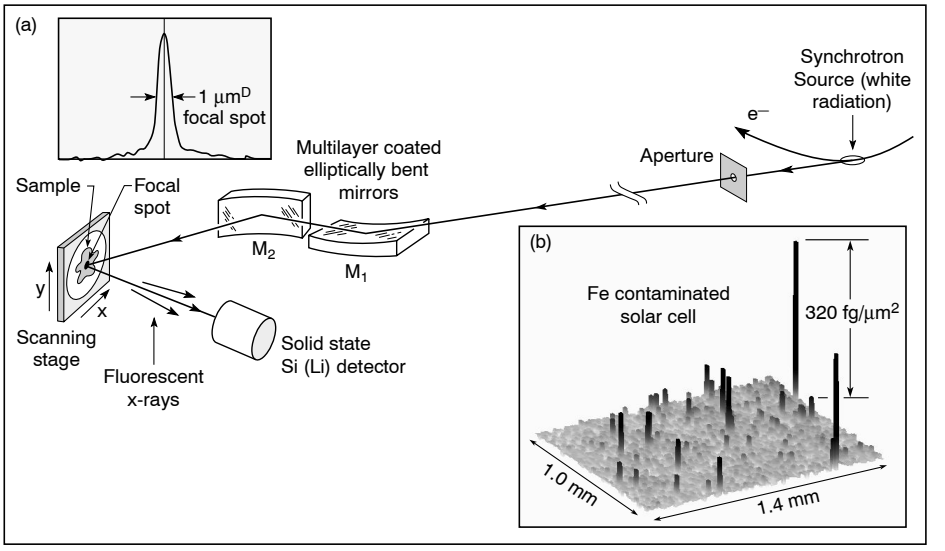

FIGURE 4.14. A fluorescence x-ray microprobe, using a pair of multilayer coated elliptically bent mirrors of varied d-spacing, to focus hard x-rays to a nominal 1 μm diameter focal spot. Three separate mirror pairs provide pass bands at 8 keV, 10 keV, and 12 keV, with $E/\Delta E \simeq 30$. Incident photons create core-level vacancies through photoemission. Subsequent characteristic line emission (fluorescence) is detected by an energy selective detector, permitting clear identification of elements present. Because of the "photon-in–photon-out" nature of the measurement, bremsstrahlung is absent and detection thresholds are very low, at the parts-per-billion and femtogram levels. This is possible even in a high Z host by using a photon energy below the host K-edge. Raster scanning the sample provides a two-dimensional concentration map for each element detected. Shown in (b) is the fluorescent emission of dilute iron particles found to be the contaminating agent in a defective solar cell. (Courtesy of A. Thompson, J. Underwood, LBNL; the sample in (b) is from unpublished work with R. Holm of Miles Laboratory in Pittsburgh, PA.)

particular embodiment broad band bending magnet radiation (see Chapter 5) is used, although both wiggler and undulator radiation offer advantages. The focusing optics consist of a pair of elliptically bent mirrors[52] employing W/B_4C multilayer coatings at a nominal incidence angle of 1°. The coatings have graded d-spacings to accommodate the variation in incidence angles. In fact there are three sets of optics: one set for 8 keV, a second set for 10 keV, and a third set for 12 keV photon energy. The nominal spectral bandpass in each case is $E/\Delta E \simeq 30$. Compared to the use of spherical or cylindrical optics, the use of elliptically bent optics reduces off-axis spherical aberrations, resulting in a smaller spot size, just under 1 μm diameter, and significantly reduced flare, i.e., a better-defined focal spot. For the configuration shown in Figure 4.14, the nominal demagnification is 400 : 1.

Such focusing optics are conveniently adapted for use in many applications, involving a variety of techniques. For example, the focused radiation has been used extensively as an x-ray fluorescence microprobe, with nominal 1-μm spatial resolution, in which the incident radiation causes photoemission of core-level electrons from a broad range of elements that may be present. Subsequent fluorescent line emissions, characteristic of the elements present, are then detected with an energy selective solid state detector, as shown in Figure 4.14. The fluorescence provides a measure of the relative concentrations of elements present and

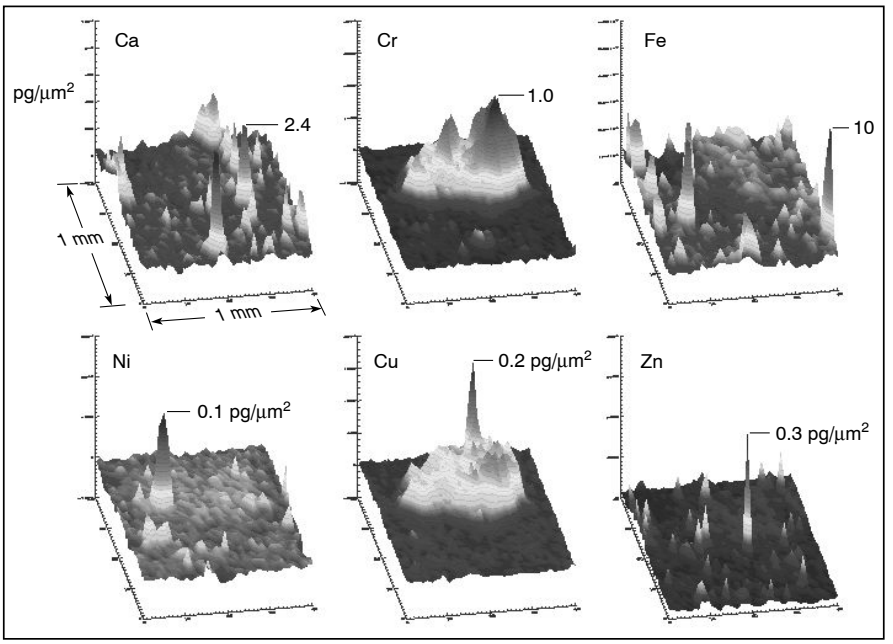

FIGURE 4.15. Elemental concentrations and size distributions of the elements Ca, Cr, Fe, Ni, Cu, and Zn found in contaminated wetlands as determined from x-ray microfluorescence. Bioremediation techniques involving organic materials are dependent on elemental concentrations and particle size. All concentrations are given in units of picograms per square micron. (Courtesy of T. Tokunaga and A. Thompson, LBNL, unpublished.)

accessible with the incident photon energy passed by the multilayer coating, i.e., with binding energies (Chapter 1, Table 1.2) below the incident photon energy.

This fluorescent emission technique is quite powerful in several ways. Because it is a "photon-in–photon-out" technique, there is no bremsstrahlung, and thus the background noise is very low, permitting detection sensitivities at the part per billion (ppb) and femtogram (fg) level. Furthermore, these dilute concentration levels can be detected in the presence of a high Z host material by selecting an incident photon energy below the host K-edge so as to avoid exciting host fluorescence. Figure 4.14(b) shows data obtained at 10 keV incident energy, which indicate the presence of iron particle contamination in a defective silicon solar cell. Figure 4.15 shows elemental concentration of Ca, Cr, Fe, Ni, Cu, and Zn, measured using this same technique, as part of an environmental remediation study involving contaminated wetlands near the San Francisco Bay. By the identification of elements present and particulate sizes, such studies can contribute to the development of appropriate bioremediation techniques.

The x-ray microprobe can also be used in combination with diffractive techniques. Figure 4.16 shows an early example of KB optics used in a microdiffraction configuration to study structural phase transformations of material under high pressure in a diamond-anvil cell. First experiments of this type were conducted by Mao, Wu, and colleagues[53–55] using synchrotron radiation at Stanford (SSRL) and Brookhaven (NSLS), and are now being implemented at third generation synchrotron facilities.[56, 57] The smaller electron beam size, high x-ray intensity, and wider availability of undulator and wiggler radiation at the third generation facilities (see Chapter 5) make these microprobe techniques very attractive.[56]

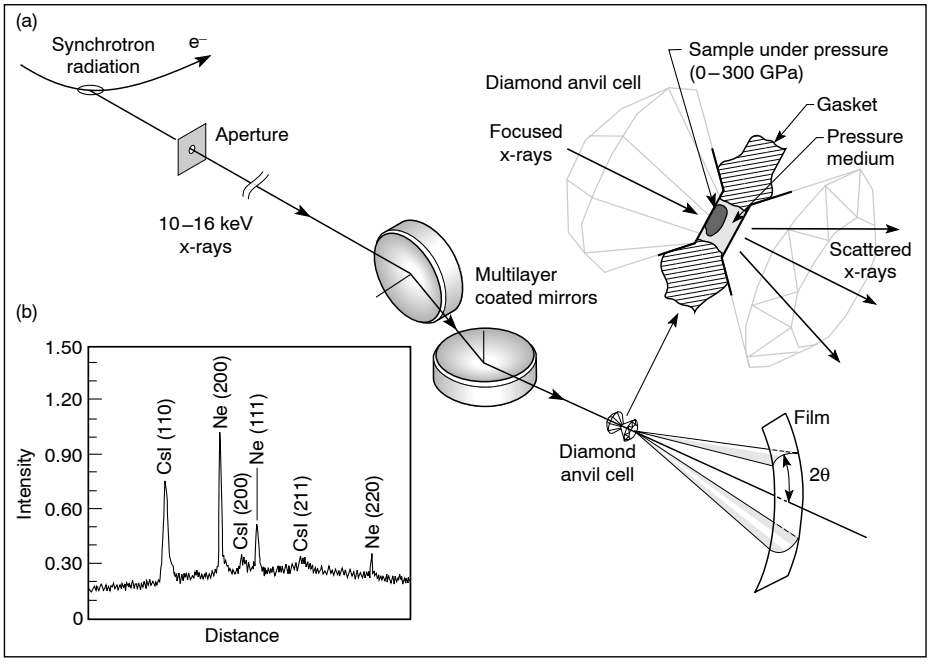

FIGURE 4.16. (a) Multilayer coated focusing optics used to deliver a high photon flux to small samples, typically 10 μm across, in a high pressure diamond-anvil cell. Monochromatic x-rays were obtained with a Si(III) double-crystal monochromator at the Stanford Synchrotron Radiation Laboratory. (b) A diffraction pattern obtained with CsI and neon at 26 GPa. Structural changes in the CsI were observed as the pressure varied from zero to 300 GPa. (From Y. Wu, Ph.D. thesis, UC Berkeley, 1990.[53])

For the microdiffraction investigation depicted in Figure 4.16, cesium iodide (CsI), with neon as a pressure medium, was studied over the pressure range from zero to 300 GPa ($\simeq 3\times10^6$ atm), simulating conditions in the earth's interior. With increasing pressure, CsI was observed through diffraction to transform in stages from a simple cubic structure to a hexagonal close-packed (hcp) structure above 200 GPa. CsI was chosen for these early studies because it is a widely used prototype for experimental and theoretical studies of crystal structures, equations of state, and metallization at high pressure.

Further topics of great interest include metallization of hydrogen,[54] and the structural phase of iron[58] at high pressure. Because these very high pressures are achieved in the laboratory over very limited dimensions (of order 10–20 μm in a diamond-anvil cell), it is important that the incident radiation be focused to a spot size of order 1 μm diameter. It is clear that these studies will be improved by the use of elliptically bent optics,[52] graded d-spacing multilayer coatings,[25–27] and third generation synchrotron radiation facilities (see Chapter 5) characterized by small (emission) beam size and divergence. These improvements will result in greatly increased photon flux within the desired spot size, as well as improved angular resolution.

REFERENCES

1. E. Spiller, *Soft X-Ray Optics* (SPIE, Bellingham, WA, 1994), and references therein.
2. T.W. Barbee and D.L. Keith, "Synthesis of Metastable Materials by Sputter Deposition Techniques,"

p. 93 in *Synthesis and Properties of Metastable Phases,* E.S. Machlin and T.J. Rowland, Editors (Metallurgical Society, Amer. Inst. Mech. Eng., Warrendale, PA, 1980).
3. J.H. Underwood and T.W. Barbee, "Soft X-Ray Imaging with a Normal Incidence Mirror," *Nature 294*, 429 (1981).
4. J.H. Underwood and T.W. Barbee, "Layered Synthetic Microstructures as Bragg Diffractors for X-Rays and Extreme Ultraviolet: Theory and Predicted Performance," *Appl. Opt. 20*, 3027 (1981).
5. R.P. Haelbich and C. Kunz, "Multilayer Interference Mirrors for the XUV Range Around 100 eV Photon Energy," *Opt. Commun. 17*, 287 (1976).
6. A.E. Rosenbluth, "Computer Search for Layer Materials that Maximize the Reflectivity of X-Ray Multilayers," *Revue Phys. Appl. (Paris) 23*, 1599 (1988); "The Reflecting Properties of Soft X-Ray Multilayer Mirrors," Ph.D. thesis, Institute for Optics, University of Rochester (1982).
7. T.W. Barbee, S. Mrowka, and M.C. Hettrick, "Molybdenum–Silicon Multilayer Mirrors for the Extreme Ultraviolet," *Appl. Opt. 24*, 883 (1985).
8. K.M. Skulina, C.S. Alford, R.M. Bionta, D.M. Makowiecki, E.M. Gullikson, R. Soufli, J.B. Kortright, and J.H. Underwood, " Molybdenum–Silicon Multilayer Mirrors for Normal Incidence in the Extreme Ultraviolet," *Appl. Opt. 34*, 3727 (1996).
9. C. Montcalm, D.G. Stearns, S.P. Bajt, R.D. Behymer, M.A. Wall, and J.A. Folta, "Multilayer Reflective Coatings for Extreme Ultraviolet Lithography," *Proc. SPIE 3331*, 42 (1998); C. Montcalm, B.T. Sullivan, H. Pepin, J.A. Dobrowski, and M. Sutton, "Extreme-Ultraviolet Mo/Si Multilayer Mirrors Deposited by Radio-Frequency-Magnetron Sputtering," *Appl. Opt. 33*, 2057 (1994).
10. T.D. Nguyen, "Microstructure-Interference-Property Relationships in Nanometer-Period X-Ray Multilayers," Ph.D. thesis, Applied Science and Technology Program, University of California, Berkeley (1993).
11. A.V. Vinogradov and B.Ya. Zeldovich, "X-Ray and Far UV Multilayer Mirrors: Principles and Possibilities," *Appl. Opt. 16*, 89 (1977).
12. E. Spiller, "Reflective Multilayer Coatings for the Far UV Region," *Appl. Opt. 15*, 2333 (1976).
13. G. Borrmann, "Über Extinktions Diagramme von Quartz," *Physikol Z. 42*, 157 (1941).
14. B.L. Henke, E.M. Gullikson, and J.C. Davis, "X-Ray Interactions: Photoabsorption, Scattering, Transmission and Reflection at $E = 50$–$30{,}000$ eV, $Z = 1$–92," *Atomic Data and Nucl. Data Tables 54*, 181 (1993).
15. J.H. Underwood, "Multilayer Mirrors for X-Rays and Extreme UV," *Optics News 12*, 20 (OSA, Washington, DC, March 1986).
16. J.H. Underwood and E.M. Gullikson, "Beamline for Measurement and Characterization of Multilayer Optics for EUV Lithography," *Proc. SPIE 3331*, 52 (1998).
17. R. Soufli and E.M. Gullikson, "Reflectance Measurements on Clean Surfaces for the Determination of Optical Constants of Silicon in the Extreme Ultraviolet-Soft X-Ray Region," *Appl. Optics. 36*, 5499 (1997); R. Soufli and E.M. Gullikson, "Absolute Photoabsorption Measurements of Molybdenum in the Range 60 to 930 eV for Optical Constant Determination," *Appl. Opt. 37*, 1713 (1998).
18. R. Soufli, "Optical Constants of Materials in the EUV/Soft X-Ray Region for Multilayer Mirror Applications," Ph.D. thesis, Electrical Engineering and Computer Science, University of California, Berkeley (1997).
19. D.G. Stearns, "X-Ray Scattering from Interfacial Roughness in Multilayer Structures," *J. Appl. Phys. 71*, 4286 (1992); *J. Appl. Phys. 65*, 491 (1989).
20. D.L. Windt, R. Hull, W.K. Waskiewicz, "Interface Imperfections in Metal/Si Multilayers," *J. Appl. Phys. 71*, 2675 (1992); D.L. Windt, W.K. Waskiewicz, and J.E. Griffith, "Surface Finish Requirements for Soft X-Ray Mirrors," *Appl. Opt. 33*, 2025 (1994).
21. E.M. Gullikson, D.G. Stearns, D.P. Gaines, and J.H. Underwood, "Non-Specular Scattering from Multilayer Mirrors at Normal Incidence," *Proc. SPIE 3113*, 55 (1998); E.M. Gullikson, "Scattering from Normal Incidence EUV Optics," *Proc. SPIE 3331*, 72 (1998).
22. R.S. Rosen, D.G. Stearns, M.A. Viliardos, M.E. Kassner, S.P. Vernon, and Y. Cheng, "Silicide Layer Growth Rates in Mo/Si Multilayers," *Appl. Opt. 32*, 6975 (1993).
23. E. Ziegler, "Multilayers for High Heat Load Synchrotron Applications," *Opt. Engr. (SPIE) 34*, 445 (1995).
24. H. Takenaka, T. Kawamura, and Y. Ishii, "Heat Resistance of Mo/Si, $MoSi_2$/Si, and Mo_5Si_3/Si

Multilayer Soft X-Ray Mirrors," *J. Appl. Phys. 78*, 5227 (1995); H. Takenaka, H. Ito, T. Haga, and T. Kawamura, "Design and Fabrication of High Heat-Resistant Mo/Si Multilayer Soft X-Ray Mirrors with Interleaved Barrier Layers," *J. Synchr. Rad. 5*, 708 (1998).

25. J.A. Folta, S. Bajt, T.W Barbee, Jr., F.R. Grabner, P.B. Mirkarimi, C. Montcalm, T. Nguyen, M.A. Schmidt, E. Spiller, C.C. Walton, and M. Wedowski, "Advances in Multilayer Reflective Coatings for Extreme Ultraviolet Lithography," *Proc. SPIE 3676* (1999); D.G. Stearns, R.S. Rosen, and S.P. Vernon, "Multilayer Mirror Technology for Soft X-Ray Projection Lithography," *Appl. Optics 32*, 6952 (1993); P.A. Kearney, C.E. Moore, S.I. Tan, S.P. Vernon, and R.A. Levesque, "Mask Blanks for Extreme Ultraviolet Lithography: Ion Beam Sputter Deposition of Low Defect Density Mo/Si Multilayers," *J. Vac. Sci. Technol. B 15*, 2452 (1997).
26. D.L. Windt and W.K. Waskiewicz, "Multilayer Facilities Required for Extreme-Ultraviolet Lithography," *J. Vac. Sci. Technol. B 12*, 3826 (1994).
27. J.B. Kortright, E.M. Gullikson, and P.E. Denham, "Masked Deposition Techniques for Achieving Multilayer Period Variations Required for Short-Wavelength (68 Å) Soft X-Ray Imaging Optics," *Appl. Opt. 32*, 6961 (1993).
28. C.M. Falco and J.M. Slaughter, "Characterization of Metallic Multilayers for X-Ray Optics," *J. Magn. and Magn. Materials 126*, 3 (1993); J.A.R. Ruffner, J.M. Slaughter, J. Eickmann, and C.M. Falco, "Epitaxial-Growth and Surface-Structure of (0001)Be on (111)Si," *Appl. Phys. Lett. 64*, 31 (1994).
29. S.V. Gaponov, S.A. Gusev, B.M. Luskin, N.N. Salashchenko, and E.S. Gluskin, "Long-Wave X-Ray Radiation Mirrors," *Opt. Commun. 38*, 7 (1981).
30. J.H. Underwood, E.M. Gullikson, and K. Nguyen, "Tarnishing of Mo/Si Multilayer X-Ray Mirrors," *Appl. Opt. 32*, 6985 (1993).
31. K. Schwarzschild, "Untersuchungen zur Geometrischen Optik II. Astronomische Mitteilungen der Königlichen Sternwarte zu Göttingen," *10*, 9 (1905).
32. F. Cerrina, G. Margaritondo, J.H. Underwood, M. Hettrick, M.A. Green, L.J. Brillson, A. Franciosi, H. Hochst, P.M. DeLuca, Jr., and M.N. Gold, "MAXIMUM, A Scanning Photoelectron Microscope at Aladden," *Nucl. Instr. Meth. A266*, 303 (1988); also J.H. Underwood, J.B. Kortright, R.C.C. Perera, F. Cerrina, C. Capasso, A.K. Ray-Chaudhuri, W. Ng, J. Welnack, J. Wallace, S. Liang, and G. Margaritondo, "X-Ray Microscopy with Multilayer Mirrors: the MAXIMUM Photoelectron Microscope," p. 601 in *Sychrotron Radiation in the Biosciences*, B. Chance, J. Deisenhofer, T. Sasaki, et al., Editors, (Oxford Univ. Press, 1994).
33. G.F. Lorusso, H. Solak, F. Cerrina, J.H. Underwood, P.J. Batson, Y. Cho, C. Kisielowski, J. Kruger, and E.R. Weber, "X-Ray Photoemission Spectromicroscopy of GaN and AlGaN," *MRS Proc. 512*, 393 (1998).
34. J.H. Underwood, T.W. Barbee, and D.C. Keith, "Layered Synthethic Microstructures: Properties and Applications in X-Ray Astronomy," *Proc. SPIE 184*, 123 (1979).
35. A.B.C. Walker, T.W. Barbee, R.B. Hoover, and J.F. Lindblom, "Soft X-Ray Images of the Solar Corona with a Normal Incidence Cassegrain Multilayer Telescope," *Science 241*, 1781 (30 September 1988); M.J. Allen, A.B.C. Walker, O. Oluseyi, R.B. Hoover, and T.W. Barbee, "Chromospheric and Coronal Structure of Polar Plumes," *Solar Phys. 174*, 367 (1997).
36. L. Golub and J.M. Pasachoff, *The Solar Corona* (Cambridge University Press, New York, 1997), Section 8.3.1; also see the TRACE website http://hea-www.harvard.edu/SSXG/TRACE/pictures. html
37. "The National Technology Roadmap for Semiconductors" (Semiconductor Industry Association, San Jose, CA 1997). http://www.semichips.org. See also Chapter 10 of this book: Figure 10.7 and Table 10.1.
38. J.E.M. Goldsmith, K.W. Berger, D.R. Bozman, G.F. Cardinale, D.R. Folk, C.C. Henderson, D.J. O'Connell, A.K. Ray-Chaudhuri, K.D. Stewart, D.A. Tichenor, H.N. Chapman, R.J. Gaughan, R.M. Hudyma, C. Montcalm, E.A. Spiller, J.S. Taylor, J.D. Williams, K.A. Goldberg, E.M. Gullikson, P. Naulleau, and J.L. Cobb, "Sub-100 nm Imaging with the EUV 10X Microstepper," *Proc. SPIE 3676* (1999); J.E. Goldsmith, P.K. Barr, K.W. Berger, L.J. Bernardez, G.F. Cardinale, J.R. Darnold, S.J. Haney, G.C. Henderson, K.J. Jefferson, K.D. Krenz, G.D. Kubiak, R.P. Nissen, Y. Perras, A.K. Ray-Chandhuri, T.G. Smith, R.H. Stulen, D.A. Tichenor, A.A. Ver Berkmoes, and J.B. Wronosky, "Recent Advances in the Sandia EUV 10× Microstepper," *Proc. SPIE 3331*,

11 (1998); C. Montcalm, E. Spiller, M. Wedowski, E.M. Gullikson and J.A. Folta, "Multilayer Coatings of 10X Projection Optics for Extreme Ultraviolet Lithography," *Proc. SPIE 3676* (1999).
39. G.L. Stradling, "Time Resolved Soft X-Ray Studies of Energy Transport in Layered and Planar Laser-Driven Targets," Ph.D. thesis, Dept. of Applied Science, Univ. of California, Davis (1982).
40. G.L. Stradling, T.W. Barbee, B.L. Henke, E.M. Campbell, and W.C. Mead, "Streaked Spectrometry Using Multilayer X-Ray Interference Mirrors to Investigate Energy Transport in Laser Plasma Applications," p. 292 in *Low Energy X-Ray Diagnostics* (Amer. Inst. Phys., New York, 1981), D.T. Attwood and B.L Henke, Editors.
41. G.L. Stradling, D.T. Attwood, and R.L. Kauffman, "A Soft X-Ray Streak Camera," *IEEE J. Quantum Electron. QE-19*, 604 (1983).
42. M.J. Freiser, "A Survey of Magnetooptic Effects," *IEEE Trans. Magn. MAG-4*, 152 (1967).
43. J.C. Suits, "Magnetooptical Properties," Chapter 9 in *Handbook of Magnetic Materials* (Reinhold, New York, 1968), P.A. Albertos and F.E. Luborsky, Editors.
44. P. Dhez, "Polarizers and Polarimeters in the X-UV Range," *Nucl. Instrum. Meth. A 261*, 66 (1987).
45. J.B. Kortright and J.H. Underwood, "Multilayer Optical Elements for Generation and Analysis of Circularly Polarized X-Rays," *Nucl. Instrum. Meth. A 291*, 272 (1990).
46. M. Yamamoto, K. Mayama, H. Kimura, Y. Gato, and M. Yanagihara, "Thin Film Ellipsometry at a Photon Energy of 97 eV," *J. Electr. Spectrosc. Rel. Phenom. 80*, 465 (1996).
47. S. DiFonzo, W. Jark, F. Schäfters, H. Petersons, A. Gaupp, and J.H. Underwood, "Phase Retardation and Full-Polarization Analysis of Soft X-Ray Synchrotron Radiation Close to the Carbon K-Edge by Use of a Multilayer Transmission Filter," *Appl. Optics 33*, 2624 (1994).
48. J.B. Kortright, M. Rice, and R. Carr, "Soft X-Ray Faraday Rotation at Fe $L_{2,3}$ Edges," *Phys. Rev. B 51*, 10240 (1995).
49. J.B. Kortright and M. Rice, "Soft X-Ray Magneto-optic Kerr Rotation and Element Specific Hysteresis Measurement," *Rev. Sci. Instrum. 67*, 1 (1996); available on CD-ROM only.
50. J.B. Kortright, S.-K. Kim, T. Warwick, and N.V. Smith, "Soft X-Ray Circular Polarizer Using Magnetic Circular Dichroism at the Fe L_3 Line," *Appl. Phys. Lett. 71*, 1446 (1997).
51. J.H. Underwood, A.C. Thompson, Y. Wu, and R.D. Giaque, "X-Ray Microprobe Using Multilayer Mirrors," *Nucl. Instrum. Meth. A 266*, (1988).
52. J.H. Underwood, A.C. Thompson,, J.B. Kortright, K.C. Chapman, and D. Lunt, "Focusing X-Rays to a 1-μm Spot Using Elastically Bent, Graded Multilayer Coated Mirrors," *Rev. Sci. Instrum. 67*, 1 (1996); available on CD-ROM only.
53. Y. Wu, "Phase Transition and Equation of State of CsI under High Pressure and the Development of a Focusing System for X-Rays," Ph.D. thesis, Physics Department, University of California, Berkeley 1990 (LBL-29844).
54. H.K. Mao, Y. Wu, R.J. Hemley, L.C. Chen, J.F. Shu, and L.W. Finger, "X-Ray Diffraction to 302 Gigapascals: High Pressure Crystal Structure of Cesium Iodide," *Science 246*, 649 (3 November 1989); note that for the experiments described in this paper crossed slits were used without focusing optics.
55. Y. Wu, A.C. Thompson, J.H. Underwood, K.H. Mao, Y.W. Fei, J.Z. Hu, J.V. Badding, and J.F. Shu, "A Focusing System for X-Ray Diffraction Studies of Materials under High Pressure in the Diamond Cell, *Adv. X-Ray Anal. 34*, (1991); H.-K. Mao, J. Shu, G. Shen, R.J. Henley, B.Li., and A.K. Singh, "Elasticity and Rheology of Iron Above 220 GPa and the Nature of the Earth's Inner Core," *Nature 396*, 741 (1998).
56. D. Clery, "New Synchrotrons Light Up Microstructure of Earth,"*Science 277*, 1220 (29 Aug. 1997).
57. R.J. Hemly and N.W. Ashcroft, "The Revealing Role of Pressure in the Condensed Matter Sciences," *Phys. Today*, 26–32 (August 1998).
58. S. Gilder and J. Glen, "Magnetic Properties of Hexagonal Close-Packed Iron Deduced from Direct Observations in a Diamond Anvil Cell," *Science 279*, 72 (2 January 1998).

HOMEWORK PROBLEMS

Homework problems for each chapter will be found at the website:
http://www.coe.berkeley.edu/AST/sxreuv

Chapter 5

SYNCHROTRON RADIATION

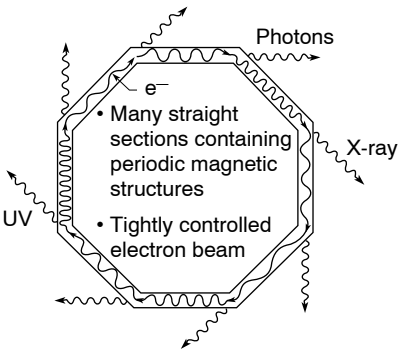

Bending Magnet:

$$\hbar\omega_c = \frac{3e\hbar B\gamma^2}{2m} \tag{5.7}$$

Wiggler:

$$\hbar\omega_c = \frac{3e\hbar B\gamma^2}{2m}$$

$$n_c = \frac{3K}{4}\left(1 + \frac{K^2}{2}\right)$$

$$P_T = \frac{\pi e K^2 \gamma^2 I N}{3\epsilon_0 \lambda_u}$$

Undulator:

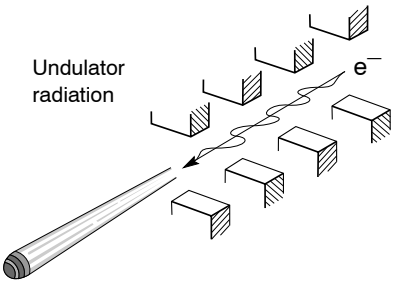

(see Colorplate X)

$$\lambda = \frac{\lambda_u}{2\gamma^2}\left(1 + \frac{K^2}{2} + \gamma^2\theta^2\right) \tag{5.28}$$

$$K = \frac{eB_0\lambda_u}{2\pi mc} \tag{5.18}$$

$$\theta_{\text{cen}} = \frac{1}{\gamma^*\sqrt{N}} \tag{5.15}$$

$$\left.\frac{\Delta\lambda}{\lambda}\right|_{\text{cen}} = \frac{1}{N} \tag{5.14}$$

$$\bar{P}_{\text{cen}} = \frac{\pi e\gamma^2 I}{\epsilon_0\lambda_u}\frac{K^2}{\left(1 + \frac{K^2}{2}\right)^2} f(K) \tag{5.41}$$

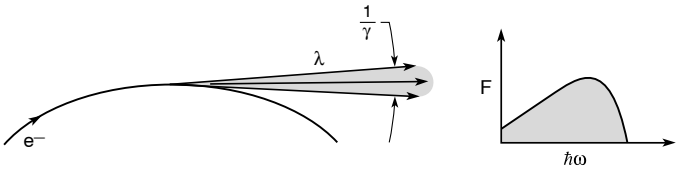

FIGURE 5.1. Bending magnet radiation occurs when a relativistic electron travels in a uniform magnetic field, executing a circular motion with acceleration directed toward the center. The radiation is directed tangentially outward in a narrow radiation cone, giving the appearance of a sweeping "searchlight." The radiation spectrum is very broad, analogous to a "white light" x-ray light bulb. The emission angle is typically $1/\gamma$, where γ is the Lorentz contraction factor.

In this chapter we briefly review the central features of synchrotron radiation, beginning with estimates of radiated photon energies and angular divergence based on the application of well-known results from the theory of relativity and Heisenberg's uncertainty principle. For bending magnet radiation, formulae describing photon flux as a function of angle and photon energy are summarized in a convenient handbook style. Undulator radiation, generated by relativistic electrons traversing a periodic magnet structure, is calculated in detail. The approach taken makes maximal use of the well-known classical results of dipole radiation. This is accomplished by solving the electron equation of motion in the laboratory frame of reference, then making a Lorentz transformation to the frame of reference moving with the average electron velocity. In this frame of reference the motion is non-relativistic, yielding the well-known $\sin^2\Theta$ angular dependence of radiated power per unit solid angle. These results are then Lorentz transformed back to the laboratory (observer) frame of reference. A central radiation cone, defined as containing a $1/N$ relative spectral bandwidth, is shown to correspond to an angular half width of $1/\gamma\sqrt{N}$, where N is the number of magnet periods. Power radiated in the central cone is readily calculated from the dipole formula. Calculations of spectral brightness follow in a straightforward manner. Wiggler radiation, the strong field extension of undulator radiation, is shown to be dominated by a large number of harmonics that merge to a continuum at high photon energy. The spectral shape of wiggler radiation is similar to that of bending magnetic radiation, but shifted to higher photon energy (by the higher magnetic fields) and to increased ($2N$) photon flux.

5.1 INTRODUCTION

It is well known that an accelerated charged particle, such as one traveling on a curved trajectory, will emit radiation. When moving at relativistic speeds, this radiation is emitted as a narrow cone tangent to the path of the particle.[1] Synchrotron radiation is generated when relativistic electrons (or positrons) are accelerated (undergo a change of direction) in a magnetic field, as seen in Figure 5.1.

There are three types of magnetic structures commonly used to produce synchrotron radiation: bending magnets, undulators, and wigglers. Bending magnets cause a single curved trajectory as pictured in Figure 5.1. The result is a fan of radiation around the bend. Undulators are periodic magnetic structures with relatively weak magnetic fields. The periodicity causes the electron to experience a harmonic oscillation as it moves in the axial direction, resulting in a motion characterized by small angular excursions called undulations,[2,3] as shown in Figure 5.2. The weak magnetic fields cause the amplitude of this undulation to be small.

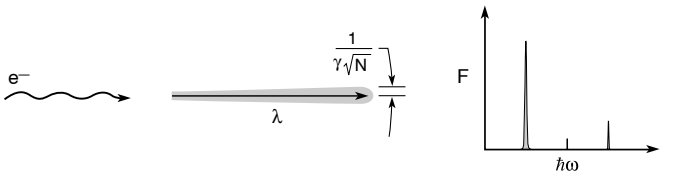

FIGURE 5.2. Undulator radiation is generated as a highly relativistic electron traverses a periodic magnetic field. In the undulator limit, the magnetic field is relatively weak and the resultant angular excursions of the electron are smaller than the angular width of the natural radiation cone, $1/\gamma$, normally associated with synchrotron radiation. The frequency spread of undulator radiation can be very narrow, and the radiation can be extremely bright and partially coherent, under certain circumstances. The characteristic emission angle is narrowed by a factor $\sqrt{N}$, where N is the number of magnetic periods. Typically N is of order 100. Depending on the magnet strength, harmonic radiation may be generated.

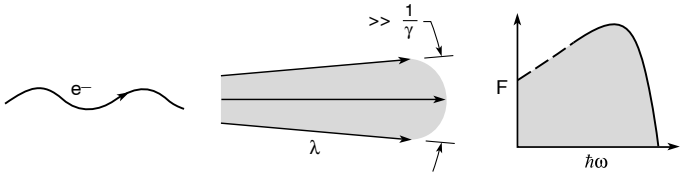

FIGURE 5.3. Wiggler radiation is also generated from a periodic magnet structure, but in the strong magnetic field limit where in at least one plane the angular excursions are significantly greater than the natural $(1/\gamma)$ radiation cone. Because accelerations are stronger in this limit, the radiation generated peaks at higher photon energies and is more abundant (higher photon flux and more power). The radiation spectrum is very broad, similar to that of the bending magnet. Although more power is radiated, wiggler radiation is less bright because of the substantially increased radiation cone.

Hence, the resultant radiation cone is narrow. In combination with a tightly confined electron beam, this leads to radiation with small angular divergence and relatively narrow spectral width, properties we generally associate with the coherence properties of lasers.[4] Wigglers are a strong magnetic field version of undulators. Due to the stronger fields, the oscillation amplitude and concomitant radiated power is larger. The radiation cone is broader in both space and angle. The radiation spectrum is similar to that of bending magnets, but characterized by a much larger photon flux and a shift to harder x-rays (shorter wavelengths), as seen in Figure 5.3.

Historically, synchrotron radiation was first observed as energy loss in electron storage rings. Logically, the first synchrotron radiation sources for general scientific use were simple parasitic beam ports utilizing otherwise lost radiation at existing storage rings. Over time, however, sources have been constructed for dedicated use as synchrotron radiation facilities (*second generation* facilities). The newest synchrotron facilities (*third generation* facilities) are composed of many straight sections specially optimized to produce high brightness undulator and wiggler radiation. Figure 5.4 illustrates yesterday's and today's synchrotron radiation facilities.

Figure 5.5 is a simple schematic of a synchrotron radiation source. The relativistic electrons are injected into the ring from a linear accelerator and (energy) booster synchrotron. Various magnetic lenses keep the electrons traveling along the desired trajectory. Synchrotron radiation is produced as the electrons pass through the bending magnets, undulators, and

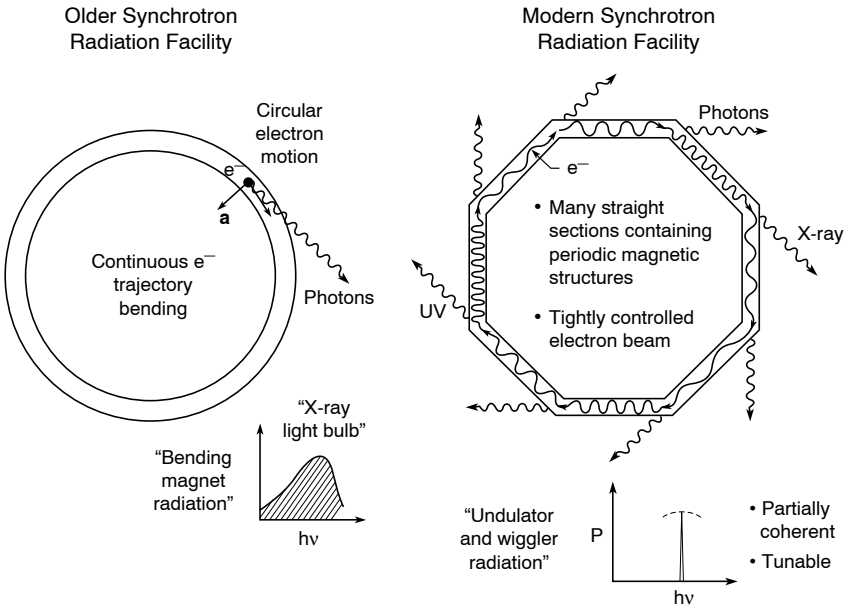

FIGURE 5.4. (a) Early synchrotron radiation facilities were basically circular rings for bending magnet radiation, although some have been retrofitted with periodic magnetic structures (undulators or wigglers). They generally have an electron beam of relatively large cross-section and angular divergence. (b) Modern storage rings are dedicated to broad scientific use and optimized for high spectral brightness through the inclusion of many long straight sections for undulators and wigglers, as well as very tightly confined (spatial and angular extent) electron beams. Bending magnet radiation is also generated in turning from one straight section to the next (not shown).

wigglers. Electron beam energy lost to synchrotron radiation is replenished with a radio-frequency accelerator (a cavity with an axial electric field oscillating at the frequency of arrival of sequential electron bunches). Typical parameters characterizing synchrotron radiation from two modern storage rings, one optimized for the generation of soft x-rays and one optimized for the generation of hard x-rays, are given in Table 5.1.

5.2 CHARACTERISTICS OF BENDING MAGNET RADIATION

In this introductory section, we wish to use simple arguments to show why one expects to see radiation at x-ray wavelengths. The arguments are based on an estimate of the time duration of the observed radiation signal and an application of Heisenberg's uncertainty principle for photon energy. Bending magnet radiation is sometimes described as a sweeping "searchlight," analogous to the headlight of a toy train on a circular track. This searchlight effect is a general manifestation associated with radiation from relativistic particles undergoing acceleration. An electron experiencing radial acceleration as it travels around a circle emits radiation through a broad angular pattern – as seen in its frame of reference. However, angular patterns are very much compressed upon Lorentz transformation from one frame of reference (that moving with the electron) to another (the laboratory frame of the observer) when the relative motion is highly relativistic. In Appendix F it is shown that angles measured from the direction of

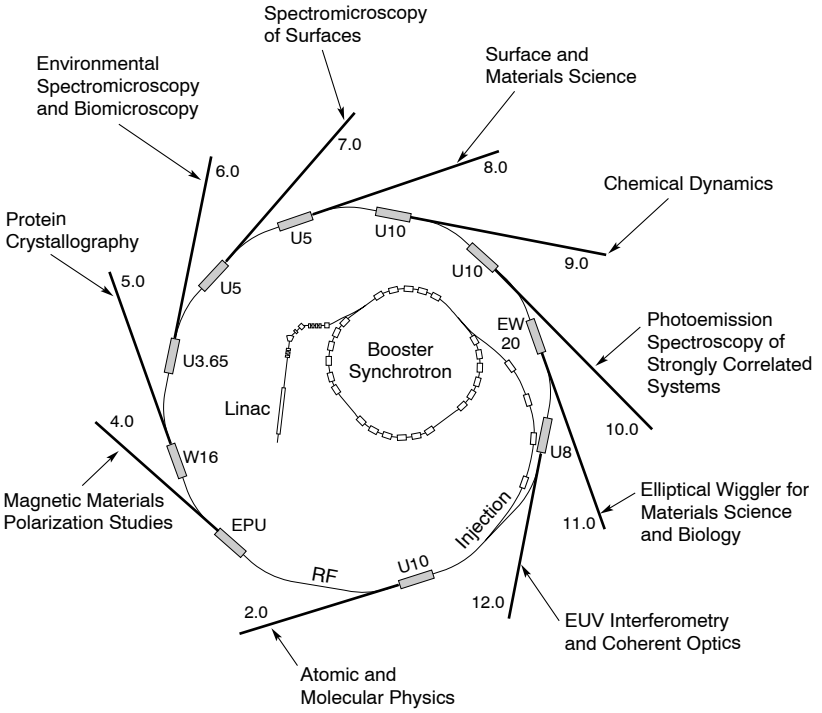

FIGURE 5.5. This sketch of an electron storage ring optimized for soft x-ray radiation shows a linear accelerator (linac) and booster synchrotron that bring electrons up to an energy matched to storage ring magnet settings, an injection system, which directs electrons into the ring, and a radio frequency (rf) generator to replenish the energy lost to synchrotron radiation as the electrons pass bending magnets, undulators, and wigglers. Straight sections for undulators and wigglers direct energy into beamlines and end sections for various scientific studies. Bending magnet radiation beamlines, located between straight sections, are not shown.

motion are related by

$$\tan\theta = \frac{\sin\theta'}{\gamma(\beta + \cos\theta')} \tag{5.1}$$

where θ' is observed in the frame of reference moving with the electron, θ is in the laboratory frame, $\beta \equiv \mathrm{v}/c$ (where v is the relative velocity between frames and c is the velocity of light), and $\gamma \equiv 1/(1 - \mathrm{v}^2/c^2)^{1/2}$. For highly relativistic electrons β approaches unity, and $\gamma \gg 1$. Thus for arbitrarily large emission angles θ', in the electron frame, the radiation is folded into a narrow forward radiation cone of half angle

$$\boxed{\theta \simeq \frac{1}{2\gamma}} \tag{5.2}$$

leading to the description of synchrotron radiation as being concentrated in a narrow "searchlight beam."

TABLE 5.1. Typical parameters for synchrotron radiation at two complementary storage ring facilities. Both rings are optimized for small electron phase space (emittance) and the use of multiple straight sections for undulators and wigglers. Bending magnet radiation is obtained as the electron beam turns from one straight section to the next. The two facilities are complementary in that one is optimized for soft x-rays while the other is optimized for hard x-rays. The Advanced Light Source (ALS) is operated by Lawrence Berkeley National Laboratory in California. The Advanced Photon Source (APS) is operated by Argonne National Laboratory in Illinois. Parameters for other facilities around the world are tabulated by Winck (Ref. 5).

Facility	**ALS**	**APS**
Electron energy	1.90 GeV	7.00 GeV
γ	3720	13,700
Current (mA)	400	100
Circumference (m)	197	1100
RF frequency (MHz)	500	352
Pulse duration (FWHM) (ps)	35–100	170
Bending Magnet Radiation:		
Bending magnet field (T)	1.27	0.599
Critical photon energy (keV)	3.05	19.5
Critical photon wavelength	0.407 nm	0.0636 nm (0.636 Å)
Bending magnet sources	24	35
Undulator Radiation:		
Number of straight sections	12	40
Undulator period (typical) (cm)	5.00	3.30
Number of periods	89	72
Photon energy ($K = 1, n = 1$)	457 eV	9.40 keV
Photon wavelength ($K = 1, n = 1$)	2.71 nm	0.132 nm (1.3 Å)
Tuning range ($n = 1$)	2.0–5.4 nm	0.10–0.35 nm
Tuning range ($n = 3$)	0.68–1.8 nm	0.033–0.12 nm
Central cone half-angle ($K = 1$)	35 μrad	11 μrad
Power in central cone ($K = 1, n = 1$) (W)	2.3	12
Flux in central cone (photons/s)	3.1×10^{16}	7.9×10^{15}
σ_x, σ_y (μm)	260, 16	320, 50
σ'_x, σ'_y (μrad)	23, 3.9	23, 7
Brightness ($K = 1, n = 1$)[a] [(photons/s)/mm^2 · mrad^2 · (0.1%BW)]	2.3×10^{19}	4.8×10^{18}
Total power ($K = 1$, all n, all θ) (W)	187	780
Other undulator periods (cm)	3.65, 8.00, 10.0	2.70, 5.50, 12.8
Wiggler Radiation:		
Wiggler period (typical) (cm)	16.0	8.5
Number of periods	19	28
Magnetic field (maximum) (T)	2.1	1.0
K (maximum)	32	7.9
Critical photon energy (keV)	5.1	33
Critical photon wavelength	0.24 nm	0.038 nm (0.38 Å)
Total power (max. K) (kW)	13	7.4

[a] Using Eq. (5.65). See comments following Eq. (5.64) for the case where $\sigma'_{x,y} \simeq \theta_{\text{cen}}$.

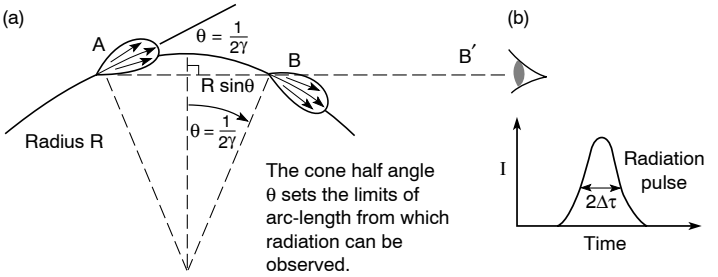

FIGURE 5.6. (a) A schematic of bending magnet radiation illustrating the "searchlight" effect, similar to that of the headlight of a train on a circular track, which is a general feature of radiation by highly relativistic electrons. (b) The time width of the observed radiation pulse is determined by transit time differences between radiation and electrons between points A and B. The uncertainty relationship between pulse duration and minimal spread of photon energy indicates that a broad range of photon energies, extending to the x-ray region, is to be expected. (Following Hofmann.[2])

As an electron traverses a curved path, radiation is emitted tangentially, as seen in Figure 5.6, in a narrow radiation cone of half width $\theta \simeq 1/2\gamma$. For electrons circulating in a ring, we can estimate the photon energies and wavelengths radiated using simple arguments based on Heisenberg's uncertainty principle, $\Delta E \cdot \Delta\tau \geq \hbar/2$, where $\Delta\tau$ is the (rms) time duration during which one detects radiation, and ΔE is the uncertainty (rms spread) in observed photon energies. We begin by estimating the detected pulse duration, $2\,\Delta\tau$, of radiation emitted by a short bunch of electrons following a circular trajectory of radius R. We estimate the time extent of the observed signal by considering a detector at point B or equivalently further to the right at B'. As the electron comes within an angle $\theta \simeq 1/2\gamma$ of the horizon at point A, the detector will be in the path of emitted photons. These photons will be detected after a transit time of the light, τ_r. The signal will continue until the electron reaches point B, beyond which the radiation cone has turned too far to permit reception by our detector. The electron will reach point B after a transit time around the bend, τ_e. The pulse width, $\Delta\tau$, shown in Figure 5.6(b) is the difference between these two transit times, i.e., the detector detects radiation after a time τ_r, and stops detecting radiation at τ_e.

Following this outline, we see that

$$2\,\Delta\tau = \tau_e - \tau_r$$

$$2\,\Delta\tau = \frac{\text{arc length}}{\text{v}} - \frac{\text{radiation path}}{c}$$

$$2\,\Delta\tau \simeq \frac{R \cdot 2\theta}{\text{v}} - \frac{2R\sin\theta}{c}$$

Noting that $\theta \simeq 1/2\gamma$, making a small angle approximation for $\sin\theta$, and substituting $\text{v} = \beta c$, one obtains

$$2\,\Delta\tau \simeq \frac{R}{\gamma\text{v}} - \frac{R}{\gamma c} = \frac{R}{\gamma}\left(\frac{1}{\text{v}} - \frac{1}{c}\right)$$

Writing $v = \beta c$, one has

$$2\,\Delta\tau \simeq \frac{R}{\gamma\beta c}(1-\beta)$$

Noting that

$$\gamma \equiv \frac{1}{\sqrt{1-\beta^2}}$$

$$\gamma^2 = \frac{1}{1-\beta^2} = \frac{1}{(1-\beta)(1+\beta)}$$

and thus for $\beta = v/c$ approaching unity

$$1-\beta \simeq \frac{1}{2\gamma^2} \tag{5.3}$$

the expression for the duration of the radiation pulse becomes

$$2\Delta\tau \simeq \frac{R}{2c\gamma^3} \tag{5.4a}$$

This can be expressed as an anticipated photon energy spread through the use of Heisenberg's uncertainty principle[6] and an expression for the radius of curvature R. From the uncertainty principle,

$$\Delta E \cdot \Delta\tau \geq \hbar/2$$

Combining this with the expression in Eq. (5.4a) for the pulse duration, we see that the photons will have an rms energy spread of order*

$$\Delta E \geq \frac{2\hbar c\gamma^3}{R} \tag{5.4b}$$

To better appreciate the photon energies implied by Eq. (5.4b) it is useful to replace the electron radius of curvature R with an expression involving γ and the magnetic field. For electrons crossing a perpendicular magnetic field, as in a bending magnet, the relativistically correct form of the equation of motion can be written as

$$\mathbf{F} = \frac{d\mathbf{p}}{dt} = -e\mathbf{v} \times \mathbf{B}$$

where $\mathbf{p} = \gamma m\mathbf{v}$ is the momentum,[6] m is the electron rest mass, γ is the Lorentz factor, $\mathbf{v}$ is the velocity, and $\mathbf{B}$ is the magnetic flux density. For electron motion in a uniform magnetic field, the electron energy and thus γ is a constant, so that only the direction of $\mathbf{v}$ changes, not its magnitude. To see this we write the rate of change of electron energy as

$$\frac{dE_e}{dt} = \mathbf{v} \cdot \mathbf{F} = \underbrace{-e\mathbf{v} \cdot (\mathbf{v} \times \mathbf{B})}_{\equiv 0}$$

*Similar arguments are given in J.D. Jackson (Ref. 1), First Edition, pp. 475–477.

which is zero by vector identity (see Appendix B). Thus the electron energy, which can be written[6] as γmc^2, is a constant, viz.,

$$\frac{dE_e}{dt} = \frac{d}{dt}(\gamma mc^2) = 0$$

Thus γ, and therefore the scalar magnitude v of the velocity, are both constant. The equation of motion can be rewritten as

$$\gamma m \frac{d\mathbf{v}}{dt} = -e\mathbf{v} \times \mathbf{B}$$

Since the magnitude of **v** is constant, the magnitude of the acceleration is also constant, equal to $e\mathrm{v}B/\gamma m$, in a plane perpendicular to **B**. This corresponds to motion along a circle, with centripetal acceleration v^2/R, so that the scalar form of the equation of motion becomes

$$\gamma m \left(-\frac{\mathrm{v}^2}{R}\right) = -e\mathrm{v}B$$

Solving for the radius of curvature, we have

$$R = \frac{\gamma m \mathrm{v}}{eB}$$

or for highly relativistic electrons

$$R \simeq \frac{\gamma mc}{eB}$$

Using this in Eq. (5.4b), the rms spread of photon energies for bending magnet radiation becomes

$$\Delta E \geq \frac{2e\hbar B\gamma^2}{m} \tag{5.4c}$$

which we note depends on the electron charge to mass ratio, e/m, and the product $B\gamma^2$. If we substitute values for e, $\hbar$, and m, Eq. (5.4c) indicates photon energies in the keV range (nanometer wavelengths) for typical values of γ and B found in modern storage rings, e.g., γ of several thousand and B of 1T or more. For highly relativistic electrons it is convenient to express the total electron energy in terms of γ and the electron rest energy, mc^2, as[6]

$$\gamma = \frac{E_e}{mc^2} = 1957E_e(\mathrm{GeV}) \tag{5.5}$$

where on the right side we have used the fact that the electron rest energy is 0.5110 MeV, and expressed the electron energy E_e in GeV.

The description of expected photon energy spread obtained above, Eq. (5.4c), is based on relatively simple arguments involving Heisenberg's uncertainty principle. It is valuable in that it provides a measure of the expected photon energies radiated by accelerated charges moving at relativistic speeds, and gives a functional dependence in terms of $B\gamma^2$. The numerical factor (2) obtained by this argument is, however, is somewhat arbitrary in that it depends on the angular distribution of radiation embodied in our assumption that $\theta \simeq 1/2\gamma$. A more precise description of the photon energy distribution, obtained by a rigorous solution of Maxwell's equations for a relativistic electron in a uniform magnetic field, introduces instead a factor of $\frac{3}{2}$ and a more useful definition of ΔE. The results are somewhat complex, involving

TABLE 5.2. Sample values of the functions $G_1(y)$ and $H_2(y)$, where $y = \omega/\omega_c$ (following Green.[7]).

y	$G_1(y)$	$H_2(y)$
0.0001	9.959×10^{-2}	6.271×10^{-3}
0.0010	2.131×10^{-1}	2.910×10^{-2}
0.0100	4.450×10^{-1}	1.348×10^{-1}
0.1000	8.182×10^{-1}	6.025×10^{-1}
0.3000	9.177×10^{-1}	1.111×10^{0}
0.5000	8.708×10^{-1}	1.356×10^{0}
0.7000	7.879×10^{-1}	1.458×10^{0}
1.000	6.514×10^{-1}	1.454×10^{0}
1.500	4.506×10^{-1}	1.250×10^{0}
2.000	3.016×10^{-1}	9.780×10^{-1}
3.000	1.286×10^{-1}	5.195×10^{-1}
4.000	5.283×10^{-2}	2.493×10^{-1}
5.000	2.125×10^{-2}	1.131×10^{-1}
7.000	3.308×10^{-3}	2.107×10^{-2}
10.00	1.922×10^{-4}	1.478×10^{-3}

modified Bessel functions of the second kind (see Refs. 1–3). Defining θ as the in-plane observation angle for radiation from relativistic electrons traveling in a circular path, and ψ as the out-of-plane (vertical) angle, Kim[3] shows that the photon flux F_B for bending magnet radiation is given on axis by

$$\left.\frac{d^3F_B}{d\theta\, d\psi\, d\omega/\omega}\right|_{\psi=0} = 1.33 \times 10^{13} E_e^2(\text{GeV}) I(\text{A}) H_2(E/E_c) \frac{\text{photons/s}}{\text{mrad}^2 \cdot (0.1\%\ \text{BW})} \tag{5.6}$$

where the electron energy E_e is in GeV, the average current I is in amperes, where the units of relative spectral bandwidth $d\omega/\omega$ are expressed non-dimensionally as a factor of 10^{-3}, or 0.1% BW, as discussed further in section 5.4.6, and the function

$$H_2(y) = y^2 K_{2/3}^2(y/2)$$

is a modified Bessel function dependence, tabulated in Table 5.2 and shown graphically in Figure 5.7. The ratio E/E_c is the photon energy normalized with respect to a *critical photon energy*

$$E_c = \hbar\omega_c = \frac{3e\hbar B\gamma^2}{2m} \tag{5.7a}$$

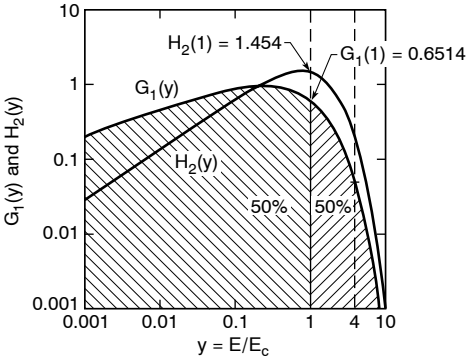

FIGURE 5.7. The functions $H_2(y)$, representing on-axis photon flux from a bending magnet, and $G_1(y)$, representing the vertically integrated photon flux, as functions of photon energy normalized to the critical photon energy. Half the radiated power is in photons of energy greater than E_c, and half in photons of energy less than E_c (following Kim[3]). Note that for a photon energy of $4E_c$ the photon flux is reduced a factor of about 10 from its value at E_c.

The critical photon energy is that for which half the radiated power is in higher energy photons and half is in lower energy photons. As such it provides a primary parameter for characterizing bending magnet radiation.

Equation (5.7a) can be rewritten in practical units as

$$E_c(\text{keV}) = 0.6650E_e^2(\text{GeV})B(\text{T}) \tag{5.7b}$$

where the critical photon energy is in keV, the electron beam energy is given in GeV, and the magnetic field in teslas. The corresponding *critical wavelength* is

$$\lambda_c = \frac{4\pi mc}{3eB\gamma^2} \tag{5.7c}$$

which can be written in practical units of nanometers, GeV, and teslas as

$$\lambda_c\ (\text{nm}) = \frac{1.864}{E_e^2(\text{GeV})B(\text{T})} \tag{5.7d}$$

Note that the critical photon energy given in Eq. (5.7a) is well within the range of photon energies estimated by Eq. (5.4c) on the basis of relativistic angular transformations and Heisenberg uncertainty arguments.

The critical photon energy is in fact a very useful parameter for characterizing synchrotron radiation from relativistic electrons as they traverse the fields of a bending magnet. For example, of two new storage rings operating in the United States, the Advanced Light Source (ALS) at Lawrence Berkeley Laboratory in California, with a beam energy of 1.9 GeV and a bending magnet field strength of 1.27 T, has a critical photon energy of 3.1 keV and a critical wavelength of 0.41 nm (4.1 Å), while the Advanced Photon Source (APS) at Argonne National Laboratory in Illinois, with a beam energy of 7.0 GeV and a bending magnet field strength of 0.60 T, has a critical photon energy of 20 keV and a critical wavelength of 0.064 nm (0.64 Å).

Typical parameters characterizing synchrotron radiation from these two representative facilities are presented in Table 5.1. Between the two they cover a broad region of the electromagnetic spectrum. In fact, inspection of Figure 5.7 shows that on axis the photon flux decreases by only a factor of 10 at a photon energy equal to $4E_c$. For many experiments this significantly extends the useful range of bending magnet radiation, for instance to 12 keV at the ALS, and to 80 keV at the APS. Further enhancements using strong field periodic wigglers are also possible. Wiggler radiation is described at the end of this chapter.

TABLE 5.3. Measures of angular divergence of bending magnet radiation in the vertical plane, as a function of normalized photon energy. Single sided rms and full width at half maximum (FWHM) measures are given. (Following Kim.[3])

E/E_c	σ'_ψ (rms)	FWHM
0.01	$5.0/\gamma$	$12/\gamma$
0.03	$3.3/\gamma$	$7.8/\gamma$
0.1	$2.0/\gamma$	$4.7/\gamma$
0.3	$1.2/\gamma$	$2.8/\gamma$
1	$0.64/\gamma$	$1.5/\gamma$
3	$0.37/\gamma$	$0.9/\gamma$
10	$0.18/\gamma$	$0.4/\gamma$

On occasion it is convenient to know the bending magnet photon flux per unit horizontal angle θ, integrating out the vertical plane ϕ-dependence. In this case Kim[3] finds that the radiated photon flux, in units of photons per second per milliradian per 0.1% relative spectral bandwidth, is given by

$$\frac{d^2F_B}{d\theta\, d\omega/\omega} = 2.46 \times 10^{13} E_e(\text{GeV}) I(\text{A}) G_1(E/E_c) \frac{\text{photons/s}}{\text{mrad} \cdot (0.1\%\text{BW})} \tag{5.8}$$

where the function

$$G_1(y) = y \int_y^\infty K_{5/3}(y')\, dy'$$

is also shown graphically in Figure 5.7. Note that by the definition of E_c, the integrals of $G_1(y)$ from zero to one and from one to infinity are equal, as suggested in Figure 5.7. Table 5.2 gives some specific values of the functions $H_2(\omega/\omega_c)$ and $G_1(\omega/\omega_c)$.

Note that the bending magnet radiation is linearly polarized when viewed in the horizontal plane of acceleration. When viewed outside this plane, bending magnet radiation is elliptically polarized. The out of plane photon flux, decomposed into horizontal and vertical polarization components, is given by Kim.[3] Kim also introduces a convenient measure of angular divergence[3] in the vertical plane, σ'_ψ, for bending magnet radiation. This divergence angle varies with normalized photon energy, E/E_c. Fitted to a Gaussian angular distribution, the rms half angle in the vertical plane is $0.64/\gamma$ at $E/E_c = 1$. Full width at half maximum (FWHM) measures are larger by a factor of 2.35. Sample values are given in Table 5.3 for sample values of E/E_c.

Since the acceleration of electrons is confined to the horizontal plane (for vertical bending magnet fields), the electric field of the resultant radiation will be linearly polarized in that

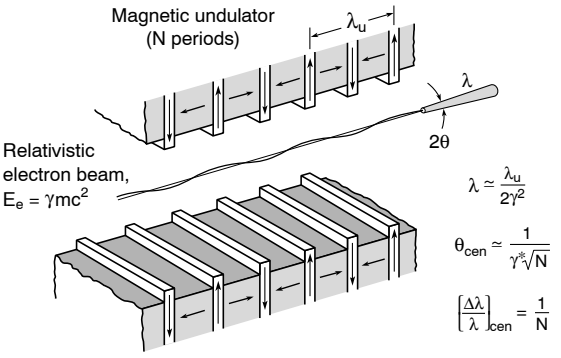

FIGURE 5.8. Illustration of narrow cone undulator radiation that is generated by electrons traversing a periodic magnet structure.

plane. The general polarization properties of bending magnet radiation for arbitrary angles of observations are discussed in Ref. 3.

5.3 CHARACTERISTICS OF UNDULATOR RADIATION

An electron traversing a periodic magnet structure[8] of moderate field strength will undergo a small amplitude oscillation and therefore radiate. If the electron's angular excursions are small compared to the natural radiation width, $\theta_e < 1/2\gamma$, the device is referred to as an *undulator* (see Figure 5.8). The resultant radiation is greatly reduced in wavelength, λ, from that of the magnet period, λ_u. We will see shortly that Lorentz contraction and relativistic Doppler shift lead to a reduction in the radiated wavelength by a factor of $2\gamma^2$. As γ can easily be several thousand, undulator periods measured in centimeters lead to observed x-ray wavelengths measured in angstroms.

While discussing undulator radiation, we will find it convenient to consider the radiation in several frames of reference. Many of the calculations will be done in the reference frame moving with the electron. We will then transform the results to the rest frame of the laboratory via Lorentz transformations (see Ref. 9 or Appendix F, Lorentz Space–Time Transformations). The following is a brief introduction to undulator radiation. A more detailed discussion will follow in subsequent sections.

In the frame moving with the electron, the electron "sees" a periodic magnet structure moving toward it with a relativistically (Lorentz) contracted period, λ', given by

$$\lambda' = \frac{\lambda_u}{\gamma} \tag{5.9}$$

where $\gamma \equiv 1/\sqrt{(1 - v^2/c^2)}$, v is the relative velocity, and c is the velocity of light in vacuum, as discussed in Appendix F. Due to the periodic magnet, the electron experiences an oscillation and consequently radiates. In the frame moving with the electron this problem is that of the classical *radiating dipole*, a point charge oscillating with an amplitude much smaller than the radiated wavelength. The frequency of this emitted radiation, in the reference frame of

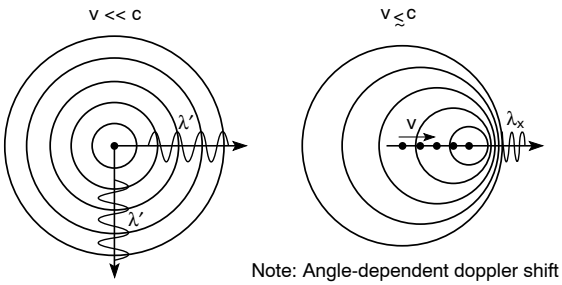

FIGURE 5.9. Radiation from an oscillating charge moving at (a) a non-relativistic and (b) a relativistic speed. Short wavelengths are observed because comparable speeds of the moving charge (v) and the radiation (c) reduce the separation of succeeding phase fronts. Indeed, as v approaches c, the spatial phase variations (λ) are dramatically compressed by many orders of magnitude. (Following J. Madey.)

the electron, is

$$f' = \frac{c}{\lambda'} = \frac{c\gamma}{\lambda_u}$$

To the observer in the fixed laboratory reference frame, the radiation wavelength is further reduced by Doppler shifting. The Doppler shift is dependent on the relative velocity and therefore is dependent on the observation angle θ, as can be deduced from Figure 5.9. The shortest wavelength is observed on axis. The relativistic form of the Doppler frequency formula is [see Appendix F, Eq. (F.8b)]

$$f = \frac{f'}{\gamma(1 - \beta\cos\theta)} = \frac{c}{\lambda_u(1 - \beta\cos\theta)} \tag{5.10}$$

where $\beta \equiv \mathrm{v}/c$ and θ is the observation angle measured from the direction of motion.

Let us first analyze the observed frequency on axis. Here $\theta = 0,\ \cos\theta = 1$, and

$$f = \frac{c}{\lambda_u(1 - \beta)}$$

As noted in Eq. (5.3), for $\beta \simeq 1$ we have $1 - \beta \simeq 1/2\gamma^2$. Therefore, the observed radiation frequency on axis is

$$f = \frac{2\gamma^2 c}{\lambda_u}$$

and the observed wavelength on axis is

$$\lambda = \frac{c}{f} = \frac{\lambda_u}{2\gamma^2} \tag{5.11}$$

Note that the observed wavelength, λ, is relativistically contracted by a factor $2\gamma^2$ from the period of the undulator. Again using the ALS as an example, with a 1.9 GeV electron energy, $\gamma \simeq 3700$ [see Eq. (5.5)]; thus $2\gamma^2 \simeq 2.8 \times 10^7$. If the undulator period is $\lambda_u = 5.0$ cm, the

resultant on-axis radiation will be relativistically shifted to an observed wavelength of order

$$\lambda \simeq \frac{5.0\text{cm}}{2.8 \times 10^7} \simeq 1.8\ \text{nm}$$

Thus the periodic magnet generates radiation peaked in the soft x-ray region of the electromagnetic spectrum.

If we wish to consider Doppler shifts at small angles off axis ($\theta \neq 0$), we can return to Eq. (5.10) and use the small angle approximation. The Taylor expansion for small angles is $\cos\theta = 1 - \theta^2/2 + \cdots$; therefore,

$$f = \frac{\frac{c}{\lambda_u}}{1 - \beta\left(1 - \frac{\theta^2}{2} + \cdots\right)} = \frac{\frac{c}{\lambda_u}}{1 - \beta + \frac{\beta\theta^2}{2} + \cdots} = \frac{\frac{c}{(1-\beta)\lambda_u}}{1 + \frac{\beta\theta^2}{2(1-\beta)}}$$

Since $\beta \simeq 1$ and by Eq. (3) $1 - \beta \simeq 1/2\gamma^2$, one has

$$f = \frac{\frac{2\gamma^2 c}{\lambda_u}}{1 + \frac{2\gamma^2\theta^2}{2} - \cdots} = \frac{2c\gamma^2}{\lambda_u(1 + \gamma^2\theta^2)}$$

In terms of the observed wavelength $\lambda = c/f$, one has to first order

$$\lambda = \frac{\lambda_u}{2\gamma^2}(1 + \gamma^2\theta^2) \tag{5.12}$$

We again see the $2\gamma^2$ contraction on axis, but now with the off-axis radiation having a wavelength increased by a factor $(1+\gamma^2\theta^2)$. Hence, to observe the narrow bandwidth characteristic of this relativistic harmonic oscillator, it is necessary to select only near-axis radiation.

As we will see explicitly in a following section, the magnetically induced undulation causes the electron to follow a somewhat longer pathlength as it traverses the undulator. Thus, the mean axial velocity is reduced, resulting in a modified Doppler shift and therefore somewhat longer wavelengths than indicated by Eq. (5.12), and a broader radiation cone as well.

5.3.1 Undulator Radiation Pattern

As we saw in Chapter 2, Eqs. (2.25)–(2.33), an oscillating electron of charge $-e$ undergoing an acceleration **a** will radiate electromagnetic waves characterized by an electric field (also see Leighton, Ref. 9).

$$E(\mathbf{r}, t) = \frac{ea(t - r/c)}{4\pi\epsilon_0 c^2 r}\sin\Theta$$

and an orthogonal magnetic field

$$H(\mathbf{r}, t) = \frac{ea(t - r/c)}{4\pi cr}\sin\Theta$$

where $t - r/c$ is the retarded time (delayed arrival at distance r), and Θ is the angle between the direction of acceleration (**a**) and the propagation direction ($\mathbf{k}_0$). Because the electric and magnetic fields are orthogonal, their cross product gives a Poynting vector **S** (power per

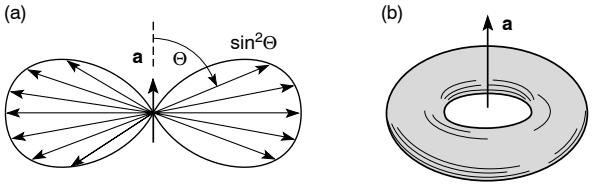

FIGURE 5.10. Illustration of an oscillating charge and the resultant radiation pattern. Note that there is no radiation in the direction of acceleration, giving the radiation pattern a doughnut-like appearance.

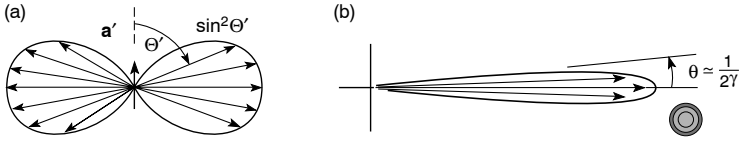

FIGURE 5.11 (see Colorplate VI). (a) Illustration of the radiation pattern of an oscillating electron in the frame of reference moving with the average electron speed. (b) Illustration of the radiation pattern of a highly relativistic electron as observed in the laboratory frame of reference. The shortest wavelengths are observed on axis. (Following Hofmann.[2])

unit area) of

$$\mathbf{S} = \mathbf{E} \times \mathbf{H} = \left[\frac{e^2 a^2 \sin^2 \Theta}{16\pi^2 \epsilon_0 c^3 r^2} \right] \mathbf{k}_0$$

The radiated power per unit solid angle is [Chapter 2, Eq. (2.34)]

$$\frac{dP}{d\Omega} = r^2 |\mathbf{S}| = \frac{e^2 a^2}{16\pi^2 \epsilon_0 c^3} \sin^2 \Theta$$

Hence, the radiation pattern has a toroidal $\sin^2 \Theta$ shape, because there is no radiation in the acceleration direction ($\Theta = 0$), as illustrated in Figure 5.10.

For an undulating electron, undergoing simple oscillations in its own reference frame (γ), one obtains the same radiation pattern. However, the radiation pattern as observed in the laboratory frame is relativistically contracted into a narrow radiation cone (the so-called searchlight effect) as shown in Figure 5.11(b). Considering the symmetry of the problem, it is convenient to work with a polar coordinate system measured from the z-axis. For instance, in the plane defined by the electron acceleration (**a**) and the z-axis, the factor $\sin^2 \Theta'$ becomes $\cos^2 \theta'$, θ' being the polar angle measured away from the z-axis in the primed coordinate system. In this primed electron frame of reference the radiation pattern has a half-intensity angle at $\cos^2 \theta' = \frac{1}{2}$ or $\theta' = 45^\circ$. According to Eq. (5.1), this corresponds to an angle in the unprimed laboratory (observer) frame of reference of $\theta \simeq 1/2\gamma$. Returning to the example of a 1.9 GeV electron ($\gamma \simeq 3700$), in this case traversing a periodic magnet structure, one anticipates that radiated x-rays will largely be confined to a cone of half angle 140 μrad. As we will see in the following paragraphs, further cone narrowing can be obtained in the case of undulator radiation.

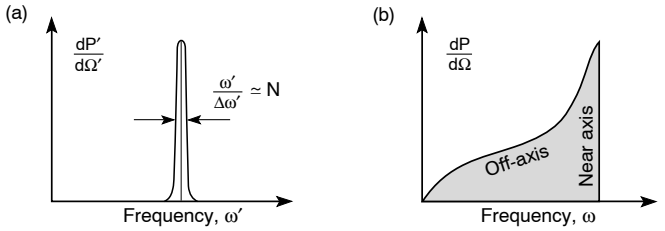

FIGURE 5.12. (a) The radiation spectrum as seen in the frame of reference moving with the electron is narrow with a relative spectral bandwidth of order $1/N$, where N is the number of oscillation periods. (b) In the laboratory frame of reference, the wavelengths are shorter, but the spectrum is broader due to off-axis Doppler effects. (Following Hofmann.[2])

5.3.2 The Central Radiation Cone

The spectrum of radiation in the two reference frames is shown in Figure 5.12(a) and (b). Figure 5.12(a) shows the narrow spectral width in the electron frame, set by the harmonic oscillation for a fixed number of periods N. This is essentially a frequency–time (Laplace) transform.

For example, the ALS has undulators of 5.0 cm period, with a length of 89 periods, so that one can expect $\Delta\omega'/\omega' = \Delta\lambda'/\lambda'$ of order 0.01. Note, however, that upon transformation to the laboratory frame of reference, off-axis Doppler effects will broaden this considerably. Figure 5.12(b) illustrates the Doppler shifted spectrum that results when the $\sin^2\Theta$ dipole radiation pattern is transformed according to Eqs. (5.1) and (5.12).

Recall that we have determined the undulator equation (5.12) in the laboratory frame, viz.,

$$\lambda \simeq \frac{\lambda_u}{2\gamma^2}(1 + \gamma^2\theta^2)$$

and have also noted that the radiation is primarily contained in a narrow cone of half angle $\theta = 1/2\gamma$. The corresponding spectral width within this cone can thus be estimated by taking the difference of Eq. (5.12) for two angles. Taking the wavelength as λ on axis ($\theta = 0$), and $\lambda + \Delta\lambda$ off axis at angle θ, then taking ratios, one obtains

$$\frac{\Delta\lambda}{\lambda} \simeq \gamma^2\theta^2 \tag{5.13}$$

where Eq. (5.13) shows how the wavelength increases as one observes the radiation off axis. Note that for radiation within the cone of half angle $\theta \simeq 1/2\gamma$ the relative spectral bandwidth given by Eq. (5.13) is $\frac{1}{4}$; thus the cone of half-intensity half angle encloses a relative spectral bandwidth of about 25%. Use of aperture spectral filtering is illustrated in Figure 5.13. Often, further spectral narrowing is desired, for instance, when probing in the vicinity of sharp atomic resonance features. In such cases, a monochromator of some type (see Chapter 8) is employed that acts as a narrow bandpass filter. In the case of radiation from a single electron or a tightly constrained bunch of electrons, modest spectral filtering (as narrow as $1/N$) can be obtained with a simple small-angle selecting aperture (pinhole). In this limit, we will see that angular width and spectral width are closely connected. The interrelationship is shown in Figure 5.14.

Further cone narrowing can be appreciated by considering the undulator equation for two angular positions, one on axis and one at angle θ, as we did previously in Eq. (5.13). If one

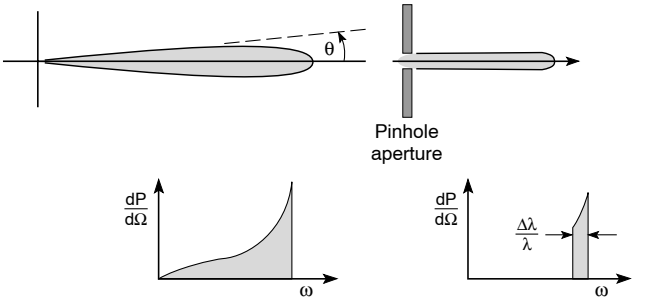

FIGURE 5.13. The spectrum of undulator radiation in the laboratory frame of reference before and after selecting an angular cone near the axis. With a sufficiently small electron beam phase space (size–angle product) this can provide a simple mechanism for monochromatization.

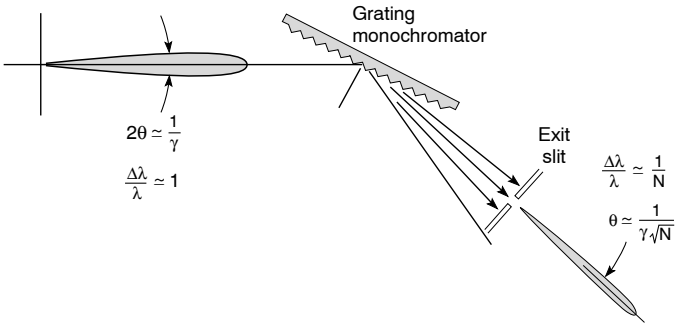

FIGURE 5.14. Illustration of a grating monochromator as used to filter undulator radiation to a "natural" spectral width $1/N$, and the concomitant cone narrowing to $1/\gamma\sqrt{N}$ that occurs with a tightly constrained electron beam.

sets the monochromator for a "natural" bandwidth $\Delta\lambda/\lambda$, set by the number of oscillation periods, N, then one obtains the condition

$$\boxed{\frac{\Delta\lambda}{\lambda} = \frac{1}{N}} \tag{5.14}$$

which, when combined with Eq. (5.13), indicates that narrower bandwidth radiation occurs in a *concomitantly narrower "central" radiation cone* of half width

$$\boxed{\theta_{\text{cen}} \simeq \frac{1}{\gamma\sqrt{N}}} \tag{5.15}$$

This narrow undulator radiation cone implies an emission solid angle reduced by a factor $1/N$. These factors become very important when considering brightness and coherence (see Chapter 8).

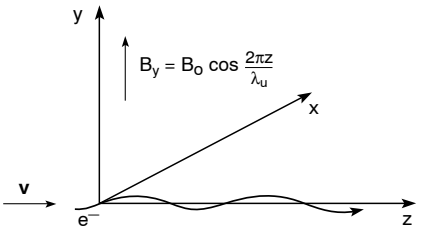

FIGURE 5.15. Electron motion in a periodic magnetic field.

The above analysis is for a single electron. For these results to hold for an electron beam with many electrons, it is necessary that all electrons in the bunch be contained within an angular variance of less than $1/\gamma\sqrt{N}$. This angular constraint on the electron beam is referred to as the *undulator condition*. Again considering 1.9 GeV electrons, with $\gamma \simeq 3720$ and $N \simeq 100$, one expects the 1% bandwidth radiation to be confined within a cone of angular half width $\theta \simeq 35\ \mu$rad.

5.4 UNDULATOR RADIATION: CALCULATIONS OF RADIATED POWER, BRIGHTNESS, AND HARMONICS

Having introduced the basic features of undulator radiation, we now wish to solve the problem by considering the equations of motion for a highly relativistic electron traversing a periodic magnetic field. In the laboratory frame, the electron experiences only the static, albeit periodic, magnetic field for small K. Hence, the laboratory is a convenient reference frame for the calculation. After calculating electron trajectories in the laboratory frame, we will transform to the frame of reference moving with the average electron motion (γ). Our next step will be to calculate the radiated fields in the electron frame where we have simple harmonic motion (dipole radiation). We will see a multiplicity of harmonics, $n\omega$, of this radiation. Finally, we will transform the radiated fields to the laboratory frame. The approach follows that of Hofmann.[2]

5.4.1 The Undulator Equation

The force equation for a charge in the presence of electric and magnetic fields can be written in any frame of reference as

$$\frac{d\mathbf{p}}{dt} = q(\mathbf{E} + \mathbf{v} \times \mathbf{B}) \tag{5.16}$$

where $\mathbf{p} = \gamma m\mathbf{v}$ is the momentum, q is the charge, $\mathbf{v}$ is the velocity, and $\mathbf{E}$ and $\mathbf{B}$ are the electric and magnetic fields, determined through Maxwell's equations. The problem we are considering is dominated by the applied dc magnetic field associated with a periodic magnet structure (undulator), as illustrated in Figure 5.15. There are no applied electric fields. Further, we consider the radiated electromagnetic fields due to the undulator radiation generated by many electrons to be relatively weak in the sense that the radiated fields have a negligible effect on the various electron motions. To this level of approximation, we take $\mathbf{E} \simeq 0$ in Eq. (5.16). Note that this would not be the case in a sufficiently long undulator. In fact, the effect of the radiated fields would lead to free electron laser (FEL) action.[10, 11] With these

approximations the momentum equation becomes

$$\frac{d\mathbf{p}}{dt} = -e(\mathbf{v} \times \mathbf{B})$$

For the undulator case with relatively weak radiated fields (pre-FEL action), we take the approximations $E \simeq 0$ and $\mathbf{B}_y = \mathbf{B}_0 \cos(2\pi z/\lambda_u)$ plus a negligible radiation field. Additionally, taking to first order $\mathbf{v} \simeq \mathbf{v}_z$, the vector components in the x-direction give

$$m\gamma \frac{d\mathrm{v}_x}{dt} = +e\mathrm{v}_z B_y$$

$$m\gamma \frac{d\mathrm{v}_x}{dt} = e\frac{dz}{dt} \cdot B_0 \cos\left(\frac{2\pi z}{\lambda_u}\right) \qquad (0 \le z \le N\lambda_u)$$

Now we can solve for the transverse oscillation v_x. This gives rise to the primary source of undulator radiation. To first order, we will find v_x as a function of axial position z. Continuing the algebra,

$$m\gamma \, d\mathrm{v}_x = e \, dz \, B_0 \cos\left(\frac{2\pi z}{\lambda_u}\right)$$

Integrating both sides gives

$$m\gamma \mathrm{v}_x = eB_0 \frac{\lambda_u}{2\pi} \int \cos\left(\frac{2\pi z}{\lambda_u}\right) \cdot d\left(\frac{2\pi z}{\lambda_u}\right)$$

or

$$m\gamma \mathrm{v}_x = \frac{eB_0\lambda_u}{2\pi} \sin\left(\frac{2\pi z}{\lambda_u}\right) \tag{5.17}$$

This is an exact solution of the simplified equation of motion, but note that z is not a linear function of time. That is, v_z is not constant, but rather involves oscillations itself. Hence, terms of the $\sin(\cdots \sin)$ type will appear, giving rise to harmonics.

Define the non-dimensional magnetic strength for a periodic magnet parameter as[12]

$$\boxed{K \equiv \frac{eB_0\lambda_u}{2\pi mc}} \tag{5.18a}$$

or, in convenient units,

$$K = 0.9337 B_0(\mathrm{T})\lambda_u(\mathrm{cm}) \tag{5.18b}$$

The electron's transverse velocity can then be written as

$$\mathrm{v}_x = \frac{Kc}{\gamma} \sin\left(\frac{2\pi z}{\lambda_u}\right) \tag{5.19}$$

Note that the angle the electron motion makes with the z-axis is a sine function bounded

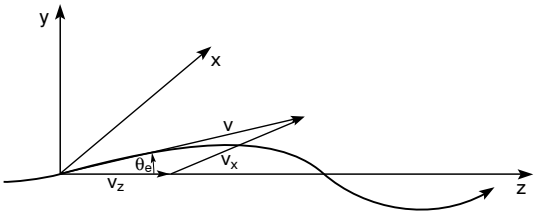

FIGURE 5.16. Electron angular excursions are harmonic, with maximum excursion K/γ. For $K < 1$ the angular excursions are within the natural radiation cone ($1/2\gamma$), leading to interesting interference effects that are manifested in cone narrowing, higher spectral brightness, and in some cases partial coherence. The case of small angular excursions ($K < 1$) is referred to as the undulator limit. For $K \gg 1$ such interference effects are not possible. This limit ($K \gg 1$) is referred to as the wiggler limit. The scales here are exaggerated in the x-direction for clarity of presentation.

by $\pm K/\gamma$, i.e.,

$$\tan\theta_e = \frac{\mathrm{v}_x}{\mathrm{v}_z} \simeq \frac{K}{\gamma}\sin\left(\frac{2\pi z}{\lambda_u}\right) \tag{5.20}$$

so that K is also referred to as the (magnetic) *deflection parameter*. Note that to good approximation we have taken $\mathrm{v}_z \simeq c$. Thus the maximum excursion angle (see Figure 5.16) is

$$|\theta_{e,\,\mathrm{max}}| \simeq \frac{K}{\gamma} \tag{5.21}$$

This is the root of differences between undulator radiation and wiggler radiation. Recall that the characteristic half angle for emission of radiation is $\theta_{\mathrm{rad}} \simeq 1/2\gamma$. Thus, for magnet strength characterized by $K \leq 1$, the electron angular excursions lie within the radiation cone. This is the undulator case where interesting interference effects can occur, narrow bandwidths result, and narrower radiation cones are obtained.

In the strong field case, $K \gg 1$, we refer to *wiggler radiation*. In this case, interference opportunities are lost because the radiation from various segments of an oscillation are widely separated in angle and therefore do not overlap in space after some propagation distance. Nonetheless, other valuable attributes appear. Primarily, wiggler radiation provides a $2N$ increase in radiated power and a broad shift to higher photon energies. We will discuss both cases ($K < 1$, $K \gg 1$) further.

Recall that Eq. (5.19) is not that of a simple time harmonic, because $z = z(t)$ is only approximately equal to ct. To see this explicitly, we recall that γ is constant in a magnetic field; thus for motion in the x, z-plane ($\mathrm{v}_y = 0$),

$$\gamma \equiv \frac{1}{\sqrt{1-\frac{\mathrm{v}^2}{c^2}}} = \frac{1}{\sqrt{1-\frac{\mathrm{v}_x^2+\mathrm{v}_z^2}{c^2}}}$$

Thus,

$$\frac{\mathrm{v}_z^2}{c^2} = 1 - \frac{1}{\gamma^2} - \frac{\mathrm{v}_x^2}{c^2} \tag{5.22}$$

Knowing v_x from Eq. (5.19), we can solve for v_z:

$$\frac{v_z^2}{c^2} = 1 - \frac{1}{\gamma^2} - \frac{K^2}{\gamma^2} \sin^2\left(\frac{2\pi z}{\lambda_u}\right)$$

To first order in the small parameter K/γ,

$$\frac{v_z}{c} = 1 - \frac{1}{2\gamma^2} - \frac{K^2}{2\gamma^2} \sin^2\left(\frac{2\pi z}{\lambda_u}\right) \tag{5.23a}$$

where $\sin^2 k_u z = \frac{1}{2}(1 - \cos 2k_u z)$, and thus

$$\frac{v_z}{c} = 1 - \frac{1 + K^2/2}{2\gamma^2} + \frac{K^2}{4\gamma^2} \cos 2k_u z \tag{5.23b}$$

Hence, the axial velocity (z-direction) has a reduced average component and a component oscillating at twice the magnet spatial frequency. By averaging over a single period, we can determine the average axial velocity, which plays a major role in the relativistic transformations. Defining an average quantity

$$\bar{v}_z \equiv \frac{L}{T} = \frac{L}{\int_0^L dz/v_z} \tag{5.24}$$

where v_z is given in Eq. (5.23b) and where T is the time required for the electron to travel a distance $L = N\lambda_u$. Then

$$\bar{v}_z = c\left[1 - \frac{1 + K^2/2}{2\gamma^2}\right]\left[\frac{L}{\int_0^L \frac{dz}{1+\alpha\cos 2k_u z}}\right]$$

where

$$\alpha = \frac{K^2}{4\gamma^2\left[1 - \frac{1+K^2/2}{2\gamma^2}\right]}$$

Expanding the denominator of the integral to second order in the small parameter α, one obtains

$$\bar{v}_z = c\left[1 - \frac{1 + K^2/2}{2\gamma^2}\right]\left(1 - \frac{\alpha^2}{2}\right)$$

where the α^2 term is of order $1/\gamma^4$ and thus can be ignored, so that the average axial velocity at finite K is given by

$$\frac{\bar{v}_z}{c} = 1 - \frac{1 + K^2/2}{2\gamma^2} \tag{5.25}$$

From this, we can define an effective axial value of the relativistic factor,

$$\boxed{\gamma^* \equiv \frac{\gamma}{\sqrt{1 + K^2/2}}} \tag{5.26}$$

where the asterisk (*) refers to the reduction of the relativistic contraction factor by an amount $\sqrt{1 + K^2/2}$. Hence Eq. (5.25) can be rewritten as

$$\frac{\bar{v}_z}{c} = 1 - \frac{1}{2\gamma^{*2}} \tag{5.27}$$

As a consequence, the observed wavelength in the laboratory frame of reference is modified from that given in Eq. (5.12), now taking the form

$$\lambda = \frac{\lambda_u}{2\gamma^{*2}}(1 + \gamma^{*2}\theta^2)$$

that is, the Lorentz contraction and relativistic Doppler shift now involve γ^* rather than γ. Expanding γ^* according to Eq. (5.26), one has

$$\lambda = \frac{\lambda_u}{2\gamma^2}\left(1 + \frac{K^2}{2}\right)\left(1 + \frac{\gamma^2}{1 + K^2/2}\theta^2\right)$$

or

$$\boxed{\lambda = \frac{\lambda_u}{2\gamma^2}\left(1 + \frac{K^2}{2} + \gamma^2\theta^2\right)} \tag{5.28}$$

where we recall that $K \equiv eB_0\lambda_u/2\pi mc$. Equation (5.28) is the *undulator equation*, which describes the generation of short (x-ray) wavelengths through the factor $\lambda_u/2\gamma^2$, magnetic tuning through $K^2/2$, and off-axis wavelength variations through $\gamma^2\theta^2$. Note that wavelength tuning through variations of K requires changing the magnet gap. This is more desirable than γ-tuning, as it affects only the desired experimental station on a multi-undulator storage ring (see Figure 5.5). In practical units the wavelength λ and corresponding photon energy $E = 2\pi\hbar c/\lambda$ are given by

$$\lambda(\text{nm}) = \frac{1.306\lambda_u(\text{cm})\left(1 + \frac{K^2}{2} + \gamma^2\theta^2\right)}{E_e^2(\text{GeV})} \tag{5.29a}$$

and

$$E(\text{keV}) = \frac{0.9496E_e^2(\text{GeV})}{\lambda_u(\text{cm})\left(1 + \frac{K^2}{2} + \gamma^2\theta^2\right)} \tag{5.29b}$$

where λ_u is to be given in centimeters and the electron energy E_e in GeV.

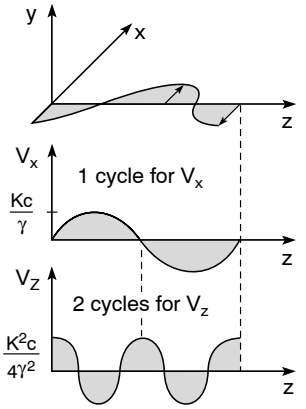

FIGURE 5.17. Illustration of the first and second harmonic motions of the electron.

5.4.2 Comments on Undulator Harmonics

In addition to modifying the observed wavelength of the fundamental [as given by Eq. (5.28)], the effect of transverse oscillations introduces higher harmonics into the motion. We will see that the harmonic amplitudes scale as K^n, where n is the harmonic number. These higher harmonics of the radiation will occur at frequencies $n\omega_1$ and wavelengths λ_1/n. Because short wavelengths are difficult to generate, harmonics are of great interest, especially since they are a natural consequence of the motion. Harmonics are frequently used to extend the photon energy range of a given undulator or facility.

We begin by considering second harmonic motion. From Eq. (23b) – repeated below – we have

$$\frac{v_z}{c} = 1 - \frac{1 + K^2/2}{2\gamma^2} + \frac{K^2}{4\gamma^2}\cos\left(2 \cdot \frac{2\pi z}{\lambda_u}\right)$$

This expression displays both the decreased axial velocity and an axial velocity modulation at twice the fundamental frequency. This is referred to as a second harmonic of the motion and is illustrated in Figure 5.17. If the first order (fundamental) motion leads to radiation at frequency ω_1' in the electron frame, then the axial harmonic will radiate at $\omega_2' = 2\omega_1'$; hence, it is called *second harmonic* radiation. Note that the magnitude of the second harmonic term scales as K^2.

Note that the second harmonic oscillations of the electron are at right angles to the fundamental oscillations. That is, the fundamental radiation results from oscillations in the x-direction, while the second harmonic (and other even harmonics) result from oscillations in the z-direction. As a result, the polarization is different. Additionally, when transformed to the laboratory frame, the angular distributions will be different. Figure 5.18 illustrates the radiation patterns of the fundamental and second harmonics.

If we further analyze details of the electron motion, we will find that for larger K-values, $K \geq 1$, additional harmonics will appear due to the continued mixing of harmonic motions. As K increases, this mixing will eventually lead to a strongly non-sinusoidal *wiggler limit*. In all cases, the observed wavelengths will be governed by an extension of the undulator equation:

$$\lambda_n = \frac{\lambda_u}{2\gamma^2 n}\left(1 + \frac{K^2}{2} + \gamma^2\theta^2\right) \tag{5.30}$$

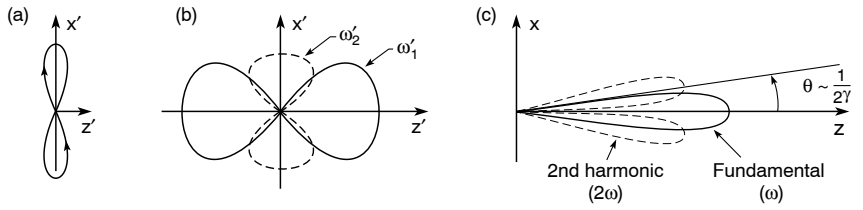

FIGURE 5.18. (a) Illustration of the figure eight electron motion in the frame of reference moving with the average electron velocity, and the resultant radiation patterns at the fundamental and second harmonic frequencies in both (b) the frame of reference moving with the electron and (c) the laboratory frame of reference.

Due to the increased number of cycles, the relative spectral bandwidth is also improved,[†] viz.,

$$\left(\frac{\Delta\lambda}{\lambda}\right)_n = \frac{1}{nN} \tag{5.31}$$

where n is the harmonic number and N is the number of magnetic periods.

From Figure 5.18, we see that the even harmonics radiate a pattern that peaks off axis and has zero intensity on axis. (Note that within a full electron bunch, this will be modified due to random individual motions slightly off axis, i.e., to finite phase space effects.) As a consequence, the even harmonics tend to be relatively weak on axis and, upon transformation to the laboratory frame, radiate into a hollow cone of radiation. We will see later that this cone has less interesting coherence and brightness properties. On the other hand, the odd harmonics ($n = 1, 3, 5, \ldots$) radiate on axis with a narrow spectrum and into a narrow forward cone. Hence, they are quite interesting as sources of high brightness and partially coherent x-rays. We will return to this subject in Section 5.5.

5.4.3 Power Radiated in the Central Radiation Cone

The undulator equation (5.28) tells us the wavelength of radiation as a function of magnet period λ_u, magnet deflection parameter K, electron energy γ (in rest energy units), and polar angle of observation θ. Now we would like to calculate the amount of power radiated. A natural and interesting choice is to calculate the power radiated into the central radiation cone, of half angle θ_{cen}, which we can identify with a relative spectral bandwidth $\lambda/\Delta\lambda \simeq N$, where N is the number of magnetic periods and thus the number of oscillations the electron executes in traversing the undulator. This has a natural appeal, common to our experience with other physical phenomena involving oscillators, gratings, etc., which we embody mathematically in our time–frequency and space–angle transformations. The choice of a central radiation cone containing the $1/N$ relative spectral bandwidth is also interesting because applications of undulator radiation generally involve the use of narrow bandwidth, quasi-monochromatic radiation, and the $1/N$ bandwidth is as small[‡] as one can obtain without use of a monochromator.

[†] In practice this narrowed spectral bandwidth is limited to the first few harmonics due to electron energy spread ($\Delta\gamma$) in a many-electron beam. Typically $\Delta\gamma/\gamma$ is of order 10^{-3} in a modern storage ring.

[‡] In fact the $1/N$ value is idealistic in that in practice one utilizes radiation from a multi-electron bunch for which there is an angular divergence due to the slightly varying electron trajectories. In specific cases considered later in this chapter, this typically contributes an additional broadening to the relative spectral bandwidth.

In Section 5.3.3 we used a simplified version of the undulator equation to introduce the concept of a central radiation cone, finding that for a bandwidth $1/N$ the cone half angle is $1/\gamma\sqrt{N}$. Having reconsidered electron motion in an undulator of finite K (Section 5.4.1), we can now follow the same arguments using the corrected undulator equation (5.28), viz.,

$$\lambda = \frac{\lambda_u}{2\gamma^2}\left(1 + \frac{K^2}{2} + \gamma^2\theta^2\right)$$

Writing this equation twice, once for a wavelength λ_0 corresponding to $\theta = 0$, and once for an off-axis angle θ_{cen} such that it encompasses a full bandwidth $\Delta\lambda$, subtracting the two equations and normalizing (as was done in Section 5.3.2, but now for finite K), one obtains a corrected formula for the central radiation cone

$$\boxed{\theta_{\text{cen}} = \frac{1}{\gamma^*\sqrt{N}} = \frac{\sqrt{1 + K^2/2}}{\gamma\sqrt{N}}} \tag{5.32}$$

of a single electron, containing a relative spectral bandwidth $\Delta\lambda/\lambda = 1/N$, where $\gamma^* = \gamma/\sqrt{1 + K^2/2}$, as defined earlier in Eq. (5.26). Thus for finite K there are not only longer wavelengths at each angle, but also an enlargement of the central radiation cone. We can trace both effects to the reduced average axial velocity of the electron for finite K, and thus to reduced effects of the angle dependent relativistic Doppler shift. A further discussion of spectral bandwidth is presented in Section 5.4.4.

Our task now is to calculate the power radiated within the central cone, at the fundamental frequency only. In later sections we will calculate other details, including the total power radiated. Our approach will be to use our knowledge of classical dipole radiation, as considered earlier in Chapter 2. We might ask how this can be done in a situation involving highly relativistic motion. The technique is to transfer the calculation to the frame of reference moving with the average electron velocity. In this frame of reference the electron motion is non-relativistic, at least for modest K, and the oscillation amplitude is small compared to the wavelength (in the frame of reference in which the calculation is made), as it should be for the dipole approximation to be valid. Having the desired power calculations, the results are then Lorentz transformed back to the laboratory (observer) frame of reference using straightforward but relativistically correct angular relationships given in Appendix F. This procedure gives us maximum leverage on the use of classical radiation results, and provides very valuable insights to the most important properties of undulator radiation. The process is outlined in Table 5.4.

Following the procedure outlined in Table 5.4, the electron velocity in the laboratory frame of reference has been derived, from Newton's second law of motion, as Eq. (5.19),

$$\mathrm{v}_x = \frac{Kc}{\gamma}\sin\frac{2\pi z}{\lambda_u}$$

which we can write as

$$\mathrm{v}_x = \frac{Kc}{\gamma}\sin k_u z$$

To obtain the acceleration we need v_x as a function of time. To first order we assume that

TABLE 5.4. An outline of the procedure for calculating power radiated by relativistic electrons traversing a periodic undulator. Electron motion is determined in the laboratory frame of reference. A Lorentz transformation to the frame of reference moving with the average electron velocity permits the use of classical dipole radiation (Chapter 2), as the electron motion is non-relativistic in this frame. The dipole radiation results are then Lorentz transformed back to the laboratory frame of reference.

x, z, t laboratory frame of reference

x', z', t' frame of reference moving with the average velocity of the electron

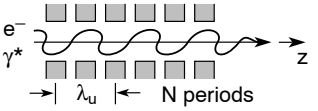

Lorentz transformation

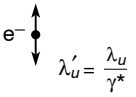

x', z', t' motion
$a'(t')$ acceleration

Determine x, z, t motion:

$$\frac{dp}{dt} = -e\,(\mathbf{E} + \mathbf{v} \times \mathbf{B})$$

$$m\gamma \frac{dv_x}{dt} = e\,\frac{dz}{dt} B_0 \cos\frac{2\pi z}{\lambda_u}$$

$$v_x(t);\ a_x(t) = \cdots$$

$$v_z(t);\ a_z(t) = \cdots$$

Dipole radiation:

$$\frac{dP'}{d\Omega'} = \frac{e^2 a'^2 \sin^2\Theta'}{16\pi^2 \epsilon_0 c^3}$$

$$\frac{dP'}{d\Omega'} = \frac{e^2 c\gamma^2}{4\epsilon_0 \lambda_u^2} \frac{K^2}{[1+K^2/2]^2} (1 - \sin^2\theta' \cos^2\phi') \cos^2 \omega'_u t'$$

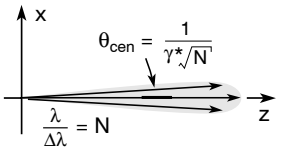

Lorentz transformation

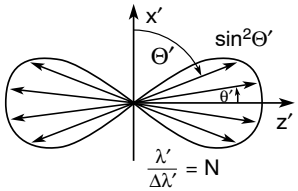

$$\frac{dP}{d\Omega} = 8\gamma^{*2} \frac{dP'}{d\Omega'}$$

$$\frac{d\bar{P}}{d\Omega} = \frac{e^2 c\gamma^4}{\epsilon_0 \lambda_u^2} \frac{K^2}{[1+K^2/2]^3} \begin{cases} K \le 1 \\ \theta \le \theta_{cen} \end{cases}$$

$$\Delta\Omega_{cen} = \pi\theta_{cen}^2 = \pi/\gamma^{*2} N$$

$$\bar{P}_{cen} = \frac{\pi e^2 c\gamma^2}{\epsilon_0 \lambda_u^2 N} \frac{K^2}{[1+K^2/2]^2}$$

N_e uncorrelated electrons:

$$N_e = IL/ec,\ L = N\lambda_u$$

$$\bar{P}_{cen} = \frac{\pi e \gamma^2 I}{\epsilon_0 \lambda_u} \frac{K^2}{[1+K^2/2]^2}$$

$z \simeq \bar{v}_z t = \beta^* ct$, where $\bar{v}_z$ is the average electron velocity in the z-direction and β^* is very close to unity. The velocity can then be written as

$$v_x \simeq \frac{Kc}{\gamma} \sin k_u \beta^* ct = \frac{Kc}{\gamma} \sin \omega_u t$$

where $\omega_u = k_u \beta^* c \simeq k_u c$. Integrating once with respect to time t, we have the first order oscillatory motion $x(t)$:

$$x \simeq -\frac{K}{k_u \gamma} \cos \omega_u t$$

The Lorentz transformations from the (x, t) laboratory frame of reference to the (x', t') frame of reference moving with the average electron velocity ($\beta^* c$ or γ^*) are given in Appendix F, Eqs. (F.1b) and (F.1c), as

$$t = \gamma^* \left(t' + \frac{\beta^* z'}{c} \right) \simeq \gamma^* \left(t' + \frac{z'}{c} \right)$$

$$x = x' \qquad \text{(non-relativistic motion transverse to } z \text{ for } K \leq 1 \text{)}$$

Thus in the electron frame of reference

$$x' \simeq -\frac{K}{k_u \gamma} \cos \omega_u \gamma^* \left(t' + \frac{z'}{c} \right)$$

where z' represents the small axial excursions about the average position in the reference frame moving with the electron. This is an important term, which we will see later provides a coupling of energy to higher harmonics. For small values of K, however, this term's contribution to the fundamental motion is minimal. Thus to a fair degree of accuracy we can write

$$x' \simeq -\frac{K}{k_u \gamma} \cos \omega_u \gamma^* t'$$

Recognizing the Lorentz shifted frequency ω'_u, this becomes

$$x' \simeq -\frac{K}{k_u \gamma} \cos \omega'_u t'$$

Taking the second derivative with respect to t', we have

$$a'_x \simeq \frac{K \omega'^2_u}{k_u \gamma} \cos \omega'_u t'$$

where $a'_x \equiv d^2 x'/dt'^2$. Noting that $\omega'_u = \gamma^* k_u c = \gamma k_u c/(1 + K^2/2)^{1/2}$, one has the desired electron acceleration in the (x', t') moving frame of reference:

$$a'_x \simeq \frac{2\pi c^2 \gamma}{\lambda_u} \frac{K}{(1 + K^2/2)} \cos \omega'_u t' \tag{5.33}$$

This acceleration can now be used in the dipole radiation formula [Chapter 2, Eq. (2.34)]

$$\frac{dP'}{d\Omega'} = \frac{e^2 a'^2 \sin^2 \Theta'}{16\pi^2 \epsilon_0 c^3}$$

where a' is the instantaneous electron acceleration, Θ' is the angle of observation measured from the direction of acceleration, and we have assumed that the amplitude of oscillation is small compared to the radiated wavelength (in the frame of reference where the calculation is

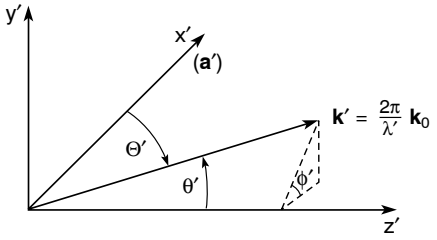

FIGURE 5.19. Illustration of the polar coordinate system (r', θ', ϕ') where $d\Omega' = \sin\theta' d\theta' d\phi'$, and where the coordinate system is oriented to have the polar axis ($\theta' = 0$) oriented along the z'-axis of symmetry for undulator radiation.

made). Using Eq. (5.33) for the electron acceleration in the moving frame of reference, and averaging over one full cycle of the motion, we obtain the average power radiated per unit solid angle to be

$$\frac{d\bar{P}'}{d\Omega'} = \frac{e^2 c\gamma^2}{8\epsilon_0 \lambda_u^2} \frac{K^2}{(1 + K^2/2)^2} \sin^2 \Theta' \tag{5.34}$$

where time averaging $\cos^2 \omega_u' t'$ over a full cycle (or N full cycles) has introduced a factor of $\frac{1}{2}$. The $\sin^2 \Theta'$ factor can be set to unity, as only radiation in the vicinity of $\Theta' \simeq \pi/2$ contributes to the central radiation cone in the laboratory frame. The angular factors will be discussed in detail in the next section. However, for clarity in understanding the approximation to various angular factors, we introduce the coordinate system shown in Figure 5.19. We recall that the Lorentz transformation to the laboratory frame will concentrate the radiation pattern into a narrow cone about the z-axis. It is sensible to organize our angular measurements about this natural symmetry axis. Hence, we introduce a polar coordinate system (r', θ', ϕ') where r' is the polar axis oriented collinear to the z-axis, θ' is the polar angle (0 to π), and ϕ' is measured from the x'-axis in the x', y'-plane (0 to 2π). For the fundamental at ω_u', with acceleration $a_{x'}'$, Θ' is measured from the x'-axis as shown in Figure 5.19.

In a polar coordinate system, the angle between the two vectors $\mathbf{k}'$ and $\mathbf{a}'$ (wave propagation direction and acceleration direction) is given by (see Appendix D)

$$\cos\Theta' = \cos\theta_k' \cos\theta_a' + \sin\theta_k' \sin\theta_a' \cos(\phi_k' - \phi_a') \tag{5.35}$$

For the fundamental radiation at ω_u', $\theta_a' = \pi/2$, and $\phi_a' = 0$. Equation (5.35) then simplifies to

$$\cos\Theta' = \sin\theta_k' \cos\phi_k'$$

so that for the radiated power,

$$\sin^2\Theta' = 1 - \sin^2\theta_k' \cos^2\phi_k' \tag{5.36}$$

In what follows we drop the subscript k for convenience. The approximation that $\sin^2\Theta' \simeq 1$ can then be understood by examining the magnitude of the $\sin^2\theta' \cos^2\phi'$ term for angles which will transform to angles $\theta \leq \theta_{\text{cen}}$ in the laboratory frame. From Appendix F, Eq. (F.14), the polar angles in the two frames of reference are related by

$$\sin\theta' = \frac{2\gamma^*\theta}{1 + \gamma^{*2}\theta^2}$$

where both θ' and θ are measured from the z-axis in their respective frames of reference. For

a central cone of half angle $\theta = 1/\gamma^*\sqrt{N}$, the corresponding angle in the primed reference frame is $\sin\theta' \simeq 2/\sqrt{N}$, so that $\theta' \simeq 2/\sqrt{N}$ for large N (of order 100). For such small angles it is clear that, for all values of ϕ, $\sin^2\Theta' \simeq 1 - \theta'^2/2 \simeq 1 - 2/N$, thus permitting, for large N, the first order approximation $\sin^2\Theta' \simeq 1$ in Eqs. (5.34) and (5.36).

Equation (5.34) above gives us the power radiated per unit solid angle, for angles near the z-axis, in the frame of reference moving with the average electron velocity. Following the procedure outlined in Table 5.4, we now want to transform this result back to the laboratory frame of reference. To do so we need a relativistically correct relation between $dP'/d\Omega'$ and $dP/d\Omega$. In the next section we will show that the desired relationship is

$$\frac{dP}{d\Omega} = \frac{8\gamma^{*2}}{(1+\gamma^{*2}\theta^2)^3}\frac{dP'}{d\Omega'}$$

which for small angles within the central radiation cone reduces to

$$\frac{dP}{d\Omega} \simeq 8\gamma^{*2}\frac{dP'}{d\Omega'}$$

Thus using Eq. (5.34) with the approximation $\sin^2\Theta' = 1$, the average power radiated per unit solid angle, as observed in the laboratory frame of reference, is

$$\left.\frac{d\bar{P}}{d\Omega}\right|_{e^-} \simeq \frac{e^2c\gamma^4}{\epsilon_0\lambda_u^2}\frac{K^2}{(1+K^2/2)^3} \quad (K \le 1,\ \theta \le \theta_{\text{cen}}) \tag{5.37}$$

where the subscript e^- reminds us that this is for a single electron. To obtain power radiated we simply multiply by the element of solid angle associated with the central radiation cone, viz.,

$$\Delta\Omega_{\text{cen}} = \int_0^{2\pi}\int_0^{1/\gamma^*\sqrt{N}} \sin\theta\, d\theta\, d\phi = \frac{\pi}{(\gamma^*\sqrt{N})^2}$$

and thus conclude that, as observed in the laboratory frame of reference, the average power radiated into the central cone, for a single electron, is given by

$$\bar{P}_{\text{cen}}\big|_{e^-} \simeq \frac{\pi e^2 c\gamma^2}{\epsilon_0\lambda_u^2 N}\frac{K^2}{(1+K^2/2)^2} \tag{5.38}$$

with an associated bandwidth of $\Delta\lambda/\lambda = 1/N$ and a radiation cone half angle of $1/\gamma^*\sqrt{N}$. This result is generally valid for $K \le 1$. We observe that the power radiated is proportional to $(K\gamma/\lambda_u)^2$, due to the dependence on electron acceleration squared, and inversely proportional to N. While the inverse dependence on N may at first seem surprising, it can be understood as a combination of increased power (N), combined with a decreased solid angle ($1/N$) of the central radiation cone and a decreased central cone bandwidth ($1/N$). The additional factor involving K in the denominator is associated with the reduced acceleration as the electron's axial motion is decreased. Recall that the wavelength of this radiation is given by the undulator equation (5.28).

An important extension of this result is to the practical case of multi-electron bunches traversing the undulator, in which case the radiated power is much greater and thus much more valuable for laboratory applications. We show in the next section that for an electron current I in the storage ring, the number of electrons radiating within an undulator, averaged over a

long time period compared to the electron bunch structure, is equal to

$$N_e = IL/ec$$

where $L = N\lambda_u$ is the length of the undulator. If the motion of the various electrons is uncorrelated, the radiated fields due to differing electrons will have no special relationship, and as a result the radiated power will increase proportionally to N_e, the number of electrons. Were the electron motions well correlated, as in an electron wave (sometimes called microbunching), this would lead to phase correlated electric and magnetic fields – as in a free electron laser (FEL). In such a case the fields of the N_e electrons would add in phase and since radiated power is proportional to E^2, far greater power could be radiated, perhaps N_e^2 times greater than for a single electron. For the uncorrelated case, generally understood as *undulator radiation*, the intensities rather than the fields add and one simply multiplies Eq. (5.38) by $N_e = IL/ec = IN\lambda_u/ec$ to obtain

$$\boxed{\bar{P}_{\text{cen}} \simeq \frac{\pi e\gamma^2 I}{\epsilon_0 \lambda_u} \frac{K^2}{(1+K^2/2)^2}} \tag{5.39}$$

for the average power radiated by electrons of current I, at the fundamental frequency ($n = 1$), within a relative spectral bandwidth $\Delta\lambda/\lambda \simeq 1/N$, and into a central radiation cone of half angle $\theta_{\text{cen}} = 1/\gamma^*\sqrt{N} = \sqrt{1+K^2/2}/\gamma\sqrt{N}$. Detailed spectral shapes and increases to the central radiation cone caused by random electron motions (divergence) within the electron beam are discussed in Section 5.4.5.

We give two examples of the use of this formula, involving soft x-ray and hard x-ray undulators at the ALS and APS, previously cited in Table 5.1. For a typical soft x-ray case ($\gamma = 3720,\ \lambda_u = 5.00$ cm, $N = 89$, and $I = 400$ mA), power of order 1–2 W is radiated into a half angle of about 35 μrad, in a wavelength region extending from 2 nm to 5 nm (250 eV to 600 eV photon energy), within a relative spectral bandwidth of approximately 1.1%. For a typical hard x-ray undulator at the APS ($\gamma = 13{,}700,\ \lambda_u = 3.30$ cm, $N = 72$, and $I = 100$ mA), power of order 10–20 W is radiated into an 11 μrad half angle cone, at wavelengths from about 0.1 nm to 0.3 nm (1 Å to 3 Å, 5 keV to 14 keV photon energy), within a relative spectral bandwidth of approximately 1.4%. Tuning curves for these two undulators are presented in Figure 5.20(a) and (b), respectively, illustrating photon energy and power in the central cone as a function of the magnetic deflection parameter K. At the lowest values of K there is little transverse acceleration and thus little power radiated. Because the electrons move through the undulator relatively fast at low K-values, the N oscillations are executed more rapidly, resulting in higher frequency radiation, higher photon energies, and shorter wavelength. For small K, power grows as K^2, peaking according to Eq. (5.39) at $K = \sqrt{2}$. At such high K-values, however, the coupling to higher harmonics becomes very efficient, and the accuracy of our results, which are valid for $K < 1$, requires further attention.

The formulation of power radiated in the central cone [Eq. (5.39)] is based in part on a small perturbation analysis in which we have assumed small K operation. These approximations were made in the development of a simplified expression for the electron acceleration [Eq. (5.33)] in the moving frame of reference, which is subsequently squared and used in the dipole radiation formula. To obtain Eq. (5.33) we started in the laboratory frame with the electron velocity [Eq. (5.19)] $\mathrm{v}_x = (Kc/\gamma)\sin k_u z$ and assumed to first order (in K) that $z \simeq \beta^* ct$, thus neglecting higher order harmonic motions, which scale as $K^2,\ K^3$, etc. Having made the

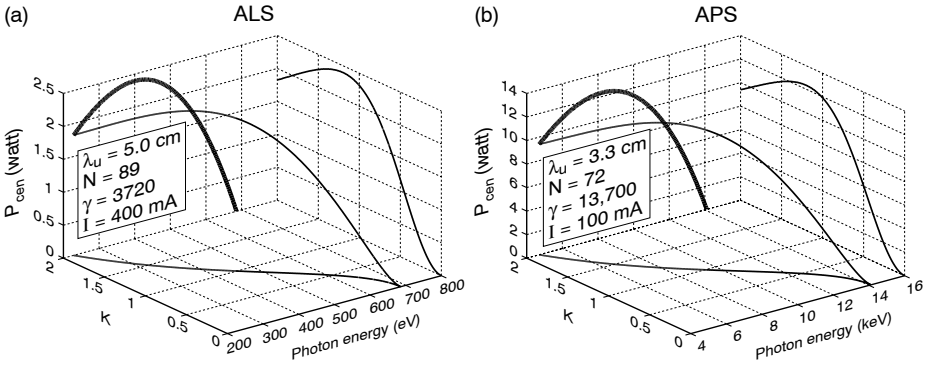

FIGURE 5.20. Power radiated into the central radiation cone ($\theta_{\text{cen}} = 1/\gamma^*\sqrt{N}$, $1/N$ relative spectral bandwidth, $n = 1$ only) as a function of photon energy and magnetic deflection parameter K, for typical soft x-ray and hard x-ray undulators. Harmonic power is not included ($n = 1$ only).

transformation to the moving reference frame, where $x' \simeq -(K/k_u\gamma)\cos\omega_u\gamma^*(t' + z'/c)$, we again assumed on the basis of K^n scaling that the z'-term, which is associated with harmonic oscillations about the average electron trajectory, could be neglected. Now, however, observing that central cone power scales as K^2 with a peak just above $K = 1$ according to Eq. (5.39), we have a great interest in understanding the accuracy of the low K results as K approaches and exceeds unity. This knowledge will be of great value in planning experiments.

Kim[3] has analyzed undulator radiation in a very complete manner, accounting for all harmonics and accurate for all K. Comparing his results [Ref. 3, Eq. (4.44)] with that of Eq. (5.39) here, there is an additional multiplicative factor, $f(K)$, associated with the transfer of power from the fundamental ($n = 1$) to the harmonics ($n > 1$) and given by the difference of Bessel functions,

$$f(K) = [J_0(x) - J_1(x)]^2 \tag{5.40a}$$

where $x = K^2/4(1 + K^2/2)$. For modest values of x (zero to $\frac{1}{3}$ for $0 \le K \le 2$),

$$J_n(x) = \sum_{s=0}^{\infty} \frac{(-1)^s}{s!(n+s)!}\left(\frac{x}{2}\right)^{n+s}$$

so that the relevant expansions are

$$J_0(x) = 1 - \left(\frac{x}{2}\right)^2 + \frac{1}{(2)^2}\left(\frac{x}{2}\right)^4 - \cdots$$

and

$$J_1(x) = \frac{x}{2} - \frac{1}{2}\left(\frac{x}{2}\right)^3 + \cdots$$

TABLE 5.5. The multiplicative correction factor $f(K)$ that enables the low K analytic formulation of undulator central cone power [Eq. (5.39)] to be extended to higher K-values.

K	$x = \frac{K^2}{4(1+K^2/2)}$	$J_0(x)$	$J_1(x)$	$f(K)$
0	0	1.0000	0	1.000
0.5	0.0556	0.9992	0.0278	0.944
1.0	0.1667	0.9931	0.0831	0.828
$\sqrt{2}$	0.2500	0.9844	0.1240	0.740
1.5	0.2647	0.9826	0.1312	0.725
2.0	0.3333	0.9724	0.1643	0.653
2.5	0.3788	0.9644	0.1860	0.606

For small K the multiplicative factor $f(K)$ is approximated by

$$f(K) = 1 - x - \frac{x^2}{4} + \frac{3x^3}{8} + \cdots \tag{5.40b}$$

The factor $f(K)$ is tabulated in Table 5.5 for selected values of K. Thus Eq. (5.39) overestimates the fundamental power radiated in the central cone by 6.6% for $K = \frac{1}{2}$, and 17% for $K = 1$. These overestimates are incurred through the omission of second order and higher terms in K, which would have had the effect of reducing the first order electron velocity and acceleration, and thus of concomitant radiated power. Nonetheless, this analytic formulation [Eq. (5.39)] has provided a valuable tool for understanding the most important features of undulator radiation, with very simply interpreted physical insights.

A modified version of Eq. (5.39), which extends its utility to higher K-values while preserving the clarity of its analytic features, is obtained by including $f(K)$ as a finite K corrective factor, so that the power in the central cone ($n = 1$, $1/N$ relative spectral bandwidth, finite K) becomes

$$\boxed{\bar{P}_{\text{cen}} = \frac{\pi e \gamma^2 I}{\epsilon_0 \lambda_u} \frac{K^2}{(1 + K^2/2)^2} f(K)} \tag{5.41a}$$

where $f(K)$ is given in Eq. (5.40). In practical units this can be written as

$$\bar{P}_{\text{cen}} = (5.69 \times 10^{-6}\ \text{W}) \frac{\gamma^2 I(\text{A})}{\lambda_{\text{u}}(\text{cm})} \frac{K^2}{(1 + K^2/2)^2} f(K) \tag{5.41b}$$

Note that for the two undulators cited, Eq. (5.41b) indicates that for $K = 1$ the 5.0 cm undulator at the ALS radiates 2.3 W in the central cone at 2.71 nm wavelength, while the 3.3 cm undulator at the APS radiates 12 W at 0.13 nm (1.3 Å).

The power in the central cone can be written explicitly as a function of photon energy through use of the undulator equation (5.28), which relates K^2 to frequency. From the undulator equation, $f = 2\gamma^2 c/\lambda_u(1 + K^2/2)$ on axis. Thus $\hbar\omega = 4\pi\hbar\gamma^2 c/\lambda_u(1 + K^2/2) = \hbar\omega_0/(1 + K^2/2)$, where $\hbar\omega_0$ is defined as the photon energy on axis for the limiting case

$K = 0$. From this one can solve for both $1 + K^2/2$ and K^2 to obtain

$$\bar{P}_{\text{cen}} = \frac{2\pi e\gamma^2 I}{\epsilon_0 \lambda_u} \cdot \frac{\hbar\omega}{\hbar\omega_0}\left(1 - \frac{\hbar\omega}{\hbar\omega_0}\right) f(\hbar\omega/\hbar\omega_0) \tag{5.41c}$$

where we replace the multiplicative factor $f(K)$ by the related function

$$f(\hbar\omega/\hbar\omega_0) \simeq \frac{7}{16} + \frac{5}{8}\frac{\hbar\omega}{\hbar\omega_0} - \frac{1}{16}\left(\frac{\hbar\omega}{\hbar\omega_0}\right)^2 + \cdots \tag{5.41d}$$

which is the finite-K correction factor (5.40) written in terms of photon energy. In numerical form this becomes

$$\bar{P}_{\text{cen}} = (1.14 \times 10^{-5}\ \text{W})\frac{\gamma^2 I(\text{A})}{\lambda_u(\text{cm})} \cdot \frac{\hbar\omega}{\hbar\omega_0}\left(1 - \frac{\hbar\omega}{\hbar\omega_0}\right) f(\hbar\omega/\hbar\omega_0) \tag{5.41e}$$

where $\hbar\omega_0 = 4\pi\hbar c\gamma^2/\lambda_u$ has the value 686 eV for $\gamma = 3720$ and $\lambda_u = 5.00$ cm, and the value 14.1 keV for $\gamma = 13{,}700$ and $\lambda_u = 3.30$ cm.

5.4.4 Power as a Function of Angle and Total Radiated Power

In this section we return to the calculation of power radiated per unit solid angle, for small K, in this case keeping the angular dependence. Again we follow the procedure outlined in Table 5.4. At the end of the section we integrate over all angles to obtain the total power radiated at the fundamental ($n = 1$) frequency. In the previous section we employed dipole radiation in the frame of reference moving with the electron,

$$\frac{dP'}{d\Omega'} = \frac{e^2 a'^2 \sin^2\Theta'}{16\pi^2\epsilon_0 c^3}$$

along with the first order acceleration of an electron traversing an undulator [Eq. (5.33)],

$$a'_x \simeq \frac{2\pi c^2\gamma}{\lambda_u}\frac{K}{(1 + K^2/2)}\cos\omega'_u t'$$

where $\omega'_u = \gamma^*\omega_u = 2\pi\gamma^*\beta^* c/\lambda_u \simeq 2\pi\gamma^* c/\lambda_u$, and where $a'_x \equiv d^2x'/dt'^2$, to obtain the average power radiated per unit solid angle in the electron frame of reference [Eq. (5.34)],

$$\frac{d\bar{P}'}{d\Omega'} = \frac{e^2 c\gamma^2}{8\epsilon_0\lambda_u^2}\frac{K^2}{(1 + K^2/2)^2}\sin^2\Theta'$$

where averaging over a full cycle of the motion has introduced a factor of one-half. Thus, comparing with Eq. (5.34), here we have kept the factor $\sin^2\Theta'$.

As illustrated in Figure 5.19 and described in Eq. (5.36), the factor $\sin^2\Theta'$ can be written in terms of the polar angles

$$\sin^2\Theta' = 1 - \sin^2\theta'\cos^2\phi'$$

where θ' is the polar angle (0 to π) measured from the z-axis and ϕ' is the azimuthal angle (0 to 2π) measured from the x'-axis in the x', y'-plane. The radiated power in the fundamental is therefore

$$\frac{d\tilde{P}'}{d\Omega'} = \frac{e^2 c\gamma^2}{8\epsilon_0 \lambda_u^2} \frac{K^2}{(1 + K^2/2)^2}(1 - \sin^2\theta' \cos^2\phi') \tag{5.42}$$

To transform this to the laboratory frame of reference we make use of angular relationships obtained in Appendix F as Eqs. (F.9) to (F.11):

$$\sin\theta' = \frac{\sin\theta}{\gamma^*(1 - \beta^* \cos\theta)}$$

$$\cos\theta' = \frac{\cos\theta - \beta^*}{1 - \beta^* \cos\theta}$$

$$\tan\theta' = \frac{\sin\theta}{\gamma^*(\cos\theta - \beta^*)}$$

and

$$\sin\theta = \frac{\sin\theta'}{\gamma^*(1 + \beta^* \cos\theta')}$$

$$\cos\theta = \frac{\cos\theta' + \beta^*}{1 + \beta^* \cos\theta'}$$

$$\tan\theta = \frac{\sin\theta'}{\gamma^*(\cos\theta' + \beta^*)}$$

In the highly relativistic case, where $\gamma^* \gg 1,\ \beta^* \simeq 1$, these take the approximate forms

$$\sin\theta' \simeq \frac{2\gamma^*\theta}{1 + \gamma^{*2}\theta^2} \tag{5.43a}$$

$$\cos\theta' \simeq \frac{1 - \gamma^{*2}\theta^2}{1 + \gamma^{*2}\theta^2} \tag{5.43b}$$

$$\tan\theta' \simeq \frac{2\gamma^*\theta}{1 - \gamma^{*2}\theta^2} \tag{5.43c}$$

Since the angles ϕ and ϕ' lie in planes perpendicular to the relativistic motion, we have

$$\phi' = \phi$$

Using the angular relations, Eq. (5.43), for $\gamma^* \gg 1$, the angular radiation pattern in Eq. (5.42) becomes

$$1 - \sin^2\theta' \cos^2\phi' = \frac{1 + 2\gamma^{*2}\theta^2(1 - 2\cos^2\phi) + \gamma^{*4}\theta^4}{(1 + \gamma^{*2}\theta^2)^2} \tag{5.44}$$

Similarly, the element of solid angle $d\Omega'$ can be rewritten as

$$d\Omega' \simeq \sin\theta' d\theta' d\phi' \simeq \frac{4\gamma^{*2}}{(1+\gamma^{*2}\theta^2)^2} \cdot \theta\, d\theta\, d\phi$$

or

$$d\Omega' \simeq \frac{4\gamma^{*2}}{(1+\gamma^{*2}\theta^2)^2}\, d\Omega \tag{5.45}$$

where we recognize that for small angles $d\Omega = \theta\, d\theta\, d\phi$.

To complete the transformation of power per unit solid angle in the moving (primed) frame of reference, $d\bar{P}'(\theta',\ \phi')/d\Omega'$, to the laboratory frame of reference, $d\bar{P}(\theta,\ \phi)/d\Omega$, we are left to consider the relationship between the radiated power, P' and P, as observed in the two frames of reference. To do this we consider the emission of a finite number of photons, $\mathcal{N}'$, during a time interval $\Delta t'$, as seen in the moving frame of reference where all photons have the same energy $\hbar\omega'$, independent of emission angle – a property of dipole radiation. These same photons, discretely counted in identical number, $\mathcal{N} = \mathcal{N}'$, in the laboratory frame of reference, are observed there in a time interval Δt, with an angle dependent photon energy [due to the angle dependent Doppler shift, Appendix F, Eq. (F.8b)] given by

$$\hbar\omega = \frac{\hbar\omega'}{\gamma^*(1-\beta^*\cos\theta)}$$

Since the Lorentz transformation forces all angles θ' to very small angles of order $\theta \simeq O(1/\gamma^*)$ in the laboratory frame, we can approximate the Doppler shift by

$$\hbar\omega \simeq \frac{2\gamma^*}{1+\gamma^{*2}\theta^2}\,\hbar\omega'$$

By noting that time intervals in the two frames of reference are related by Appendix F, Eq. (F.13) as

$$\Delta t = \gamma^* \Delta t'$$

we can likewise relate the incremental radiated power in the two frames of reference,

$$\Delta P' = \frac{\mathcal{N}'\hbar\omega'}{\Delta t'}$$

and

$$\Delta P = \frac{\mathcal{N}\hbar\omega}{\Delta t}$$

Rewriting the expression for ΔP and then substituting relationships in terms of primed quantities for $\mathcal{N}$, ω and Δt, one obtains

$$\Delta P = \frac{\mathcal{N}\hbar\omega}{\Delta t} = \frac{\mathcal{N}'\left(\dfrac{2\gamma^*}{1+\gamma^{*2}\theta^2}\right)\hbar\omega'}{\gamma^*\Delta t'}$$

$$\Delta P = \frac{2}{1+\gamma^{*2}\theta^2}\frac{\mathcal{N}'\hbar\omega'}{\Delta t'}$$

Recognizing the quantity on the right as $\Delta P'$, and writing this in differential form, one has

$$dP = \frac{2}{1+\gamma^{*2}\theta^2}\, dP'$$

Using the relation given in Eq. (5.45) between $d\Omega'$ and $d\Omega$, the relationship for power per unit solid angle between the two reference frames becomes

$$\frac{dP}{d\Omega} = \frac{8\gamma^{*2}}{(1+\gamma^{*2}\theta^2)^3}\frac{dP'}{d\Omega'} \tag{5.46}$$

Combining Eqs. (5.42), (5.44), and (5.46), one obtains the average power radiated per unit solid angle at the fundamental frequency ($n = 1$), for small K, as observed in the laboratory frame of reference:

$$\left.\frac{d\tilde{P}}{d\Omega}\right|_{e^-} = \frac{e^2cK^2\gamma^4}{\epsilon_0\lambda_u^2(1+K^2/2)^3}\left[\frac{1+2\gamma^{*2}\theta^2(1-2\cos^2\phi)+\gamma^{*4}\theta^4}{(1+\gamma^{*2}\theta^2)^5}\right] \tag{5.47}$$

This result is for a single electron. A more useful result would be the power radiated by an electron bunch in which the individual motions within the bunch are random. In this case the radiated fields due to different electrons are uncorrelated and the average power radiated is a simple sum of the radiated power from individual electrons; that is, we sum intensities, not fields. For the moment let us consider the electron bunch to be sufficiently constrained in spatial and angular extent that the angular dependencies are to first order as given by Eq. (5.47). We will see in the next section that this requires that the extent of random angular deviation within the electron bunch be limited to values $\sigma' < 1/\gamma^*\sqrt{N}$, where σ' is the rms measure of width of the electron angular distribution function about the z-axis.

To generalize Eq. (5.47) to the many electron case we must determine how many electrons, on average, are radiating from within the undulator at any given time. It is convenient to do this in terms of the current in the storage ring. Current is defined as the charge per unit time crossing a given plane. For electrons of velocity v the magnitude of the current can be written as

$$I = e\mathrm{v}n_l$$

where n_l is the number of electrons per unit length in the direction of motion. For a magnet structure (undulator) of length L containing on average N_e electrons in its entire length, each traveling with a velocity $\mathrm{v} \simeq c$, the average current is

$$I = \frac{ecN_e}{L}$$

so that the total number of electrons radiating within the magnet structure at a given time is

$$N_e = \frac{IL}{ec} \tag{5.48}$$

which was cited without proof in the previous section. The average power radiated per unit solid angle by a distribution of relativistic electrons of average current I is then obtained, following the same arguments regarding uncorrelated motions which led to Eq. (5.39), by

simply multiplying the single electron result [Eq. (5.47)] by the average number of electrons within the undulator [Eq. (5.48)] to obtain

$$\frac{d\bar{P}}{d\Omega} = N_e \frac{d\bar{P}}{d\Omega}\bigg|_{e^-} = \frac{eN\gamma^4 I}{\epsilon_0 \lambda_u} \cdot \frac{K^2}{(1+K^2/2)^3} \underbrace{\left[\frac{1+2\gamma^{*2}\theta^2(1-2\cos^2\phi)+\gamma^{*4}\theta^4}{(1+\gamma^{*2}\theta^2)^5}\right]}_{F(\theta,\,\phi)} \tag{5.49}$$

where we have used the fact that the undulator length L is equal to $N\lambda_u$.

This is a significant result for undulator radiation ($K < 1$). Note that the angular function $F(\theta, \phi)$ in Eq. (5.49) is unity on axis, is approximately $\frac{1}{3}$ for an angle $\theta = 1/2\gamma^*$, and goes rapidly to zero for $\theta > 1/\gamma^*$. Thus we again see the generally anticipated searchlight effect for synchrotron radiation, this time with an explicit power dependence on angle.

For small amplitude oscillations, e.g., $K \leq 1$, the K^2 dependence reflects the acceleration (a^2) dependence on magnetic field. For $K > 1$ the power radiated in the fundamental begins to decline as the strong magnetic field couples energy into successively higher harmonics, thus beginning an evolution towards wiggler radiation. The γ^4 dependence reflects the relativistic photon energy shift (γ^2) and the ever narrowing emission solid angle ($1/\gamma^2$). The angular distribution given in Eq. (5.49) can be used to provide a small (several percent) correction to the previously derived power in the central radiation cone.

In the derivation of Eqs. (5.38) and (5.39) we assumed that the power per unit solid angle, $dP/d\Omega$, was to first order independent of θ for $\theta \leq \theta_{\text{cen}} = 1/\gamma^*\sqrt{N}$, where typically $N = 100$. We see, however, in Eq. (5.49) that there are several terms involving $\gamma^{*2}\theta^2$ which reach values of order $1/N$ within the central cone. Thus for improved accuracy in predicting undulator performance, attention should be paid to these angular factors. Towards this end, numerical integration programs such as that described by Walker and Diviacco,[13] are an important complement to the simplified analytic formulation. These computer codes also permit the inclusion of finite electron beam size, angular divergence, and energy spread, as is discussed in the next section.

Our next task is to calculate the undulator power radiated at the fundamental wavelength to all angles and all wavelengths, which is achieved by integrating Eq. (5.49) over all solid angles $d\Omega = \sin\theta\, d\theta\, d\phi$. Recalling that the integrand falls off rapidly for angles beyond $1/\gamma^*$, we can take $d\Omega \simeq \theta\, d\theta\, d\phi$, and proceed beyond that with an exact integration. Note that ϕ appears in only one term, which integrates to zero, viz.,

$$\int_0^{2\pi} (1-2\cos^2\phi)\, d\phi = -\frac{1}{2}\int_0^{2\pi} \cos 2\phi \cdot d(2\phi) = -\frac{1}{2}\sin 2\phi\Big|_0^{2\pi} = 0$$

In all other terms there is no ϕ-dependence, so that the ϕ-integration gives a simple 2π factor. The remaining integration is performed (see Appendix F) by introducing $u = \gamma^*\theta$ and $x = 1 + u^2$, then integrating the resultant polynomial over $dx = 2u\, du$ to obtain

$$\int_0^{\pi}\int_0^{2\pi} \frac{1+\gamma^{*4}\theta^4}{(1+\gamma^{*2}\theta^2)^5}\theta\, d\theta\, d\phi = \frac{\pi}{3\gamma^{*2}}$$

The total radiated power in the fundamental ($n = 1$), to all angles and wavelengths, for small

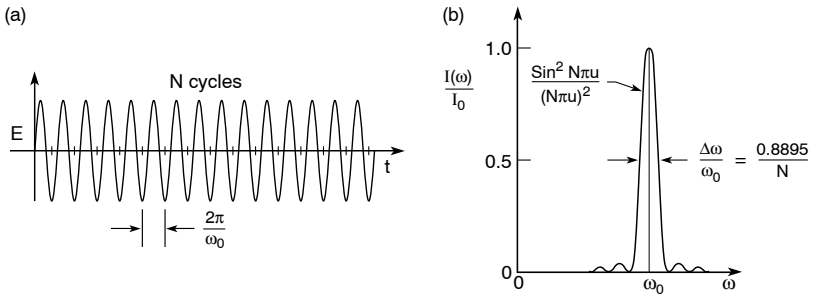

FIGURE 5.21. (a) Radiated wavetrain from a single electron traversing an undulator, as detected in the laboratory frame of reference, and (b) the corresponding spectral distribution function, where $u = \Delta\omega/\omega_0$ and $\Delta\omega = \omega - \omega_0$.

K, is then

$$P_{T,1} = \frac{\pi e \gamma^2 I N}{3\epsilon_0 \lambda_u} \cdot \frac{K^2}{(1 + K^2/2)^2} \tag{5.50a}$$

where we have made the identification $L = N\lambda_u$. Note that the total power is larger than that in the central cone [Eq. (5.39)] by a factor $N/3$. Rewriting in practical units, the total power in the fundamental for small K is

$$P_{T,1}(\mathrm{W}) = \frac{(1.90 \times 10^{-6}\ \mathrm{W})\gamma^2 N I(\mathrm{A})}{\lambda_u(\mathrm{cm})} \cdot \frac{K^2}{(1 + K^2/2)^2} \tag{5.50b}$$

where I is in amperes and λ_u is in centimeters. We note that for the two undulators cited in Table 5.1, the soft x-ray undulator radiates 69 W into the fundamental at all angles, while the hard x-ray undulator generates 350 W in the fundamental. The subject of harmonic motion and power radiated at harmonic frequencies is discussed in later sections.

The preceding analysis appears to imply that with a sufficiently small angular aperture one could measure power into an infinitely narrow spectral bandwidth. Consideration of finite undulator length obviates this unphysical conclusion. Electron oscillation through a finite number of periods ($L = N\lambda_u$) will give rise to a minimum relative spectral bandwidth of order N^{-1}. Finite random motion within the electron bunch, giving rise to instantaneous trajectories at various angles to the z-axis, also contributes to spectral width at any given observation angle. Although finite lateral width of the electron bunch has little effect upon spectral characteristics, the considerable longitudinal depth of the radiation source can contribute a discernible broadening to the observable radiation characteristics through what could be described as a depth of focus effect. These topics are discussed further in the following section.

5.4.5 Spectral Bandwidth of Undulator Radiation

For an undulator of N periods each electron oscillates through N cycles of its motion and thus radiates a wavetrain consisting of N well-defined cycles of the electric field as illustrated in Figure 5.21(a). The Fourier transform of this waveform,[14] which gives the spectral content

of the fields, is a $(\sin x)/x$, or sinc x, function, where as used here $x = N\pi u$, $u = \Delta\omega/\omega_0$, and $\Delta\omega = \omega - \omega_0$ is the frequency shift away from the central maximum at ω_0, as observed at a given angle and K-value. The intensity observed in the laboratory frame is proportional to the square of the electric field, so that in normalized form

$$\frac{I(\omega)}{I_0} = \frac{\sin^2(N\pi\,\Delta\omega/\omega_0)}{(N\pi\,\Delta\omega/\omega_0)^2} \tag{5.51}$$

For large N the major contribution to the fundamental occurs for small values of $\Delta\omega/\omega_0$. This is a commonly encountered function, tabulated[14] as $\text{sinc}^2 x$, which is normalized to unity with a full width at half maximum (FWHM) of approximately $1/N$, centered at ω_0, as illustrated in Figure 5.21(b). For undulator radiation the central frequency ω_0 is equal to $2\pi c/\lambda_0$, which we determined earlier (without the use of a subscript zero) to be given by [Eq. (5.28)].

$$\lambda = \frac{\lambda_u}{2\gamma^2}\left[1 + \frac{K^2}{2} + \gamma^2\theta^2\right]$$

Thus the central maximum of the spectral distribution function (5.51b) occurs at a frequency (subscript zero suppressed)

$$\omega = \frac{4\pi c\gamma^2}{\lambda_u\left(1 + \frac{K^2}{2} + \gamma^2\theta^2\right)} \tag{5.52}$$

which we recall is a function of the observation angle θ in the laboratory frame. Thus for undulator radiation from a single electron moving along the undulator (z) axis, we expect to see radiation centered at a photon energy $\hbar\omega_0$ given as a function of angle by Eq. (5.52), with a spectral distribution of intensity given by Eq. (5.51b), and having a relative spectral bandwidth of approximately $1/N$. If the acceptance cone for this observation, $\Delta\theta$ at θ, is finite, the detected frequency or energy bandwidth may be broader.

In a previous section we used a general knowledge of Fourier transform pairs to predict that undulator radiation would have a "natural" spectral bandwidth of $1/N$ and, on the basis of this, defined a *central radiation cone* with an inclusive half angle of [Eq. (5.32)]

$$\theta_{\text{cen}} = \frac{1}{\gamma^*\sqrt{N}}$$

Beyond the natural or *lifetime* broadening, due to the finite number N of oscillations, further spectral broadening can be incurred with the passage of many electrons through the undulator in a bunch of finite size, divergence, and energy spread. Parameters describing electron beam size and divergence[¶] are illustrated in Figure 5.22. If there is an electron energy spread within

[¶]In an electron storage ring the beam size and divergence, σ and σ', are described in terms of a phase space product, known as the *emittance*, and a β-function, a parameter characterizing the magnet's structure (*lattice*) that confines the electrons within the ring. The phase space volume is the region of a six-dimensional position–momentum, or position–angle, space that encloses all particles. For particles with a Gaussian distribution of rms spatial and angular measures, σ and σ' respectively, accelerator physicists refer to the electron beam phase space volume ϵ as the emittance, where $\epsilon = \pi\sigma\sigma'$ is generally written separately for the horizontal and vertical planes, i.e., $\epsilon_h = \pi\sigma_x\sigma_x'$ and $\epsilon_v = \pi\sigma_y\sigma_y'$. The rms electron beam parameters are given by $\sigma_{x,y} = \sqrt{\epsilon_{x,y}\beta_{x,y}}$ and $\sigma'_{x,y} = \sqrt{\epsilon_{x,y}/\beta_{x,y}}$. where the emittances ϵ_x and ϵ_y are fixed for a given storage ring, while β_x and β_y have different values around

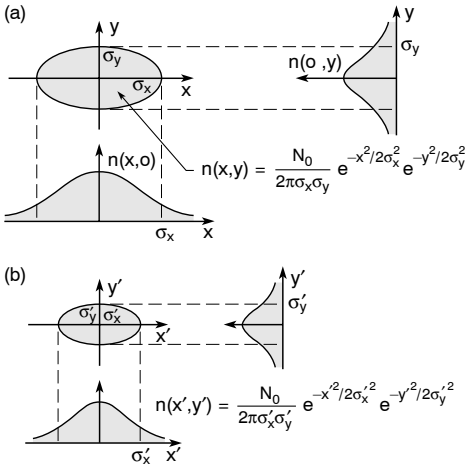

FIGURE 5.22. Cross-sectional view of an electron beam of elliptical cross-section with Gaussian distribution of density in both (a) spatial and (b) angular coordinates, where $x' = dx/dz$ and $y' = dy/dz$.

the bunch, $\Delta E_e/E_e = \Delta\gamma/\gamma$, there will be a corresponding photon energy spread according to Eq. (5.52), given by

$$\frac{\Delta E}{E} = \frac{2\,\Delta\gamma}{\gamma} \tag{5.53}$$

where the factor of two is due to the squared relationship between photon energy and electron energy. Since typical energy spreads in modern storage rings are of order $\Delta\gamma/\gamma = 10^{-3}$, this is generally negligible in the fundamental for undulators of about 100 periods, although it can be an observable factor for higher harmonic (n) radiation where the effective number of cycles in the observed radiation is nN.

A more significant effect is that due to random angular motion within the bunch. As a result some electrons traverse the magnet structure not along or parallel to the z-axis, but at a small angle α thereto. These electrons undergo the same number N of oscillations, but experience a somewhat longer period, and further, the observed radiation is affected by a non-axial relativistic Doppler shift. The net result is a Doppler-dominated energy shift, always to lower photon energy (longer wavelength), given by[§]

$$\frac{\Delta E}{E} = \gamma^{*2}\alpha^2 \tag{5.54}$$

This term is important for electron trajectories such that the angle α causes a photon energy shift $\Delta E/E$ of order $1/N$. For a collection of electrons passing through the undulator in a bunch, maintenance of the sharp single-electron spectral features requires that the rms angular divergence σ' cause a spectral broadening less than $1/N$. From Eq. (5.54), with α replaced by σ', and $\Delta E/E < 1/N$, one obtains the *undulator condition* restricting electron beam

the ring depending on local magnetic fields. The ratio ϵ_y/ϵ_x is referred to historically as the coupling ratio. Typically the coupling ratio is of order 1% in modern storage rings. For further discussion see the article by Cornacchia.[15]

[§]Write the undulator equation (5.28) for an increased period $\lambda_u/\cos\alpha$, and for an observation angle $\theta = \alpha$; then compare this with the $\alpha = 0$ case and normalize to form $\Delta\lambda/\lambda$ and $\Delta E/E$.

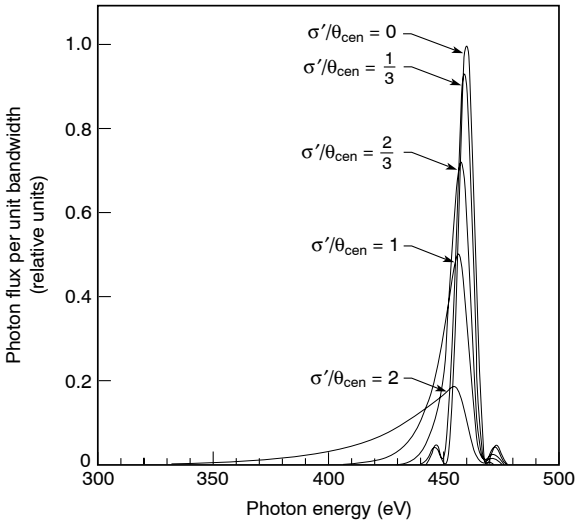

FIGURE 5.23. Spectral line shape and relative spectral brightness of undulator radiation as a function of electron beam angular divergence σ' divided by the central cone half angle θ_{cen}, for a soft x-ray undulator having $\gamma = 3720$, $\lambda_u = 5.00$ cm, $N = 89$, and $K = 1$. (Following Kitamura.[16])

divergence, as anticipated in earlier sections:

$$\sigma'^2 \ll \frac{1}{\gamma^{*2} N} \tag{5.55a}$$

or

$$\boxed{\sigma'^2 \ll \theta_{\text{cen}}^2} \tag{5.55b}$$

A far-field computation of the predicted spectral distribution of undulator radiation for various values of electron beam divergence is presented in Figure 5.23. Note that this is a summation of $\text{sinc}^2 N\pi u$ individual electron spectral functions, shifted to lower photon energies ΔE for an assumed Gaussian distribution of electron trajectories at an angle α to the z-axis. The example is chosen with $N = 89$, for a natural bandwidth of about 1.1%, and a (single electron) central cone of half angle 35 μrad. The rms electron angular distributions (σ'), ranging from zero to 70 μrad, illustrate the transition from a $\sin^2 N\pi u$ behavior for many parallel electrons, to an extended low photon energy (red shifted) tail when the rms values are comparable to the characteristic central cone angle. As these curves illustrate, when σ' is comparable to the single electron value of θ_{cen}, the observed on-axis spectrum is spread to varying degrees. This requires some adjustment to our characterization of the observed radiation. For instance, we calculated in an earlier section the power radiated in the central cone. Clearly that power is not confined within the central cone of a single electron, but rather is spread to a larger angle by random electron trajectories within the beam. As a first approximation we can define a *total* central radiation cone θ_T as a near-Gaussian square root of the sum of squares. As storage ring electron beams are generally elliptical in cross-section, as was illustrated in Figure 5.22, we choose to define horizontal and vertical values, θ_{Tx}

and θ_{Ty}, as

$$\theta_{Tx} = \sqrt{\theta_{\text{cen}}^2 + \sigma_x'^2} \tag{5.56a}$$

and

$$\theta_{Ty} = \sqrt{\theta_{\text{cen}}^2 + \sigma_y'^2} \tag{5.56b}$$

To appreciate the magnitude of these corrections we take as an example the ALS 5 cm period undulator operating at $K = 1$, which has a single electron central radiation cone half angle (θ_{cen}) of 35 μrad. For the ALS $\sigma_x' = 23$ μrad and $\sigma_y' = 3.9$ μrad, so that the total central cone half angles are $\theta_{Tx} \simeq 42$ μrad and $\theta_{Ty} = 35$ μrad. Adding angles in quadrature, as in Eqs. (5.56), is correct for Gaussian distributions, but only a convenient approximation for broadening of the central radiation cone. Nonetheless the model is simple, with a clear physical concept, and gives an easily obtained estimate of the degree to which single-electron calculations of power and divergence are modified by beam divergence. More accurate estimates require numerical studies, which include finite angular acceptance, real measures of electron angular distribution, and other storage-ring–beamline characteristics.[13]

Further spectral broadening can be incurred due to the finite electron bunch size, as was illustrated in Figure 5.22(a) in terms of a Gaussian radial measure σ, with subscripts indicating differing widths in the various coordinate directions. Although spatial effects can be quite large in older storage rings with large beam sizes, in modern storage rings spatial effects are typically somewhat smaller than those due to angular divergence. The effect of spatial broadening is due to the fact that electrons traveling parallel to the z-axis, but displaced at some lateral coordinates (x, y), will be observed at some finite angle, and thus again be Doppler shifted to longer wavelengths. As typical values of σ are of order 100 μm in modern storage rings, and observations (experimental chambers) are typically 10 m or more downstream, angular measures due to source size are of order 10 μrad, and thus cause less of a spectral broadening effect than that due to electron beam divergence (σ') as estimated by Eq. (5.56).

5.4.6 Spectral Brightness of Undulator Radiation

As measures of the radiation emitted by electrons traversing a periodic magnet undulator we have calculated the power, photon flux, and power per unit solid angle. Another important measure is brightness, or in fact spectral brightness.‖ Brightness is defined here as radiated power per unit area and per unit solid angle at the source, or equivalently the photon flux per unit area and per unit solid angle. Spectral brightness is the brightness per unit relative spectral bandwidth, i.e., the brightness contained within a relative spectral bandwidth ($\Delta\lambda/\lambda$ or $\Delta\omega/\omega$) of interest. Brightness has an important conceptual role, as it is a conserved quantity in perfect optical systems. That is, in a lossless unaberrated optical system the brightness is equal in the source and image planes. For instance, in a simple imaging system the size magnification is matched by an equal angular demagnification, so that the size–angle product is fixed. The

‖Some use the phrase "spectral brilliance." Refer to Born and Wolf, Ref. 17.

area–solid-angle product is therefore also equal in the object and image planes. It is thus an important quantity in designing microscopes, microprobes, and other imaging systems. Furthermore, it has very interesting wavelength limits when considering experiments that utilize the partially coherent nature of undulator radiation, a subject we return to in Chapter 8.

To first order one can define *brightness* as the power ΔP radiated from an area ΔA into a solid angle $\Delta\Omega$ as

$$B = \frac{\Delta P}{\Delta A \cdot \Delta\Omega} \tag{5.57}$$

and the *spectral brightness* as that portion of the brightness lying within a relative spectral bandwidth $\Delta\omega/\omega$ as

$$B_{\Delta\omega/\omega} = \frac{\Delta P}{\Delta A \cdot \Delta\Omega \cdot \Delta\omega/\omega} \tag{5.58}$$

To specialize this to the case of undulator radiation we can use the previously calculated power in the central radiation cone, P_{cen}, which was defined as having a relative spectral bandwidth (BW) of $\Delta\omega/\omega = 1/N$ and a radiation cone of half angle θ_{cen}, which in the presence of an elliptically divergent electron beam becomes elliptical itself with half angles θ_{Tx} and θ_{Ty} as defined in Eq. (5.56). In the synchrotron community the tradition is to define spectral brightness in terms of photon flux (photons per unit time), rather than power, and furthermore to express the result in terms of a relative spectral bandwidth of 10^{-3}, often written as 0.1%BW. To accommodate this tradition we introduce the photon flux within the central cone, F_{cen}, which we define as the radiated power divided by the energy per photon, viz.,

$$\bar{F}_{\text{cen}} = \frac{\bar{P}_{\text{cen}}}{\hbar\omega/\text{photon}} \tag{5.59}$$

Defining the *undulator spectral brightness in terms of photon flux* within the central cone, one has

$$\bar{B}_{\Delta\omega/\omega} = \frac{\bar{F}_{\text{cen}}}{\Delta A \cdot \Delta\Omega \cdot N^{-1}} \tag{5.60a}$$

To write this in terms of a 0.1% bandwidth, rather than $1/N$, we multiply numerator and denominator by a unitless factor 10^{-3} to obtain

$$\bar{B}_{\Delta\omega/\omega} = \frac{\bar{F}_{\text{cen}} \cdot (N/1000)}{\Delta A \cdot \Delta\Omega \cdot (0.1\%\text{BW})} \tag{5.60b}$$

The factor $N/1000$, which appears in the numerator, takes account of the fact that with a choice of photon flux within a unit relative bandwidth less than $1/N$, only a portion of the flux within the central cone is utilized, e.g., for $N = 100$ only $N/1000 = 10^{-1}$ of the central cone flux is within a relative bandwidth of 0.1%.

If the radiation emits from a source of elliptical cross-section, having a Gaussian distribution of density across both horizontal (x) and vertical (y) coordinates, the photon flux per

unit area can be written as**

$$\frac{dF}{dA} = \frac{F_{\text{cen}}}{2\pi\sigma_x\sigma_y} e^{-x^2/2\sigma_x^2} e^{-y^2/2\sigma_y^2} \tag{5.61}$$

where the spatially integrated distribution is normalized to F_{cen}, the total flux within a $1/N$ relative spectral bandwidth without divergence. For the assumed Gaussian spatial distribution the on-axis value of photon flux per unit area is $\bar{F}_{\text{cen}}/2\pi\sigma_x\sigma_y$, where $\pi\sigma_x\sigma_y$ is the area of a cross-sectional ellipse of semi-major and semi-minor axes σ_x and σ_y.

To complete the brightness calculation an expression is needed for $dF/d\Omega$ within the central cone. Various forms of this function will be appropriate, depending on the relative measures of $\sigma'_{x,y}$ and θ_{cen}. If the undulator condition (5.55) is well satisfied, so that $\sigma'_{x,y} \ll \theta_{\text{cen}}$, the central cone will be rather well defined in terms of both its angular definition and spectrum. The spectrum will approximate the limiting case illustrated in Figure 5.23, while the cone half angle will be only slightly larger than θ_{cen}, which we can approximate by θ_{Tx} and θ_{Ty}, in the respective planes, as given in Eq. (5.56). In this case the central cone solid angle will be only slightly elliptical, and well approximated by $\Delta\Omega_{\text{cen}} = \pi\theta_{Tx}\theta_{Ty}$, so that within this cone

$$\frac{dF}{d\Omega} = \frac{\bar{F}_{\text{cen}}}{\pi\theta_{Tx}\theta_{Ty}} \tag{5.62}$$

which is the expression we will use in Eq. (5.60), as it captures our sense of the ideal circumstances for observing undulator radiation. In other cases, however, where the undulator condition is not well satisfied, such as $\sigma'_{x,y} \simeq \theta_{\text{cen}}$, the concept of a well-defined central cone is somewhat diminished. As we observed in Figure 5.23, this leads to a broader emission spectrum of reduced spectral intensity. In such a case the angular distribution of central cone photon flux will also be spread. We distinguish this from the central cone arguments developed in this chapter, for which to first order the various electrons travel parallel to the z-axis and radiate a nearly uniform angular pattern out to θ_{cen}. Rather, the Gaussian distribution argument follows from a convolution of the many single electron radiation patterns (θ_{cen}) with an angular distribution function whose measures are σ'_x and σ'_y. This leads to a smoother angular distribution, which can in some cases be fitted with a Gaussian distribution, particularly when the values of σ'_x and σ'_y approach that of θ_{cen}. This is the type of argument that led to the definitions of θ_{Tx} and θ_{Ty} as total central cone angles in their respective planes, as defined in Eqs. (5.56a) and (5.56b). In this case the angular distribution of radiation within a narrow bandwidth would be approximated by a Gaussian distribution of the form

$$\frac{d\bar{F}}{d\Omega} = \frac{\bar{F}_{\text{cen}}}{2\pi\theta_{Tx}\theta_{Ty}} e^{-(x')^2/2\theta_{Tx}^2} e^{-(y')^2/2\theta_{Ty}^2}$$

where x' is an abbreviation for the radiation angle in the x, z-plane measured from the z-axis, y' is an abbreviation for the radiation angle in the y, z-plane, and integration over all angles would be normalized to $\bar{F}_{\text{cen}}/2\pi\theta_{Tx}\theta_{Ty}$. Keeping to the spirit of a well-defined central radiation cone, with the undulator condition well satisfied, we will use the formulation of photon flux angular distribution given by Eq. (5.62). Where the condition $\sigma'_{x,y} \ll \theta_{\text{cen}}$ is not well satisfied, computational techniques will be very useful.

**This is confirmed by integrating dF/dA over all x and y, and noting (Appendix D) that $\int_0^\infty e^{-a^2x^2}dx = \sqrt{\pi}/2a$.

Combining expressions for a Gaussian spatial distribution [Eq. (5.61)] with the central cone angular distribution given by [Eq. (5.62)], the on-axis photon flux per unit area and per unit solid angle is

$$\frac{d^2\bar{F}}{dA\,d\Omega} = \frac{\bar{F}_{\text{cen}}}{2\pi^2\sigma_x\sigma_y\theta_{Tx}\theta_{Ty}} \tag{5.63}$$

so that the on-axis spectral brightness follows from Eq. (5.60b) as

$$\bar{B}_{\Delta\omega/\omega}(0) = \frac{\bar{F}_{\text{cen}} \cdot (N/1000)}{2\pi^2\sigma_x\sigma_y\theta_{Tx}\theta_{Ty}(0.1\%\text{BW})} \tag{5.64}$$

where $\bar{F}_{\text{cen}}$ is given in Eq. (5.59) and where the zero in parentheses refers to an on-axis value with respect to both position and angle. Combining this with Eqs. (5.41b) and (5.59) for P_{cen} and F_{cen}, the expression for on-axis spectral brightness can be rewritten in practical units as

$$B_{\Delta\omega/\omega}(0) = \frac{7.25 \times 10^6\gamma^2N^2I(\text{A})}{\sigma_x(\text{mm})\sigma_y(\text{mm})\left(1+\dfrac{\sigma_x'^2}{\theta_{\text{cen}}^2}\right)^{1/2}\left(1+\dfrac{\sigma_y'^2}{\theta_{\text{cen}}^2}\right)^{1/2}} \times \frac{K^2f(K)}{\left(1+\frac{K^2}{2}\right)^2}\frac{\text{photons/s}}{\text{mm}^2\text{mrad}^2(0.1\%\text{BW})} \tag{5.65}$$

where σ_x and σ_y are in millimeters, I is in amperes, and $f(K)$ is the finite-K correction factor given in Eq. (5.40) and Table 5.5. This formulation is most accurate when the electron beam divergences σ_x' and σ_y' are significantly less than θ_{cen} so that the undulator condition is well satisfied. For large electron beam divergence, such that $\sigma_{x,y}' \simeq \theta_{\text{cen}}$, the undulator condition is not satisfied, so that the spectral content is significantly broadened, as illustrated in Figure 5.23, and Eq. (5.65) overestimates spectral brightness by a factor approaching two. In this case it is best to utilize numerical simulations, although the analytic formulation will continue to give useful insights. Sample values of spectral brightness for soft and hard x-ray undulators are given in Table 5.1, and general trends are shown in Figure 5.24, where brightness values for bending magnet radiation and wiggler radiation are shown for comparison. Note that the expression (5.65) for spectral brightness can be written explicitly in terms of photon energy by relating K^2 to photon energy, as was done in Eqs. 5.41(c), (d), and (e).

5.4.7 Time Structure

The electron beam in a storage ring is not a continuous stream, but rather a highly modulated density function consisting of axial bunches. The spacing of these bunches is set by the radio frequency (rf) used to restore power to electrons, once each turn around the storage ring, to compensate for power lost to synchrotron radiation. The rf is fed to a microwave cavity operating in a mode with an axial electric field, synchronized so that slower electrons receive a small acceleration, while faster electrons experience a small deceleration. In this manner a sequence of potential wells is set up that tends to trap available electrons into a series of *buckets* that travel around the ring at the speed of light, with a bunch-to-bunch separation

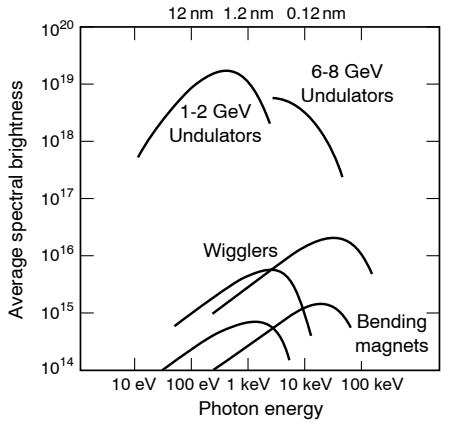

FIGURE 5.24. General trends of spectral brightness for undulator radiation, wiggler radiation, and bending magnet radiation, showing the complementary nature of soft x-ray (1–2 GeV) and hard x-ray (6–8 GeV) storage ring facilities. High spectral brightness is particularly useful for experiments involving scanning microscopy and partial coherence, diffraction from small crystalline samples, and other studies which generally benefit from radiation of minimal divergence emanating from a small source size. Units as in Eq. (5.65).

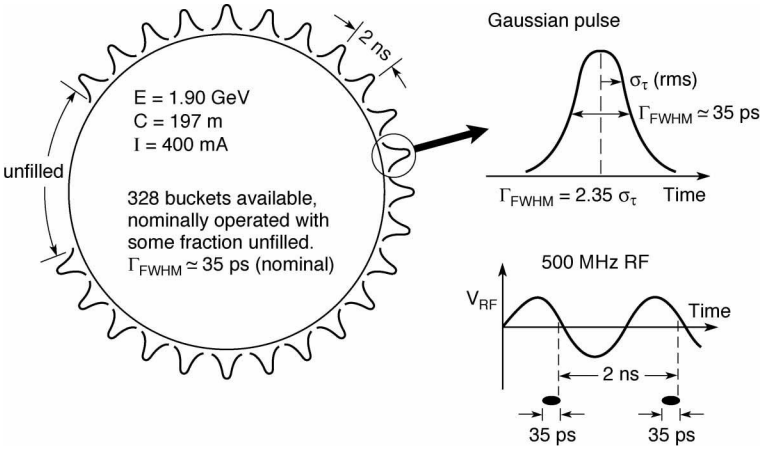

FIGURE 5.25. Illustration showing how the time structure of synchrotron radiation is related to rf power replenishment and resultant electron bunch structure (axial electron density modulation) for a typical storage ring. In the example shown here the radio frequency (rf) and storage ring circumference are matched for a 60 cm peak to peak structure of 328 axial buckets, of which a pre-selected fraction are filled with electrons. At the speed of light, 60 cm corresponds to a 2 ns x-ray pulse separation. The individual pulse duration, set by the rf voltage and beam dynamics, is 35 ps FWHM in the example shown, which corresponds to a Gaussian axial bunch length ($2\sigma_z$) of 8.9 mm rms.

equal to the rf wavelength. Figure 5.25 illustrates electron bunch structure in the ALS storage ring for a multibunch operation in which all of the buckets are filled. By proper timing of electron injection into the ring any sequence of filled buckets can be obtained. A less common, but regularly used mode of operation employs only two filled bunches, which is convenient for use with time-of-flight measurements of chemical reaction products in photodissociation products.

For some experiments involving time-of-flight detection of photofragments (chemical dynamics) very few buckets contain electrons. More generally, most buckets are filled, leaving some sequence unfilled to counteract beam propagation instabilities that are thought to involve ion trapping within the ring. For the case illustrated in Figure 5.25 a 500 MHz rf produces a

bunch-to-bunch separation of 60 cm, which accommodates a 328 bucket axial charge distribution within a 197 m storage ring circumference set by the beam energy and bending magnet fields. In the case illustrated, 288 of the 328 buckets are filled. Each of the electron bunches has a near-Gaussian pulse shape with a nominal 35 ps FWHM duration, corresponding to an axial charge distribution of $\sigma_z = 4.5$ mm rms. The pulse-to-pulse separation seen at any given position along the ring is 2.0 ns, corresponding to the 60 cm electron bunch separation traveling around the ring at near the velocity of light.

In many of the examples considered throughout this chapter, the average power, photon flux, etc., were calculated on a time average basis (indicated by a bar over the assigned symbol, as in $\bar{P}_{\text{cen}}$). To calculate peak powers ($\hat{P}$) one must know the exact time dependence. For instance, in the case illustrated in Figure 5.25, where a sequence of 35 ps FWHM Gaussian pulses occurs every 2.0 ns, the ratio of peak to average power, $\hat{P}/\bar{F}$, is 54. Thus the peak power, photon flux, and spectral brightness values are higher than the time-averaged values cited by a factor of 54. Other operating parameters can give significantly different ratios depending on optimizations of interest. For instance, in single-bunch operation the ratio would be larger by several hundred. The pulse duration can also be adjusted through the choice of rf voltage and the use of third harmonic cavities (1.5 GHz at the ALS), which are used to extend pulse duration (to 100 ps, nominal operation) and thus extend the beam lifetime due to the reduced electron density in the bunch. The APS typically operates with nominal 170 ps FWHM pulses with a pulse to pulse separation of 2.8 ns, so that with all buckets full the ratio of peak to average power is about 16. However, a typical choice of operation at this facility is to fill only 200 of 1296 available buckets, so that the ratio of peak to average power is more typically 100.

5.4.8 Polarization Properties of Undulator Radiation

For electron motion directed along the z-axis of an undulator (see Figures 5.8 and 5.17) with periodic magnetic fields oriented in the vertical (y) direction, electron oscillations are in the horizontal (x) direction for low K-values. This generates radiation at a fundamental ($n = 1$) wavelength given by the so-called undulator equation (5.28), having fields within the central cone polarized with the electric field in the horizontal (x) direction. For somewhat higher K-values, of order one, second and third harmonics become important, as was illustrated in Figure 5.17 and is discussed further in Section 5.5, which follows. For these modest K-values the second harmonic motion consists of a velocity modulation in the z-direction so that in the primed frame of reference, moving with the mean electron motion, the second harmonic radiation (ω_2') is polarized in the z'-direction, with maximum intensity off axis at $\theta' = \pi/2$, as shown in Figure 5.18(b). This radiation is then transformed to the laboratory frame of reference as an axisymmetric second harmonic radiation cone, with a peak intensity off axis having a radial electric field polarization, and an intensity null on axis. Thus by moving the point of observation circularly around the second harmonic peak $0 \leq \phi \leq 2\pi$, at an angle of $1/\gamma$ off axis, the polarization detected will vary smoothly from vertical to horizontal. Third harmonic radiation ($n = 3$) is similar to the fundamental, being horizontally polarized for angles of observation near the central (z) axis. The subject of off-axis polarization for arbitrary K-values is discussed by Kim in Ref. 3.

Specialized magnet structures for the generation of arbitrarily polarized undulator radiation are of great interest for probing magnetic materials, helical structures, and other samples with polarization dependent properties.[18] In general the greatest freedom in varying both polarization state and wavelength is valued. Toward this end efforts have been made to construct magnet structures that can provide orthogonal linear polarizations, left or right circularly

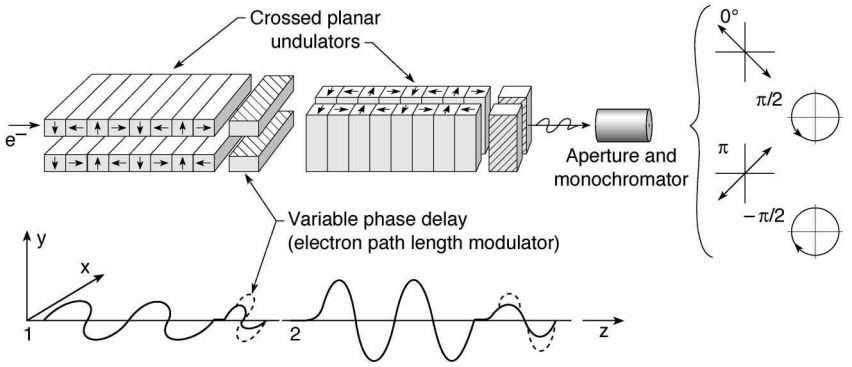

FIGURE 5.26. Schematic of a pair of crossed undulators that can be used to generate linearly polarized, circularly polarized, or elliptically polarized radiation across a broad range of EUV and soft x-ray energies. (Courtesy of K.-J. Kim.[19])

polarized radiation, and elliptically polarized radiation. Figure 5.26 shows a pair of axially separated crossed undulators.[19, 20] As electrons sequentially traverse the two undulators, radiation is generated with orthogonal polarizations. In each magnet structure the emitted phase is related to the motion of the electron. By controlling the electron transit time between the two undulators through the use of a variable-field magnet, the relative phase of the radiated field amplitudes (**E**) can be selected. Thus linearly polarized radiation can be obtained with field orientations set to $\pm\pi/4$ from the vertical. By modulating the electron transit time between undulators one can switch between these two orthogonal polarizations. Similarly one can generate left or right circular polarization through proper phasing. The wavelength is controlled independently by setting the magnet gap. A pair of crossed undulators such as these has been installed at the BESSY Facility in Berlin for the study of spin resolved photoemission at soft x-ray and EUV wavelengths.[21] As noted earlier in Eq. (5.55a), optimum undulator performance is obtained with small electron beam divergence, $\sigma' < 1/\gamma\sqrt{N}$, which limits devices such as this to modern storage rings.

A number of other magnet structures have been designed with various additional attributes. Onuki and colleagues[22, 23] have designed and built a system in which two orthogonal undulators are placed side by side so that the electrons experience a net magnetic force due to the combined fields at each point along their trajectory. By phase shifting one undulator magnet set (say the horizontal field set) by a quarter period, that is, moving it axially by a distance $\pm\lambda_u/4$, one can induce left or right handed helical motion of the electrons as they traverse the magnet structure. This has the great advantage of avoiding harmonic radiation.[12] An 8 cm period prototype of this helical undulator has been built and tested in the 0.6 GeV Teras storage ring in Japan, where it produced 63 nm circular and linear polarized radiation. Elleaume at ESRF in Grenoble,[24] and Di Viacco and Walker at Sincrotrone Trieste[25] in Italy, have designed planar magnet structures that generate circularly polarized radiation with minimal effect on the vacuum chamber configuration.

S. Sasaki and colleagues[26, 27] in Japan have developed an undulator concept for the generation of linear and circular polarized radiation based on the use of four rows of periodic magnet arrays, as illustrated in Figure 5.27. In this structure all the magnets are above or below the electron orbit plane, thus avoiding horizontal gap–electron-beam interactions. In this device the four rows of periodic magnets are arranged with two rows above and two rows below the electron orbit plane. In both the upper and lower magnet planes one row of magnets is fixed

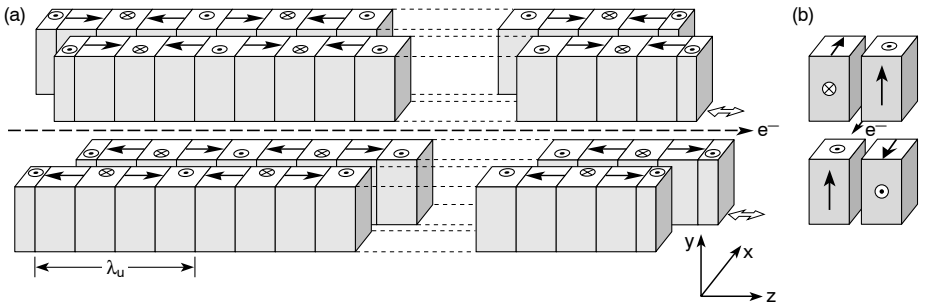

FIGURE 5.27. Schematic view of a magnetic structure for generating variably polarized undulator radiation in which there are no magnets in the plane of electron motion. (a) Isometric view showing two fixed rows (upper right and lower left) and two axially movable rows (upper left and lower right), shown displaced forward by one quarter period. (b) End-on view in a midplane of the magnet structure in a configuration that produces both horizontal and vertical magnetic fields on axis, which will result in a helical electron motion and the concomitant emission of elliptically polarized radiation. (Following Sasaki et al.[26, 27])

and one is movable (in the axial direction). The two movable magnet sets, upper front and lower back in Figure 5.27, move together. In combination, the four magnet structures create an on-axis magnetic field that can induce linear or helical electron motion as the position of the diagonally opposed moveable set is translated in the axial direction.

Versions of this elliptically polarizing undulator have been constructed for use at both the 3 GeV Stanford Synchrotron Radiation Laboratory (SSRL) and the 1.9 GeV Advanced Light Source (ALS) in Berkeley. The SSRL elliptically polarizing undulator (EPU) employs a 6.5 cm period, with 0.2 T horizontal and vertical fields, optimized for elliptically polarized undulator radiation in the 300–1000 eV spectral region.[28] The ALS EPU has a 5.0 cm period, with maximum horizontal and vertical magnetic fields of 0.55 and 0.80 T, respectively. It has 37 periods and provides circularly polarized radiation tunable from 130 eV to 700 eV.[29] Higher photon energies are accessible with elliptical polarization. Recent reviews of periodic magnet structures (insertion devices) for third generation hard x-ray facilities are presented in Refs. 30–32.

5.5 THE SCALE OF HARMONIC MOTION

To understand undulator harmonic motion and the resultant radiated power, it is instructive to continue the analysis of electron dynamics for the case of K approaching unity. We will transform to the frame of reference moving with the average electron velocity $\bar{v}_z$. In this frame, the motion is a simple harmonic, or described in terms of Fourier coefficients of simple harmonics. Therefore, we can utilize the well-known results for radiation from an oscillating electron, summarized earlier in this chapter.

To begin the analysis, we recall the earlier result, Eq. (5.19):

$$v_x = \frac{Kc}{\gamma} \sin\left(\frac{2\pi z}{\lambda_u}\right)$$

To determine the oscillation amplitude and accelerations we must find $v_x(t)$, rather than $v_x(z)$.

To do so, we must utilize our knowledge of $z = z(t)$ and do the necessary transformations to the frame of reference moving with the average electron motion. In this frame of reference, at least in the low-K undulator regime, the motion is described in terms of a few simply related harmonic motions. To do this, we recall Eq. (5.23a):

$$\mathrm{v}_z \simeq c\left[1 - \frac{1}{2\gamma^2} - \frac{K^2}{2\gamma^2}\sin^2\frac{2\pi z}{\lambda_u}\right]$$

Recalling that $\sin^2\alpha = (1-\cos 2\alpha)/2$ and defining $k_u z = 2\pi z/\lambda_u$, where k_u is the wavenumber, we rewrite the above as previously in Eq. (5.23b):

$$\mathrm{v}_z = c\left[1 - \frac{1 + K^2/2}{2\gamma^2} + \frac{K^2}{4\gamma^2}\cos(2k_u z)\right]$$

Noting that $z = \int \mathrm{v}_z\, dt$, we have

$$z(t) = c\underbrace{\left(1 - \frac{1}{2\gamma^{*2}}\right)}_{\beta^*} t + \frac{cK^2}{4\gamma^2}\int \cos[2k_u z(t)]\, dt$$

where $z(t)$ appears twice. Noting that the cosine term is bounded, and approximating $z(t) \simeq \beta^* ct$ in the integral, this gives, to first order,

$$z \simeq c\beta^* t + \frac{cK^2}{4\gamma^2 \cdot 2k_u c\beta^*}\sin 2k_u\beta^* ct \tag{5.66}$$

where we have used the following definitions:

$$\gamma = \frac{1}{\sqrt{1-\beta^2}}$$

and

$$\gamma^* = \frac{1}{\sqrt{1-\beta^{*2}}} = \frac{\gamma}{\sqrt{1+K^2/2}}$$

Therefore, for β approaching unity,

$$\beta^* = 1 - \frac{1}{2\gamma^{*2}} \tag{5.67a}$$

$$\beta^* = 1 - \frac{1 + K^2/2}{2\gamma^2} \tag{5.67b}$$

Substituting $\omega_u = \beta^* k_u c$ and rearranging terms, Eq. (5.66) becomes

$$z - \beta^* ct \simeq \frac{K^2}{8\gamma^2 k_u \beta^*}\sin 2\omega_u t$$

The Lorentz transformation, as described in Appendix F, can be used to transform this equation from the laboratory frame of reference $(z,\ t)$ to the electron frame of reference $(z',\ t')$.

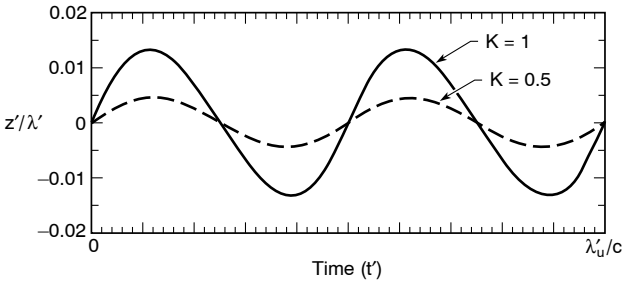

FIGURE 5.28. Axial motion $z'(t')$ for an electron traversing a low K undulator, as seen in the moving (γ^*) frame of reference. Note the double oscillation for a single period of the magnet structure, and the distortion for higher K as a $4\omega'$ contribution pulls the positive amplitude peaks earlier in time and pushes the negative peaks later in time.

Using the transformation [Appendix F, Eq. (F.1)], the z'-motion takes the form

$$\frac{z'}{\gamma^*} \simeq \frac{K^2}{8\gamma^2 k_u \beta^*} \sin 2\omega_u \left[\gamma^* \left(t' + \frac{\beta^* z'}{c} \right) \right]$$

Multiplying through by γ^*, noting that $\omega_u = k_u c$, and taking $\beta^* \simeq 1$, one has

$$z' \simeq \frac{K^2}{8\gamma k_u (1 + K^2/2)^{1/2}} \sin(2\omega_u \gamma^* t' + 2k_u \gamma^* z')$$

For convenience, we define

$$K^* \equiv \frac{K}{(1 + K^2/2)^{1/2}} \tag{5.68}$$

where we note that for large K, K^* approaches $\sqrt{2}$. We also note that because of the Lorentz contraction $k'_u = \gamma^* k_u$, with corresponding frequency $\omega'_u = \gamma^* \omega_u$. Thus z' can be written as

$$z'(t') = \frac{K^{*2}}{8k'_u} \sin(2\omega'_u t' + 2k'_u z') \tag{5.69}$$

where we observe the complexity of this equation in that z' appears both on the left and in a phase term on the right. A numerical solution of this equation is illustrated in Figure 5.28, showing the basic second harmonic motion for a relatively low K-value (two full cycles of motion in a time period λ'_u/c), with an observable asymmetry for $K = 1$, where the sine function peaks early in the first half cycle and late in the second half cycle. This asymmetric behavior indicates the growing presence of still higher harmonics as K grows from very small values to unity and beyond. Before proceeding to the consideration of higher K-values, we first examine the low K case somewhat further for a better insight into the motion and amplitude scaling in this important parameter regime.

Since z', as described in Eq. (5.69), is bounded by the sine function to an oscillation amplitude $z' \simeq K^{*2}/8k'_u$, the second phase term, $2k'_u z'$, never exceeds $K^{*2}/4$. This is in contrast with the first phase term, $2\omega'_u t'$, which dominates the oscillations for small K^*. In

this limit the lowest order solution for $z'(t')$ is

$$z'(t') \simeq \frac{K^{*2}}{8k'_u} \sin 2\omega'_u t' \tag{5.70}$$

which displays a double-frequency oscillation in the axial direction, with an amplitude that scales as K^{*2}. Note that the validity of this approximation, for instance $K^{*2}/4 < 0.1$, corresponds to $K < 0.7$, while $K^{*2}/4 < 0.2$ corresponds to $K < 1.1$. As the axial "sloshing amplitude," the z' motion serves as the amplitude for second harmonic radiation, and also as the coupling mechanism between fundamental and higher harmonics. Note that the axial oscillation velocity, $v'_z = dz'/dt'$, is bounded by $K^{*2}c/4$.

To determine the third harmonic of the motion, we return to the calculation of $x(t)$, where, as we found in Section 5.4.3 [in the development of Eq. (5.33)],

$$x \simeq -\frac{K}{\gamma k_u} \cos \omega_u t$$

Again using the Lorentz transformations $x = x'$ and $t = \gamma^*(t' + \beta^* z'/c) \simeq \gamma^*(t' + z'/c)$,

$$x' \simeq -\frac{K}{k_u \gamma} \cos \omega_u \gamma^* \left(t' + \frac{z'}{c} \right)$$

Using Eq. (5.70) for $z'(t')$, and noting that the Doppler shifted wavenumber and frequency are $k'_u = \gamma^* k_u$, and $\omega'_u = \gamma^* \omega'_u$, the x'-motion becomes

$$x'(t') \simeq -\frac{K^*}{k'_u} \cos \left(\omega'_u t' + \frac{K^{*2}}{8} \sin 2\omega'_u t' \right) \tag{5.71}$$

If we let $\epsilon = K^{*2}/8$, Eq. (5.71) becomes

$$x'(t') \simeq -\frac{K^*}{k'_u} \cos(\omega'_u t' + \epsilon \sin 2\omega'_u t')$$

Using the trigonometric identity (Appendix D) that $\cos(\alpha + \beta) = \cos\alpha \cos\beta - \sin\alpha \sin\beta$, the expression for $x'(t')$ can be expanded as

$$x'(t') \simeq -\frac{K^*}{k'_u} [\cos \omega'_u t' \cos(\epsilon \sin 2\omega'_u t') - \sin \omega'_u t' \sin(\epsilon \sin 2\omega'_u t')]$$

For $\epsilon \ll 1$ this becomes

$$x'(t') \simeq -\frac{K^*}{k'_u} [\cos \omega'_u t' - \epsilon \sin \omega'_u t' \sin 2\omega'_u t']$$

The third harmonic component is obtained from the last term by using the trigonometric identity (Appendix D) $\sin\alpha \sin\beta = [\cos(\alpha - \beta) - \cos(\alpha + \beta)]/2$. The expression for $x'(t')$ is then

$$x'(t') \simeq \frac{-K^*}{k'_u} \left[\cos \omega'_u t' - \frac{\epsilon}{2} \cos \omega'_u t' + \frac{\epsilon}{2} \cos 3\omega'_u t' \right]$$

For $\epsilon = K^{*2}/8 \ll 1$ the dominant terms are

$$x'(t') \simeq -\frac{1}{k'_u}\left[K^* \cos\omega'_u t' + \frac{K^{*3}}{16}\cos 3\omega'_u t'\right] \tag{5.72}$$

The first term describes the fundamental oscillation as the electron traverses the periodic magnet structure, while the second term describes the third harmonic component of the motion. Thus both first and third harmonic radiations will have the same (x') polarization.

For the low-K undulator case the lowest order harmonic motions are described by Eqs. (5.70) and (5.72), which we restate below in terms of the fundamental wavelength in the moving reference frame, $\lambda'_u = 2\pi/k'_u$, as

$$\frac{x'(t')}{\lambda'_u} \simeq -\frac{1}{2\pi}\left[K^* \cos\omega'_u t' + \frac{K^{*3}}{16}\cos 3\omega'_u t'\right] \tag{5.72}$$

$$\frac{z'(t')}{\lambda'_u} \simeq \frac{1}{2\pi}\left[\frac{K^{*2}}{8}\sin 2\omega'_u t'\right] \tag{5.70}$$

We observe that the various harmonic amplitudes scale as K^{*n}, so that harmonic motion can be expected to grow very rapidly as K approaches and exceeds unity (a subject for the next section). Furthermore, since the power radiated scales as the square of acceleration for the respective harmonics, we can anticipate that harmonic power per unit solid angle will scale as

$$\frac{dP'}{d\Omega'} \propto n^4 K^{*2n}$$

i.e., $a_n \propto n^2 K^{*n}$, $dP'/d\Omega' \propto a_n^2$. Thus the radiated power will indeed grow very quickly with increasing K. Note, however, that the growth scales with K^*, so that for a given harmonic there is a built-in saturation as K^* levels off at a value of $\sqrt{2}$ for large K. Rather, as we will see in the following section, the radiation evolves to ever higher harmonics. Note also, from Eqs. (5.70) and (5.72), that the harmonic amplitudes, scaled to their respective wavelengths (λ'_u/n), are each bounded to values less than $K^{*n}/2\pi$, so that for $K \ll 1$ the dipole approximations $x'_u/\lambda'_u \ll 1$ are well satisfied, i.e.,

$$\frac{\left|x'_{\omega'_u}\right|}{\lambda_u} \leq \frac{K^*}{2\pi} \tag{5.73a}$$

$$\frac{\left|z'_{2\omega'_u}\right|}{\lambda'_u/2} \leq \frac{1}{4}\frac{K^{*2}}{2\pi} \tag{5.73b}$$

$$\frac{\left|x'_{3\omega'_u}\right|}{\lambda'_u/3} \leq \frac{3}{16}\frac{K^{*3}}{2\pi} \tag{5.73c}$$

For modest K-values the motion in the electron reference frame approximates a figure eight. This can be seen by combining the fundamental and second harmonic terms in Eqs. (5.70) and (5.72), viz., for small K

$$\frac{x'}{\lambda'_u} \simeq -\frac{K}{2\pi}\cos\omega'_u t'$$

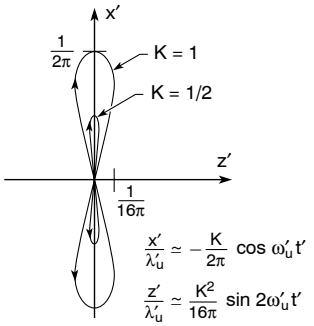

FIGURE 5.29. The x', z'-motion of an electron in the moving (γ^*) frame of reference, as it traverses a low-K undulator.

and

$$\frac{z'}{\lambda'_u} \simeq \frac{K^2}{16\pi} \sin 2\omega'_u t'$$

so that the electron executes two z' oscillations for each x' oscillation, as illustrated in Figure 5.29.

Note that the relative width of the figure eight grows with increasing K, as x' is proportional to K, while the z'-motion is proportional to K^2. In the following section we consider the more complex transition from undulator to wiggler radiation as K exceeds unity, taking on very large values and thus leading to a domination by higher harmonics. In this limit the harmonics become very close, and various practical effects lead to their (laboratory) observation as a smoothed continuum at very high photon energies.

5.6 THE TRANSITION FROM UNDULATOR TO WIGGLER RADIATION

We have seen in the preceding sections that as K increases toward unity the radiated power in higher harmonics grows rapidly. Indeed, for $K \gg 1$ analysis shows the emergence of a large number of ever stronger harmonics, extending to ever higher photon energies. Figure 5.30 shows the development of this comblike harmonic structure for increasing values of the magnetic deflection parameter K. The curves shown are for the limiting case in which all the electrons are contained within a vanishingly small phase space volume, $\epsilon = \pi\sigma\sigma' \to 0$, with the radiation observed in a very small acceptance cone of half angle $\Delta\theta \to 0$. Note that in these limits the even harmonics, which are zero on axis, do not appear. Although the harmonic spikes seen in Figure 5.30 would be broadened for finite emittance, a more important factor in the case of high K wiggler radiation is the observation cone angle, $\Delta\theta$. With the radiated energy spread into so many harmonics, and into a fan of angular width K/γ, it is natural to utilize the available photons by accepting a larger radiation cone. In this case the relative spectral bandwidth of each harmonic expands in frequency from values of order $1/N$ to values dominated by the $\gamma^2\theta^2$ term in the undulator equation (5.28). The harmonic spikes then merge into a quasi-continuum, much like that seen earlier for bending magnet radiation, with interesting consequences.

The broadening of harmonics and their merger into a smooth continuum can be understood better if we consider the various mechanisms involved and estimate the effect of each. We again follow the path of considering a small phase space electron beam traversing a periodic

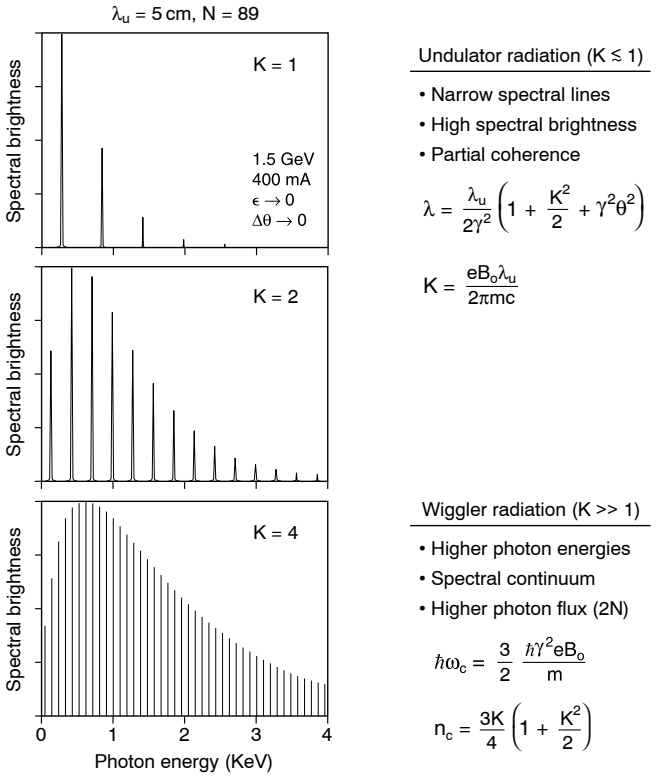

FIGURE 5.30. The transition from undulator radiation ($K \leq 1$) to wiggler radiation ($K \gg 1$) is illustrated. The emergence of bright and more numerous harmonics is evident as the magnetic strength (K) is increased. Spectral brightness is indicated on axis in the limits of very small electron beam phase space (ϵ) and very small angular acceptance ($\Delta\theta$). The comblike spectrum eventually merges to a continuum for finite emittance and acceptance angle in the wiggler limit ($K \gg 1$). (With K.J. Kim, unpublished.)

magnet structure of N periods, and initially consider a near-axial observation of radiation within a relatively narrow acceptance cone. In this case the even harmonics are, at least initially, not observed. Through a little algebraic manipulation of the undulator equation for harmonic n [see Eq. (5.30)] one can show that the separation between harmonics on axis (only odd harmonics appear) is given by

$$\Delta f_{\Delta n=2} = 2\left(\frac{2c\gamma^{*2}}{\lambda_u}\right) = 2f_1 \tag{5.74}$$

where f_1 is the frequency of the fundamental and the subscript $\Delta n = 2$ reminds us that the separation is between harmonics n and $n + 2$. Since the relative bandwidth [Eq. (5.31)] for the nth harmonic of an N-period undulator in terms of frequency is

$$\frac{\Delta f_{n,N}}{f_n} = \frac{1}{nN}$$

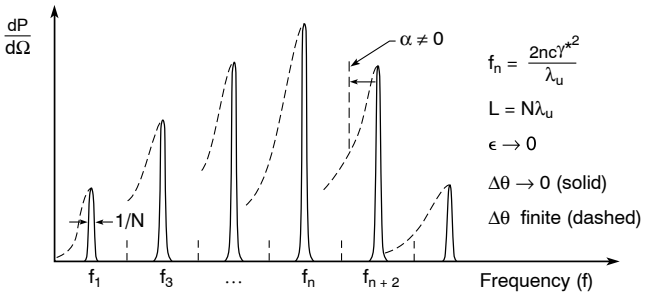

FIGURE 5.31. The effect of finite acceptance angle ($\Delta\theta$) is shown by dashed lines superposed on the spectrum of harmonic radiation for zero acceptance angle (solid lines). A small electron beam phase space ($\epsilon = 0$) is assumed in both cases. The solid lines also shift to lower frequencies (lower photon energies hf) for electron trajectories at angle α to the z-axis. For sufficiently large acceptance angle and magnetic field strength the harmonics merge into a smooth continuum. However, for finite K and $\Delta\theta$ the spectrum may continue to display many sharp peaks and valleys, particularly in the lower photon energy region.

the absolute bandwidth can be written as

$$\Delta f_{n,N} = \frac{f_n}{nN} = \frac{1}{N} \cdot f_1 \tag{5.75}$$

The bandwidth of radiation collected within an angular aperture 2θ (radiation cone of half angle θ) is, for the nth harmonic [an extension of Eq. (5.13) for finite K]

$$\Delta f_{n,\gamma^*\theta} = \gamma^{*2}\theta^2 f_n = n\gamma^{*2}\theta^2 f_1 \tag{5.76}$$

Finally, we note that an individual electron traveling somewhat off axis at an angle α will experience a somewhat longer period, and further, the observed radiation will be affected by the equivalent of an off-axis Doppler shift. The net result is a shifted frequency [see Eq. (5.54)]

$$\Delta f_{n,\alpha} = n\gamma^{*2}\alpha^2 f_1 \tag{5.77a}$$

Note that for an electron storage ring there are many electrons in each bunch with random angular excursions described statistically by σ'. Thus the frequency spread due to random Doppler shifts [Eq. (5.77a)] becomes

$$\Delta f_{n,\alpha} = n\gamma^{*2}\sigma'^2 f_1 \tag{5.77b}$$

With substantial off-axis motion even harmonics are also observed on axis so that the harmonic separation, Eq. (5.74), is replaced by $\Delta f_{\Delta n=1} = f_1$. Combining this with Eq. (5.77b) one obtains the conditions for harmonic merging due to finite electron beam divergence

$$n_m\gamma^{*2}\sigma'^2 \geq 1 \tag{5.78}$$

Based on these estimates, Figure 5.31 sketches the expected frequency spectrum. The sketch is for a modest value of K where the various effects can still be distinguished. Note that it is presented in frequency space; conversion to photon energy requires multiplication by Planck's constant (h). The solid lines, corresponding to a small acceptance angle $\Delta\theta$, show

a series of harmonics at frequencies n times the fundamental ($2c\gamma^{*2}/\lambda_u$), with only the odd harmonics observed on axis. According to Eq. (5.74) they are separated by an interval $2f_1$, and according to Eq. (5.75) they each have a width $1/N$ times the fundamental.

A very important consideration is that of finite angular acceptance at moderate to high K operation. To understand this merging to a continuum for finite acceptance angle θ, we note that even harmonics will be observed off axis, and thus again replace Eq. (5.74) by $\Delta f_{\Delta n=1} = f_1$. Combining this with Eq. (5.76) we obtain the condition for harmonic merging due to a finite acceptance angle

$$n_m \gamma^{*2} \theta_m^2 = 1 \tag{5.79a}$$

Thus the condition for harmonic merging within a finite acceptance angle θ is

$$n \geq \frac{1}{\gamma^{*2}\theta^2} \tag{5.79b}$$

Eq. (5.79) suggests an evolution to a quasi-continuum spectrum, particularly for the higher harmonic region of the spectrum where much of the radiated energy resides.

To better understand the evolution from a spectrum characterized by sharply peaked harmonics to a relatively smooth continuum similar to that from a bending magnet, it is useful to consider further the relationship between harmonic number (n) and K. In an earlier section on bending magnet radiation we discussed the critical photon energy [Eq. (5.7)]:

$$E_c = \hbar\omega_c = \frac{3e\hbar B\gamma^2}{2m}$$

for which half of the radiated energy appears at higher photon energy, and half at lower photon energy. Here on the other hand we have been discussing the generation of a comblike structure of very high harmonics from a wiggler. A useful notion is to combine the two and introduce the concept of a critical harmonic number for which half the radiated energy is in higher harmonics, and half is in lower harmonics.

A few simple substitutions provide the desired result. Rewriting the critical energy in terms of the non-dimensional magnetic deflection parameter [Eq. (5.18)]

$$K = \frac{eB_0\lambda_u}{2\pi mc}$$

this becomes

$$\hbar\omega_c = \frac{3\pi c\hbar\gamma^2 K}{\lambda_u} \tag{5.80}$$

For a periodic structure the harmonic frequencies, from the harmonic undulator equation (5.30), are

$$\omega_n = \frac{2\pi c}{\lambda_n} = \frac{4\pi nc\gamma^2}{\lambda_u(1 + K^2/2)} \tag{5.81}$$

Equating Eqs. (5.80) and (5.81), we can define a *critical harmonic number*, n_c, viz.,

$$\omega_c \equiv \omega_{n,c} = n_c\omega_1$$

Thus

$$\frac{3\pi c\gamma^2 K}{\lambda_u} = \frac{4\pi c\gamma^2}{\lambda_u(1+K^2/2)} \cdot n_c$$

or

$$\boxed{n_c = \frac{3K}{4}\left(1+\frac{K^2}{2}\right)} \tag{5.82}$$

which for large K takes the form

$$n_c \simeq \frac{3K^3}{8}, \quad K \gg 1 \tag{5.83}$$

The 19-period wiggler at the 1.9 GeV ALS, as indicated in Table 5.1, has a peak magnetic flux density on axis of $B_0 = 2.13$ T, a period of 16.0 cm, a critical photon energy of 5.1 keV (0.24 nm wavelength), and a deflection parameter at peak field of $K = 32$, with a corresponding critical harmonic number n_c in excess of 12,000.

Under the circumstances it is interesting to reconsider the condition for harmonic merging given by Eq. (5.79a). For very large K the condition for spectral merging of the harmonics becomes

$$\theta_m = \frac{\sqrt{1+K^2/2}}{\gamma\sqrt{n/2}} \simeq \frac{K}{\gamma\sqrt{2n}} \tag{5.84a}$$

or for n_c

$$\theta_{m,c} \simeq \frac{1.2}{\gamma\sqrt{K}} \tag{5.84b}$$

For the example cited, with $K = 32$, this corresponds to a collection angle of $\theta_{m,c} \simeq 0.2/\gamma$, or only 50 μrad for $\gamma = 3914$. Indeed, with a horizontal radiation fan of $\pm K/\gamma$, one might use a significantly larger acceptance angle to collect the radiation, thus ensuring spectral merging for very low harmonics, well below n_c.

The picture that emerges for very large K operation, where the spectral energy density shifts to very high harmonics, is one of spectrally isolated lower harmonics, a merger into a quasi-continuum well below the critical harmonic, and finally a relatively smooth continuum for $n > n_c$. The high photon energy portion of the spectrum is similar to that of a bending magnet, but intensified by a factor $2N$ (two peak field locations per period), and shifted to a higher critical photon energy because the peak wiggler field is much greater than that of a bending magnet.[††] An example of a detailed calculation is presented in Figure 5.32 for a 6 cm period magnet structure, operating at $K = 3.7$, in the 2 GeV storage ring Elettra in Trieste, Italy.[13] In this example $n_c = 22$, and with an acceptance angle of 0.1 mrad, harmonic merging

[††] In a circular orbit the beam energy and magnetic field are matched so as to maintain a path of constant radius and thus avoid hitting the vacuum wall. In a periodic structure the magnetic fields can be considerably larger, as alternate poles redirect the beam, keeping it near the vacuum chamber axis at all times.

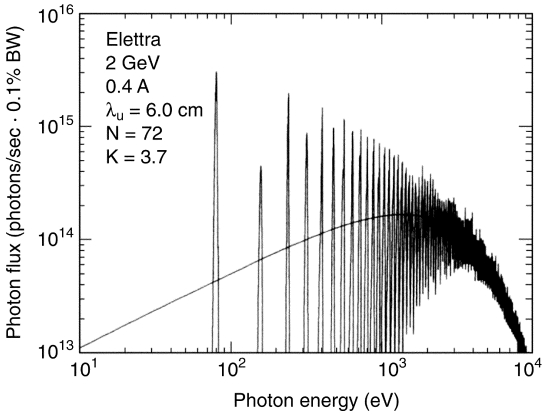

FIGURE 5.32. Calculated photon flux near the central axis for a 6 cm periodic magnet structure operating at an intermediate K-value of 3.7. The calculation is performed for the third generation 2 GeV synchrotron radiation facility Elettra in Trieste, Italy. The critical harmonic number, n_c is 22 for this K-value. The acceptance half angle is 0.1 mrad. Harmonic merging occurs for this acceptance angle at $n_m \simeq 51$. (Courtesy of R.P. Walker and B. Diviacco.[13])

occurs at $n \simeq 51$. This is an interesting illustration of the evolution from undulator to wiggler radiation. For significantly higher K and larger acceptance angle, harmonic merging occurs for $n \ll n_c$. This corresponds to the wiggler limit, which is discussed in the following section.

5.7 WIGGLER POWER AND FLUX

We have approached the subject of radiation from relativistic electrons traversing periodic magnet structures from a small K theory of undulator radiation. While this has clear advantages, the approximations made are not valid for large K wiggler radiation. The advantages of small K theory are that one is able to borrow significant results from well-known classical dipole radiation, transform the results to the laboratory frame of reference, and obtain simple analytic expressions and a clear physical model for the major features of undulator radiation, including observable wavelengths, bandwidth, polarization, power scaling, and the emergence of harmonics. For wiggler radiation with $K \gg 1$ the motion becomes significantly more complex – relativistic even in the electron (γ^*) frame of reference – and the acceleration becomes very strong at the extremes of its off-axis excursions. Indeed, the accelerations become so strong at the extrema that the radiation appears not to come from a near-point-source oscillator on axis, but rather from an alternating sequence of two points at the extremes of motion in a highly non-sinusoidal trajectory. Fourier analysis of this radiation would clearly involve very sharp temporal gradients (time derivatives), and thus lead to very high harmonics of the basic periodic motion. This causes a shift to higher photon energies, and thus shorter wavelengths. Because the accelerations are greater (the time derivatives are sharper), there is also a substantial increase in radiated power. The angular width however is increased in the horizontal plane to a value K/γ, and the apparent source size is increased, particularly if observed from a position somewhat off axis, thus significantly reducing overall brightness.

A discussion of the relevant physics, including analytic and numerical solutions for arbitrary K, is given by Kim (Ref. 3). For example, the total radiated power in *all* harmonics,

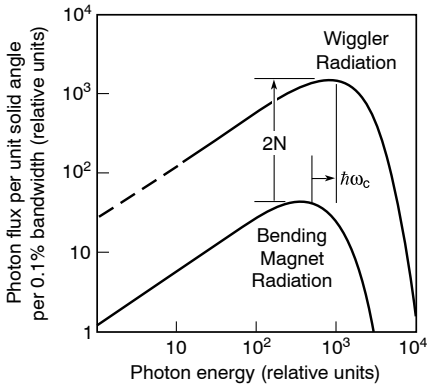

FIGURE 5.33. Comparison of on-axis photon flux per unit solid angle and per unit relative spectral bandwidth for bending magnet radiation and wiggler magnet radiation from the same storage ring. The shape of the curves is basically the same, $H_2(\omega/\omega_c)$. The photon flux from the wiggler is $2N$ higher in the case illustrated, and shifted $2\times$ to higher photon energy by the critical energy $\hbar\omega_c$. The wiggler curve below the critical photon energy (shown dashed here) has a complex harmonic content that may not be smooth, depending on the acceptance angle and electron beam divergence (see text).

integrated over all angles and wavelengths, for arbitrary K, is given by

$$P_T = \frac{\pi e K^2 \gamma^2 I N}{3\epsilon_0 \lambda_u} \tag{5.85a}$$

Note that this is similar to our earlier result for $P_{T,1}$, the total power radiated to all angles in the fundamental ($n = 1$ only), Eq. (5.50a), except that the factor $(1 + K^2/2)^2$ is absent from Eq. (5.85a). This factor accounts for the power radiated to *all harmonics*. In practical units the total power radiated to all harmonics, for arbitrary K, is given by

$$P_T = \frac{1.90 \times 10^{-6}(\mathrm{W}) K^2 \gamma^2 N I(\mathrm{A})}{\lambda_u(\mathrm{cm})} \tag{5.85b}$$

Typical values for radiated power from high K wigglers are given in Table 5.1. Both radiate about 10 kW of x-ray power, with critical photon energies of 5.1 keV and 33 keV for the soft x-ray and hard x-ray facilities, respectively. Expressions for the photon flux from a wiggler, in the limits $K \gg 1$ and $n \gg 1$, are similar to those for bending magnet radiation, but increased by a factor of $2N$ due to the strong acceleration that occurs twice in each period at the peaks of magnetic field. For instance the on-axis photon flux per unit solid angle, per unit relative spectral bandwidth, is given by (Kim[3])

$$\left.\frac{d^2F}{d\Omega\, d\omega/\omega}\right|_0 = 2.65 \times 10^{13} N E_e^2(\mathrm{GeV}) I(\mathrm{A}) H_2(E/E_c) \frac{\text{photons/s}}{\text{mrad}^2(0.1\%\text{BW})} \tag{5.86}$$

where $H_2(y)$ is illustrated in Figure 5.7 and partially tabulated in Table 5.2. Relative spectra for both a bending magnet and a wiggler are presented in Figure 5.33. Note the $2N$ times larger photon flux for the wiggler, and the shift to higher photon energies ($\hbar\omega_c$). Expressions for off-axis photon flux in the two orthogonal polarizations are given by Kim.[3]

To calculate the photon flux or power radiated by a wiggler within a given spectral bandwidth we can begin with Eq. (5.8) for bending magnet radiation with the dependence on vertical angle (ψ) already integrated out. To adapt this to wiggler radiation we multiply by $2N$ to obtained the photon flux per unit horizontal angle θ, and per unit relative spectral bandwidth

$$\frac{d^2F}{d\theta\, d\omega/\omega} = 4.92 \times 10^{13} N E_e(\text{GeV}) I(\text{A}) G_1(E/E_c) \frac{\text{photons/s}}{\text{mrad} \cdot (0.1\%\text{BW})} \tag{5.87}$$

where the various parameters are described below Eq. (5.8), and where the function $G_1(E/E_c)$ is tabulated in Table 5.2 and shown graphically in Figure 5.7. As we have seen, wiggler radiation in the horizontal plane is dominated by the electron trajectory [Eq. (5.20)] with angular deflection limits $\pm K/\gamma$. This results in an angular photon flux dependence[3] $dF/d\theta = F_0\sqrt{1-(\gamma\theta/K)^2}$, which has a characteristic angular extent $(2\theta)_{\text{FWHM}} = \sqrt{3}K/\gamma$. With this θ-dependence an angular integration of Eq. (5.87) leads to a multiplicative factor[‡‡] of $1.57K/\gamma$, giving a wiggler radiated photon flux per unit relative spectral bandwidth of

$$F = 3.94 \times 10^{13} N K I(\text{A}) G_1(E/E_c) \frac{\text{photons/s}}{(0.1\%\text{BW})} \tag{5.88a}$$

where we have used Eq. (5.5) to replace γ by E_e. This equation can be written alternatively in terms of the magnetic flux density B_0 and the wiggler length $L = N\lambda_w$, using Eq. (5.18b) to express K in terms of $B_0(T)$ and λ_w(cm), as

$$F = 3.68 \times 10^{15} L(m) B_0(T) I(\text{A}) G_1(E/E_c) \frac{\text{photons/s}}{(0.1\%\text{BW})} \tag{5.88b}$$

where $E = \hbar\omega$ is the photon energy, and from Eq. (5.76b) E_c (keV) = $0.665E_e^2$ (GeV)$B_0(T)$. Inspection of Eq. (5.88b) indicates that there is a linear dependence on wiggler length, peak magnetic flux density, and current as expected. To first order there is no dependence on electron beam energy, only a very slow dependence through E_c in $G_1(E/E_c)$. A potential application of these formulas is the use of wiggler radiation as a source for EUV lithography (see Chapter 4, Section 4.5.3, and Chapter 10, Section 10.2). At a wavelength of 13.4 nm (92.5 eV photon energy), and within a relative spectral bandwidth of 0.1%, Eq. (5.88b) gives a radiated wiggler power of

$$P_{13.4\text{nm},0.1\%\text{BW}} = (5.46 \times 10^{-2}\text{W}) L(m) B_0(T) I(\text{A}) G_1(E/E_c) \tag{5.89}$$

To understand what performance might be achieved in a practical application we consider a wiggler similar to that employed at the ALS ($B_0 = 2.1$ T, $\lambda_w = 16$ cm, $K = 32$, $N = 19$, and $L = 3.0$ m) in an optomized[¶¶] 0.5 GeV, 1A storage ring, which would provide a radiated power of 8.1 W within a 2.5% relative spectral bandwidth at 13.4 nm, and within a 3 mrad by 56 mrad angular emission fan.

[‡‡] Y. Liu, private communication.

[¶¶] A small circumference ring, perhaps having room temperature magnets, with a low energy, high current, large phase-space electron beam, and a value of $G_1(E/E_c) = 0.92$ at $E/E_c = 0.26$. For example see the paper by D.C. Ockwell, et al., "A Synchrotron Light Source for EUV Lithography," *J. Vac. Sci. Technol. B17* (1999) and also product literature for Aurora 2s and 2d by the Sumitomo Heavy Industry Corporation.

5.8 FEMTOSECOND PULSE GENERATION

The study of dynamics in physical systems often requires time resolution beyond the picosecond capabilities presently available with synchrotron radiation. Femtosecond (10^{-15} s) capabilities have been available for many years at visible wavelengths.[33] There exists a wide interest in the extension of femtosecond techniques to the EUV, soft x-ray, and x-ray regions of the spectrum. Proposed techniques include the generation of very short electron bunches that would subsequently radiate femtosecond pulses, techniques that would slice a short electron bunch out of a longer bunch, and techniques involving the upconversion of femtosecond visible light pulses to significantly shorter wavelengths. Pellegrini and a broadly based group of collaborators[34] have proposed building a high power free electron laser (FEL) that, if successful, would accelerate 160 fs pulses at wavelengths of order 4 nm. The proposal is based on high gain self-amplified spontaneous emission (SASE), using the existing SLAC[§§] linear accelerator (linac) operating at 7 GeV electron energy, and a 60 m long 8.3 cm period undulator. Recent papers about this and other options are discussed by Kulipanov, Skrinsky, and Vinokurov[35] and by Kim.[36]

Schoenlein, Leemans, Shank, and colleagues[37–39] have taken a different approach, employing strongly Doppler shifted Thomson scattering of femtosecond infrared (800 nm) laser pulses. In their experiments 100 fs (FWHM) laser pulses are scattered off the 50 MeV electrons ($\gamma = 98$) of a linear accelerator at the ALS in Berkeley. Nominal 300 fs duration pulses of 30 keV photons (0.04 nm wavelength) are scattered 90° into a narrow cone ($\theta \simeq 1/\gamma$) in the direction of the electron beam.[37–39] The 300 fs x-rays have been used in time resolved diffraction experiments to study lattice expansion in InSb under high intensity short duration laser excitation.[40]

Zholents and Zolotorev[41] have suggested procedures to extract very short electron bunches from longer electron bunches through the use of high intensity short duration laser pulses. In their proposal, intense femtosecond light pulses are resonantly matched to electron periodic motion in an undulator. The excited electrons are spatially separated from their neighbors. In subsequent passage through a bending magnet field they radiate normal bending magnet radiation, but of very short temporal duration. Experiments are currently underway at the ALS in Berkeley, led by Schoenlein et al., employing 800 fs infrared laser pulses at 800 nm wavelength, followed by a 1.27 T bending magnet with 3.1 keV critical energy photons (0.41 nm wavelength). To resonantly match the laser-induced electron oscillations to those of the undulator, they utilize first harmonic motion ($n = 1$) in a high K wiggler mode of operation ($K = 16.5$ for $\lambda_u = 16$ cm). In a third approach, Larsson, Heimann, Falcone, and their colleagues have developed a technique for carving a nominal 1 ps x-ray pulse out of longer synchrotron radiation pulses, using femtosecond laser (Ti : Al_2O_3, 800 nm wavelength) irradiated crystals. Using a double crystal, double laser pulse irradiation technique with variable delay, they have observed time dependent Bragg reflection at 5 keV. In a cross-correlation mode, they have detected variations in the crystal structure to a time resolution[42] of 2 ps, with the potential of reducing this to sub-picosecond resolution with improved statistics. Using cross-correlated x-ray diffraction, they have studied reversible disordering of the structure of an InSb crystal.[43] This offers another option for the pursuit of femtosecond short wavelength radiation. Further options, involving high harmonic generation in neutral gases, and lasing at EUV/soft x-ray wavelengths, are discussed in Chapters 6 and 7.

[§§]Stanford Linear Accelerator Center, at Stanford University.

REFERENCES

1. J.D. Jackson, *Classical Electrodynamics* (Wiley, New York, 1998), Third Edition, Chapter 14; also see First Edition (1962), Section 14.4.
2. A. Hofmann, "Quasi-Monochromatic Radiation from Undulators," *Nucl. Instrum. and Meth. 152*, 17 (1978); also see "Theory of Synchrotron Radiation," Stanford Synchrotron Radiation Laboratory report ACD-Note 38 (unpublished).
3. K.-J. Kim, "Characteristics of Synchrotron Radiation," pp. 565–632 in *Physics of Particle Accelerators*, AIP Conference Proccedings 184 (Amer. Inst. of Physics, New York, 1989), M. Month and M. Dienes, Editors; also see K.-J. Kim, "Characteristics of Synchrotron Radiation," *X-Ray Data Booklet*, (Center for X-Ray Optics, Lawrence Berkeley National Laboratory, 1999), Second Edition; K.-J Kim, "Optical and Power Characteristics of Synchrotron Radiation Sources," Opt. Engr. *34*, 342 (1995).
4. D.T. Attwood, K. Halbach, and K.-J. Kim, "Tunable Coherent Radiation," *Science 228*, 1265 (14, June, 1985).
5. H. Winick (editor), *Synchrotron Radiation Sources* (World Scientific, Singapore, 1994).
6. P.A. Tipler, *Modern Physics* (Worth, New York, 1978).
7. G.K. Green, Brookhaven National Laboratory, Upton, NY, Report 50522 (also in Report 50595, Vol. II), 1977.
8. K. Halbach, "Physical and Optical Properties of Rare Earth Cobalt Magnets," *Nucl. Instrum. and Meth. 187*, 109 (1981); also "Permanent Magent Undulators," *J. Phys.* (Paris), 44, Colloque C1, Suppl. 2, 211 (1983).
9. R.B. Leighton, *Principles of Modern Physics* (McGraw-Hill, New York, 1959), Chapter 12.
10. J.M.J. Madey, *J. Appl. Phys. 42*, 1906 (1971).
11. T.C. Marshall, *Free Electron Lasers* (Macmillan, New York, 1985).
12. B.M. Kincaid, "A Short-Period Helical Wiggler as an Improved Source of Synchrotron Radiation," *J. Appl. Phys. 48*, 2684 (1977); also see M.R. Howells and B.M. Kincaid, "The Properties of Undulator Radiation," pp. 315–359 in *New Directions in Research with Third Generation Soft X-Ray Synchrotron Radiation Sources* (Kluwer, Dordrecht, 1994), A.S. Schlachter and F.J. Wuilleumier, Editors,
13. R.P. Walker and B. Diviaco, "A Computer Program for Calculating Undulator Radiation and Spectral, Angular, Polarization, and Power Density Properties," *Rev. Sci. Instrum. 63*, 392 (1992); also see R.P. Walker, "Interference Effects in Undulator and Wiggler Radiation Sources," *Nucl. Instr. Methods A 335*, 328 (1993).
14. D.C. Champeney, *Fourier Transforms and their Applications* (Academic Press, NY, 1973), p. 26; E. Hecht, *Optics* (Addison-Wesley, Reading, MA, 1988), Third Edition, pp. 307–308 and p. 649.
15. M. Cornacchia, "Lattices," Chapter 2, pp. 30–58 in *Synchrotron Radiation Sources: A Primer* (World Science, Singapore, 1994), H. Winick, Editor.
16. H. Kitamura, "Future of Synchrotron Radiation," *Kasokuki Kagaku (Accelerator Sci.) 1*, 45 (Ionics Publishing, Tokyo, 1986).
17. M. Born and E. Wolf, *Principles of Optics* (Cambridge Univ. Press, New York, 1999), Sections 4.8.1 and 4.8.3, which deal with photometry and brightness.
18. R.D. Schlueter, "Wiggler and Undulator Insertion Devices," Chapter 14, p. 377 in *Synchrotron Radiation Sources: A Primer* (World Science, Singapore, 1994), H. Winick, Editor.
19. K.-J. Kim, "A Synchrotron Radiation Source with Arbitrarily Adjustable Elliptical Polarization," *Nucl. Instrum. and Meth. A 219*, 425 (1984).
20. M.B. Moissev, M.M. Nikitin, and N.I. Fedosov, "Change in the Kind of Polarization of Undulator Radiation," *Sov. Phys. J. 21*, 332 (1978).
21. J. Bahrdt, A. Gaupp, W. Gudat, M. Mast, K. Molter, W.B. Peatman, M. Scheer, Th. Schroeter, and Ch. Wang, "Circularly Polarized Synchrotron Radiation from the Crossed Undulator at BESSY," *Rev. Sci. Instrum. 63*, 339 (1992); R. David, P. Stoppmanns, S.-W. Yu, R. Kuntze, N. Müller, and U. Heinzmann, "Circularly Polarized Undulator Radiation from the New Double Crossed Undulator Beamline at BESSY and its First Use for Spin Resolved Auger Electron Emission Spectroscopy," *Nucl. Instrum. and Meth. A 343*, 650 (1994).

22. H. Onuki, "Elliptically Polarized Synchrotron Radiation Source with Crossed and Retarded Magnetic Fields," *Nucl. Instrum. and Meth. A 246*, 94 (1986).
23. H. Onuki, N. Saito, and T. Saito, "Undulator Generating any Kind of Elliptically Polarized Radiation," *Appl. Phys. Lett. 52*, 173 (1988).
24. P. Elleaume, "A Flexible Planar/Helical Undulator Design for Synchrotron Sources," *Nucl. Instrum. and Meth. A 291*, 371 (1990).
25. B. Di Viacco and R.P. Walker, "Fields and Trajectories in Some New Types of Permanent Magnet Helical Undulators," *Nucl. Instrum. Meth. A 292*, 517 (1990).
26. S. Sasaki, K. Kakunori, T. Takada, T. Shimada, K. Yanagida, and Y. Miyahara, "Design of a New Type of Planar Undulator for Generating Variably Polarized Radiation," *Nucl. Instrum. Meth. A 331*, 763 (1993).
27. S. Sasaki,"Analysis for a Planar Variably-Polarizing Undulator," *Nucl. Instrum. and Meth. A347*, 83 (1994).
28. R. Carr and S. Lidia, "The Adjustable Phase Planar Helical Undulator," *Proc. SPIE 2013*, 56 (1993); S. Lidia and R. Carr, "An Elliptically Polarizing Undulator with Phase Adjustable Polarization and Energy," *Nucl. Instrum. and Meth. A 347*, 77 (1994); R. Carr, J.B. Kortright, M. Rice, and S. Lidia, "Performance of the Elliptically Polarizing Undulator at SPEAR," *Rev. Sci. Instrum. 66*, 1862 (1995).
29. S. Marks, C. Cortopassi, J. De Vries, E. Hoyer, R. Leinbach, Y. Minamihara, H. Padmore, P. Pipersky, D. Plate, R. Schlueter, and A. Young, "Advanced Light Source Elliptically Polarizing Undulator," *Proc. 1997 Particle Accelerator Conference (1998)*, p. 3221; A. Young, V. Martynov, and H. Padmore, "An Elliptically Polarizing Undulator Beamline at the Advanced Light Source," *J. Electr. Spectr.* (to be published, 1999).
30. H. Kitamura, "Present Status of SPring-8 Insertion Devices," *J. Synchr. Rad. 5*, 184 (1998).
31. E. Gluskin, "APS Insertion Devices: Recent Developments and Results," *J. Synchr. Rad. 5*, 189 (1998).
32. J. Chavanne, P. Elleaume, and P. van Vaerenbergh, "The ESRF Insertion Devices," *J. Synchr. Rad. 5*, 196 (1998).
33. E.P. Ippen, C.V. Shank, and A. Dienes, "Passive Mode Locking of the CW Dye Laseer," *Appl. Phys. Lett. 21*, 348 (1972); R.L. Fork, B.I. Greene, and C.V. Shank, "Generation of Optical Pulses Shorter than 0.1 psec by Colliding Pulse Mode Locking," *Appl. Phys. Lett. 38*, 671 (1981).
34. C. Pellegrini, J. Rosenzweig, G. Travish, K. Bane, R. Boyce, G. Loew, P. Morton, H.-D. Nuhn, J. Paterson, P. Pianetta, T. Raubenheimer, J. Seeman, R. Tatchyn, V. Vylet, H. Winick, K. Halbach, K.-J. Kim, M. Xie, D. Prosnitz, E.T. Scharlemann, R. Bonifacio, L. De Salvo, and P. Pierini, "The SLAC Soft X-Ray High Power FEL," *Nucl. Instrum. Meth. A 341*, 326 (1994).
35. G.N. Kulipanov, A.N. Skrinsky, and N.A. Vinokurov, "Synchrotron Light Sources and Recent Developments of Accelerator Technology," *J. Synchr. Rad. 5*, 176 (1998).
36. K.-J. Kim, "Advanced Capabilities for Future Light Sources," *J. Synchr. Rad. 5*, 202 (1998).
37. R.W. Schoenlein, W.P. Leemans, A.H. Chin, P. Volfbeyn, T.E. Glover, P. Balling, M.S Zolotorev, K.-J. Kim, S. Chattopadhyay, and C.V. Shank, "Femtosecond X-Ray Pulses at 0.4 Å Generated by 90° Thomson Scattering: A Tool for Probing the Structural Dynamics of Materials," *Science 274*, 236 (11 October 1996).
38. W.P. Leemans, R.W. Schoenlein, P. Volfbeyn, A.H. Chin, T.E. Glover, P. Balling, M.S Zolotorev, K.-J. Kim, S. Chattopadhyay, and C.V. Shank, "Interaction of Relativistic Electrons with Ultrashort Laser Pulses: Generation of Femtosecond X-Rays and Microprobing of Electronbeams," *IEEE J. Quant. Electr. 33*, 1925 (1997); W.P. Leemans et al., "X-Ray Based Subpicosecond Electron Bunch Characterization Using 90° Thomson Scattering," *Phys. Rev. Lett. 77*, 4182 (1996).
39. K.-J. Kim, S. Chattopadhyay, and C.V. Shank, "Generation of Femtosecond X-Rays by 90° Thomson Scattering," *Nucl. Instrum. Meth. A 341*, 351 (1994).
40. A.H. Chin, R.W. Schoenlein, T.E. Glover, P. Balling, W.P. Leemans, and C.V. Shank, "Ultrafast Structural Dynamics in InSb Probed by Time-Resolved X-Ray Diffraction," *Phys. Rev. Lett.* (to be published, 1999); A.H. Chin, "Ultrashort X-Ray Pulse Science," Ph.D. thesis, Physics Department, University of California, Berkeley (1998).
41. A.A. Zholents and M.S. Zolotorev, "Femtosecond X-Ray Pulses of Synchrotron Radiation," *Phys. Rev. Lett. 76*, 912 (1996).

42. J. Larsson, Z. Chang, E. Judd, P.J. Schuck, R.W. Falcone, P.A. Heinmann, H.A. Padmore, H.C. Kapteyn, P.H. Buchsbaum, M.M. Murnane, R.W. Lee, A. Machacek, J.S. Wark, X. Liu, and B. Shan, "Ultrafast X-Ray Diffraction Using a Streak Camera Detector in Averaging Mode," *Optics Lett. 22*, 1012 (1997).
43. J. Larsson, P.A. Heinmann, A.M. Lindenberg, P.J. Schuck, P.H. Buchsbaum, R.W. Lee, H.A. Padmore, J.S. Wark, and R.W. Falcone, "Ultrafast Structural Changes Measured by Time-Resolved X-Ray Diffraction," *Appl. Phys. A* (London) *66*, 587 (1998).
44. Further reading: there is much material relevant to this chapter in the proceedings of the international and national Synchrotron Radiation Instrumentation (SRI) conferences. These are generally published as special issues of the journals Nucl. Instrum. and Meth. (NIM), Rev. Sci. Instr. (RSI), and J. Synchr. Rad. Listed here are the editors and years of recent SRI proceedings:

International
F. Wuilleumier and Y. Farge, Editors, NIM *152* (1978).
E.E. Koch, Editor, NIM *203* (1983).
G.S. Brown and I. Lindau, Editors, NIMA *246* (1986)
M. Ando and T. Miyahara, Editors, RSI *60* (1989)
I.H. Munro and D.J. Thompson, Editors, RSI *63* (1992)
J.B. Hastings, S.L. Hulbert, and G.P. Williams, Editors, RSI *66* (1995)
S.S. Hasnain, J.R. Helliwell, and H. Kamitsubo, Editors, *J. Synchr. Rad. 5* (1998).

U.S. National
D.L. Ederer and J.B. West, Editors, NIM *172* (1980)
D.M. Mills and B.W. Batterman, Editors, NIM *195* (1982)
W. Thomlinson and G.P. Williams, Editors, NIM *222* (1984)
M.A. Green, J.P. Stott and P.R. Woodruff, Editors NIMA *266* (1988)
R.C.C. Perera and A.C. Thompson, Editors, NIMA *291* (1990)
R.L. Stockbauer, E.D. Poliakoff and V. Saile, Editors, NIMA *319* (1992)
G.G. Long, D.R. Mueller, and S.K. Southworth, Editors, NIMA *347* (1994)
G.K. Shenoy and J.L. Dehmer, Editors, RSI *67* (1996), [CD-ROM only].
E. Fontes, Editors, AIP *417* (1997).

HOMEWORK PROBLEMS

Homework problems for each chapter will be found at the website:
http://www.coe.berkeley.edu/AST/sxreuv

Chapter 6

PHYSICS OF HOT DENSE PLASMAS

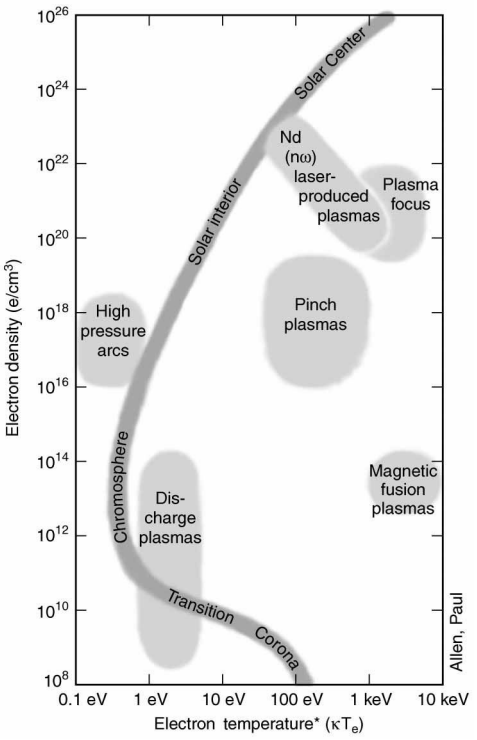

$$f(\mathrm{v}) = \frac{1}{(2\pi)^{3/2}\mathrm{v_e^3}}\, \mathrm{e}^{-\mathrm{v}^2/2\mathrm{v_e^2}} \tag{6.1}$$

$$\mathrm{v}_e = \left(\frac{\kappa T_e}{m}\right)^{1/2} \tag{6.2}$$

$$a^* = \left(\frac{Z\gamma\kappa T_e}{M}\right)^{1/2} \tag{6.97}$$

$$\omega_c = \frac{eB}{m} \tag{6.8}$$

$$\nu_{\mathrm{ei}} \simeq \frac{Z\omega_p}{11N_D}\ln\left(\frac{9\mathrm{N_D}}{2\mathrm{Z}}\right) \tag{6.120c}$$

$$l_{abs} = \frac{n_c}{n_e}\frac{\mathrm{v}_g}{\nu_{ei}} \tag{6.119c}$$

$$n = \left(1 - \frac{n_e}{n_c}\right)^{1/2} \tag{6.114b}$$

$$n_c = \frac{\epsilon_0 m\omega^2}{e^2} \tag{6.112a}$$

$$\left|\frac{\mathrm{v_{os}}}{\mathrm{v_e}}\right|^2 = \frac{I/c}{n_c\kappa T_{\mathrm{e}}} \tag{6.131a}$$

$$I = \sigma T^4 \tag{6.141b}$$

$$\hbar\omega\,\Big|_{\mathrm{max}} = 2.82\kappa T \tag{6.137}$$

$$\omega_p^2 = \frac{e^2 n_e}{\epsilon_0 m} \tag{6.5}$$

$$\lambda_D = \left(\frac{\epsilon_0\kappa T_{\mathrm{e}}}{e^2 n_e}\right)^{1/2} \tag{6.6}$$

$$N_D = \frac{4\pi}{3}\lambda_D^3 n_e \tag{6.7}$$

* $\kappa T_e = 100$ eV corresponds to $T_e = 1.6 \times 10^6$ K

In this chapter the physics of hot dense plasmas is considered. Combining both high temperature and high density, such plasmas are particularly bright sources of EUV through soft x-ray radiation. In general the radiation consists of a broad spectral continuum, plus narrow line emission from the various ionization stages of those elements present. Such plasmas are found in the stars and, on a laboratory scale, at the focus of intense laser beams irradiating material surfaces.

6.1 INTRODUCTION

The study of hot dense plasmas constitutes a subset of plasma physics relevant to the generation of intense x-rays. Such plasmas are found in the stars and, on a smaller scale, at the focus of intense laser beams irradiating material surfaces (see chapter frontispiece). The physics of plasmas involves interaction between many charged particles on a microscopic scale through the electric and magnetic fields associated with their positions and velocities. Fortunately, this extremely complex *many body* problem often may be simplified by the consideration of macroscopic, collective interactions where the charges are described in terms of charge densities and currents. The study of plasmas is rich in interesting phenomena at both the linear and the non-linear level.[1–15] The term "non-linear" refers to various phenomena, such as wave growth or particle acceleration, which depend on some parameter, like temperature or density, in other than a linear manner, or on some combination of such parameters. Non-linear processes can involve frequency sums and differences, harmonics, and mixing phenomena.

Hot dense plasmas have a natural tendency to push at the threshold of many of these strong non-linear mixing processes. In order to generate EUV and soft x-ray radiation, the plasma must consist of particles at very high energies – of the order 100 eV to several keV if they are to radiate such energies during particle–particle interactions, since total energy must be conserved. This may also be understood in terms of blackbody radiation. The peak photon energy is related to the temperature of the radiating body, so that soft x-rays require radiators that are extremely hot. In addition, for the radiation to be intense, the emissions must come from a large number of particles in a small volume, perhaps approaching densities characteristic of solids. Thus the descriptive phrase "hot dense plasma."

Of course, these conditions are far from equilibrium in our $\frac{1}{40}$ eV world. As a consequence, such plasmas are inherently short-lived. The high temperatures imply high velocities that cause the plasmas to rapidly expand and cool. For electron temperatures of 1 keV, a plasma of electrons and silicon ions that is electrically neutral overall will expand at a velocity of order 0.3 μm/ps (where 1 ps $= 10^{-12}$ s, and 1 μm $= 10^{-6}$ m). For comparison, the speed of light in these units is 300 μm/ps. Since a great deal of energy must be imparted to each particle, and there are so many particles per unit volume, these plasmas tend to be very small, on the order of 100 μm in dimension. Thus, a typical time for expansion is

$$\Delta t = \frac{\Delta x}{\mathrm{v}} = \frac{100\ \mu\mathrm{m}}{0.3\ \mu\mathrm{m/ps}} \simeq 300\ \mathrm{ps}$$

As a result the world of hot dense plasmas is generally one of microns (μm) and picoseconds. Clearly, there are detailed phenomena that occur on both shorter and longer time scales, but these simple arguments give a general idea of the domains involved.

This raises a question: How can we create a plasma quickly enough to deliver significant energy to a small volume in a short time? The primary technology with this capability is high peak power lasers, which can deliver single pulses with gigawatt to terawatt peak powers to spot

sizes of characteristic dimension 100 μm in sub-nanosecond pulses. Sub-picosecond pulses may also be used, but these provide less input energy, and thus less energy radiates out of the resulting plasma. Such short pulse lasers are primarily employed in cases where extremely short time scales are required. On longer time scales, of order 10–100 ns, other technologies such as electrical discharges may be employed, but these generally involve larger volumes at lower densities and temperatures, tending to be better optimized for extreme ultraviolet radiation.

Hot dense plasmas are of interest in basic physics research because of the multitude of interesting phenomena that arise. Moreover, they are of technological and industrial importance in such research areas as laser fusion, EUV and soft x-ray lasers, lithography, and other areas well known for concentrated energy densities. Because of the high energy concentration, which implies high temperatures and pressures, these plasmas tend to involve rapid expansions and thus sharp gradients in density and other parameters. This introduces a fair degree of complexity into the description of plasma processes, requiring the use of several tools. Theoretical models are created that attempt to explain the behavior of these plasmas within limited parameter ranges, perhaps of density and temperature. They describe the system in purely analytic terms, and strive to find closed form mathematical descriptions of various phenomena. To deal with the wide variations of density, temperature, and field intensities, numerical simulations are employed.

Several types of computer modeling are used. On a small scale, the detailed motion of a finite number of particles is tracked, for instance, to study non-linear plasma motion in the presence of extremely high incident laser radiation. On a somewhat larger scale, fluid-like zoning techniques are used to follow energy and particle transport in the presence of sharp spatial and temporal gradients in the presence of localized heating.

Finally, it is essential that theory and simulations be compared with real experiments. Only in the laboratory (or the stars) can the plasma be studied in a rigorous manner, with all Mother Nature's interactions present and accounted for. However, to understand these experiments, they must be carefully considered and executed with appropriate diagnostic instrumentation. Indeed, because of the considerable complexity, a satisfactory interpretation of the experiments generally requires substantial use of both theory and simulations.

Of primary interest here is the resultant emission of radiation, particularly at short wavelengths. As hot dense plasmas are fully ionized, the radiation consists of a broad continuum of so-called *bremsstrahlung*,* due to free-electron–ion interactions, and narrow line emissions due to bound–bound transitions in the atoms (ions) of various charge states. A composite sketch of what such an emission spectrum might look like is shown in Figure 6.1.

The spectrum consists of a broad continuum, perhaps near-thermal in nature, with narrow atomic emission lines of characteristic L-shell and K-shell transitions. These atoms have generally lost several, perhaps many, electrons in collisions with energetic free plasma electrons, and thus radiate emission lines characteristic of ions of several ionization states. In addition, there may be a long tail of energetic x-rays emitted by hot, or *suprathermal*, electrons generated by non-linear wave–particle processes in the plasma.

6.2 SHORT AND LONG RANGE INTERACTIONS IN PLASMAS

Several basic processes occur in plasmas. Among these are short distance binary *collisions*, and longer distance many-particle interactions better described in terms of collective phenomena.

*German word for "braking radiation."

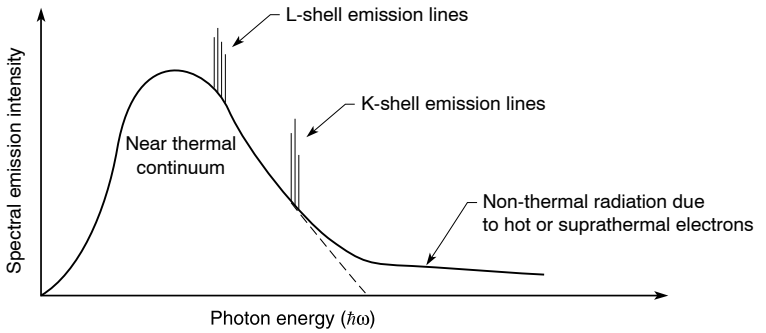

FIGURE 6.1. Line and continuum radiation from a hot dense plasma. The narrow emission lines are from ions of various ionization states.

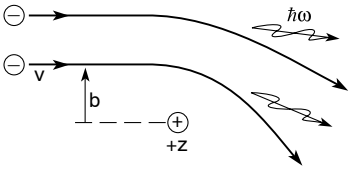

FIGURE 6.2. Bremsstrahlung occurs when a passing electron is accelerated by an ion, causing it to radiate. Because of the wide range of incident electron velocities and the range of distances of closest approach (*impact parameter b*) a broad continuum of radiation is generated in a plasma, with a spectrum closely related to the electron velocity distribution, or its characteristic temperature.

The short distance collisions transfer energy from particle to particle, in a somewhat random fashion, thereby thermalizing the plasma and ionizing the atoms. The level of ionization (the number of electrons lost) is set by the electron temperature of the plasma and the atomic binding energies, a topic we discuss further in a later section. Generally, multiple ionization states are formed, each with its own characteristic emission lines, leading to a rich complex of lines, often useful for diagnostic purposes, providing information regarding the electron and ion temperatures and the density. Collisions also cause the plasma to radiate. When an electron collides with an ion, as illustrated in Figure 6.2, it is accelerated and therefore radiates.

If the electron comes very close to the ion (small value of the *impact parameter b* in Figure 6.2), the acceleration is strong, the deflection angle is large, and the radiated photon is of high energy. For a more distant interaction (larger impact parameter) the acceleration is weaker and the radiated photon is of lower energy. With a random interaction process involving many electrons of differing velocity and impact parameter, one can expect a rather smooth continuum spectrum, related to the plasma's electron velocity distribution, or more simply its temperature. By a *thermal* plasma we mean an idealized equilibrium plasma in which all species (electrons, ions, radiation) are characterized by a single temperature and appropriate energy or velocity distributions. In practice the different particles will be characterized by different temperatures that vary with space and time. Indeed, we may find that for a single species, such as electrons, the velocity distribution cannot be described by a single temperature. This then leads us to concepts such as *near-thermal radiation* and the use of two-temperature models involving a thermal component and a suprathermal component, as used in Figure 6.1. Nonetheless, it is very useful to consider the thermal limit. For electrons characterized by a

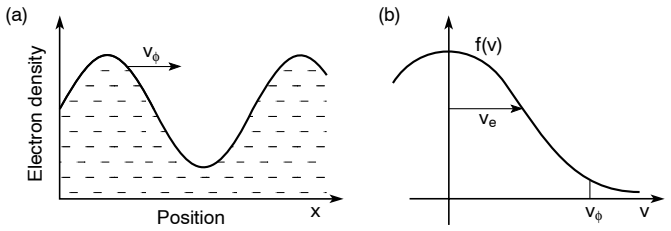

FIGURE 6.3. (a) An electron-acoustic wave, typically oscillating near the plasma frequency ω_p, propagates as an electron density modulation. Uniformly distributed ions (not shown) are too massive to participate in this relatively high frequency wave, but do provide overall charge neutrality. The wave is shown propagating to the right with a phase velocity v_ϕ. (b) The velocity distribution function $f(v)$ of individual electrons with a characteristic (rms) "thermal velocity," v_e. Electron-acoustic waves, as described in (a), generally propagate with a phase velocity v_ϕ significantly greater than the thermal velocity $v_e = (\kappa T_e/m)^{1/2}$.

single electron temperature† κT_e, the Maxwellian velocity distribution is[16]

$$f(v) = \frac{n_e}{(2\pi)^3 v_e^{3/2}} e^{-v^2/2v_e^2} \tag{6.1}$$

where

$$v_e = (\kappa T_e/m)^{1/2} \tag{6.2}$$

is the root mean square thermal velocity, n_e is the electron density, and m is the electron mass. The closely related topic of blackbody thermal radiation is described in a later section.

Longer range interactions are also important in plasmas, and especially so in hot dense plasmas. These often take the form of plasma oscillations, collective waves that propagate naturally, much like sound waves or deep water waves in their respective media. Generally these are high frequency waves associated with electrons, and lower frequency waves associated with the heavier ions, referred to respectively as electron-acoustic and ion-acoustic waves. A sketch of a propagating electron-acoustic wave is shown in Figure 6.3.

It is longitudinal in nature and propagates at a very high phase velocity, as we will see in the theory section that follows. Indeed, at long plasma wavelengths this wave propagates at phase velocities much greater than the electron thermal velocity, as shown in Figure 6.3(b). Collective oscillations such as these are naturally damped at short wavelengths by wave–particle interactions. This occurs on a scale related to the Debye screening distance λ_D, which gives a measure of the transition between short and long range interactions in a plasma. It is discussed in the following section. Where circumstances conspire to cause such a wave to grow to large amplitude, the crest regions of high electron density can form a very high potential well in which individual electrons can be trapped and accelerated to enormous energies. These energetic suprathermal or "hot" electrons will eventually exhibit their presence through the ensuing bremsstrahlung process, giving off a high photon energy tail as suggested in Figure 6.1. Such high amplitude waves are indeed encountered in hot dense plasmas. They are driven

†The Boltzmann constant is $\kappa = 8.6174 \times 10^{-5}$ eV/K (see Appendix A), so that when expressed in energy units a temperature of 100 eV corresponds to 1.16×10^6 kelvin (K).

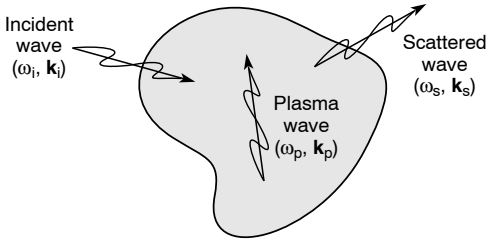

FIGURE 6.4. Three wave mixing among natural modes of the plasma. In resonant mixing the three satisfy conservation of energy and momentum.

to high amplitude by various non-linear processes involving wave–wave and wave–particle interactions, as suggested in Figure 6.4.

These non-linear processes are particularly strong in hot dense plasmas because the energy, time, and space scales require very high power densities, and thus high field amplitudes. These high field amplitudes (electric field, velocity, etc.) tend to force the plasma away from equilibrium, near-thermal states toward highly non-thermal states. For instance, a high intensity focused laser pulse can excite plasma waves out of the noise of random particle motions (which are always present). As an example, in what is known as *stimulated Raman scattering* (SRS), an intense incoming electromagnetic (laser) wave rattles all electrons at a single frequency, with well-defined spatial periodicity (**k**), and with high velocity. This can lead to a well-organized, large amplitude electron-acoustic wave. A portion of the incoming electromagnetic wave can be scattered collectively from the growing plasma wave, creating an outgoing scattered wave with appropriate Doppler frequency shift and directional change. This can lead to a *resonant* three-wave interaction in which the wave frequencies (ω) and wave vectors (**k**) satisfy conservation of energy and momentum relations of the form

$$\hbar\omega_i = \hbar\omega_p + \hbar\omega_s \tag{6.3}$$

$$\hbar\mathbf{k}_i = \hbar\mathbf{k}_p + \hbar\mathbf{k}_s \tag{6.4}$$

where $(\omega_i, \mathbf{k}_i)$ characterizes the incoming or incident radiation, $(\omega_p, \mathbf{k}_p)$ characterizes the particular plasma wave involved, and $(\omega_s, \mathbf{k}_s)$ represents the outgoing scattered wave. With a very intense incident wave the plasma wave can be amplified to very high amplitude at the beat frequency ($\omega_p = \omega_i - \omega_s$) between the two electromagnetic waves, growing quickly out of the noise (of many plasma waves), and soon dominating the process. This can then seriously affect the observed emission spectrum as the excited plasma wave, now characterized by high fields (electric potential) and generally high velocities (ω_p/k_p), traps and accelerates individual electrons to very high velocities, to a large fraction of the speed of light in some cases, resulting in the emission of very high energy photons, as mentioned earlier. Where this process involves excitement of a high frequency electron-acoustic wave, there is a substantial shift of the scattered wave frequency and the process is called stimulated Raman scattering – stimulated because the plasma wave's growth from noise is driven by the strong incident wave it eventually scatters and resonates with. Where the process involves the emergence of a high amplitude ion-acoustic wave, the scattered wave experiences only a small frequency shift and the process is referred to as *stimulated Brillouin scattering* (SBS).

As the generation of suprathermal processes necessarily takes energy away from thermal processes, and often is deleterious in its own right, the avoidance of such processes is often of

great interest. Thresholds are thus well studied, and countermeasures, principally operating at lower intensities and high frequencies, are employed. In laser-produced plasmas this generally requires that the incident intensity I be kept below a threshold $I\lambda^2/\kappa T_e$, depending on the wavelength λ and temperature κT_e, which we will discuss in a later section.

6.3 BASIC PARAMETERS FOR DESCRIBING A PLASMA

To further explore basic processes in a plasma it is necessary to develop an appropriate framework. This will necessarily involve important physical quantities such as the electron density n_e the electron temperature T, and the magnetic induction **B**. These in turn will lead to the natural introduction of characteristic parameters such as the plasma frequency ω_p, the Debye screening distance λ_D, the cyclotron frequency ω_c, and the collision mean free path l_{mfp}, among others. In general the plasmas are electrically neutral, so that the ion density differs from the electron density only by the average ionization state. Hot dense plasmas are effectively fully ionized, so that neutral atoms are of little consequence. The electron density n_e determines the electron plasma frequency

$$\omega_p = \left(\frac{e^2 n_e}{\epsilon_0 m}\right)^{1/2} \tag{6.5}$$

a natural frequency at which electrons tend to oscillate. In Eq. (6.5) e and m are the electron charge and mass, respectively, and ϵ_0 is the permittivity of free space.

In the next section we will see that electron-acoustic waves tend to oscillate at frequencies at or just above ω_p. Furthermore, we will see that electromagnetic waves can propagate in a plasma only if their frequency ω is greater than ω_p. For a plasma with an electron density gradient, as shown in Figure 6.5, the incident electromagnetic wave is totally reflected at the critical electron density n_c where $\omega = \omega_p$. Except for a short exponential penetration depth, the wave is totally excluded from the region characterized by $\omega < \omega_p$.

For hot dense plasmas, particularly laser produced plasmas, the electron densities of interest are near-solid densities. For a common neodymium (Nd) laser of 1.06 μm wavelength, the laser-plasma interaction occurs near the critical electron density, $n_c = 1 \times 10^{21}\ e/\text{cm}^3$, where the plasma frequency is just equal to the laser light radian frequency, about 1.8×10^{15} rad/s. The absorption and various scattering processes, some of which were discussed in the previous section, occur predominantly in the low density ($10^{19}\ e/\text{cm}^3$ to $10^{21}\ e/\text{cm}^3$) region just below the critical region. Classical absorption occurs here, as the incident radiation causes the electrons to oscillate, giving them energy that is then lost in part to random collisions with ions, as was illustrated in Figure 6.2. X-ray emission tends to come predominantly from a thin, somewhat higher density region ($10^{21}\ e/\text{cm}^3$ to $10^{23}\ e/\text{cm}^3$), just behind the critical layer, where energy has been transported by charged particles and radiation. This region characterized by high density and high temperature (see Figure 6.5), is ideal for intense x-ray generation.

A second important plasma parameter is the Debye screening distance

$$\lambda_D = \left(\frac{\epsilon_0 \kappa T_e}{e^2 n_e}\right)^{1/2} \tag{6.6}$$

– a distance beyond which individual charges tend to be screened by the presence of other nearby and mobile charges. For a 1 keV plasma at $10^{21}\ e/\text{cm}^3$, the Deybe screening distance

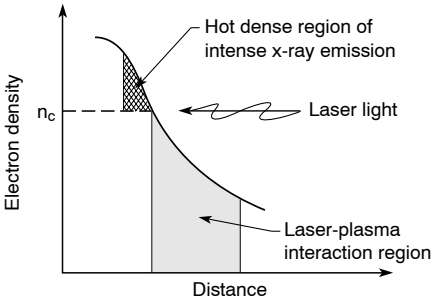

FIGURE 6.5. Intense laser light is absorbed in the region just below and at the critical density region. Energy transport to a thin region just beyond the critical density region creates a region of intense x-ray emission. Laser light that reaches the critical surface, of electron density n_c, is reflected.

is about 7 nm. On spatial scales shorter than λ_D the presence and effects of individual charges are evident. On longer spatial scales the individual charges tend to be screened by neighboring charges, so that on this longer scale charged particle interactions tend to occur through collective motions, such as the electron- and ion-acoustic waves.

In the theoretical study of plasma waves, one finds that the dispersion relation $\omega(k)$ contains a damping term due to individual electron–wave interactions which, although negligible at long wavelengths, become very strong for plasma of wavenumber $k > 1/\lambda_D$. This natural decay of short wavelength plasma waves is known as Landau damping. It is an example of a plasma process whose understanding and theoretical description require not only use of fluid mechanical quantities, such as density and temperature, but also a detailed knowledge of the shape of the velocity distribution function $f(\mathrm{v})$, shown earlier in Figure 6.3(b). We will return to this subject in the next section.

What begins to emerge here is a more detailed understanding of the manner in which the Debye screening distance separates short-range from long-range interactions in a plasma. In describing collective effects in plasma an important parameter is the number of electrons in the Debye sphere

$$N_D = \frac{4\pi}{3}\lambda_D^3 n_e \tag{6.7}$$

For $N_D \gg 1$, fluctuations in the microscopic fields are small, and as a result the collective description in terms of averaged field quantities is more effective.

A further important plasma parameter, associated with a directional or imposed magnetic induction **B**, is the electron cyclotron frequency

$$\omega_c = \frac{eB}{m} \tag{6.8}$$

with which electrons circle about the magnetic field. For a 1 MG field the electron cyclotron frequency is about 2×10^{13} rad/s. The electron cyclotron frequency is important for the understanding of energy transport in plasmas, as electrons tend to circle about magnetic field lines with a Larmor radius $r_L = \mathrm{v}/\omega_c = m\mathrm{v}/eB$, interrupted only by collisions. This tends to inhibit energy transport to density regions of potentially intense x-ray emission. For instance, x-ray emission from the sun shows dark spots and bright coronal loops, which are clear evidence for the presence of strong magnetic fields and constrained charged particle transport. The cyclotron frequency can also play an important role in the collective plasma oscillations, at both low and high frequency, introducing strong dispersion and polarization effects. Cyclotron *resonances*, where the dispersion relation is flat, can play an important role in absorption of low frequency electromagnetic waves (microwaves) by magnetic fusion plasmas.

A fourth parameter, also important to energy transport by charged particles, is the electron–ion collision mean free path, l_{mfp}, which has various dependencies on basic plasma properties, but typically is proportional to $(\kappa T)^2/n_i Z$, where n_i is the ion density and $+Ze$ the average charge state. For a 1 keV electron in a 10^{20} ion /cm^3 plasma of +10 charge state, the mean free path is about 4 μm (that is, at the critical electron density 10^{21} e/cm^3). A 10 keV electron, well out on the velocity distribution curve, would have a similar mean free path at the $100n_c$ surface, which could be only a few microns away for a sharp density gradient in the supracritical region of a laser-produced plasma. Thus much of the absorbed energy could be stopped by classical collisions in a distance of only a few microns from the critical surface, causing this region to light up with intense (radiated power per unit area) x-ray emissions.

6.4 MICROSCOPIC, KINETIC, AND FLUID DESCRIPTIONS OF A PLASMA

The theoretical description of a plasma may take several forms with varying levels of detail.[1, 3–6] The most exact and complex model involves a description of the position and velocity of each and every particle in the plasma as a function of time. With so many particles present, this level of description is mathematically intractable and must be left to numerical simulations with small numbers of particles.

A simplification is obtained by averaging over a spatial volume containing a large number of particles. This leads to a kinetic description in terms of a more tractable velocity distribution function, which can still have a slow space and time dependence, but omits the details of any particular particle. Further simplification results from averaging over all velocities and describing the plasma in terms of fluid parameters such as density, temperature, and pressure. We begin our analysis at the microscopic level and work our way to the fluid description.

6.4.1 The Microscopic Description

A formal description of plasma dynamics suggested by Klimontovich[5] involves a microscopic distribution function describing the position and velocity of all particles in a six dimensional velocity–position phase space:

$$f(\mathbf{v}, \mathbf{r}; t) = \sum_{i=1}^{N} \delta[\mathbf{r} - \mathbf{r}_i(t)]\delta[\mathbf{v} - \mathbf{v}_i(t)] \tag{6.9}$$

where the detailed motion of the ith point particle is described by $\mathbf{r}_i(t)$ and $\mathbf{v}_i(t)$. The distribution function is normalized to the total number of particles, N, by the phase space integral

$$\int_{\mathbf{r}} \int_{\mathbf{v}} f(\mathbf{v}, \mathbf{r}; t)\, d\mathbf{r}\, d\mathbf{v} = N \tag{6.10}$$

where we define the shorthand notation, for example in Cartesian coordinates

$$\delta(\mathbf{r}) \equiv \delta(x)\delta(y)\delta(z) \tag{6.11}$$

$$\delta(\mathbf{v}) \equiv \delta(\mathrm{v}_x)\delta(\mathrm{v}_y)\delta(\mathrm{v}_z) \tag{6.12}$$

and

$$d\mathbf{r} \equiv dx\, dy\, dz \tag{6.13}$$

$$d\mathbf{v} \equiv d\mathrm{v}_x\, d\mathrm{v}_y\, d\mathrm{v}_z \tag{6.14}$$

where the properties of the Dirac delta function $\delta(x)$ are described in Appendix B.

The particle dynamics of the particle distribution can be determined by taking a partial derivative of $f(\mathbf{v}, \mathbf{r}; t)$ with respect to time:

$$\frac{\partial f}{\partial t} = \sum_i \left[\frac{\partial}{\partial t}\delta(\mathbf{r} - \mathbf{r}_i)\right]\delta(\mathbf{v} - \mathbf{v}_i) + \sum_i \left[\frac{\partial}{\partial t}\delta(\mathbf{v} - \mathbf{v}_i)\right]\delta(\mathbf{r} - \mathbf{r}_i)$$

The first bracketed quantity can be simplified by use of the chain rule for differentiation. For simplicity we first use a scalar, one-dimensional version, defining the functions $g(t) = r_i(t)$ and $f(g) = \delta(r - r_i(t)) = \delta(r - g(t))$, so that by the chain rule

$$\frac{\partial f(g)}{\partial t} = \frac{\partial g}{\partial t} \cdot \frac{\partial f}{\partial g}$$

or explicitly

$$\frac{\partial}{\partial t}\delta(r - r_i(t)) = \frac{\partial r_i}{\partial t}\frac{\partial \delta(r - r_i)}{\partial r_i}$$

Noting that for delta functions (see Appendix B) $(d/dx)(x - a) = -(d/da)(x - a)$, we can interchange differentials to obtain

$$\frac{\partial (r - r_i)}{\partial r_i} = -\frac{\partial \delta(r - r_i)}{\partial r}$$

and thus

$$\frac{\partial}{\partial t}\delta(r - r_i(t)) = -\frac{\partial r_i}{\partial t}\frac{\partial}{\partial r}\delta(r - r_i)$$

In its three-dimensional generalization this becomes

$$\frac{\partial}{\partial t}\delta(\mathbf{r} - \mathbf{r}_i(t)) = -\frac{\partial \mathbf{r}_i}{\partial t} \cdot \nabla\delta(\mathbf{r} - \mathbf{r}_i(t))$$

where we recognize the differential $\partial \mathbf{r}_i/\partial t = d\mathbf{r}_i/dt = \mathbf{v}_i$, so that

$$\frac{\partial}{\partial t}\delta(\mathbf{r} - \mathbf{r}_i(t)) = -\mathbf{v}_i \cdot \nabla\delta(\mathbf{r} - \mathbf{r}_i(t))$$

Likewise, for the second bracketed quantity one obtains

$$\frac{\partial}{\partial t}\delta(\mathbf{v} - \mathbf{v}_i(t)) = -\frac{\partial \mathbf{v}_i}{\partial t} \cdot \nabla_{\mathrm{v}}\delta(\mathbf{v} - \mathbf{v}_i(t))$$

where use of the Lorentz force on each particle permits the substitution

$$\frac{\partial}{\partial t}\delta(\mathbf{v} - \mathbf{v}_i(t)) = -\frac{q_i}{m}(\mathbf{E} + \mathbf{v}_i \times \mathbf{B}) \cdot \nabla_{\mathrm{v}}\delta(\mathbf{v} - \mathbf{v}_i(t))$$

Combining these results for the two bracketed quantities, we see that the microscopic particle distribution function $f(\mathbf{v}, \mathbf{r}; t)$ obeys the equation

$$\frac{\partial f}{\partial t} = \sum_i (-\mathbf{v}_i) \cdot \nabla[\delta(\mathbf{r} - \mathbf{r}_i)\delta(\mathbf{v} - \mathbf{v}_i)] + \sum_i -\frac{q_i}{m}(\mathbf{E} + \mathbf{v}_i \times \mathbf{B}) \cdot \nabla_{\mathrm{v}}[\delta(\mathbf{r} - \mathbf{r}_i)\delta(\mathbf{v} - \mathbf{v}_i)]$$

By identifying $f(\mathbf{v}, \mathbf{r}; t)$ in each term above one obtains the *Klimontovich equation*

$$\boxed{\frac{\partial f}{\partial t} + \mathbf{v} \cdot \nabla f + \frac{q}{m}(\mathbf{E} + \mathbf{v} \times \mathbf{B}) \cdot \nabla_{\mathrm{v}} f = 0} \tag{6.15}$$

which describes the evolution of the microscopic distribution function, as a function of time, in phase space.

A self-consistent solution is required because of the interdependence of variables, namely, the velocity distribution function $f(\mathbf{v})$ depends on the electric and magnetic fields $\mathbf{E}$ and $\mathbf{B}$, which in turn depend on $f(\mathbf{v})$ through the charge density ρ and current $\mathbf{J}$ as they appear in Maxwell's equations. To find such a solution we note that the charge and current densities can be written in terms of the distribution functions $f_j(\mathbf{v}, \mathbf{r}; t)$, for each particle type present ($j = 1$ for electrons, $j = 2$ for ions) as

$$\rho_j(\mathbf{r}, t) = \sum_i q_j \delta(\mathbf{r} - \mathbf{r}_i) = \sum_i q_j \int \delta(\mathbf{r} - \mathbf{r}_i)\delta(\mathbf{v} - \mathbf{v}_i)\, d\mathbf{v} = q_j \int f_j(\mathbf{v}, \mathbf{r}; t)\, d\mathbf{v} \tag{6.16}$$

and

$$\begin{aligned} \mathbf{J}_j(\mathbf{r}, t) &= \sum_i q_j \mathbf{v}_i \delta(\mathbf{r} - \mathbf{r}_i) = \sum_i q_j \int \mathbf{v}\delta(\mathbf{r} - \mathbf{r}_i)\delta(\mathbf{v} - \mathbf{v}_i)\, d\mathbf{v} \\ &= q_j \int \mathbf{v} f_j(\mathbf{v}, \mathbf{r}; t)\, d\mathbf{v} \end{aligned} \tag{6.17}$$

where for electrons $q_1 = -e$ and the sum $\sum_i$ is over all individual electrons, and for ions $q_2 = +Ze$ and the sum $\sum_i$ is over all individual ions. The formal set of self-consistent field equations, which describe plasma dynamics at the microscopic level, are called the *Maxwell–Klimontovich equations*. They take the form [see Chapter 2, Eqs. (2.1–2.6)]

$$\nabla \times \mathbf{H} = \frac{\partial \mathbf{D}}{\partial t} + \sum_j q_j \int \mathbf{v} f_j(\mathbf{v}, \mathbf{r}; t)\, d\mathbf{v} \tag{6.18}$$

$$\nabla \times \mathbf{E} = -\frac{\partial \mathbf{B}}{\partial t} \tag{6.19}$$

$$\nabla \cdot \mathbf{D} = \sum_j q_j \int f_j(\mathbf{v}, \mathbf{r}; t)\, d\mathbf{v} \tag{6.20}$$

$$\nabla \cdot \mathbf{B} = 0 \tag{6.21}$$

with constitutive relations

$$\mathbf{D} = \epsilon_0 \mathbf{E} \tag{6.22}$$

$$\mathbf{B} = \mu_0 \mathbf{H} \tag{6.23}$$

and for each particle species (j)

$$\frac{\partial f_j}{\partial t} + \mathbf{v} \cdot \nabla f_j + \frac{q_j}{m_j}(\mathbf{E} + \mathbf{v} \times \mathbf{B}) \cdot \nabla_{\mathrm{v}} f_j = 0 \tag{6.24}$$

where the field equations are written for a multicomponent plasma (electrons and ions) with respective distribution functions $f_j(\mathbf{v}, \mathbf{r}; t)$, for species of charge q_j and mass m_j (see Ref. 2).

The Klimontovich description is a simple yet formal approach to the microscopic description of plasma phenomena. It postulates a distribution function, takes its time derivative, and writes it in a form that easily evolves into a reduced *kinetic theory*, which we consider in the next section.

6.4.2 The Kinetic Description

The microscopic description in terms of Klimontovich's density function is highly stochastic, varying rapidly over space and time, and involves details regarding too many individual particles for analytic treatment. A reduced description, averaged somewhat over a space containing a large number of particles, forms a more slowly varying distribution, $f(\mathbf{v}, \mathbf{r}; t)$, which contains no information regarding individual particles, but rather describes an average velocity distribution function $f(\mathrm{v})$, with a slow space–time dependence. We drop the subscript j here for convenience, but understand that this process must be followed separately for each species. Whereas Klimontovich's distribution function is discontinuous and stochastic, with wildly varying amplitude, the kinetic distribution function f is analytic. Integrating the Maxwell–Klimontovich equations over a spatial volume sufficient to include many particles – so that statistical fluctuations are not so wild – produces such a distribution.[3]

We can write the distribution function in terms of a slowly varying part and a fluctuating part, as

$$f(\mathbf{v}, \mathbf{r}; t) = \bar{f}\,(\mathbf{v}, \mathbf{r}; t) + \tilde{f}\,(\mathbf{v}, \mathbf{r}; t)$$

with a similar description for the fields

$$\mathbf{E}(r, t) = \bar{\mathbf{E}}(\mathbf{r}, t) + \tilde{\mathbf{E}}(\mathbf{r}, t), \qquad \text{etc.}$$

Then substituting these into the Klimontovich equation [Eq. (6.15)], and averaging over a spatial scale sufficiently large to give a smoothed kinetic equation for the velocity distribution

function, gives us a kinetic equation formally equivalent to the Boltzmann equation:

$$\frac{\partial f}{\partial t} + \mathbf{v}\cdot\nabla f + \frac{q}{m}(\mathbf{E}\times\mathbf{v}\times\mathbf{B})\cdot\nabla_{\mathrm{v}} f(\mathbf{v},\mathbf{r};t) = -\frac{q}{m}\nabla_{\mathrm{v}}\cdot\overline{(\tilde{\mathbf{E}}+\mathbf{v}\times\tilde{\mathbf{B}})\tilde{f}} \tag{6.25}$$

where for simplicity of notation we have dropped, on the left side of the equation, the overbars denoting slowly varying variables, i.e., $\bar{f}$, $\bar{E}$, and $\bar{B}$. The right side is a symbolic "collision" term, non-linear (because of the product terms) in fluctuations from the mean, which tends to bring the distribution function back toward an equilibrium. In situations not too distant from equilibrium, and not turbulent, the collision term may be small. In such a case one has the *collisionless Vlasov equation,* which is valuable in solving many plasma kinetic problems. Of course this must be solved self-consistently with similarly smoothed Maxwell's equations for the slowly varying quantities $\bar{\mathbf{E}}$, $\bar{\mathbf{H}}$, $\bar{\mathbf{B}}$, $\bar{\mathbf{D}}$, and $\bar{f}$. Substituting in Eqs. (6.18–6.24) quantities such as $\mathbf{E} = \bar{\mathbf{E}} + \tilde{\mathbf{E}}$, $\mathbf{H} = \bar{\mathbf{H}} + \tilde{\mathbf{H}}$, etc., retaining only the slowly varying quantities ($\bar{}$), and then, for simplicity of notation, dropping the bars, we obtain the *collisionless Maxwell–Vlasov equations* for a plasma,

$$\nabla\times\mathbf{H} = \frac{\partial\mathbf{D}}{\partial t} + \sum_j q_j \int \mathbf{v} f_j(\mathbf{v},\mathbf{r};t)\,d\mathbf{v} \tag{6.26}$$

$$\nabla\times\mathbf{E} = -\frac{\partial\mathbf{B}}{\partial t} \tag{6.27}$$

$$\nabla\cdot\mathbf{D} = \sum_j q_j \int f_j(\mathbf{v},\mathbf{r};t)\,d\mathbf{v} \tag{6.28}$$

$$\nabla\cdot\mathbf{B} = 0 \tag{6.29}$$

plus the constitutive relations in vacuum,

$$\mathbf{D} = \epsilon_0\mathbf{E} \tag{6.30}$$

$$\mathbf{B} = \mu_0\mathbf{H} \tag{6.31}$$

and the collisionless Vlasov equations for each species (electrons, ions),

$$\frac{\partial f_j(\mathbf{v},\mathbf{r};t)}{\partial t} + \mathbf{v}\cdot\nabla f_j(\mathbf{v},\mathbf{r};t) + \frac{q_j}{m_j}(\mathbf{E}+\mathbf{v}\times\mathbf{B})\cdot\nabla_{\mathrm{v}} f_j(\mathbf{v},\mathbf{r};t) = 0 \tag{6.32}$$

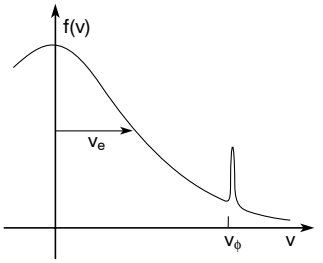

FIGURE 6.6. Velocity distribution function with an injected electron beam.

These equations are formally identical to the Maxwell–Klimontovich equations [Eqs. (6.18–6.24)], but contain significantly less detail, making them mathematically more tractable. Whereas the Maxwell–Klimontovich equations were written for an N-particle distribution function, containing detailed positions and velocities of all N particles, the Maxwell–Vlasov equations involved a simpler *kinetic* distribution function, which does not distinguish (or recognize) any individual particles. This kinetic distribution function is sometimes referred to in the literature as the "single particle" distribution function, emphasizing that it does not have discrete N-particle information.

Examples of phenomena that can be mathematically described by the use of a kinetic description are those of electron-acoustic wave amplification and collisionless decay, known commonly as Landau growth and damping. The distribution function for thermal electrons takes the form shown previously in Figure 6.3(b). For example, in the case of the electron-acoustic wave, which is a longitudinal wave of electrons in a uniform positive ion density background, a charge density modulation propagates in some direction as shown in Figure 6.3(a). Most of the electrons do not move with the wave, but rather oscillate in a nearly fixed position as the wave passes by, as in the case of the motion of molecules in a sound wave. However, as shown by the distribution function, some electrons travel at a velocity near that of the wave. Electrons that move slightly slower than the wave are pushed by the negative potential of the charge density peak; therefore, these electrons accelerate, taking energy from the wave. Likewise, electrons traveling slightly faster than the wave push the charge density peaks, thus decelerating themselves while imparting energy to the wave. In a thermal distribution, there are more electrons traveling slower than the phase velocity of the wave, v_ϕ, so the wave is damped [see Figure 6.3(b)].

On the other hand, if a beam of electrons with velocities slightly larger than the wave velocity (v_ϕ) is injected into the plasma, the new electron velocity distribution function, shown in Figure 6.6, causes wave growth. In this case the injected electrons tend to "push" the potential crests of the wave, transferring energy to the wave, and losing energy themselves as they merge into it. Mathematical solutions to Eqs. (6.26–6.32) show that the Landau damping or growth rate is related to the slope of $f(v)$ at $v = v_\phi$ (Refs. 4 and 18).

6.4.3 The Fluid Description

The Vlasov equation has a great deal of information about velocity distributions and how they evolve in space and time. In some problems velocity information is critical, but in some it is not needed and further simplification is possible. A set of fluid mechanical equations,[4] containing physical variables such as the particle density $n_j(\mathbf{r}, t)$ for each species, the average velocity $\bar{\mathbf{v}}_j(\mathbf{r}, t)$, partial pressure $P_j(\mathbf{r}, t)$, and others, can be developed directly from the kinetic Vlasov equation. These common fluid mechanical quantities correspond to so-called

velocity moments, or velocity weighted integrals, of the kinetic velocity distribution function $f_j(\mathbf{v}, \mathbf{r}; t)$ with scalar, vector, and dyadic multipliers of the velocity. Specifically, for the electrons ($q_j = -e$) one defines

$$n_e(\mathbf{r}, t) = \int f(\mathbf{v}, \mathbf{r}; t)\, d\mathbf{v} \tag{6.33}$$

$$n_e \bar{\mathbf{v}}(\mathbf{r}, t) = \int \mathbf{v} f(\mathbf{v}, \mathbf{r}; t)\, d\mathbf{v} \tag{6.34}$$

where the subscript e has been suppressed for simplicity on both $\bar{\mathrm{v}}_j$ and $f_j(\mathbf{v}, \mathbf{r}; t)$. In terms of the random (thermal) component of the velocity, $\tilde{\mathbf{v}}$, that is, the departure from the average velocity $\bar{\mathbf{v}}$, higher velocity moments are

$$\mathbb{P}_e = n_e m \overline{\tilde{\mathbf{v}}\tilde{\mathbf{v}}} = m \int \tilde{\mathbf{v}}\tilde{\mathbf{v}} f(\mathbf{v}, \mathbf{r}; t)\, d\mathbf{v} \tag{6.35}$$

$$n_e U_e = \frac{1}{2} n_e m \overline{\tilde{\mathbf{v}}^2} = \frac{1}{2} m \int \tilde{\mathbf{v}}^2 f(\mathbf{v}, \mathbf{r}; t)\, d\mathbf{v} \tag{6.36}$$

and

$$\mathbf{Q}_e = \frac{1}{2} n_e m \overline{\tilde{\mathbf{v}}^2 \tilde{\mathbf{v}}} = \frac{1}{2} m \int \tilde{\mathbf{v}}^2 \tilde{\mathbf{v}} f(\mathbf{v}, \mathbf{r}; t)\, d\mathbf{v} \tag{6.37}$$

where $n_e(\mathbf{r}, t)$ is the local electron (particle) density, $\bar{\mathbf{v}}(\mathbf{r}; t)$ is the distribution weighted average velocity, the fluctuation component of fluid velocity is defined by $\mathbf{v} = \bar{\mathbf{v}} + \tilde{\mathbf{v}}$, $\mathbb{P}_e$ is the tensor electron pressure dyadic, U_e is the electron thermal (kinetic) energy density, and $\mathbf{Q}_e$ is the vector heat flux or thermal flux density carried by electrons. Note that the notation $\tilde{\mathbf{v}}^2$ is understood to represent the scalar quantity $\tilde{\mathbf{v}} \cdot \tilde{\mathbf{v}}$ and that simple juxtaposition ($\tilde{\mathbf{v}}\tilde{\mathbf{v}}$) indicates a nine component tensor multiplication of two vectors, as described in Appendix D. As a specific example, the pressure dyadic $\mathbb{P}_e$ of Eq. (6.35), which involves the tensor velocity product $\tilde{\mathbf{v}}\tilde{\mathbf{v}}$, can be written out in terms of its components as

$$\mathbb{P}_e = n_e m \begin{bmatrix} \overline{\tilde{\mathrm{v}}_x^2}\, \mathbf{x}_0\mathbf{x}_0 & \overline{\tilde{\mathrm{v}}_x \tilde{\mathrm{v}}_y}\, \mathbf{x}_0\mathbf{y}_0 & \overline{\tilde{\mathrm{v}}_x \tilde{\mathrm{v}}_z}\, \mathbf{x}_0\mathbf{z}_0 \\ \overline{\tilde{\mathrm{v}}_y \tilde{\mathrm{v}}_x}\, \mathbf{y}_0\mathbf{x}_0 & \overline{\tilde{\mathrm{v}}_y^2}\, \mathbf{y}_0\mathbf{y}_0 & \overline{\tilde{\mathrm{v}}_y \tilde{\mathrm{v}}_z}\, \mathbf{y}_0\mathbf{z}_0 \\ \overline{\tilde{\mathrm{v}}_z \tilde{\mathrm{v}}_x}\, \mathbf{z}_0\mathbf{x}_0 & \overline{\tilde{\mathrm{v}}_z \tilde{\mathrm{v}}_y}\, \mathbf{z}_0\mathbf{y}_0 & \overline{\tilde{\mathrm{v}}_z^2}\, \mathbf{z}_0\mathbf{z}_0 \end{bmatrix} \tag{6.38}$$

where $\mathbf{v} = \mathrm{v}_x\mathbf{x}_0 + \mathrm{v}_y\mathbf{y}_0 + \mathrm{v}_z\mathbf{z}_0$ in Cartesian coordinates, with unit vectors $\mathbf{x}_0$, $\mathbf{y}_0$, $\mathbf{z}_0$. The unit dyad has diagonal units equal to one, and zeros elsewhere, so that its dot product with any vector equals the vector, i.e., $\mathbf{1} \cdot \mathbf{v} = \mathbf{v}$. One can show (see Appendix B) that in general, for two vectors $\mathbf{A}$ and $\mathbf{B}$, $\nabla \cdot (\mathbf{AB}) = \mathbf{A} \cdot \nabla\mathbf{B} + \mathbf{B}\nabla \cdot \mathbf{A}$, a relationship we will find useful in following paragraphs.

The relevant equations for these fluid mechanical quantities (n, $\bar{\mathbf{v}}$, $\mathbb{P}$, etc.,) can be obtained by multiplying the Vlasov equation by 1, $\mathbf{v}$, $\mathbf{vv}$, etc., and integrating over all velocities. These are the so called *moment* equations, as they each multiply the Vlasov equation by some quantity before integration. Assuming for the moment that the collision term is small, we start with the

collisionless Vlasov equation [Eq. (6.32)] and integrate over velocity, viz.,

$$\int \left[\frac{\partial f}{\partial t} + \mathbf{v} \cdot \nabla f + \frac{q}{m}(\mathbf{E} + \mathbf{v} \times \mathbf{B}) \cdot \nabla_{\mathrm{v}} f \right] d\mathbf{v} = 0 \tag{6.39}$$

where we have written this for a specific species j, for instance for the electrons or for a particular ionic species. Recall that $d\mathbf{v}$ is not a vector quantity, but rather shorthand notation for the volume element in velocity space, e.g., $d\mathbf{v} = d\mathrm{v}_x\, d\mathrm{v}_y\, d\mathrm{v}_z$. Long range interactions between various species are included through the slowly varying electromagnetic fields. Short range interactions (collisions) that involve strong space–time variations of these fields are included, where appropriate, through the product of fluctuation term on the right-hand side of Eq. (6.25).

To perform the indicated integrations we note that the independent coordinates in this non-relativistic kinetic plasma are $\mathbf{v}$, $\mathbf{r}$, and t. Thus in the first term of Eq. (6.39) the time derivative passes through the velocity integral, leaving

$$\frac{\partial}{\partial t} \int f(\mathbf{v})\, d\mathbf{v} = \frac{\partial}{\partial t} n(\mathbf{r}, t)$$

by the definition in Eq. (6.32). The second term of Eq. (6.39), involving $\mathbf{v} \cdot \nabla f$, can be integrated using the vector identity $\nabla \cdot (\phi \mathbf{A}) = \phi \nabla \cdot \mathbf{A} + \mathbf{A} \cdot \nabla \phi$, so that

$$\mathbf{v} \cdot \nabla f = \nabla \cdot (f\mathbf{v}) - \underbrace{f \nabla \cdot \mathbf{v}}_{=0}$$

The last term above is zero, as $\mathbf{v}$ is not a function of $\mathbf{r}$ and thus $\nabla \cdot \equiv 0$. The second term of Eq. (6.39) is then integrated as follows:

$$\int \mathbf{v} \cdot \nabla f(\mathbf{v})\, d\mathbf{v} = \int \nabla \cdot f\mathbf{v}\, d\mathbf{v} = \nabla \cdot \int f(\mathbf{v})\, \mathbf{v}\, d\mathbf{v} \equiv \nabla \cdot n\bar{\mathrm{v}}$$

using the definition given in Eq. (6.33). The fluid equation now emerging from Eq. (6.39) becomes

$$\frac{\partial n}{\partial t} + \nabla \cdot (n\bar{\mathrm{v}}) + \frac{q}{m} \int (\mathbf{E} + \mathbf{v} \times \mathbf{B}) \cdot \nabla_{\mathrm{v}} f(\mathbf{v})\, d\mathbf{v} = 0$$

With a few steps we will show that for this first fluid equation the Lorentz force term does not contribute; however, in higher order fluid equations, to be considered next, it will contribute. Considering the remaining integral in Eq. (6.39), we again use the $\nabla \cdot (\phi \mathbf{A})$ vector relation, i.e.,

$$(\mathbf{E} + \mathbf{v} \times \mathbf{B}) \cdot \nabla_{\mathrm{v}} f(\mathbf{v}) = \nabla_{\mathrm{v}} \cdot [(\mathbf{E} + \mathbf{v} \times \mathbf{B}) f] - \underbrace{f \nabla_{\mathrm{v}} \cdot (\mathbf{E} + \mathbf{v} \times \mathbf{B})}_{=0}$$

where we note that in the term $\nabla_{\mathrm{v}} \cdot \mathbf{E}$, $\mathbf{E}$ is not a function of $\mathbf{v}$, and $\nabla_{\mathrm{v}} \cdot (\mathbf{v} \times \mathbf{B}) = (\nabla_{\mathrm{v}} \times \mathbf{v}) \cdot \mathbf{B} = 0$ since $\nabla_{\mathrm{v}} \times \mathbf{v} = 0$. The remaining term can then be integrated using Gauss's theorem for an arbitrary vector $\mathbf{A}$:

$$\int_{\text{volume}} (\nabla \cdot \mathbf{A})\, dV = \oint_{\text{surface}} \mathbf{A} \cdot d\mathbf{S}$$

so that in velocity space

$$\int \nabla_{\mathrm{v}} \cdot [(\mathbf{E} + \mathbf{v} \times \mathbf{B}) f(\mathbf{v})]\, d\mathbf{v} = \int_{\substack{\text{velocity} \\ \text{space} \\ \text{surface}}} [(\mathbf{E} + \mathbf{v} \times \mathbf{B}) f(\mathbf{v})] \cdot d\mathbf{S}_{\mathrm{v}} = 0$$

where the integral is evaluated at a velocity space surface where $\mathbf{v}$ approaches infinity (or some other sufficiently large value not exceeding c). Taking $d\mathbf{S} = 4\pi \mathrm{v}^2\, d\Omega \mathbf{v}_0$, where $\mathbf{v}_0$ is a unit vector in the outgoing velocity direction, the $\mathbf{v} \times \mathbf{B}$ term is normal to $\mathbf{v}_0$ and thus does not contribute.

The remaining surface integral involving $\mathbf{E} f(\mathbf{v})$ does not contribute for the case where $f(\mathbf{v})$ goes to zero faster than $1/\mathrm{v}^2$ for large v, a very reasonable assumption for any physical plasma. The resultant fluid equation, the *first moment* (lever arm) of the collisionless Vlasov equation for electrons, is then

$$\boxed{\frac{\partial n_e}{\partial t} + \nabla \cdot (n_e \bar{\mathbf{v}}) = 0} \tag{6.40}$$

which in fluid mechanics is referred to as the *continuity equation*, and expresses the conservation of particles of a certain type, in this case electrons.

The next fluid equation, involving conservation of momentum, takes on the form of Newton's second law of motion for a fluid. It is obtained by taking a second moment of the collisionless Vlasov equation [Eq. (6.32)], this time by multiplying all terms by the momentum $m\mathbf{v}$ and then integrating over all velocities to obtain

$$\int m\mathbf{v} \left[\frac{\partial f}{\partial t} + \mathbf{v} \cdot \nabla f - \frac{e}{m} (\mathbf{E} + \mathbf{v} \times \mathbf{B}) \cdot \nabla_{\mathrm{v}} f \right] d\mathbf{v} = 0 \tag{6.41}$$

Noting again the fluid definitions of Eqs. (6.33) to (6.37), and the interchangeability of order among $\mathbf{r}$, t, and $\mathbf{v}$ derivatives, one has

$$m \frac{\partial}{\partial t} (n_e \bar{\mathbf{v}}) + m \nabla \cdot \int \mathbf{v}\mathbf{v} f(\mathbf{v})\, d\mathbf{v} - e \int \mathbf{v} [(\mathbf{E} + \mathbf{v} \times \mathbf{B}) \cdot \nabla_{\mathrm{v}} f]\, d\mathbf{v} = 0$$

$$m \frac{\partial}{\partial t} (n_e \bar{\mathbf{v}}) + m \nabla \cdot (n_e \overline{\mathbf{v}\mathbf{v}}) - e \int \mathbf{v} [(\mathbf{E} + \mathbf{v} \times \mathbf{B}) \cdot \nabla_{\mathrm{v}} f(\mathbf{v})]\, d\mathbf{v} = 0$$

This begins to look like the desired fluid mechanical momentum equation if we expand the first two terms. If we write the velocity as the sum of a slowly varying component $\bar{\mathbf{v}}(\mathbf{r}; t)$ and a faster fluctuating component $\tilde{\mathbf{v}}$, such that $\mathbf{v} = \bar{\mathbf{v}} + \tilde{\mathbf{v}}$, then the product $\overline{\mathbf{v}\mathbf{v}}$ becomes

$$\overline{\mathbf{v}\mathbf{v}} = \overline{(\bar{\mathbf{v}} + \tilde{\mathbf{v}})(\bar{\mathbf{v}} + \tilde{\mathbf{v}})} = \bar{\mathbf{v}}\bar{\mathbf{v}} + 2 \underbrace{\overline{\bar{\mathbf{v}}\tilde{\mathbf{v}}}}_{=0} + \overline{\tilde{\mathbf{v}}\tilde{\mathbf{v}}}$$

where $\overline{\bar{\mathbf{v}}\tilde{\mathbf{v}}} = \bar{\mathbf{v}}\overline{\tilde{\mathbf{v}}} = 0$, since $\overline{\tilde{\mathbf{v}}} \equiv 0$. The $\tilde{\mathbf{v}}\tilde{\mathbf{v}}$ term is a non-linear product of velocities that gives rise to interesting fluid mechanical properties, including aerodynamic flight. With expansion

of the differential product terms, the second fluid equation (6.39) takes the form

$$mn_e\frac{\partial\bar{\mathbf{v}}}{\partial t}+m\bar{\mathbf{v}}\overbrace{\left[\frac{\partial n_e}{\partial t}+mn_e\bar{\mathbf{v}}\cdot\nabla\bar{\mathbf{v}}+m\bar{\mathbf{v}}\nabla\cdot\right]}n\bar{\mathbf{v}}+m\nabla\cdot(n_e\overline{\bar{\mathbf{v}}\bar{\mathbf{v}}})$$
$$-e\int\mathbf{v}\,[(\mathrm{E}+\mathbf{v}\times\mathrm{B})\cdot\nabla_{\mathrm{v}}f(\mathbf{v})]\,d\mathbf{v}=0$$

where the second and fourth terms cancel by the continuity equation [Eq. (6.40)], where the expansion of the $\nabla\cdot(n\overline{\mathbf{vv}})$ term made use of the dyadic relation $\nabla\cdot(\mathbf{AB})=\mathbf{A}\cdot\nabla\mathbf{B}+\mathbf{B}\nabla\cdot\mathbf{A}$, and where we recognize $mn_e\overline{\bar{\mathbf{v}}\bar{\mathbf{v}}}$ from Eq. (6.35) as the dyadic pressure $\mathbb{P}_e$. To simplify the remaining integral involving the Lorentz force term, we replace $-e(\mathbf{E}+\mathbf{v}\times\mathbf{B})$ by $\mathbf{F}(\mathbf{v},\mathbf{r};t)$. The remaining integral is then

$$\int\mathbf{v}[\mathbf{F}(\mathbf{v})\cdot\nabla_{\mathrm{v}}f(\mathbf{v})]\,d\mathbf{v}=\int\mathbf{v}\{\nabla_{\mathrm{v}}\cdot[\mathbf{F}(\mathbf{v})f(\mathbf{v})]-\underbrace{f(\mathbf{v})\nabla_{\mathrm{v}}\cdot\mathbf{F}}_{=0}\}\,d\mathbf{v}$$

where we have used the vector identity $\nabla\cdot(\phi\mathbf{A})=\phi\nabla\cdot\mathbf{A}+\mathbf{A}\cdot\nabla\phi$, and noted that $\nabla_{\mathrm{v}}\cdot\mathbf{F}=-e\nabla_{\mathrm{v}}\cdot(\mathbf{E}+\mathbf{v}\times\mathbf{B})=0$ (since $\mathbf{E}$ is not a function of $\mathbf{v}$) and $\nabla_{\mathrm{v}}\cdot\mathbf{v}\times\mathbf{B}=\nabla_{\mathrm{v}}\times\mathbf{v}\cdot\mathbf{B}=0$ (since $\nabla_{\mathrm{v}}\times\mathbf{v}=0$). Again using the dyadic expansion of $\nabla\cdot(\mathbf{AB})$, this time with $\mathbf{A}=\mathbf{F}(\mathbf{v})f(\mathbf{v})$ and $\mathbf{B}=\mathbf{v}$, the remaining integral becomes

$$\int\mathbf{v}\{\nabla_{\mathrm{v}}\cdot[\mathbf{F}(\mathbf{v})f(\mathbf{v})]\}\,d\mathbf{v}=\int\{\nabla_{\mathrm{v}}\cdot[\mathbf{F}(\mathbf{v})f(\mathbf{v})\mathbf{v}]-\mathbf{F}(\mathbf{v})f(\mathbf{v})\cdot\underbrace{\nabla_{\mathrm{v}}\mathbf{v}}_{\mathbf{1}}\}\,d\mathbf{v}$$

The first term is again set equal to zero on the basis of Gauss's theorem in velocity space for the dyadic quantity $\mathbf{F}f(\mathbf{v})\mathbf{v}$, which requires a somewhat faster decay of $f(\mathbf{v})$ with large $\mathbf{v}$ than in the first moment equation (for the continuity equation). The second term, however, contributes in this case. Note that $-\mathbf{F}(\mathbf{v})f(\mathbf{v})\cdot\mathbf{1}=-\mathbf{F}(\mathbf{v})f(\mathbf{v})=e(\mathbf{E}+\mathbf{v}\times\mathbf{B})f(\mathbf{v})$, so that the remaining integral in Eq. (6.41) becomes

$$-e\int[(\mathbf{E}+\mathbf{v}\times\mathbf{B})\cdot\nabla_{\mathrm{v}}f(\mathbf{v})]\mathbf{v}\,d\mathbf{v}=e\int(\mathbf{E}+\mathbf{v}\times\mathbf{B})f(\mathbf{v})\,d\mathbf{v}=en_e(\mathbf{E}+\bar{\mathbf{v}}\times\mathbf{B})$$

where we have again used the definitions for $n_e(\mathbf{r},t)$ and $n_e(\mathbf{r},t)\bar{\mathbf{v}}(\mathbf{r};t)$ given by Eqs. (6.33) and (6.34). Combining all terms, we obtain the fluid mechanical equation expressing conservation of momentum for electrons:

$$m\underbrace{\left[\frac{\partial}{\partial t}+\bar{\mathbf{v}}\cdot\nabla\right]}_{D/Dt}\bar{\mathbf{v}}=-\frac{1}{n_e}\nabla\cdot\mathbb{P}_e-e(\mathbf{E}+\bar{\mathbf{v}}\times\mathbf{B})\tag{6.42}$$

where $D/Dt=\partial/\partial t+\bar{\mathbf{v}}\cdot\nabla$ is the *substantial* derivative, a time derivative moving with the average velocity, and where $\mathbb{P}_e=mn_e\overline{\bar{\mathbf{v}}\bar{\mathbf{v}}}$ is the dyadic electron pressure, as defined in Eq. (6.34).

Equation (6.37) provides a mathematical description for the rate of change of momentum for a compressible fluid – it is essentially Newton's second law of motion where the unbalanced forces are due to a gradient in pressure along the fluid trajectory, and to the Lorentz force $-e(\mathbf{E}+\bar{\mathbf{v}}\times\mathbf{B})$ on the electrons (charged particles). In many cases, involving an isotropic

distribution function, the dyadic pressure reduces to a scalar pressure P such that $\mathbb{P} = P\mathbf{1}$, and $\nabla \cdot \mathbb{P} = \nabla P$, yielding a more common form of the fluid mechanical *momentum equation* for electrons:

$$m\left(\frac{\partial}{\partial t} + \bar{\mathbf{v}} \cdot \nabla\right)\bar{\mathbf{v}} = -\frac{1}{n_e}\nabla P_e - e(\mathbf{E} + \bar{\mathbf{v}} \times \mathbf{B}) \tag{6.43}$$

The inclusion of viscosity, a frictional effect involving velocity differences (gradients) among adjoining regions of the same species, leads to an additional term in the momentum equation [Eq. (6.43)], which is then referred to in fluid mechanics as the *Navier–Stokes equation.*[17] In its most common form this involves the addition of a viscous force term $\mu\nabla^2\mathbf{v}$ to the right-hand side of Eq. (6.43). A discussion of the fluid transport equations including viscosity (for uncharged particles) is given in Ref. 16.

Another commonly encountered situation in which an alternative form of Eq. (6.43) occurs is that in which short range collisions between the various species (electrons, ions, and neutrals) leads to a transfer of momentum among species, such as between electrons and ions, or between electrons and neutrals. For this to arise naturally would require an appropriate collision term on the right side of the kinetic Vlasov equation (6.25). Inclusion of such a collision term produces no additional term in the continuity equation (6.40), but a collision term of the form $-m\nu\bar{\mathbf{v}}$ will appear in Eq. (6.43), where ν is an effective collision frequency for momentum transfer among different species due to short-range collisions.[16] In the absence of such viscosity and inter-particle collisions, the fluid equations are referred to as the *Euler equations.* Collecting the fluid equations (6.40) and (6.43) for each species j along with Maxwell's equations, we now have the *Maxwell–Euler equations* that describe plasma dynamics on fluid level:

$$\nabla \times \mathbf{H} = \frac{\partial \mathbf{D}}{\partial t} + \sum_j q_j n_j \mathbf{v}_j \tag{6.44}$$

$$\nabla \times \mathbf{E} = -\frac{\partial \mathbf{B}}{\partial t} \tag{6.45}$$

$$\nabla \cdot \mathbf{D} = \sum_j q_j n_j \tag{6.46}$$

$$\nabla \cdot \mathbf{B} = 0 \tag{6.47}$$

with the constitutive relations

$$\mathbf{D} = \epsilon_0 \mathbf{E} \tag{6.48}$$

$$\mathbf{B} = \mu_0 \mathbf{H} \tag{6.49}$$

and for each particle species (j)

$$\frac{\partial n_j}{\partial t} + \nabla \cdot (n_j \mathrm{v}_j) = 0 \tag{6.50}$$

$$m\left(\frac{\partial}{\partial t} + \mathrm{v}_j \cdot \nabla\right)\mathrm{v}_j = -\frac{1}{n_j}\nabla P_j + q_j(\mathbf{E} + \mathbf{v}_j \times \mathbf{B}) \tag{6.51}$$

where for electrons $q = -e$ and for ions $q = +eZ$. Note that for simplicity we have dropped the overbar on the average velocities $\bar{\mathbf{v}}_j$ with the understanding that the simpler notation $\mathbf{v}_j$ now carries the connotation of a slowly varying function of space and time.

The Maxwell–Euler equations are an *independent* set in that the particles affect the electromagnetic fields, through the charge [Eq. (6.46)] and current [Eq. (6.44)] distributions, while the fluid equations are in turn affected by $\mathbf{E}$ and $\mathbf{B}$ [Eq. (6.38)]. The coupled set of equations as described here is *incomplete* in that for each species we have added five new fluid quantities (n_j, $\mathbf{v}_j$, and the scalar P_j), but only four new scalar equations, one from Eq. (6.40) and three from Eq. (6.43). An additional equation is required for each. To complete the set of coupled fluid–electromagnetic equations we must generate another equation – an energy related equation – by taking an additional moment of the Vlasov equation (6.32) for each species, this time by multiplying through by a scalar factor $m\mathrm{v}^2/2$ and then proceeding with the velocity-space integrals. From Eq. (6.32) we form equations for each species:

$$\int \frac{m\mathrm{v}^2}{2}\left[\frac{\partial f_j}{\partial t} + \mathbf{v} \cdot \nabla f_j + \frac{q_j}{m}(\mathbf{E} + \mathbf{v} \times \mathbf{B}) \cdot \nabla_{\mathrm{v}} f_j\right] d\mathbf{v} = 0 \tag{6.52}$$

Integration techniques similar to those used to obtain Eqs. (6.40) and (6.43), yield[2] a *conservation of energy* equation:

$$n_j\left[\frac{\partial}{\partial t} + \mathbf{v} \cdot \nabla\right] U_j + (\mathbb{P}_j \cdot \nabla) \cdot \mathbf{v} + \nabla \cdot \mathbf{Q}_j = 0 \tag{6.53}$$

where for each species U_j is the (random) thermal energy defined by Eq. (6.36), $\mathbf{Q}_j$ is the thermal flux vector defined by Eq. (6.37), and we recall that $\tilde{\mathbf{v}}^2 \equiv \tilde{\mathbf{v}} \cdot \tilde{\mathbf{v}}$.

For an isotropic plasma (no directional preference) with a symmetric distribution function [$f(\mathbf{v}) = f(-\mathbf{v})$] the pressure dyad reduces to a scalar pressure times the unit dyad $\mathrm{P_j}\mathbf{1}$, and the thermal energy flux $\mathbf{Q}_j$ is zero. The simplified *adiabatic* ($\mathbf{Q} = 0$) equation (6.53) is then

$$n_j \frac{DU_j}{Dt} + P_j \nabla \cdot \mathbf{v} = 0 \tag{6.54}$$

where we use the substantial derivative $D/Dt = \partial/\partial t + \mathbf{v} \cdot \nabla$, and where we recall that there is a separate $\mathbf{v}_j$ for each species, but that we have suppressed the j for simplicity. Writing the

continuity equation (6.40) in terms of the substantial derivative as

$$\nabla \cdot \mathbf{v} = -\frac{1}{n_j}\frac{Dn_j}{Dt}$$

the adiabatic energy equation (6.54) can be written as

$$n_j \frac{DU_j}{Dt} - \frac{P_j}{n_j}\frac{Dn_j}{Dt} = 0 \tag{6.55}$$

As we shall see, this leads to a very simple relation between P and n, as needed to complete the Maxwell–Euler equation set.

For a fluid with three degrees of translational freedom, elementary kinetic theory tells us that the thermal energy U can be expressed in terms of a temperature T, for each species, by

$$U_j = \frac{1}{2}m\overline{\tilde{\mathbf{v}}^2} \equiv \frac{3}{2}\kappa T_j \tag{6.56}$$

e.g., an energy of $\frac{1}{2}\kappa T$ per degree of freedom. From our definition of the pressure dyadic [Eq. (6.35)], for the symmetric and isotropic case,

$$\mathbb{P} = nm\overline{\tilde{\mathbf{v}}\tilde{\mathbf{v}}} = nm\left(\overline{\tilde{v}_x^2}\mathbf{x}_0\mathbf{x}_0 + \overline{\tilde{v}_y^2}\mathbf{y}_0\mathbf{y}_0 + \overline{\tilde{v}_z^2}\mathbf{z}_0\mathbf{z}_0\right)$$

where $\overline{\tilde{v}_x^2} = \overline{\tilde{v}_y^2} = \overline{\tilde{v}_z^2} = \frac{1}{3}\overline{\tilde{\mathbf{v}}^2}$, so that

$$\mathbb{P}_j = m\overline{\tilde{\mathbf{v}}^2} \cdot \mathbf{1} = P_j\mathbf{1} \tag{6.57}$$

Combining Eqs. (6.56) and (6.57), we obtain the perfect gas relation for partial pressures,

$$\boxed{P_j = n_j\kappa T_j} \tag{6.58}$$

From Eq. (6.56) the thermal energy can now be written as

$$U_j = \frac{3}{2}\frac{P_j}{n_j} \tag{6.59}$$

From Eq. (6.55) we can write the adiabatic energy equation as

$$\frac{DU_j}{Dt} = \frac{P_j}{n_j^2}\frac{Dn_j}{Dt} = -P_j\frac{D}{Dt}\left(\frac{1}{n_j}\right)$$

so that with Eq. (6.59)

$$\frac{3}{2}\frac{D}{Dt}\left(\frac{P_j}{n_j}\right) = -P_j\frac{D}{Dt}\left(\frac{1}{n_j}\right)$$

Moving along a streamline, i.e., with D/Dt, the differential relation takes the form

$$\frac{3}{2}\left[\frac{dP_j}{n_j} + P_j d\left(\frac{1}{n_j}\right)\right] = -P_j d\left(\frac{1}{n_j}\right)$$

or

$$\frac{dP_j}{P_j} = \left(1 + \frac{2}{3}\right)\frac{dn_j}{n_j} = \gamma\frac{dn_j}{n_j} \tag{6.60a}$$

Integrating, one obtains the desired *adiabatic condition* between pressure and density for processes (wave motions, etc.) involving no heat transfer:

$$\boxed{\frac{P_j}{P_{0j}} = \left(\frac{n_j}{n_{0j}}\right)^{\gamma}} \tag{6.60b}$$

where P_{0j} and n_{0j} are background values, and $\gamma = 1 + 2/N$ is the thermodynamic *ratio of specific heats* for a system with N degrees of freedom. In this case $\gamma = \frac{5}{3}$, for three degrees of translational motion. For a diatomic molecule, one would have two additional degrees of rotational freedom, and one degree of vibrational freedom. This then completes the Maxwell–Euler equation set for a fluid mechanical description of an isotropic, collisionless plasma with a symmetric velocity distribution function.

Using Eq. (6.60), the pressure P can be eliminated from Eq. (6.43) so that there are an equal number of equations and unknowns. The coupled set of equations then permits a mathematical or computational description of fluid level plasma phenomena (particle transport, wave motion, radiation, etc.) in which the particle densities and currents determine the electromagnetic fields, and these fields *self-consistently* determine the particle densities and velocities. Descriptions of various plasma phenomena are presented in Refs. 1–12.

The fluid model has an appropriate level of detail to describe some of the basic properties of wave propagation in plasmas. For instance, the propagation of both transverse and longitudinal waves is easily described, dispersion relations obtained, and some dominant wave–wave couplings identified. Wave mixing occurs as a result of the non-linear terms in the Maxwell–Euler equations: $n_j\mathbf{v}$, $\mathbf{v}\cdot\nabla\mathbf{v}$, and $\mathbf{v}\times\mathbf{B}$. For instance, if waves with frequencies ω_1 and ω_2 propagate in the plasma, then the density and velocity will have terms that vary in space and time as

$$e^{-i(\omega_1 t - \mathbf{k}_1\cdot\mathbf{r})} \quad \text{and} \quad e^{-i(\omega_2 t - \mathbf{k}_2\cdot\mathbf{r})}.$$

Multiplying these terms together results in a cross term with beat frequencies $\omega_3 = \omega_1 \pm \omega_2$. Thus, these terms can lead to scattering processes where two waves create a third, or the inverse process where a wave decays into two other waves. Examples of this are stimulated Raman scattering (SRS), stimulated Brillouin scattering (SBS), and the $2\omega_{pe}$ instability. These will be discussed later.

An example of something missing from the fluid treatment of a plasma is the collisionless Landau damping discussed earlier. Since the magnitude and sign of this damping process depend entirely upon the shape of the velocity distribution near the electron-acoustic wave phase velocity, it cannot be described by the fluid equations, in which all information about the velocity distribution has been integrated out. In general, any process that involves velocity specific wave–particle interactions cannot be described in the fluid description. However, in some cases the averaged consequences of these processes can be included, for instance by adding a collision term or damping rate to the fluid equations.

6.4.4 Plasma Expansion

An important characteristic of hot dense plasmas is the fact that they expand into vacuum with a speed determined by the temperature of the electrons (usually hotter than the ions) and the mass of the ions. The rate at which this occurs determines how fast energy must be supplied to the plasma if it is to reach a high temperature. The expansion rate of a plasma may be described in terms of the one-dimensional isothermal expansion of a hot fluid with two species: electrons and ions. This can be seen by examination of the conservation of mass and momentum equations (6.40) and (6.43) for both electrons and ions. Because the resultant expansion velocity is small (because of the ion mass), the electron momentum equation is dominated by the non-velocity terms, so that for a dimensional plasma of electron density n_e and electron pressure P_e

$$n_e eE = -\frac{\partial}{\partial x} P_e. \tag{6.61}$$

The one-dimensional continuity (6.40) and momentum (6.43) equations describing ions of density n_i, partial pressure P_i, charge $+Ze$ and mass M are

$$\frac{\partial n_i}{\partial t} + \frac{\partial}{\partial x}(n_i \mathrm{v}) = 0 \tag{6.62}$$

$$M n_i \left[\frac{\partial}{\partial t} + \mathrm{v}\frac{\partial}{\partial x}\right] \mathrm{v} = n_i Z e E - \frac{\partial}{\partial x} P_i. \tag{6.63}$$

The attraction of the electrons to the ions maintains an overall neutrality in the plasma, so that

$$n_e = Z n_i \tag{6.64}$$

The pressure terms in the electron and ion momentum equations (6.61) and (6.63) can be replaced with expressions involving the respective densities through use of the adiabatic energy condition, Eq. (6.60b), in the form

$$dP = \frac{\gamma P}{n}\, dn$$

Writing this separately for the electron and ion partial pressures, and using the perfect gas relation, Eq. (6.58), for both, the pressure gradient terms in Eqs. (6.61) and (6.63) become

$$\frac{\partial P_e}{\partial x} = \gamma \kappa T_e \frac{\partial n_e}{\partial x} \tag{6.65}$$

and

$$\frac{\partial P_i}{\partial x} = \gamma \kappa T_i \frac{\partial n_i}{\partial x} \tag{6.66}$$

The momentum equation for ions then becomes

$$M n_i \left[\frac{\partial}{\partial t} + \mathrm{v}\frac{\partial}{\partial x}\right] \mathrm{v} = n_i Z e E - \gamma \kappa T_i \frac{\partial n_i}{\partial x} \tag{6.67}$$

Substituting for the electric field E from Eq. (6.61), which couples electron and ion motion, i.e.,

$$E = -\frac{1}{en_e}\frac{\partial P_e}{\partial x} = -\frac{\gamma\kappa T_e}{en_e}\frac{\partial n_e}{\partial x}$$

the ion momentum equation (6.67) becomes

$$Mn_i\left[\frac{\partial}{\partial t} + \mathrm{v}\frac{\partial}{\partial x}\right]\mathrm{v} = -(Z\gamma\kappa T_e + \gamma\kappa T_i)\frac{\partial n_i}{\partial x}$$

or for $T_e \gg T_i$

$$\left[\frac{\partial}{\partial t} + \mathrm{v}\frac{\partial}{\partial x}\right]\mathrm{v} = -\mathrm{v}_{\mathrm{exp}}^2\frac{1}{n_i}\frac{\partial n_i}{\partial x} \tag{6.68}$$

where we define an electron–ion thermal expansion velocity

$$\boxed{\mathrm{v}_{\mathrm{exp}} = \left(\frac{Z\gamma\kappa T_e}{M}\right)^{1/2}} \tag{6.69a}$$

driven by the electron pressure (through $n_e\kappa T_e$), but limited by the inertia of the ions through their mass M. In practical units the expansion velocity can be expressed as[‡]

$$\boxed{\mathrm{v}_{\mathrm{exp}} = 0.28\left(\frac{Z\kappa T_e}{M}\right)^{1/2}\ \mu\mathrm{m/ps}} \tag{6.69b}$$

where Z is in units of ten, κT is in keV, the ion mass M is expressed in units of 20 times that of a proton, and γ is taken as $\frac{5}{3}$.

The ion continuity equation (6.62) can be written as

$$\left[\frac{\partial}{\partial t} + \mathrm{v}\frac{\partial}{\partial x}\right]n_i + n_i\frac{\partial \mathrm{v}}{\partial x} = 0 \tag{6.70}$$

As can be seen by substitution, a solution to the fluid equations (6.68) and (6.70) is[1]

$$\mathrm{v} = \mathrm{v}_{\mathrm{exp}} + \frac{x}{t} \tag{6.71}$$

and

$$n_i = N_{i0}e^{-x/\mathrm{v}_{\mathrm{exp}}t} \tag{6.72}$$

[‡]For comparison, the speed of light in vacuum, in these units, is $c \simeq 300\ \mu$m/ps.

Thus the plasma expands from an initial ion density n_{i0}, at a surface $x = 0$, with the electron–ion thermal velocity, v_{exp}. Examining the density function $n_i(x, t)$ we see that the density gradient length l_{exp}, due to the expansion, is given by

$$l_{exp} \equiv -n_i/(\partial n_i/\partial x) = v_{exp} t \tag{6.73}$$

and increases with time at a rate set by the expansion velocity v_{exp}. According to Eq. (6.69), a 1 keV plasma of ions with an average charge state of $Z = +12$ will expand at a velocity of approximately 0.21 μm/ps.

6.4.5 Electron-Acoustic Waves

The propagation of high frequency longitudinal waves in a plasma, known widely as electron-acoustic waves, and also known as electron-plasma waves or as Langmuir oscillations, is readily described on the basis of the Maxwell–Euler fluid equations (6.40) and (6.43–6.49). For high frequency waves the more massive ions are relatively immobile and simply provide a uniform, electrically neutralizing charge distribution. For longitudinal waves in which the field quantities n, $\mathbf{v}$, P, $\mathbf{E}$, etc., vary only in the wave propagation ($\mathbf{k}$) direction, one need consider only the equations of continuity (6.40), momentum conservation (6.43), and Gauss's law (6.46), which for electrons are written as

$$\frac{\partial n_e}{\partial t} + \nabla \cdot (n_e \mathbf{v}) = 0$$

$$m\left(\frac{\partial}{\partial t} + \mathbf{v} \cdot \nabla\right)\mathbf{v} = -\frac{1}{n_e}\nabla P_e - e(\mathbf{E} + \mathbf{v} \times \mathbf{B})$$

$$\nabla \cdot \mathbf{E} = -e n_e/\epsilon_0$$

where the uniform ion distribution does not contribute to the last equation.

The non-linear terms, involving products like $n_e\mathbf{v}$, $\mathbf{v} \cdot \nabla\mathbf{v}$, and $\mathbf{v} \times \mathbf{B}$, can be simplified through a *linearization* process in which one assumes that each field can be written as the sum of a background value and a small fluctuation therefrom. Thus we write

$$n_e = n_0 + \tilde{n}_e \tag{6.74a}$$

$$\mathbf{v} = \mathbf{v}_0 + \tilde{\mathbf{v}} \tag{6.74b}$$

$$\mathbf{E} = \mathbf{E}_0 + \tilde{\mathbf{E}} \tag{6.74c}$$

and so on. We then assume that the waves of interest are of small amplitude, such that $\tilde{n}_e/n_0 \ll 1$, etc. In the case of the velocity modulation we assume that there is no directed average motion, so that $\mathbf{v}_0 = 0$. Substituting Eqs. (6.74) into the fluid equations and dropping all product of fluctuation terms as being of second order (very small), we have (dropping the tildes for fluctuating quantities)

$$\frac{\partial n_e}{\partial t} + n_0 \nabla \cdot \mathbf{v} + \underbrace{\mathbf{v}_0 \cdot \nabla n_e}_{=0} = 0 \tag{6.75}$$

$$m\frac{\partial \mathbf{v}}{\partial t} = -\frac{1}{n_0}\gamma\kappa T_e \nabla n_e - e\mathbf{E} \tag{6.76}$$

$$\nabla \cdot \mathbf{E} = -\frac{en_e}{\epsilon_0} \tag{6.77}$$

where the pressure gradient was handled as in Eq. (6.65). Taking $\partial/\partial t$ of Eq. (6.75),

$$\frac{\partial^2 n_e}{\partial t^2} + n_0 \frac{\partial}{\partial t}(\nabla \cdot \mathbf{v}) = 0$$

and the divergence $(\nabla\cdot)$ of Eq. (6.76),

$$m\frac{\partial}{\partial t}(\nabla \cdot \mathbf{v}) = -\frac{\gamma\kappa T_e}{n_0}\nabla^2 n_e - e\nabla \cdot \mathbf{E}$$

these can be combined to form a wave equation

$$\frac{\partial^2 n_e}{\partial t^2} - \frac{\gamma\kappa T_e}{m}\nabla^2 n_e - \frac{en_0}{m}\nabla \cdot \mathbf{E} = 0$$

Using Eqs. (6.46) and (6.48), this can be written as

$$\frac{\partial^2 n_e}{\partial t^2} + \frac{e^2 n_0}{\epsilon_0 m} n_e - \frac{\gamma\kappa T_e}{m}\nabla^2 n_e = 0$$

or

$$\boxed{\left[\frac{\partial^2}{\partial t^2} + \omega_p^2 - a_e^2\nabla^2\right] n_e(\mathbf{r}, t) = 0} \tag{6.78}$$

which we recognize as a longitudinal wave equation for electron density fluctuations, with *electron sound speed* a_e given by

$$\boxed{a_e = \left(\frac{\gamma\kappa T_e}{m}\right)^{1/2}} \tag{6.79}$$

where $\gamma = 1+2/N$, as described below Eq. (6.60b), and where, as we will understand shortly, the natural frequency of oscillation ω_p, known as the *plasma frequency*, is given by

$$\boxed{\omega_p = \left(\frac{e^2 n_0}{\epsilon_0 m}\right)^{1/2}} \tag{6.80}$$

for background electron density n_0. For the 1 keV electron temperature plasma considered earlier, the electron sound speed is $a_e \simeq 17\ \mu$m/ps.

To better appreciate the plasma frequency, we consider an electron density wave of the form

$$n_e(\mathbf{r}, t) = n_e e^{-i(\omega t - \mathbf{k}\cdot\mathbf{r})} \tag{6.81}$$

where the wave is of frequency ω and wavevector $\mathbf{k}$, with scalar wavenumber $k = 2\pi/\lambda$. For a wave of this form the time and space differentials are replaced by (see Chapter 2, Section 2.2)

$$\frac{\partial}{\partial t} \rightarrow -i\omega \tag{6.82a}$$

and

$$\nabla \rightarrow i\mathbf{k} \tag{6.82b}$$

so that the wave equation (6.78) takes the form

$$\left[\omega^2 - \omega_p^2 - k^2 a_e^2\right] n_e = 0 \tag{6.83}$$

where the exponential with time and space dependence is suppressed. Following the same procedures as in Chapter 2 for electromagnetic waves, we observe that Eq. (6.83) has solutions for finite n when the bracketed quantity is zero. This then is a natural oscillation or wave of the system, requiring, in principle, no driving term. Setting the bracketed quantity equal to zero yields the *dispersion relation for the electron-acoustic wave*,

$$\boxed{\omega^2 = \omega_p^2 + k^2 a_e^2} \tag{6.84}$$

This tells us that for long period plasma waves, where k goes to zero, there is natural oscillation at the electron plasma frequency, $\omega \simeq \omega_p$. For waves of finite k, in the range of $0 \leq k \leq \omega_p/a_e$, the frequency increases somewhat, to a value of $\sqrt{2}\omega_p$ at $k = \omega_p/a_e$, as shown in the dispersion diagram of Figure 6.7.

Here the frequency as a function of wavenumber is shown for naturally occurring waves in a plasma. The parameter $\omega_p/a_e = 1/\sqrt{\gamma}\lambda_D$ is approximately equal to one over the Debye screening distance, discussed earlier in Section 6.3, Eq. (6.6). For waves characterized by $k < k_D \equiv 1/\lambda_D$, the wavelength λ is greater than λ_D and the discreteness of individual charges within the plasma is not "seen" by the wave – they are screened. In this region ($k < 1/\lambda_D$), the fluid model is quite accurate and the wave propagates as indicated. However, for $k > 1/\lambda_D$, the wavelength of the plasma wave is less than the Debye screening distance and the discreteness or individuality of charges should be apparent, i.e., *not* screened. As a consequence we can suspect that the fluid theory, which averages out (ignores) individual charge effects, might be inadequate.

Indeed, if one considers the propagation of the electron-acoustic wave based on a kinetic theory, as discussed in Section 6.4.2, one obtains the same basic dispersion relation [Eq. (6.84)], but the frequency is found to be complex, with an imaginary component ω_i corresponding to wave decay,[1, 3, 4, 12] where for $\omega = \omega_r + \omega_i$

$$\omega_i = \frac{\pi}{2}\frac{\omega_p^2 \omega_r}{k^2}\frac{\partial f}{\partial v}\bigg|_{v=\omega/k} \tag{6.85}$$

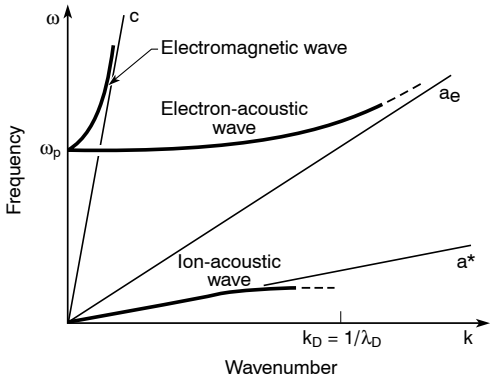

FIGURE 6.7. The dispersion diagram for naturally occurring waves in an isotropic plasma. Shown are the transverse electromagnetic wave with cutoff at the plasma frequency ω_p, a high frequency longitudinal wave called the electron-acoustic wave, and a low frequency longitudinal wave called the ion-acoustic wave.

so that a negative slope for $\partial f/\partial \mathrm{v}$ corresponds to damping. The expression for a three-dimensional Maxwellian distribution $f(\mathrm{v})$ is given by

$$f(\mathrm{v}) = \frac{1}{(2\pi)^{3/2}\mathrm{v}_e^3} e^{-\mathrm{v}^2/2\mathrm{v}_e^2} \tag{6.86a}$$

However, in Eq. (6.85), $f(\mathrm{v})$ may be considered to be a one-dimensional Maxwellian electron velocity distribution as follows:

$$f(\mathrm{v}) = \frac{1}{\sqrt{2\pi}\mathrm{v}_e} e^{-\mathrm{v}^2/2\mathrm{v}_e^2} \tag{6.86b}$$

where the electron thermal velocity is

$$\mathrm{v}_e = (\kappa T_e/m)^{1/2} \tag{6.86c}$$

the damping term becomes

$$\frac{\omega_i}{\omega_r} = -\sqrt{\frac{\pi}{8}} \frac{\omega_p^2 \omega_r}{k^3 \mathrm{v}_e^3} e^{-\frac{\omega_r^2}{2k^2\mathrm{v}_e^2}} \tag{6.87}$$

where from Eq. (6.84) $\omega_r^2 \simeq \omega_p^2(1 + k^2/k_D^2)$, and where $k_D = \omega_p/\mathrm{v}_e$. For $k \ll k_D$ the exponential factor in Eq. (6.87) dominates, so that ω_i/ω_r goes to zero and damping is negligible. However, for larger k, near k_D, damping is very strong, with

$$\frac{\omega_i}{\omega_r} \simeq -\sqrt{\frac{\pi}{4}} \left(\frac{k_D}{k}\right)^3 e^{-(k_D/k)^2}$$

so that for $k = k_D$ the wave decays to a $1/e$ field amplitude in just a few oscillations. Decay of electron-acoustic waves is known as Landau damping,[18] ¶ and is due to particle–wave

¶Named for the Russian scientist L.D. Landau.

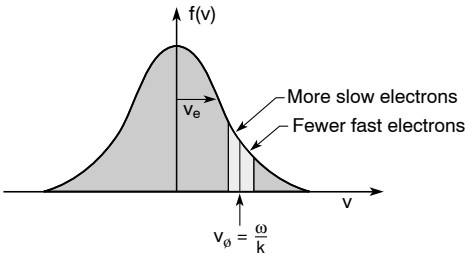

FIGURE 6.8. The electron velocity distribution [Eq. (6.86)] in a thermal plasma has more slow electrons than fast electrons in the vicinity of v_ϕ, the phase velocity electron-acoustic waves. This is particularly troublesome for short period (high k) waves for which $v_\phi \geq v_e$. In this region there are many resonant electrons and the gradient in velocity is sharp, leading to strong damping of the wave. This process, called *Landau damping*, is a collisionless wave–particle interaction in which energy is transferred from the wave to the individual electrons.

interactions, particularly for electrons traveling in the wave direction with velocities approximately equal to the wave's phase velocity.

As was suggested earlier in Figure 6.3, the electron-acoustic wave consists of regions of high charge density that propagate at high phase velocity v_ϕ. From Eq. (6.84) we can now conclude, with a little algebraic manipulation, that

$$v_\phi = \frac{\omega}{k} = a_e\sqrt{1 + \frac{k_D^2}{k^2}} \tag{6.88}$$

so that in general $v_\phi > a_e$ for propagating waves ($k < k_D$). In this region ($v > a_e$) the velocity distribution (6.86) falls very rapidly with increasing velocity (negative slope), so that in general there are more slow electrons ($v \leq v_\phi$) than fast electrons ($v \geq v_\phi$) interacting with the wave. Because the velocities of these *resonant* electrons are close to that of the wave, there is a relatively long interaction time in which energy can be exchanged between the electrons and the wave. Traveling with the wave, the somewhat faster electrons tend to "push" the potential crest of the wave, giving up energy as they merge with it. Somewhat slower electrons must be dragged along, taking energy from the wave, As shown in Figure 6.8, the thermal velocity distribution is negative in slope for $v > a_e$, so that there are more slow electrons taking energy away from the wave than fast electrons contributing energy. Thus on balance, there is a net loss of energy for a plasma wave of high phase velocity ($v_b > a_e$). In this case the complete electron velocity distribution has a positive slope (more fast than slow electrons) near v_b, leading to wave growth, sometimes described as "inverse Landau damping."

6.4.6 Ion-Acoustic Waves

The fluid level plasma equations (6.40, 6.43–6.49) also have a low frequency solution, a natural mode of oscillation at a frequency $\omega \ll \omega_p$. In this longitudinal wave the frequency is sufficiently low that the ions play a major role and, as we will see, the electrons also participate. At these very low frequencies the electron and ion charge densities are very closely coupled, a condition called *quasi-neutrality.* We again seek a linearized version of the fluid equations (6.40, 6.43), through a perturbation analysis $n_i = n_{0i} + \tilde{n}_i$, $n_e = n_{0e} + \tilde{n}_e$, $\mathbf{v}_i = \mathbf{v}_{0i} + \tilde{\mathbf{v}}_i$, and

$\mathbf{v}_e = \mathbf{v}_{0e} + \tilde{\mathbf{v}}_e$. With no long scale average motion $\mathbf{v}_{0e} = \mathbf{v}_{0i} = 0$. For ions of charge Z and mass M, the condition of quasi-neutrality permits us to make the approximations $n_{0i} = n_{0e}/Z$, $\tilde{n}_i \simeq \tilde{n}_e/Z$, and $\tilde{\mathbf{v}}_e \simeq \tilde{\mathbf{v}}_i$. Furthermore, for small amplitude waves the process is adiabatic (no heat transfer), so that the pressure gradients can be replaced by density gradients [as seen previously in Eqs. (6.65) and (6.66)], viz.,

$$\nabla \tilde{P}_i = \gamma \kappa T_i \nabla \tilde{n}_i \tag{6.89}$$

and

$$\nabla \tilde{P}_e = \gamma \kappa T_e \nabla \tilde{n}_e \tag{6.90}$$

where the values of γ will depend on the nature of the wave and thus could be different for ions and electrons.

With these approximations the linearized fluid equations for the ions can be written as

$$\frac{\partial n_i}{\partial t} + \frac{n_0}{Z} \nabla \cdot \mathbf{v}_i = 0 \tag{6.91}$$

$$\frac{M n_0}{Z} \frac{\partial \mathbf{v}_i}{\partial t} = -\gamma \kappa T_i \nabla n_i + e n_0 \mathbf{E} \tag{6.92}$$

and the electron momentum equation, with $\mathbf{v}_e \simeq \mathbf{v}_i$ and $n_e \simeq Z n_i$, is

$$m n_0 \frac{\partial \mathbf{v}_i}{\partial t} = -Z \gamma \kappa T_e \nabla n_i - e n_0 \mathbf{E} \tag{6.93}$$

where we have dropped the tildes for simplicity (they appear on all but background quantities), have replaced $\mathbf{v}_e$ by $\mathbf{v}_i$ as discussed above, and have simplified the background charge densities by writing $n_{0e} = n_0$ and $n_{0i} = n_0/Z$. With these low-frequency approximations the electron continuity equation offers no additional information. Adding the two momentum equations (6.91) and (6.92) to eliminate $\mathbf{E}$, and noting that $m \ll M/Z$, we have

$$\frac{M n_0}{Z} \frac{\partial \mathbf{v}_i}{\partial t} = -(\gamma \kappa T_i + Z \gamma \kappa T_e) \nabla n_i \tag{6.94}$$

A wave equation can now be formed by taking $\partial/\partial t$ (6.91) and $\nabla \cdot$ (6.94):

$$\frac{\partial^2 n_i}{\partial t^2} + \frac{n_0}{Z} \frac{\partial}{\partial t} (\nabla \cdot \mathbf{v}_i) = 0$$

$$\frac{M n_0}{Z} \frac{\partial}{\partial t} (\nabla \cdot \mathbf{v}_i) = -(\gamma \kappa T_i + Z \gamma \kappa T_e) \nabla^2 n_i$$

which can be combined to form the *ion-acoustic wave equation*

$$\frac{\partial^2 n_i}{\partial t^2} - \left(\frac{\gamma \kappa T_i + Z \gamma \kappa T_e}{M} \right) \nabla^2 n_i = 0 \tag{6.95}$$

For the common case $T_e \gg T_i$, generally resulting from the fact that energy is delivered to the

electrons and only indirectly transferred to the ions through collisions, the *ion-acoustic wave equation* can be written as

$$\frac{\partial^2 n_i}{\partial t^2} - a^{*2}\nabla^2 n_i = 0 \tag{6.96}$$

where the wave propagates with a hybrid sound speed

$$a^* = \sqrt{\frac{Z\gamma\kappa T_e}{M}} \tag{6.97}$$

which has the characteristics of an electron temperature and an ion mass.[4] This low-frequency plasma oscillation is thus seen to be driven by electron thermal energy, but with an inertia set by the more massive ions. Due to the quasi-neutrality at this low frequency, each electron must drag an equivalent (per unit charge) mass of M/Z.

Following our usual procedures, the dispersion relation for an ion-acoustic wave with $n_i = n_{i0}\exp[-i(\omega t - \mathbf{k}\cdot\mathbf{r})]$ follows from Eq. (6.96) as

$$\omega = ka^* \tag{6.98}$$

as illustrated by the lower branch in Figure 6.7. This dispersion relation indicates a linear relationship between k and ω, so that in fact it lacks dispersion – all frequencies propagate at the same phase velocity, a^*. A somewhat more refined analysis shows a rollover to lower phase velocities as k approaches the Debye wavenumber. Again Landau damping can be important, but in this case it is the ions that do the damping, and the degree of damping is a function of ZT_e/T_i due to the variation in sound speed. At the phase velocity of this wave, a^*, the electron velocity distribution is nearly flat [$f'(\mathrm{v}) \simeq 0$], so that the number of relatively fast and slow electrons is about equal, and there is little transfer of energy. For the ions, with $ZT_e/T_i \gg 1$, a^* is much greater than the ion thermal speed ($a_i = \sqrt{\gamma\kappa T_i/M}$) and thus the phase velocity of the ion-acoustic wave is so far out on the ion velocity distribution curve that $f_i(a^*)$ goes to zero and again there is little damping, i.e., although $f_i'(\mathrm{v})$ is sharp, there are few ions in this velocity region. For ZT_e/T_i approaching unity, a^* approaches a_i and ion damping becomes very strong for k near the Debye wavenumber

6.4.7 Transverse Electromagnetic Waves in a Plasma

Transverse electromagnetic waves also propagate in a plasma, much like those considered in Chapter 2, but with a cutoff appearing at the plasma frequency $\omega \simeq \omega_p$, which has important consequences for energy delivery in laser-produced plasmas. The Maxwell–Euler fluid equations give a very satisfactory description of these waves. At these high frequencies the ions are immobile, so that we need consider only the electrons in Eqs. (6.44–6.51). For transverse electromagnetic waves of relatively weak intensity these equations simplify considerably. The current term in Eq. (6.44), which in general is non-linear, simplifies in this case to $\mathbf{J} = -en_0\mathbf{v}$, where n_0 is the background electron density, assumed in this weak field limit to be unmodulated

by the passing electromagnetic wave. In this case Maxwell's equations (6.44–6.49) can be written as

$$\nabla \times \mathbf{H} = \epsilon_0 \frac{\partial \mathbf{E}}{\partial t} - e n_0 \mathbf{v} \tag{6.99}$$

$$\nabla \times \mathbf{E} = -\mu_0 \frac{\partial \mathbf{H}}{\partial t} \tag{6.100}$$

In Eqs. (6.50) and (6.51), which describe particle motion, all non-linear terms can be neglected in the weak field limit, so that with only electrons mobile, these become

$$\frac{\partial n_e}{\partial t} + n_0 \nabla \cdot \mathbf{v} = 0 \tag{6.101}$$

and

$$m \frac{\partial \mathbf{v}}{\partial t} = -\frac{\gamma \kappa T_e}{n_0} \nabla n_0 - e\mathbf{E} \tag{6.102}$$

For transverse electromagnetic waves, as seen earlier in Chapters 2 and 3, only the transverse component of the current density $\mathbf{J}_\mathrm{T}$ contributes to the wave, and thus only to the transverse component of $\mathbf{v}$. This is also the case for the plasma in the weak-field limit. Thus in Eqs. (6.101) and (6.102), the $\nabla \rightarrow i\mathbf{k}$ terms are longitudinal and thus do not contribute to the transverse motion. The remaining terms in Eq. (6.102) yield a simplified version of Newton's law, $\mathbf{F} = m\mathbf{a}$, for the electrons:

$$m \frac{\partial \mathbf{v}}{\partial t} = -e\mathbf{E} \tag{6.103}$$

We can now develop a wave equation by differentiating Eq. (6.99) with respect to time,

$$\nabla \times \frac{\partial \mathbf{H}}{\partial t} = \epsilon_0 \frac{\partial^2 \mathbf{E}}{\partial t^2} - e n_0 \frac{\partial \mathbf{v}}{\partial t} \tag{6.104}$$

and taking the curl of Eq. (6.100),

$$\nabla \times (\nabla \times \mathbf{E}) = -\mu_0 \nabla \times \frac{\partial \mathbf{H}}{\partial t} \tag{6.105}$$

We combine Eqs. (6.104) and (6.105) by eliminating $\nabla \times \partial \mathbf{H}/\partial t$, and use the vector relation $\nabla \times (\nabla \times \mathbf{E}) = \nabla(\nabla \cdot \mathbf{E}) - \nabla^2 \mathbf{E}$ (see Appendix D) to obtain

$$\nabla(\nabla \cdot \mathbf{E}) - \nabla^2 \mathbf{E} = -\mu_0 \epsilon_0 \frac{\partial^2 \mathbf{E}}{\partial t^2} + \mu_0 e n_0 \frac{\partial \mathbf{v}}{\partial t} \tag{6.106}$$

For transverse waves $\nabla \cdot \mathbf{E} = 0$ (recall from Chapter 2 that $\nabla \rightarrow i\mathbf{k}$). Furthermore, we can replace $\partial \mathbf{v}/\partial t$ with an expression involving $\mathbf{E}$ by use of Eq. (6.103), so that

$$\frac{\partial^2 \mathbf{E}}{\partial t^2} + \frac{e n_0}{\epsilon_0} \left(\frac{e\mathbf{E}}{m} \right) - \frac{1}{\epsilon_0 \mu_0} \nabla^2 \mathbf{E} = 0$$

Recognizing $c^2 = 1/\epsilon_0 \mu_0$ and $\omega_p^2 = e^2 n_0 / \epsilon_0 m$ [Eq. (6.80)], we have the *wave equation for a*

transverse wave in a plasma,

$$\left(\frac{\partial^2}{\partial t^2} + \omega_p^2 - c^2\nabla^2\right)\mathbf{E}(\mathbf{r}, t) = 0 \tag{6.107}$$

For a plane wave of the form $\mathbf{E}(\mathbf{r}, t) = E_0 e^{-i(\omega t - \mathbf{k}\cdot\mathbf{r})}$ Eq. (6.107) yields a dispersion relation

$$\omega^2 = \omega_p^2 + k^2c^2 \tag{6.108}$$

where we have essentially taken the indicated derivatives, or equivalently used the identification of Eqs. (6.82a) and (6.82b). The dispersion relation for waves propagating in plasma differs from that in vacuum by the appearance of the ω_p^2 term. In vacuum this term is zero, giving $\omega^2 = k^2c^2$, or equivalently $f\lambda = c$, whereby waves of all frequencies propagate with the same phase velocity c. According to Eq. (6.108) there is a cutoff frequency in the plasma at $\omega = \omega_p$. For $\omega < \omega_p$, the solution for k is imaginary, indicating that the wave cannot propagate in this *overdense* plasma. Rather the wave decays exponentially with wavenumber

$$k = \frac{\sqrt{\omega^2 - \omega_p^2}}{c} \tag{6.109}$$

or in the highly overdense limit $\omega^2 \ll \omega_p^2$

$$k = i\frac{\omega_p}{c} \tag{6.110}$$

which corresponds to a penetration depth l into the highly overdense plasma of

$$l = c/\omega_p \tag{6.111}$$

The frequency for which $\omega = \omega_p$ is often referred to as the *critical frequency*, and the corresponding electron density is defined as the *critical electron density*, n_c, where from Eq. (6.5)

$$n_c \equiv \frac{\epsilon_0 m\omega^2}{e^2} \tag{6.112a}$$

or in terms of the wavelength (in microns)

$$n_c = \frac{1.11 \times 10^{21}\ \ e/\mathrm{cm}^3}{\lambda^2(\mu\mathrm{m})} \tag{6.112b}$$

TABLE 6.1. Electron density, plasma frequency, critical photon energy for $\omega_c = \omega_p$, and critical wavelength for electromagnetic radiation.

$n_e(e/\text{cm}^3)$	$\omega_p/2\pi$	$\hbar\omega_c$ (eV)	λ_c	Comments
1.00×10^6	8.94 MHz		33.5 m	Between AM and FM radio
1.00×10^{14}	89.4 GHz		3.35 mm	Microwaves
1.00×10^{19}			10.6 μm	CO_2 laser
1.00×10^{21}		1.17	1.06 μm	Nd laser
1.60×10^{22}		4.86	266 nm	4ω of Nd laser
4.60×10^{24}		80.0	15.5 nm	Ne-like Y laser

Thus for a Nd laser of wavelength 1.06 μm, the critical density is $n_c \simeq 1 \times 10^{21}\ e/\text{cm}^3$. For frequency doubled light at 0.53 μm wavelength (green light) the critical electron density quadruples to 4×10^{21}.

Referring back to Figure 6.5, we can now better appreciate the role of the critical density region. There we see the laser light incident from the right on a plasma of sharply rising electron density. During passage through the *underdense* region of the plasma ($n < n_c$) the wave experiences classical absorption as it causes electrons to oscillate, some of which then lose their energy through electron–ion collisions, thermally heating the plasma in the process. This transfer of energy to the plasma increases in efficiency as the light wave propagates to higher densities. Eventually the laser light of frequency ω reaches the critical density n_c, beyond which it cannot propagate ($\omega_p > \omega$, k imaginary), and the wave is reflected back toward the vacuum and lost.

The overdense plasma is important in several other well-known situations. Astronauts and cosmonauts regularly experience a communication blackout during reentry into the earth's atmosphere as their capsules are engulfed in an overdense plasma created as it heat and ionizes atmospheric molecules, preventing the transmission or reception of shortwave or microwave signals. Common AM broadcasts, at frequencies around 1 MHz, are reflected from the earth's ionosphere[17] ($10^5\ e/\text{cm}^3$ to $10^6\ e/\text{cm}^3$ at heights of 100 km to 400 km), often permitting distant reception at night when absorption is minimal. There are interesting daily and seasonal variations to this phenomenon, affected by cycles of ionizing radiation from the sun, longer charged particle lifetimes at higher altitudes, and increased collisional absorption during the day as the sun's heat warms the atmosphere below, causing it to expand outward into the lower regions of the ionosphere where 1 MHz radiation is typically reflected (or absorbed). Broadcast emissions in the 100 MHz region ($n_c \sim 10^8\ e/\text{cm}^3$), typically used for FM, are of sufficiently high frequency that they propagate through the ionosphere and into outer space, which explains why the reflection phenomena experienced with AM radio do not occur for FM broadcasts. Critical parameters are given for representative values of n_e in Table 6.1.

For waves of frequency $\omega > \omega_p$ there is a real propagating wave in the plasma, with properties much like those considered in Chapters 2 and 3, except that now there is considerable dispersion (the phase velocity is not constant) and the refractive index, or dielectric constant, is different. The wave's dispersion relation [Eq. (6.108)] is shown in Figure 6.7 with phase velocity (Chapter 3, Section 3.2) $v_\phi = \omega/k$ approaching c, the phase velocity of light in vacuum, for $\omega \gg \omega_p$. From Eq. (6.108) the phase velocity of the wave is

$$v_\phi = \frac{\omega}{k} = \frac{c}{\sqrt{1 - \omega_p^2/\omega^2}} = \frac{c}{\sqrt{1 - n_e/n_c}} \tag{6.113a}$$

while the group velocity $\partial\omega/\partial k$, is given by

$$\mathrm{v}_g = \frac{\partial\omega}{\partial k} = c\sqrt{1 - \frac{\omega_p^2}{\omega^2}} = c\sqrt{1 - \frac{n_e}{n_c}} \tag{6.113b}$$

We see that these velocities are not constant, but vary with ω_p/ω, or n_e/n_c. For low electron densities, where n_e/n_c is small, both the phase and group velocities approach c. However, for n_e/n_c approaching unity the phase velocity can be very large and the group velocity, with which we associate with the transport of energy, can be very small.[20, 21] From Eq. (6.113a) we can see that the refractive index (see Chapter 3) of the plasma, $n \simeq c/\mathrm{v}_\phi = ck/\omega$, is given by

$$\boxed{n = \sqrt{1 - \frac{\omega_p^2}{\omega^2}}} \tag{6.114a}$$

or equivalently

$$\boxed{n = \sqrt{1 - \frac{n_e}{n_c}}} \tag{6.114b}$$

This analysis is readily extended to include the effect of collisions between electrons, oscillating due to the transverse wave, and ions. By including a collision term,[4, 6, 16] the electron momentum transfer equation (6.103) becomes

$$m\frac{\partial \mathbf{v}}{\partial t} = -e\mathbf{E} - m\nu_{ei}\mathbf{v} \tag{6.115}$$

where the momentum transfer is proportional to the electron momentum $m\mathbf{v}$ and where ν_{ei} is the electron–ion collision frequency. The electron velocity can now be written as

$$\mathbf{v} = -\frac{ie}{m(\omega + i\nu_{ei})}\mathbf{E} \tag{6.116}$$

and the dispersion relation (6.108) is modified, for $\nu_{ei} \ll \omega$, to

$$\omega^2 = \omega_p^2\left(1 - i\frac{\nu_{ei}}{\omega}\right) + k^2c^2 \tag{6.117}$$

If we set $\omega = \omega_r + i\omega_i$, substitute into Eq. (6.117), and solve separately for the real and imaginary parts, we find, for $\nu_{ei}/\omega \ll 1$, that the real part of the frequency satisfies

$$\omega_r^2 = \omega_p^2 + k^2c^2 \tag{6.118a}$$

much as before, but we now have an imaginary component

$$\omega_i \simeq -\frac{\nu_{ei}\,\omega_p^2}{2\,\omega^2} = -\frac{n_e}{2n_c}\nu_{ei} \tag{6.18b}$$

where the negative sign indicates damping. Physically, as the electromagnetic wave propagates through the plasma, its electric field induces an oscillatory component to the velocity of all electrons, superposed on their otherwise random motion. As the electrons experience collision with ions, their energy of oscillation is converted to random energy, thus heating the electrons to a higher temperature. Thus there is a transfer of energy from the wave to the plasma, increasing the thermal energy of the plasma and decreasing the intensity of the wave. This linear damping mechanism, referred to as collisional damping or inverse bremsstrahlung, is very important for the creation and heating of laser-produced plasmas.[1, 23]

In this connection we note that for real ω, the dispersion relation (6.117) yields real and imaginary components of the magnitude of the propagation vector, $k = k_r + ik_i$, given by

$$k_r = \frac{\sqrt{\omega^2 - \omega_p^2}}{c} \tag{6.119a}$$

and

$$k_i = \frac{\nu_{ei}\omega_p^2}{2c\omega\sqrt{\omega^2 - \omega_p^2}} = \frac{\nu_{ei}\omega_p^2}{2\mathrm{v}_g\omega^2} \tag{6.119b}$$

The attenuation length for $1/e$ intensity decay is a distance

$$l_{\mathrm{abs}} = \frac{1}{2k_i} = \frac{\omega^2}{\omega_p^2}\frac{\mathrm{v}_g}{\nu_{ei}}$$

In terms of electron densities, the absorption length for a transverse wave in a plasma is given by[1]

$$l_{\mathrm{abs}} = \frac{n_c}{n_e}\frac{\mathrm{v}_g}{\nu_{ei}} \tag{6.119c}$$

The collision frequency ν_{ei} in a hot plasma is complicated, as it depends on many long range relatively weak interactions. There are, however, many of the these interactions, and the result can lead to a very strong absorption process,[22–24] as we shall see for the case of laser-produced plasmas of even relatively short density scale lengths, e.g., tens of wavelengths. The momentum transfer in collisions can be studied by considering Figure 6.2, where the distance b is called the impact parameter. The amount of momentum transfer clearly depends on the velocity of the electron v, the ion charge Z, and b. The change in momentum $\Delta p = m\ \Delta\mathbf{v}$ is equal to the force experienced multiplied by the interaction time $\mathbf{F}\ \Delta t$. For an interaction

time $\Delta t \simeq 2b/\mathrm{v}$ and a Coulomb force $e^2 Z/4\pi\epsilon_0 b^2$, the resultant hyperbolic trajectory has a corresponding scalar momentum change[1]

$$m\ \Delta \mathrm{v} \simeq \frac{e^2 Z}{4\pi\epsilon_0 b^2} \cdot \frac{2b}{\mathrm{v}}$$

or

$$\Delta \mathrm{v} \simeq \frac{e^2 Z}{2\pi\epsilon_0 m \mathrm{v} b}$$

We see that the velocity change in a collision has an inverse dependence on both v and b. The time required to undergo a substantial momentum change such that $\Delta \mathrm{v}_{\mathrm{rms}} \sim \mathrm{v}$ clearly depends on the range of values of v and b, and on the ion density. The reciprocal of this *collision time* is the effective electron–ion collision frequency ν_{ei}.

Dawson and his colleagues[23, 24] have determined the collision frequency for a Maxwellian velocity distribution, as a function of density, temperature, and ion charge. According to Johnson and Dawson,[24]

$$\nu_{ei} = \frac{e^4 Z n_e \ln \Lambda}{3(2\pi)^{3/2}\epsilon_0^2 m^{1/2}(\kappa T_e)^{3/2}} \tag{6.120a}$$

or

$$\frac{\nu_{ei}}{\omega_p} = \frac{Z\omega_p^3 \ln \Lambda}{3(2\pi)^{3/2} n_e \mathrm{v}_e^3} \tag{6.120b}$$

where v_e is the electron thermal velocity [Eq. (6.86b)], $\mathrm{v}_e = (\kappa T_e/m)^{1/2}$, and Λ is the ratio $b_{\max}/b_{\min}$ of the impact parameters corresponding to the Debye length ($b_{\max}$) beyond which the individual ion is effectively screened and the classical distance of closest approach ($b_{\min}$) without capture, the latter determined by equating the energy in the Coulomb field of the ion at closest approach, $e^2 Z/4\pi\epsilon_0 b_{\min}$, to the average electron thermal energy $\frac{3}{2}m\mathrm{v}_e^2$ (i.e., $\frac{1}{2}m\bar{\mathrm{v}}^2 = \frac{3}{2}\kappa T_e = \frac{3}{2}m\mathrm{v}_e^2$). Observing that the Debye length [Eq. (6.6)] can be written as $\lambda_D = \mathrm{v}_e/\omega_p$, the electron collision frequency can be written as

$$\boxed{\frac{\nu_{ei}}{\omega_p} = \frac{1}{9}\sqrt{\frac{2}{\pi}}\frac{Z}{N_D}\ln\left(\frac{9N_D}{2Z}\right)} \tag{6.120c}$$

where $N_D = (4\pi/3)\lambda_D^3 n$ is the number of electrons in a Debye sphere, given in practical units as

$$\boxed{N_D = \frac{4\pi}{3}\lambda_D^3 n_e = 1.7 \times 10^3 \frac{(\kappa T_e)^{3/2}}{n_e^{1/2}}} \tag{6.121}$$

for κT_e in keV and n_e in units of $10^{21}\ e/\mathrm{cm}^2$.

For a plasma with $\kappa T_e = 1$ keV, created by a 1.06 μm laser, at half-critical density $0.5 \times 10^{21}\ e/\text{cm}^3$ and with $Z = +14$ (neon-like chromium, discussed later in this chapter) one has $N_D \simeq 3.4 \times 10^3$ and $\nu_{ei}/\omega_p \simeq 2.5 \times 10^{-3}$. At half-critical density, $\omega_p \simeq 1.3 \times 10^{15}$ rad/s, so that $\nu_{ei} \simeq 3.3 \times 10^{12}$/s. In this example the absorption length [Eq. (6.119c)] at this density is $l_{\text{abs}} \simeq 130\ \mu$m. In view of the density scale length [Eq. (6.73)] for an expanding plasma, this same chromium plasma would have an expansion velocity [Eq. (6.69)] of $\text{v}_{\text{exp}} \simeq 0.21\ \mu$m/ps and thus a density scale length $l_{\text{exp}} \simeq 110\ \mu$m after 500 ps of irradiation.

As this scale length is about equal to the absorption length, we expect a fairly significant collisional absorption of 1.06 μm light for nanosecond duration or longer pulses, especially in the region approaching the critical density. This can be seen more clearly by algebraically rearranging the parameters in Eqs. (6.119c) and (6.120a) so as to better illustrate the scaling of collisional absorption with density, temperature, and ion charge state:

$$l_{\text{abs}} \propto \frac{\sqrt{1 - n_e/n_c}(\kappa T_e)^{3/2}}{n_e^2 Z} \tag{6.122}$$

Thus in the example above the absorption scale length decreases substantially as the wave progression propagates into more dense plasma (above $n_c/2$), leading to rapidly increasing absorption. The advantage of short wavelength illumination is also clear. Using a harmonic of Nd at 2ω or 3ω (0.53 μm or 0.35 μm), where harmonic conversion can be done very efficiently, raises the critical density by a factor of four or nine, respectively, again leading to a substantial decrease of the absorption length in the subcritical density region. Furthermore, as the wave approaches the critical surface the group velocity goes to zero, again enhancing absorption as represented by the factor $\sqrt{1 - n_e/n_c}$ in Eq. (6.122).

Kruer has solved Maxwell's equations for a wave propagating into a one-dimensional expanding plasma with density profile $n/n_c = \exp(-l/Z)$. For the case of non-resonant (see next section) s-polarized light he obtains an analytic solution for the collisional absorption fraction[1]

$$f_{\text{abs}} = 1 - \exp\left[-\left(\frac{8\nu_{ei}^*\ l \cos^3\theta}{3c}\right)\right]$$

where θ is the angle of incidence measured from the surface normal and ν_{ei}^* is the value of ν_{ei} at $n_e = n_c$, where much of the absorption occurs. The strong angular dependence is due to refraction in the plasma. For the 1 keV temperature chromium plasma considered above, with normal incidence irradiation ($\theta = 0$) at 1.06 μm wavelength, the wave will experience 80% absorption with a density scale length of about 30 μm, thus ensuring high absorption of nanosecond duration irradiation at modest intensity. For frequency-doubled Nd at 0.53 μm wavelength the required scale length for 80% absorption is only about 7 μm, permitting strong collisional absorption even with rather short duration modest scale length plasmas.

In a following section we will discuss the effect of high-intensity irradiation on expanding density profiles. In such cases the intense illumination can generate a radiation pressure that steepens the electron density profile and thus reduces the role of collisional absorption in the underdense plasma. In very steep density profiles, collision absorption is compromised, but the incident wave can approach very close to the critical region where, depending on the electric field polarization, an enhanced *resonance absorption* can become important. This is discussed in the following section.

6.4.8 Resonance Absorption

In very steep gradient plasmas the incident wave is very close to the critical density surface before it is reflected (or, more accurately in an expanding plasma, refracted away). Steep gradient plasmas are encountered with very short pulse irradiations where expansion is minimized, and in very high intensity illuminations where radiation pressure inhibits the expansion. For a one-dimensional plasma expanding from a planar surface with a density gradient ∇n_e and an incident wave vector $\mathbf{k}$ at an angle of incidence θ from the surface normal, the wave is refracted out of the plasma, reaching a highest electron density $n_c \cos^2\theta$ at the turning point, beyond which k is imaginary, representing an evanescent or tunneling field.[25, 26] Depending on the polarization of the incident radiation, it is possible to directly excite plasma waves through the resonance $\omega = \omega_p$ at the critical density. For p-polarized radiation, with the electric field lying in the plane of incidence defined by $\mathbf{k}_i$ and the surface normal, the electric field at the turning point has a component in the direction of the gradient that tunnels into the critical region. As we saw in Chapters 2 and 3, Maxwell's equations must satisfy the condition $\nabla \cdot (\epsilon \mathbf{E}) = 0$ at an interface, where for a plasma $\epsilon = \epsilon_0 n^2 = \epsilon_0 (1 - n_e/n_c)$ and $n = c/\mathrm{v}_\phi$ is the refractive index as given in Eq. (6.113a). One then has $\epsilon_0 \nabla \cdot [(1 - n_e/n_c)\,\mathbf{E}] = 0$, which shows that the tunneling field $\mathbf{E}$ will drive a resonant response at the critical surface $n = n_c$, strongly driving plasma oscillation at $\omega = \omega_p$. A solution of Maxwell's equations in the critical region[26] shows that the fraction of energy absorbed depends on the parameter $(k_i l)^{1/3} \sin\theta$, where l is the density scale length. The absorption peaks at about 50% when the parameter is equal to about 0.8. For normal incidence, $\theta = 0$, there is no axial component of electric field to drive the resonance, and for glancing incidence (large θ) the wave is refracted away from the critical surface, so that the tunneling field is weak.

6.4.9 Waves in a Magnetized Plasma

The presence of a static magnetic field $\mathbf{B}_0$ can substantially modify the nature of waves that propagate in a plasma, particularly if the cyclotron frequency $\omega_c = eB_0/m$ is comparable to or greater than the plasma frequency. Magnetized plasmas such as this are of great interest in astrophysics[27–30] and for the pursuit of fusion energy using magnetic confinement techniques. Not surprisingly, the orientation of the static magnetic field with respect to the propagation direction and electric field polarization is a significant factor. An example of dispersion curves for a magnetized plasma with $\omega_c < \omega_p$ is shown in Figure 6.9, for electromagnetic waves propagating along ($\theta = 0$) and perpendicular ($\theta = \pi/2$) to the static magnetic field direction ($\mathbf{B}_0$). Solutions for intermediate angles are shaded. The subject of magnetized plasma is beyond the scope of this text, but the interested reader will find substantial material in the plasma literature.[4, 6, 11, 14]

6.4.10 Non-linear Processes in a Plasma

If we look back at the fluid level Maxwell–Euler equations, we see that product terms, which are inherently non-linear,[27] appear in several places. For convenience we repeat these equations here and box the terms that involve a product of field quantities:

$$\nabla \times \mathbf{H} = \epsilon_0 \frac{\partial \mathbf{E}}{\partial t} + \sum_j \boxed{(nq\mathrm{v})_j} \tag{6.123a}$$

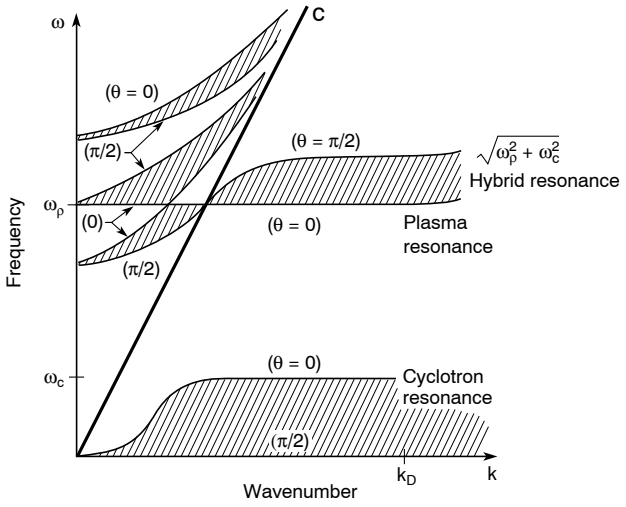

FIGURE 6.9. Dispersion diagram for plasma waves in the presence of an external magnetic field with $\omega_c < \omega_p$. (Courtesy of N. Marcuvitz.[3])

$$\nabla \times \mathbf{E} = -\mu_0 \frac{\partial \mathbf{H}}{\partial t} \tag{6.123b}$$

$$\frac{\partial n_j}{\partial t} + \nabla \cdot \boxed{(n_j \mathbf{v})} = 0 \tag{6.123c}$$

$$m_j \boxed{n_j \left(\frac{\partial}{\partial t} + \overline{\mathbf{v} \cdot \nabla} \right) \mathbf{v}} = -\nabla P_j + q_j \overline{\boxed{n_j (\mathbf{E} + \mathbf{v} \times \mathbf{B})}} \tag{6.123d}$$

where we have used $\mathbf{D} = \epsilon_0 \mathbf{E}$ and $\mathbf{B} = \mu_0 \mathbf{H}$, and where Eqs. (6.123c) and (6.123d) must be written for both electrons and ions ($j = 1$ and 2) with appropriate mass and charge. We see that in at least four places there is a term involving a product of fields. These introduce the possibility for both non-linear growth and frequency mixing, and are known to play a major role in the development of non-thermal processes such as continuum x-ray emission, in favor of sometimes deleterious processes such as runaway suprathermal electrons and hard x-ray emission tails.

If we Fourier analyze one of these terms, we can gain some appreciation of the manner in which these processes operate, as well as some insight into the characteristic signatures we might look for. For instance, we can analyze the current term for electrons in Eq. (6.44),

$$\mathbf{J}(\mathbf{r}, t) = -e n_e(\mathbf{r}, t) \mathbf{v}(\mathbf{r}; t) \tag{6.124a}$$

by writing each field in terms of its respective wave component, viz.,

$$\mathbf{J} e^{-i(\omega_1 t - \mathbf{k}_1 \cdot \mathbf{r})} = -e n_e e^{-i(\omega_2 t - \mathbf{k}_2 \cdot r)} \mathbf{v} e^{-i(\omega_3 t - \mathbf{k}_3 \cdot \mathbf{r})} \tag{6.124b}$$

where a term by term match shows that for the amplitudes

$$\mathbf{J} = -e n_e \mathbf{v}$$

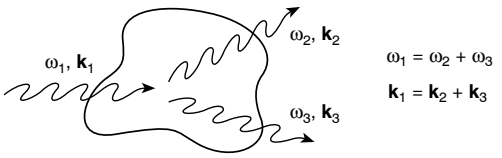

FIGURE 6.10. A three-wave mixing process.

while for the frequencies and wavenumbers

$$\boxed{\omega_1 = \omega_2 \pm \omega_3} \tag{6.125a}$$

and

$$\boxed{\mathbf{k}_1 = \mathbf{k}_2 \pm \mathbf{k}_3} \tag{6.125b}$$

Equations (6.125a) and (6.125b) are sometimes referred to as *conservation of energy* and *conservation of momentum* equations for three-wave interactions, as is suggested by multiplying through by $\hbar$. Figure 6.10 captures the simplicity of this idea.

The process can in fact be either linear or non-linear. If a wave exists at a certain fixed amplitude, such as a density wave $n_e(\mathbf{r}, t)$, or even a fixed grating, then incoming waves $\omega_1, \mathbf{k}_1$ scatter from it in linear fashion to a new frequency (for a moving wave) and wavevector $\omega_3, \mathbf{k}_3$. This is a linear process: n is fixed, and the scattered field $\omega_3, \mathbf{k}_3$ depends linearly on the incident field $\omega_1, \mathbf{k}_1$. This specific example was the subject of Figure 6.4 in Section 6.2.

These processes can also be non-linear, and may apply to or grow out of any of the boxed non-linear terms in Eq. (6.123). For instance, it may occur that the incoming wave $\omega_1, \mathbf{k}_1$ is very intense, and as a result, as it propagates into or through the plasma, it scatters from a spectrum of natural waves $\omega_2, \mathbf{k}_2$ which pre-exist in the normal noise of random low level plasma oscillations. Of course $\omega_1, \mathbf{k}_1$ will scatter from this spectrum of natural waves $\omega_2, \mathbf{k}_2$, generating a spectrum of scattered waves $\omega_3, \mathbf{k}_3$. Not all wave combinations will satisfy the conservation equations (6.125a, b) – matching of frequency and wavevectors is simply not guaranteed for three natural modes, each with its own dispersion relation. However, in some cases they may match, perhaps only at some special density.[28, 29] In those cases the three waves are said to *resonate*. The incoming wave scatters off waves in the noise. The new scattered wave grows in amplitude, and interferes with the incident wave at the beat frequency $\omega_3 - \omega_1$ and difference wavevector $\mathbf{k}_3 - \mathbf{k}_1$, causing the initial noise at $\omega_2 = \omega_3 - \omega_1$, $\mathbf{k}_2 = \mathbf{k}_3 - \mathbf{k}_1$ to grow in amplitude. This of course causes further scattering, and the process of growth and scattering continues. This process is called *stimulated* scattering. An incoming wave drives a plasma wave out of the noise and stimulates it to grow, by the very process of scattering from it in a resonant three-wave mixing process. Note that since these processes are resonant, they are sensitive to the background plasma parameters and to gradients of these quantities.

Figure 6.11 shows dispersion diagrams[7] for two such processes involving intense incident electromagnetic radiation: stimulated Brillouin scattering (SBS) and stimulated Raman scattering (SRS). In SBS the incident wave scatters from a low-frequency ion-acoustic wave generating a scattered wave (ω_R, k_R) of slightly shifted frequency. In SRS the incident wave

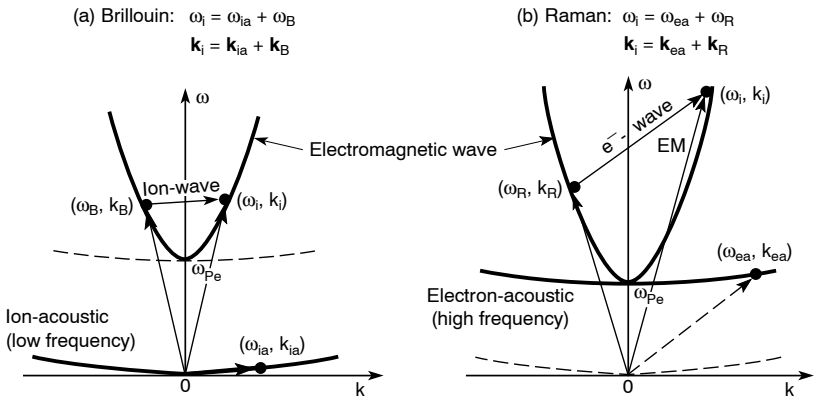

FIGURE 6.11. Dispersion diagrams for (a) Brillouin and (b) Raman scattering of incident electromagnetic radiation by ion-acoustic and electron-acoustic waves, respectively. The scattered wave experiences a relatively small frequency shift in the Brillouin case. Negative k-values indicate backscattered waves. Note that **k**-vector matching occurs for a strong incident wave participating in a three-wave process in which frequency and wavevector matching occur, i.e., when the ω, **k** for all three waves lie on the naturally occurring dispersion curves. (Following H. Motz.[7])

scatters from a high-frequency electron-acoustic wave, generating a scattered wave $(\omega_{\rm R}, \omega_{\rm R})$ at a substantially shifted frequency.

The first is called Brillouin scattering because of the small scattered wave frequency shift, analogous to light scattering from acoustic waves in (neutral) gases. The second is called Raman scattering because of the large frequency shift reminiscent of light scattering from vibrational states in molecules. Both are called "stimulated" because the third wave – ion-acoustic in one case, electron-acoustic in the other – is caused to grow out of the noise through stimulation at the beat frequency. In each case the wave equations can be written with the non-linear terms appearing as driving terms on the right-hand side of the otherwise homogeneous (source-free) wave equation – now inhomogeneous. Whether the wave grows, and to what amplitude is determined by the balance of loss processes (collisions or Landau damping, non-linear saturation processes, etc.) against the gain provided by the resonant beat frequency driver.

To further illustrate this three-wave mixing, we consider the stimulated Raman scattering of Figure 6.10(b) in some additional detail. We consider backscattered radiation in which the incident frequency ω_i is somewhat greater that $2\omega_p$, so that both the scattered transverse wave frequency ω_R and the excited electron-acoustic wave frequency $\omega_{\rm ea}$ are just slightly above ω_p as indicated in Figure 6.11. Because $\omega_i = 2\omega_p$, this corresponds to the quarter-critical density region, $n \simeq n_c/4$. Since the scattered wave has $\omega_R \simeq \omega_p$, it has a very small wave wavenumber in the plasma, $\Delta k \ll k_i/2$, smaller than it would have in vacuum. In order to resonantly match both frequencies and wavenumbers, as required by Eqs. (6.123), the electron-acoustic wave must have a wavenumber $k_{\rm ea} = k_i + \Delta k$, as shown in Figure 6.12. The frequency matching condition, $\omega_i = \omega_R + \omega_{\rm ea}$, for waves with dispersion relations given by Eqs. (6.84) and (6.108) is given by

$$\omega_i = \omega_p \left[1 + \frac{(\Delta k)^2 c^2}{\omega_p^2}\right]^{1/2} + \omega_p \left[1 + \frac{(k_i + \Delta k)^2 a_{\rm e}^2}{\omega_p^2}\right]^{1/2} \tag{6.126}$$

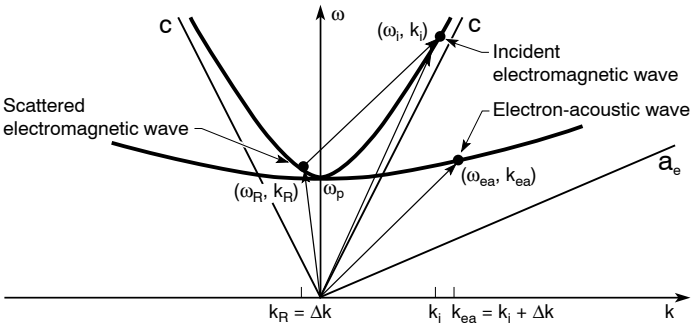

FIGURE 6.12. Three-wave mixing is illustrated for stimulated Raman backscattering at the quarter-critical electron density surface, $n_e \simeq n_c/4$.

or for small Δk,

$$\omega_i = \omega_p + \omega_p \left(1 + \frac{k_i^2 a_e^2}{\omega_p^2}\right)^{1/2} \tag{6.127}$$

We can eliminate k_i through use of the transverse dispersion relation, Eq. (6.107), where

$$k_i = \left(\frac{\omega_i^2 - \omega_p^2}{c^2}\right)^{1/2} \simeq \left(\frac{4\omega_p^2 - \omega_p^2}{c^2}\right)^{1/2} \simeq \frac{\sqrt{3}\omega_p}{c} \tag{6.128}$$

The frequency matching condition (6.127) then becomes

$$\omega_i \simeq \omega_p + \underbrace{\omega_p \left(1 + \frac{3a_e^2}{c^2}\right)^{1/2}}_{\omega_{ea}} \tag{6.129}$$

For a 1 keV electron temperature, $a_e \simeq c/18$, so that the electron-acoustic frequency is $\omega_{ea} \simeq 1.005\omega_p$, and thus by Eq. (6.127) $\omega_i = 2.005\omega_p$. The three-wave mixing therefore occurs at an electron density in the vicinity of $n \simeq 0.249\, n_c$, that is, very close to the quarter-critical surface.

Note that an electron density gradient, as depicted in Figure 6.5, will limit this three-wave resonant mixing to a small region of the plasma. Note also that the phase velocity of the electron-acoustic wave is

$$v_\phi = \frac{\omega_{ea}}{k_{ea}} \simeq \frac{\omega_p}{\sqrt{3}\omega_p/c} \simeq \frac{c}{\sqrt{3}} \tag{6.130}$$

If this wave is driven to large amplitude by the high intensity three-wave resonance, it offers the possibility of trapping electrons within its high potential crests and accelerating them to velocities of $c/\sqrt{3}$, or to energies of order 100 keV. Turner, Drake, Campbell, and their colleagues[34, 35] report experiments in which suprathermal electrons of order 100 keV energy are generated in a nominally 1 keV plasma by high intensity laser irradiation experiments in which SRS is identified as the non-linear acceleration mechanism. Once accelerated to

high energies, these suprathermal electrons will eventually generate suprathermal x-rays as they collide with ions and nearby dense materials. In the following two subsections we consider intensity thresholds for non-linear processes, and numerical simulations of just such processes.

6.4.11 Threshold for Non-linear Processes

As we have seen in the previous subsection, the Maxwell–Euler equations (6.123a–d) are non-linear, with several product terms available for mode mixing and large amplitude growth. It is possible to determine the initial growth rate of such processes by expanding the fields in a power series, as was done earlier in the linearization process, but now carrying selected second order, or *product of fluctuation*, terms. The procedure is to keep linear terms to the left side of the equal signs, and treat the second order (non-linear) terms to the right as driving terms, much as in the treatment of inhomogeneous differential equations. At relatively small amplitude it is then possible to consider the product terms as exciting the natural (linear) modes to finite *initial* growth rates. Thresholds for the onset of non-linear growth of fields are then obtained by comparing these initial growth rates with natural wave decay rates such as collisional or collisionless (Landau) damping. For instance, in the stimulated Raman process just considered, one would determine what incident electric field **E**, or equivalently wave intensity I, would be required to overcome collisional and Landau damping of the electron-acoustic wave, and collisional damping (ν_{ei} of the two transverse waves). This would be a threshold intensity; below this intensity the waves naturally decay, and above it they grow.

We will not consider quasi-linear growth rates of plasma waves here, as we are generally confronted in hot dense plasmas, particularly in intense laser-produced plasmas, by growth rates that rapidly exceed these thresholds and for which further tools are required. These tools include numerical simulations in which a finite number of individual charged particles, constrained to a limited range of background density and temperature variations, are followed in the presence of high intensity laser illumination. Examples of such "particle in cell" calculations are described in the following section. By numerically studying the growth of waves and the acceleration of particles as a function of laser intensity, it is possible both to determine threshold values and to gain a better insight into the evolution of non-linear processes and their resultant field distributions.

Before proceeding to the numerical simulations, however, it is useful to develop some intuitive appreciation for the general nature of these stimulated processes and a likely order of magnitude estimate of threshold conditions. For instance, in the stimulated Raman process we can imagine a relatively weak electromagnetic wave, of frequency ω and electric field E, incident on a thermal plasma of electron density n_e and temperature κT_e. At low intensity the electron motions are dominated by random interactions (collisions) with other electrons and ions, both at short distances and through longer range wave motions. Superimposed on this random motion is a small sinusoidal velocity component, v_{os}. As the incident laser intensity increases, the oscillatory component of the velocity becomes more important and there evolves a distinctive *coherent* nature to the electron motions – phase locked in both space and time to the electric field of the transverse wave. Where the imposed frequency and wavenumber of the collective electron motion are a close match to a natural mode of the system – an electron-acoustic wave – we can expect the physics to change from one of random thermal processes to coherently driven wave motions. A measure of this transition is the intensity at which the imposed oscillation velocity v_{os} is comparable to a random thermal velocity, which we can take as v_e in Eq. (6.86c).

We can determine the oscillating component of velocity, v_{os}, as we did earlier using Eq. (6.103), which in scalar form gives

$$m\frac{\partial v_{os}}{\partial t} = -eE$$

or with imposed time dependence $e^{-i\omega t}$ is

$$v_{os} = -i\frac{eE}{m\omega}$$

We then compare this with a measure of the electron's random thermal motion, v_e from Eq. (6.86c):

$$v_e = \left(\frac{\kappa T_e}{m}\right)^{1/2}$$

We take the ratio and square it so that it represents a ratio of energies, that is, the ratio of electron energy in coherent oscillations to that in random motion. The result is

$$\boxed{\left|\frac{v_{os}}{v_e}\right|^2 = \frac{e^2E^2}{m\omega^2\kappa T_e} = \frac{I/c}{n_c\kappa T_e}} \tag{6.131a}$$

where I and E^2 follows from Chapter 3, Eq. (3.20). For a plasma produced by a 1.06 μm wavelength Nd laser, with critical electron density $n_c = 1\times10^{21}\, e/\text{cm}^2$ and an assumed (typical) electron temperature of 1 keV, the ratio of coherent to thermal electron energies is unity for a focused laser intensity $I = 4.7\times10^{15}$ W/cm^2. This is a commonly achieved value – and one such that the effects of non-linear processes are readily evident in the literature.[36] We can rewrite this ratio of energies in terms of common laboratory values as

$$\boxed{\left|\frac{v_{os}}{v_e}\right|^2 = \frac{0.021I(10^{14}\ \text{W/cm}^2)\lambda^2(\mu\text{m})}{\kappa T_e(\text{keV})}} \tag{6.131b}$$

where I is in units of 10^{14} W/cm^2, λ is in microns, and κT_e is in keV.

To avoid the excitation of non-thermal processes in a laser-produced plasma it is clearly advantageous to utilize low intensities and short wavelengths where possible. For instance, in laser-driven inertial fusion, where high intensities are essential, the use of short wavelengths through harmonic generation is common.[37] The achievable thermal temperature κT_e is also closely related to the incident intensity I, as we will see in a following section on blackbody radiation, so there too it may be more convenient to use a shorter wavelength. This is particularly true for the generation of thermal x-rays, but less so for extreme ultraviolet radiation where the requisite laser intensities are rather modest, in the 10^{12} W/cm^2 to 10^{13} W/cm^2 range.

For further discussion of these non-linear processes the reader is referred to the book by Kruer[1] and the article by Baldis, Campbell, and Kruer[33] in which they describe in detail several stimulated processes, their specific thresholds, and in particular, limits to growth rates in sharp gradient plasmas where energy and momentum matching can only be achieved over limited

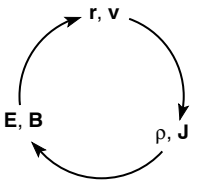

FIGURE 6.13. The basic cycle of a particle simulation code. (Following Kruer.[1])

spatial dimensions. In the case of sharp gradients the intensity–wavelength thresholds, $I\lambda^2$ in Eq. (6.131b), evolve to $I\lambda l$ thresholds, where l is the density scale length. For instance, see Table 2 of Baldis, Campbell, and Kruer.[33] Experiments confirming several of these thresholds are reviewed by Drake.[38]

6.5 NUMERICAL SIMULATIONS

The plasma theories considered in Section 6.4 are complicated in several ways. As we have seen, they are highly non-linear, the parameters vary sharply in space and in time, and they involve both fluid and kinetic details characteristic of long range and short range interactions. Linearized theories built around slowly varying background quantities are very useful for understanding the basic phenomena and obtaining initial growth rates for non-linear processes, but they are not adequate in themselves for the inherent complexities of hot dense plasmas. Numerical simulations offer additional tools to address these complex phenomena. We discuss two methods in particular that address different aspects of this problem. One technique, called *particle in cell* calculations, follows the detailed kinetic motion of a finite number of particles in a background of limited space–time variations. These techniques are particularly useful for studying particle kinetics and wave growth in highly non-linear laser plasma interactions. A second numerical technique, sometimes referred to as "hydrodynamic transport codes," utilizes zonal tracking of fluid properties such as density, temperature, and velocity in the presence of strong localized heating (laser energy deposition), including thermal and non-thermal energy transport among zones, with the use of energy bins as needed. These are generally called *Lagrangian techniques* in that they tend to follow identifiable mass regions as their positions and shape evolve in time.

6.5.1 Particle in Cell Simulations

In the particle in cell numerical simulations, a finite number of charged particles are tracked as their positions and velocity evolve in response to the self-consistent fields, electric and magnetic, they themselves produce, as well as any applied fields. As an initial condition, a distribution of charged particle positions and velocities is selected, perhaps to represent a modest one-dimensional density ramp, with electron velocities chosen to represent a selected electron temperature, and ions immobile. From these initial positions and velocities the charge distributions and currents are determined on a spatial scale (grid) sufficient to resolve collective motion. These are then used with Maxwell's equations to calculate the electric and magnetic fields generated. These fields, averaged over a suitable grid, are then used with the Lorentz force to determine changes in the position and velocity of all the particles. This constitutes one step in the simulation. The process is continued,[1, 10] as shown in Figure 6.13, with charge densities and currents re-determined for each step. The process is repeated through many

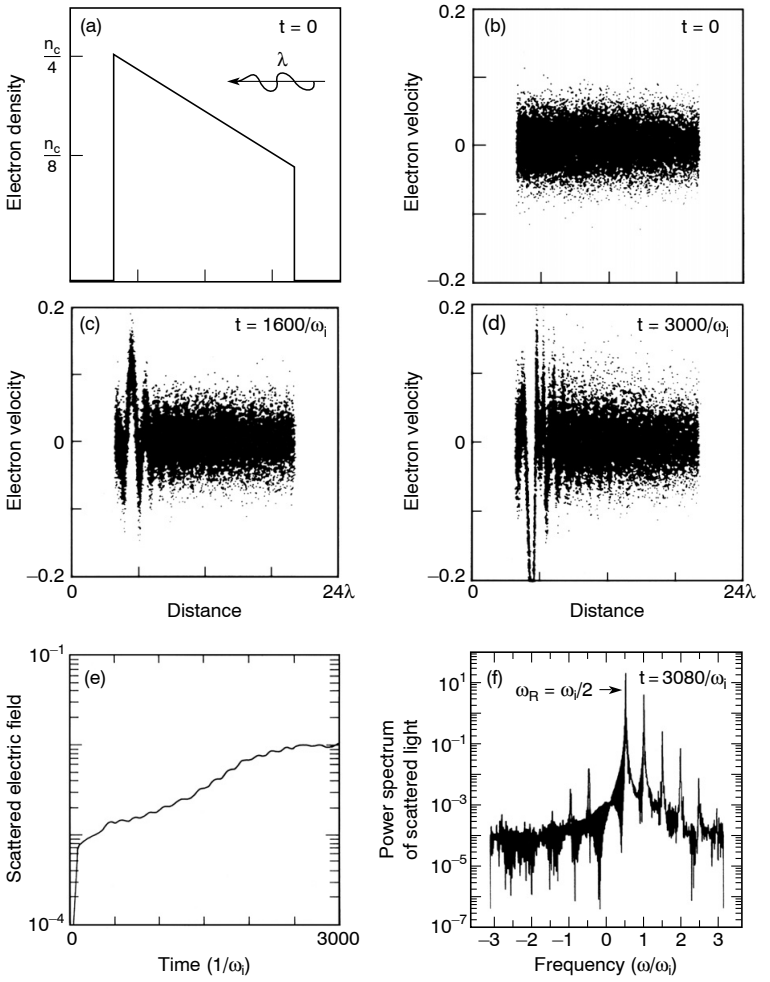

FIGURE 6.14. Numerical simulation of stimulated Raman scattering from a plasma with an electron density ramp (a) just reaching $n_c/4$ in a distance of about 16 wavelengths of the incident laser radiation. The initial electron (thermal) temperature (b) is $v_e/c = 0.028$, and the incident laser intensity is such that $(v_{os}/v_e)^2 = 1.1$. The electron velocities as a function of position are shown at 1600 (c) and 3000 (d) cycles. The Raman scattered electromagnetic wave at $\omega_i/2$ and other half harmonics is shown in (e) and (f). (Courtesy of D. Forslund, J. Kindel, and E. Lindman, Los Alamos National Laboratory.)

cycles at small time intervals, sufficient to resolve the phenomena of interest, but typically on a time scale equal to a small fraction of $1/\omega_p$.

Figure 6.14 shows the results of a numerical simulation of stimulated Raman scattering by Forslund, Kindel, and Lindman,[39] in which the motion of 15,000 electrons, initially distributed in an electron density map extending from $n_c/8$ to $n_c/4$, with a thermal velocity distribution $v_e/c = 0.028$, is tracked as a function of time during irradiation by intense laser light (λ) that induces an oscillatory motion of the electrons at $v_{os}/c = 0.30$, thus just above the condition for $|v_{os}/v_e|^2 = 1$ in Eq. (6.122). The ions are held immobile. The electron density map and initial (thermal) velocity distribution are shown in Figure 6.14(a) and (b), respectively. The

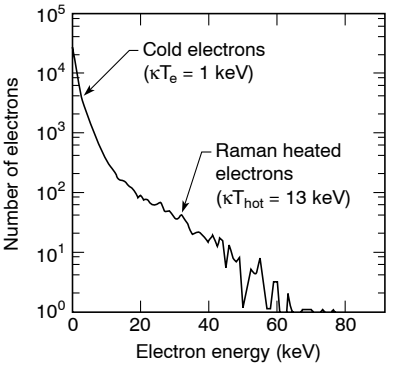

FIGURE 6.15. The electron energy distribution determined in a numerical simulation of the stimulated Raman scattering process, for a uniform plasma of electron density $n = n_c/10$, plasma length of 127 electromagnetic wavelengths, initial electron temperature of 1 keV, and incident laser intensity I corresponding to $(v_{os}/v_e)^2 = 0.53$. The simulation shows a heated electron tail at $\kappa T_{hot} = 13$ keV, essentially corresponding to electrons of velocity equal to the phase velocity of the simulated electron-acoustic wave. (Courtesy of Estabrook, Kruer, and Lasinski, Lawrence Livermore National Laboratory.)

velocity distributions are shown later, after 1600 and 3000 oscillations, in Figure 6.14(c) and (d), displaying very large amplitude oscillations, much larger than v_e, near the quarter-critical density. The amplitude of the scattered wave's electric field is shown in Figure 6.14(e), indicating an extremely sharp rise, with a growth period measured in tens of cycles of the incident radiation, essentially equal to the transit time across the density ramp. The power spectrum of scattered radiation shows a very strong component at $\omega = \omega_i/2$, as would be expected for Raman scattering, and many additional half-frequency harmonics due to the onset of further wave mixing in this very intense and highly non-linear interaction. In these calculations about 30% of the incident electromagnetic energy goes to the plasma oscillation.

Further simulations by Estabrook, Kruer, and Lasinski[40] explore the electron heating due to the intense stimulated Raman process in a wide range of electron densities, with mobile ions, and with competition among non-linear processes. Figure 6.15 shows the heated electron energy distribution for a simulation in which an incident laser wave (λ) of intensity I, such that the ratio in Eq. (6.131), $|v_{os}/v_e|^2 = 0.53$, traverses a uniform plasma of electron density $n = n_c/10$ and length $L = 127\lambda$, and initial electron temperature 1 keV. The figure shows a cold (thermal) component and a heated electron component characterized by $\kappa T_{hot} \simeq 13$ keV, due to the wave–particle interaction between electrons and the stimulated electron-acoustic wave. Further simulations show that, as expected from the arguments in Section 6.4.10, Eqs. (6.126) to (6.130), the energy of the heated electrons is largely dependent on the phase velocity of the Raman stimulated electron-acoustic wave (e.g., on κT_e and n_e or ω_p), and only weakly dependent on the incident wave intensity. Indeed, the simulations show that through control of the phase velocity of the electron-acoustic wave, largely the choice of n_e/n_c, it is possible to generate a Raman heated electron tail of energy up to 100 keV, as was suggested below Eq. (6.130).

6.5.2 Lagrangian Zonal Calculations of Plasma Mass and Energy Transport

Our description of the hot dense plasma includes sharp density profiles, rapid thermal expansion, and a host of non-linear terms, which in general cannot be linearized. Furthermore, we have seen that the energy distributions of particles and radiation can have substantial non-thermal components. Under these circumstances the mathematical problem of describing the plasma evolution is analytically intractable. Rather we again seek numerical solutions, in this case fluidlike Lagrangian computer codes in which the plasma mass is grouped into zones of specified mass, with appropriate fluid level parameters, whose evolution is followed as they absorb energy, increase in temperature and pressure, and expand. Basic parameters in

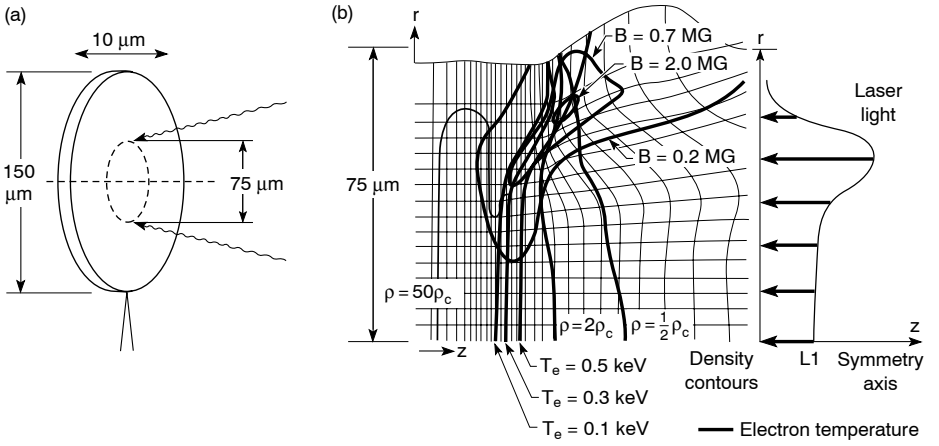

FIGURE 6.16. Results of Lagrangian calculation of hot dense plasma expansion from a laser-heated parylene disk (a) at the peak of a nominally 1×10^{14} W/cm^2, 150 ps FWHM pulse of 1.06 μm light. The non-uniform laser light intensity is shown to the right in (b). Shown in (b) are mass density contours corresponding to electron densities of $n_c/2,\ 2n_c$, and $50n_c$ at the peak of the 0.5 nsec laser pulse. Also shown are electron temperature contours for 0.5 keV, 0.3 keV, and 0.1 keV in the dense region of the plasma (higher in the low-density region). Various contours for calculated off-axis "dc" (varying only on the time scale of the expansion, not of the laser light) magnetic fields in megagauss are also shown. (Courtesy of G. Dahlbacka, M. Mead, C. Max, and J. Thomson, Lawrence Livermore National Laboratory.)

each zone include density, temperature, pressure, vector velocity, multiple species, perhaps energy bins for electrons and photons, etc. As an example, Figure 6.16 shows a Lagrangian mesh calculated for a hot dense plasma as it expands from a laser-heated parylene (CH) disk. These computations are done with the program LASNEX developed by Zimmerman and colleagues[41] at Lawrence Livermore National Laboratory.

Shown are the expanded zones at the peak of the laser pulse after each has absorbed prescribed amounts of laser energy and increased in temperature and pressure, thus exerting pressure on surrounding zones causing fluid motion. Note that one side is shown for this axisymmetric problem. Larger zone size indicates lower density; thus we see directly the plasma expansion into vacuum at the right. Mass density contours corresponding to electron densities of $n_c/2,\ 2n_c$, and $50n_c$ are shown, as are electron temperature contours for 0.1, 0.3, and 0.5 keV. Expansion velocities of the critical density surface in these numerical simulations, obtained by comparing zone positions at the two different times in the calculation, are typically 0.3 μm/ps, similar to the values estimated in Section 6.4.4 following Eq. (6.69). These Lagrangian computer codes are of great utility in understanding the complex fluid (plasma) dynamics, and also in the interpretation of experimental data, as the measurements generally involve finite space–time and spectral resolution in the presence of the sharp space–time gradients.

The simulation in Figure 6.15 was part of an effort to determine possible mechanisms for inhibiting energy transport from the sub-critical absorption region to the more dense supra-critical region, and thus a possible explanation of hard x-ray (suprathermal) tails. Two candidates considered were turbulent electron density fluctuations that would enhance electron scattering and thus inhibit energy transport, and megagauss magnetic fields that might also inhibit energy transport to the dense plasma region. In the particular case examined in Figure 6.15 a somewhat annular laser light illumination pattern was used to generate strong lateral gradients, creating a $\nabla n_e \times \nabla T_e$ driven annular magnetic field, in this case reaching

levels as high as 2 MG in a wrap-around (toroidal) field. Although not confirmed in early experiments, the subject of laser-generated megagauss magnetic fields continues to be of great interest.[43]

Through this example we see that numerical techniques can provide a very valuable tool for the study of complex hot dense plasmas, and also provide substantial assistance for interpreting experimental results that themselves are limited by finite spatial and temporal resolution, and thus not uniquely understandable without further information. These numerical simulation techniques provide a major capability for the planning and subsequent analysis of laser-fusion experiments,[41] as well as the emission characteristics from laser plasma sources.

6.6 DENSITY GRADIENTS: UV AND EUV PROBING

We have seen in preceding chapters that the electron density scale length plays an important role in determining which of several possible mechanisms dominates the absorption process. For a long scale, at moderate laser intensity, collisional absorption is very efficient, while for short scale length resonant absorption can also be important. For long scale lengths several non-linear processes can be important at high intensity. However, at high intensities the plasma density distribution can be strongly affected by radiation pressure, which we will discuss shortly. In any event it is important to measure the electron density scale length to better understand the competition among linear and non-linear mechanisms, and to quantitatively understand the dominant process. Toward that end we discuss measurements of electron density through the use of short wavelength interferometry in this section.

First we note that for high intensity radiation it is possible to generate sufficiently strong radiation pressure P_{r}, comparable to the plasma's electron thermal pressure P_e, such that the plasma is partially excluded from regions of otherwise high density.[1] The size of this effect can be estimated by considering the momentum transfer of absorbed and reflected photons near the region. For absorbed photons that deliver a momentum $\hbar k$, and reflected photons that have a change of momentum $2\hbar k$, one can readily show that the radiation pressure, expressed as the momentum change per unit area, is approximately

$$P_{\mathrm{r}} = \frac{(2 - f_{\mathrm{abs}})F\hbar k}{A}$$

where f_{abs} is the absorption fraction and F is the incident photon flux within an area A. With $k = \omega/c$ and intensity $I = \hbar\omega F/A$, the radiation pressure is

$$P_{\mathrm{r}} = \frac{(2 - f_{\mathrm{abs}})I}{c}$$

For a plasma of electron density n_e and temperature κT_e, the electron thermal pressure P_e is

$$P_e = n_e \kappa T_{\mathrm{e}}$$

so that the ratio is

$$\frac{P_{\mathrm{r}}}{P_e} \simeq \frac{(2 - f_{\mathrm{abs}})I}{cn_c\kappa T_{\mathrm{e}}}$$

For a 1 keV plasma at 10^{21} e/cm^3 and an absorption fraction (near critical) of 0.5, the ratio is unity for a laser intensity of about 3×10^{15} W/cm^3. Thus even for some fraction of this intensity the radiation pressure can significantly affect the sub-critical electron density

profile,[44] and thus the competition and effectiveness of the various linear and non-linear absorption processes.

It is possible to measure electron density distributions in the critical region using interferometric probing techniques. Generally the experiments employ a shorter wavelength probe to minimize refractive bending in the steep gradient plasma, and small targets so as to minimize the path length and thus the total turning angle. For plasma of a given electron density $n_e \ll n_c$, the refractive index n is given by Eq. (6.114b) as

$$n \simeq 1 - \frac{1}{2}\frac{n_e}{n_c}$$

where by Eq. (6.112)

$$n_c = \frac{1.11 \times 10^{21}\ e/\mathrm{cm}^3}{\lambda(\mu\mathrm{m})^2}$$

for a probe of wavelength λ in microns. The first experiments[45, 46] to successfully probe the critical region of a Nd-laser irradiated target utilized a frequency quadrupled (4ω) probe of ultraviolet wavelength 266 nm, so that the plasma contribution to the refractive index was reduced by a factor of 16. The number of fringes N_F observed after propagating a distance L in a medium of refractive index n, and comparing with an equal path L in vacuum, is (see Chapter 3)

$$N_\mathrm{F} = \frac{1}{\lambda_p}\int_0^L (1-n)\,ds \tag{6.132}$$

where λ_p is the probe wavelength, ds is the incremental path length, and L is the total extent of propagation in the medium. For a region or relatively uniform density over a path length L, the number of fringes is then $N_\mathrm{F} = n_e L/2n_c\lambda_p$, where n_c is the critical density for the probe at λ_p. For a laser heating pulse of wavelength λ and associated critical density n_c, the number of fringes is $N_F = \lambda_p L/2\lambda^2$. To avoid the difficulty of too many fringes, perhaps too closely spaced, to be optically resolved or so close that they are easily time smeared, it is clearly advantageous to choose a short probe wavelength λ_p and a short plasma propagation path L. If the axial gradient is such that the electron density falls to a value $1/e$ in a distance l, then the fringe separation distance[45] at critical is

$$\Delta z|_c = \frac{l}{N_F/e} \simeq \frac{5.4 l\lambda^2}{\lambda_p L} \tag{6.133a}$$

or in terms of the critical electron density [Eq. (6.112)]

$$\Delta z|_c \simeq 2.1 \times 10^2 \frac{m}{\mu_0 e^2}\cdot\frac{l}{\lambda_p L n_c} \tag{6.133b}$$

which explicitly shows the functional dependence of required spatial resolution for short wavelength interferometry on the plasma parameters l, L, and n_c, for a probe wavelength λ_p. Clearly, to probe high electron densities in steep gradient plasmas it is necessary to minimize the product $\lambda_p L$. To probe the critical density associated with a laser heating pulse of wavelength $\lambda = 1.06\ \mu$m, with a 4ω probe at wavelength $\lambda_p = 266$ nm, assuming a gradient length $\lambda = 1.5\lambda \simeq 1.6\ \mu$m and a plasma lateral extent of $L = 30\ \mu$m requires a spatial resolution [Eq. (6.133)] of about 1.1 μm, which can be accomplished at 266 nm with a commercially available UV objective lens.

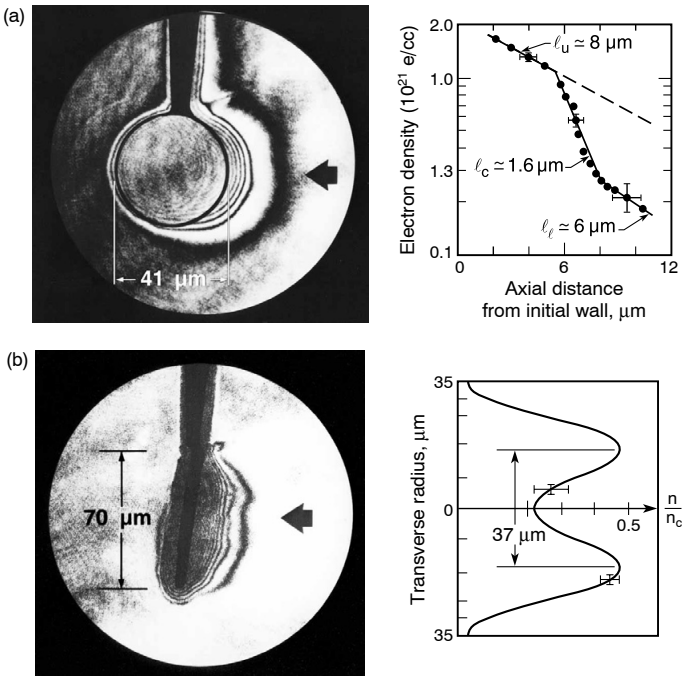

FIGURE 6.17. UV interferograms of laser produced plasmas, created with a 1.06 μm laser pulse, 30 ps FWHM, with nominal intensities of 3×10^{14} W/cm^2. The probe pulse wavelength is 266 nm, with a 15 ps FWHM duration, timed to arrive at the peak of the heating pulse. The interferograms are obtained using a holographic technique. The lack of temporal smearing in many such experiments suggests that critical surface moves more slowly than predicted, perhaps due to radiation pressure.[45, 46]

Figure 6.17 shows two such interferograms,[45] obtained using a holographic interferometer at 266 nm wavelength to probe plasma irradiated at 3×10^{14} W/cm^2 with a spherical shell target (a) and with a flat disk target (b). In both cases the electron density distribution was determined assuming axial symmetry. Both show clear effects of radiation pressure pushing plasma (partially) out of the near-critical interaction region. Assuming an electron temperature of 1 keV, the ratio of p_r to P_e is about 0.1 in these experiments. The spherical glass shell target experiment [Figure 6.17(a)] had the advantage of a short propagation path and thus was able to probe to just above the critical density. The target diameter was only 41 μm, and the lateral probing distance, equivalent to L, was shorter still. Note that the axial density profile shows a pronounced steepening just below critical, with a measured scale length $l \simeq 1.6$ μm. This is quite similar to values seen in numerical simulations and is perhaps affected somewhat by the finite resolution of the UV objective lens, which is just under 1 μm at 266 nm wavelength. The flat disk targets are of larger diameter, that in Figure 6.17(b) having a 70 μm diameter, thus limiting the measurements to about half-critical density. Their analysis, however, is to first order simpler. All the targets in this series show relatively flat fringe patterns, which for an axisymmetric geometry indicate very clearly[46] the presence of a density depression, or cavity, in the sub-critical region.

It is evident from Eq. (6.133) that to resolve fringes at high electron density, one key is to probe at shorter wavelength. Toward this end Da Silva and his colleagues[47] have developed a 15.5 nm probe beam based on EUV lasing, a subject discussed in Chapter 7, and have used it to probe relatively large scale plasmas at $L \simeq 1$ mm and electron densities in excess of

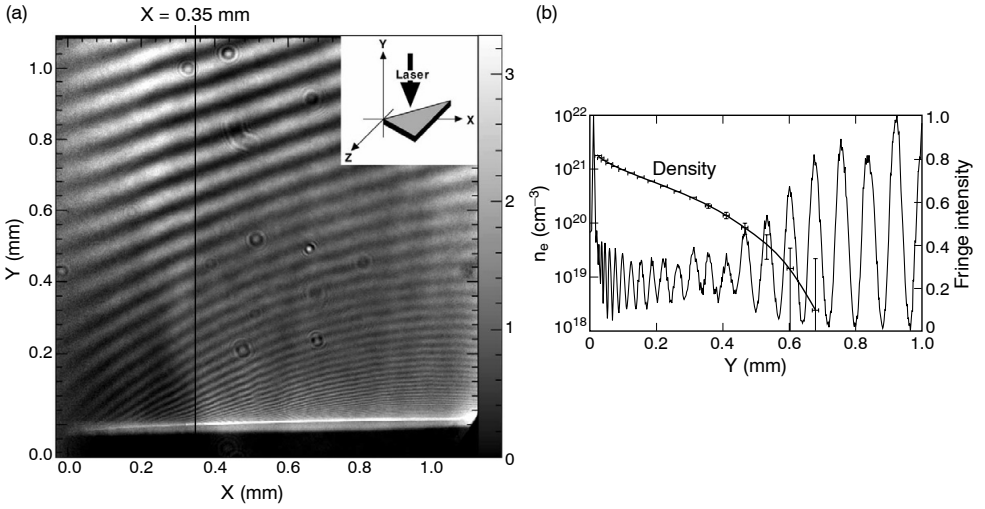

FIGURE 6.18. (a) An interferogram of an expanding CH plasma obtained with a 15.5 nm wavelength, 350 ps duration laser pulse. The plasma is produced by a 1 ns square pulse of 0.5 μm laser light at an intensity of 2.7×10^{13} W/cm^2 on a triangular shaped CH target. The probe pulse, from a neon-like yttrium laser, is of 300 ps duration, timed to arrive 1.1 nsec after initiation of the heating pulse. (b) Measured electron density, to values above 10^{21} e/cm^2, are shown for a position 0.35 mm from the target surface. (Courtesy of L. Da Silva, Lawrence Livermore National Laboratory.)

10^{21} e/cm^2. Figure 6.18 shows (a) a fringe pattern obtained with a hot dense plasma expanding from a laser heated Mylar (CH) target, and (b) the measured electron density as a function of position away from the target surface. The target is irradiated with a 1 ns duration rectangular pulse of 0.53 μm (frequency doubled Nd) laser light, at an intensity of 2.7×10^{13} W/cm^2, in a 0.7 mm diameter focal spot. The expanding plasma was integrated with a 350 ps duration, 15.5 nm probe pulse, arriving 1.1 ns after the arrival of the laser heating pulse. Analysis of the fringe pattern indicates a peak electron density of 3×10^{21} e/cm^3 and a scale length of $l \simeq 40$ μm. This clearly represents a new capability of the study of electron density distributions in hot dense plasmas, extendible to densities of 10^{22} e/cm^3 in sub-millimeter plasmas. Indeed, the authors have used the 15.5 nm laser pulse to interferometrically probe colliding high density plasmas of interest to the inertial confinement fusion (ICF, or laser fusion) community.[47] Moreno, Rocca, and colleagues have recently reported the study of plasma dynamics in a capillary discharge using shadowgrams at 48.9 nm with a table top Ne-like laser (see Chapter 7, Section 7.5).

6.7 X-RAY EMISSION FROM A HOT DENSE PLASMA

That a plasma is both hot and dense, characterized by keV temperatures and near-solid densities, ensures that it will be a bright source of short wavelength radiation. As we have seen in the preceding sections, there is the possibility of both thermal and non-thermal processes taking place, from classical electron–ion collisions to highly non-linear three-wave mixing processes, each impressing its own signatures on the electron velocity distribution, and eventually on the observed emission spectra as the electrons collide with ions or nearby dense material. In the following subsections we consider various aspects of the emission process, with examples of line and continuum radiation.

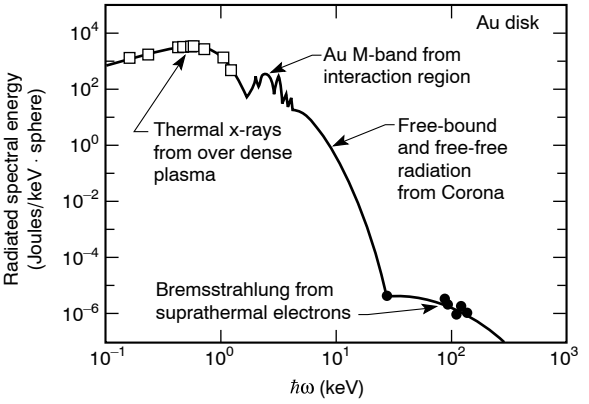

FIGURE 6.19. Typical x-ray spectra from a laser irradiated high Z target at moderate $I\lambda^2$. The data was obtained at Lawrence Livermore National Laboratory's Nova Laser Facility. (Courtesy of R. Kauffman.)

Figure 6.19 shows data of the type we might expect to encounter.[49] It shows the radiated spectral energy density, in joules per keV bandwidth, radiated into 4π sr, for a gold disk target irradiated with 0.35 μm light (3ω of Nd) at an intensity of 5×10^{14} W/cm^2, in a 1 nsec duration pulse. The emission spectrum shows a near-thermal continuum in the sub-kilovolt photon energy range, characteristic line spectra at a few keV (relatively broad M-band structure in this case), an exponentially falling spectrum of mixed free–bound and free–free bremsstrahlung radiation extending to photon energies of order 10 keV, and finally a suprathermal tail extending to 100 keV and beyond. In the following sections we consider separately general aspects of the thermal component, followed by various examples of line and continuum radiation is the sub-kilovolt and kilovolt photon energy ranges.

6.7.1 Continuum Radiation and BlackBody Spectra

We have seen in previous sections that hot dense plasmas are characterized by sharp spatial and temporal gradients, rapid expansion, and a variety of characteristic temperatures ($T_e,\ T_i,\ T_{hot}, \ldots$). Such a plasma is clearly far from equilibrium. Nonetheless, a great fraction of the plasma energy is invested in a near-thermal distribution, and thus it is valuable to pause and consider the limiting case of *blackbody radiation,* that emitted by material characterized by a single temperature T that is in thermodynamic equilibrium with its surroundings.

In 1900 Max Planck, in an early contribution to the quantum theory of matter,[50] showed that if one assumed radiation to be emitted in discrete quanta of energy, with energy proportional to frequency, that the spectral energy density of radiation for such a body in equilibrium is[51, 52]

$$U_{\Delta\omega} = \frac{\hbar\omega^3/\pi^2c^3}{e^{\hbar\omega/\kappa T} - 1} \tag{6.134a}$$

in units of energy per unit volume, per unit frequency interval $\Delta\omega$, at frequency ω, i.e., $\Delta^2E/\Delta V\ \Delta\omega$. Expressing this in terms of relative spectral bandwidth ($\Delta\omega/\omega$), the spectral energy density $[\Delta^2E/\Delta V(\Delta\omega/\omega)]$ becomes

$$U_{\Delta\omega/\omega} = \frac{\hbar\omega^4/\pi^2c^3}{e^{\hbar\omega/\kappa T} - 1} \tag{6.134b}$$

Since the radiation is isotropic and propagating at the speed of light, we may write the spectral brightness as

$$B_{\Delta\omega/\omega} = \frac{cU_{\Delta\omega/\omega}}{4\pi} = \frac{\hbar\omega^4/4\pi^3c^2}{e^{\hbar\omega/\kappa T} - 1} \tag{6.135a}$$

now in units of energy per unit time, per unit area, per steradian, per unit relative spectral bandwidth $[\Delta^4 E/\Delta t\ \Delta A\ \Delta\Omega\,(\Delta\omega/\omega)]$. Observing that energy per unit time can be written in terms of energy per photon ($\hbar\omega$) times the photon flux, the spectral brightness can be rewritten in terms of photon flux, rather than energy, as

$$B_{\Delta\omega/\omega} = \frac{(\hbar\omega)^3}{4\pi^3\hbar^3c^2}\ \frac{1}{e^{\hbar\omega/\kappa T} - 1} \tag{6.135b}$$

now in photons per second per steradian per unit area · per unit $\Delta\omega/\omega$. Normalizing to κT and substituting standard values for $\hbar$ and c (from Appendix A), the *spectral brightness of blackbody radiation* can be expressed as

$$B_{\Delta\omega/\omega} = 3.146 \times 10^{20} \left(\frac{\kappa T}{eV}\right)^3 \frac{(\hbar\omega/\kappa T)^3}{(e^{\hbar\omega/\kappa T} - 1)} \frac{\text{photons/s}}{\text{mm}^2 \cdot \text{sr} \cdot (\Delta\omega/\omega)} \tag{6.136a}$$

This can also be expressed in units previously used for the brightness of synchrotron radiation (Chapter 5, Section 5.4.6) by noting that 1 sr $= 10^6$ mrad^2, and that for the special case $\Delta\omega/\omega = 0.1\%$BW,

$$B_{\Delta\omega/\omega} = 3.146 \times 10^{11} \left(\frac{\kappa T}{eV}\right)^3 \frac{(\hbar\omega/\kappa T)^3}{(e^{\hbar\omega/\kappa T} - 1)} \frac{\text{photons/s}}{\text{mm}^2 \cdot \text{mrad}^2 \cdot (0.1\%\text{BW})} \tag{6.136b}$$

The spectral brightness has a functional dependence of the form $x^3/(e^x - 1)$, as plotted in Figure 6.20, where $x = \hbar\omega/\kappa T$. This Planckian function has a maximum value of 1.421 at $x = 2.822$, so that the peak spectral brightness occurs at a photon energy

$$\hbar\omega|_{\text{pk}} = 2.822\kappa T \tag{6.137}$$

where the peak spectral brightness is, per steradian and per unit relative spectral bandwidth,

$$B_{\Delta\omega/\omega}(2.822\kappa T) = 4.472 \times 10^{20} \left(\frac{\kappa T}{eV}\right)^3 \frac{\text{photons/sec}}{\text{mm}^2 \cdot \text{sr} \cdot (\Delta\omega/\omega)} \tag{6.138a}$$

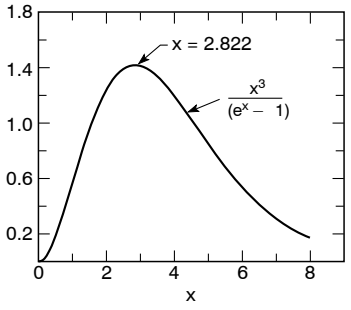

FIGURE 6.20. The Planck distribution function, of the form $x^3/(e^x - 1)$ where $x = \hbar\omega/\kappa T$, for the spectral distribution of radiation from a body in equilibrium with its surroundings, a so-called *blackbody*. The function peaks at $x = 2.822$, or $\hbar\omega = 2.822\kappa T$, where κT is the temperature in eV.

or, per square milliradian and per 0.1% bandwidth,

$$B_{\Delta\omega/\omega}(2.822\kappa T) = 4.472 \times 10^{11} \left(\frac{\kappa T}{eV}\right)^3 \frac{\text{photons/sec}}{\text{mm}^2 \cdot \text{mrad}^2 \cdot (0.1\%\text{BW})} \tag{6.138b}$$

Thus for example, at a radiation temperature of $\kappa T = 100$ eV, the peak spectral brightness at 282 eV is 4.47×10^{26} (photons/s)/mm$^2 \cdot$ sr, or 4.47×10^{17} (photons/s)/mm$^2 \cdot$ mrad$^2 \cdot$ (0.1%BW), falling to half these values to either side of the peak, at photon energies of 116 eV and 541 eV. We see that a blackbody with κT of order 100 eV is a copious radiator of EUV and soft x-ray radiation, indeed with a high spectral brightness. For laboratory plasmas we will find that this provides a useful, if idealistic, limit for the consideration of near-thermal radiation.

An important issue for laboratory plasmas is that the lifetime of the hot dense plasma is in general very close to the duration of the heating pulse, which is typically measured in nanoseconds for such high temperatures. Thus in order to obtain substantial time averaged emission it becomes important to have a very high repetition rate, for instance, kilohertz lasers in which each individual pulse is focused to an intensity of order 10^{12} W/cm^2 or higher. These numbers will become more meaningful as this section continues.

It is often of interest to know the radiant energy flux (power per unit area) passing a given surface, as, for instance, through the hole in the cavity in Figure 6.21. Since the radiation is isotropic within the blackbody, we understand that the *net* energy flow across any given surface is zero. However, we may consider the single-sided integral of energy flux crossing a specified area in one direction, which is non-zero. From Eq. (6.135a) we can compute the spectral intensity of radiation crossing in one direction as

$$I_{\Delta\omega/\omega} = \int_{2\pi} B_{\Delta\omega/\omega} \cos\theta \, d\Omega \tag{6.139}$$

where θ is measured from the surface normal, $d\Omega = \sin\theta \, d\theta \, d\phi = 2\pi \sin\theta$, for $0 \le \theta \le \pi/2$, and where $I_{\Delta\omega/\omega}$ has units of energy per unit area per unit of relative spectral bandwidth $\Delta\omega/\omega$. Since the spectral brightness is isotropic (no θ-dependence), and $\int_0^{2\pi} 2\pi \sin\theta \cos\theta \, d\theta = \pi$, one has

$$I_{\Delta\omega/\omega} = \frac{1}{4\pi^2\hbar^3c^2} \frac{(\hbar\omega)^4}{e^{\hbar\omega/\kappa T} - 1}$$

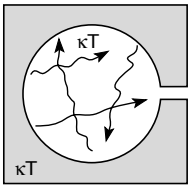

FIGURE 6.21. A cavity, or *hohlraum*, in which the contained radiation field is in radiative equilibrium with the surrounding wall.

Integrating this over all (normalized) frequencies $d\omega/\omega$, one has the (single-sided) intensity in units of energy per unit area, passing a given interface from one side to the other,

$$I = \int_0^\infty \frac{1}{4\pi^2\hbar^3c^2}\,\frac{(\hbar\omega)^3}{e^{\hbar\omega/\kappa T}-1}\,\hbar\,d\omega \tag{6.140a}$$

$$I = \frac{(\kappa T)^4}{4\pi^2\hbar^3c^2}\int_0^\infty \frac{x^3\,dx}{e^x-1} \tag{6.140b}$$

where the integral can be found in standard integral tables[53] as equal to $\pi^4/15$, so that the *blackbody intensity* at any interface is

$$I = \frac{\pi^2}{60c^2\hbar^3}(\kappa T)^4 \tag{6.141a}$$

or

$$\boxed{I = \sigma T^4} \tag{6.141b}$$

where

$$\sigma = \frac{\pi^2\kappa^4}{60c^2\hbar^3} \tag{6.142}$$

is the Stefan–Boltzmann constant, written in terms of the Boltzmann constant κ.

Equation (6.141) is known as the Stefan–Boltzmann radiation law; it says that the radiant energy flux per unit area crossing any surface or interface of a blackbody is proportional to the fourth power of the absolute temperature. This applies to the energy received by a nearby surface, and to the energy radiated back if the two are in radiative equilibrium.

Figure 6.21 illustrates a small cavity, or *hohlraum*, for which the radiation field is Planckian of temperature κT, in equilibrium with the surrounding walls, also at temperature κT. For a very small hole, small enough so as not to upset the overall radiative equilibrium, the radiated intensity per unit area is given by Eq. (6.141). This relationship is very useful for estimating an upper bound to the radiated intensity from a laser heated surface, the sun, a fireplace, or any hot object to the extent that it approximates radiative equilibrium. In many cases the emission spectrum is quite complex and we define an *equivalent blackbody temperature* by setting the radiated intensity equal to σT^4.

Equation (6.141) can be written in terms of κT, expressed in electron volts, which is more convenient for application involving EUV and soft x-ray radiation, i.e.,

$$I = \widehat{\sigma}(\kappa T)^4 \tag{6.143a}$$

in terms of a modified Stefan–Boltzmann constant

$$\widehat{\sigma} = \frac{\pi^2}{60\hbar^3 c^2} = 1.027 \times 10^5 \frac{\mathrm{W}}{\mathrm{cm}^2 \cdot \mathrm{eV}^4} \tag{6.143b}$$

In these units we readily see that a blackbody with temperature $\kappa T = 100$ eV radiates at an intensity $I \simeq 1.0 \times 10^{13}$ W/cm^2, and according to Eq. (6.137) peaks at $\hbar\omega = 282$ eV.

We might ask under what practical circumstance such emission characteristics might be achieved with a laboratory laser produced plasma, with finite fractional absorption of the incident laser radiation, and fractional conversion of absorbed light to re-radiated near-thermal emission. Experience with high intensity, nominally nanosecond duration laser pulses tells that the plasmas produced reach a steady state in a matter of picoseconds, during which the hot dense plasma is formed and energy partition between the charged particles, radiation field, and surrounding material is achieved, albeit briefly. Depending on various parameters, including intensity, laser wavelength, material (Z), and achieved temperature, as discussed earlier in Sections 6.4.9 and 6.4.10, this can lead to the creation of a rather efficient hot dense plasma radiator of soft x-rays and extreme ultraviolet radiation. For example, with a laser of 0.53 μm wavelength and incident intensity of 10^{14} W/cm^2 in a half nanosecond duration pulse incident on a medium to high Z solid target, one can expect to produce a near-thermal plasma with typically 80% absorption[33] of the incident laser energy, and 10% of the absorbed energy re-radiated at short wavelengths, for a total radiation conversion efficiency[49] of about 50% (see Section 6.7.6 regarding laser wavelength trends). Thus the re-radiated intensity would be 5×10^{13} W/cm^2, which for a blackbody according to Eq. (143a) would correspond to a temperature $T \simeq 150$ eV, with a peak [Eq. (6.137)] at 420 eV. Even with an incident laser intensity of 10^{12} W/cm^2, with similar assumptions, the equivalent blackbody temperature is reduced by only a factor of about 3.2 (fourth root), so that $\kappa T \simeq 50$ eV, with peak emission at a photon energy of about 140 eV, sufficiently energetic to create the desired ionization states among the plasma ions and to radiate strongly in the EUV region of the spectrum. We discuss the departures for the idealized blackbody emission in the following sections.

6.7.2 Line Emission and Ionization Bottlenecks

Hot dense plasmas are essentially fully ionized, that is, every atom has at least one electron removed. In fact the temperatures are sufficiently high that most atoms have many fewer bound electrons than protons in the nucleus. The ionization state (number of electrons removed) depends primarily on the binding energies of the various electrons and on the electron plasma temperature. Typically the outer electrons in a multi-electron atom are held by only a few electron volts, while the core K, L, and M shell electrons (principal quantum numbers $n = 1$, 2, and 3) are closer to the nucleus and held more tightly, with binding energies of hundreds of thousands of electron volts.[54] Table 6.2 gives the binding energies calculated by Scofield[55] for selected ions. The elements listed vertically extend from a carbon nucleus ($Z = 6$) to a xenon nucleus ($Z = 54$). Shown in the body of the table is the energy in electron volts required to remove an additional electron from an ion having 1 ("hydrogen-like"), 2 ("helium-like"), . . . , 10 ("neon-like"), etc., remaining electrons.

For example, aluminum in its neutral state has 13 electrons. Table 6.2 indicates that with one electron already gone and 12 remaining ("magnesium-like" in electron configuration) the

TABLE 6.2. Ionization energies for selected ionic species. Each column is labeled with the number of electrons bound to the ion before ionization and, in parenthesis, the symbol of the neutral atom with the same number of electrons. (Courtesy of J. Scofield, Lawrence Livermore National Laboratory.)

	Ionization energy (eV)									
Element	1 (H)	2 (He)	3 (Li)	4 (Be)	10 (Ne)	11 (Na)	12 (Mg)	27 (Co)	28 (Ni)	29 (Cu)
6 C	490.0	392.1	64.49	47.89						
7 N	667.1	552.1	97.89	77.48						
8 O	871.4	739.3	138.11	113.90						
9 F	1103.1	953.9	185.18	157.15						
10 Ne	1362.2	1195.8	239.09	207.26	21.564					
11 Na	1648.7	1465.1	299.86	264.21	47.286	5.139				
12 Mg	1962.7	1761.8	367.5	328.0	80.143	15.035	7.646			
13 Al	2304.2	2086.0	442.0	398.7	119.99	28.447	18.828			
14 Si	2673.2	2437.7	523.4	476.3	166.42	45.12	33.64			
15 P	3070	2816.9	611.7	560.8	220.31	65.02	51.80			
16 S	3494	3224	707.0	652.1	281.00	88.05	72.59			
17 Cl	3946	3658	809.2	750.5	348.5	114.20	96.84			
18 Ar	4426	4121	918.4	855.8	422.8	143.46	124.24			
19 K	4934	4611	1034.6	968.0	503.9	175.82	145.75			
20 Ca	5470	5129	1157.7	1087.3	591.9	211.28	188.38			
21 Sc	6034	5675	1288.0	1213.6	686.6	249.84	225.13			
22 Ti	6626	6249	1425.3	1346.9	788.2	291.50	264.98			
23 V	7246	6851	1569.7	1487.3	896.6	336.3	307.9			
24 Cr	7895	7482	1721.1	1634.8	1011.8	384.2	354.0			
25 Mn	8572	8141	1879.9	1789.5	1133.8	435.2	403.2			
26 Fe	9278	8828	2045.8	1951.3	1262.7	489.3	455.6			
27 Co	10012	9544	2218.9	2120.4	1389.3	546.6	511.0	7.86		
28 Ni	10775	10289	2399.3	2296.7	1540.8	607.0	569.7	18.17	7.63	
29 Cu	11568	11063	2587.0	2480.2	1690.2	670.6	631.4	36.83	20.29	7.73
30 Zn	12389	11865	2782.0	2671.1	1846.4	737.3	696.4	59.57	39.72	17.96
31 Ga	13239	12696	2984.4	2869.4	2009.4	807.3	764.5	86.0	63.4	30.7
32 Ge	14119	13557	3194	3075	2179.3	880.4	835.8	115.9	90.5	45.72
33 As	15029	14448	3412	3288	2356.0	956.8	910.3	149.2	121.2	62.3
34 Se	15968	15367	3637	3509	2539.6	1036.3	988.1	185.5	155.4	81.7
35 Br	16937	16317	3869	3737	2730.1	1119.1	1069.1	225.4	192.8	103.0
36 Kr	17936	17296	4109	3973	2927.4	1205.2	1153.3	268.2	233.4	125.9
37 Rb	18965	18306	4357	4216	3132	1294.5	1240.8	314.2	277.1	150.7
38 Sr	20025	19345	4612	4467	3343	1387.2	1331.5	363.3	324.1	177.3
39 Y	21115	20415	4876	4726	3561	1483.1	1425.6	413.6	374.0	205.9
40 Zr	22237	21516	5147	4993	3786	1582.4	1523.0	471	427.4	236.2
41 Nb	23389	22648	5426	5268	4017	1684.9	1623.7	530	483.8	268.5
42 Mo	24572	23810	5713	5550	4256	1790.9	1727.8	592	541.7	302.6
43 Tc	25787	25004	6008	5841	4502	1900.3	1835.2	656	605.8	338.5
44 Ru	27033	26230	6312	6140	4754	2013.0	1946.1	724	671.4	376.3
45 Rh	28312	27487	6623	6447	5014	2129.2	2060.3	795	740.1	416.0
46 Pd	29623	28776	6943	6762	5280	2248.9	2178.0	869	811.8	457.5
47 Ag	30966	30097	7271	7086	5553	2372.0	2299.2	946	886.6	500.9
48 Cd	32341	31451	7608	7418	5834	2498.6	2423.9	1026	964.5	546.2
49 In	33750	32837	7953	7758	6121	2628.8	2552.1	1109	1045.4	593.3
50 Sn	35192	34257	8307	8107	6415	2762.5	2683.9	1196	1129.1	642.3
51 Sb	36668	35710	8670	8465	6717	2899.8	2819.2	1285	1215.3	693.2
52 Te	38177	37196	9041	8832	7025	3041	2958.1	1377	1306.3	746.1
53 I	39721	38716	9421	9207	7340	3185	3101	1472	1399.3	800.8
54 Xe	41300	40271	9810	9591	7663	3334	3247	1571	1495.4	857.4

calculated energy to remove the twelfth electron is 18.8 eV. That would leave 11 electrons. The energy required to remove another electron (the eleventh) is 28.4 eV. Having removed the eleventh, there are 10 remaining electrons, forming a closed shell in the neon-like ($1s^2\ 2s^2\ 2p^6$) configuration. The symmetry of the closed shell makes removal of an additional electron more difficult, and the ionization potential (binding energy) jumps significantly to 120 eV for neon-like aluminum. This significantly increased threshold for further electron removal can be considered an *ionization bottleneck* for a plasma of a given temperature.

For instance, if irradiation conditions (intensity, etc.) were adjusted to produce an electron temperature of 60 eV, as cited in the previous subsection, one could expect that relatively direct electron–ion collisions would easily remove the outermost electrons of most aluminum ions, including the eleventh electron, of binding energy equal to 28.4 eV. However, removal of electrons from the remaining 10-electron neon-like configuration, of binding energy equal to 120 eV, would be substantially more difficult for a 60 eV temperature plasma. As the temperature represents a distribution of energies, there are certainly higher energy electrons that can cause further ionization, but the energy distribution [Eq. (6.86)] falls off exponentially beyond κT, so that the process quickly decreases in efficiency.

We will show data in Section 6.8.4 for the line emission from a laser-produced titanium ($Z = 22$) plasma at high laser intensity, with $\kappa T_e \simeq 1$–2 keV, where the ionization thresholds (Table 6.2) permit relatively easy removal of all but the last two electrons. For example, with only three electrons remaining, the energy required to remove an additional electron is 1.4 keV, which occurs rather efficiently in a 1–2 keV plasma. With two remaining electrons, the ion is then in a helium-like closed shell configuration and the threshold for further ionization jumps to 6.2 keV, creating a well-defined step (bottleneck) in this sequential ionization process. As a result the plasma at this temperature consists largely of helium-like titanium atoms with some lithium-like and beryllium-like ions, but little else. As we will see in Section 6.7.4, this leads to very strong line emission from helium-like titanium ions. The principal $n = 2$ to $n = 1$ transitions for helium-like (and hydrogen-like) ions, again calculated by Scofield,[55] are given in Table 6.3. For the helium-like titanium ion the table shows principal emission lines at 4.727 keV and 4.750 keV: the $^1P_1$ and $^3P_1$ to $^1S_0$ resonance and intercombination $1s2p \rightarrow 1s^2$ transitions.

6.7.3 Sub-Kilovolt Line and Continuum Emissions

Hot dense laboratory plasmas are copious emitters of extreme ultraviolet and soft x-ray radiation, have a generally complex internal density and temperature structure, and are not in equilibrium with their surroundings, although they may reach some quasi-steady state for a brief period during their expansion. These laboratory plasmas generally exhibit an emission spectrum different from the ideal blackbody considered in Section 6.7.1. Recall that the highest electron temperature occurs in the relatively low density ($n_e \leq n_c$) absorption region. The absorbed energy is transported by random charged particle motion and radiation to a cooler, higher density ($n_e > n_c$) region. Radiation from this relatively high density region tends to dominate the emission process, generating the bulk of low to medium photon energies. As the propagation path is relatively long, through a dense plasma region, the line spectra due to the various ions tends to be smoothed to a modulated continuum. Where the modulation is relatively modest, blackbody radiation characteristics can be helpful in understanding and scaling problems. In some cases it is useful to introduce an equivalent blackbody temperature T_{eq} that would generate the same radiated intensity when integrated over a broad spectral region. We will consider such radiation in this section.

TABLE 6.3. Transition energies for transitions from the $n = 2$ state to the $n = 1$ ground state of H- and He-like ions. (Courtesy of Scofield, Lawrence Livermore National Labortory.)

	Transition energy (eV)			
	Hydrogen-like		*Helium-like*	
Element	$2p_{1/2}$	$2p_{3/2}$	$2p\ ^3P_1$	$2p\ ^1P_1$
5 B	255.17	255.20	202.78	205.37
6 C	367.5	367.5	304.3	307.8
7 N	500.3	500.4	426.3	430.7
8 O	653.5	653.7	568.7	574.0
9 F	827.3	827.6	731.5	737.8
10 Ne	1021.5	1022.0	914.9	922.1
11 Na	1236.3	1237.0	1118.8	1126.9
12 Mg	1471.7	1472.7	1343.2	1352.3
13 Al	1727.7	1729.0	1588.3	1598.4
14 Si	2004.3	2006.1	1853.9	1865.1
15 P	2301.7	2304.0	2140.3	2152.6
16 S	2619.7	2622.7	2447.3	2460.8
17 Cl	2958.5	2962.4	2775.1	2789.8
18 Ar	3318	3323	3124	3140
19 K	3699	3705	3493	3511
20 Ca	4100	4108	3883	3903
21 Sc	4523	4532	4295	4316
22 Ti	4966	4977	4727	4750
23 V	5431	5444	5180	5205
24 Cr	5917	5932	5655	5682
25 Mn	6424	6442	6151	6181
26 Fe	6952	6973	6668	6701
27 Co	7502	7526	7206	7242
28 Ni	8073	8102	7766	7806
29 Cu	8666	8699	8347	8392
30 Zn	9281	9318	8950	8999
31 Ga	9917	9960	9575	9628
32 Ge	10575	10624	10221	10280
33 As	11255	11311	10889	10955
34 Se	11958	12021	11579	11652
35 Br	12682	12753	12292	12372
36 Kr	13429	13509	13026	13114
37 Rb	14199	14288	13783	13880
38 Sr	14990	15090	14562	14669
39 Y	15805	15916	15364	15482
40 Zr	16643	16765	16189	16318
41 Nb	17503	17639	17036	17178
42 Mo	18387	18537	17907	18062
43 Tc	19294	19459	18800	18971
44 Ru	20224	20406	19717	19904
45 Rh	21178	21377	20658	20861
46 Pd	22156	22374	21622	21843
47 Ag	23157	23396	22609	22851
48 Cd	24183	24444	23621	23884
49 In	25233	25518	24657	24942
50 Sn	26308	26617	25717	26027

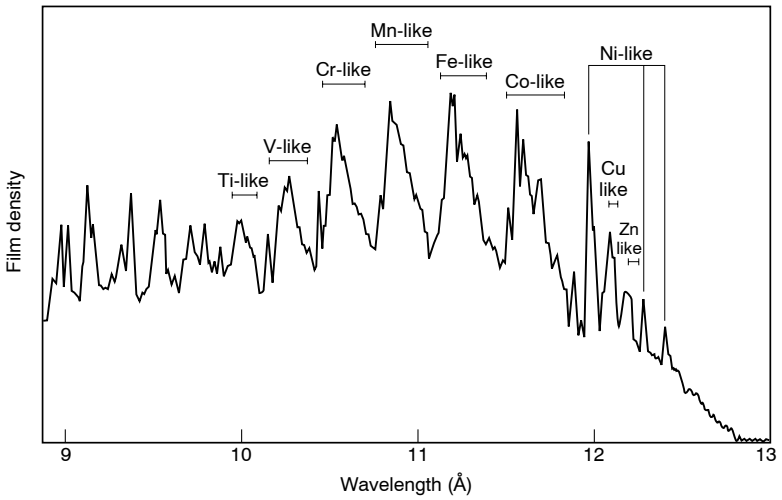

FIGURE 6.22. Emission spectrum from a laser-heated lanthanum target, showing 4f to 3d line structure due to ions in various ionization states from zinc-like (+27 charge state) to titanium-like (+35 charge state). Laser energy is 70 J, 3.5 ns FWHM, 1.06 μm wavelength at about 10^{14} W/cm^2. (Courtesy of A. Zigler, Hebrew University, Jerusalem.)

In the following section we will consider higher photon energy radiation from the hotter low density region in which the propagation path to vacuum is shorter, involves less absorption and scattering, and results in a significantly modulated spectrum with pronounced line structure characteristic of the various ionization states present. For a discussion of radiation transport in optically thick (much absorption and scattering) and optically thin (minimal absorption and scattering) regions of plasma see the book by Griem.[9]

An example of near-thermal emission from a moderate intensity high-Z laser-produced plasma is shown in Figure 6.22. The experiment, conducted by Zigler and colleagues,[56] utilized a 70 J, 3.5 ns FWHM Nd laser pulse at 1.06 μm wavelength, focused to an intensity of about 10^{14} W/cm^2 on a lanthanum ($Z = 57$) target. Dispersion of the emitted spectrum was achieved through use of a potassium ammonium phosphate (KAP) crystal and recorded on RAR 2495 x-ray film. The observed modulation of the emission spectrum is ascribed to 4f $\rightarrow$ 3d transitions in lanthanum ions of various ionization states, extending from zinc-like (30 remaining electrons, +27 charge state) to titanium-like (22 remaining electrons, +35 charge state). The various peaks consist of numerous closely packed lines in what the authors call an unresolved transition array. After correcting for the non-linear film response,[57, 58] the modulation is only about 20%, peak to valley. The ionization energy for lanthanum in this range of charge states (+35 to +27) is typically several hundred electron volts. At an irradiation intensity of 10^{14} W/cm^2 the maximum equivalent blackbody temperature is about 170 eV, with a peak photon energy near 500 eV, or a wavelength of 25 Å. Thus the observed lines in Figure 6.22 are likely somewhat on the high photon energy side of the emission peak. In similar experiments, but with 20 times less laser energy, the authors report that the transition arrays due to the higher ionization states are significantly less pronounced, merging into a noisy continuum for Cr-like and beyond.

Emission from a moderate Z laser-produced plasma, also at moderate laser intensity, is shown in Figure 6.23. In this case a chromium target ($Z = 24$) is irradiated with 1.06 μm wavelength light, at 2×10^{14} W/cm^2, in a 150 ps duration pulse. Well-defined lines of

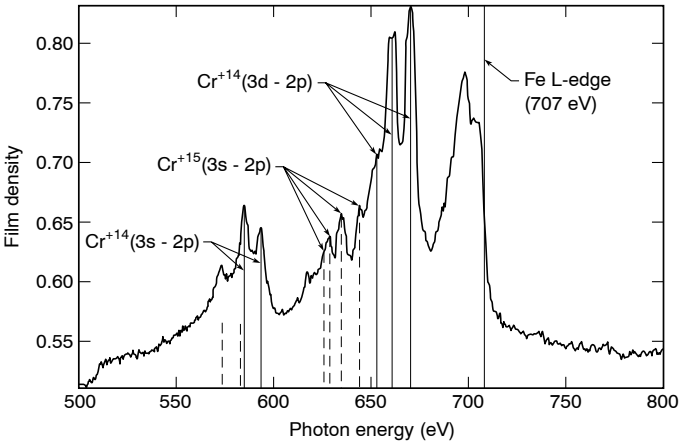

FIGURE 6.23. The emission spectrum recorded for a chromium target irradiated by a 1.06 μm Nd laser pulse of 150-ps duration and 2×10^{14} W/cm^2 incident intensity. Prominent lines of neon-like Cr^{+14} are evident, as well as weaker Cr^{+15} (fluorine-like) lines. (Courtesy of R. Kauffman and L. Koppel, Lawrence Livermore National Laboratory.)

neon-like Cr^{+14}, and weaker Cr^{+15}, are seen. The high photon energy limit of the observed spectrum is set by the L-absorption edge of neutral iron (707 eV, Appendix D) in an overlying filter. Dispersion here is provided by a lead behenate crystal ($2d \simeq 120$ Å), with the data recorded on x-ray film. According to Table 6.2, the ionization energy for Cr^{+13} (11 electrons) is 384 eV, while that for neon-like Cr^{+14} (10 electrons) is 1012 eV. With an irradiation intensity of 2×10^{14} W/cm^2 we can expect an equivalent blackbody temperature $\kappa T_{eq} \simeq 200$ eV, with a spectral emission peak approaching 600 eV. This is then consistent with a neon-like ionization bottleneck in which most Cr^{+13} ions are ionized further to Cr^{+14}, explaining the observation of strong Cr^{+14} lines and weak Cr^{+15} lines. According to Kelly,[54] the principal 3s to 2p and 3d to 2p emission lines[§] should lie at photon energies of 586 eV, 594 eV, 660 eV, and 670 eV, respectively, very close to experimental values seen in Figure 6.23. Note that the Cr^{+15} 3s to 2p lines are of somewhat higher energy than those for Cr^{+14}, as there is one fewer electron and thus somewhat reduced screening of the nuclear charge, leading to tighter binding of the remaining electrons and somewhat larger transition energies. In general the spectral evidence here appears to be quite consistent with an electron temperature, or equivalent blackbody temperature, approaching 200 eV in the strong emission region of the plasma.

In many applications fine details of the emission spectra are not essential, except for diagnostic purposes. Rather, what is essential is an accurate understanding of energy transport. Toward this end it is often useful to measure the radiated energy in rather broad energy *bins* (intervals). Slivinsky, Kornblum, Tirsell, and their colleagues[59] have done this for the laser fusion program at Lawrence Livermore National Laboratory using a series of glancing incidence mirrors, K- and L-edge transmission filters, and absolutely calibrated x-ray diodes, in instruments they refer to as "Dante." These instruments have been used extensively, and provide the basic data for many studies of the conversion efficiency of laser light to soft x-rays. An interpretive summary of experiments at 1.06 μm, 0.53 μm, 0.35 μm, and 0.26 μm wavelengths is given by Mead et al.[36]

[§]More completely, $1s^2\,2s\,2p^5\,3s$ to $1s^2\,2s\,2p^6$, etc.

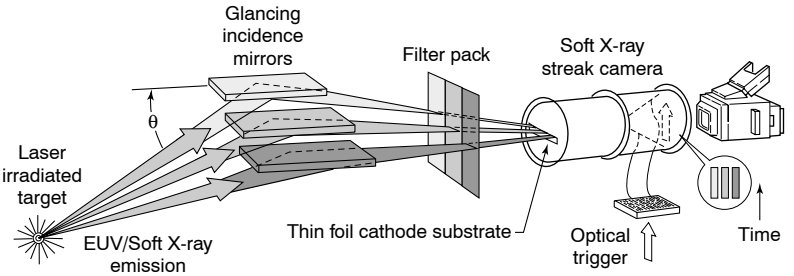

FIGURE 6.24. A schematic drawing of a time resolved three channel soft x-ray spectrometer, employing a 15-ps resolution soft x-ray streak camera and three side-by-side "notch filters" nominally centered at 200 eV, 400eV, and 600 eV, each consisting of a glancing incidence soft x-ray mirror and a matching K- or L-edge absorption filter. (Courtesy of G. Stradling, LANL, and R. Kauffman LLNL.)

Time resolved studies of thermal emission from laser-produced targets have been conducted using a 15-psec resolution streak camera[60] and a series of glancing incidence mirrors with matching transmission filters,[61, 62] as illustrated in Figure 6.24. The combination of low pass glancing incidence mirrors and high pass transmission filters was described in Chapter 3, Figure 3.11, as a notch filter with relative spectral pass band $E/\Delta E \simeq 3$ to 5. The streak camera has a slit photocathode sensitive to soft x-rays and x-rays. The emerging photoelectrons inside the tube are refocused as a slit image on a rear face phosphor plate. By optically triggering a properly timed ramp voltage the passing (time dependent) slit-shaped electron beam is swept vertically across the output phosphor screen, producing a time resolved *streak* of the slit, which is optically recorded. By placing information along the slit, such as three side-by-side notch filtered soft x-ray signals, one can obtain a time history of emission in the three selected photon energy bands. G. Stradling, R. Kauffman, H. Medecki, and colleagues[61, 62] conducted such studies with nominal 200 eV, 400 eV, and 600 eV channels of, respectively, a 5° carbon mirror with a carbon K-edge filter, a 5° nickel mirror with a vanadium L-edge filter, and a 3° nickel mirror with an iron L-edge filter. Figure 6.25 shows the soft x-ray channels for a laser irradiated gold disk target.

Spectral integration of the three channels, also shown in Figure 6.25, has a temporal peak of radiated soft x-ray power equal to 1.5×10^{10} W, assuming isotropic radiation into 4π sr. With an emission area equal to the laser focal spot area, this gives a temporally peaked soft x-ray emission intensity of 3×10^{14} W/cm^2. The equivalent blackbody temperature required to radiate at this intensity, according to Eq. (6.143), is 230 eV, with a spectral peak at 660 eV. Similar temperatures are quoted in the article by Sigel.[63] Note that the time history is similar to that of the irradiating laser pulse, 680 ps FWHM, except for a somewhat faster rise, presumably due to heating of the initially cold target and a long temporal decay as the target cools and energy flows to the low photon energy (200 eV) channel. Thus the soft x-ray emission has a somewhat longer pulse duration of 790 ps FWHM. Note that a recording instrument with a slower response would indicate a lower peak power (same radiated energy, longer time) and thus a reduced equivalent radiation temperature. In Figure 6.25 the equivalent temperature drops to about 160 eV at times ± 0.5 nsec to either side of the temporal peak. Further time resolved experiments, involving energy transport in layered targets, have been reported in the thesis by Stradling[61] in which the mirror–filter channels are replaced with narrow band multilayer mirrors coated to match selected emission lines from various layers of the target as thermal energy arrives (see Chapter 4, Section 4.5.4).

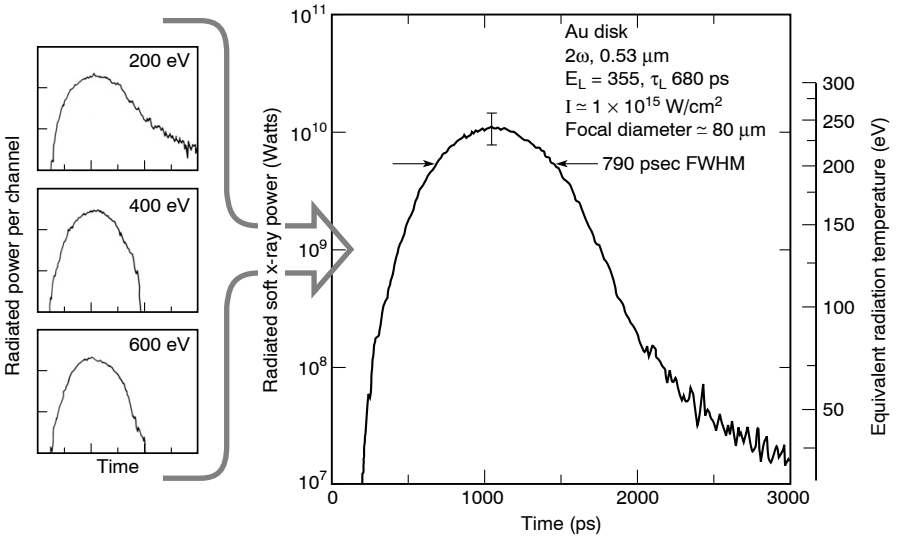

FIGURE 6.25. Time histories of soft x-ray emission in the 200, 400, and 600 eV channels for a laser irradiated gold disk target at an incident intensity of about 10^{15} W/cm^2, in a 680-ps pulse of frequency-doubled (2ω) Nd laser light at 0.53 μm wavelength. Spectral integration of the three channels shows a total soft x-ray power that peaks at about 1.5×10^{10} W, assuming isotropic radiation into 4π sr. The equivalent radiation temperature has a temperature peak at about 230 eV. (Following R. Kauffman, unpublished, Lawrence Livermore National Laboratory.)

According to the blackbody scaling, it should be possible to obtain significant EUV radiation at relatively low laser intensity on target. For instance, according to Eqs. (6.137) and (6.143), it should be possible to obtain peak photon emission at 100 eV with an equivalent blackbody temperature of only 35 eV, which radiates at only 1.5×10^{11} W/cm^2. At these low intensities laser light absorption is very efficient, perhaps 80%, with high ($\simeq 60\%$) fractional conversion to near-thermal radiation. The model then suggests that a laser intensity of order 3×10^{11} W/cm^2 on a medium or high Z target is sufficient. There is no need to employ a laser wavelength of less than 1 μm at these low intensities, as non-linear processes leading to the generation of suprathermal electrons would be unimportant. Several authors have pursued the generation of EUV radiation with low intensity laser produced plasmas. Spitzer et al.[64] have studied tin (Sn) and gold (Au) laser produced plasmas at incident intensities from 10^9 W/cm^2 to 10^{13} W/cm^2, at 1.06 μm and 0.53 μm wavelength, with a 7.5 ns duration commercial laser.

Effort toward developing a suitable laser plasma source for EUV lithography has been reported by Kubiak and colleagues,[65] who have developed a gas jet target with laser irradiation so as to eliminate the particulate debris that emerges from solid targets. For this particular study emission just below the L-edge of silicon (99.2 eV; see Chapter 1, Table 1.2) is of particular interest because of the desire to use Mo/Si multilayer interference coatings for EUV lithography (see Chapter 4, Section 4.5.3). For their work they employ a supersonic Xe gas jet irradiated at about 10^{12} W/cm^2, with a commercial 1.06 μm Nd laser of nominal 5 ns duration, at a repetition rate of 100 Hz. The focal region is typically 100 μm in diameter in a larger gas jet plume. With this laser intensity it is possible to reach an electron temperature near 50 eV, sufficient to generate strong emission in the 100–150 eV spectral region. The authors find that the use of cluster seeding techniques enhances EUV yield by permitting the achievement of

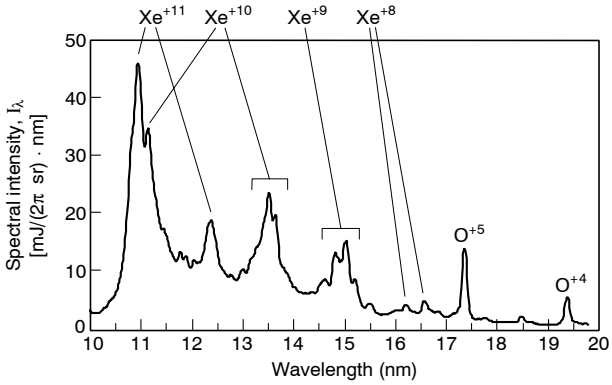

FIGURE 6.26. Emission spectra of a xenon plasma, produced in a 0.2 torr capillary discharge at 6 kA peak current. (Courtesy of M. Klosner and W. Silfvast, U. Central Florida.)

greater than critical density in the laser–gas-jet interaction region. The conversion efficiency with the seeded Xe jet is comparable to that of solid targets. Approximately 1% of the incident light is converted to EUV radiation in a 2.5% relative spectral bandwidth at 13.4 nm, and into 2π sr. The emission within this band is dominated by spectrally unresolved $4d^9 4f$ and $4d^{10}$ transitions of Xe^{+8} to Xe^{+10}, which give a local enhancement to the spectrum.[66]

Of course the plasma exists only during irradiation, so that high repetition rates are the key to achieving high time-averaged photon flux or high time-averaged EUV power. Several authors have also pursued the generation of intense EUV radiation for these same purposes, but using discharge plasmas. Klosner and Silfvast have reported the generation of intense EUV radiation in the 10–16 nm wavelength region using a xenon discharge in a capillary tube.[67] An example of their data, obtained at a Xe pressure of 0.2 torr, is shown in Figure 6.26. Prominent emission lines‖ of Xe^{+10} at 13.5 nm wavelength, and Xe^{+11} at 11.0 nm, suitable for use with Mo/Si and Mo/Be multilayer mirrors, are seen. McGeoch has conducted similar studies using a xenon Z-pinch discharge plasma,[68] showing the advantages of employing Xe–He gas mixtures to modify the emission spectrum to some degree.

6.7.4 Multi-kilovolt Line Emission

Emission lines at higher photon energies, in the multi-kilovolt region, are generated predominantly in the sub-critical plasma where electron temperatures are high and densities are low. Here the line emissions are quite prominent, especially when dealing with K-shell spectra, as there are few ionization states (He-like and H-like), the background continuum is relatively low, and, because of the low density and high temperature, opacity effects are minimal.[69, 70] This low density high temperature region is sometimes called the *plasma corona.*

Figure 6.27 shows the well resolved 2–3 keV silicon K lines obtained from a 0.35 μm, 2 ns, 3×10^{14} W/cm^2 irradiation of a glass (SiO_2) disk, obtained by Kauffman[49] using a

‖Xenon has the electron configuration $[Kr]4d^{10}5s^25p^6$. Removal of the last 5p and the two 5s electrons requires ionization energies of 82 eV, 100 eV, and 120 eV, respectively. On reaching the Kr-like closed shell, the ionization energy then jumps to 210 eV for removal of a 4d electron. This is the ionization bottleneck discussed in Section 6.7.2. These ionization energies are from Allen, *Astrophysical Quantities*, pp. 37–39 (Ref. 27).

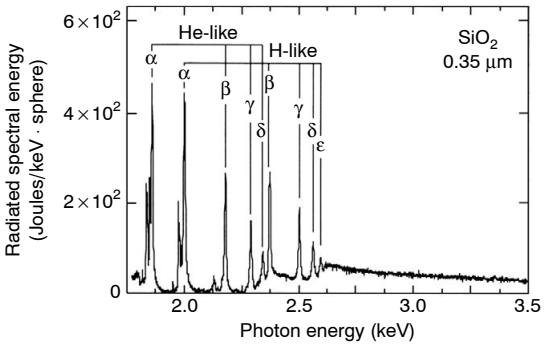

FIGURE 6.27. High resolution spectrum of He-like and H-like silicon emission lines from a glass (SiO_2) disk irradiated by a 0.35 W/cm^2 wavelength, 2-nsec laser pulse at 3×10^{14} W/cm^2. (Courtesy of R. Kauffman, Lawrence Livermore National Laboratory.)

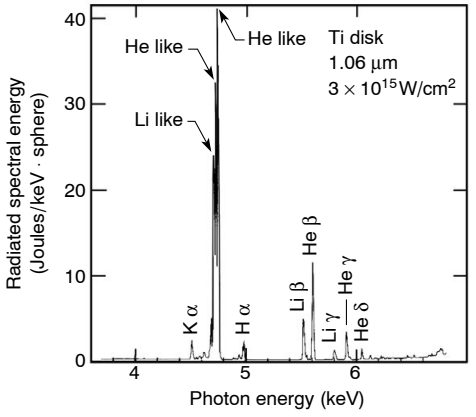

FIGURE 6.28. X-ray emission lines from a laser heated titanium disk, showing prominent He-like 1s2p to 1s^2 lines, less intense Li-like lines, and a barely observable H-like line. Irradiation is at 1.06 μm wavelength at an intensity of 3×10^{15} W/cm^2, in a 600 ps pulse. With 3 kJ of incident laser light, nearly 2 J is radiated in the lines at 4.75 keV. (Courtesy of D. Matthews, Lawrence Livermore National Laboratory.)

crystal for dispersion and x-ray recording film. The data shows several prominent lines of H-like and He-like silicon merging into the continuum at longer wavelengths. Following early spectroscopic notation, α corresponds to an $n = 2$ to $n = 1$ transition, β to $n = 3$ to $n = 1$, γ to $n = 4$ to $n = 1$, etc., for each ionization state present.

Data from Matthews and his colleagues[71] having higher photon energy lines from He-like and Li-like titanium are shown in Figure 6.28. The 2p1s to 1s^2 He-like lines at 4.7 keV clearly dominate the spectra, while Li-like lines are present but far less intense, and the H-like 2p to 1s (H-like K_α) is barely visible. From Table 6.2 (from Ref. 55) we see that the ionization energy of Li-like titanium is 1.4 keV, while that of He-like titanium jumps to 6.2 keV. This is a clear example of an ionization bottleneck. The hot plasma has stripped off the outer electrons until there are only two electrons remaining (He-like). The fact that the Li-like lines are so weak indicates that there are few ions present with three electrons; thus the electron temperature is certainly of order 1 keV or more. The fact that the hydrogen-like lines are relatively weak as well suggests that the 6.2 keV binding energy of the helium-like electrons is too high for the electron energies present in this plasma, and therefore that the electron temperature is well below 6 keV, thereby setting a bound on the electron temperature. In this particular experiment[71, 72] a titanium disk was irradiated at 3×10^{15} W/cm^2, with 3 kJ of 1.06 μm light in a 600 ps pulse delivered to a 450 μm diameter spot. Dispersion is achieved with a PET

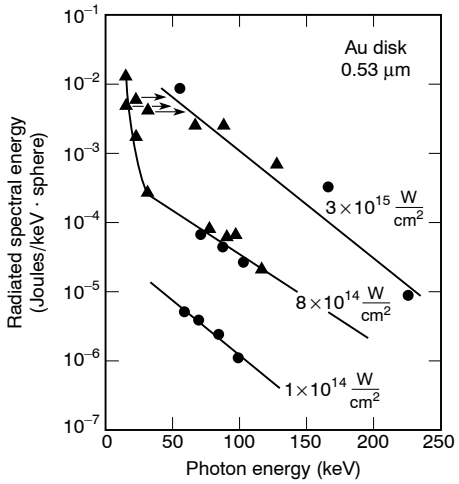

FIGURE 6.29. Hard x-ray emission, in the form of a suprathermal tail, from gold disk targets irradiated with 0.53 μm (2ω) of nominal 3.5 kJ energy in a 1 nsec pulse. The hard x-ray signal is seen to rise dramatically with intensity above 10^{14} W/cm^2. Hot electron temperatures of 20–35 keV are inferred at the higher intensities. Circular data points were obtained with a K-edge filter; triangular data points with a filter–fluorescer combination. The solid line is a fit to the data. (Courtesy of P. Drake and Lawrence Livermore National Laboratory.)

crystal, with data recorded on Kodak no-screen film. In this experiment approximately 2 J is radiated in the $1s2p \rightarrow 1s^2$ helium-like lines (He_α) at 4.75 keV, for a conversion efficiency (into 4π sr) of approximately 0.05% into this one prominent spectral feature. The conversion efficiency for these lines varies considerably with the illumination intensity, which, of course, is closely related to the corona electron temperature.

These studies have been extended to shorter wavelengths (0.53 μm and 0.35 μm) and shorter pulse duration (60–120 ps), and a wider range of target materials, by Yaakobi et al.[73] and by Phillion and Hailey,[74] seeking to further refine the parameters for optimization of a short wavelength probe pulse, or *flash backlighter*, for high density laser fusion implosion studies.[72] In addition, because of their short wavelength, these emissions can be used to infer valuable plasma temperature and density information through the appearance of lines, line widths, line intensity ratios, and merger into the continuum.[69, 73–77]

6.7.5 Suprathermal X-Rays

In laser irradiation experiments at high intensity it is common to observe a suprathermal tail of x-ray emission extending beyond 100 keV, and in some cases to several hundred keV. These high energy tails can be very strong at a laser wavelength of 1.06 μm, and even more so at 10.6 μm (CO_2 laser). Figure 6.29 shows typical data[33, 35] obtained with 0.53 μm light on a gold disk target at intensities from 10^{14} W/cm^2 to 3×10^{15} W/cm^2. The data is collected with a series of K-absorption edge filters with calibrated diode detection, and with a set of filter–fluorescers with photomultiplier recording.[78] The emission at very high photon energy is sensitive to wavelength, and is generally described in terms of the parameter $I\lambda^2$ as suggested in Section 6.4.11. Temperatures of the suprathermal tail can be in the range of 10–40 keV at high values of $I\lambda^2$. Figure 6.30 shows an example of data, described by Campbell et al.,[79] for gold disks irradiated at a nominal intensity of 10^{14} W/cm^2 to 3×10^{15} W/cm^2, for wavelengths of 1.06 μm, 0.53 μm, and 0.35 μm, with nominal focal spot diameters of 150 μm. The measured photon flux in the 45–50 keV channel is nearly 100 times less for the 0.35 μm irradiation than for the 1.06 μm experiment at this intensity. Correlation with optical data indicates that the suprathermal tail is associated with stimulated Raman scattering,[35] as was described in Section 6.4.10.

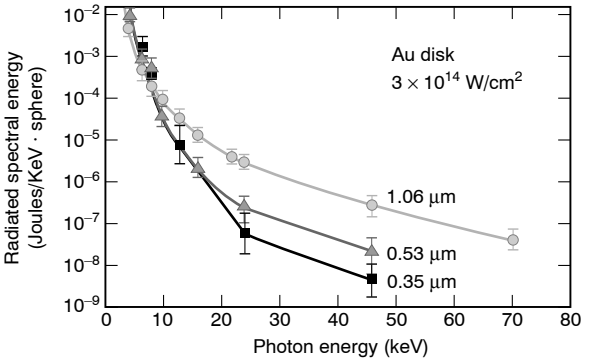

FIGURE 6.30. Suprathermal x-ray emission from gold disk targets at 3×10^{14} W/cm^2, for wavelengths of 1.06 μm, 0.53 μm, and 0.35 μm. Incident energies ranged from 20 J to 30 J. Nominal pulse duration and focal spot diameters were 700 psec and 150 μm, respectively. The units assume isotropic radiation into a sphere. (Courtesy of M. Campbell, B. Pruett, R. Turner, F. Ze, and W. Mead, Lawrence Livermore National Laboratory.)

6.7.6 Laser Wavelength Trends

To conclude this section we summarize the general trends of laser light absorption and conversion to thermal and suprathermal x-rays as functions of laser wavelength and intensity on targets. The trends are illustrated for nominal nanosecond duration pulses, where the expansion time is sufficient to permit significant collisional absorption, particularly at the low range of intensities. The trends are shown for a planar gold disk target. As discussed in the previous sections, plasma properties and processes can vary widely with the electron density and its gradient, the electron temperature and its spatial variation, and the ion charge state (and thus target material) – all of which are affected by the irradiation wavelength (through n_c), intensity, and pulse duration (through the scale length l_{exp}). Thus these trends must be taken as illustrative only, but are nonetheless valuable for guiding the choice of operating parameters for specific applications. The curves are generally derived from specific references with extensive diagnostic capabilities and from sufficient data to cover large intensity and wavelength variations; the trends represented by them reflect a broad consensus developed within the international community based on measurements at many facilities.

Figure 6.31 shows general trends of laser light absorption as a function of intensity on a gold disk target, for nominally 1 nsec duration pulses of Nd laser light at 1.06 μm and its harmonics ($n = 2,\ 3$) at 0.53 μm and 0.35 μm. Collisional absorption clearly favors shorter wavelength radiation where n_c, proportional to $1/\lambda^2$, is significantly higher, and thus collisional absorption, proportional to n^2Z, is far more effective. At high intensities radiation pressure can depress sub-critical electron densities, thus reducing absorption, while non-linear mechanisms increase energy losses due to scattering and deposit absorbed energy in non-thermal particle and photon distributions.

Conversion of laser light to near-thermal x-rays is addressed in Figure 6.32, as a function of laser intensity and wavelength. Conversion efficiency is defined as radiated energy within the broad window extending from 0.1 keV to 1.5 keV divided by the incident laser energy. The data assume a Lambertian ($\cos\theta$) angular distribution of thermal x-rays from the flat disk target. Again the example is for a gold disk irradiated with a nominally 1 nsec duration pulse. The curves are of course affected by the finite absorption values from Figure 6.31. For low intensity illumination, especially at short wavelength, the conversion efficiency to

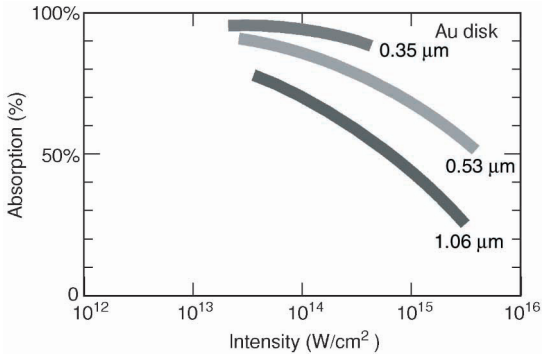

FIGURE 6.31. Curves showing the general trend of laser light absorption as a function of incident light intensity and wavelength, for nanosecond duration light pulses. In this example the target is a gold disk. For lower Z material the absorption is generally less [see Eqs. (6.120–6.122)]. These curves are derived from the data of Campbell, Turner, Ze, Max, and colleagues,[33, 79–81] Lawrence Livermore National Laboratory.

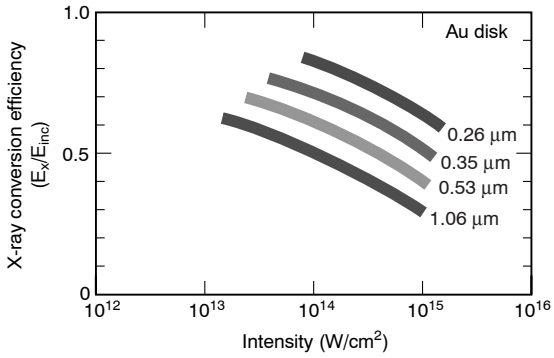

FIGURE 6.32 (see Colorplate VII). Curves showing the trend of x-ray conversion energy within the broad 0.1 keV to 1.5 keV spectral window, divided by the incident laser energy, assuming a Lambertian ($\cos\theta$) angular distribution in the emission hemisphere. Efficiency is shown as a function of intensity for Nd laser light at 1.06 μm (red) and its harmonics at 0.53 μm (green), 0.35 μm (blue), and 0.26 μm (ultraviolet) for nanosecond duration pulses. The target is a gold disk. The curves are derived largely from the data of Kauffman, Kornblum, Tirsell, Lee, Turner, and colleagues,[36, 49, 82–84] Lawrence Livermore National Laboratory.

thermal radiation is high. For the shorter wavelengths the absorption is at high densities where collisional thermalization is very efficient. At longer wavelengths and higher intensities non-thermal processes result in decreased absorption (increased stimulated scattering processes) and in increased radiation at multi-keV photon energies. Except for the lowest intensities shown, there is a great advantage to the use of harmonic conversion to short wavelength.

At high irradiation intensity, non-linear processes tend to dominate laser–plasma interaction physics as stimulated scattering processes drive high amplitude, high phase velocity plasma waves, trapping and accelerating some electrons to very high energy. One signature of these processes is the appearance of high energy suprathermal x-rays, such as illustrated in Figure 6.33, where the growth of 40–50 keV x-rays is shown as a function of intensity and wavelength, again for a gold disk target and a nominally nanosecond irradiation pulse. Again

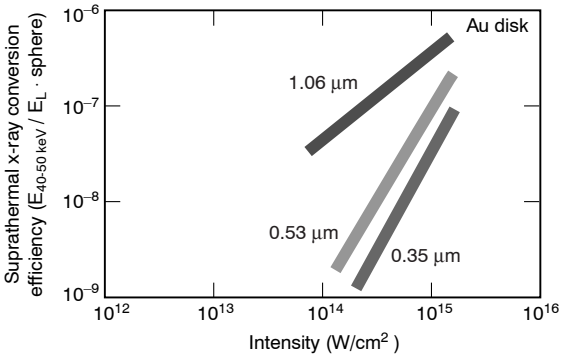

FIGURE 6.33 (see Colorplate VIII). Curves showing the general trend of suprathermal x-ray generation vs. laser intensity and wavelength. The specific data here shows radiated energy in a 40–50 keV spectral window, as a function of incident laser intensity for three wavelengths: 1.06 μm (red), 0.53 μm (green), and 0.35 μm (blue). The curves are derived from the data of Campbell, Pruett, Turner, Ze, and Mead,[78, 79] Lawrence Livermore National Laboratory.

the message is clear: suppression of non-thermal processes is best accomplished through use of modest irradiation intensity and short wavelength.

As indicated in the literature, there are many ways to affect the specific numerical values given in the illustrations presented in this section (target material, geometry, laser bandwidth, focal spot uniformity, etc.), but the general trends as functions of wavelength and intensity are essentially universal. At high laser intensities use of the shorter wavelengths is mandated and widely used.[37] This is permissible in large part because of the very high efficiencies with which Nd laser light at 1.06 μm wavelength can be converted to its harmonics – for example, 80% conversion to 3ω for both small and large scale lasers.[37]

6.8 HIGH HARMONIC GENERATION WITH FEMTOSECOND LASER PULSES

A very active area of current research is generating very high harmonics of intense femtosecond duration laser pulses in noble gases. The harmonics result from a strongly non-linear interaction between the electric field of the incident laser pulse and the individual atoms. The laser intensities and pulse durations are just at the limits of ionizing the neutral atoms. The incident field simultaneously drives the non-linear generation of harmonics in a large number of atoms, all phase coherent with the incident laser field. Thus, the resultant harmonics add in phase in the direction of the driving pulse, leading to the appearance of intense high harmonics in a relatively narrow forward radiation cone. In a typical experiment 800 nm wavelength linearly polarized laser pulses of 20–100 fs duration, corresponding to 8–40 oscillation periods, are focused to an intensity of 10^{14} W/cm^2 to 10^{15} W/cm^2 in a gas of neutral He, Ne, Ar, or Xe. In such experiments several groups[86–90] report the observation of a long spectral sequence (a *comb*) of very strong, well-defined odd harmonics, to order 100 or greater. With incident photons of 1.55 eV, the $n = 101$ harmonic (odd only) corresponds to nearly 160 eV photon energy, well into the EUV. In some experiments these harmonics merge into a quasi-continuum that extends into the soft x-ray region beyond the carbon K-absorption edge at 284 eV. These harmonics typically appear in a narrow forward radiation cone of half angle less than 1 mrad.

The major features of these experiments are explained by a strong field laser–atom interaction model[91–93] in which the linearly polarized electric field suppresses the binding potential of the atom, permitting an electron to tunnel free. The electron is then accelerated to high kinetic energy in the first half cycle of the laser field and reversed in the second half cycle, returning to the vicinity of the atom at high kinetic energy. Through recombination, or scattering, the electron undergoes a very strong short duration (much less than one optical cycle) acceleration, leading to the emission of radiation at very high photon energies. These photon energies extend to values as high as the electron kinetic energy plus the atomic binding energy, described in current theories[91, 92] as

$$(\hbar\omega)_{\max} \simeq I_p + 3.2U_p \tag{6.144}$$

Here I_p is the atomic ionization potential, and U_p is the cycle-averaged kinetic energy of the electron in an electric field E_0 and frequency ω_0, i.e., where

$$U_p = \frac{e^2E_0^2}{4m\omega_0^2} \tag{6.145a}$$

or

$$U_p = 2\pi c r_e I_{\mathrm{L}}/\omega_0^2 \tag{6.145b}$$

Here U_p is sometimes called the ponderomotive potential, I_{L} is the laser field intensity, and r_e is the classical electron radius as given in Chapter 3, Eq. (3.44). For an intensity of 10^{15} W/cm^2, a laser frequency $\omega_0 = 2.4 \times 10^{15}$ rad/s, and $r_e = 2.8 \times 10^{-13}$ cm, we have $U_p \simeq 60$ eV. Thus by Eq. (6.144) one could expect the highest harmonic to have a photon energy of 192 eV + I_p, about 220 eV in helium, which has an ionization potential of 24.5 eV. The radiation occurs in odd harmonics due to the cyclic nature of the process, which is driven by the incident laser field. Constructive interference of the various harmonics can be affected by propagation through the gas, particularly as partial ionization begins to cause variations in the frequency dependent refractive index near the peak of the pulse. This would clearly affect the highest harmonics, which are generated by the strongest electric fields. As a consequence the highest harmonics can be expected to appear in the shortest pulse, highest intensity experiments, where detrimental ionization effects have less opportunity to degrade the high field harmonic generation or the subsequent propagation and collective interference. Needless to say, it is essential in these experiments that there be no laser pre-pulse, which would cause early ionization and preclude the intense laser–atom interaction described by this model.

Examples of data from recent high harmonic experiments are shown in Figure 6.34. Figure 6.34(a) shows data from experiments reported by L'Huillier and Balcou[86] of Saclay, in which radiation up to the 135th harmonic of Nd was obtained with a 1 ps duration 1.053 μm laser pulse at an intensity of 1.5×10^{15} W/cm^2 in neon (21.5 eV ionization potential). These data show the long sequence of odd harmonics, extending to a wavelength of less than 8 nm (155 eV). The harmonics typically correspond to about 10^5 detected photons.

Figure 6.34(b) shows harmonic spectra reported by Chang et al.[88] in the group of Murnane and Kapteyn at the University of Michigan. In this example radiation from a Ti : sapphire laser, at a wavelength of 800 nm and a pulse duration of only 26 fs, is used to irradiate neon atoms at an intensity of approximately 6×10^{15} W/cm^2. Harmonics to $n = 155$ are observed, corresponding to a wavelength of 5.2 nm, or a photon energy of 240 eV. This demonstrates the advantage of shorter pulse duration and higher laser intensity. The use of helium in these same studies permitted extension to higher harmonics, as predicted by Eq. (6.144). In a later

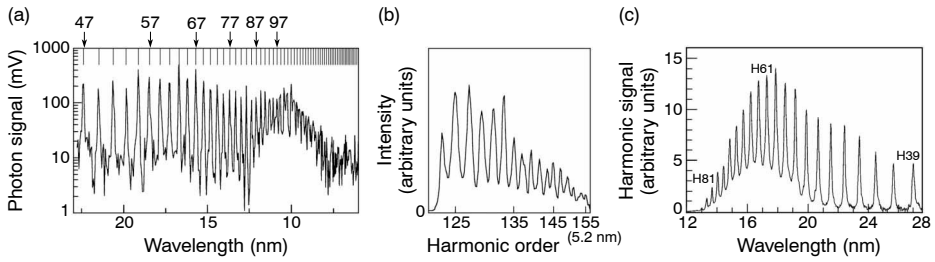

FIGURE 6.34. High harmonics of femtosecond near-infrared laser pulses are shown for three separate experiments. In each of the three a comb of harmonics is generated that extends through the EUV and into the soft x-ray spectral region. The harmonics are generated by the strongly non-linear interaction between individual atoms and the intense laser field. Through the use of very short duration fields the experiments are performed just on the threshold of ionization. The interactions are all phase coherent with the incident wave, and thus interfere coherently in a narrow forward cone. The time symmetry of the process leads to odd only harmonics. (a) Data from L'Huillier and Balcou[86] showing the harmonic spectrum obtained in neutral neon gas at 40 torr with a 1 ps duration 1.053 μm Nd laser pulse at an intensity of 1.5×10^{15} W/cm^2. The harmonics extend to order $n = 135$. (b) Data from Chang and colleagues[88] showing well-resolved harmonics to order $n = 155$, obtained in neutral neon gas at 8 torr with a 26 fs duration, 800 nm wavelength pulse from a Ti : sapphire laser, at an incident intensity of approximately 6×10^{15} W/cm^2. Harmonics to order $n = 211$, corresponding to a wavelength of 3.79 nm and a photon energy of 327 eV, were observed in helium under similar irradiation conditions. (c) Data from Schulze and colleagues[90] showing harmonic data obtained in neutral neon, with a 700 fs duration, 1053 nm wavelength laser pulse at approximately 5×10^{14} W/cm^2, showing clearly resolved high harmonics that extend about 13 nm. Their data show that the high harmonics are of the same polarization as the high intensity laser pump pulse.

publication this same group increased the output power in high harmonics through the use of phase matching techniques in which the phase velocity and divergence of the driving laser pulse were controlled using waveguide propagation in gas filled capillary tubes.[94]

Finally, Figure 6.34(c) shows data reported by Schulze and colleagues[90] at the Max Born Institute in Berlin and the Universität Bielefeld. In these experiments a 700 fs duration, 1053 nm wavelength, Nd : glass amplified Ti : sapphire laser pulse is focused to an intensity of 5×10^{14} W/cm^2 in neon gas jet at a focal diameter of about 65 μm. Figure 6.34(c) shows well-defined harmonics that extend to about 13 nm. In this study the polarization of high harmonics is shown to be the same as that of the high intensity laser pump.

The use of high intensity femtosecond laser pulses of only a few cycles duration, essentially "optical transients,"[89] to drive highly non-linear processes in neutral atoms has opened new opportunities for the generation and application[95] of short wavelength coherent radiation.[96] Present techniques result in the generation of a broad comb of odd harmonics throughout the EUV and into the soft x-ray region of the spectrum. This work is complemented by recent developments in short wavelength lasers, discussed in the following chapter, which tend to generate radiation in a single spectral line.

REFERENCES

1. W.L. Kruer, *The Physics of Laser Plasma Interactions* (Addison-Wesley, Redwood City, CA, 1988).
2. A. Rubenchik and S. Witkowski, Editors, *Physics of Laser-Plasma*, Handbook of Plasma Physics, Vol. 3 (North-Holland, Amsterdam, 1991).

3. N. Marcuvitz, "Notes on Plasma Dynamics," New York University, unpublished (1970).
4. D. Nicholson, *Introduction to Plasma Theory* (Wiley, New York, 1983).
5. Yu.L. Klimontovich, *The Statistical Theory of Non-equilibrium Processes in a Plasma* (MIT Press, Cambridge, MA, 1967).
6. P.C. Clemmow and J.P. Dougherty, *Electrodynamics of Particles and Plasmas* (Addison-Wesley, Reading, MA, 1979).
7. H. Motz, *The Physics of Laser Fusion* (Academic Press, New York, 1979).
8. G. Bekefi, *Radiation Processes in Plasmas* (Wiley, New York, 1966).
9. H. Griem, *Principles of Plasma Spectroscopy* (Cambridge Univ. Press, Cambridge, UK, 1997).
10. C.K. Birdsall and A.B. Langdon, *Plasma Physics via Computer Simulation* (McGraw-Hill, New York, 1985).
11. T. Stix, *The Theory of Plasma Waves* (McGraw-Hill, New York, 1962).
12. S. Ichimaru, *Statistical Plasma Physics* (Addison-Wesley, Reading, MA, 1992).
13. N.G. Basov, Yu. A. Zakharenkov, N.N. Zorev, A.A. Rupasov, G.V. Sklizkov, and A.S. Shikanov, *Heating and Compression of Thermonuclear Targets by Laser Beam* (Cambridge Univ. Press, Cambridge, UK, 1986).
14. T. Dolan, *Fusion Research* (Pergamon, New York, 1982).
15. P.A. Charles and F. Seward, *Exploring the X-Ray Universe* (Cambridge Univ. Press, Cambridge, UK, 1995).
16. S. Chapman and T.G. Cowling, *The Mathematical Theory of Non-uniform Gases* (Cambridge Univ. Press, Cambridge, UK, 1964).
17. R.B. Bird, *Transport Phenomena* (Wiley, New York, 1960).
18. L.D. Landau, "On the Vibrations of the Electron Plasma," *J. Physics (USSR) 10*, 25 (1946).
19. E.C. Jordon, *Electromagnetic Waves and Radiating Systems* (Prentice-Hall, Englewood Cliffs, NJ, 1950).
20. J.A. Stratton, *Electromagnetic Theory* (McGraw-Hill, New York, 1941).
21. J.D. Jackson, *Classical Electrodynamics* (Wiley, New York, 1975), Second Edition, p. 301.
22. I.P. Shkarofsky, T.W. Johnston, and M.P Bachynski, *Particle Kinetics of Plasmas* (Addison-Wesley, Reading, MA, 1966).
23. J. Dawson and C. Oberman, "High-Frequency Conductivity and the Emission and Absorption Coefficients of a Fully Ionized Plasma," *Phys. Fluids 5*, 517 (1962); J.M. Dawson, "On the Production of Plasma by Giant Pulse Lasers," *Phys. Fluids 7*, 981 (1964).
24. T.W. Johnston and J.M Dawson, "Correct Values for High Frequency Power Absorption by Inverse Bremsstrahlung in Plasmas," *Phys. Fluids 16*, 722 (1973).
25. V.L. Ginzburg, *Propagation of Electromagnetic Waves in Plasmas* (Pergamon Press, New York, 1970); P. Mulser, "Resonance Absorption and Ponderomotive Action," in Ref. 2.
26. D.W. Forslund, J.M. Kindel, K. Lee, E.L. Lindman, and R.L. Morse, "Theory and Simulation of Resonant Absorption in a Hot Plasma," *Phys. Fluids 11*, 679 (1975).
27. C.W. Allen, *Astrophysical Quantities* (Athlone Press, London, 1997), Third Edition.
28. E.N. Parker, *Spontaneous Current Sheets in Magnetic Fields with Applications to Stellar X-Rays* (Oxford Univ. Press, Oxford, 1994).
29. A.L. Peratt, *Physics of the Plasma Universe* (Springer-Verlag, Berlin, 1992).
30. R.L. Bowers and T. Deeming, *Astrophysics* (Jones and Bartlett, Portola Valley, CA, 1984).
31. N. Marcuvitz, "Notes on Plasma Turbulence," New York University, unpublished (1969).
32. C.S. Liu, M.N. Rosenbluth, and R.B. White, "Raman and Brillouin Scattering of Electromagnetic Waves in Inhomogeneous Plasmas," *Phys. Fluids 17*, 1211 (1974).
33. H.A. Baldis, E.M. Campbell, and W.L. Kruer, "Laser-Plasma Interactions," Chapter 9 in *Physics of Laser-Plasma* (North Holland, Amsterdam, 1991), A. Rubenchik and S. Witkowski, Editors.
34. R.E. Turner, K. Estabrook, R.P. Williams, H.N. Kornblum, W.L. Kruer, and E.M. Campbell, "Observation of Forward Raman Scattering in Laser-Produced Plasmas," *Phys. Rev. Lett. 67*, 1725 (1986).
35. R.P. Drake, R.E. Turner, B.F. Lasinski, K.G. Estabrook, E.M. Campbell, C.L. Wang, D.W. Phillion, E.A. Williams, and W.L, Kruer, "Efficient Raman Sidescatter and Hot-Electron Production in Laser-Plasma Interaction Experiments," *Phys. Rev. Lett. 53*, 1739 (1984); R.P. Drake, R.E. Turner, B.F.

Lasinski, E.A. Williams, K. Estabrook, W.L. Kruer, and E.M. Campbell, "X-Ray Emission Caused by Raman Scattering in Long-Scale-Length Plasmas," *Phys. Rev. A 40*, 3219 (1989).
36. W.F. Mead, E.K. Stover, R.L. Kauffman, H.N. Kornblum, and B.F. Lasinski, "Modeling, Measurements, and Analysis of X-Ray Emission from 0.26 μm Laser-Irradiated Gold Disks," *Phys. Rev. A 38*, 5275 (1988); R.E. Turner et al., "Evidence for Collisional Damping in High Energy Raman Scattering Experiments at 0.26 Microns," *Phys. Rev. Lett. 54*, 189 (1985).
37. R.S. Craxton, R.L. McCrory, and J.M. Soures, "Progress in Laser Fusion," *Sci. Amer. 255*, 68 (1986); B.M. Van Wonterghem, J.R. Murray, J.H. Cambell, D.R. Speck, C.E. Barker, I.C. Smith, D.F. Browning, and W.C. Behrendt, "Performance of a Prototype for a Large-Aperture Multipass Nd : Glass Laser for Inertial Confinement Fusion," *Appl. Opt. 36*, 4932 (1997).
38. R.P. Drake, "Three-Wave Parametric Instabilities in Long-Scale-Length, Somewhat Planar, Laser Produced Plasmas," *Laser Part. Beams 10*, 599 (1992); R.P. Drake, R.G. Watt, and K. Estabrook, "Onset and Saturation of the Spectral Intensity of Stimulated Scattering in Inhomogeneous Laser-Produced Plasmas," *Phys. Rev. Lett. 77*, 79 (1996).
39. D.W. Forslund, J.M. Kindel, and E.L. Lindman, "Plasma Simulation Studies of Stimulated Scattering Processes in Laser-Irradiated Plasmas," *Phys. Fluids 18*, 1017 (1975).
40. K. Estabrook, W.L. Kruer, and B. Lasinski, "Heating by Raman Backscatter and Forward Scatter," *Phys. Rev. Lett. 45*, 1399 (1980).
41. G.B. Zimmerman, LLNL Report UCRL-75881, 1974 (unpublished); also G.B. Zimmerman and W.L. Kruer, "Numerical Simulation of Laser-Initiated Fusion," *Comments Plasma Phys. Controlled Fusion 2*, 51 (1975).
42. G.H. Dahlbacka, W.C. Mead, C.E. Max, and J.J. Thomson, "Calculations of Self-Generated Magnetic Fields in Parylene Disk Experiments," Laser Program Annual Report 1975, UCRL 50021-75, A.J. Glass, Editor, Lawrence Livermore National Laboratory (4975), p. 271.
43. J. Stamper, "Laser-Generated Jets and Megagauss Magnetic Fields," *Science 281*, 1469 (1998).
44. X. Liu and D. Umstadter, "Competition between Ponderomotive and Thermal Pressures in Short-Scale-Length Laser Plasmas," *Phys. Rev. Lett. 69*, 1935 (1992).
45. D.T. Attwood, D. Sweeny, J. Auerbach, and P.H.Y. Lee, "Interferometric Confirmation of Radiation-Pressure Effects in Laser-Plasma Interactions," *Phys. Rev. Lett. 40*, 184 (1978); D.W. Sweeny, D.T. Attwood, and L.W. Coleman, "Interferometric Probing of Laser-Produced Plasmas," *Appl. Opt. 15*, 1126 (1976).
46. D.T. Attwood, "Diagnostics for the Laser Fusion Program – Plasma Physics on the Scale of Microns and Picoseconds," *IEEE J. Quant. Electr. QE-14*, 909 (1978).
47. L.B. Da Silva, T.W. Barbee, R. Cauble, P. Celliers, D. Ciarlo, S. Libby, R.A. London, D. Matthews, S. Mrowka, J.C. Moreno, D. Ross, J.E. Trebes, A.S. Wan, and F. Weber, "Electron Density Measurements of High Density Plasmas Using Soft X-Ray Laser Interferometry," *Phys. Rev. Lett. 74*, 3991 (1995); A.S. Wan, T.W. Barbee, R. Cauble, P. Celliers, L.B. Da Silva, J.C. Moreno, P.W. Rambo, G.F. Stone, J.E. Trebes, and F. Weber, "Electron Density Measurement of a Colliding Plasma Using Soft X-Ray Laser Interferometry," *Phys. Rev. E 55*, 6293 (1997).
48. C.H. Moreno, M.C. Marconi, V.N. Shlyaptsev, and J.J. Rocca, "Shadowgrams of a Dense Microcapillary Plasma Obtained with a Table-Top Soft X-Ray Laser," *IEEE Trans. Plasma Sci.* (February 1999); J.J. Rocca, C.H. Moreno, M.C. Marconi, and K. Kanizay, "Soft X-ray Laser Interferometry of a Plasma with a Table-Top Laser and Lloyd's Mirror," *Opt. Lett.* (15 March 1999).
49. R. Kauffman, "X-Ray Radiation from Laser Plasma," Chapter 3 in *Physics of Laser Plasma* (North Holland, Amsterdam, 1991), A. Rubenchik and S. Witkowski, Editors.
50. P.A. Tipler, *Modern Physics* (Worth, New York, 1978), p. 105.
51. Ya.B. Zel'dovich and Yu.P. Rasier, *Physics of Shock Waves and High Temperature Hydrodynamic Phenomena* (Academic Press, New York, 1966).
52. C. Kittel and H. Kroemer, *Thermal Physics* (Freeman, New York, 1980).
53. I.S. Gradshteyn and I.M. Ryzhik, *Tables of Integrals, Series, and Products* (Academic Press, New York, 1994), Fifth Edition, p. 370, No. 3.411-1, and p. xxxi.
54. R.L. Kelly, "Atomic and Ionic Spectrum Lines Below 2000 Å: Hydrogen Through Krypton," *J. Phys. Chem. Ref. Data 16*, Suppl. 1 (1987); also R.L. Kelly and L.J. Palumbo, "Atomic and Ionic

Emission Lines Below 2000 Angstroms: Hydrogen Through Krypton," Naval Research Laboratory Report 7599, NRL, Washington, DC (1973).
55. J.H. Scofield, "Energy Levels for Hydrogen-, Helium-, and Neon-Like Ions," in *X-Ray Booklet*, Lawrence Berkeley Laboratory PUB-490 rev. (April 1986), D, Vaughan, Editor: also LLNL Report UCID-16848 (1975). Extended to Co, Ni, and Cu-like ions by J. Scofield (1999, private communication) in part using data from C.E. Moore, NBS Pub. NSRDS-NBS 34 (1970), and J. Sugar and A. Musgrove, *J. Chem. Phys. Ref. Data 24*, 1803 (1995), and others referenced therein.
56. A. Zigler, M. Givon, E. Yarkoni, M. Kishinevsky, E. Goldberg, B. Arad, and M. Klapish, "Use of Unresolved Transition Arrays for Plasma Diagnostics," *Phys. Rev. A 35*, 280 (1987).
57. C.M. Dozier, D.B. Brown, L.S. Birks, P.B. Lyons, and R.F. Benjamin, *J. Appl. Phys. 47*, 3732 (1976).
58. B.L. Henke, F.G. Fujiwara, M.A. Tester, C.H. Dittmore, and M.A. Palmer, *J. Opt. Soc. Amer. B 1*, 828 (1984).
59. K.G. Tirsell, H.N. Kornblum, and V.W. Slivinsky, "Time Resolved, Sub-keV X-Ray Measurements Using Filtered X-Ray Diodes," Report UCRL-81478, Lawrence Livermore National Laboratory; also P.H.Y. Lee and K.G. Tirsell, "X-Ray Conversion Efficiency," Laser Fusion Annual Report 1980, Report UCRL-50021-80, Lawrence Livermore National Laboratory, p. 7-10; also R.A. Heinle and K.G. Tirsell, "Filtered-Mirror Sub-keV X-Ray Measurement System," Laser Program Annual Report 1979, Report UCRL-50021-79, L.W. Coleman, Editor, Lawrence Livermore National Laboratory, p. 5-5.
60. C.F. McConaghy and L.W. Coleman, "Picosecond X-Ray Streak Camera," *Appl. Phys. Lett. 25*, 268 (1974).
61. G.L. Stradling, D.T. Attwood, and R.L. Kauffman, "A Soft X-Ray Streak Camera," *IEEE J. Quant. Electr. QE-19*, 604 (1983); also G.L. Stradling, "Time Resolved Soft X-Ray Studies of Energy Transport in Layered and Planar Laser-Driven Targets," Ph.D. thesis, University of California, Davis (1982).
62. R.L. Kauffman, G.L. Stradling, D.T. Attwood, and H. Medecki, "Quantitive Intensity Measurement Using a Soft X-Ray Streak Camera," *IEEE J. Quant. Electr. QE-19*, 616 (1983).
63. R. Sigel, "Laser-Generated Intense Thermal Radiation," Chapter 4 in Ref. 2.
64. R.C. Spitzer, R.L. Kauffman, T. Orzechowski, D.W. Phillion, and C. Cerjan, "Soft X-Ray Production from Laser-Produced Plasmas for Lithography Applications," *J. Vac. Sci. Technol. B 11*, 2986 (1993).
65. G.D. Kubiak, L.J. Bernardez, K.D. Krenz, D.J. O'Connell, R. Gutowski, and A.M. Todd, "Debris-Free EUVL Sources Based on Gas Jets," p. 66 in *Extreme Ultraviolet Lithography* (Opt. Soc. Amer., Washington, DC, 1996), G.D. Kubiak and D. Kania, Editors; G.D. Kubiak, L.J. Bernardez, and K. Krenz, "High Power Extreme Ultraviolet Source Based on Gas Jets," *Proc SPIE 3331*, 81 (1998).
66. G. O'Sullivan, "Charge-Dependent Wavefront Collapse in Ionized Xenon," *J. Phys. B (London) 15*, L765 (1982).
67. M.A. Klosner and W.T. Silfvast, "Intense Xenon Capillary Discharge Extreme-Ultraviolet Source in the 10–16 nm Wavelength Region," *Opt. Lett. 23*, 1609 (1998); also see W.T. Silfvast, M. Klosner, G. Shimkaveg, H. Bender, G. Kubiak, and N. Fornaciari, "High Power Plasma Discharge Source at 13.5 nm and 11.4 nm for EUV Lithography," *Proc. SPIE 3676* (1999).
68. M. McGeoch, "Radio-Frequency Preionized Xenon Z-Pinch Source for Extreme Ultraviolet Lithography," *Appl. Opt. 37*, 1651 (1998); also see M. McGeoch, "High Power Extreme Ultraviolet Source Based on a *Z*-Pinch," *Proc. SPIE 3676* (1999).
69. H.R. Green, *Principles of Plasma Spectroscopy* (Cambridge Univ. Press, 1997).
70. D. Milhalas and B.W. Mihalas, *Foundations of Radiation Hydrodynamics* (Oxford Univ. Press, 1984); D. Mihalas, *Stellar Atmospheres* (Freeman, San Francisco, 1978), Second Edition.
71. D.L. Matthews. E.M. Campbell, N.H. Ceglio, G. Hermes, R. Kauffman, L. Koppel, R. Lee, K. Manes, V. Rupert, V.W. Slivinsky, R. Turner, and F. Ze, "Characterization of Laser-Produced Plasma X-Ray Sources for Use in X-Ray Radiography," *J. Appl. Phys. 54*, 4260 (1983).
72. D.T. Attwood, N.H. Ceglio, E.M. Campbell, J.T. Larsen, D.M. Matthews, and S.L. Lane, "Compression Measurement in Laser Driven Implosion Experiments," p. 423 in *Laser Interaction and Related Plasma Phenomena*, Vol. 5 (Plenum, New York, 1981), H. Schwarz, H. Hora, M. Lubin, and B. Yaakobi, Editors.

73. B. Yaakobi, P. Bourke, Y. Conturie, J. Delettrez, J.M. Forsyth, R.D. Frankel,, L.M. Goldman, R.L. McCrory, W. Seka, and J.M. Soures, "High X-Ray Conversion Efficiency with Target Irradiation by a Frequency-Tripled Nd : Glass Laser," *Opt. Commun. 38*, 196 (1981).
74. D.W. Phillion and C.J. Hurley, "Brightness and Duration of X-Ray Line Sources Irradiated with Intense 0.53-μm Laser Light at 60 and 120 ps Pulse Width," *Phys. Rev. A 34*, 4886 (1986).
75. B. Yaakobi, D. Steel, E. Thoros, A. Hauser, and B. Perry, "Direct Measurement of Compression of Laser-Imploded Targets Using X-Ray Spectroscopy," *Phys. Rev. Lett. 39*, 1526 (1977); also B. Yaakobi, D.M. Villeneuve, M.C. Richardson, J.M. Soures, R.J. Hutchinson, and S.A. Letzring, "X-Ray Spectroscopy Measurements of Laser-Compressed, Argon Filled Shells," *Opt. Commun. 43*, 343 (1982); B. Yaakobi, F.J. Marshall, D.K. Bradley, J.A. Delettrez, R.S. Craxton, and R. Epstein, "Signatures of Target Performance and Mixing in Titanium Doped, Laser-Driven Target Implosions," *Plasma Phys. 4*, 3021 (1997).
76. C.F. Hooper, D.P. Kilcrease, R.C. Mancini, L.A. Woltz, D.K. Bradley, P.A. Jaanimagi, and M.C. Richardson, "Time-Resolved Spectroscopic Measurements of High Density in Ar-Filled Microballoon Implosions," *Phys. Rev. Lett. 63*, 267 (1989).
77. T.D. Shepard, C.A. Back, D.H. Kalantar, R.L. Kauffman, C.J. Keane, D.E. Klem, B.F. Lasinski, B.J. MacGowan, L.V. Powers, L.J. Sutter, and R.E. Turner, "T_e Measurements in Open- and Closed-Geometry Long-Scale-Length Laser Plasmas via Isoelectronic X-Ray Spectral Line Ratios," *Rev. Sci. Instrum. 66*, 749 (1995).
78. V.W. Slivinsky, H.N. Kornblum, and H.D. Shay, "Determination of Suprathermal Electron Distributions in Laser-Produced Plasmas," *J. Appl. Phys. 46*, 1973 (1975).
79. E.M. Campbell, "Dependence of Laser-Plasma Interaction Physics on Laser Wavelength and Plasma Scalelength," p. 579 in *Radiation in Plasmas*, Vol. II (World Science, Singapore, 1983), B. McNamara, Editor; E.M. Campbell, B. Pruett, R.E. Turner, F. Ze, and W.C. Mead, "Suprathermal Electrons from Disks," p. 6-36 in *1981 Laser Program Annual Report*, E.V. George, Editor, Lawrence Livermore National Laboratory Report UCRL-50021-81.
80. C.E. Max, F. Ze, E.M. Campbell, W.C. Mead, R.E. Turner, K.G. Estabrook, V.C. Rupert, and D.W. Phillion, "Agrus and Shiva Experiments: Absorption and Stimulated Brillouin Scatter," p. 6-30 in *1981 Laser Program Annual Report*, E.V. George, Editor, Lawrence Livermore National Laboratory Report UCRL-50021-81.
81. F. Ze, E.M. Campbell, V.C. Rupert, and R.E. Turner, "Target-Interaction Experiments at 0.53 μm and 0.35 μm: Absorption," p. 7-8 in *1980 Laser Program Annual Report*, L.W. Coleman and W.F. Krupke, Editors, Lawrence Livermore National Laboratory Report UCRL-50021-80.
82. R.L. Kauffman, M.D. Cable, H.N. Kornblum, and J.A. Smith, "X-Ray Conversion Efficiency," p. 4-8 in *1985 Laser Program Annual Report*, M.L Rufer and P.W. Murphy, Editors, Lawrence Livermore National Laboratory Report UCRL-50021-85.
83. R.E. Turner, W.C. Mead, C.E. Max, E.M. Campbell, F. Ze, G.K. Tirsell, and P.H.Y. Lee, "X-Ray Conversion Efficiency at 1ω, 2ω, and 3ω," p. 6-34 in *1981 Laser Program Annual Report*, E.V. George, Editor, Lawrence Livermore National Laboratory Report UCRL-50021-81.
84. P.D. Goldstone, S.R. Goldman, W.C. Mead, J.A. Cobble, G. Stradling, R.H. Day, A. Hauer, M.C. Richardson, R.S. Marjoribanks, P.A. Jaanimagi, R.L. Keck, F.J. Marshall, W. Seka, O. Barnouin, B. Yaakobi, and S.A. Letzring, "Dynamics of High-Z Plasmas Produced by a Short-Wavelength Laser," *Phys. Rev. Lett. 59*, 56 (1987).
85. R.S. Craxton, "High Efficiency Frequency Tripling Schemes for High Power Nd : Glass Lasers," *IEEE J. Quant. Electr. QE-17*, 1771 (1981).
86. A. L'Huillier and Ph. Balcou, "High-Order Harmonic Generation in Rare Gases with a 1-ps 1053-nm Laser," *Phys. Rev. Lett. 70*, 774 (1993).
87. J.J. Macklin, J.D. Kmetric, and C.L. Gordon, "High-Order Harmonic Generation Using Intense Femtosecond Pulses," *Phys. Rev. Lett. 70*, 766 (1993).
88. Z. Chang, A. Rundquist, H. Wang, M.M. Murnane, and H.C. Kapteyn, "Generation of Coherent Soft X-Rays at 2.7 nm Using High Harmonics," *Phys. Rev. Lett. 79*, 2967 (1997); J. Zhou, J. Peatross, M.M. Murnane, H.C. Kapteyn, and I.P.Z. Christov, "Enhanced High Harmonic Generation Using 25 fs Laser Pulses," *Phys. Rev. Lett. 79*, 752 (1996).

89. Ch. Spielmann, N.H. Burnett, S. Sartania, R. Koppitsch, M. Schnürer, C. Kan, M. Lenzner, P. Wobrauschek, and F. Krausz, "Generation of Coherent X-Rays in the Water Window Using 5-Femtosecond Laser Pulses," *Science 278*, 661 (24 October 1997).
90. D. Schulze, M. Dörr, G. Sommerer, J. Ludwig, P.V. Nickles, T. Schlegel, W. Sandner, M. Drescher, U. Kleineberg, and U. Heinzmann, "Polarization of the 61st Harmonic from 1053-nm Laser Irradiation in Neon," *Phys. Rev. A 57*, 3003 (1998).
91. K.J. Schafer and K.C. Kulander, "High Harmonic Generation from Ultrafast Pump Lasers," *Phys. Rev. Lett. 78*, 638 (1997); J.L. Krause, K.J. Schafer, and K.C. Kulander, "High Harmonic Generation from Atoms and Ions in the High Intensity Regime," *Phys. Rev. Lett. 68*, 3535 (1992).
92. P.B. Corkum, "Plasma Perspective on Strong-Field Multiphoton Ionization," *Phys. Rev. Lett. 71*, 1994 (1993); P.B. Corkum, N.H. Burnett, and F. Brunnel, *Atoms in Intense Laser Fields* (Academic, New York, 1992), p. 109.
93. S.E. Harris, J.J. Macklin, and T.W. Hänsch, "Atomic Scale Temporal Structure Inherent to High-Order Harmonic Generation," *Opt. Commun. 100*, 487 (1993).
94. A. Rundquist, C.G. Durfee, Z. Chang, C. Herne, S. Backus, M.M. Murnane, and H.C. Kapteyn, "Phase-Matched Generation of Coherent Soft X-Rays," *Science 280*, 1412 (29 May 1998).
95. T.E. Glover, R.W. Schoenlein, A.H. Chin, and C.V. Shank, "Observation of Laser Assisted Photoelectric Effect and Femtosecond High Order Harmonic Radiation," *Phys. Rev. Lett. 76*, 2468 (1996).
96. T. Ditmire, E.T. Gumbrell, R.A. Smith, J.W.G. Tisch, D.D. Meyerhofer, and M.H.R. Hutchinson, "Spatial Coherence Measurement of Soft X-Ray Radiation Produced by High Harmonic Generation," *Phys. Rev. Lett. 77*, 4756 (1996).

HOMEWORK PROBLEMS

Homework problems for each chapter will be found at the website:
http://www.coe.berkeley.edu/AST/sxreuv

Chapter 7

EXTREME ULTRAVIOLET AND SOFT X-RAY LASERS

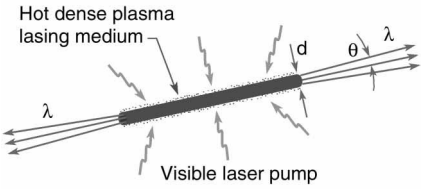

(see Colorplate XII)

$$\frac{I}{I_0} = e^{GL} \tag{7.2}$$

$$G = n_u \sigma_{\text{stim}} F \tag{7.4}$$

$$\sigma_{\text{stim}} = \frac{\pi \lambda r_e}{(\Delta\lambda/\lambda)} \left(\frac{g_l}{g_u}\right) f_{lu} \tag{7.18}$$

$$\frac{P}{A} = \frac{16\pi^2 c^2 \hbar (\Delta\lambda/\lambda) GL}{\lambda^4} \tag{7.22}$$

Lasing at short wavelengths in the EUV and soft x-ray regions of the spectrum is achieved in hot dense plasmas. Temperatures of several hundred electron volts to above 1 keV are required to collisionally excite atoms (ions) to the required energy levels. As these are well above the binding energies of outer electrons, the atoms are necessarily ionized to a high degree. Upper state lifetimes are typically measured in picoseconds, so that energy delivery (pumping) must be fast. As a result high power infrared, visible, and ultraviolet lasers are generally employed to create and heat the plasma, although in some cases fast electrical discharges are employed. Population inversion is generally accomplished through selective depopulation, rather than selective population. High gain lasing requires a high density of excited state ions, thus mandating a high density plasma. Preferred electron configurations are hydrogen-like (single electron, nuclear charge $+Ze$), neon-like (10 electrons), and nickel-like (28 electrons) ions, which tend to have a large fraction of the plasma ions in a desired ionization state. The short lifetime of hot dense plasmas limits the effectiveness of cavity end mirrors, so that in general these are high gain single pass lasers, albeit with some exceptions. Lacking multipass mode control, short wavelength lasers typically are far from diffraction limited. Temporal coherence lengths, set largely by ion Doppler line broadening, are typically 10^4 waves. The pumping power necessary to produce short wavelength lasers scales as $1/\lambda^4$. Recent high gain experiments demonstrate a capability for saturated lasing throughout much of this spectral region.

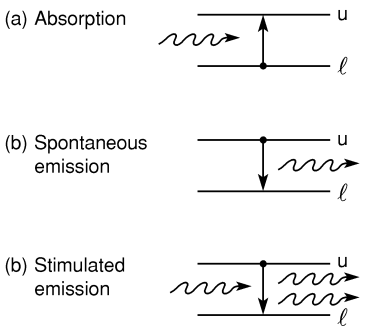

FIGURE 7.1. The processes of absorption, spontaneous emission, and stimulated emission.

7.1 BASIC PROCESSES

Lasing involves the stimulated emission and amplification of resonant electromagnetic radiation by quantized atomic systems in identical excited states.* [1–6] In such interactions the passing radiation stimulates the excited atoms to undergo transitions from their upper state to a lower state, resulting in the emission of radiation at the same frequency and phase coherent with the stimulating radiation. For lasing to occur there must be a population inversion in which there are more atoms in the upper excited state than in the lower state.

We begin the discussion of lasing with a review of absorption, spontaneous emission, and stimulated emission of radiation involving quantized atomic states, as illustrated in Figure 7.1. For the absorption process the atom is initially in the lower energy state, labeled l in Figure 7.1(a). Incident radiation of precise energy $\hbar\omega = E_u - E_l$ causes the bound electron to oscillate, acquiring the necessary energy to make a transition to the upper energy state u. For states whose difference in energy is defined to a specificity $\Delta E/E = \Delta\omega/\omega = \Delta\lambda/\lambda$, the transition involves a large number of oscillations between the two states, with the atom eventually residing in the upper level. The number of oscillations, of order $E/\Delta E$, is typically 10^6 or more. For the spontaneous emission process, described previously in Chapter 1 and shown here in Figure 7.1(b), the atom is initially in an excited state. Perhaps due to background field fluctuations, the electron is perturbed and begins to oscillate between the upper and lower energy states, emitting radiation at frequency ω in a wavetrain of duration (in cycles) of order $E/\Delta E$, eventually residing in the lower energy state. The third process, shown in Figure 7.1(c), is that of *stimulated emission*, which occurs when incident radiation of resonant frequency ω encounters an atom already in the upper excited state. Here again the electron is caused to oscillate at the frequency ω by the incident radiation, undergoing many oscillations and thus resulting in the emission of radiation with the atom eventually residing in the lower energy level. In this case the emitted radiation is not only at the same frequency, but is *phase coherent* with the stimulating radiation, and of the same polarization.

Lasing occurs when many atoms are initially in the same upper states and a cascading occurs in which some initial radiation, perhaps building from spontaneous emission (noise) or from an incident wave, causes the sequential stimulation of many phase coherent emissions, leading to substantial wave amplitude or energy amplification.[7–9] The spatial and temporal coherence properties of the resultant radiation will depend on the control of this initiating process. Known as *mode control*, this involves phase space, bandwidth, and polarization limitations imposed by geometry and cavity optics, a topic we take up later in this section.

*The acronym "laser" is derived[3] from "**l**ight **a**mplification through **s**timulated **e**mission of **r**adiation."

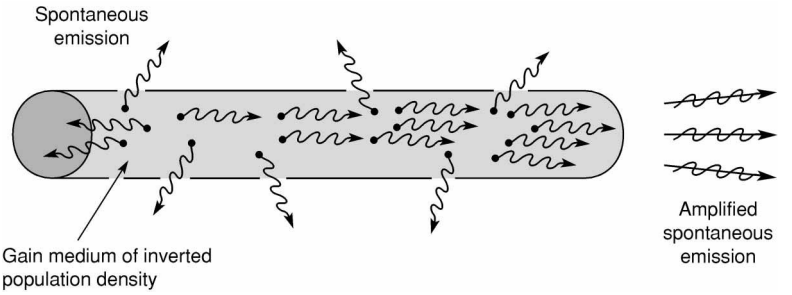

FIGURE 7.2. The lasing process begins with amplified spontaneous emission (ASE) in directions for which there is a long axial path length. The illustration shows amplification only toward the right, but it would actually occur in both directions. Radiation to the side leaves the gain medium after too short a propagation path to experience significant gain.

The initiation of lasing is illustrated in Figure 7.2, which shows the random emission from a collection of atoms, initially all in the same excited state. Due to variations in background field perturbations and the initial absence of a stimulating field, the atoms begin to spontaneously emit radiation at random times and in various directions. Early in the process, although at the same frequency ω, the various emissions are phase incoherent, as the initiation of the emission processes in different atoms is random and uncorrelated. As time progresses the situation changes. For emission in the lateral directions there is little chance for substantial amplification, due to the short path lengths; thus these emissions continue to be spontaneous and incoherent. However, for radiation emitted along the longer axial path there is a much increased probability of interacting with excited atoms, leading to stimulated phase coherent emission in a cascading, ever more intense propagating wave. This is the process of amplified spontaneous emission (ASE), which, with sufficient path length and density of excited atoms, evolves to lasing action. As we will see in the following section, it leads to exponential growth in the long path axial direction.

In some of the earliest EUV and soft x-ray laser demonstrations,[10–13] the observation of exponential intensity growth with length, in a well-defined axial direction, was a primary diagnostic, giving clear evidence that lasing had occurred. This was contrasted with lateral emissions that grew only linearly with axial path length, with little chance for amplification before exiting the active (inverted population density) region.

The process of lasing described above is dependent on a population inversion: the presence of more atoms in the upper excited state u than in the lower state l. Without such an inversion there is likely to be more absorption of radiation than stimulated emission, leading to a net decrease of wave intensity with propagation distance. Figure 7.3 shows population density versus energy level for two cases, (a) an equilibrium situation in which the upper state u is less populated than the lower state l, and (b) a non-equilibrium situation with an inverted population distribution between the upper and lower states. The inverted case, with more atoms in the upper state than in the lower state, can lead to lasing, while the equilibrium distribution leads to net absorption. The question then is, how can an inverted population distribution be obtained?

One method is to flood the atoms with radiation of sufficiently high photon energy to excite them to higher energy levels, permitting the atoms to evolve back to the ground state through transitions to various intermediate excited states. Because of differences in decay times for the various states, some of which may be *metastable* or relatively long lived due to less favorable quantum transition rates, temporary population inversions may occur. Thus for a

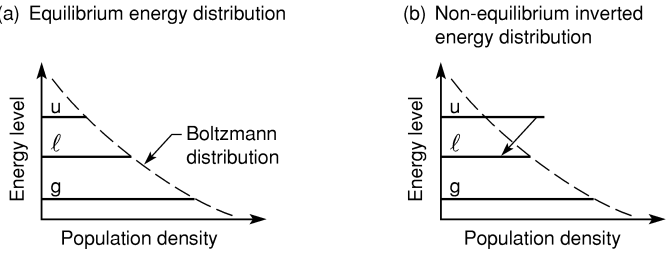

FIGURE 7.3. Equilibrium and non-equilibrium energy distributions. Lasing requires an inverted population density (more atoms in the upper state than in the lower state), as in (b).

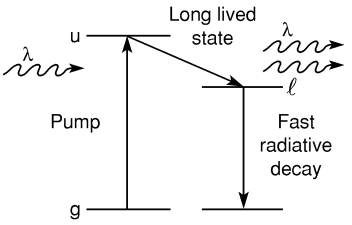

FIGURE 7.4. Three-level lasing between an upper state u and a lower state l. A pumping mechanism from the ground state g is also shown. Population inversion is obtained with many such atoms if the transition from u to l is relatively slow, while that from l to the ground state is relatively fast. This avoids subsequent reabsorption of the stimulated emission, or so-called radiation trapping.

brief period conditions for lasing may be present. In the presence of a sufficiently high density of excited states and a sufficiently long length of such lasing material, lasing will occur. Many visible light lasers operate with nanosecond, picosecond, and shorter pulse durations. Some operate in a pulse repetition mode, or in a continuous wave (cw) mode, where the cycle of pumping, excitation, and de-excitation through lasing is constantly repeated.

Other forms of pumping the inversion, more typical of short wavelength lasers, involve collisional excitation or recombination into a higher excited state. Figure 7.4 shows several energy levels of an atom to which energy has been provided by a pump that raises the atom to a long-lived excited state u, or to a higher excited state (not shown) from which it cascades down to the state u, and eventually lases to the state labeled l. The pump could consist, for example, of a collision with an energetic electron in a plasma. The lower level is unoccupied, perhaps because of its relatively rapid radiative decay. Thus for some period of time, determined by quantum transition rates, the atom resides in the upper state, available to participate in stimulated emission. The key to producing the inverted population density is the availability of upper and lower states with sufficiently dissimilar lifetimes.

Figure 7.5 shows a somewhat more realistic energy level diagram for a particularly simple one-electron (hydrogen-like) ion. This diagram will help us understand the energetics of EUV and soft x-ray lasing. In this spectral region the photon energies of interest for laboratory lasers extend from perhaps 50 eV to 500 eV. The requisite pump energies are necessarily higher, in that the atom must be lifted from the ground state to an energy at least equal to that of the upper excited state. With such energetic pump processes the atoms will surely be ionized to some high degree, as was described in Chapter 6, Section 6.7.2. In fact all successful EUV and short wavelength lasers to date have involved highly ionized plasmas,[10–21] either laser-produced plasmas or discharge plasmas.

The simplified energy level diagram in Figure 7.5 relates to a hydrogen-like (single electron) ion of nuclear charge Z. In this case the highly ionized atom is stripped of all electrons through energetic collisions in a hot plasma. As the plasma cools, a nearby free electron recombines with the ion, into a high level excited state. The electron then drops down

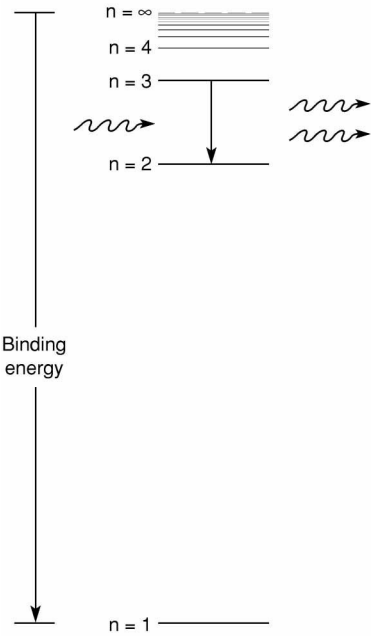

FIGURE 7.5. Energy levels for a hydrogen-like (single electron) ion of nuclear charge Z. Stimulated emission is shown for an $n = 3$ to $n = 2$, Balmer α transition. Energy levels scale according to Z^2. See Eq. (7.1) and Table 7.1 for values.

through the bound states, emitting characteristic radiation. In Figure 7.5 the ion is shown undergoing a stimulated $n = 3$ to $n = 2$ (Balmer α) transition, emitting a characteristic photon of energy [see Chapter 1, Eq. (1.8)]

$$\hbar\omega = (13.606 \text{ eV})\, Z^2 \left(\frac{1}{n_f^2} - \frac{1}{n_i^2} \right) \tag{7.1}$$

where for $n_i = 3$, $n_f = 2$, and a carbon nucleus of charge $Z = 6$ we have $\hbar\omega = 68.03$ eV (18.22 nm wavelength). Indeed, studies of this transition in hydrogen-like carbon played an important role in the early development of short wavelength lasers.[22–26] Note that the ionization energy required to remove the last electron from the carbon atom is 490 eV [$n_i = 1$, $n_f = \infty$ in Eq. (7.1)], so that preparation of such an ion for recombination laser studies requires an electron temperature of 100 eV to 200 eV.

With regard to favorable lifetimes and oscillator strengths, summarized here in Table 7.1 for a hydrogen-like ion of nuclear charge Z, the 3d $\rightarrow$ 2p transition has an oscillator strength f_{32} of 0.696, with thus a high probability for transition, and a lifetime of 12 ps.[27] The subsequent 2p $\rightarrow$ 1s transition to the ground state has an oscillator strength of 0.416 and a lifetime of only 1.2 ps, allowing for a fast depopulation of the lower state, as desired. Note that energy levels in Eq. (7.1) scale as Z^2, a general trend for higher photon energy lasers. The ionization energies scale in the same manner, so that requisite temperatures scale as $\hbar\omega$ and Z^2 as well.

Earlier in this section reference was made to the use of cavity optics for the control of coherence, spectral bandwidth, and polarization, techniques frequently employed at visible wavelengths[7, 9] Figure 7.6 illustrates (a) cavity optics for a visible light laser, and (b) a high gain, single pass EUV/soft x-ray laser. The visible light laser is configured for best spatial and temporal coherence. High reflectivity front and back mirrors are used to return the initial amplified spontaneous emission (ASE) many times through the gain medium (gas or solid with population inverted atoms – the "active" region). This improves energy extraction,

TABLE 7.1. Transitions in single electron, hydrogen-like carbon ions ($Z = 6$ nuclear charge). Photon energies, according to Eq. (7.1), scale as Z^2. Oscillator strengths are independent of Z. Radiative lifetimes,[27] which are the reciprocals of the Einstein coefficients A_{ul} given in Eq. (7.17), scale as Z^4, i.e., $\tau_Z = \tau_H / Z^4$

Transition u–l	Photon energy $\hbar\omega$(eV)	Wavelength λ (nm)	Oscillator strength[a] f_{lu}	Lifetime $\tau = 1/A_{ul}$ (ps)
2p–1s	367.0	3.378	0.4162	1.2
3p–1s	435.0	3.350	0.0791	
4p–1s	458.7	2.703	0.0290	
3p–2s	68.03	18.22	0.435	4.1
3s–2p	68.03	18.22	0.0136	
3d–2p	68.03	18.22	0.696	12.0
4p–2s	91.84	13.50	0.103	
4s–2p	91.84	13.50	0.0030	
4d–2p	91.84	13.50	0.122	
4p–3s	23.81	52.07	0.485	

[a] The emission oscillator strength f_{ul} (which has a negative value) and absorption oscillator strength f_{lu} are related by $f_{ul} = -(g_l/g_u) f_{lu}$.

providing a higher output power and permitting many passes for phase space control, spectral bandwidth selection, and choice of polarization. (Phase space control refers to the product of beam diameter and divergence at the lasing wavelength. The relationship between phase space product and full spatial coherence, $d \cdot \theta = \lambda/2\pi$ for Gaussian beams, is discussed in Chapter 8.)

Typically the rear mirror in Figure 7.6(a) would have a reflectivity of 99.9% for a visible light laser, while the partially transmitting front mirror might have a reflectivity of 90%, allowing some laser radiation to pass once for each round trip within the cavity. A transverse mode selector, typically a pinhole, blocks all ASE in the laser startup period except that which will eventually satisfy the stringent phase space constraint for full spatial coherence – in cavity parlance a transverse electromagnetic mode, TEM_{00}. The accepted ASE, which passes through the pinhole aperture, is reflected back through the gain medium, amplified, and returned again by the focusing rear mirror. Through many round trip passes the phase-space-selected radiation is selectively and exponentially amplified, easily dominating random ASE in undesired directions. At the same time a longitudinal mode selector – typically two axially separated resonant thin films, forming a high spectral selectivity Fabry–Perot bandpass – is used to narrow the laser line width to as little as a single axial mode of the cavity, typically narrower than the natural line width of stimulated emission. Narrowing the spectral bandwidth $\Delta\lambda$ increases the temporal (longitudinal) coherence length $l_{\text{coh}} = \lambda^2/\Delta\lambda$, also discussed in Chapter 8.

In some cases the narrow spectrum mode selector is replaced by an axial mode-locking *saturable dye* absorber. This passes only large intra-cavity intensity spikes, which tend to include contributions from all possible axial modes. Possessing the largest possible lasing bandwidth, this tends to produce the shortest time duration pulses. This and other gain controlling techniques are commonly used to extract available laser energy in short pulses, providing high peak power output.

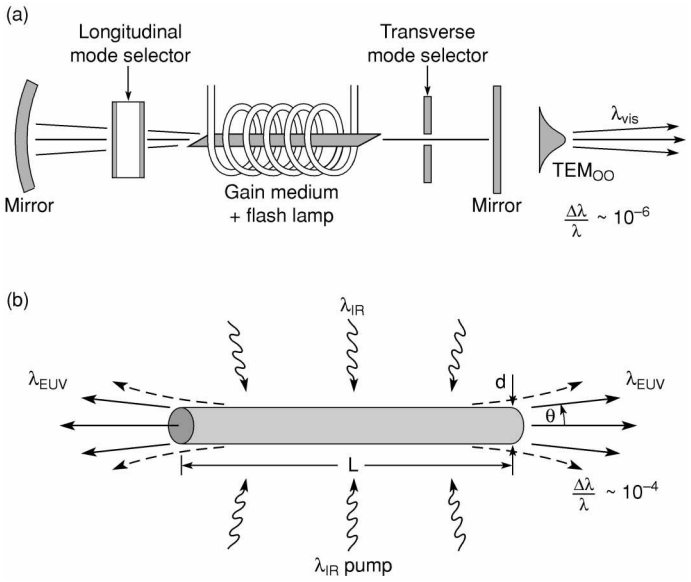

FIGURE 7.6. (a) Diagram of a visible light laser employing cavity defining feedback mirrors, an etalon for spectral narrowing through the enhancement of selected longitudinal cavity modes, a pinhole aperture for transverse mode control (spatial coherence), the gain medium, and a flashlamp pump to lift atoms into desired energy states. (b) Diagram of an EUV or soft x-ray laser based on high gain amplified spontaneous emission from an elongated laser-produced plasma (pump wavelength λ_{ir}) containing an inverted population density of ions in an upper excited state. The divergence of emitted radiation is set largely by the aspect ratio, d/L, but is also affected by refraction in the steep transverse density gradient plasma, as suggested by the dashed lines.

The gain medium shown in Figure 7.6(a) is a solid state rod, perhaps ruby, YAG, or glass, cut at Brewster's angle† (see Chapter 3, Section 3.6) for polarization control, and pumped by a flash lamp of incoherent light to achieve the initial population inversion. Both gaseous and solid state lasing media are common at visible wavelengths.[7, 9]

By comparison the EUV/soft x-ray laser, at least in its typical configuration as shown in Figure 7.6(b), is much simpler. In order to simultaneously achieve the requisite high temperature and high density, energy is deposited in a short time, typically sub-picosecond to several nanoseconds in duration, generally by a high power infrared or visible Laser or, for longer EUV wavelength lasers, by a short pulse, high current electrical discharge. Since light travels at a speed of 300 μm/ps, a 1 ns duration laser pulse would permit use of a single mirror at 15 cm or two mirrors each 7.5 cm from the center for full cavity operation. Generally mirror damage due to pum–laser scattering and plasma debris limit the use of cavity end mirrors at EUV and soft x-ray wavelengths, although some work has been done.[12, 28, 29] For shorter pulse duration the cavity length would be even shorter than the required gain length, typically measured in centimeters, thus excluding the possibility of multipass operation, unless regenerated plasma

†For lasing rods cut at Brewster's angle (see Chapter 3, Section 3.6), properly polarized light experiences no reflective loss at the air–solid interface, giving a slight intensity advantage over other ASE polarizations in the round trip gain competition, which rapidly leads to single polarization dominance in the multipass exponential lasing process.

techniques are developed. As a consequence, present EUV/soft x-ray lasers are largely single pass, high gain devices. Without cavity mirrors, the ability to control spatial coherence is limited to geometrical considerations, such as the ratio of output aperture diameter to axial lasing length.

These considerations are further complicated by refractive effects that tend to increase the divergence of laser radiation due to sharp lateral density gradients encountered in these rapidly expanding hot dense plasmas.[11, 14, 30] The subject of refraction in plasmas is discussed in Chapter 6, Section 6.6. Efforts to control the effects of refraction on short wavelength lasers, including prepulses, multiple pulses, double targets and special pump focusing techniques, are currently of great interest.[29, 31–33] In part this interest is due to the fact that the phase space product of EUV/soft x-ray lasers (the product of beam diameter and divergence) is generally much larger than the wavelength, indicating that the radiation consists of many transverse modes, and indicating minimal spatial coherence, particularly at the shorter wavelengths.[34]

Further discussion of spatial coherence, and improvements through techniques such as pinhole spatial filters and staged amplifiers, is presented in Chapter 8, Section 8.5. Laser line widths, typically dominated by Doppler broadening[14] due to motion of the relatively hot lasing ions, are generally of order $\Delta\lambda/\lambda \sim 10^{-4}$, leading to temporal coherence lengths approaching a millimeter, values quite useful for many applications.

7.2 GAIN

Obtaining exponential gain from stimulated emission of radiation requires a substantial population density inversion. Generally we inquire as to what difference in upper state and lower state ion densities, n_u and n_l, will lead to a substantial gain–length product GL, such that an initial emission intensity I_0 grows according to

$$\frac{I}{I_0} = e^{GL} \tag{7.2}$$

where I_0 is an initial EUV/soft x-ray intensity (power per unit area) that grows to a value I after propagating a distance L in a lasing media of gain per unit length G.[‡] The gain is often expressed in terms of atomic cross-sections for stimulated emission and absorption, σ_{stim} and σ_{abs}:

$$G = n_u\sigma_{\text{stim}} - n_l\sigma_{\text{abs}} \tag{7.3}$$

which can be written in terms of a density inversion factor F, as

$$\boxed{G \equiv n_u\sigma_{\text{stim}}F} \tag{7.4}$$

[‡]For short-wavelength lasers a more appropriate model is that of uniformly distributed spontaneous emission, amplified by stimulated emission as it propagates to the exit surface of the gain medium. In this case the integrated output intensity I, for an active medium gain G and length L, is $I = J_s(e^{GL} - 1)^{3/2}/G(GLe^{GL})^{1/2}$ where J_s is the spontaneously emitted power per unit volume within the lasing line. This is often referred to as the Linford formula.[35] It is widely used to assign gain values G in experimental studies of laser intensity versus length, such as we shall encounter here in Sections 7.3 and 7.4.

where the density inversion factor is given by

$$F \equiv 1 - \frac{n_l \sigma_{\text{abs}}}{n_u \sigma_{\text{stim}}} = 1 - \frac{n_l g_u}{n_u g_l} \tag{7.5}$$

and where the otherwise symmetrical cross-sections for stimulated emission and absorption may differ by statistical weights g_u and g_l, which are due to degeneracies (same energy, different quantum numbers) in the upper and lower lasing states.

Expressions for the cross-section for stimulated emission and gain can be obtained in terms of the Einstein A and B coefficients,[36–38] which appear when one considers rate equations for transitions among quantum states. For example, if we consider the rate of transitions, per unit volume, between the upper and lower states u and l, then *in radiative equilibrium* (as many transitions up as down)

$$n_u A_{ul} + n_u B_{ul} U_{\Delta\omega}(\hbar\omega) = n_l B_{lu} U_{\Delta\omega}(\hbar\omega) \tag{7.6}$$

where again n_u and n_l are the densities of atoms (ions) in the upper and lower states, A_{ul} is the spontaneous decay rate (number per second) from u to l, B_{ul} is the stimulated transition rate from u to l in the presence of radiation of spectral energy density[¶] $U_{\Delta\omega}(\hbar\omega)$, and B_{lu} is the absorption coefficient for transition from the lower state l to the upper state u. Again B_{ul} and B_{lu} would be equivalent, due to the symmetric nature of the two processes, except for the degeneracies, so that in general $g_l B_{lu} = g_u B_{ul}$. In equilibrium, $U_{\Delta\omega}$ is the Planckian distribution

$$U_{\Delta\omega}(\hbar\omega) = \frac{\hbar\omega^3}{\pi^2 c^3 (e^{\hbar\omega/\kappa T} - 1)} \tag{7.7}$$

where the density of states follows the Boltzmann energy distribution[34]

$$\frac{n_l}{n_u} = \frac{g_l}{g_u} e^{(E_u - E_l)/\kappa T} = \frac{g_l}{g_u} e^{\hbar\omega/\kappa T} \tag{7.8}$$

A consistent solution of Eqs. (7.6–7.8) requires that the Einstein coefficients be related[36] by[§]

$$\frac{A_{ul}}{B_{ul}} = \frac{\hbar\omega^3}{\pi^2 c^3} \tag{7.9}$$

an expression we will make use of shortly.

For lasing the idea is to get out of equilibrium, creating a temporary population inversion where $n_u > n_l$, with a sufficient spectral energy density of photons at $\hbar\omega = E_u - E_l$ that the stimulated process dominates, resulting in the preferential phase-coherent emission of radiation in a narrow spectral band. For the situation where stimulated emission far exceeds spontaneous emission, the rate equation for the increase in energy per unit time, within a narrow spectral bandwidth $\Delta\omega$, can be written [in distinction to Eq. (7.6) for equilibrium] as

$$\frac{\Delta E}{\Delta t} = \Delta I \cdot \Delta A = [n_u B_{ul} U_{\Delta\omega}(\hbar\omega) - n_l B_{lu} U_{\Delta\omega}(\hbar\omega)]\hbar\omega \cdot \Delta A \cdot \Delta L \tag{7.10}$$

[¶] See Chapter 6, Eq. (6.134a). $U_{\Delta\omega}(\hbar\omega)$ has units of energy per unit volume, per unit frequency interval $\Delta\omega$, at frequency ω.

[§] $A_{ul}/B_{ul} = 8\pi h\nu^3/c^3$ when expressed in terms of ν rather than ω. See Ref. 38, pp. 688, 712, and 63.

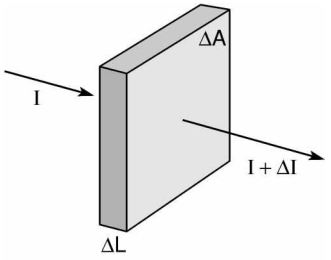

FIGURE 7.7. Geometry for considering laser amplification in a gain medium, in terms of an incremental increase ΔI in intensity.

where, as shown in Figure 7.7, ΔI is the incremental increase in intensity within the resonant bandwidth of the transition from u to l, ΔA is the element of cross-sectional area, and ΔL is the thickness of the volume element in the direction of propagation, and where we have neglected the spontaneous emission term as being relatively small. The incremental increase in intensity due to stimulated emission, contributed by the population inversion in the element of length ΔL, is then

$$\Delta I = n_u F B_{ul} U_{\Delta\omega}(\hbar\omega)\hbar\omega \cdot \Delta L \tag{7.11}$$

where we have used the density inversion factor defined earlier in Eq. (7.5). Writing the radiation spectral energy density in terms of the local intensity per unit bandwidth (see Chapter 6, Section 6.7.1), we have

$$U_{\Delta\omega}(\hbar\omega) = \frac{I(\hbar\omega)}{(\Delta\omega)c} \tag{7.12}$$

so that the incremental increase in intensity due to stimulated emission can be written as

$$\frac{\Delta I}{I} = \frac{\hbar\omega n_u F B_{ul} \cdot \Delta L}{(\Delta\omega)c} \tag{7.13}$$

Recalling the relation between A and B coefficients [Eq. (7.9)], this can be rewritten as

$$\frac{\Delta I}{I} = \frac{\pi^2 c^2 n_u F A_{ul} \cdot \Delta L}{(\Delta\omega)\omega^2} \tag{7.14a}$$

Noting that $(\Delta\omega)\omega^2 = (\Delta\omega/\omega)\omega^3 = (\Delta\lambda/\lambda)(2\pi)^3 c^3/\lambda^3$, the increase in intensity as a function of wavelength is

$$\frac{\Delta I}{I} = \frac{\lambda^3 n_u F A_{ul} \cdot \Delta L}{8\pi c(\Delta\lambda/\lambda)} \tag{7.14b}$$

Integrating this from $\Delta L = 0$ to L, over which the intensity increases from I_0 to I, one obtains the expression previously written as Eq. (7.2):

$$\frac{I}{I_0} = e^{GL}$$

where now the gain G is given explicitly as

$$G = \frac{\lambda^3 n_u F A_{ul}}{8\pi c(\Delta\lambda/\lambda)} \tag{7.15}$$

Recalling our earlier definition of the stimulated emission cross-section σ_{stim} in terms of the gain [Eq. (7.4)] as

$$G = n_u \sigma_{\text{stim}} F$$

we now identify the cross-section as[14]

$$\sigma_{\text{stim}} = \frac{\lambda^3 A_{ul}}{8\pi c(\Delta\lambda/\lambda)} \tag{7.16}$$

where $\Delta\lambda/\lambda$ is the full spectral bandwidth.

Quantum mechanically the Einstein A coefficient can be expressed in terms of the oscillator strength[‖] f_{lu} as[9, 27]

$$A_{ul} = \frac{e^2\omega^2}{2\pi\epsilon_0 mc^3}\left(\frac{g_l}{g_u}\right) f_{lu} \tag{7.17}$$

The cross-section for stimulated emission is then

$$\boxed{\sigma_{\text{stim}} = \frac{\pi\lambda r_e}{\Delta\lambda/\lambda}\left(\frac{g_l}{g_u}\right) f_{lu}} \tag{7.18}$$

where we have introduced the classical electron radius $r_e = e^2/4\pi\epsilon_0 mc^2 = 2.82 \times 10^{-13}$ cm, as described in Chapter 2, Eqs. (2.44) and (2.46).

For EUV and soft x-ray lasers the observed linewidth is dominated by Doppler broadening in the hot plasma. For a Maxwellian velocity distribution [see Chapter 6, Eq. (6.86), written for ions] the resultant spectral bandwidth, for full width at half maximum (FWHM) of intensity, is given by

$$\boxed{\left.\frac{(\Delta\lambda)}{\lambda}\right|_{\text{FWHM}} = \frac{v_i}{c} = \frac{2\sqrt{2\ln 2}}{c}\sqrt{\frac{\kappa T_i}{M}}} \tag{7.19a}$$

where v_i is the rms ion thermal velocity, κT_{i} is the ion temperature, and M is the ion mass. Expressing κT_{i} in electron volts and the ion mass as $2m_p Z$, where m_{p} is the proton mass and Z is the number of protons, the Doppler broadened linewidth can be expressed as

$$\left.\frac{(\Delta\lambda)}{\lambda}\right|_{\text{FWHM}} = 7.69 \times 10^{-5}\left(\frac{\kappa T_i}{2Z}\right)^{1/2} \tag{7.19b}$$

Returning to the calculation of gain, from Eq. (7.4),

[‖] In this chapter we return to the standard use of f for the oscillator strength, with subscripts u and l to show the upper and lower states. In Chapters 2 and 3 f was used to represent the atomic scattering factor. Also, we use g here, again with u and l subscripts, to denote the degeneracy of atomic states.

$$G = \pi r_e f_{lu} \frac{\lambda n_u F}{(\Delta\lambda/\lambda)} \frac{g_l}{g_u} \tag{7.20}$$

Expressions for gain as an explicit function of wavelength, for given line shapes, are derived by Silfvast in Ref. 9, Chapter 7.

For the previously cited example, with a 3d $\rightarrow$ 2p Balmer α transition at $\hbar\omega = 68.03$ eV (18.22 nm wavelength) in hydrogen-like carbon (see Figure 7.5 and Table 7.1), we can estimate the cross-section for stimulated emission from Eq. (7.18). For a carbon plasma initially heated to an electron temperature of several hundred electron volts to ensure full ionization, then quickly cooled to an ion temperature[12] of $\kappa T_i = 10$ eV, with an ion mass of $M = 2Zm_p = 12$ atomic mass units, the FWHM relative spectral bandwidth is $\Delta\lambda/\lambda = 7.0 \times 10^{-5}$. For the 3d to 2p transition,[27] (see Table 7.1), $f_{23} = 0.696$ and $g_l/g_u = 3/5$, so that from Eq. (7.18), $\sigma_{\text{stim}} \simeq 9.6 \times 10^{-15}$ cm^2. The associated gain, given by Eq. (7.4), is $G \simeq (9.6 \times 10^{-15}\ \text{cm}^2) n_u F$. For exponential amplification one requires, by Eq. (7.2), a length L such that $GL > 1$, or an inversion density–length product

$$n_u F L > 1/(9.6 \times 10^{-15}\ \text{cm}^2)$$

Assuming a lasing medium of length $L = 0.3$ cm and a density inversion factor approaching unity, this requires an initial excited state ($n = 3$) ion density of greater than $3.5 \times 10^{14}/\text{cm}^3$. Calculations of ion density and excited state distributions[26] for C^{+5} (one electron) in plasmas in the assumed temperature ranges typically indicate a fraction of order 10^{-3} in the $n = 3$ excited state, thus requiring a total C^{+5} ion density of order 4×10^{17} ions/cm^2, and thus an electron density (five times greater for charge neutrality) of $n_e \simeq 2 \times 10^{18} e/\text{cm}^2$. This electron density is below the critical value for CO_2 and Nd lasers, 10^{19} and 10^{21} e/cm^2 respectively (see Chapter 6, Table 6.1), and thus is reasonably approached with plasma formation by either system. In the next section we discuss early lasing experiments conducted with plasmas produced by both Nd and CO_2 lasers.

Having some understanding now of the temperatures and densities required to achieve lasing, it is interesting to inquire as to what power and intensity this requires of the driver, and how these scale with lasing wavelength. To estimate the required power that must be delivered to the lasing medium (plasma) in order to maintain the inverted population density, we can write

$$P = \frac{\hbar\omega n_u F V}{\tau} \tag{7.21}$$

where $n_u F$ is the inverted population density, V is the plasma volume, and $\hbar\omega$ is the photon energy that would be emitted by spontaneous emission in a transition of lifetime τ. In fact this is a lower limit on the required power, as the pumping is far from 100% efficient, involving several ionization stages, many energy states, and a general investment in thermal energy. Observing that $\tau = 1/A_{ul}$, and using Eq. (7.15) to replace $n_u F A_{ul} = 8\pi c(\Delta\lambda/\lambda)G/\lambda^3$, the required power per unit volume of plasma is

$$\frac{P}{V} = \frac{16\pi^2 c^2 \hbar (\Delta\lambda/\lambda) G}{\lambda^4}$$

so that in terms of the gain–length product, with $V = AL$, the required power per unit area (i.e., intensity) is

$$\frac{P}{A} = \frac{16\pi^2 c^2 \hbar (\Delta\lambda/\lambda) GL}{\lambda^4} \tag{7.22}$$

Thus to maintain a population inversion density with a given gain–length product and a linewidth ($\Delta\lambda/\lambda$) determined by the ion temperature κT_i as given in Eq. (7.19), the requisite laser intensity scales as $1/\lambda^4$. Actually, the linewidth $\Delta\lambda/\lambda \propto \sqrt{\kappa T_i}$, so that if $T_i \propto T_e$ and $\kappa T_e \propto \hbar\omega \propto 1/\lambda$, one has the proportionality $\Delta\lambda/\lambda \propto 1/\sqrt{\lambda}$. Where this is so, the required laser intensity scales[39, 40] as $1/\lambda^{4.5}$. This very rapid scaling of required pump intensity with lasing wavelength provides a significant challenge for the achievement of laser action at soft x-ray wavelengths.

7.3 RECOMBINATION LASING WITH HYDROGEN-LIKE CARBON IONS

The early history of EUV/soft x-ray lasing is associated with the pursuit of population inversion in hydrogen-like carbon plasmas, formed by the irradiation of carbon fibers at the focus of high power, short duration Nd lasers. The work was motivated in part by the observation of intense EUV lines and the possibility for population inversion as pointed out by Jaeglé, Carillon, and their colleagues,[41] as well as early theoretical predictions by Gudzenko and Shelepin[42] and others.

The first experimental inferences of population inversion, albeit small, were reported by Irons and Peacock,[22] followed by scalable threshold observations by Pert, Ramsden, and their colleagues[23, 25] and by Key, Lewis, and Lamb.[24] These pioneering experiments were all based on recombination in rapidly cooling, fully ionized carbon plasmas, described by the energy level diagram in Figure 7.5, in geometries similar to that of Figure 7.6(b). The general idea is to produce fully stripped carbon ions in a hot dense laser-produced plasma. By Eq. (7.1), removal of the last electron requires an energy of 490 eV, thus requiring an initial electron temperature of 100–200 eV, a value achievable with laser intensities of order[24, 25] 10^{13} W/cm^2 to 10^{14} W/cm^2, depending on the laser wavelength (see Chapter 6, Section 6.7.1). With rapid cooling by expansion and radiation, recombination takes place with low energy electrons populating upper excited levels, forming hydrogen-like (single electron) carbon ions. In this collisional recombination a third particle (an additional electron) is required to satisfy conservation of energy. As a consequence the rate of recombination is proportional to $n_e^2 n_i$, and thus occurs most efficiently at high electron density. Recombination is dependent on a low electron temperature; thus fast cooling is critical to this lasing technique. As the single bound electrons cascade down to lower excited states, a population inversion is created between the $n = 3$ and $n = 2$ levels due to the faster decay rates from $n = 2$ to $n = 1$, as indicated in Table 7.1. The 3d $\rightarrow$ 2p transition, with a 0.696 oscillation strength and a 12 ps lifetime, is then a good candidate for amplified spontaneous emission, as discussed in the previous section.

Suckewer and his colleagues introduced a novel[43] and successful[12, 13] approach to the idea of recombination lasing by suggesting the use of an axial magnetic field to constrain the lateral expansion of the laser-produced carbon plasma, thus tending to maintain high densities for a longer time while introducing a more favorable geometry for lasing. The basic geometry is illustrated in Figure 7.8(a). As electron densities under 10^{19} e/cm^2 are consistent with required ion densities, as discussed in the preceding section, use was made of a CO_2

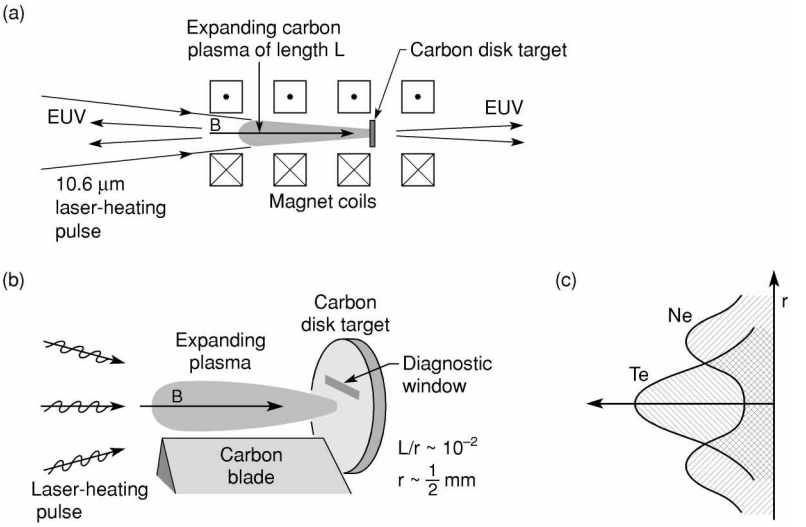

FIGURE 7.8. (a) A CO_2-laser-produced plasma constrained to a primary axial expansion by a solenoidal magnetic field. (b) The plasma is seen expanding away from a carbon disk target. A perpendicular carbon blade is shown, whose role is to enhance cooling, plasma density, and uniformity in the expanding plasma. A diagnostic window (slot) is shown in the carbon disk, which permits collection and spectral analysis of radiation in the axial direction through use of a spectrometer. A second spectrometer is used to study emissions in the transverse direction. (c) The presence of a strong axial magnetic field, through pressure balance, tends to produce an annular plasma with a density depression on-axis. (Courtesy of S. Suckewer, Princeton University.)

laser, which delivered approximately 300 J in a 70 ns FWHM pulse, resulting in an incident intensity of 5×10^{12} W/cm^2 on the solid carbon disk target. At this intensity the plasma should reach a temperature approaching 100 eV at peak irradiation intensity, permitting at least a fair fraction of the desired C^{+5} density.** Furthermore, with a CO_2 laser wavelength of 10.6 μm, this intensity corresponds to a rather high value of $I\lambda^2$ (see Chapter 6, Section 6.4.11). This leads to the generation of a non-Maxwellian energy distribution in which the hot-electron tail may further assist in the ionization process. With a solenoidal magnetic field of 90 kG, the electrons tend to circle the axial field lines with a Larmor radius†† of order one micron as they expand (axially) away from the irradiated disk region, typically 1 mm in diameter. Aspect ratios (L/r) of order 10 to 100 were obtained with the magnetically confined plasma expansion.

Shown in Figure 7.8(a) is the incident CO_2 laser beam irradiating a solid carbon disk target, the solenoidal magnetic field, and the expanding target. In these experiments one to four carbon blades [see Figure 7.8(b)], mounted perpendicular to the solid disk in off axis positions, were utilized to enhance plasma density, cooling, and uniformity in the axial direction.[13] The presence of a strong axial magnetic field tends to produce a plasma with

**Note that many authors follow the spectroscopic notation in which C VI is equivalent to C^{+5} (neutral carbon is C I).

††The Larmor radius, $r_L = mv/eB$, is 3.7 μm for a 100 eV electron in a 90 kG, or 9 T, magnetic field.

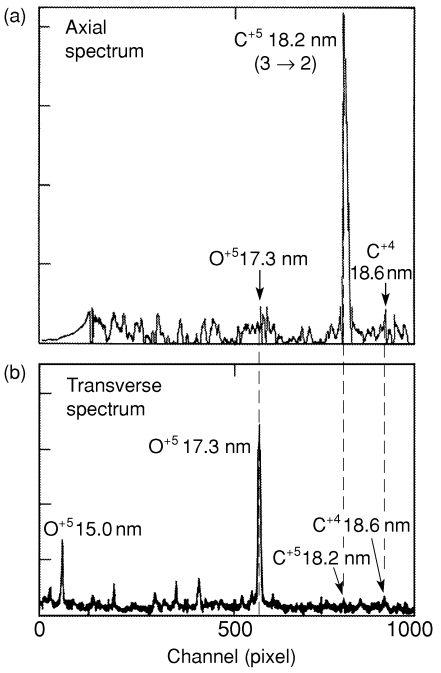

FIGURE 7.9. Emission spectra observed in the (a) axial and (b) transverse directions from a CO_2 laser-produced plasma formed by irradiating a carbon disk target located in a strong axial magnetic field. The laser energy was 300 J in an 80 ns pulse. (Courtesy of S. Suckewer, Princeton University.)

electron temperature peaked on axis (set by the laser irradiation profile), but with density peaked off axis, as illustrated in Figure 7.8(c), tending to produce favorable lasing conditions in an annular geometry.

Spectrally resolved emissions were observed both axially and in a transverse direction. Sample spectra are shown in Figure 7.9 for a single CO_2 laser pulse. In the axial direction there is a dominant emission line identified as that of the $3 \rightarrow 2$ transition in C^{+5}. In the transverse direction this line is barely discernible. This particular experiment[13] employed a 300 J CO_2 laser pulse of nominal 80 ns duration, and four symmetrically located carbon blades. Measurements in this series showed that maximum gain occurred off axis in a 200 μm thick annular shell at a radius of 1.3 mm to 1.5 mm, as observed through the diagnostic viewing slot. The maximum gain in these experiments[13] corresponds to a gain–length product $GL \simeq 8$. The gain was determined by the simultaneous observation of lasing and non-lasing emission lines in C^{+5}: the $n = 3$ to $n = 2$ line at 18.22 nm, the $n = 4$ to $n = 2$ line at 13.50 nm, and the spontaneous emission $n = 2$ to $n = 1$ line at 3.378 nm used to monitor reproducibility of plasma conditions. Lasing energies of 3 mJ per pulse were recorded at a repetition rate of 0.05 Hz, within a divergence angle of 5–10 mrad.

In a continuation of these early recombination lasing experiments with hydrogen-like carbon, the Princeton group conducted a further series of experiments[44] utilizing a 25 J, 3 ns duration Nd laser pulse to irradiate carbon targets with a 100 μm by several millimeter cylindrical focus, designed to generate lasing in a direction parallel to the target surface. A stainless steel (C + Fe) blade was again used, parallel and near (0.8 mm) to the line focus, to assist in plasma cooling.[44, 45] A magnetic field parallel to the line focus was employed, but played a less essential role due to the natural plasma line shape associated with the line focus. The laser intensity was nominally $(0.8–1) \times 10^{13}$ W/cm^2. Spectrally resolved emission lines observed in the long plasma direction are shown in Figure 7.10, for plasma lengths

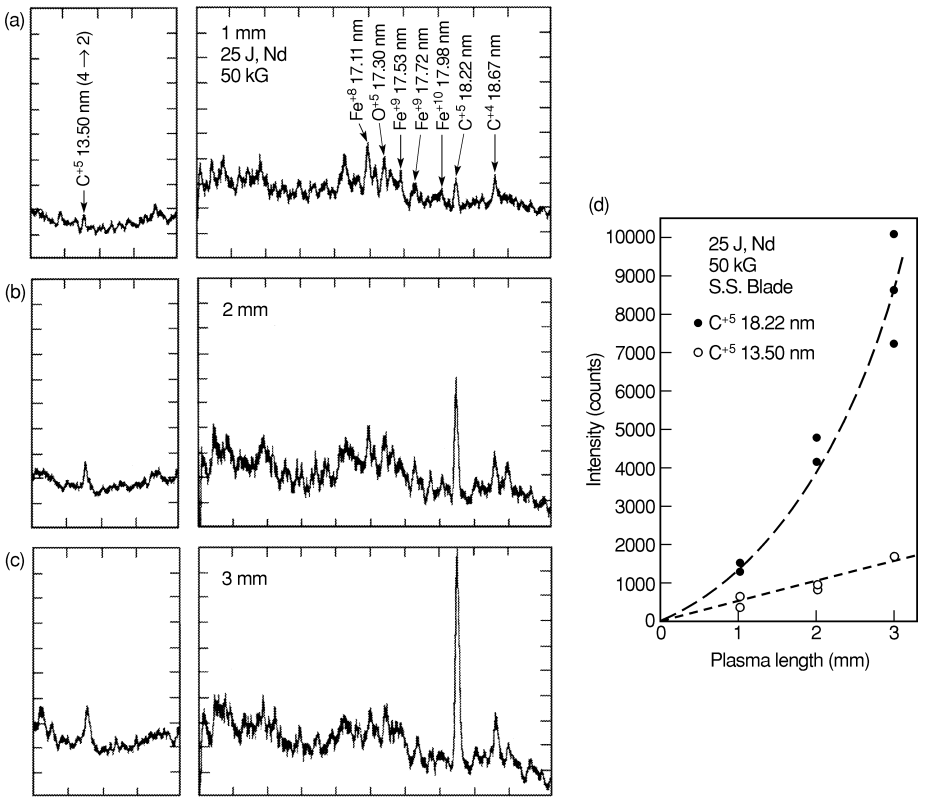

FIGURE 7.10. (a–c) Emission spectra from a hydrogen-like carbon plasma formed by a Nd : glass laser. The line focus length is varied from 1 mm to 3 mm across the surface of a carbon target. Emission is observed in the elongated plasma direction. With longer plasma length the emission line at 18.22 nm grows exponentially out of the noise to become a prominent spectral feature. A companion line, less likely to lase, at 13.50 nm, is shown for comparison. (d) Relative emission intensities of C^{+5} lines at 18.22 nm (solid circles) and 13.50 nm (open circles), showing an exponential growth with plasma length for the $n = 3$ to $n = 2$ line at 18.22 nm. Nd laser energy was 25 J (15 J on target), with a magnetic field of 50 kG. The dashed curve is a theoretical fit to a gain of 8.1/cm. Growth of the 13.50 nm line ($n = 4$ to 2) is linear with length. (Courtesy of S. Suckewer, Princeton University.)

of 1–3 mm. For the shortest plasma length (1 mm) a number of weak emission lines are observed just above the continuum, including lines of iron (Fe) and oxygen associated with the nearby stainless steel blade. As the plasma length is increased to 2 mm and 3 mm, by elongating the line focus, the C^{+5} $n = 3$ to 2 transition at 18.22 nm grows rapidly out of the noise. A companion line at 13.50 nm, corresponding to an $n = 4$ to 2 transition in C^{+5} (see Table 7.1), shows weaker growth with plasma length. This 13.50 nm line has a shorter wavelength and smaller oscillator strength (see Table 7.1), and is thus expected by Eq. (7.20) to have a smaller gain. In Figure 7.10(d) the intensity increase of these two lines is shown as a function of plasma length. The lasing line at 18.22 nm is observed to exponentiate with a gain of $G \simeq 8.1$/cm, while the reference line at 13.50 nm grows linearly with length. The observation of exponential intensity growth with plasma length was used as proof of lasing in these early studies. Further research at the Rutherford-Appleton Laboratory[46] has led to

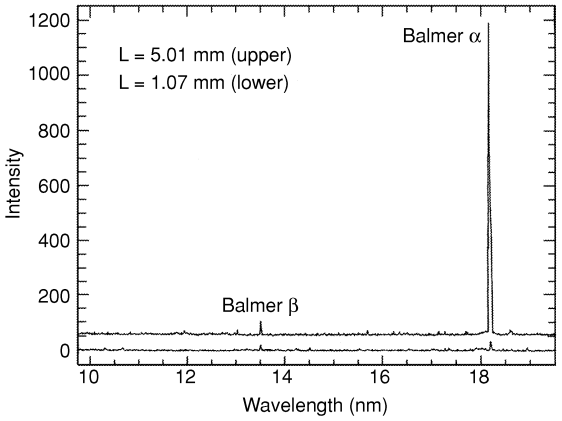

FIGURE 7.11. On-axis emission spectra from Nd laser irradiated carbon fibers of 7 μm diameter and different lengths. The data show substantial growth for the $n = 3$ to $n = 2$ Balmer α line of C^{+5} at 18.22 nm. Laser intensity is nominally 6×10^{15} W/cm^2 in a 2 ps duration pulse. The gain length product was $GL = 6.5$ for the 5.0 mm long plasma. (Courtesy of J. Zhang and M.H. Key,[46] Rutherford-Appleton Laboratory.)

beautifully resolved 18.22 nm lines in higher intensity, 3×10^{15} W/cm^2, 2 ps duration Nd laser irradiations of 7 μm diameter, 5 mm long carbon fibers, achieving gains up to 12.5/cm. An example of their data is shown in Figure 7.11.

7.4 COLLISIONALLY PUMPED NEON-LIKE AND NICKEL-LIKE LASERS

Collisionally pumped lasers, involving closed shell, highly ionized ions, offer an alternative path toward high gain at short wavelengths. The technique makes use of ionization bottlenecks, associated with closed electron shells as discussed in Chapter 6, Section 6.7.2, to ensure a high density of ions in a particular ionization state. It employs cylindrical illumination of thin, elongated foils, which are laser-heated to high density and high electron temperature, as illustrated in Figure 7.12. The irradiation intensity is chosen to produce an electron temperature that is well matched to the ionization potential of the desired closed shell ion. Excited states are mostly produced by collisions with plasma electrons, but also by cascading down from higher-still Ne-like (10 electrons) excited states, and by recombination of overly ionized F-like ions. Population inversion is by selective depopulation of the lower lasing state, rather than by selective population of the upper state. These techniques were pioneered at Lawrence Livermore National Laboratory by Matthews,[10, 47] Rosen,[11, 48] Hagelstein, MacGowan,[49–52] and their colleagues,[53–57] based in part on the early theoretical work of Vinogradov and Shlyaptsev[58] and others.

The earliest demonstration[10, 11] of high gain at short wavelength utilizing collisionally pumped closed shell ions employed neon-like selenium ($Z = 34$, 10 electrons, net charge +24). The ionization energy required to remove an electron from an 11-electron Na-like ion is 1036 eV, while that for a 10-electron Ne-like ion is 2540 eV due to the closed shell.[‡‡] With an electron temperature of about 1 keV one can then expect a large fraction of the ions to be in the Ne-like state, with fewer in the Na-like and lower ionization states. Simulations indicate,[48]

[‡‡]See Chapter 6, Table 6.2, in Section 6.7.2.

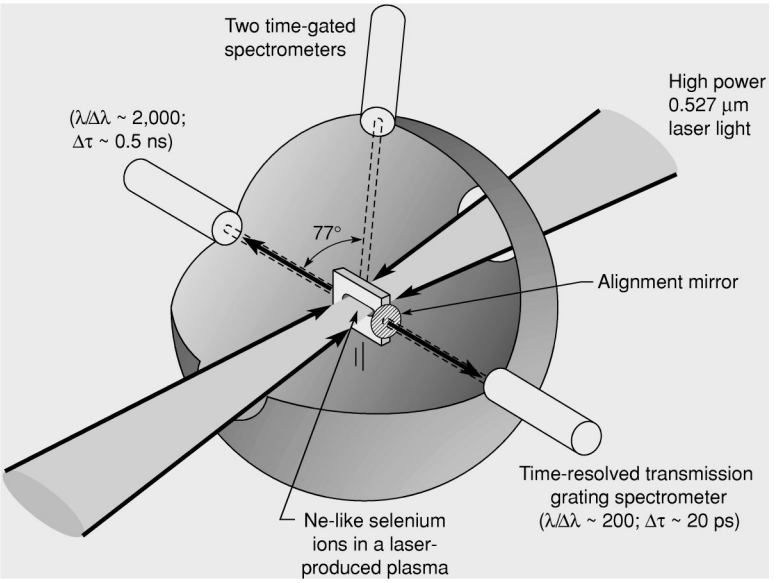

FIGURE 7.12. Double-sided irradiation of a thin film selenium target for high gain lasing at 20.65 nm and 20.98 nm wavelengths. High gain amplified spontaneous emission (ASE) grows exponentially in the elongated plasma column, resulting in intense narrow band lasing in two opposite directions. Irradiation is by high power visible light (nominally 2.4 TW, 0.527 μm wavelength, 450 ps FWHM, 7×10^{13} W/cm^2, 200 μm $\times$ 1.1 cm elongated focal spot). Two time-gated spectrometers record axial and off-axis emission spectra. A time resolved transmission grating streak spectrometer records axial emission spectra in the opposite direction. (Courtesy of D. Matthews, Lawrence Livermore National Laboratory.)

for instance, that about 20% of all ions are Ne-like, a similar number are F-like (9 electrons), and the rest are dispersed over a broad range of ionization states. These observations are confirmed by experimental emission spectra.[11] For the Ne-like ions, a population inversion is produced between the $1s^2\,2s^2\,2p^5\,3p$ and $1s^2\,2s^2\,2p^5\,3s$ states, as shown in the energy level diagram of Figure 7.13. Both states are filled by collisions from below, and by recombination and cascading from higher level states. Population inversion results as the $2p^5\,3p$ to $2p^6$ (ground state) transition is dipole forbidden (see Chapter 1, Section 1.3), while the $2p^5\,3s$ to $2p^6$ transition is radiatively allowed with a high oscillation strength and a short lifetime, of order $\frac{1}{3}$ ps. Lasing then occurs on the 3p ($J = 2$) to 3s ($J = 1$) transitions. Electron collisional excitation from the ground state to these and higher excited states requires at least 1.5 keV,[59] thus also requiring a high electron temperature.

Experimental data[10] obtained with thin film selenium foils of three lengths are shown in Figure 7.14. The targets were irradiated with frequency doubled Nd laser light (0.527 μm wavelength), line focused to a nominal intensity of 7×10^{13} W/cm^2, in a pulse of 450 ps duration (FWHM). The foil targets consisted of a 750 Å thick layer of selenium, vapor deposited on a nominally 1500 Å thick Formvar ($C_{11}H_{18}O_5$) substrate. Using a cylindrical lens, a line focus of 200 μm $\times$ 1.1 cm was obtained. With two beam illumination from opposite sides of the Novette laser, plasmas up to 2.2 cm length were formed. Due to the thin nature of the target material, the entire irradiated area was vaporized, creating a single elongated plasma. The combination of experimental data and computer simulations indicates[57] that at the time of

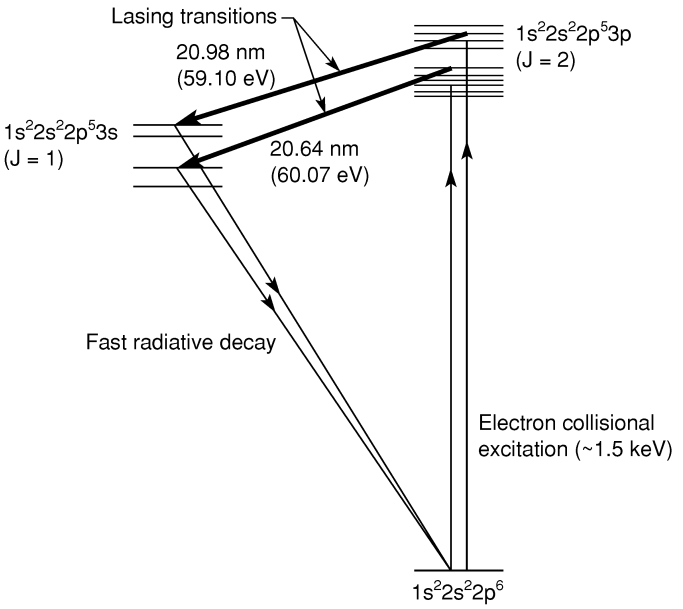

FIGURE 7.13. Simplified energy diagrams showing two lasing lines, at 20.64 nm and 20.98 nm, in neon-like (10 electron) selenium ions. The ground state has a $1s^2\ 2s^2\ 2p^6$ configuration. The Ne-like ions are produced in a hot dense plasma. The ions are pumped into excited states by direct electron collisional excitation, and by downward cascading from overly ionized F-like ions. Population inversion results from selective depopulation. The 3p to 2p transition is a long-lived dipole forbidden transition, while the 3s to 2p is dipole allowed with a fast radiative decay of about $\frac{1}{3}$ ps. This creates a population inversion between the 3p and 3s states. (Courtesy of M. Rosen, Lawrence Livermore National Laboratory.)

lasing the electron density was about (3–5) $\times 10^{20}\ e/\text{cm}^3$ with a density scale length in excess of 100 μm, electron temperature approximately 900 eV, and ion temperature approximately 400 eV.

Figure 7.14 shows time-gated axially observed emission spectra for plasma lengths of 4.6 mm, 10.1 mm, and 22.4 mm. For the 4.6 mm long plasma the $2p^5$ 3p to $2p^5$ 3s lines,[52, 53] at 20.64 nm and 20.98 nm, are evident but comparable in intensity to many other emission lines, just above the background continuum. Observed at an angle away from the axis, with a companion instrument, these lines are barely discernible above the background continuum.[10] As seen in Figure 7.14(b), with a plasma length of 10.1 mm the two lasing lines begin to dominate the spectrum. For the 22.4 mm plasma length, Figure 7.14(c), the lasing lines at 20.64 nm and 20.98 nm completely dominate the observed axial emission spectra. Integrated line intensities versus target length are shown in Figure 7.14(d) for (laterally displaced) double sided target irradiations. The exponential growth of intensity for both 20.64 nm and 20.98 nm lines is a clear diagnostic of amplification by stimulated emission. This exponential growth is observed only in the axial direction, where a sufficient gain–length (GL) product exists. Fits to the experimental data in Figure 7.14 indicate a gain of approximately 5/cm for the two-sided irradiations.

Further confirmation of lasing, obtained in later experiments, involved measurement of the emission line spectral shape ($\Delta\lambda$), and the observation of gain narrowing of the 20.64 nm

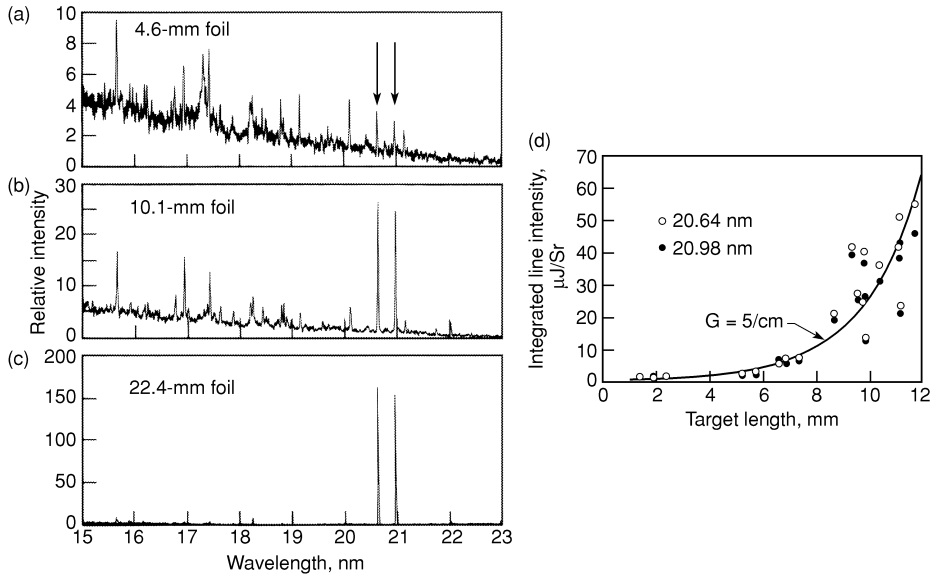

FIGURE 7.14. (a–c) Axial emission spectra are observed for selenium plasmas of lengths 4.6 mm, 10.1 mm, and 22.4 mm. The Ne-like selenium lasing lines, at 20.64 nm and 20.98 nm wavelengths, are observed to grow dramatically in intensity with increasing plasma length. Data are obtained with the time-gated spectrometer shown in Figure 7.12. Observation of the same spectral range from an off-axis position shows these same lines to be very weak, lacking a sufficient propagation distance for growth by stimulated emission. (d) Exponential growth of integrated line intensity with target length provided the primary evidence for lasing on the 3p to 3s transitions at 20.64 nm and 20.98 nm wavelength in Ne-like selenium ions. (Courtesy of D. Matthews and colleagues,[10] Lawrence Livermore National Laboratory.)

line in time resolved high spectral resolution studies by Koch et al.[56, 57] Neon-like lasing was extended to relatively modest facilities by Lee, McLean, and Elton,[60] who used a 400 J, 2 ns Nd laser and solid targets to demonstrate lasing in Cu and Ge, albeit at the somewhat longer wavelengths of 27.93 nm and 23.22 nm, respectively. Collisionally pumped lasing in Ne-like electron configurations was extended to shorter wavelengths[15–17, 47, 49] using Ne-like Y at 15.50 nm and 15.71 nm, and Ne-like Mo at 13.10 nm and 13.27 nm.¶¶

Continuation to still shorter wavelengths using this same isoelectronic sequence requires ever higher electron temperatures and thus higher visible laser intensities, which is problematic because of power requirements for these large area targets. Recent experiments utilizing double pulse *transient excitation* offer a new and more efficient route to collisionally pumped lasing. In this technique two time-separated laser pulses are used to heat a plasma. The first is a relatively modest intensity nanosecond duration pulse that pre-forms a plasma to the desired ionization stage. The plasma is then allowed to expand for 1–2 ns, creating a larger plasma with more gentle density gradients. A second, more intense pulse, typically one picosecond in duration, is then used to rapidly heat the pre-formed plasma, collisionally exciting the existing neon-like atoms to higher excited states. Differences in radiative decay rates among

¶¶A comparison of experimentally observed and calculated Ne-like lasing wavelengths is given by Nilson and Scofield.[53]

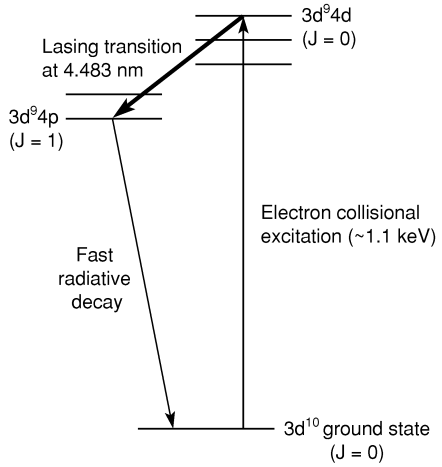

FIGURE 7.15. Simplified energy level diagram for Ni-like Ta^{+45}, showing the 4d to 4p lasing transition at 4.483 nm (276 eV). (Following MacGowan et al.[52])

the various excited states provide the desired population inversion. The more gentle density gradients reduce refraction in the plasma, increase the potential lasing volume, and permit more efficient extraction of energy from the picosecond heating pulse.

Nickels and his colleagues[61] have used this transient inversion technique with a relatively modest laser facility to achieve lasing in neon-like titanium at 32.6 nm. In their experiments a total of only about 10 J was used to obtain clear lasing results, pointing a path toward future table top capabilities. Using a 30 μm by 5 mm line focus on a solid titanium target, 7 J of 1.053 nm laser light in a 1.5 ns FWHM pulse is delivered to the target, at an intensity of about 10^{12} W/cm^2. This is followed by a 1.5 ns delayed pulse of 4 J in 0.7 ps, at a nominal intensity of 10^{15} W/cm^2. The 0.7 ps transient pulse permits a favorable inversion condition with respect to the longer lifetimes of the excited upper states. With an irradiated target length of 5 mm, a gain of 19/cm was achieved, for a gain–length product of $GL = 9.5$. Continuation of these transient population inversion experiments is described toward the end of this section in experiments involving collisionally pumped nickel-like lasers.

A second route in the pursuit of ever shorter wavelength lasers, also utilizing collisional pumping of closed electron shells, is that involving nickel-like ions.[50–52, 54] In this case the closed-shell ground state is $1s^2\,2s^2\,2p^6\,3s^2\,3p^6\,3d^{10}$, a 28-electron ion, with lasing between the $3d^9\,4d$ and $3d^9\,4p$ excited states. Key advantages of the Ni-like schemes are the lower ionization potentials of $n = 4$ levels, vs. $n = 3$ levels for Ne-like, and the lower excitation energies from the $3d^{10}$ ground state, about 1.1 keV vs. about 1.5 keV for Ne-like (from $2p^6$). Figure 7.15 shows a simplified energy level diagram[52, 54] for Ni-like tantalum ($Z = 73$, 28 electrons, net charge +45). Pumping is largely through direct electron collisional excitation and through cascading down from upper levels. Population inversion is again achieved through selective depopulation of the lower $3d^9\,4p$ level in a fast radiative decay to the ground state.

Experimental data[51, 52] for axial emissions of Ni-like Ta^{+45} are shown in Figure 7.16. With a small increase in plasma length from 1.7 cm to 2.5 cm, the 4.483 nm line is seen to emerge dramatically from the noise. The intense line of the 2.5 cm case has a gain–length product $GL \simeq 8$. Axially observed lasing lines at 5.023 nm, 4.483 nm, 4.318 nm, and 3.556 nm, observed with Ni-like ions of ytterbium, tantalum, tungsten (wolfram), and gold, are shown in Figure 7.17. The lines of Ta and W are selected as they straddle the K-absorption edge of carbon at 4.36 nm, an important feature for many scientific and technological applications, as

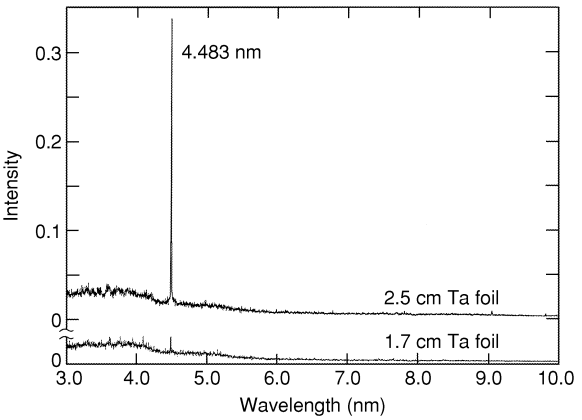

FIGURE 7.16. Measured axial emission spectrum for 1.7 cm and 2.5 cm long tantalum foils, showing the emergence of the 4d to 4p lasing line in Ni-like Ta, at 4.483 nm wavelength. (Courtesy of B. MacGowan and colleagues,[52] Lawrence Livermore National Laboratory.)

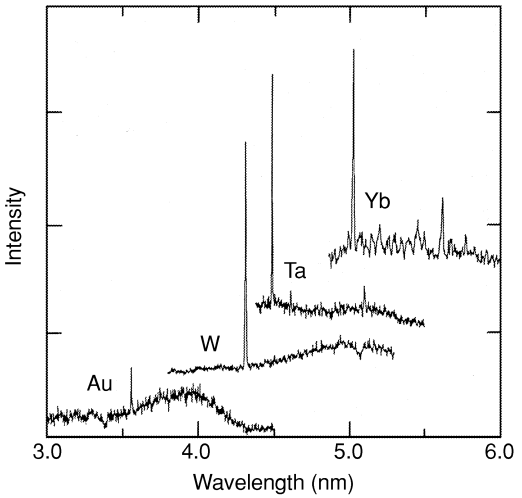

FIGURE 7.17. Examples of on-axis spectra from Ni-like lasers, showing strong 4d to 4p lines in Yb at 5.023 nm, in Ta at 4.483 nm, in W at 4.318 nm, and in Au at 3.556 nm wavelength. (Courtesy of B. MacGowan and colleagues,[52] Lawrence Livermore National Laboratory.)

discussed for instance by London, Rosen, and Trebes.[55] For the Ta^{+45} laser, the output energy is estimated[62] to be about 30 μJ in a 250 ps pulse, radiating into a horizontal divergence angle of about 12 mrad (FWHM).

Work on Ni-like lasers, in pursuit of saturated lasing at shorter wavelengths, continues. In a collaboration between the Institute for Laser Engineering in Osaka and the National Laboratory for High Power Lasers and Physics in Shanghai, Kato, Wang, Daido, and their colleagues[29, 63, 64] have employed multiple pulse irradiation techniques to control refraction, and multilayer mirrors to provide feedback, in experiments involving Ni-like lasing in Nd ($Z = 60$) at 7.905 nm wavelength. Their technique employs four pulses of 1.053 μm, each of nominal 100 ps duration and 7×10^{13} W/cm^2 intensity. The first pulse is used to pre-form the

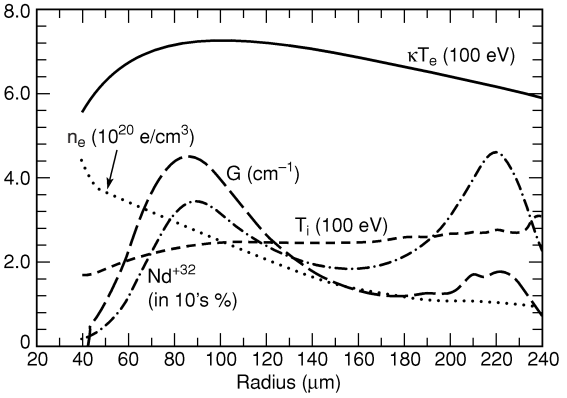

FIGURE 7.18. Radial distributions of electron temperature, electron density, ion temperature, percentage of Nd ions in the Ni-like ionization stage, and predicted gain, at the peak of the third pulse in a multipulse irradiation of coaxial Nd slab targets at nominal 7×10^{13} W/cm^2, 100 ps, cylindrically focused Nd laser pulses. The simulations are based on experiments conducted with the GEKKO XII laser at the Institute of Laser Engineering in Osaka. At peak gain (expansion radius 81 μm) the predicted values are $\kappa T_e = 820$ eV, $n_e = 2.8 \times 10^{20}\ e/\text{cm}^3$, $\kappa T_\text{i} \simeq 340$ eV, 35% of Nd ions in the Ni-like ionization state, and gain 4.8/cm. (Courtesy of Y. Kato, H. Daido, and colleagues,[29] ILE, Osaka University, and S. Wang and colleagues, NLHPLP, Shanghai.)

plasma, allowing free expansion to set a relatively long density scale length so as to minimize refractive turning during subsequent irradiations. Cylindrical focusing is used on side-by-side slab targets, illuminated from opposite sides and aligned for double plasma path length. The two targets are separated axially by 3 cm center to center, are curved to compensate for refraction, and are laterally displaced. The double targets are irradiated with this sequence of four pulses, in each case with one target irradiation delayed by 100 ps to enhance gain in one direction ($\Delta\tau = \Delta l/c$). A Ru–B_4C multilayer mirror,[§§] with 7% reflectivity at 7.9 nm wavelength, is placed 6 cm from the center of the closest target. This separation matches the 400 ps interval between pulses (2×6 cm$/c$). With feedback from the mirrors, lasing is enhanced on the third and fourth pulses. The combination of multipass lasing in refraction-compensated, quasi-traveling-wave illumination (delayed by one target) of solid Nd targets generates a sequence of three 130 ps duration pulses, of 40 μJ energy each,[64] at 7.905 nm wavelength in a nickel-like neodymium plasma.

Numerical simulations of plasma conditions at the peak of the third pulse, obtained using a one-dimensional (radial) computer code, are reproduced here in Figure 7.18. The figure shows radial profiles of electron density, electron temperature, ion temperature, percentage of Ni-like Nd^{+32} ions, and predicted gain. A maximum gain of 4.8/cm is predicted during the third pulse, for a double length target of 4.6 cm. Maximum gain is predicted to occur at an expansion radius 81 μm from the initial surface, in a radial region about 40 μm wide, radiating into a divergence angle of about 3 mrad. At maximum gain, the computer code predicts an electron temperature of 820 eV, an electron density of $2.8 \times 10^{20}\ e/\text{cm}^3$, an ion temperature of about 340 eV, and a Ni-like Nd^{+32} ion fraction of about 35%.

Saturation of Ni-like lasers at a variety of wavelengths, as short as 7.355 nm in Sm, has been achieved in experiments at the Rutherford-Appleton Laboratory using 75 ps, 1.05 μm

[§§]See Chapter 4, Refs. 24 and 27.

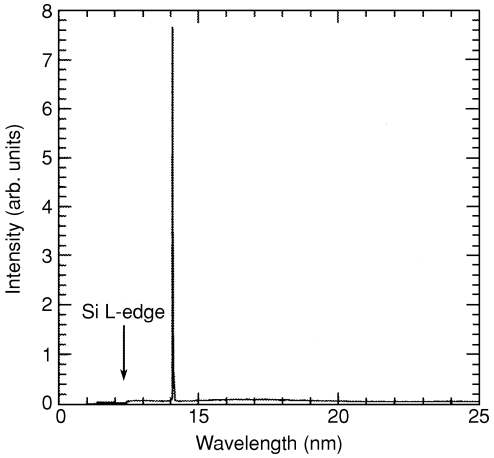

FIGURE 7.19. Axial emission spectrum from a single 18 mm long curved silver target, showing the dominant Ni-like Ag 4d to 4p lasing line at 13.99 nm. (Courtesy of J. Zhang and colleagues,[65] Rutherford-Appleton Laboratory.)

laser heating pulses, cylindrically focused to (1–4) $\times 10^{13}$ W/cm^2 irradiation intensity. Zhang, MacPhee, Lin, and their colleagues[32, 65] have employed double pulses (2.2 ns separation) to irradiate side-by-side slab targets, axially aligned and oppositely illuminated, up to 3.6 cm total length. With the resultant opposed density gradients, refraction in the sequential plasmas is partially compensated, with resultant divergence angles of 1–2 mrad. These saturation results are particularly interesting in that they are obtained with modest laser intensities (2×10^{12} W/cm^2) that are accessible at many smaller laser facilities, thus showing a path towards wider access to short wavelength lasing.

Figure 7.19 shows the axial emission spectrum of a single 18 mm long curved silver target.[65] The spectrum is dominated by the 4d $\rightarrow$ 4p ($J = 0 \rightarrow 1$) lasing line of nickel-like Ag at 13.99 nm.[‖‖] The small signal gain in these experiments was about 7.2/cm. Saturation, as shown in Figure 7.20(a), was achieved with a gain–length product of $GL \simeq 1.6$). Based on best estimates of source size (43 μm $\times$57 μm FWHM) and divergence (1.5 mrad $\times$ 3.5 mrad FWHM), a pulse peak spectral brightness of 1.1×10^{25} photons/s $\cdot$ mm^2 $\cdot$ mrad is estimated. This is based on a laser output energy of 90 μJ in a single 43 ps pulse, corresponding to an output intensity of 69 GW/cm^2. Saturation curves[66] for nickel-like lasing in Ag, In, Sn, and Sm, at wavelengths of 13.99 nm, 12.59 nm, 11.98 nm, and 7.355 nm, respectively, are shown in Figure 7.20. The Sm laser at 7.355 nm has a smaller angular divergence than silver (1.3 mrad versus 2.8 mrad) and a significantly higher output intensity, 2.5×10^{11} W/cm^2.

The efficiency with which saturation is achieved in these Ni-like lasers has recently been improved by an order of magnitude using picosecond transient inversion techniques combined with a true traveling wave illumination. In these experiments, also at the Rutherford-Appelton Laboratory, MacPhee, Lewis, Pert, and colleagues[67] use a 280 ps FWHM, nominal 10^{13} W/cm^2 prepulse followed 550 ps later by a 3 ps FWHM, nominal 10^{15} W/cm^2 heating pulse (both 1.053 μm wavelength) to drive a transient population inversion. By using off-axis illumination the transient heating pulse travels along the gain medium at the same velocity as

[‖‖] The wavelengths quoted here follow the predicted values of Scofield and MacGowan,[54] and are within the uncertainties of measurements.

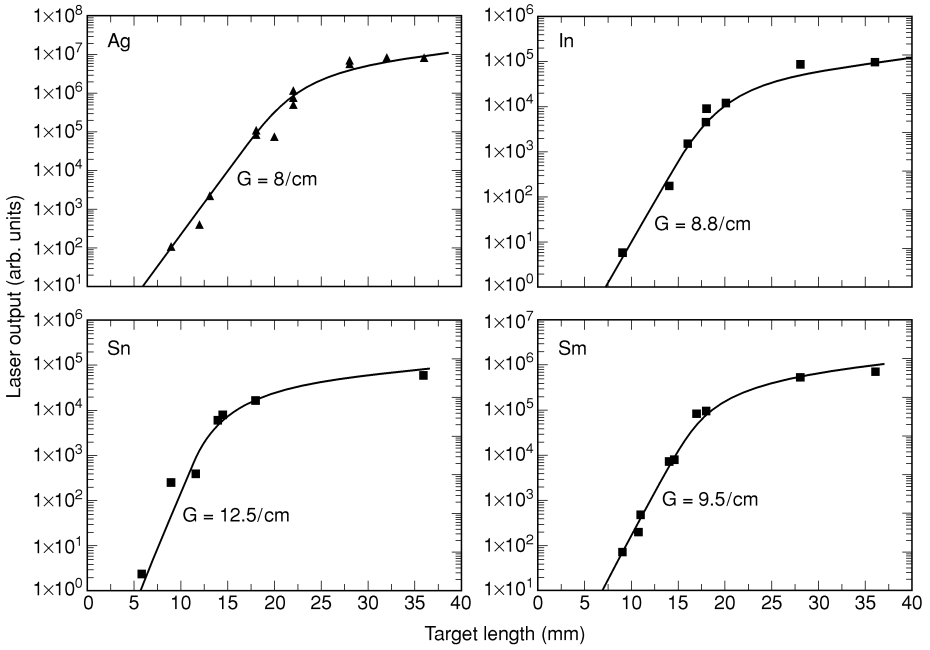

FIGURE 7.20. Laser output versus target length, showing saturation for nickel-like silver (13.99 nm), indium (12.59 nm), tin (11.98 nm), and samarium (7.355 nm). Gains are shown in inverse centimeters. For these experiments refraction compensating double targets were irradiated by a pair of 75 ps, 2×10^{13} W/cm^2 Nd pulses (1.053 μm) separated by 2.2 ns. (Courtesy of J.Y. Lin and colleagues, Rutherford-Appleton Laboratory,[66] with permission of Elsevier Science.)

the exponentially growing short wavelength laser pulse. Using tin coated strips on solid glass targets, very high gains of 31/cm were obtained on the Ni-like Sn line at 11.98 nm wavelength. Full saturation was obtained[67] with a target length of only 1 cm, yielding an output energy of about 60 μJ in a nominal 3 ps duration pulse, for a peak power of order 20 MW. The measured beam divergence was approximately 6 mrad. The total energy input for this experiment was approximately 30 J, most of it in the prepulse. The achievement of saturated lasing with modest pump energy, at these relatively short wavelengths, portends well for the development of table top soft x-ray lasers, especially as further improvements in irradiation efficiency are realized.

7.5 COMPACT EUV LASERS

While relatively large visible and infrared laser drivers are used to form laser produced plasmas for the generation of soft x-ray and EUV laser radiation, discharge tube plasmas provide an alternate route, at least for EUV lasing that may not require as high a density or temperature. Rocca and his colleagues[68–74] at Colorado State University have developed an electrical-discharge-driven EUV laser operating at 46.86 nm wavelength[73] on a 3p to 3s transition ($J = 0$ to 1) in Ne-like argon. The discharge, in a 500–700 mtorr argon gas, is driven by a 70 ns, 37 kA peak current from a 3 nF capacitor. The high current pulse drives a $\mathbf{J} \times \mathbf{B}$ radial compression[74] of the plasma, as shown in Figure 7.21. The discharge occurs through the argon plasma in a 16 cm long, 4 mm diameter capillary tube. Electron densities of $(5–8) \times 10^{18}$ e/cm^3 are obtained, with electron temperatures of 65–90 eV, across a plasma

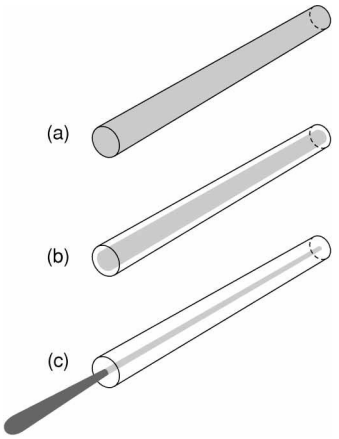

FIGURE 7.21. A fast high current electrical discharge compresses and heats a plasma column for use in EUV laser generation experiments. Current density increases in the sequence from (a) to (b) and (c). The optimum electron density and temperature for lasing are obtained near the end of the compression. (After Rocca et al.[74])

column of order 300 μm diameter. The elongated plasma column thus has an aspect ratio of up to 1000 : 1. Examples of axial emission spectra are shown in Figure 7.22, for plasma lengths of 3, 6, and 12 cm. For the 3 cm plasma length, many lines are observed, including several identified as Al-like (13 electrons) and Mg-like argon (12 electrons). The Ne-like Ar^{+8} $3p \rightarrow 3s$ line is not particularly intense. With a 6 cm plasma length, amplified spontaneous emission has intensified the $3p \rightarrow 3s$ line to prominence. With a 12 cm plasma length the Ne-like Ar^{+8} $3p \rightarrow 3s$ line at 46.86 nm has grown to an intensity one hundred times that of all other lines. The early data matches an exponential gain of about 0.6/cm, giving a gain–length product $GL \simeq 7$. Later experiments achieve a gain coefficient of 1.2/cm and single pass gains larger than[70] $GL = 13$. Single pass saturation[70] is achieved [Figure 7.22(d)] with a 16 cm capillary length yielding an output laser energy of 6 μJ on this line. Use of a normal incidence iridium mirror ($R \simeq 20\%$), permitted double pass experiments that achieved $GL \simeq 28$, with an output energy of 30 μJ at 46.86 nm wavelength, in a 0.8 ns FWHM duration pulse. In more recent experiments, single pulse energies of 130 μJ have been achieved.[70] Near- and far-field images[71] indicate an exit beam size of 150–300 μm diameter (FWHM) and a divergence angle (2θ) of 2–5 mrad (FWHM), with the smaller numbers corresponding to the highest initial argon pressure (750 mtorr). This corresponds to radiation approximately 20–70 times diffraction limited at this wavelength.*** Measurements of spatial coherence, using diffraction from a knife-edge, show expected correlations with column length and discharge parameters.[72] The extension of discharge-driven lasers to shorter wavelengths using Ni-like ions is clearly of interest for future table top experiments.

An alternative approach to compact laser systems is the pursuit of short pulse *transient inversions*, such as that discussed by Nickels et al.[61] earlier, in the section on collisionally pumped neon-like schemes. Transient inversions significantly enhance the efficiency of lasing and thus permit a decreased scale of operation. An important component to such pursuits is that of using femtosecond duration excitation of atoms and ions in what is known as optical field ionization (OFI).[75, 76] OFI involves the application of very high intensity pulses, of order

***See Chapter 8, Eq. (8.5), and the footnote following. For a diffraction limited radiation source of Gaussian spatial distribution and Gaussian far-field angular distribution, the product of source size (d) and divergance angle (2θ) is given in terms of FWHM values as $(d \cdot 2\theta)_{\mathrm{FWHM}} = 0.44\lambda$. For further discussion see the footnote following Eqs. (8–5) in Chapter 8.

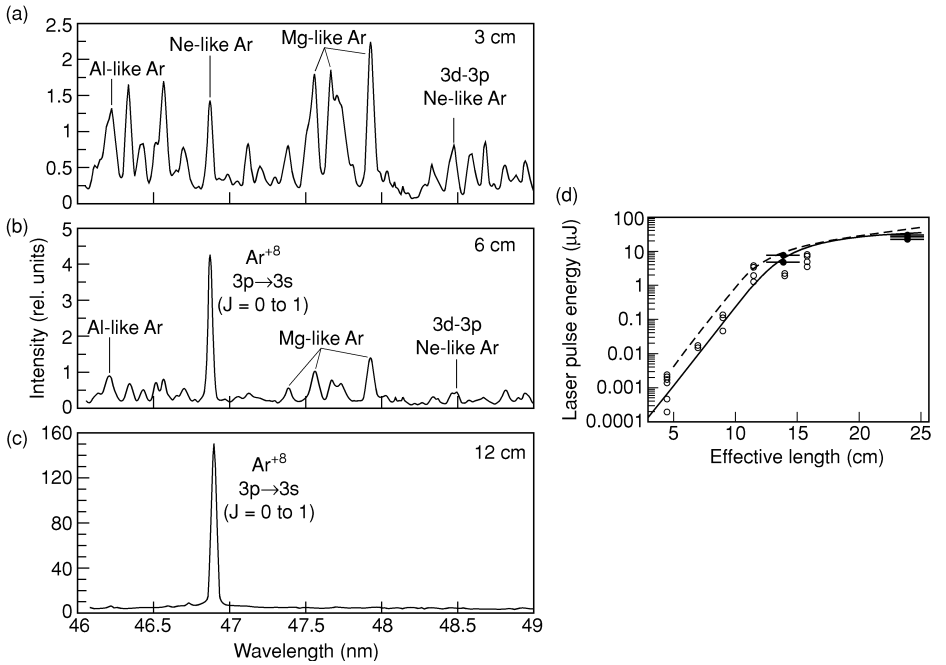

FIGURE 7.22. EUV lasing at 46.86 nm on the 3p → 3s, $J = 0$ to 1 transition in neon-like argon. Axial emission spectra are shown[68] for (plasma) capillary lengths of (a) 3 cm, (b) 6 cm, and (c) 12 cm. Later results extended these experiments to saturation at 16 cm capillary length, with an output energy of 6 μJ in a 0.8 ns FWHM pulse, and a gain–length product $GL \simeq 13$. Double pass experiments, utilizing an iridium mirror, extend this further, to $GL \simeq 28$, with an output energy of 30 μJ at 46.86 nm wavelength (26.46 eV photon energy), also in a 0.8 ns duration pulse. (See Rocca et al.[70, 73]) Recent results have extended the time averaged power to 0.9 mW using a modified capillary and a 7 Hz repetition rate (Courtesy of B.R. Benware, J. Rocca and colleagues, Colorado State University.)

10^{17} W/cm^2, in a pulse of perhaps 20–200 fs. In this fast excitation process a fair fraction of the electrons are accelerated to high energies, into the continuum, but do not become well separated from the parent atom or ion. The technique can lead to very high harmonic generation[77–80] (HHG), as discussed in Chapter 6, but can also be employed in the development of efficient lasing systems, which have the advantage that they radiate their energy in a single emission line.

Pursuits of this approach include that of Lemoff, Harris, and their colleagues[81] at Stanford, who observed lasing at 41.8 nm in Pd-like Xe^{+8}, using nominal 40 fs, 70 mJ, 800 nm wavelength (Ti : sapphire laser) pulses at 10 Hz, focused longitudinally into a Xe gas (5 torr to 12 torr) at an intensity of about 3×10^{16} W/cm^2. The pulse duration in this case is only about 15 cycles, well matched to the OFI model. The kinetic energy of the eight liberated electrons, equal to the quiver energy gained in the high intensity optical field minus the sequentially increased binding energies, ranges from about 9 eV to 550 eV, and thus contributes to the collisional excitation of the remaining bound electrons on the Xe^{+8} ion. Lasing on the 5d to 5p transition is reported at a gain of 13/cm, with a total gain–length product of $GL = 11$.

Nagata, Toyoda, and their colleagues[82] at RIKEN in Japan, and Korobkin, Nam, and Suckewer[83] at Princeton, have pursued lasing to the ground state in hydrogen-like lithium, Li^{+2}. Nagata et al.[82] used double pulse irradiation, a 20 ns prepulse followed by a 500 fs, 10^{17} W/cm^2, 248 nm wavelength pulse, to create an inversion with cylindrical illumination

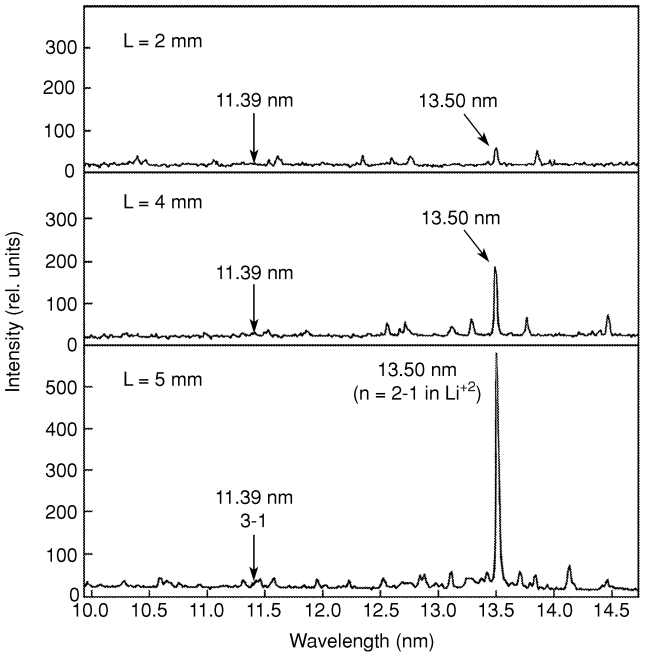

FIGURE 7.23. Axial spectra obtained with femtosecond laser heating of a lithium plasma, in which the $n = 2$ to 1 transition in Li^{+2}, at 13.50 nm wavelength, is observed to grow rapidly out of the noise as the microcapillary length is increased from 2 mm to 5 mm. The 13.50 nm line grows with a gain $G \simeq 11/\text{cm}$, while a nearby non-lasing line ($n = 3$ to 1) at 11.39 nm barely emerges from the noise. (Courtesy of D.V. Korobkin, C.H. Nam, and S. Suckewer, Princeton University.)

of solid targets. Recombination lasing on the Lyman α 2p to 1s transition in Li^{+2} at 13.5 nm wavelength was observed with a modest gain–length product $GL \simeq 4$.

These efforts have been extended by the Princeton group,[83] who improved the efficiency and gain–length product by pumping the plasma axially in a hollowed LiF microcapillary tube, using a modest prepulse followed several hundred nanoseconds later by an intense 250 fs, 248 nm wavelength inversion pump at about 2×10^{17} W/cm^2 and 2 Hz repetition rate. By fully stripping the Li ions by OFI, lasing is then possible by three body recombination to highly excited states on a sub-picosecond time scale. The inversion pulse is nominally 0.25 ps, while the 2p to 1s transition in Li^{+2} has a lifetime of 26 ps, giving stimulated emission a significant time advantage. Figure 7.23 shows the emergence of the $n = 2$ to 1 emission in Li^{+2}, at 13.50 nm wavelength, as a function of microcapillary length. While a nearby $n = 3$ to 1 line at 11.39 nm shows very little growth with increased plasma length from 2 mm to 5 mm, essentially remaining in the noise, the 13.50 nm line grows exponentially with a gain $G \simeq 11/\text{cm}$, for a gain–length product of $GL \simeq 5.5$.

The authors believe that laser waveguiding by the plasma radial density profile plays a significant role in both guiding the high intensity KrF laser pulse and guiding the axially propagating stimulated radiation. Their model derives from the initial plasma formation process in which the relatively low power Nd pulse enters the initially evacuated LiF capillary, causing ablation of plasma from the inner surface, which expands towards the axis. This creates a plasma with lower electron density, and thus higher refractive index (see Chapter 6, Section 6.4.7), on axis. The phase velocity of radiation is thus slower on axis, tending to create a

situation that guides radiation in the axial direction for a relatively long propagation distance. Radiation guiding effects such as this are common at all wavelengths. Such effects have been used for microwave plasma diagnostics, and are critical to future plans for a high gain, short wavelength free electron laser (FEL).

REFERENCES

1. J.P. Gordon, H.J. Zeiger, and C.H Townes, "The Maser – New Type of Microwave Amplifier, Frequency Standard and Spectrometer," *Phys. Rev. 99*, 1264 (1955).
2. N.G. Basov and A.M. Prokhorov, "3-Level Gas Oscillator," *Zh. Eksp. Teor. Fiz. (Moscow), 27*, 431, (1954); also *28*, 249 (1955).
3. A.L. Schawlow and C.H. Townes, "Infrared and Optical Masers," *Phys. Rev. 112*, 1940 (1958); also see C.H. Townes, *How the Laser Happened* (Oxford Univ. Press, 1999).
4. A.M. Prokhorov, "Molecular Amplifier and Generator for Submillimeter Waves," *Zh. Eksperim. Teor. Fiz. (Moscow) 34*, 1658 (1958); also "Quantum Electronics," *Science 149*, 828 (20 August 1965).
5. T. Maiman, "Stimulated Optical Radiation in Ruby," *Nature 187*, 493 (6 August 1960).
6. A. Javan, W.R. Bennett, and D.R. Herriott,"Population Inversion and Continuous Optical Maser Oscillation in a Gas Discharge Containing a He–Ne Mixture," *Phys. Rev. Lett. 6*, 106 (1961).
7. A.D. Siegman, *Lasers* (Univ. Sci. Books, Mill Valley, CA, 1986). In particular see pp. 28–35 regarding the relationship between the field description of stimulated transitions and the resultant coherence and directionality properties of the radiation.
8. M. Sargent, M.O. Scully, and W.E. Lamb, *Laser Physics* (Addison-Wesley, Reading, MA, 1974). In particular, see pp. 38–41 regarding an ensemble of stimulated oscillators and the resultant directionality of the emitted photons.
9. W.T. Silfvast, *Laser Fundamentals* (Cambridge Univ. Press, Cambridge, 1996).
10. D.L. Matthews, P.L. Hagelstein, M.D. Resen, M.J. Eckart, N.M. Ceglio, A.U. Hazi, H. Medecki, B.J. MacGowan, J.E. Trebes, B.L. Whitten, E.M. Campbell, C.W. Hatcher, A.M. Hawryluk, R.L Kauffman, L.D. Pleasance, G. Rambach, J.H. Scofield, G. Stone, and T.A. Weaver, "Demonstration of a Soft X-Ray Amplifier," *Phys. Rev. Lett. 54*, 110 (1985).
11. M.D. Rosen, P.L. Hagelstein, D.L Matthews, E.M. Campbell, A.U. Hazi, B.L. Whitten, B. MacGowan, R.E. Turner, and R.W. Lee, "Exploding-Foil Technique for Achieving a Soft X-Ray Laser," *Phys. Rev. Lett. 54*, 106 (1985).
12. S. Suckewer, C.H. Skinner, H. Milchberg, C. Keane, and D. Voorhees, "Amplification of Stimulated Soft X-Ray Emission in a Confined Plasma Column," *Phys. Rev. Lett. 55*, 1753 (1985).
13. S. Suckewer, D.H. Skinner, D. Kim, E. Valeo, D. Voorhees, and A. Wouters, "Divergence Measurements of Soft X-Ray Laser Beam," *Phys. Rev. Lett. 57*, 1004 (1986).
14. R.C. Elton, *X-Ray Lasers* (Academic Press, San Diego, 1990).
15. P. Jaeglé and A. Sureau, Editors, *X-Ray Lasers* (Editions de Physique, Les Ulis, France, 1986); also see P. Jaeglé, "Vacuum Ultraviolet Lasers," pp. 101–118 in *Vacuum Ultraviolet Spectroscopy I* (Academic, New York, 1998), J.A.R Samson and D.L. Ederer, Editors.
16. G.J. Tallents, Editor, *X-Ray Lasers 1990* (Inst. Phys., Bristol, England, 1990).
17. E.E. Fill, Editor, *X-Ray Lasers 1992* (Inst. Phys., Bristol, England, 1992).
18. D.C. Eder and D.L. Matthews, Editors, *X-Ray Lasers 1994* (Amer. Inst. Phys., New York, 1994).
19. S. Svanberg and C.-G. Wahlström, Editors, *X-Ray Lasers 1996* (Inst. Phys., Bristol, England, 1996).
20. J.J. Rocca and L.B. DaSilva, Editors, *Soft X-Rays Lasers and Applications II* (SPIE, Bellingham, WA, 1997).
21. Y. Kato, H. Takuma, and H. Daido, Editors, *X-Ray Lasers 1998* (Inst. Phys., Bristol, England, 1999).
22. F.E. Irons and N.J. Peacock, "Experimental Evidence for Population Inversion in C^{+5} in an Expanding Laser-Produced Plasma," *J. Phys. B.: Atom. Molec. Phys. (London) 7*, 1109 (1974).

23. R.J. Dewhurst, D. Jacoby, G.J. Pert, and S.A. Ramsden, "Observation of a Population Inversion in a Possible Extreme Ultraviolet Lasing System," *Phys. Rev. Lett. 37*, 1265 (1976).
24. M.H. Key, C.L.S. Lewis, and M.J. Lamb, "Transient Population Inversion at 18.2 nm in a Laser Produced C VI Plasma," *Opt. Comm. 28*, 331 (1979).
25. D. Jacoby, G.J. Pert, S.A. Ramsden, L.D. Shorrock, and G.J. Talents, "Observation of Gain in a Possible Extreme Ultraviolet Lasing System," *Opt. Comm. 37*, 193 (1981).
26. G.J. Pert, "Model Calculations of XUV Gain in Rapidly Expanding Cylindrical Plasmas," *J. Phys. B.: Atom. Molec. Phys. (London) 9*, 3301 (1976); part II, *12*, 2076 (1979).
27. A. Corney, *Atomic and Laser Spectroscopy* (Oxford Univ. Press, Oxford, 1977), pp. 106–115.
28. N.M. Ceglio, D.G. Stearns, D.P. Gaines, A.M. Hawryluk, and J.E. Trebes, "Multipass Amplification of Soft X-Rays in a Laser Cavity," *Opt. Lett. 13*, 108 (1988).
29. Y. Kato, S. Wang, H. Daido, Z. Lin, G. Zhang, Y. Gu, G. Huang, H. Tang, T.Imani, S. Sezaki, S. Hirose, K. Murai, G.-Y. Yoon, T. Jitsuno, M. Takagi, H. Takenaka, K. Mima, and X. Deng, "Generation of Intense X-Ray Laser Radiation at 8 nm in Ni-like Nd Ions," *Proc. SPIE 3156*, 2 (1997).
30. M.D. Rosen and P.L. Hagelstein, "X-Ray Lasing: Theory," p. 2 in *Energy and Technology Review* (Lawrence Livermore National Laboratory, November 1985), UCRL-52000-85-11.
31. G.J. Pert, S.B. Healy, J.A. Plowes, and P.A. Simms, "Effects of Density Structures and Pulse Temporal Shaping," p. 260 in *X-Ray Lasers 1996* (Inst. Phys., Bristol, 1996), S. Svanberg and C.-G. Wahlström, Editors; S.B. Healy, G.F. Cairns, C.L.S. Lewis, G.J. Pert, and J.A. Plowes, "A Computational Investigation of the Ne-like Germanium Collisionally Pumped Laser Considering the Effect of Prepulses," *IEEE J. Select. Top. Quant. Electr. 1*, 949 (1995); J.A. Plowes, G.J. Pert, S.B. Healy, and A. Toft, "Beam Modelling for X-Ray Lasers," *Opt. and Quant. Elect (London) 28*, 219 (1996).
32. J. Zhang, A.G. MacPhee, J. Lin, E. Woflrum, J. Nilson, T.W. Barbee, C. Dansen, M.H. Key, C.L.S. Lewis, D. Neely, R.M.N. O'Rourke, G.J. Pert, R. Smith, G.J. Tallents, and J.S. Wark, "Recent Progress in Nickel-Like X-Ray Lasers at RAL," p. 53 in Ref. 20.
33. Y. Li, P. Lu, J. Maruhn, J. Nilsen, G. Pretzler, and E. Fill, "Study of Prepulse-Induced Ne- and Ni-Like X-Ray Lasers," p. 21 in Ref. 20.
34. T.-N. Lee, S.-H. Kim and H.-J. Shin, "Comparison of X-Ray Lasers and Third Generation Sychrotron Radiation Sources," p. 250 in Ref. 20.
35. G.J. Linford, E.R. Peressini, W.R. Sooy, and M.L. Spaeth, "Very Long Lasers," *Appl. Opt. 13*, 379 (1974).
36. A. Einstein, "Zur Quantentheorie der Strahlung," *Phys. Z. 18*, 121 (1917); English translation, "On the Quantum Theory of Radiation," p. 167 in *The Old Quantum Theory* (Pergamon, Oxford, 1967), D. Ter Haar, Editor.
37. R. Loudon, *The Quantum Theory of Light* (Oxford Univ. Press, Oxford, 1983), Sections 1.5, 2.4, and 2.12.
38. R. L. Liboff, *Introductory Quantum Mechanics* (Addison-Wesley, Reading, MA, 1998), Third Edition, Chapter 13, Sections 7 and 9.
39. A.V. Vinogradov and I.I. Silverman, "On the Possibility of Lasers in the UV and X-Ray Ranges," *Sov. Phys. JETP 36*, 1115 (1973).
40. M.H. Key,"Laboratory Production of X-Ray Lasers," *Nature 316*, 314 (25 July 1985).
41. P. Jaegle, A. Carillon, P. Dhez, G. Jamelot, A. Sureau, and M. Cukier, "Experimental Evidence for the Possible Existence of a Stimulated Emission in the Extreme UV Range," *Phys. Lett. (Netherlands) 36A*, 167 (1971); B. Rus, A. Carillon, P. Dhez, P. Jaeglé, G. Jamelot, A. Klisnick, M. Nantel, and P. Zeitoun, "Efficient, High Brightness Soft X-ray Laser at 21.2 nm," *Phys. Rev. A 55*, 3858 (1997).
42. L.I. Gudzenko and L.A. Shelepin, "Radiation Enhancement in a Recombining Plasma," *Dokl. Akad. Nauk. SSSR 160*, 1296 (1965) [*Sov. Phys. Dokl. 10*, 147 (1965)].
43. S. Suckewer and H. Fishman, "Conditions for Soft X-Ray Lasing Action in a Confined Plasma Column," *J. Appl. Phys. 51*, 1922 (1980).
44. D. Kim, C.H. Skinner, G. Umesh, and S. Suckewer, "Gain Measurements at 18.22 nm in C VI Generated by a Nd : Glass Laser," *Opt. Lett. 14*, 665 (1989).

45. V.A. Bhagavatula and B. Yaakobi, "Direct Observation of Population Inversion Between Al^{+11} Levels in a Laser-Produced Plasma," *Opt. Commun. 24*, 331 (1978).
46. J. Zhang, M.H. Key, P.A. Norreys, G.J. Tallents, A. Behjat, C. Danson, A. Demir, L. Dwivedi. M. Holden, P.B. Holden, C.L.S. Lewis, A.G. MacPhee, D. Neely, G.J. Pert, S.A. Ramsden, S.J. Rose, Y.F. Shao, O. Thomas, F. Walsh, and Y.L. You, "Experiments of High Gain C VI X-Ray Lasing in Rapidly Recombining Plasmas," p. 80 in *X-Ray Lasers 1994* (Amer. Inst. Phys., New York, 1994), D.C. Eder and D.L. Matthews, Editors.
47. D.L. Matthews, M. Eckart, D. Eder, P. Hagelstein, A. Hazi, R. London, B. MacGowan, S. Maxon, D. Nilson, T. Phillips, M. Rosen, J. Scofield, G. Shimkaveg, R. Stewart, J. Trebes, D. Whelen, B. Whitten, J. Woodworth, and S. Brown, "Review of Livermore's Soft X-Ray Laser Program," p. C6-1 in *X-Ray Lasers* (J. de Physique, Tome 47, Editions de Physique, Les Udis, France, 1986), P. Jaelge and A. Sureau, Editors.
48. M.D. Rosen J.E. Trebes, B.J. MacGowan, P.L. Hagelstein, R.A. London, D.L. Matthews, D.G. Nilson, T.W. Phillips, and D.A. Whelen, "Dynamics of Collisional-Excitation X-Ray Lasers," *Phys. Rev. Lett. 59*, 2283 (1987).
49. B.J. MacGowan, M.D. Rosen, M.J. Eckart, P.L. Hagelstein, D.L. Matthews, D.G. Nilson, T.W. Phillips, J.H. Scofield, G. Shimkaveg, J.E. Trebes, R.S. Walling, B.L. Witten, and J.G. Woodworth, "Observation of Soft X-Ray Amplification in Neon-like Molybdenum," *J. Appl. Phys. 61*, 5243 (1987).
50. B.J. MacGowan, S. Maxon, P.L. Hagelstein, C.J. Keane, R.A. London, D.L. Matthews, M.D. Rosen, J.H. Scofield, and D.A. Whelan, "Demonstration of Soft X-Ray Amplification in Nickel-like Ions," *Phys. Rev. Lett. 59*, 2157 (1987).
51. B.J. MacGowan, S. Maxon, L.B. DaSilva, D.J. Fields, C.J. Keane, D.L. Matthews, A.L. Osterheld, J.H. Scofield, G. Shimkaveg, and G.F. Stone, "Demonstration of X-Ray Amplifiers Near the Carbon K Edge," *Phys. Rev. Lett. 65*, 420 (1990).
52. B.J. MacGowan, L.B. DaSilva, D.J. Fields, C.J. Keane, J.A. Koch, R.A. London, D.L. Matthews, S. Maxon, S. Mrowka, A.L. Osterheld, J.H. Scofield, G. Shimkaveg, J.E. Trebes, and R.S. Walling, "Short Wavelength X-Ray Laser Research at the Lawrence Livermore National Laboratory," *Phys. Fluids B 4*, 2326 (1992).
53. J. Nilsen and J. Scofield, "Wavelengths of Neon-like 3p $\rightarrow$ 3s X-Ray Laser Transitions," *Phys. Scripta 49*, 558 (1994).
54. J.H. Scofield and B.J. MacGowan, "Energies of Nickel-like 4d to 4p Laser Lines," *Phys. Scripta, 46*, 361 (1992).
55. R.A. London, M.D. Rosen, and J.E. Trebes, "Wavelength Choice for Soft X-Ray Laser Holography of Biological Samples," *Appl. Opt. 28*, 3397 (1989).
56. J.A. Koch, B.J. MacGowan, L.B. DaSilva, D.L. Matthews, J.H. Underwood, P.H. Baton, and S. Mrowka, "Observation of Gain-Narrowing and Saturation Behavior in Se X-Ray Laser Line Profiles," *Phys. Rev. Lett. 68*, 3291 (1992).
57. J.A. Koch, B.J. MacGowan, L.B. DaSilva, D.L. Matthews, J.H. Underwood, P.H. Batson, R.W. Lee, R.A. London, and S. Mrowka, "Experimental and Theoretical Investigation of Neon-like Selenium X-Ray Laser Spectral Linewidths and Their Variation with Amplification," *Phys. Rev. A 50*, 1877 (1994).
58. A.V. Vinogradov and V.N. Shlyaptsev, "Amplification of Ultraviolet Radiation in a Laser Plasma," *Kvant. Elektr. (Moscow) 10*, 2325 (1983); *Sov. J. Quant. Electr. 13*, 1511, (1983).
59. R.L. Kelly, *Atomic and Ionic Spectrum Lines Below 2000 Angstroms: Hydrogen through Krypton, Part II (Mn–Kr)* (Amer. Inst. Phys., New York, 1987), published as *J. Phys. Chem. Ref. Data 16*, Suppl. 1 (1987). See p. 1332.
60. T.N. Lee, E.A. McLean, and R.C. Elton, "Soft X-Ray Lasing in Neon-Like Germanium and Copper Plasmas," *Phys. Rev. Lett. 59*, 1185 (1987).
61. P.V. Nickels, V.N. Shlyaptsev, M. Kalachnikov, M. Schnürer, I. Will, and W. Sander, "Short Pulse X-Ray Laser at 32.6 nm Based on Transient Gain in Ne-Like Titanium," *Phys. Rev. Lett. 78*, 2748 (1997).
62. B.J. MacGowan, L.B. DaSilva, D.J. Fields, A.R. Fry, C.J. Keane, J.A. Koch, D.L. Matthews,

S. Maxon, S. Mrowka, A.L. Osterheld, J.H. Scofield, and G. Shimkaveg, "Short Wavelength Nickel-Like X-Ray Laser Development," p. 221 in Ref. 16.

63. S. Wang, Z. Lin, Y. Gu, G. Huang, H. Tang, D. Ximing, G. Zhang, Y. Kato, H. Daido, T. Imani, S. Sezaki, S. Hirose, G.-Y. Yoon, T. Jitsuno, M. Takagi, K. Mima, K. Murai, and H. Takenaka, "Intense Nickel-Like Neodymium X-Ray Laser at 7.9 nm with a Double-Curved Slab Target," *Jpn. J. Appl. Phys. Lett. 37,* L1 234 (1998).
64. S. Sebban, N. Sakaya, H. Daido, Y. Kato, K. Murai, A. Klisnick, P. Zeitoun, H. Tang, Y. Gu, G. Huang, S. Wang, A Kashihara, Y. Takigawa, T. Desai, and H. Takenaka, "Optimization of a Ni-Like Silver Collisional Soft X-Ray Laser Using Prepulse Technique and Double Target Geometry," in *X-Ray Lasers 1998* (Inst. Phys., Bristol, England, 1999), K. Kato, H. Takuma, and H. Daido, Editors.
65. J. Zhang, A.G. MacPhee, J. Nilsen, J. Lin, T.W. Barbee, C. Danson, M.H. Key, C.L.S. Lewis, D. Neely, R.M.N. O'Rourke, G.J. Pert, R. Smith, G.J. Tallents, J.S. Wark, and E. Wolfrum, "Demonstration of Saturation in a Ni-Like Ag X-Ray Laser at 14 nm," *Phys. Rev. Lett. 78*, 3856 (1997).
66. J.Y. Lin, G.J. Tallents, J. Zhang, A.G. MacPhee, C.L.S. Lewis, D. Neely, J. Nilsen, G.J. Pert, R.M.N. O'Rourke, R. Smith, and E. Wolfrum, "Gain Saturation of Ni-Like X-Ray Lasers," *Opt. Commun. 158*, 55 (1998); R. Smith et al., *Phys. Rev. A 59*, R47 (1999).
67. A.G. MacPhee, C.L.S. Lewis, R.M.N. O'Rourke, A. Demir, G.J. Tallents, D. Neely, D. Ros, Ph. Zeitoun, S.P. McCabe, and G.J. Pert, "Transient Gain in Ni-Like X-Ray Lasers," *Phys. Rev. A* (to be published).
68. J.J. Rocca, V. Shlyaptsev, F.G. Tomasel, O.D. Cortázar, D. Hartshorn, and J.L.A. Chilla, "Demonstration of a Discharge Pumped Table-Top Soft X-Ray Laser," *Phys. Rev. Lett. 73*, 2192 (17 October 1994).
69. J.J. Rocca, M.C. Marconi, J.L.A. Chilla, D.P. Clark, F.G. Tomasel, and V.N. Shlyaptsev, "Discharge-Driven 46.9 nm Amplifier with Gain–Length Approaching Saturation," *IEEE J. Sel. Top. Quant. Electr. 1*, 945 (1995).
70. J.J. Rocca, D.P. Clark, J.L.A. Chilla, and V.N. Shlyaptsev, "Energy Extraction and Achievement of the Saturation Limit in a Discharge-Pumped Table-Top Soft X-Ray Amplifier," *Phys. Rev. Lett. 77*, 1476 (1996); B.R. Benware, C.D. Macchieto, C.H. Moreno, and J.J. Rocca, "Demonstration of a High Average Power Table-Top Soft X-Ray Laser," *Phys. Rev. Lett. 81*, 5804 (1998).
71. C.H. Moreno, M.C. Marconi, V.N. Shlyaptsev, B.R. Benware, C.D. Macchietto, J.L.A. Chilla, J.J. Rocca, and A.L. Osterheld, "Two-Dimensional Near-Field and Far-Field Imaging of a Ne-like Ar Capillary Discharge Table-Top Soft X-Ray Laser," *Phys. Rev. A 58*, 1509 (1998).
72. M.C. Marconi, J.L.A. Chilla, C.H. Moreno, B.R. Benware, and J.J. Rocca, "Measurement of the Spatial Coherence Buildup in a Discharge Pumped Table-Top Soft X-Ray Laser," *Phys. Rev. Lett. 79*, 2799 (1997).
73. J.J. Rocca, F.G. Tomasel, M.C. Marconi, V.N. Shlyaptsev, J.L.A. Chilla, B.T. Szapiro, and G. Guidice, "Discharge-Pumped Soft X-Ray Laser in Neon-Like Argon," *Phys. Plasmas 2*, 2547 (1995).
74. J.J. Rocca, O.D. Cortázar, B. Szapiro, K. Floyd, and F.G. Tomasel, "Fast-Discharge Excitation of Hot Capillary Plasmas for Soft X-Ray Amplifers," *Phys. Rev. E 47*, 1299 (1993).
75. P.B. Corkum and N.H. Burnett, "Multiphoton Ionization for the Production of X-Ray Laser Plasmas," p. 225 in *OSA Proceedings on Short Wavelength Coherent Radiation: Generation and Applications* (OSA, Washington, DC, 1988), R.W. Falcone and J. Kirz, Editors.
76. P.B. Corkum, "Plasma Perspective on Strong-Field Multiphoton Ionization," *Phys. Rev. Lett. 71*, 1994 (1993).
77. Ch. Spielman, N.H. Burnett, S. Sartania, R. Koppitsch, M. Schnürer, C. Kan, M. Lenzner, P. Wobrauschek, and F. Krausz, "Generation of Coherent X-Rays in the Water Window Using 5-Femtosecond Laser Pulses," *Science 278*, 661 (1997).
78. A. Rundquist, C.G. Durfee, Z. Chang, C. Herne, S. Backus, M.M. Murnane, and H.C. Kapteyn, "Phase-Matched Generation of Coherent Soft X-Rays," *Science 280*, 1412 (1998).
79. K.J. Schafer and K.C. Kulander, "High Harmonic Generation from Ultrafast Pump Lasers," *Phys. Rev. Lett. 78*, 638 (1997).
80. A. L'Huillier and Ph. Balcou, "High Order Harmonic Generation in Rare Gases with a 1-ps 1053-nm Laser," *Phys. Rev. Lett. 70*, 774 (1993).

81. B.E. Lemoff, G.Y. Yin, C.L. Gordon, C.P.J. Barty, and S.E. Harris, "Demonstration of a 10 Hz Femtosecond-Pulse-Driven XUV Laser at 41.8 nm in Xe IX," *Phys. Rev. Lett. 74*, 1574 (1995).
82. Y. Nagata, K. Midorikawa, S. Kubodera, M. Obara, H. Tashiro, and K. Toyoda, "Soft X-Ray Amplification of the Lyman-α Transition by Optical-Field-Induced Ionization," *Phys. Rev. Lett. 71*, 3774 (1993).
83. D.V. Korobkin, C.H.Nam, and S. Suckewer, "Demonstration of Soft X-Ray Lasing to Ground State in Li III," *Phys. Rev. Lett. 77*, 5206 (23 December 1996).
84. Yu.A. Uspenskii, V.E. Levashov, A.V. Vinogradov, A.I. Fedorenko, V.V. Kondratenko, Yu.P. Pershin, and E.N. Zubarev, "High Reflectivity Multilayer Mirrors for a Vacuum-Ultraviolet Interval of 35–50 nm," *Opt. Lett. 23*, 771 (1998).

HOMEWORK PROBLEMS

Homework problems for each chapter will be found at the website:
http://www.coe.berkeley.edu/ AST/sxreuv

Chapter 8

COHERENCE AT SHORT WAVELENGTHS

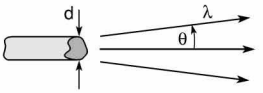

$$l_{\mathrm{coh}} = \lambda^2/(2\,\Delta\lambda) \text{ [temporal (longitudinal) coherence]} \tag{8.3}$$

$$d \cdot \theta = \lambda/2\pi \text{ [spatial (transverse) coherence]} \tag{8.5}$$

$$\text{or } d \cdot 2\theta\big|_{\mathrm{FWHM}} = 0.44\,\lambda \tag{8.5*}$$

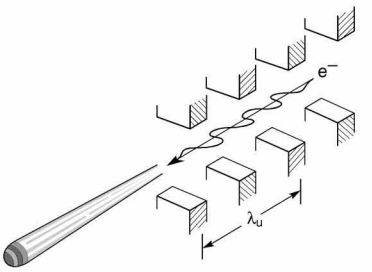

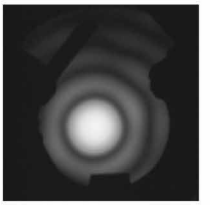

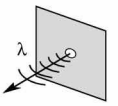

$$\bar{P}_{\mathrm{coh},N} = \frac{(\lambda/2\pi)^2}{(d_x\theta_x)(d_y\theta_y)}\,\bar{P}_{\mathrm{cen}} \tag{8.6}$$

$$\bar{P}_{\mathrm{coh},\lambda/\Delta\lambda} = \frac{e\lambda_u I\eta(\Delta\lambda/\lambda)N^2}{8\pi\epsilon_0 d_x d_y} \cdot \left[1 - \frac{\hbar\omega}{\hbar\omega_0}\right] f(K) \tag{8.9}$$

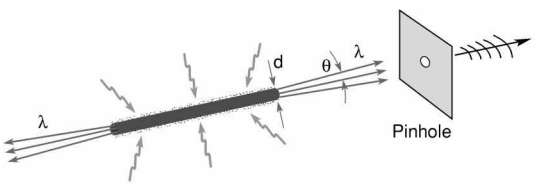

$$P_{\mathrm{coh}} = \frac{(\lambda/2\pi)^2}{(d_x\theta_x)(d_y\theta_y)}\,P_{\mathrm{laser}} \tag{8.11}$$

Whereas spatially and temporally coherent radiation is plentiful at visible wavelengths due to the availability of lasers, it is just becoming available at shorter wavelengths. In this chapter we review the concepts of spatial and temporal coherence, some applications that require radiation with these properties, and methods to generate spatially and spectrally filtered radiation at extreme ultraviolet, soft x-ray, and x-ray wavelengths.

8.1 CONCEPTS OF SPATIAL AND TEMPORAL COHERENCE

The ability to focus radiation to the smallest possible spot size, to propagate it great distances with minimal divergence, to encode wavefronts, and in general to form interference patterns, requires well-defined phase and amplitude variations of the fields throughout the regions of interest. In general, simple phase distributions approaching those of plane or spherical waves are of greatest interest in those applications. Real laboratory sources, especially at very short wavelengths, generally radiate fields with more complex phase relationships that are well defined over only limited spatial and temporal scales. This brings us to the subject of coherence, its technical definition, and various convenient measures.

Coherence in our daily lives refers to a systematic connection or logical relationship between events, actions, or policies. In physics the word implies similar relationships among the complex field amplitudes used to describe electromagnetic radiation. Mathematically, one utilizes a *mutual coherence function*, Γ, as a measure of the degree to which the electric field at one point in space can be predicted, if known at some other point, as a function of their separation in space and time[1, 2]:

$$\Gamma_{12}(\tau) \equiv \langle E_1(t+\tau)E_2^*(t)\rangle \tag{8.1}$$

where in this scalar form E_1 and E_2 are the electric fields at points 1 and 2, and τ is the time delay. The angular brackets denote an expectation value, or a time average of the indicated product. It is often convenient to introduce a normalized *complex degree of coherence*, γ_{12}, again in scalar form, as

$$\gamma_{12}(\tau) = \frac{\Gamma_{12}(\tau)}{\sqrt{\langle|E_1|^2\rangle}\sqrt{\langle|E_2|^2\rangle}} \tag{8.2}$$

where the normalizing factors in the denominator are clearly related to the local intensities at the respective points, as was discussed in Chapter 2, Section 2.3. Thus, for example, in the case of a uniform plane wave, of very well-defined frequency, if the electric field is known at any given space–time point, it can be predicted everywhere else with certainty. As we quantify this later for real physical systems, we will consider this uniform plane wave as *coherent radiation*, meaning that $|\gamma| = 1$ everywhere. The counterexample would be one in which there were a large number of atoms moving randomly and radiating independently, at various frequencies, so that fields at the two separated points have almost no relationship. In this case the resultant degree of coherence, μ, approaches zero, and the fields are considered *incoherent*.

One could write similar functions to describe amplitude and phase correlations in other physical systems. For a well-behaved water wave, for instance, one would expect the surface amplitude to be predictable over great distances, so that $|\gamma|$ would be near unity, implying a high degree of coherence, over much of the observed field. On the other hand, the introduction of randomly thrown pebbles would create a jumble of uncorrelated disturbances, so that $|\gamma|$

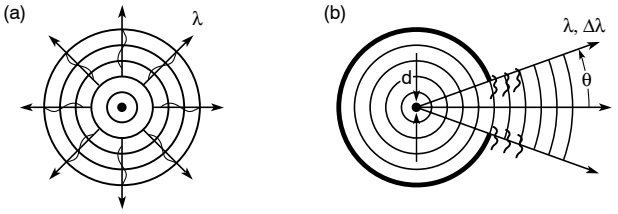

FIGURE 8.1. (a) Fully coherent radiation from a point source oscillator, which oscillates for all time. Note the circular or spherical nature of the outgoing waves. (b) Partially coherent radiation from a source of finite size, emission angle, and duration. Note that the outgoing radiation only approximates circular or spherical waves.

would approach zero in the immediate vicinity, leading us to conclude that the fields in this vicinity were largely incoherent.

To introduce the concept of a *coherence region*, we consider first the rather visual example of soldiers marching across a field. The coherent limit corresponds to all the soldiers in perfect step. In the presence of a strong wind, however, some soldiers might not hear the leader calling the cadence. In this case those soldiers close enough to hear would remain in step, while those further away would become out of step – so there would be a region of coherence near the leader. The distance over which there is a reasonable expectation that the soldiers were marching in step could be called a "coherence length." Note that the coherence length need not be the same in all directions, in this case being dependent on wind direction. The complete absence of cadence would result in uncorrelated stepping, a state of incoherence where $|\gamma|$ goes to zero for the smallest separations, and where the coherence length is essentially zero. In the following paragraphs we will attempt to provide measures of the distances over which electromagnetic fields can be expected to be well correlated, and thus useful for interference experiments as discussed in the first paragraph of this chapter.

In the theoretical limit of a point source oscillating at a single frequency for all time, from minus infinity to plus infinity, the radiated field quantities would be perfectly correlated everywhere. That is, if one knew the electric field amplitude and phase at a given point and time, one would know these quantities at all points and for all time. In this limiting case the radiation field is said to be *coherent*. Real physical sources, however, are made up of spatially distributed radiators that emit with a finite spectral bandwidth for a finite period of time. Consequently, well-defined phase relationships between field amplitudes are in practice restricted to a finite *region of coherence*.

Real sources are neither fully coherent nor fully incoherent, but rather are *partially coherent*.[1] In Figure 8.1(a) the point source radiates fields that are perfectly correlated, and thus coherently related everywhere. In Figure 8.1(b) a source of finite size and spectral bandwidth, restricted to radiate over a limited angular extent, generates fields with strong phase and amplitude correlation over only a limited extent. This brings us again to notions of "regions of coherence" and "coherence time": that is, spatial and temporal measures over which the fields are well correlated. In cases where there is a well-defined direction of propagation, it is convenient to decompose the region of coherence into orthogonal components, one in the direction of propagation and one transverse to it, as illustrated in Figure 8.2. Throughout the remainder of this chapter we will confine ourselves to the subject of partially coherent radiation in which there is a relatively well-defined direction of energy transport.

In the direction of propagation it is common to introduce a longitudinal, or *temporal*, coherence length l_{coh} over which phase relationships are maintained. For a source of bandwidth

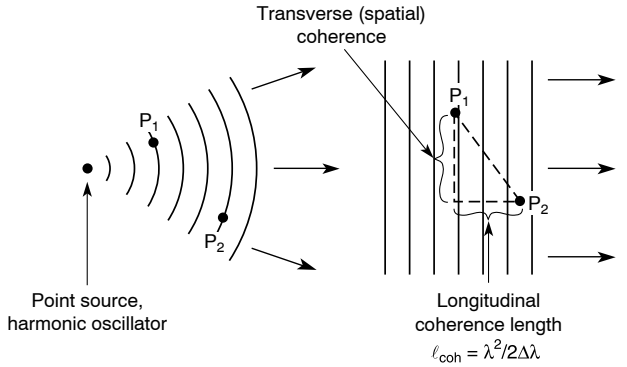

FIGURE 8.2. Transverse and longitudinal coherence.

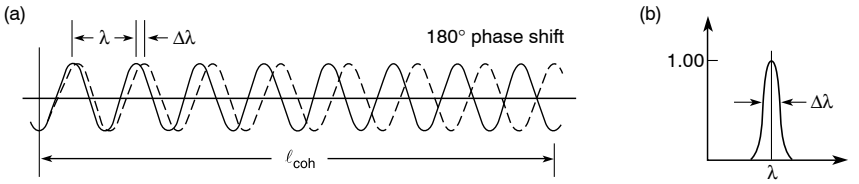

FIGURE 8.3. (a) Spectral bandwidth and (b) coherence length: destructive interference due to finite spectral bandwidth for radiation of wavelength λ and spectral bandwidth $\Delta\lambda$.

$\Delta\lambda$, one can define a coherence length

$$l_{\text{coh}} = \frac{\lambda^2}{2\,\Delta\lambda} \tag{8.3}$$

where $\Delta\lambda$ is the spectral width, as discussed by several authors.[2, 3] The relationship between longitudinal coherence length (e.g., in the direction of propagation) and spectral bandwidth is illustrated in Figure 8.3. Here the coherence length is taken as that distance that results in two waves, of wavelength difference just equal to the bandwidth $\Delta\lambda$, becoming 180° out of phase. Over such a distance one would expect the waves emanating from a source of continuous spectral width to become largely uncorrelated, and thus not contribute significantly to a well-defined interference pattern. Equation (8.3) follows from Figure 8.3 on writing $l_{\text{coh}} = N\lambda$ for the first wave and $l_{\text{coh}} = (N - \frac{1}{2})(\lambda + \Delta\lambda)$ for the spectrally shifted wave, which executes one-half less oscillation (one-half fewer wavelengths) to travel the same distance, and then equating the two to solve for the "number of waves of coherence," $N = \lambda/(2\,\Delta\lambda)$. Equation (8.3) then follows on multiplying N by the wavelength, giving the coherence length for which radiation of continuous bandwidth $\Delta\lambda$ becomes substantially dephased. The resultant numerical factor of $\frac{1}{2}$ appearing in Eq. (8.3) is somewhat arbitrary as obtained here, as it depends on the criteria selected. The numerical factors' dependence on spectral line shape is discussed by Goodman[2] in his Section 5.1.3. In the experimental formation of interference (fringe) patterns by amplitude dissection (e.g., using a beamsplitter) and recombination, as in interferometry[1] and holography,[3] it is essential that differences in propagation length

be less than the coherence length; otherwise high contrast interference patterns will not be obtained.

Transverse, or *spatial*, coherence is related to the finite source size and the characteristic emission (or observation) angle of the radiation. In this case one is interested in phase correlation in planes orthogonal to the direction of propagation. It is instructive to consider the relationship of spatial coherence to spherical waves in the limit of phase being perfectly correlated everywhere. Clearly this limit corresponds to concentric spherical waves with constant phase across every spherical surface and with phase maxima separated by a wavelength in the outward propagation direction. Although somewhat restrictive, we consider the spherical case because it is common to our experience and yields a clear physical insight. Again we consider only a small portion of the spherical wave propagating in a relatively well-defined direction. With some appropriate bandwidth, and thus finite coherence length, such a spherical wave could provide a reference wave for encoding complex wavefronts, as in holography. Near-spherical waves can be focused to a spot size approaching finite wavelength limits, as in a scanning microscope, or collimated to travel with minimal divergence for use in precision diffraction experiments.

Full spatial coherence, the situation in which phase is perfectly correlated at all points transverse to the propagation direction, can be achieved with a spherical wavefront, which we associate with a point source. We might then ask, "How small is a point source?" or more accurately, "How small must the source be to produce wavefronts suitable for our purpose?" and "How small must our undulator electron beam or x-ray laser aperture appear to be in order to provide spatially coherent radiation?" We can obtain a simple estimate based on Heisenberg's uncertainty principle

$$\Delta\mathbf{x} \cdot \Delta\mathbf{p} \geq \hbar/2 \tag{8.4}$$

Here $\Delta\mathbf{x}$ is the uncertainty in position and $\Delta\mathbf{p}$ the uncertainty in momentum, both being single-sided rms ($1/\sqrt{e}$) measures of Gaussian probability distributions.[4] Using Eq. (8.4), we can determine the smallest source size d resolvable with finite wavelength λ and observation half angle θ. For photons the momentum is $\hbar\mathbf{k}$, where the scalar wavenumber $|\mathbf{k}|$ is $2\pi/\lambda$. If the relative spectral bandwidth $\Delta\lambda/\lambda$, which is equal to $\Delta k/k$, is small, then the uncertainty in momentum, $\Delta\mathbf{p} = \hbar\,\Delta\mathbf{k}$, is due largely to the uncertainty in direction θ, so that for small angles $|\Delta\mathbf{p}| = \hbar k\,\Delta\theta$. Substituting into the uncertainty relation (8.4)

$$\Delta x \cdot \hbar k\,\Delta\theta \geq \hbar/2$$

and noting that $k = 2\pi/\lambda$, one has

$$\Delta x \cdot \Delta\theta \geq \lambda/4\pi$$

Identifying the source diameter as $d = 2\,\Delta x$ and the divergence half angle θ with the uncertainty $\Delta\theta$, as illustrated in Figure 8.4, we obtain the limiting relationship[5–7]

$$\boxed{d \cdot \theta = \lambda/2\pi} \tag{8.5}$$

which determines the smallest source size we can discern; that is, within the constraints of physical law we would not be able to tell if our "point" source were any smaller. We recall from Eq. (8.4) that this relationship is for Gaussian rms quantities (d and θ). For non-rms

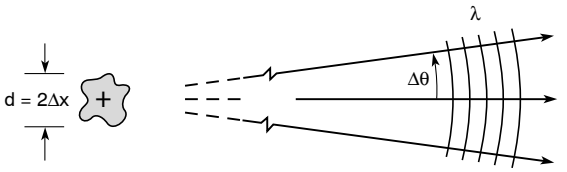

FIGURE 8.4. Spherical wavefronts and spatially coherent radiation are approached when the source size and far-field divergence angle are related to wavelength as indicated in Eq. (8.5).

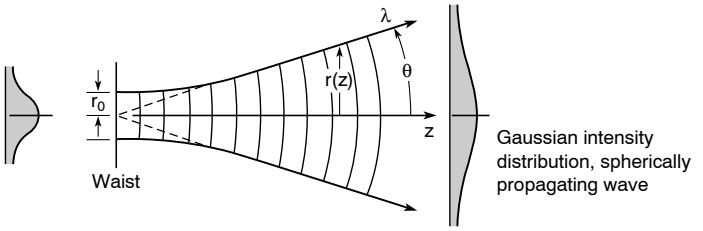

FIGURE 8.5. Propagation of a Gaussian beam.

measures the numerical factor $(1/2\pi)$ will be different.* Radiation satisfying the equality (8.5) is said to be *diffraction limited* – that is, limited by the finite wavelength and observation angle (or numerical aperture θ). To generate a spatially coherent spherical wave we must develop a source – at x-ray wavelengths – that approaches the limiting values set by Eq. (8.5). For symmetry purposes some researchers prefer to introduce a "spatial coherence length," rather than θ. This would clearly depend on distance z from the source; e.g., if one defines $l_{\text{transverse}} \equiv z\theta$, one has

$$l_{\text{transverse}} = \frac{z\lambda}{2\pi d}$$

In this text, we will confine ourselves to the use of the space–angle relationship given in Eq. (8.5).

For comparison, a laser radiating in a single transverse mode TEM_{00} satisfies this same condition when the waist diameter d and far-field divergence half angle θ are written in terms of rms quantities, as illustrated in Figure 8.5. For a spherical wave propagating with a Gaussian intensity distribution, $I/I_0 = \exp(-r^2/2r_0)$, where r_0 is the $1/\sqrt{e}$ waist radius at the origin $(z = 0)$, the intensity distribution grows with a $1/\sqrt{e}$ radius given by[5, 6]

$$r(z) = r_0\sqrt{1 + \left(\frac{\lambda z}{4\pi r_0^2}\right)^2}$$

Thus in the far field, where $z \gg 4\pi r_0^2/\lambda$, the $1/\sqrt{e}$ divergence half angle is

$$\theta \equiv \frac{r(z)}{z} = \frac{\lambda}{4\pi r_0}$$

*For Gaussian intensity distributions measured in terms of FWHM diameter (d) and FWHM angle (2θ), the equivalent relation is $(d \cdot 2\theta)_{\text{FWHM}} = \frac{2\ln 2}{\pi}\lambda = 0.441\lambda$, or approximately $\lambda/2$.

With a waist diameter $d = 2r_0$, this TEM_{00} laser cavity mode exhibits a waist diameter times far-field divergence half angle (both in terms of $1/\sqrt{e}$ measures) given by

$$d \cdot \theta = \frac{\lambda}{2\pi}$$

as found previously in Eq. (8.5) on the basis of Heisenberg's uncertainty principle.

In summary, we now have two convenient relationships by which to gauge the coherence properties of a radiation field for the purpose of conducting phase sensitive interference experiments, Eqs. (8.3) and (8.5):

$$l_{\text{coh}} = \frac{\lambda^2}{2\,\Delta\lambda} \qquad \text{(temporal or longitudinal coherence)}$$

and

$$d \cdot \theta = \lambda/2\pi \qquad \text{(spatial or transverse coherence)}$$

In the next section we will use these measures to determine what fraction of radiated power, or photon flux, from a given source is useful for experiments requiring spatially or temporally coherent radiation within required bounds.

8.2 EXAMPLES OF EXPERIMENTS THAT REQUIRE COHERENCE

As discussed in the preceding section, radiation from a real physical source cannot be truly coherent, because of both the finite spectral width and the finite physical extent. Nonetheless, in many experiments we require a high degree of coherence across only a limited region, and as a consequence may wish to employ spatial and temporal filtering techniques. For example, if one wishes to focus radiation to the smallest possible spot size, at a given wavelength (λ) and lens numerical aperture, the lens must be coherently illuminated, as illustrated in Figure 8.6.

Such focusing is essential for the achievement of highest spatial resolution in a scanning x-ray microscope, a topic we take up in Chapter 9. The advantage of scanning x-ray microscopy is that it is capable of achieving significantly smaller focal spots than are achievable with visible or ultraviolet radiation, and thus it is becoming a widely used tool for the study of material surfaces, chemical fibers, and biological materials. For the case of the smallest possible focal spot size, the lens forms a wavelength-limited image of the source. This process is referred to as *diffraction limited* focusing because the intensity distribution in the focal region is limited by the finite wavelength and lens numerical aperture, rather than the actual source size. This is, of course, a limiting case. For a larger source size the image would simply be demagnified by the ratio $M = q/p$, where q is the source to lens distance, p is the lens to image distance, and these are related to the lens focal length f by the reciprocal thin lens equation $1/f = 1/p + 1/q$. In the diffraction limited case, however, the source size d is sufficiently small that the radiation intercepted by the lens (see θ in Figure 8.6) approximately satisfies the spatial coherence condition set by Eq. (8.5), or its equivalent. In this case the focal

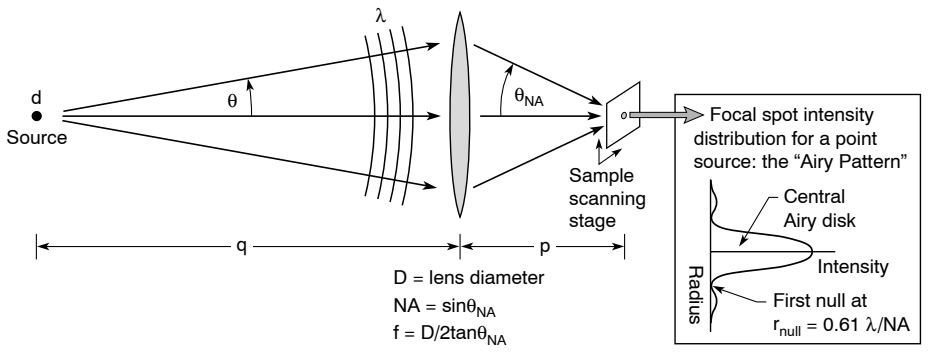

FIGURE 8.6. Diffraction limited focusing – that is, limited only by the finite wavelength and lens numerical aperture (NA) – requires a perfect lens and coherent illumination. The refractive lens shown is for illustration only. At x-ray wavelengths this would require diffractive or reflective optics, such as a Fresnel zone plate or a multilayer coated spherical mirror. In a scanning microscope a sample would be placed at the focus and raster scanned with a suitable translation stage while observing an appropriate signal such as transmitted x-rays, fluorescent emission of characteristic radiation, or photoelectrons. The spatial resolution of the measurement would be set by the focal spot size, assuming this is not compromised by lens imperfections, mounting-related aberrations, improper illumination, or scanning stage limitations such as placement accuracy or non-uniform dwell times.

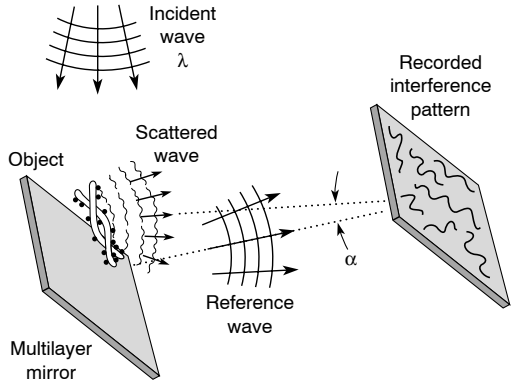

FIGURE 8.7. A possible approach to off-axis x-ray holography, which would require spatially and temporally coherent radiation to achieve high contrast interference patterns.

region intensity pattern approximate an Airy pattern,[1,8] with a focal region radius to the first null given by $0.61\lambda/\mathrm{NA}$. The fact that this is a spherical wave illumination, rather than a plane wave illumination, simply moves the focal plane to a conjugate point determined by the thin lens equation for finite source distance q. Departures from spatially coherent illumination of the lens, due to finite source size and divergence, are addressed in Section 8.6.

A second example in which coherence plays an important role is that of encoding complex wavefronts, as in holography.[3] A typical setup, such as might be used with a weak x-ray scattering object, is shown in Figure 8.7. The incident wave is shown illuminating a flat mirror and a nearby object. After reflection from the multilayer mirror, the radiation propagates

toward the recording medium, and is referred to now as the *reference wave*. In the presence of a weakly scattering object, secondary radiation is scattered in all directions, although Figure 8.7 shows only that portion directed toward the recording plane.

To form an interference pattern in the plane of the recording medium, the reference and scattered waves must maintain a time averaged phase relation, that is, the detected fields must at every point in this plane have a complex degree of coherence [Eq. (8.2)] of order unity, or some fraction thereof, in order to form a recordable interference pattern. Because a complex object, such as the double stranded structure in Figure 8.7, redirects radiation at various angles, leading to a complex jumble of interacting waves at the detector, it is essential that the incident and reference wavefronts maintain a simple variation across the field, such as with the spherical wavefront invoked for development of the spatial coherence condition [Eq. (8.5)], so as to provide a clear mechanism for wavefront encoding and subsequent decoding, or reconstruction, with a similar spherical wavefront. Furthermore, to ensure high contrast encoding (interference) it is essential that all path lengths from the source (not shown) to the detector be equal to within a longitudinal coherence length [Eq. (8.3)], $l_{coh} = \lambda^2/(2\,\Delta\lambda)$, whether that path involves a reflection from the mirror or scattering from the object. The latter condition must be satisfied at every point in the detector plane. Having satisfied these conditions, and with sufficient coherent photon flux or power, a suitable interference pattern can be produced and recorded with an appropriate detector.

In general, the interference pattern at x-ray wavelengths will be characterized by a very fine spatial scale, of order $\lambda/\sin\alpha$, where α is the angle between reference and scattered waves. The geometry of Figure 8.7 is designed to keep these two waves nearly collinear (small α), but sufficiently separated to permit an unambiguous reconstruction – an attribute of off-axis holography. Note that the selected geometry imposes a condition whereby the angle of recorded scattering, which is due to spatial features of the sample, is about equal to the change in direction of the reference wave, which is due to the spatial periodicity of the multilayer mirror. Thus by this technique one would expect, if successful, to image features in the sample with a scale size about equal to a multilayer period. By the Bragg condition discussed in Chapter 4, this is equal to $\lambda/\sqrt{2}$ for a total turning angle of 90°.

This example, however, is presented here to illustrate ideas and concepts rather than to suggest its practical implementation. Although in principle it achieves a resolution equal to the wavelength, large angle x-ray scattering from a non-periodic structure can be expected to be weak. Success for such an experiment would require a high resolution ($\lambda/\sin\alpha$) detector with high (quantum) sensitivity, good dynamic range and linearity, and a radiation source capable of generating radiation with the requisite spatial and temporal coherence at sufficiently high coherent photon flux or coherent power. In the following section we discuss the procedures by which a partially coherent radiation field can be spatially and temporally filtered to achieve the desired degree of coherence. Early examples that demonstrate off-axis holography with a spatially and temporally filtered x-rays are presented in the literature by Aoki, Kikuta, Kohra, and their colleagues.[9] Gabor holography is discussed by Howells, Jacobsen, Kirz, and their colleagues,[10] and soft x-ray interferometry is discussed by Joyeaux and Pollack.[11]

A clever approach to atomic resolution holographic imaging of surface structures is based on the scattering and interference of fluorescence emission. Known as *inside source holography*, the technique does not require coherent illumination, but rather utilizes the inherent coherence of single atom emissions scattered off near neighbors. The resultant interference patterns are summed in the far field over the contributions of many atoms in an identical geometric lattice. First proposed for this application by Szöke, recent experiments are described by Fiagel, Tegze, Marchesini, and their colleagues in reference 9–101.

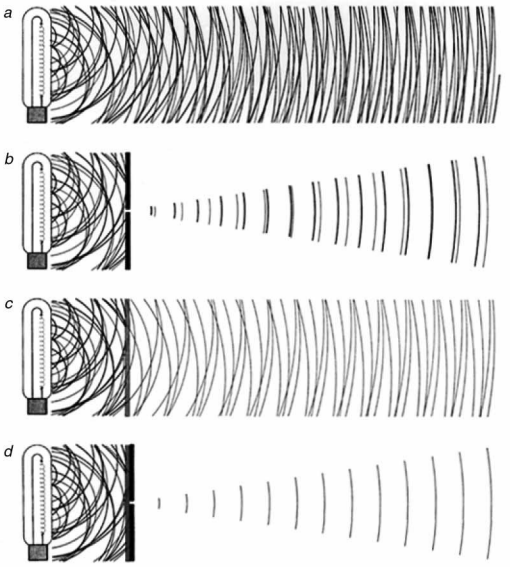

FIGURE 8.8 (see Colorplate IX). Spatial and spectral filtering is illustrated as a procedure to produce coherent radiation, albeit at greatly diminished power, from an ordinary thermal source of visible light. In the nomenclature used here, d would be the diameter of the pinhole shown in part (d), and θ would be the divergence half angle in part (d), set either by the radiation emission characteristics, by a downstream acceptance aperture, or by a lens. (From A. Schawlow,[12] Stanford University.)

8.3 SPATIAL AND SPECTRAL FILTERING

We concluded in Section 8.1 that the limiting condition of spatially coherent radiation is a space–angle product [Eq. (8.5)], or phase space[†] volume

$$d \cdot \theta = \lambda/2\pi$$

where d is a Gaussian $1/\sqrt{e}$ diameter and θ is the Gaussian half angle. All physical sources generate radiation of space–angle product larger than this, often considerably larger. At visible wavelengths, for instance, only lasers with intra-cavity mode control approach this limit, those operating in the so-called TEM_{00} mode.[5] The question here is: what if your source generates radiation into a larger phase space, largely incoherent in nature, but you wish to use it for phase sensitive experiments that require a higher degree of coherence? Schawlow,[12] in his article on lasers, introduces a very informative illustration to show how such radiation can be filtered, both spectrally and spatially, to obtain radiation of greatly improved coherence properties, albeit at the loss of considerable power.

The illustration is reproduced in part here in Figure 8.8. Shown is a typical thermal light bulb with an extended filament heated to a temperature such that many excited atoms randomly

[†]This space–angle product is often referred to as a "phase space" volume. This derives from the study of dynamics, where particles are followed in a position–momentum phase space ($\Delta\mathbf{x}$, $\Delta\mathbf{p}$). For photons $p = \hbar\mathbf{k}$, and for nearly monochromatic radiation the interval in momentum $\Delta\mathbf{p} = \hbar\,\Delta\mathbf{k}$ becomes $\Delta\mathbf{p} = \hbar k\,\Delta\boldsymbol{\theta}$, where $\Delta\boldsymbol{\theta}$ is transverse to $\mathbf{k}$. Thus for nearly monochromatic photons the interval of position–momentum phase space becomes $\Delta\mathbf{x} \cdot \Delta\boldsymbol{\theta}$, which has a scalar minimum given by Eq. (8.5).

radiate a broad spectrum of white light – that is, radiate a continuum containing all colors of the spectrum visible to the human eye. The radiation is filtered in two ways. A pinhole is used [Figure 8.8(b)] to obtain spatially coherent radiation (over some angular extent), as set here by Eq. (8.5). A color filter is used [Figure 8.8(c)] to narrow the spectral bandwidth, thus providing a degree of longitudinal coherence, as described here in Eq. (8.3). Combining both the pinhole and the filter, one obtains radiation that is both spatially and temporally coherent, as is seen in Figure 8.8(d), but with a power that is only a small fraction of the total power radiated by the light bulb.

As Schawlow points out in his article, a visible light laser has the great advantage of providing these desired coherence properties, often with very long temporal coherence length (very narrow $\Delta\lambda/\lambda$), without compromising available power. As we have seen, however, this is a much greater challenge at x-ray wavelengths, both because the energetics make lasing at high photon energy more difficult, and because the very short wavelengths place great demands on the achievement of substantial spatial coherence [Eq. (8.5)]. As a consequence, lasing to date has been accomplished largely at the longer wavelengths of extreme ultraviolet (EUV) and soft x-rays, and has lacked spatial coherence. The techniques of spatial and spectral filtering are therefore very important, and are now commonly used at EUV through x-ray wavelengths. In the following section we discuss the use of spatial and temporal filtering of undulator radiation at powers sufficient to permit experimentation at these very short wavelengths.

8.4 SPATIAL AND SPECTRAL FILTERING OF UNDULATOR RADIATION

As an example of pinhole spatial filtering, Figure 8.9 illustrates how the technique is used to obtain spatially coherent radiation from a periodic undulator,[7, 13] as was described in Chapter 5. The secret to success in this spatial filtering process is that the electron beam cross-section and divergence must be sufficiently small, so that a fair fraction of the radiated flux is able to pass through a pinhole–aperture combination for which $d \cdot \theta = \lambda/2\pi$, as described earlier in Eq. (8.5). That is, viewed through an appropriate pinhole and angular aperture, the radiation must appear to come from a point source. Figure 8.9(a) depicts both the undulator and one form of a spatial filter. Within the indicated central radiation cone (θ_{cen}), the emitted radiation is characterized by a relative spectral bandwidth $\lambda/\Delta\lambda$ equal to N, which is the number of magnet periods and thus the number of oscillations executed by the electrons as they traverse the magnet structure. Figure 8.9(b) shows the calculated power radiated within the central cone [Chapter 5, Eq. (5.41)] for an undulator at the Advanced Light Source (E = 1.9 GeV), which was described previously in Chapter 5, with parameters summarized in Chapter 5, Table 5.1.

In general the phase space of the central radiation cone is larger than the limiting condition [Eq. (8.5)] required for spatial coherence. That is, if we take a typical electron beam diameter of 100 μm and a typical central cone half angle of 50 μrad, the product $d \cdot \theta$ is 5 nm, generally much greater than $\lambda/2\pi$ for EUV and soft x-ray wavelengths. Thus for experiments that require spatial coherence, a pinhole and angular acceptance aperture are introduced, as shown in Figure 8.9(a). This *pinhole spatial filter* is used to narrow, or filter, the phase–space of transmitted radiation, much as was illustrated in Figure 8.8. Filtering to $d \cdot \theta = \lambda/2\pi$ requires the use of both a small pinhole (d) as shown, and some limitation on θ, such that the product is equal to $\lambda/2\pi$. For example, one could accept the full central cone (θ_{cen}) and choose an appropriate pinhole diameter $d = \lambda/2\pi\theta_{\text{cen}}$. Alternatively, one could use a downstream angular aperture (perhaps another pinhole or a lens) of acceptance angle $\theta < \theta_{\text{cen}}$, and choose d accordingly. Both forms of spatial filter are used in practice.

To calculate the spatially coherent power transmitted by the pinhole spatial filter, one must consider the phase–space of the emitted radiation in both the vertical (y–z) and horizontal

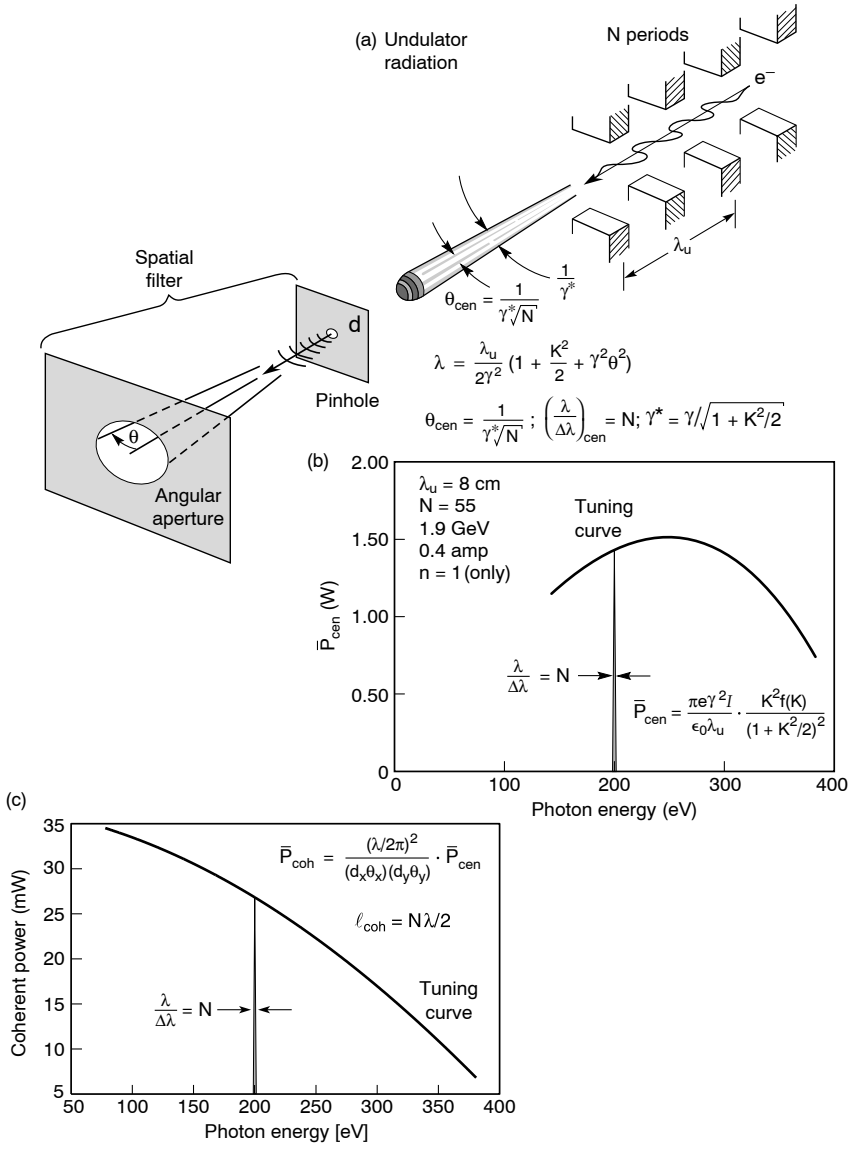

FIGURE 8.9 (see Colorplate X). (a) Undulator radiation with a pinhole spatial filter. (b) Power in the central radiation cone (θ_{cen}, $1/N$ relative spectral bandwidth) for an 8 cm period undulator at the ALS (Table 5.1). (c) Time-averaged coherent power after spatial filtering ($d \cdot \theta = \lambda/2\pi$).

(x–z) planes, as the condition $d \cdot \theta = \lambda/2\pi$ must be satisfied for both. If the electron beam is elliptical, as was discussed in Chapter 5, Section 5.4.5, and illustrated in Figure 5.22, with major and minor diameters $d_x = 2\sigma_x$ and $d_y = 2\sigma_y$, and if the central radiation cone is also somewhat elliptical due to differences in the horizontal and vertical electron beam divergence, so that the characteristic half angles[‡] are θ_x and θ_y, then the respective phase–space volume

[‡]In Eqs. (5.56) these were described as the "total" central cone half angles $\theta_{Tx} = \sqrt{\theta_{\text{cen}}^2 + \sigma_x'^2}$ and $\theta_{Ty} = \sqrt{\theta_{\text{cen}}^2 + \sigma_y'^2}$, where σ_x' and σ_y' are the respective measures of electron beam divergence in the two planes. For simplicity in this chapter we have replaced θ_{Tx} by θ_x and θ_{Ty} by θ_y.

containing the emitted power in the radiation cone, $\bar{P}_{\text{cen}}$ of Eq. (5.41), will be $(d_x\theta_x)(d_y\theta_y)$. The pinhole spatial filter must reduce both $d_x\theta_x$ and $d_y\theta_y$ to $\lambda/2\pi$. The transmitted *spatially coherent power*[7] will therefore be reduced, proportionally, to a value

$$\boxed{\bar{P}_{\text{coh},N} = \left(\frac{\lambda/2\pi}{d_x\theta_x}\right)\left(\frac{\lambda/2\pi}{d_y\theta_y}\right)\bar{P}_{\text{cen}}} \tag{8.6}$$

where the horizontal (x) and vertical (y) phase–space filter factors are written separately to remind us that each alone has a maximum value of unity. In much of what follows we will assume that in both planes $d \cdot \theta > \lambda/2\pi$, permitting some simplifications to the formulae.¶

We recall from Chapter 5, Eq. (5.41a), that

$$\bar{P}_{\text{cen}} = \frac{\pi e\gamma^2 I}{\epsilon_0 \lambda_u} \cdot \frac{K^2}{(1 + K^2/2)^2} f(K)$$

where I is the average current, λ_u is the undulator period, and $f(K)$ is a finite-K correction factor of order unity which is given in Chapter 5, Eq. (5.41). The longitudinal coherence length is understood to be $l_{\text{coh}} = \lambda^2/(2\,\Delta\lambda) = N\lambda$ for N undulator periods and no further spectral filtering. This is consistent with our formulations of $\bar{P}_{\text{cen}}$ and θ_{cen}, which are defined for a relative spectral bandwidth of $\lambda/\Delta\lambda = N$. According to Eq. (8.6), the spatially coherent power can generally be expected to decline with a λ^2 behavior for shorter wavelengths. This phase–space scaling, however, is modified for undulator radiation by several factors that arise from the K-dependence of radiated power, involving the electrons' transverse acceleration, reduced axial velocity, and electron beam divergence parameters.

To examine the wavelength dependence of coherent power further we note that $\bar{P}_{\text{cen}}$ contains a factor $K^2/(1+K^2/2)^2$ that is related to wavelength through the undulator equation [Eq. (5.28)]

$$\lambda = \frac{\lambda_u}{2\gamma^2}\left(1 + \frac{K^2}{2} + \gamma^2\theta^2\right)$$

For on-axis radiation ($\theta = 0$) one has

$$\lambda = \frac{\lambda_u}{2\gamma^2}\left(1 + \frac{K^2}{2}\right)$$

or more conveniently, in terms of photon energy ($\hbar\omega = 2\pi\hbar c/\lambda$),

$$\hbar\omega = \frac{\hbar\omega_0}{1 + K^2/2} \tag{8.7a}$$

where

$$\hbar\omega_0 \equiv 4\pi\hbar c\gamma^2/\lambda_u \tag{8.7b}$$

¶The phase–space assumption $d \cdot \theta > \lambda/2\pi$ is generally valid for the undulator radiation, but is near its limit (diffraction limited radiation) in the vertical plane for longer wavelength radiation at third generation facilities.

is the highest photon energy that can be radiated in the fundamental ($n = 1$) by a given undulator, and that corresponds to the limiting case $K = 0$. With some algebraic manipulation one can show that the three wavelength-dependent factors, λ^2 due to the coherent phase–space constraint, K^2 due to the transverse electron acceleration, and $(1+K^2/2)^2$ due to the decreased axial velocity ($\gamma^* = \gamma/\sqrt{1+K^2/2}$) for finite K, combine to give a photon energy dependence $(\hbar\omega_0 - \hbar\omega)/\hbar\omega$, so that the spatially coherent power [Eq. (8.6)] for an undulator wavetrain of N cycles takes the form

$$\bar{P}_{\mathrm{coh},N} = \frac{e\lambda_u I}{8\pi\epsilon_0 d_x d_y \theta_x \theta_y \gamma^2}\left(\frac{\hbar\omega_0}{\hbar\omega} - 1\right) f(\hbar\omega/\hbar\omega_0) \tag{8.7c}$$

where in terms of photon energy the finite-K correction factor [Eq. 5.41(d)] can be rewritten as

$$f(\hbar\omega/\hbar\omega_0) = \frac{7}{16} + \frac{5}{8}\frac{\hbar\omega}{\hbar\omega_0} - \frac{1}{16}\left(\frac{\hbar\omega}{\hbar\omega_0}\right)^2 + \cdots \tag{8.8}$$

Note that for magnetic tuning of the undulator through a range $0 \le K \le 2$, the photon energy is varied by a factor of three, where now in terms of $\hbar\omega/\hbar\omega_0$ the factor $f(1) = 1$, while for instance $f(\frac{1}{3}) = 0.65$. Equation (8.7), however, does not give the full story, as the product $\theta_x\theta_y$ in the denominator may also contain a noticeable photon energy dependence, depending on the relative values of electron beam divergence $\sigma'_{x,y}$ and the central cone half angle, θ_{cen} [see the footnote below Eq. (8.6)]. For the case where the undulator condition $\sigma'^2_{x,y} \ll \theta^2_{\mathrm{cen}}$ is well satisfied, which corresponds to a relatively narrow spectral shape (see Figure 5.23), the product $\theta_x\theta_y$ can be approximated as

$$\theta_x\theta_y \simeq \theta^2_{\mathrm{cen}} = \frac{1+K^2/2}{\gamma^2 N}$$

which by Eq. (8.7a) becomes $\theta_x\theta_y \simeq \hbar\omega_0/\hbar\omega\gamma^2 N$. The spatially coherent power in this important special case then takes the form

$$\bar{P}_{\mathrm{coh},N} = \frac{e\lambda_u I N}{8\pi\epsilon_0 d_x d_y}\left(1 - \frac{\hbar\omega}{\hbar\omega_0}\right) f(\hbar\omega/\hbar\omega_0) \qquad \left(\sigma'^2 \ll \theta^2_{\mathrm{cen}}\right) \tag{8.9}$$

An example of coherent power versus photon energy is given in Figure 8.9(c) for the case of an 8 cm undulator at the ALS, where $\sigma'_x = 23$ μrad, $\sigma'_y = 3.9$ μrad, and for $K = 1$ (286 eV photon energy, 4.34 nm wavelength) the central cone half angle is 44 μrad, so that the undulator condition is well satisfied. The values of d_x and d_y are 520 μm and 32 μm, respectively. The spatially coherent fraction $(\lambda/2\pi)^2/d_x\theta_x d_y\theta_y$, given in Eq. (8.6), is 1.3×10^{-2} for this undulator at a wavelength of 4.34 nm ($K = 1$, $\hbar\omega = 286$ eV). Thus the 1.4 W power in the central cone is reduced by spatial filtering to a value of 18 mW of spatially coherent power. According to Eq. (8.9), the coherent power is a linearly decreasing function of photon energy, going to zero at $\hbar\omega_0 = 428$ eV. Although the curve in Figure 8.9(c) derives from the more general Eq. (8.7), it very closely follows the specialized form given in Eq. (8.9) for this case where $\sigma'_{x,y} \ll \theta_{\mathrm{cen}}$.

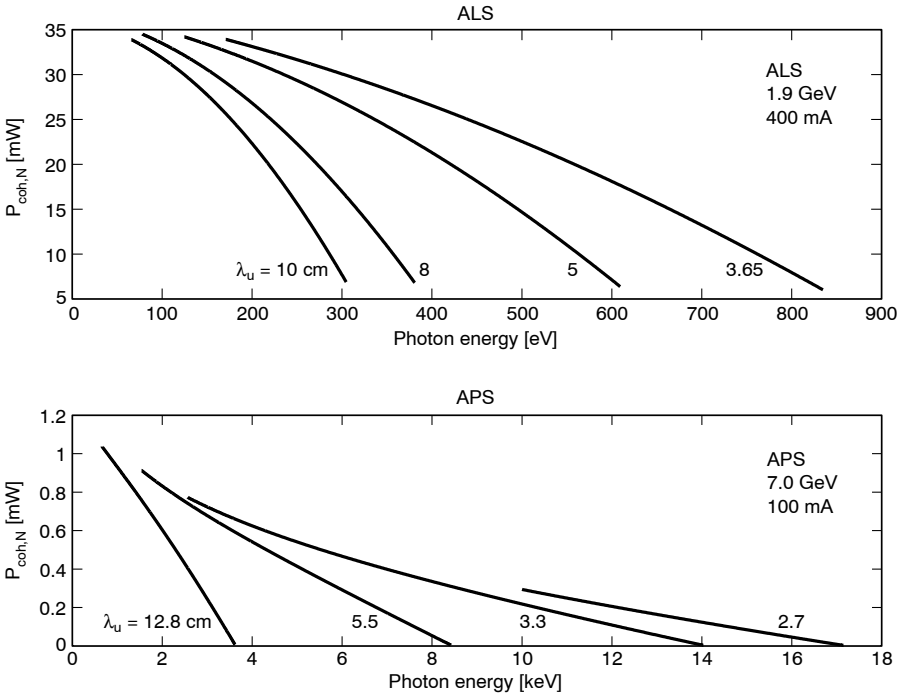

FIGURE 8.10. Spatially coherent average power within a $1/N$ relative spectral bandwidth for undulators at the Advanced Light Source and the Advanced Photon Source, previously described in Chapter 5, with electron beam parameters summarized in Table 5.1. Note that coherent power is shown for the ALS at 1.9 GeV, and for the APS at 7.0 GeV beam energy. Harmonics ($n = 3,\ 5$) can be used to bridge photon energies between those shown. Note that peak powers are nominally 54 times higher than average power values at the ALS, and 100 times higher than average power values at the APS.

Coherent power can be obtained at higher photon energies through the use of shorter undulator periods (λ_u) and higher electron beam energies. This point is illustrated in Figure 8.10, which shows spatially coherent power [Eq. (8.7)] versus photon energy for several undulator periods and differing electron beam energies at the two U.S. synchrotron radiation facilities described in Chapter 5 (Section 5.1 and Table 5.1). These curves are for a longitudinal coherence length $l_{\text{coh}} = N\lambda/2$, where N is the number of periods for each specific undulator. Note that spatially coherent power of order 100 μW is achievable to photon energies as high as 10 keV at the Advanced Photon Source ($E = 7.0$ GeV).

The scaling of coherent power at high photon energy can best be appreciated through examination of Eq. (8.7), where θ_x and θ_y are retained as variables because at high values of γ, θ_{cen} is smaller and possibly comparable to σ_x' and σ_y'. Typical values are given in Table 5.1. With $d_x,\ d_y,\ \theta_x$, and θ_y fixed or slowly varying, and with the factors $(\hbar\omega_0/\hbar\omega - 1)\, f\,(\hbar\omega/\hbar\omega_0)$ providing a local photon energy *shape factor* for a given undulator in the vicinity of its own $\hbar\omega_0$, the wavelength scaling of coherent power is dominated by λ_u/γ^2, which is proportional to λ, or inversely to photon energy, as seen on the more global scale of Figure 8.10. In the vicinity of $\hbar\omega_0$ for any given undulator, λ_u and γ are fixed and the dependence on photon

energy is dominated by the local shape factor described above. The absolute values of coherent power are also affected by the storage ring current I, which is generally less at higher beam energies. Again see Table 5.1 for typical values.

On a more global scale, the coherent power is observed in Figure 8.10 to scale roughly as λ, when corrected for differences in current. From Eq. (8.6) we expect coherent power to scale as λ^2, but higher values of γ are required to reach shorter wavelengths, and the power in the central cone scales as γ^2/λ_u, or as $1/\lambda$, thus giving a net scaling proportional to λ, as seen in Figure 8.10. Note that because of the duty cycle of the synchrotron facilities (e.g., 35 ps FWHM Gaussian pulses every 2.0 ns at the ALS), the peak power can be considerably higher than the average power, for instance, a factor of 54 at the ALS and a factor of 100 at the APS, as discussed in Section 5.4.7.

For many experiments it is also desirable to narrow the spectral bandwidth, either because improved spectral resolution is required to probe atomic or molecular states, because a chromatically sensitive zone plate focusing lens requires a relatively narrow spectral bandwidth (narrower than one divided by the number of zones), or because a longer longitudinal coherence length is required for high contrast interferometric or holographic fringe formation. The radiation must then be spectrally filtered by a monochromator (not shown in Figure 8.9) to further narrow the relative spectral bandwidth to a suitable value of $\Delta\lambda/\lambda$, thus increasing the longitudinal coherence length from a value of $N\lambda/2$ to a greater length $l_{\text{coh}} = \lambda^2/(2\,\Delta\lambda)$. For example, if monochromatization to a value $\lambda/\Delta\lambda = 10^3$ were desired, the longitudinal coherence length would become $l_{\text{coh}} = 10^3\lambda/2$. This of course is accomplished at a reduction in spatially coherent power. By filtering from $\Delta\lambda/\lambda = 1/N$ to $\Delta\lambda/\lambda = 1/10^3$, the transmitted power is necessarily reduced by a multiplicative factor $(\Delta\lambda/\lambda)/(1/N)$, or $N/10^3$ in the example cited. Furthermore, there will be an *insertion loss* due to the finite monochromator efficiency, including such factors as the grating or crystal efficiency, finite mirror reflectivities, etc. If we collect these factors into an inclusive *beamline efficiency* η, then the available coherent power can be written as

$$\bar{P}_{\text{coh},\lambda/\Delta\lambda} = \underbrace{\eta}_{\substack{\text{beamline}\\ \text{efficiency}}} \underbrace{\frac{(\lambda/2\pi)^2}{(d_x\theta_x)(d_y,\theta_y)}}_{\substack{\text{spatial}\\ \text{filtering}}} \cdot \underbrace{N\frac{\Delta\lambda}{\lambda}}_{\substack{\text{spectral}\\ \text{filtering}}} \cdot \bar{P}_{\text{cen}} \tag{8.10a}$$

which can be rewritten following the logic that led to Eq. (8.7) as

$$\bar{P}_{\text{coh},\lambda/\Delta\lambda} = \frac{e\lambda_u I(\eta N\,\Delta\lambda/\lambda)}{8\pi\epsilon_0 d_x d_y \theta_x \theta_y \gamma^2}\left(\frac{\hbar\omega_0}{\hbar\omega} - 1\right) f(\hbar\omega/\hbar\omega_0) \tag{8.10b}$$

where $\lambda/\Delta\lambda$ is the relative spectral bandwidth, N is the number of undulator periods, η is the beamline efficiency (insertion loss), $\hbar\omega_0 = 4\pi c\hbar\gamma^2/\lambda_u$ is the highest photon energy achievable with the fundamental ($n = 1$) of a given undulator in the limit $K = 0$, and $f(\hbar\omega/\hbar\omega_0)$ is the finite-K correction factor for central cone radiation expressed in terms of $\hbar\omega/\hbar\omega_0$ as in Eq. (8.8). To emphasize the penalty paid for this further monochromatization we have bracketed the quantity $\eta N\,\Delta\lambda/\lambda$, which is a numerical factor less than unity that represents the loss of power incurred through monochromatization.

In the case where the undulator condition is well satisfied ($\sigma'_{x,y} \ll \theta_{\text{cen}}$), such that $\theta_x \theta_y \simeq (1 + K^2/2)/N\gamma^2$, the expression for coherent power takes the form

$$\bar{P}_{\text{coh},\lambda/\Delta\lambda} = \frac{e\lambda_u I \eta(\Delta\lambda/\lambda)N^2}{8\pi\epsilon_0 d_x d_y} \cdot \left(1 - \frac{\hbar\omega}{\hbar\omega_0}\right) f(\hbar\omega/\hbar\omega_0) \qquad \left(\sigma'^2 \ll \theta_{\text{cen}}^2\right) \tag{8.10c}$$

which we note scales as N^2 in this limit. This expression is quite accurate for low emittance[§] soft x-ray synchrotron facilities such as the ALS and its equivalent elsewhere, as the condition $\sigma_{x,y}^2 \ll \theta_{\text{cen}}^2$ is reasonably well satisfied for $\gamma \simeq 3728$, $N \simeq 50$–100, and $\sigma' \leq 20$ μrad. Note that while in this case the coherent power scales as N^2, in the case where $\sigma' \simeq \theta_{\text{cen}}$, as may occur for high γ facilities, Eq. (8.10b) must be used and the scaling of coherent power will be closer to linear in N.

In the example cited previously for an 8 cm period undulator at the Advanced Light Source, a monochromator and beamline optics, with an overall efficiency η of 10% (30% grating efficiency and five glancing incidence mirrors at 0.8 reflectivity each) are used to obtain $\lambda/\Delta\lambda = 10^3$. The resultant coherent power at 4.3 nm wavelength (286 eV) would be [following Eq. (8.10a)] $(\frac{1}{10})(0.013)(55/10^3)(1.4\text{ W})$, or about 100 μW, with a longitudinal coherence length of $10^3\lambda = 3.5$ μm. The detailed photon energy (wavelength) dependence is included in Eq. (8.10c).

An example of a beamline designed for spatial and spectral filtering of soft x-ray and extreme ultraviolet (EUV) undulator radiation is shown in Figure 8.11. It employs a grazing incidence grating monochromator[14, 15] as appropriate for use at these wavelengths. (There is extensive recent literature on the design of grating monochromators.[16–18])

The first optical element (M1) is a water cooled plane mirror set at an angle that reflects the desired radiation but absorbs the unwanted power residing in higher harmonics. Following this are curved reflective optics that form an image of the radiating electrons at 65 : 1 spatial demagnification on a downstream entrance pinhole. As with any imaging system, this provides a concomitant increase in angular illumination ($65\theta_{\text{cen}} \simeq 2.9$ mrad at $K = 1$), as required in this case for the downstream experiment, which here involves coherent interferometry of EUV optical systems. With this relatively large angular illumination, pinholes of about 1 μm diameter are required to approximate the condition [Eq. (8.5)] for spatial coherence at 13 nm wavelength.[‖] Also included in the beamline optics is a combined grazing incidence grating and exit slit that provides the desired wavelength and spectral bandpass. Use of a varied line space grating permits wavelength tuning without movement of the (fixed) exit slit.[14, 15] The remaining mirrors permit an intermediate image of the source at the exit slit of the monochromator, with final vertical and horizontal image formation at the pinhole. Though separate branchlines for coherent optics and photoemission microscopy are shown, details of the beamline optics are omitted.

Calculations of the anticipated coherent power available with this undulator and beamline combination are shown in Figure 8.11(b), for a monochromator setting of $\lambda/\Delta\lambda = 10^3$, so that

[§]The phrase "low emittance" refers to an electron beam of small (phase space) product $\pi\sigma\sigma'$. The phrase is occasionally used to describe the facility as well.

[‖]The work at 13 nm wavelength involves the use of Mo–Si multilayer mirrors, as discussed in Chapter 4. The coated optics are used for reduction imaging in the EUV lithography program, as discussed in Chapter 10, Section 10.2.

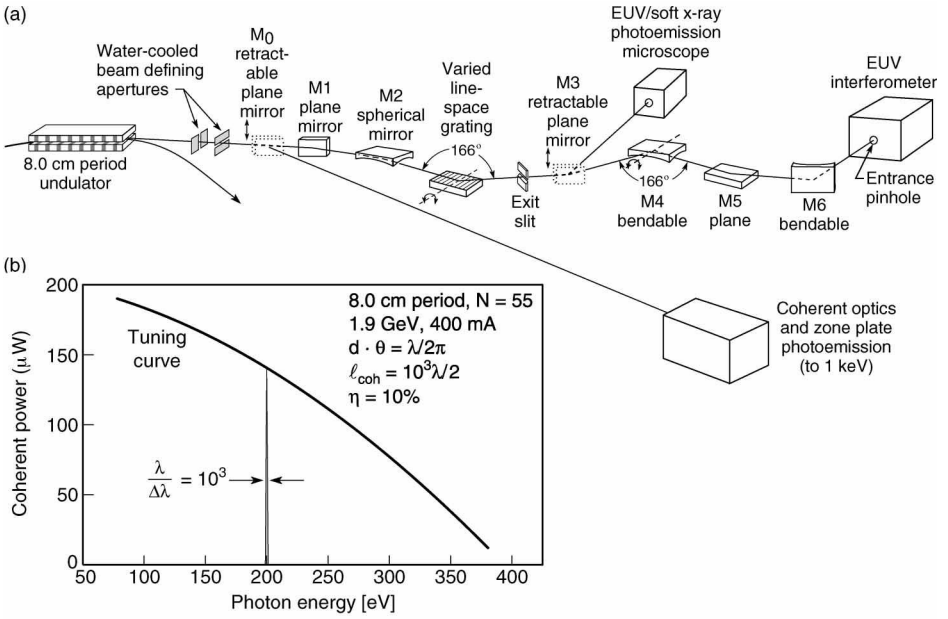

FIGURE 8.11. A coherent optics beamline used for spatial and spectral filtering of undulator radiation. The grating and exit slit provide spectral filtering, typically to $\lambda/\Delta\lambda = 1000$, for a fixed and stable electron beam position. The reflective optics (mirrors) refocus the source at a 65 : 1 demagnification on an entrance pinhole at each station. The pinhole diameter is selected to provide spatial filtering for the given incident radiation cone and/or the acceptance cone within each experimental chamber. Three separate branch lines are available as shown, and are selected by retractable mirrors. Resultant coherent power is shown in (b) for radiation satisfying $d \cdot \theta = \lambda/2\pi$, $\lambda/\Delta\lambda = 1000$, and an assumed beamline efficiency of 10% as described by Eq. (8.10a). Advanced Light Source (ALS) electron beam parameters are assumed (see Chapter 5, Table 5.1).

the longitudinal coherence length is $10^3\lambda/2$, and for a pinhole diameter such that a high degree of spatial coherence is obtained. The resultant coherent power is shown in Figure 8.11(b) to be broadly tunable from 80 eV to 400 eV photon energy (3 nm to 15 nm wavelength), with about 5 μW to 30 μW within this narrow (10^{-3}) spectral band. The coherent optics branchline, though not shown in detail in Figure 8.11(a), is designed to cover higher photon energies, including third harmonic ($n = 3$) undulator radiation to 1 keV, using mirrors closer to glancing incidence so as to reflect well at the shorter wavelengths.

Experiments have been performed to record spatially and spectrally filtered radiation using the undulator and beamline described in Figures 8.9 and 8.11. The exit slit of the monochromator was set for a relative spectral bandwidth $\Delta\lambda/\lambda$ of 1/1100. Downstream of a 1.1 μm diameter pinhole, Airy diffraction patterns[1, 8] were recorded with a CCD electronic array detector** having single photon detection sensitivity at these wavelengths. Recorded images[19] are shown in Figure 8.12 for several undulator wavelengths. All show the characteristic central Airy disk surrounded by several dark and bright rings. The integrated power in the central Airy disk at 13.4 nm corresponds to a time averaged coherent power of 11 μW, or

**A back-thinned charge coupled device (CCD), with single photon detection capability for photons just below the silicon L-absorption edge at 99 eV.

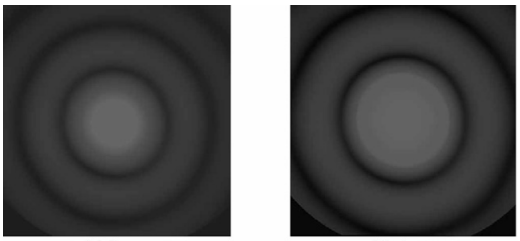

FIGURE 8.12 (see Colorplate XI). Far-field images (Airy patterns) of spatially filtered undulator radiation at wavelengths of 11.2 nm and 13.4 nm. Wavelength tuning is accomplished through variation of the magnetic field, and thus K, for an 8 cm period undulator at the Advanced Light Source. The beamline and pinhole spatial filter are illustrated in Figure 8.11 and discussed in the text. A 1.1 μm diameter pinhole was used, and the monochromator was set for a relative spectral bandwidth of 1/1100. The measured power in the central Airy disk is 11 μW at 13.4 nm wavelength. Radiation within the central Airy disk is used for spatially coherent experimentation. (Courtesy of P. Naulleau and colleagues,[19] Lawrence Berkeley National Laboratory.)

7×10^{11} coherent photons per second. The longitudinal coherence length, set by the measured spectral bandwidth and wavelength, is 7.4 μm.

A further examination of the scaling of spatially and temporally filtered undulator radiation, for both soft and hard x-rays, is shown in Figure 8.13, which follows Eq. (8.10b) with the assumption in all cases that $\eta = 10\%$ and that $\lambda/\Delta\lambda = 10^3$. This permits one to see the general trend as a function of photon energy. One observes the general λ-dependence discussed earlier (in connection with Figure 8.10), with local shape factors near the respective

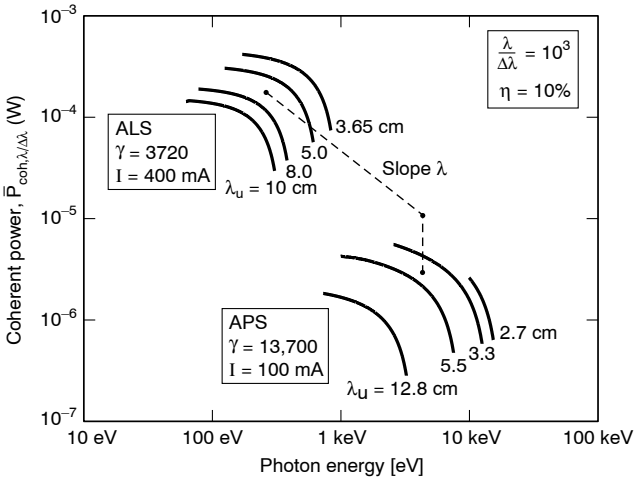

FIGURE 8.13. Spatially and temporally coherent power for a variety of undulators at both the ALS and APS, following Eq. (8.10b). Only the fundamental ($n = 1$) is shown; higher harmonics ($n = 3$, etc.) would extend this coverage in each case. Spatial coherence satisfying $d \cdot \theta = \lambda/2\pi$ and a relative spectral bandwidth of 10^3 is assumed in each case. An overall beamline efficiency of 10% is assumed in each case. Specific undulator, current, and electron beam parameters are summarized in Chapter 5, Table 5.1. When adjusted for differences in current (dashed vertical line), the undulator coherent power scales roughly proportionally to λ, as discussed in the text. Further analyses of the theoretical[21] and experimental[22–24] coherence properties of undulator radiation are presented in the literature.

values of $\hbar\omega_0$. Account is taken of differences in electron beam parameters and average current. Similar scaling curves appear in the literature,[7, 20] occasionally in terms of coherent photon flux, or with an imposed constraint of fixed coherence length (rather than fixed relative spectral bandwidth). In each of these manners of presenting information an additional factor of $\lambda\,(\propto 1/\hbar\omega)$ is introduced, leading to a sharper λ^2 fall-off (scaling) with increasing photon energy. In the first case this is because there are proportionally fewer photons per radiated Joule of energy at higher photon energy, and in the second case because fixed coherence length requires narrower relative spectral bandwidth at higher photon energy (shorter wavelength) and thus proportionally less available power.

8.5 SPATIALLY COHERENT EUV AND SOFT X-RAY LASERS

Spatial filtering requirements for extreme ultraviolet and soft x-ray lasers are similar to those for undulators. In general these lasers lack transverse mode[25–27] control and as a result generate radiation characterized by $d \cdot \theta \gg \lambda/2\pi$, thus requiring substantial spatial filtering for applications requiring spatial coherence. Spectral filtering, on the other hand, is generally not required, as these lasers naturally radiate with a very narrow linewidth,[28] typically with $\Delta\lambda/\lambda$ of order 10^{-4}. The coherent power available after spatial filtering can be written in a manner similar to that for undulators [Eq. (8.6)]:

$$P_{\text{coh}} = \frac{(\lambda/2\pi)^2}{(d_x\theta_x)\,(d_y\theta_y)} P_{\text{laser}} \tag{8.11}$$

where P_{laser} is the radiated laser power occupying an elliptical phase–space $(d_x\theta_x)\,(d_y\theta_y)$. Recalling the nickel-like tantalum laser[29] of Chapter 7, radiating 100 kW in a single 250 ps pulse at a wavelength of 4.483 nm, we can now estimate the coherent power that would be available after spatial filtering. The laser is shown schematically in Figure 8.14 along with measured emission spectra. With a source diameter d estimated at 100 μm and a divergence half angle θ of 5 mrad, the space product $d\cdot\theta$ is approximately 700 times larger than $\lambda/2\pi$. The single pulse coherent power available after spatial filtering is therefore about 100 kW/$(700)^2$, or 200 mW. Considering the pulse duration of 200 ps, this corresponds to an energy of 40 pJ, or about 10^6 spatially coherent photons within a temporal (longitudinal) coherence length of about 25 μm.

Importantly, the soft x-ray laser does not require a monochromator, because of its already narrow spectral width. There are, however, incoherent line emissions and continuum emissions from the hot dense plasma, and in some cases nearby but less intense lasing lines, all of which must in general be suppressed. Often this can be done with a single multilayer mirror, which at these wavelengths can achieve a reflectivity of about 10% for a 90° deflection. Thus one expects a 20 mW pulse of coherent power into an experiment, or about 10^5 spatially coherent photons, at 4.483 nm wavelength. Similar results have been obtained on the high side of the (neutral) carbon K-absorption edge, with lasing in nickel-like tungsten at 4.318 nm (287.1 eV), thus permitting wavelength differential imaging or other experiments around the carbon edge.[29] Methods for measuring the coherence properties of EUV/soft x-ray lasers are described in the literature.[30, 31]

In addition to post-lasing pinhole spatial filtering, one can imagine effective mode control within the laser itself, as in a conventional visible light laser such as that illustrated in Figure 8.15, or within a laser amplification chain as illustrated in Figure 8.16. Spatial filtering within the oscillator is the most energy efficient way to proceed, as it stimulates atoms to radiate only within the desired phase space. This, however, requires multipass lasing, which in general

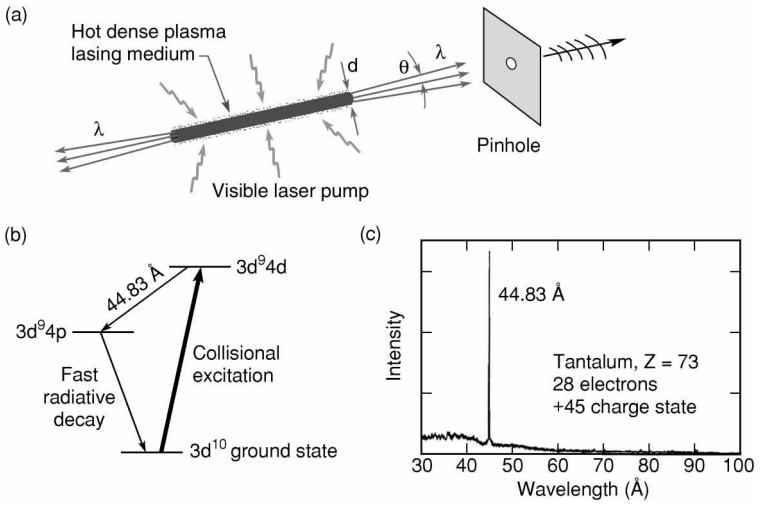

FIGURE 8.14 (see Colorplate XII). Soft x-ray lasing is demonstrated on a 4d to 4p ($J = 0$ to 1) transition at 4.483 nm wavelength (276.6 eV) in nickel-like tantalum atoms ($Z = 73$, 28 electrons, +45 charge state). The highly stripped atoms are created and collisionally pumped in a hot dense laser plasma created by a high power 250 psec pulse duration terawatt laser pulse. A multimode 100 kW pulse is produced in both directions at 4.483 nm wavelength. Spatial filtering to a single transverse mode would yield a 20 mW pulse of spatially coherent radiation with a 25-μm longitudinal coherence length. (Data courtesy of B. MacGowan, Lawrence Livermore National Laboratory.)

is difficult for lasing in hot dense plasmas created by intense, very short duration visible light lasers or electronic discharges. For a half-nanosecond duration plasma, this permits a propagation path length of only 15 cm (at the speed of light); thus for just one round trip, the cavity end mirrors[32, 33] would be just 7.5 cm apart and an intracavity pinhole would at most be only a few centimeters from a very intense pump pulse. Such a configuration would tend to vaporize the pinhole and create an additionally complicated refractive medium within the cavity. This might have a better chance of success with longer pulse duration lasers or discharges, perhaps more toward extreme ultraviolet wavelengths where the energetics of atomic lasing (lower photon energy, lower excitation energies) require less intense pumping, and where phase–space constraints are less demanding.

A second approach is to use a sequence of collinear laser amplifiers in a chain that incorporates a pinhole spatial filter following the first stage.[25, 26] Thus the second and sequential amplification stages are driven by single mode spatially coherent radiation, rather than growing from noise as in the first stage, and have the possibility of growing to high coherent power levels. Such staging requires precise timing and alignment as well as careful attention to the control of transverse gradients in the amplification stages, which could lead to increased angular divergence and thus reduced spatial coherence. Further ideas for enhancing the spatial coherence of EUV and soft x-ray laser radiation, including the use of gain guiding and other transverse mode control techniques, are discussed in the literature.[26, 27, 34, 35]

Several additional routes toward spatially coherent EUV radiation have recently been developed, both involving table top sized equipment. Marconi, Rocca, and colleagues[36] have measured a high degree of spatial coherence, of order ten times diffraction limited, with 46.9 nm radiation from a neon-like argon laser driven by a capillary discharge plasma. Their work is described further in Chapter 7, Section 7.5. Murnane, Kapteyn, and colleagues[37]

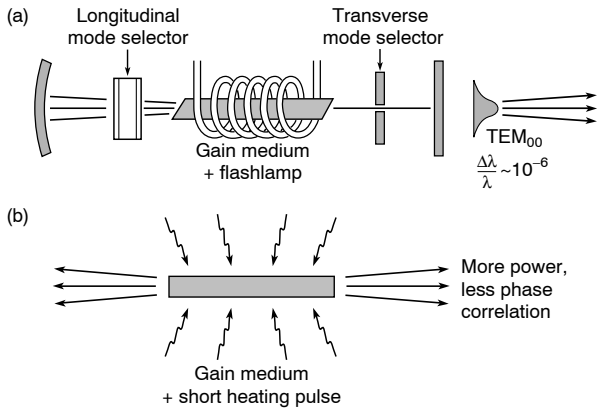

FIGURE 8.15. Comparison of a multipass visible light laser employing intra-cavity longitudinal and transverse mode selectors, with a typical EUV or soft x-ray laser that generally lacks cavity mirrors and mode selecting optics.

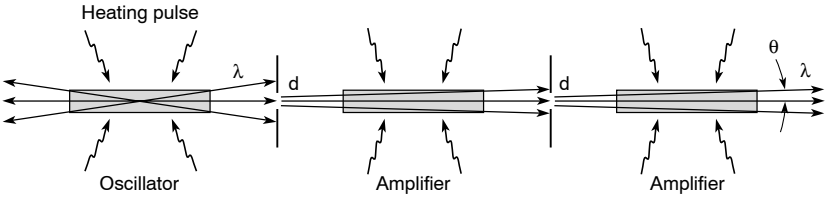

FIGURE 8.16. A laser oscillator followed by a pinhole spatial filter and a chain of laser amplifiers – similar to the first stage but stimulated to emit by spatially filtered radiation, rather than growing from noise as in the first stage. In this manner energy from the second and later stages contributes only to the TEM_{00} (spatially coherent) mode.[25]

have recently reported a sharp increase in the generation of high harmonics of femtosecond laser pulses when phase velocity matching techniques are employed. Their pump wave is a nominal 20 fs duration, 800 nm laser pulse incident on neutral argon gas in a capillary tube. They observe harmonics of order $n = 23$ to 31 (26 nm to 35 nm wavelength) with a divergence angle of about 1 mrad and a source diameter of 40–70 μm. This suggests that the harmonics are about three to six times diffraction limited. Each harmonic has an energy of about 0.2 nJ per pulse, at an repetition rate of 1 kHz. The work is described further in Chapter 6, Section 6.8.

8.6 THE VAN CITTERT–ZERNIKE THEOREM

In the previous sections of this chapter we have compared the phase–space of emitted radiation from an incoherent source with that from a nearly point source for which the radiated fields approach perfect correlation in the transverse plane and for which the phase–space is given by the limiting condition $d \cdot \theta = \lambda/2\pi$. We then compared the phase–space ratios to estimate the spatially coherent power available, assuming that this could be obtained by appropriate spatial filtering. In this section we discuss the finite degree of spatial coherence that results when an extended incoherent source of quasi-monochromatic radiation is observed through the use of

spatial and angular apertures. The complex degree of coherence in such a radiation field is described by the van Cittert–Zernike theorem.[1, 2, 38–39] It is of particular interest to us as a means to predict the degree of spatial coherence that will result from pinhole spatial filtering of both undulator radiation and EUV/soft x-ray laser radiation, each of which is, to a large degree, spatially incoherent in nature. For the consideration of spatially coherent radiation one is primarily interested in the correlation of quasi-monochromatic fields in the limit that the time separation τ goes to zero. In this limit the normalized degree of coherence between fields at points 1 and 2 [Eq. (8.2)] takes a simpler form as $\gamma_{12}(0) \rightarrow \mu_{12}$, where now[1, 2]

$$\mu_{12} = \frac{\langle E_1(t)E_2^*(t)\rangle}{\sqrt{\langle|E_1|^2\rangle}\sqrt{\langle|E_2|^2\rangle}} \tag{8.12}$$

with absolute values bounded by $0 \leq |\mu_{12}| \leq 1$. While still generally referred to as the normalized degree of coherence, μ_{12} is also known as the complex coherence factor.

The van Cittert–Zernike theorem provides a very convenient method for calculating the degree of spatial coherence that can be derived from a collection of mutually incoherent but quasi-monochromatic radiators. That spatially coherent radiation can be obtained in any circumstance involving uncorrelated radiators may at first seem surprising. Figure 8.17 introduces the subject.

Imagine first that in Figure 8.17 there is only the point source S_1, whose radiation at wavelength λ illuminates a mask with two small openings at points P_1 and P_2 in what we call the *test plane*, because we will use it to test the degree of coherence as a function of separation distance between the two observation points. Radiation will pass these two small openings, propagating to a distant screen where the two beams will overlap. Because the emission is quasi-monochromatic and from a point source (S_1), a well-defined interference pattern will be formed on the screen, as indicated by the solid sinusoidal pattern. Note that the exact location of maxima and minima in this self-interference pattern will depend on the phase difference of the paths from S_1 to P_1 and P_2, indicated as ψ_{21} in Figure 8.17. This phase difference is due entirely to the geometry (and wavelength) and is therefore constant in time, so that the interference pattern (maxima and minima) is also constant in time. Now consider a second point source S_2 at a very small distance from the first (S_1). Its radiation paths are indicated by the dashed lines, resulting in a second stationary interference pattern at the screen, also shown as a dashed line in Figure 8.17. Because the two point radiators are uncorrelated, their fields do not combine to form a mixed (time averaged) interference pattern. Rather, they each form separate self-interference patterns that are quite similar, in fact displaced on the distant screen by only a small phase difference $\delta\psi_{21}$, which is evidently due to the small spatial separation between S_1 and S_2.

We thus begin to see the emerging picture. With some constraints on lateral source size, wavelength, and observation angles, it is possible to obtain rather well-defined interference patterns even with completely uncorrelated emissions. On the other hand, it is also possible to scramble the resultant interference pattern completely by observing a collection of such radiators whose positions in the source plane are sufficiently separated that the resultant phase shifts $\delta\psi_{21}$ are of order π rad or larger, so that the summed intensity patterns at the screen show no net modulation, indicating a total absence of coherence in the test plane. Following Wolf,[1] we will now detail the geometry of propagation paths involved and explore under what circumstances a finite degree of coherence can be obtained, and what the resultant degree of coherence will be.

In Figure 8.18(a) we revisit this geometry for the single point source S, showing propagation paths to two points in the test plane, the origin O, which we use to define an optical axis,

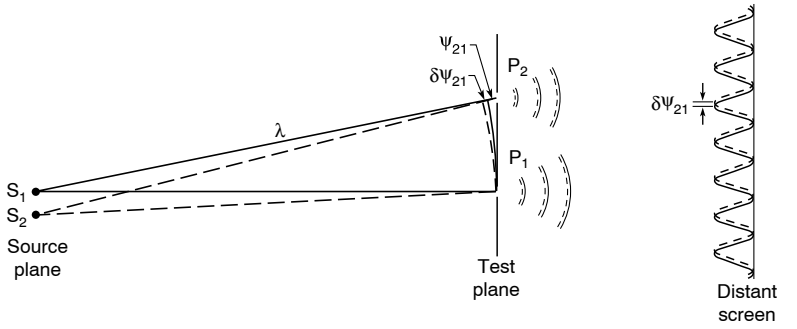

FIGURE 8.17. The persistence of interference fringes as observed in a distant plane is dependent on the spatial separation of two mutually incoherent quasi-monochromatic point sources, the angles, and the wavelength. The source S_1 illuminates small openings at points P_1 and P_2 in a *test plane*. For a single point source S_1 there is a fixed variation ψ_{21} between the two observation points. The resulting interference pattern is observed at a distant screen (solid line). Placing a second point source S_2 at a small distance from S_1 results in a second interference pattern, mutually incoherent with the first, that very nearly overlaps the interference pattern due to S_1, but is shifted by a small amount, $\delta\psi_{21}$. This small phase increment is due to the separation between S_1 and S_2. Thus one sees that within some as yet to be determined limits on source size, observation geometry, and wavelength, mutually incoherent sources of emission can provide a highly coherent radiation field at a distant plane. This is the basis of the van Cittert–Zernike theorem.

and a point P a distance x away in the transverse plane. The distance z separating the parallel source and observation (test) planes is assumed very large compared to the lateral source and observation distances, so that the angle θ is very small. The phase difference between the two paths (ψ_{21} in Figure 8.17) is

$$\psi = \frac{2\pi l}{\lambda} = \frac{kx^2}{2z} = \frac{kz\theta^2}{2} \tag{8.13}$$

where l is the difference in physical path lengths, determined by comparing the sides of the triangle with equal radial distances measured from S. This difference gives the additional path length for a propagating wave. In Figure 8.18(b) we show the point source displaced a distance ξ in the source plane, and again calculate the various path lengths. With the source displaced a distance ξ we observe that a ξ-dependent increment of path difference is introduced, $\delta\psi$, where from the geometry

$$\delta l = -\xi x/z = -\xi\theta$$

with a corresponding increment in phase

$$\delta\psi = \frac{2\pi\,\delta l}{\lambda}$$

or

$$\delta\psi = -k\xi x/z = -k\xi\theta \tag{8.14}$$

These relations can be seen by forming a right angle from the path $\overline{\mathrm{SO}}$ to the line from S to P.

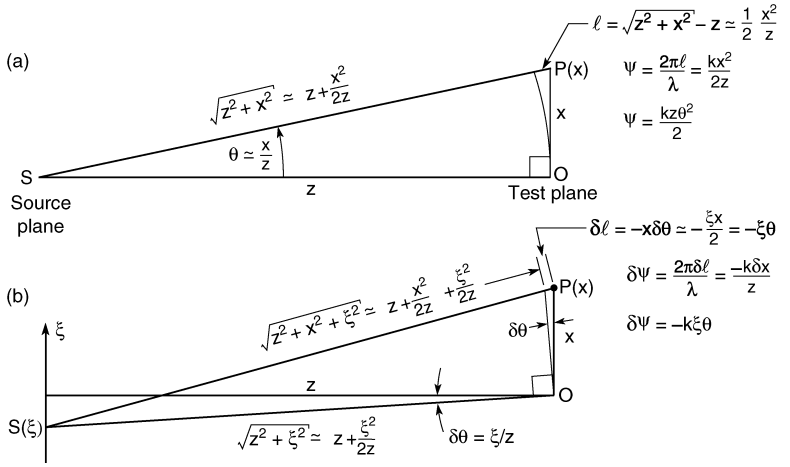

FIGURE 8.18. Propagation paths for radiation from a single point source to two observation points O and P at a distant observation plane. The separation distance z between the two parallel planes is large compared to the lateral source (ξ) and observation (x) distances in their respective planes ($z \gg \xi,\ x$). Shown in (a) are the differences in path length and the resulting phase difference ψ for a spherical wave propagating from a point source at the origin in the source plane to two points in the test (observation) plane, one at the origin O and one a distance x off axis at a point P(x). In (b) the path lengths and phase difference $\delta\psi$ are shown when the source point is displaced a distance ξ from the origin in the source plane.

The increment δl, due to displacement ξ, is also dependent on the distance x from O to P in the test plane.

The scalar electric field at a distance R from a point source of field E_ξ can be written as

$$E = \frac{E_\xi e^{ikR}}{R}$$

where the time dependence $e^{-i\omega t}$ and an arbitrary phase factor are suppressed. Thus the electric field at points O and P due to the source S at ξ can be written for $x,\ \xi \ll z$ as

$$E_{\mathrm{O}} = \frac{E_\xi e^{ik(z+\xi^2/2z)}}{z + \xi^2/2z} \simeq \frac{E_\xi e^{ikz}\, e^{ik\xi^2/2z}}{z} \tag{8.15}$$

and

$$E_{\mathrm{P}} = \frac{E_\xi \exp\left[ik\left(z + \frac{x^2}{2z} + \frac{\xi^2}{2z} - \frac{\xi x}{z}\right)\right]}{z + \frac{x^2}{2z} + \frac{\xi^2}{2z} - \frac{\xi x}{z}} \simeq \frac{E_\xi e^{ikz}\, e^{ik\xi^2/2z}\, e^{ikx^2/2z}\, e^{-ik\xi x/z}}{z}$$

or

$$E_{\mathrm{P}} \simeq \frac{E_\xi e^{ikz}\, e^{ik\xi^2/2z}\, e^{i\psi}\, e^{-ik\xi\theta}}{z} \tag{8.16}$$

where ψ is given by Eq. (8.12) and where we observe that E_{O} and E_{P} contain two identical

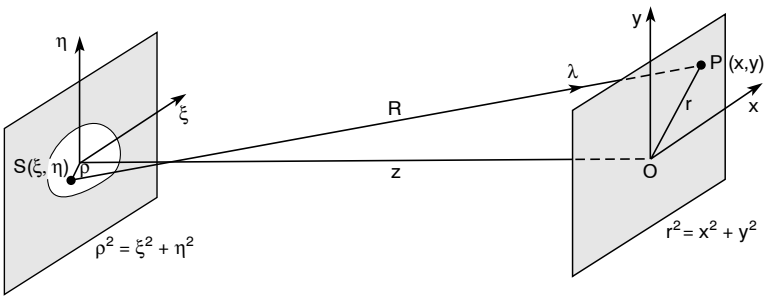

FIGURE 8.19. The geometry for calculation of the van Cittert–Zernike theorem, which involves integration in the $(\xi,\ \eta)$ source plane of the contributions from a continuum of quasi-monochromatic mutually incoherent sources of radiation to the fields at a distant observation plane at the origin O and the off-axis point P(x, y). (Following M. Born and E. Wolf[1].)

phase factors, e^{ikz} and $e^{ik\xi^2/2z}$. Thus for a single point source at ξ, the normalized degree of coherence for electric fields at a point O on the optic axis and a point P at distance x off axis can be obtained by combining Eqs. (8.12), (8.15), and (8.16) to form

$$\mu_{\mathrm{OP}} = \frac{\langle E_{\mathrm{O}} E_{\mathrm{P}}^{*} \rangle}{\sqrt{\langle |E_{\mathrm{O}}|^2 \rangle}\sqrt{\langle |E_{\mathrm{P}}|^2 \rangle}} = e^{-i\psi}\, e^{ik\xi\theta} \tag{8.17}$$

where for $z \gg x,\ \xi$ both normalizing fields can be approximated by

$$\sqrt{\langle |E_{\mathrm{O}}|^2 \rangle} \simeq \sqrt{\langle |E_{\mathrm{P}}|^2 \rangle} \simeq \frac{|E_{\xi}|}{z}$$

In Eq. (8.17) ψ is an x-dependent phase shift (for fixed z) due to the displacement of P from the axis, and the $ik\xi\theta$ factor is due to the ξ-dependent tilt of the wavefront, with a leverage due to x, where $\theta \simeq x/z$. Equation (8.17) is readily extended to three dimensions (ξ, η, z and x, y, z), as illustrated in Figure 8.19. The normalized correlation function becomes

$$\mu_{\mathrm{OP}} = e^{-i\psi}\, e^{ik(\xi\theta_x + \eta\theta_y)} \tag{8.18a}$$

where in the three dimensional coordinate system

$$\psi = k\frac{x^2 + y^2}{2z} = kz\frac{\theta_x^2 + \theta_y^2}{2} \tag{8.18b}$$

$$\theta_x = \frac{x}{z} \tag{8.18c}$$

$$\theta_y = \frac{y}{z} \tag{8.18d}$$

Again, the ψ factor is strictly due to the angular projection of the observation point P as measured from the optic axis, with no dependence on the source point location, while the $k(\xi\theta_x + \eta\theta_y)$ factor is now generalized to take account of the wavefront tilt due to both source point coordinates ξ and η.

If we now assume that there is a distribution of quasi-monochromatic source points in the ξ, η-plane, all mutually incoherent, then we can sum their individual contributions to the fields at O and P in the x, y-plane. Integrating over the extended source as suggested in Figure 8.19, one obtains the complex degree of coherence by combining Eqs. (8.12) and (8.18):

$$\mu_{\mathrm{OP}} = \frac{e^{-i\psi} \iint |E(\xi,\eta)|^2 \, e^{ik(\xi\theta_x + \eta\theta_y)} \, d\xi \, d\eta}{\iint |E(\xi,\eta)|^2 \, d\xi \, d\eta}$$

or in terms of the source plane intensity distribution $I(\xi, \eta) \propto |E(\xi, \eta)|^2$,

$$\boxed{\mu_{\mathrm{OP}} = \frac{e^{-i\psi} \iint I(\xi,\eta) e^{ik(\xi\theta_x + \eta\theta_y)} \, d\xi \, d\eta}{\iint I(\xi,\eta) \, d\xi \, d\eta}} \tag{8.19}$$

This is the *van Cittert–Zernike theorem.* It states that the normalized degree of coherence for a distribution of uncorrelated quasi-monochromatic emissions, observed in a distant plane, is equal to the two dimensional Fourier transform of the source intensity function. Again the phase $\psi = k(x^2 + y^2)/2z$ is purely geometrical, giving the predictable oscillation of phase as the observation point P is moved from the reference position O at the origin.

Of particular interest to us is the axisymmetric case, as might be encountered in pinhole spatial filtering of undulator or EUV/soft x-ray laser radiation. For an axisymmetric geometry it is convenient to introduce cylindrical coordinates, $(\rho, \phi_{\mathrm{S}})$, in the (ξ, η) source plane, and (r, ϕ_{P}) in the (x, y) observation (test) plane. The geometrical details are clarified in Figure 8.20. The normalized degree of coherence can now be written as

$$\mu_{\mathrm{OP}} = \frac{e^{-i\psi} \int_0^\infty \int_0^{2\pi} I(\rho,\phi_{\mathrm{S}}) e^{ik(\rho\cos\phi_{\mathrm{S}}\cdot\theta\cos\phi_{\mathrm{P}} + \rho\sin\phi_{\mathrm{S}}\cdot\theta\sin\phi_{\mathrm{P}})} \, \rho \, d\rho \, d\phi_{\mathrm{S}}}{\int_0^\infty \int_0^{2\pi} I(\rho,\phi_{\mathrm{S}}) \rho \, d\rho \, d\phi_{\mathrm{S}}}$$

$$\mu_{\mathrm{OP}} = \frac{e^{-i\psi} \int_0^\infty \int_0^{2\pi} I(\rho,\phi_{\mathrm{S}}) e^{ik\rho\theta\cos(\phi_{\mathrm{S}} - \phi_{\mathrm{P}})} \rho \, d\rho \, d\phi_{\mathrm{S}}}{\int_0^\infty \int_0^{2\pi} I(\rho,\phi_{\mathrm{S}}) \rho \, d\rho \, d\phi_{\mathrm{S}}}$$

where $\cos(\phi_{\mathrm{S}} - \phi_{\mathrm{P}}) = \cos\phi_S \cos\phi_{\mathrm{P}} + \sin\phi_{\mathrm{S}} \sin\phi_{\mathrm{P}}$. For the axisymmetric case, where $I(\rho, \phi_{\mathrm{S}}) = I(\rho)$, this becomes

$$\boxed{\mu_{\mathrm{OP}} = \frac{e^{-i\psi} \int_0^\infty I(\rho) J_0(k\rho\theta) \, \rho \, d\rho}{\int_0^\infty I(\rho) \, \rho \, d\rho}} \tag{8.20}$$

where we have made the identification[40–42]

$$J_0(k\rho\theta) = \frac{1}{2\pi} \int_0^{2\pi} e^{ik\rho\theta\cos(\phi_{\mathrm{S}} - \phi_{\mathrm{P}})} \, d\phi_{\mathrm{S}} \tag{8.21}$$

for a Bessel function[43] $J_0(\nu)$ of the first kind, order zero. In this axisymmetric geometry, the degree of coherence is described in terms of a Fourier–Bessel transform of the radial source function, sometimes described as a Hankel transform.[44, 45]

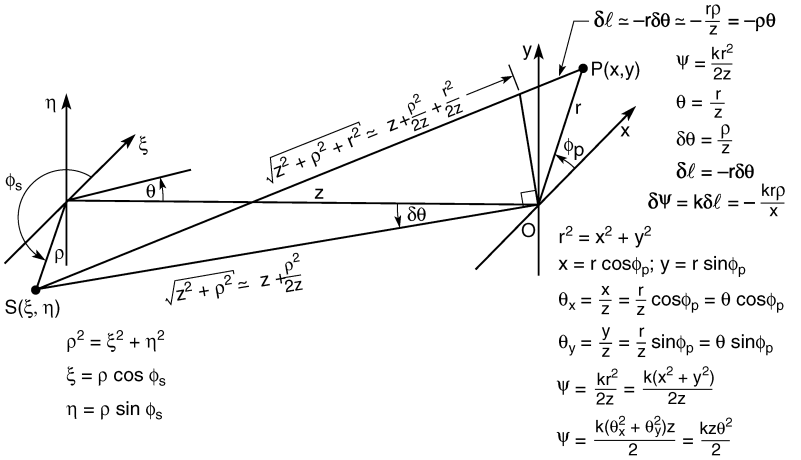

FIGURE 8.20. Geometry of the various propagation path lengths and phase differences (ψ) as a function of cylindrical coordinates (ρ, ϕ_S) in the source plane and (r, ϕ_P) in the observation (test) plane. The angle θ is measured from the optic axis to the point P.

We will next consider three axisymmetric cases of interest, (1) a point source, (2) a Gaussian intensity distribution, and (3) a uniformly but incoherently illuminated pinhole. The analysis of each follows.

(1) **A Point Source:** For a point source described by a normalized delta function[††] in cylindrical coordinates,

$$I = I_0\delta(\rho)/2\pi\rho \tag{8.22}$$

the degree of coherence is given by [Eq. (8.20)]

$$\mu_{OP} = \frac{e^{-i\psi}\int_0^\infty \delta(\rho)J_0(k\rho\theta)\,d\rho}{\int_0^\infty \delta(\rho)\,d\rho} = e^{-i\psi}J_0(0)$$

or

$$\mu_{OP} = e^{-i\psi} \tag{8.23a}$$

where $J_0(0) = 1$ and from Figure 8.20 $\psi = kr^2/2z = kz\theta^2/2$. Thus for a true point source the normalized degree of coherence $|\mu_{OP}| = 1$, so that the radiated field is *fully coherent* in the distant (z) plane, with a *perfectly described phase variation* $\psi(r)$ as a function of off-axis position, i.e., the field variations in the observation or test plane are completely predictable, with a variation for distance z between the source and observation planes given by

$$\mu_{OP} = e^{-ikz\theta^2/2} \tag{8.23b}$$

with a θ^2 phase variation as was first encountered in Figure 8.18(a).

[††]The normalization condition is determined by $\int_0^\infty\int_0^{2\pi} f(\rho,\phi)\,\rho\,d\rho\,d\phi = 2\pi\int_0^\infty f(\rho)\,\rho\,d\rho = 1$.

(2) **A Gaussian Intensity Distribution:** For an axisymmetric Gaussian source of standard deviation a such that

$$I = I_0 e^{-\rho^2/2a^2} \tag{8.24}$$

the normalized degree of coherence [Eq. (8.20)] takes the form

$$\mu_{\mathrm{OP}} = \frac{e^{-i\psi} \int_0^\infty e^{-\rho^2/2a^2} J_0(k\theta\rho)\, \rho\, d\rho}{\int_0^\infty e^{-\rho^2/2a^2}\, \rho\, d\rho}$$

These are standard integrals,[46] which yield the result

$$\boxed{\mu_{\mathrm{OP}} = e^{-i\psi} e^{-(ka\theta)^2/2}} \tag{8.25}$$

This degree of coherence for a Gaussian distributed source exhibits the same geometrical phase variation, $\psi = kz\theta^2/2$, as did the point source, now however with an additional Gaussian amplitude dependence as a function of θ. Note that for $ka\theta = \frac{1}{2}$, corresponding to $d \cdot \theta = \lambda/2\pi$, the normalized degree of coherence is

$$|\mu_{\mathrm{OP}}| = e^{-1/8} = 0.88$$

which is just 12% less than the maximum value of unity. Thus for a radiation source described statistically as a point source to within a standard deviation a, the far-field angular distribution is concomitantly determined to within one standard deviation θ, as described earlier in this chapter on the basis of uncertainty arguments, i.e., the quantities a and θ constitute an *uncertainty pair* or *transform pair*, more usually written as uncertainties in position and momentum $\Delta r \cdot \Delta p = \hbar/2$, where $\Delta r = a$ and $\Delta p = \hbar \Delta k = 2\pi\hbar\theta/\lambda$. We now see by use of the van Cittert–Zernike theorem that in the case where the uncertainty condition, written as $d \cdot \theta = \lambda/2\pi$ earlier in this chapter, is just met, the finite degree of coherence is not unity, but somewhat less at 0.88. That is to say, if we knew the electric field on axis, the expectation that we could predict the field at an off-axis angular position θ would be 0.88. Since the degree of coherence varies as θ^2 in this case [Eq. (8.23b)], the degree of coherence can be increased substantially, to $e^{-1/32} = 0.97$, by halving the observation angle to $ka\theta = \frac{1}{4}$, albeit at a considerable loss of flux or power.

(3) **A Uniformly but Incoherently Illuminated Pinhole:** For a uniform circular disk of uncorrelated emitters, the equivalent of an incoherently illuminated pinhole, we can write the source function as

$$I(\rho) = \begin{cases} I_0 & \text{for } \rho \le a \\ 0 & \text{for } \rho > a \end{cases} \tag{8.26}$$

where $d = 2a$ is the pinhole diameter. The degree of coherence [Eq. (8.20)] then becomes

$$\mu_{\mathrm{OP}} = \frac{e^{-i\psi} I_0 \int_0^a J_0(k\rho\theta)\, \rho\, d\rho}{I_0 \int_0^a \rho\, d\rho}$$

$$\mu_{\mathrm{OP}} = \frac{8e^{-i\psi}}{d^2} \int_0^a J_0(k\rho\theta)\rho\, d\rho$$

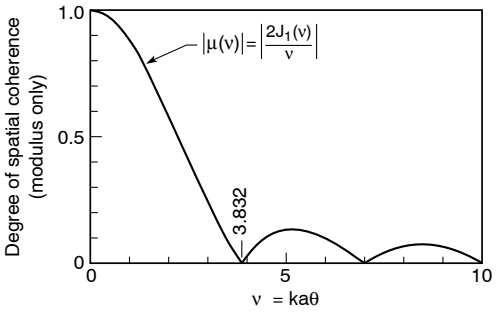

FIGURE 8.21. The degree of coherence for a uniformly but incoherently illuminated pinhole as observed at an angle θ in the far field. The modulus of the degree of spatial coherence follows a $2J_1(\nu)/\nu$ behavior.

which is of the standard integral form[47]

$$\int_0^1 xJ_0(\nu x)\,dx = \frac{J_1(\nu)}{\nu}$$

where we have made the substitutions $\rho = ax$ and $k\rho\theta = \nu x$ so that $\nu = ka\theta$. Making these substitutions, one finds that for the *incoherently illuminated pinhole* the normalized degree of coherence is

$$\boxed{\mu_{\mathrm{OP}}(\theta) = e^{-i\psi}\frac{2J_1(ka\theta)}{ka\theta}} \tag{8.27}$$

where $J_1(\nu)$ is a Bessel function of the first kind, of order one, and where again $\psi = kz\theta^2/2$.

The function $2J_1(\nu)/\nu$ is plotted[43] in Figure 8.21. It has a maximum value of unity at $ka\theta = 0$, drops to 0.88 at $ka\theta = 1$, and is zero, corresponding to complete incoherence (no correlation among the fields at these two points), for $ka\theta = 3.832$. The latter corresponds to $d\cdot\theta = 1.22\lambda$. These results are particularly interesting in a practical sense in that circular pinhole apertures, back-illuminated by essentially incoherent radiation, provide a particularly attractive method by which to obtain spatially coherent radiation at these very short wavelengths, as was stated without proof in Section 8.4 and illustrated in Figure 8.9. Further tradeoffs, gaining improved spatial coherence at a cost of reduced coherent power, can be made by further constraining the product $ka\theta$. For example, rather than accepting a degree of coherence of 0.88 with $ka\theta = 1$, choose smaller values of both a and θ. Expanding $J_1(ka\theta)$ for small values[48] of $ka\theta$ in Eq. (8.27), the degree of coherence for an incoherently illuminated pinhole becomes

$$|\mu_{\mathrm{OP}}| \simeq 1 - \frac{1}{8}(ka\theta)^2 + \frac{1}{384}(ka\theta)^4 - \cdots \tag{8.28}$$

One finds, for instance, that for a space–angle constraint $ka\theta = \frac{1}{4}$ corresponding to $d\cdot\theta = \lambda/4\pi$, the degree of coherence is 0.99, and thus within 1% of perfect spatial coherence over this limited phase–space product. Compared to the case $ka\theta = 1$, with a 0.88 degree of coherence,

this improvement comes at a cost of reduced coherent power by a factor of 16, because, the loss scales as $(ka\theta)^2$ in an axisymmetric system. Nonetheless, this provides an interesting exercise in the use of the powerful van Cittert–Zernike theorem, permitting a quantitative evaluation of the tradeoff between available coherent power and degree of spatial coherence in a very practical application.

Thompson and Wolf[49] have taken this work further in both experiments and analysis. In much referenced experiments[1, 2, 50] with incoherent visible light and a geometry similar to that of Figure 8.17, the contrast in fringe (interference) patterns is observed to follow the $J_1(v)/v$ behavior of Eq. (8.26), illustrated in Figure 8.21, with fringe visibility rising and falling as predicted. Furthermore, Thompson and his colleagues have extended the analysis of far-field pinhole diffraction patterns for partially coherent radiation[51, 52] with varying degrees of spatial coherence across the pinholes. Their diffraction results are described further in Chapter 9, where diffraction from pinholes and zone plates is considered (see Section 9.3, Figure 9.11).

8.7 EXAMPLES OF HIGH CONTRAST FRINGES FORMED AT SHORT WAVELENGTHS

High quality interference patterns have been recorded at very short wavelengths utilizing radiation from an extended, essentially incoherent source of quasi-monochromatic radiation taking advantage of the quantitative limits of source size and divergence permitted by the van Cittert–Zernike theorem. The experiments are part of a developmental activity led by J. Bokor and his colleagues[53–56] involving at-wavelength interferometry[57, 58] for the metrology and ultimate improvement of both multilayer coated and diffractive optics. Pinhole spatial filtering of largely incoherent radiation, as discussed in the preceding paragraphs, is employed with undulator radiation in a geometry illustrated earlier in Figures 8.9 and 8.11.

The geometry for the particular phase shifting point diffraction interferometer [54, 55] utilized is shown in Figure 8.22. It is a common-path interferometer, thus requiring minimal longitudinal coherence length and requiring no beamsplitter (for which flatness is problematic at these wavelengths). The grating provides a phase shifting capability to assist in fractional fringe analysis and with a relatively high throughput. As seen in Figure 8.22, undulator radiation characterized by a large phase space overfills a pinhole of diameter d. The acceptance angle θ is set by the aperture of the optic under test and its distance downstream of the pinhole. The optical system under test forms an image of the pinhole at its conjugate (image) plane. The grating, which is employed to provide a fractional fringe phase shifting capability when moved laterally, generates several orders, two of which are permitted to reach the image plane. For the example shown in Figure 8.22 the zeroth order and one of the first orders are selected by an image plane mask. With a perfect optic both would form Airy patterns[1] at the focal plane.[‡‡] This, of course, is not the case; aberrations of the optical system cause departures of the wavefronts from sphericity, which is precisely what is to be measured in the interferometer. To do so, one of the two waves reaching the image plane is spatially filtered a second time, using an image plane mask *reference* pinhole to remove these wavefront distortions. This then provides a near-perfect spherical reference wave against which to compare the second (still aberrated) wavefront of the remaining order. The two then propagate on to overlap and form an interface pattern, which is recorded by the CCD camera.[¶¶]

[‡‡] The subject of pinhole diffraction and Airy patterns is discussed in Chapter 9, Section 9.3.

[¶¶] Charged coupled device, an electronic array detector, back-thinned in this case to provide detection sensitivity at EUV and soft x-ray wavelengths.

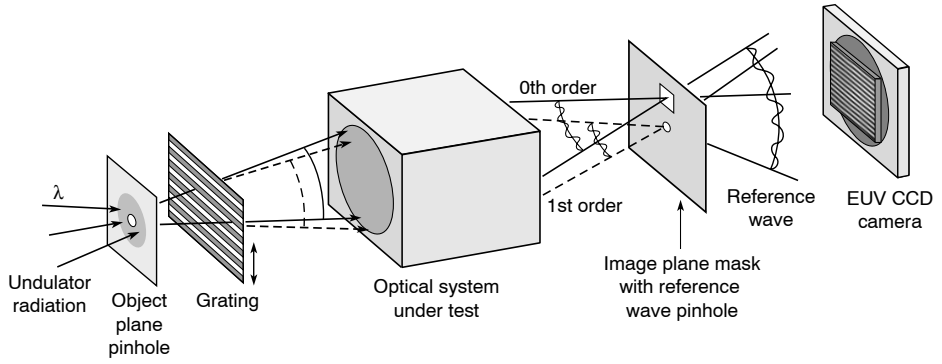

FIGURE 8.22. A phase shifting point diffraction interferometer (PS/PDI) for testing reflective and diffractive optics at EUV and soft x-ray wavelengths. Largely incoherent undulator radiation enters from the left, over-filling a pinhole spatial filter. The grating generates several orders, two of which are permitted (by an image plane mask) to pass through the interferometer. The optical system under test forms an image of the pinhole with each of the transmitted orders. Because the optic is not perfect, it distorts both wavefronts, which therefore now carry information regarding the aberrations of the optical system. By removing the wavefront distortion in one of the two wavefronts, through the use of a second, image-plane pinhole spatial filter, a short wavelength optical interferometer is formed. The two wavefronts propagate to a distant plane, where they overlap and their interference is recorded on a CCD electronic array detector. (Courtesy of H. Medecki, E. Tejnil, K. Goldberg, P. Naulleau, J. Bokor, and colleagues,[54–56] Lawrence Berkeley National Laboratory.)

An interference pattern[59] recorded in this manner is shown in Figure 8.23(a). The period of the interference pattern is controlled by the choice of grating period and geometry. A line-out showing the fringe contrast (visibility) is shown in Figure 8.23(b). The optical system under test in this case was a 10× magnification, 0.08 NA Schwarzschild optic (see Chapter 4), multilayer coated[60, 61] for peak reflectivity at a wavelength of 13.4 nm. The undulator was tuned for maximum output at this wavelength. A recorded Airy pattern, showing the emissions from the first (upstream) pinhole used to illuminate the optic under test, was shown earlier in Figure 8.12 and in the frontispiece for this chapter. About half of the central radiation lobe is used. For the interference pattern shown in Figure 8.23(a), the upstream spatial filter consists of a 0.75 μm diameter pinhole and an acceptance half angle of 0.008 (i.e., NA/10), so that for $\lambda = 13.4$ nm the parameter appearing in Eq. (8.26) is $ka\theta = 1.4$. According to the previous paragraphs this corresponds to a degree of coherence of approximately 0.8 radially across the test wavefront. The image plane pinhole, used to generate the final reference wave, has a 120 nm diameter.

Note that fringe contrast in this experiment is affected by the grating period, which sets the shear angle between the two interfering wavefronts. The fringe contrast shown in Figure 8.23(b) is about 0.7. For the particular optic under test in these experiments,[59] analysis of the interference pattern indicates an optical wavefront error of 0.86 nm rms at 13.4 nm ($\lambda_{euv}/15$), indicating a capability for near-diffraction-limited imaging over a small field. The subject of better quality optics and the use of aspheres to cover a larger field of view is discussed in Chapter 10, in Section 10.2 on extreme ultraviolet lithography.

The accuracy of this interferometer ultimately depends on minimizing departures from sphericity of the wavefront incident on the optic under test, and a similar constraint on the reference wavefront incident on the CCD. To improve the accuracy, at the cost of reduced photon flux, the pinhole-aperture spatial filter can be operated at smaller values of the parameter $ka\theta$. To assess the accuracy of the interferometer one can spatially filter both waves (grating orders)

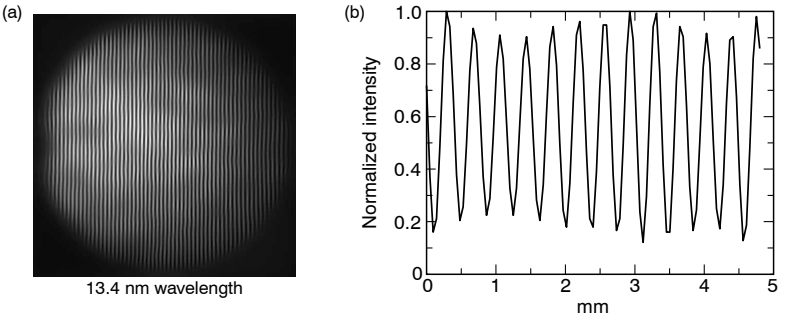

FIGURE 8.23. An interference pattern (a) obtained using the interferometer of Figure 8.22, recorded at a wavelength of 13.4 nm. The intensity variation (b) for a line through the center of the fringe pattern shows a contrast (visibility) of approximately 0.7. The optical system under test in these measurements, a multilayer coated 10× reduction Schwarzschild (see Chapter 10, Figure 10.10), has a figure error of 0.86 nm rms ($\lambda_{euv}/15$). (Courtesy of K. Goldberg and colleagues,[59] Lawrence Berkeley National Laboratory.)

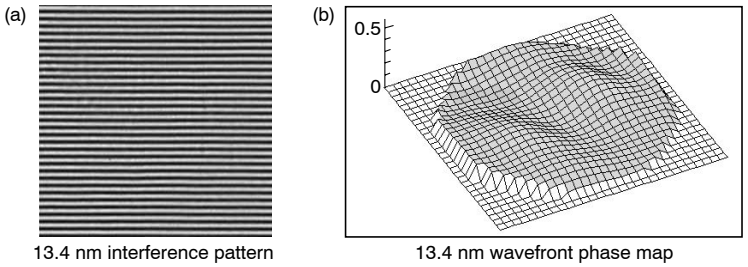

FIGURE 8.24. (a) An interference pattern recorded at 13.4 nm wavelength using two 100 nm diameter pinholes and an EUV CCD in the point diffraction interferometer shown in Figure 8.22. Through use of this two-pinhole *null mask* the wavefront accuracy of the interferometer can be determined. (b) Analysis of the interference pattern yields data on wavefront uniformity, measured to be 0.054 nm rms, or $\lambda_{euv}/250$ with these 100 nm pinholes. Wavefront uniformity has been measured to $\lambda_{euv}/330$ using 80 nm pinholes. (Courtesy of P. Naulleau and colleagues,[63] Lawrence Berkeley National Laboratory.)

using two pinholes in the mask plane. This is accomplished by replacing the image plane mask shown in Figure 8.22 by one containing two side-by-side pinholes. Figure 8.24(a) shows a recorded interference pattern obtained with two side-by-side 100 nm diameter pinholes, separated from each other by 4.5 μm. The mask was fabricated using electron beam lithography techniques,[62] as discussed in the following chapter, Section 9.10. Analysis of the interference pattern indicates that the reference wave has a departure from sphericity [Figure 8.2(b)] of 0.054 nm rms over a numerical aperture of 0.08, or $\lambda_{euv}/250$ at 13.4 nm wavelength.[63] Experiments using a pair of 80 nm pinholes have achieved a wavefront error of 0.041 nm rms, or $\lambda_{euv}/330$. In an rms sense, this is a metrological accuracy smaller than the first Bohr radius of the hydrogen atom ($a_0 = 0.053$ nm). A comparison of visible light and EUV interferometry is described by Goldberg, Naulleau, Chapman, and colleagues in Ref. 64. Note that this interferometer can also be used to test Fresnel zone plate lenses, a subject discussed in the following chapter on diffractive optics.

Chang[65] has begun efforts to repeat at short wavelength the classic two pinhole fringe visibility experiments of Thompson and Wolf[49]. Figure 8.24(a) shows the recorded interference pattern at 13.4 nm wavelength of overlapping Airy patterns from two 420 nm diameter

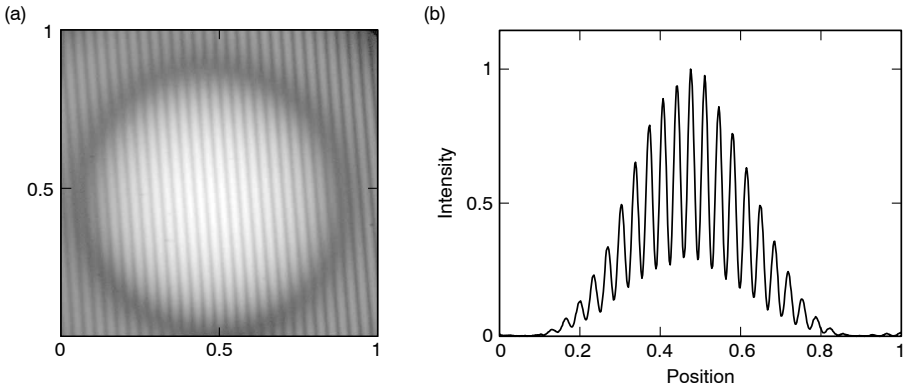

FIGURE 8.25. (a) The recorded interference pattern at 13.4 nm wavelength of two 420 nm diameter pinholes separated by 5 μm as part of experiments to measure the partial coherence of reimaged undulator radiation. (b) The normalized intensity modulation through the center of (a) showing approximately 70% fringe contrast at this separation. (Courtesy of C. Chang, University of California, Berkeley, and Lawrence Berkeley National Laboratory.)

pinholes seperated by 5 μm. The interference pattern is recorded on a one inch square, 512 by 512, EUV sensitive CCD camera at a distance of 26 cm. The radiation is derived from the undulator beamline[19] described in Figures 8.11 and 8.12. Intensity modulation of the recorded interference pattern is shown in Figure 8.24(b). At this separation the fringe contrast is approximately 70%. Increasing the pinhole separation to 9 μm in these continuing experiments, the contrast decreases significantly, indicating a decreased coherence.

REFERENCES

1. M. Born and E. Wolf, *Principles of Optics* (Pergamon, New York, 1983), Chapter 10; see also Section 8.5.2 for a discussion of the Airy pattern; For a more advanced discussion see L. Mandel and E. Wolf, *Optical Coherence and Quantum Optics* (Cambridge Univ. Press, 1995).
2. J.W. Goodman, *Statistical Optics* (Wiley, New York, 1985).
3. R.J. Collier, C. Burkhardt, and L.H. Lim, *Optical Holography* (Academic Press, New York, 1985).
4. P.A. Tipler, *Modern Physics* (Worth, New York, 1978), Section 5.7.; also see R.N. Bracewell, *The Fourier Transform and Its Applications* (McGraw-Hill, NY, 1986), Second edition, p. 160.
5. A.E. Siegman, *Lasers* (University Science, Mill Valley, CA, 1986), Chapters 1, 14, and 17, and Eq. 17-5, recast here in terms of rms quantities.
6. G.R. Fowles, *Introduction to Modern Optics* (Dover, New York, 1989), Chapters 3 and 9.
7. D. Attwood, K. Halbach, and K.-J. Kim, "Tunable Coherent X-Rays," *Science 228*, 1265 (14 June 1985). Coherence length and spectral bandwidth are defined slightly differently in this paper.
8. E. Hecht, *Optics* (Addison-Wesley, Reading, PA, 1998), Third Edition, Chapters 10 and 12; see Sec. 10.2.5 and 10.2.6 regarding diffraction by a circular aperture and the Airy pattern.
9. S. Aoki, Y. Ichihara, and S. Kikuta, *Jpn. J. Appl. Phys. 11*, 1857 (1972). The outline of this paper is repeated in Ref. 7. Also see S. Kikuta and K. Kohra, *Opt. Commun. 5*, 86 (1972).
10. Much work in this area has been reported by M. Howells, C. Jacobsen, J. Kirz, and their colleagues. For an extensive list of references to their work and that of others see S. Lindaas, M. Howells, C. Jacobsen, and A. Kalinovsky, "X-Ray Holographic Microscopy by Means of Photoresist Recording and Atomic Force Microscope Readout," *J. Opt. Soc. Amer. 13*, 1788 (1996).
11. D. Joyeaux and F. Pollack, "Carbon Index Measurement Near K-Edge, by Interferometry with Optoelectronic Detection," p. II-103 in *X-Ray Microscopy and Spectromicroscopy* (Springer, Berlin, 1998), J. Thieme, G. Schmahl, D. Rudolph, and E. Umbach, Editors.

12. A.L. Schawlow, "Laser Light," *Sci. Amer. 219*, 120 (September 1968).
13. A.M. Kondratenko and A.N. Skrinsky, "Use of Radiation of Electron Storage Rings in X-Ray Holography of Objects," *Opt. Spectrosc. (USSR) 42*, 189 (February 1977); p. 338 in the original Russian journal.
14. The monochromator illustrated in Figure 8.11 is similar to that described in J. Underwood, E. Gullikson, M. Koike, P. Batson, P. Denham, K. Franck, R. Tackaberry, and W. Steele, "Calibration and Standards Beamline 6.3.2 at the Advanced Light Source," *Rev. Sci. Instrum. 67(9)*, 1 (September 1996); also R. Beguiristain, "Thermal Distortion Effects on Beamline Design for High Flux Synchrotron Radiation," Ph.D. Thesis, Nuclear Engineering Department, University of California at Berkeley, Oct. 1997.
15. M. Hettrick, J. Underwood, P. Batson, and M. Eckart, "Resolving Power of 35,000 in the Extreme Ultraviolet Employing a Grazing Incidence Spectrometer," *Appl. Opt. 27*, 200 (15 January 1988), and references therein.
16. W.B. Peatman, *Gratings, Mirrors and Slits* (Gordon and Breach, Amsterdam, 1997). For synchrotron beamlines with high thermal loading see the review article by A.K. Freund, "Synchrotron X-ray Beam Optics" in *Complementarity Between Neutron and Synchrotron X-Ray Scattering*, A. Furrer, Editor (World Sci. Press, Singapore, 1998).
17. J.A.R. Samson and D.L. Ederer, *Vacuum Ultraviolet Spectroscopy*, Vol. I, II (Academic, San Diego, CA, 1997).
18. E.G. Loewen and E. Popov, *Diffraction Gratings and Applications* (Marcel Dekker, New York, 1997).
19. D.T. Attwood, P. Naulleau, K.A. Goldberg, E. Tejnil, C. Chang, R. Beguiristain, P. Batson, J. Bokor, E.M. Gullikson, H. Medecki, and J.H. Underwood, "Tunable Coherent Radiation in the Soft X-Ray and Extreme Ultraviolet Spectral Regions," *IEEE J. Quant. Electr. 35* (May 1999).
20. D. Attwood, K.-J. Kim, N. Wang, and N. Iskander, "Partially Coherent Radiation at X-Ray Wavelengths," *J. de Phys. (Paris) 47*, C6-203, Suppl. 10 (October 1986).
21. R. Coïsson, "Spatial Coherence of Synchrotron Radiation," *Appl. Opt. 34*, 904 (1995); K. Fezzaa, F. Comin, S. Marchesini, R. Coïsson, and M. Belakhovsky, "X-Ray Interferometry at ESRF Using Two Coherent Beams from Fresnel Mirrors," *J. X-Ray Sci. Technol. 7*, 12 (1997).
22. D.L. Abernathy, G. Grübel, S. Bauer, I. McNulty, G.B. Stephenson, S.G.J. Mochrie, A.R. Sandy, N. Mulders, and M. Sutton, "Small-Angle X-Ray Scattering Using Coherent Undulator Radiation at ESRF," *J. Synchr. Rad. 5*, 37 (1998).
23. A. Snigirev, I. Snigireva, V. Kohn, S. Kuznetsov, and I. Schelokov, "On the Possibilities of X-Ray Phase Contrast Microimaging by Coherent High-Energy Synchrotron Radiation," *Rev. Sci. Instrum. 66*, 5486 (1995); Z.H. Hu, P.A. Thomas, A. Snigerev, I. Snigireva, A. Souvorov, P.G.R. Smith, G.W. Ross, and S. Teats, "Phase-Mapping of Periodically Domain-Inverted $LiNbO_3$ with Coherent X-Rays," *Nature 392*, 690 (1998).
24. Y. Takayama, R.Z. Tai, T. Hatano, T. Miyahara, W. Okamoto, and Y. Kagoshima, "Measurement of the Coherence of Synchrotron Radiation," *J. Synchr. Rad. 5*, 456 (1998); Y. Takayama et al., "Relationship between Spatial Coherence of Synchrotron Radiation and Emittance," *J. Synchr. Rad. 5*, 1187 (1998).
25. D. Attwood, "Comparative Features of Partially Coherent X-Ray Sources," in *Proceedings of the First Symposium on the Applications of Laboratory X-Ray Lasers, Asilomar, February 1985*, N.M. Ceglio, Editor; published by Lawrence Livermore National Laboratory as CONF-850293-Abstracts.
26. M.D. Rosen, J.E. Trebes, and D.L Matthews, "A Strategy for Achieving Spatially Coherent Output from Laboratory X-Ray Lasers," *Comments Plasma Phys. Fusion 10*, 245 (1987).
27. R.A. London, M. Strauss, and M.D. Rosen, "Model Analysis of X-Ray Laser Coherence," *Phys. Rev. Lett. 65*, 563 (30 July 1990); see also R.A. London, P Amendt, M. Strauss, M.D. Rosen, M.D. Feit, and J.A. Fleck, "Coherent X-Ray Lasers for Applications," p. 363 in *X-Ray Lasers 1990* (Instit. of Physics, Bristol, England, 1990), G.J. Tallents Editor.
28. J.A. Koch, B.J. MacGowan, L.B. DaSilva, D.L. Mathews, S. Mrowka, J.H. Underwood, and P.J. Batson, "Selenium X-Ray Laser Line Profile Measurements," in *X-Ray Lasers 1992* (Inst. Phys., Bristol, England, 1992), E.E. Fill, Editor; also J.A. Koch et al., *Phys. Rev. Lett. 68*, 3291 (1992).
29. B.MacGowan, S. Maxon, P. Hagelstein, C. Keane, R. London, D. Mathews, M. Rosen, J. Scofield, and D. Whelan, "Demonstration of Soft X-Ray Amplification in Nickel-Like Ions," *Phys. Rev. Lett.*

59, 2157 (9 November 1987); see also B.J. MacGowan, S. Maxon, L.B. Da Silva, D.J. Fields, C.J. Keane, D.L. Matthews, A.L. Osterheld, J.H. Scofield, G. Shimkaveg, and G.F. Stone, "Demonstration of X-Ray Amplifiers Near the Carbon K Edge," *Phys. Rev. Lett. 65*, 420 (1990).

30. L. Da Silva, T. Barbee, R. Cauble, P.Celliers, D. Ciarlo, S. Libby, R. London, D. Matthews, S. Mrowka, J. Trebes, A. Wan, and F. Weber, "Development of XUV-Interferometry (155 Å) Using a Soft X-Ray Laser," in *Soft X-Ray Lasers and Applications* (SPIE, Bellingham, WA, 1995), J. Rocca and P. Hagelstein, Editors, *Proc. SPIE 2520*, 288 (1995).
31. R. Burge, G. E. Slark, M.T., Browne, X.C. Yuan, P. Charalambous, X.H. Cheng, C.L.S. Lewis, G.F. Cairns, A.G. MacPhee, and D. Neely, "Dependence of the Spatial Coherence of 23.2–23.6 nm Radiation on the Geometry of a Multielement Germanium X-Ray Laser Target," *J. Opt. Soc. Amer. B, 15*, 2515 (1998); R.E. Burge et al., "Time Dependence of the Spatial Coherence of the 23.6 and 23.2-nm Radiation from the Germanium Soft X-Ray Laser," *J. Opt. Soc. Amer. B, 15,* 1620 (1998).
32. N. M. Ceglio, D.G. Stearns, D.P. Gaines, A.M. Hawryluk, and J.E. Trebes, "Multipass Amplification of Soft X-Rays in a Laser Cavity," *Opt. Lett. 13,* 108 (1988); N.M. Ceglio, D.P. Gaines, J.E. Trebes, R.A. London, and D.G. Stearns, "Time Resolved Measurement of Double Pass Amplification of Soft X-Rays," *Appl. Opt. 7,* 5022 (1988; N.M. Ceglio, D.P. Gaines, D.G. Stearns, and A.M. Hawryluk, "Double Pass Amplification of Laser Radiation at 131 Å," *Opt. Commun. 69,* 285 (1989).
33. B.J. MacGowan, S. Mrowka, T.W. Barbee, L.B. Da Silva, D.C. Eder, J.A. Koch, L.S. Pan, J.A. Turner, J.H. Underwood, and P.E. Young, "Investigation of Damage to Multilayer Optics in X-Ray Laser Cavities: W/C, WRe/C, WC/C, Stainless Steel/C, and Cr_3C_2/C Mirrors," *J. X-Ray Sci. Techn. 3*, 231 (1992).
34. G.J. Pert, S.B. Healy, J.A. Plowes, and P.S. Simms, "Effects of Density Structures and Temporal Shaping of the Pump Pulse in X-Ray Lasing," in *X-Ray Lasers '96,* S. Svanberg and C.-G. Wahlström, Editors, p. 260.
35. F. Albert, A. Carillon, P. Jaeglé, G. Jamelot, A. Klisnick, D. Ros, B. Rus, S. Sebban, and P. Zeitoun, "New Approach for Measurement of the X-Ray Laser Transverse Coherence," p. 427 in *X-Ray Laser '96*, S. Svanberg and C.-G. Wahlström, Editors, to be published.
36. M.C. Marconi, J.L.A. Chila, C.H. Moreno, B.R. Benware, and J.J. Rocca, "Measurement of the Spatial Coherence Buildup in a Discharge Pumped Table-Top Soft X-Ray Laser," *Phys. Rev. Lett. 79*, 2799 (1997); B.R. Benware, C.D. Macchieto, C.H. Moreno, and J.J. Rocca, "Demonstration of a High Average Power Table-Top Soft X-Ray Laser," *Phys. Rev. Lett. 81*, 5804 (1998). C.H. Moreno, M.C. Marconi, V.N. Shlyaptev, B.R. Benware, C.D. Macchietto, J.L.A. Chila, and J.J. Rocca, "Two-Dimensional Near-Field and Far-Field Imaging of a Ne-like Ar Capillary Discharge Table-Top Soft X-Ray Laser," *Phys. Rev. A 58*, 1509 (1998).
37. A. Rundquist, C.G. Durfee, Z. Chang, C. Herne, S. Backus, M.M. Murnane, and H.C. Kapteyn, "Phase-Matched Generation of Coherent Soft X-Rays," *Science 280*, 1412 (1998).
38. P.H. van Cittert, "Die Wahrscheinliche Schwingungsverteilung in Einer von Einer Lichtquelle Direkt oder Mittels Einer Linse Beleuchteten Ebene" [The Probable Distribution of Vibrations in a Plane Illuminated by a Light Source Either Directly or Through a Lens], *Physica 1*, 210 (1934); see *Coherence and Fluctuations of Light (1850–1966)* (SPIE, Bellingham, WA, 1990), L. Mandel and E. Wolf, Editors, p. 1.
39. F. Zernike, "The Concept of Degree of Coherence and its Application to Optical Problems," *Physica 5*, 785 (1938); see *Coherence and Fluctuations of Light (1850–1966)* (SPIE, Bellingham, WA, 1990), L. Mandel and E. Wolf, Editors, p. 100.
40. G.N. Watson, *A Treatise on the Theory of Bessel Functions* (Cambridge Univ. Press, 1944), p. 20.
41. I.S. Gradshteyn and I.M. Ryzhik, *Table of Integrals, Series and Products* (Academic Press, New York, 1994), Fifth Edition, Section 8.411, No. 1, p. 961.
42. F.W. Oliver, "Bessel Functions of Integer Order," p. 360, No. 9.1.21, in *Handbook of Mathematical Functions* (Dover, New York, 1972), M. Abramowitz and I. Stegun, Editors.
43. E. Kreyszig, *Advanced Engineering Mathematics* (Wiley, New York, 1993), Seventh Edition, pp. 225 and A97.
44. R.N. Bracewell, *The Fourier Transform and Its Applications* (McGraw-Hill, New York, 1978), Second Edition, Chapter 12.

45. I.N. Sneddon, *Fourier Transforms* (Dover, New York, 1995).
46. Reference 41, p. 382, Section 3.460, No. 3, and p. 738, Section 6.632, No. 4.
47. Reference 41, p. 707, Section 6.561, No. 5.
48. Reference 43, p. 228.
49. B.J. Thompson and E. Wolf, "Two-Beam Interference with Partially Coherent Light," *J. Opt. Soc. Amer. 47*, 898 (1957).
50. Reference 8, p. 560.
51. R.A. Shore, B.J. Thompson, and R.E. Whitney, "Diffraction by Apertures Illuminated with Partially Coherent Light," *J. Opt. Soc. Amer. 56*, 733 (1966).
52. Reference 2, pp. 207–229.
53. D. Attwood, G. Sommargren, R. Beguiristain, K. Nguyen, J. Bokor, N. Ceglio, K. Jackson, M. Koike, and J. Underwood, "Undulator Radiation for At-Wavelength Interferometry of Optics for Extreme Ultraviolet Lithography," *Appl. Opt. 32*, 7022 (1 December 1993).
54. H. Medecki, E. Tejnil, K. Goldberg, and J. Bokor, "A Phase-Shifting Point Diffraction Interferometer," *Opt. Lett. 21*, 1526 (1 October 1996).
55. E. Tejnil, K.A. Goldberg, H. Medecki, R. Beguiristian, J. Bokor, and D. Attwood, "Phase-Shifting Point Diffraction Interferometry for At-Wavelength Testing of Lithographic Optics," p. 118 in *Extreme Ultraviolet Lithography* (OSA TOPS Series, Washington, DC, 1996); G.D. Kubiak and D.R. Kania, Editors; E. Tejnil, K.A. Goldberg, S.H. Lee, H. Medecki, P. Batson, P. Denham, A. McDowell, J. Bokor, and D. Attwood, "At-Wavelength Interferometry for EUV Lithography," *J. Vac. Soc. Technol. B 15(6)*, 2455 (November–December 1997); E. Tejnil, "Characterization of Extreme Ultraviolet Imaging Systems," Ph.D. thesis, Department of Electrical Engineering and Computer Science, University of California, Berkeley (1997).
56. K.A. Goldberg, E. Tejnil, S.-H. Lee, H. Medecki, D.T. Attwood, K.H. Jackson, and J. Bokor, "Characterization of an EUV Schwrzschild Objective Using Phase-Shifting Point Diffraction Interferometry," *Proc. SPIE 3048*, 264 (1997); K.A. Goldberg, "Extreme Ultraviolet Interferometry," Ph.D. thesis, Physics Department, University of California, Berkeley (1997).
57. For a general discussion of interferometry consult M. Françon, *Optical Interferometry* (Academic Press, New York, 1966).
58. For a general discussion of interferometry consult Ref. 1, Chapter VII,
59. K.A. Goldberg, P. Naulleau, S.-H. Lee, C. Bresloff, C. Henderson, D.T. Attwood, and J. Bokor, "High-Accuracy Interferometry of EUV Lithographic Optical Systems," *J. Vac. Sci. Technol. B 16*, 3435 (1998).
60. C. Montcalm, S. Bajt, P.B. Mirkarimi, E. Spiller, F.J. Weber, and J.A. Folta, "Multilayer Reflective Coatings for Extreme-Ultraviolet Lithography," *Proc. SPIE 3331*, 42 (1998).
61. E. Spiller, F.J. Weber, C. Montcalm, S.L. Baker, E.M. Gullikson, and J.H. Underwood, "Multilayer Coating Tests of a 10× Extreme Ultraviolet Lithographic Camera," *Proc. SPIE 3331* 62 (1998).
62. E.H. Anderson, Private communication, Lawrence Berkeley National Laboratory.
63. P. Naulleau, K.A. Goldberg, S.-H. Lee, C. Chang, C. Bresloff, P. Batson, D.T. Attwood, and J. Bokor, "Characterization of the Accuracy of EUV Phase-Shifting Point Diffraction Interferometry, *Proc. SPIE 3331*, 114 (1998).
64. K.A. Goldberg, P. Naulleau, H.N. Chapman, R. Gaughan, and J. Bokor, "Direct Comparison of EUV and Visible Light Interferometries," *Proc. SPIE 3676* (1999).
65. C. Chang, EECS UC Berkeley and CXRO Lawrence Berkeley National Laboratory, private communication.

HOMEWORK PROBLEMS

Homework problems for each chapter will be found at the website:
http://www.coe.berkeley.edu/AST/sxreuv

Chapter 9

SOFT X-RAY MICROSCOPY WITH DIFFRACTIVE OPTICS

Zone Plate Lens

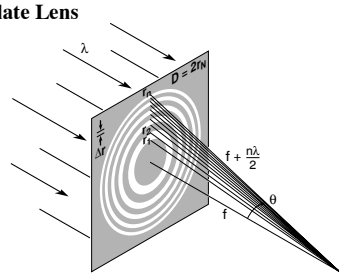

Soft X-Ray Microscope

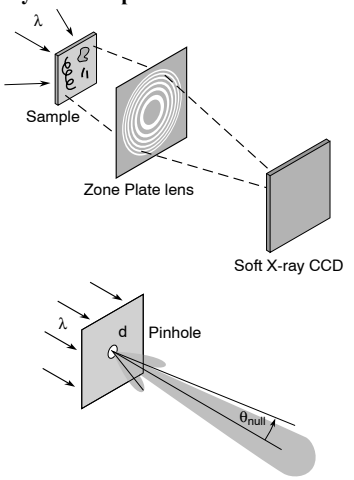

Scanning Soft X-Ray Microscope

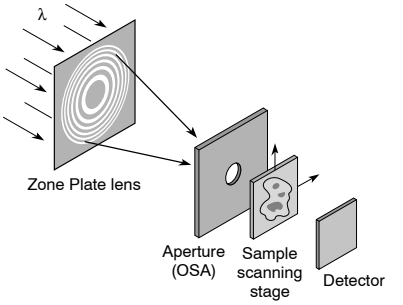

Zone Plate Formulae

$$r_n^2 = n\lambda f + \frac{n^2\lambda^2}{4} \tag{9.9}$$

$$D = 4N\Delta r \tag{9.13}$$

$$f = \frac{4N(\Delta r)^2}{\lambda} \tag{9.14}$$

$$NA = \frac{\lambda}{2\Delta r} \tag{9.15}$$

$$F^{\#} = \Delta r/\lambda \tag{9.16}$$

$$\text{Rayleigh res.} = \frac{0.610\lambda}{\text{NA}} = 1.22\Delta r \tag{9.47, 9.48}$$

$$\text{DOF} = \pm\frac{1}{2}\frac{\lambda}{(\text{NA})^2} = \pm\frac{2(\Delta r)^2}{\lambda} \tag{9.50, 9.51}$$

$$\frac{\Delta\lambda}{\lambda} \leq \frac{1}{N} \tag{9.52}$$

Pinhole Formula

$$\theta_{\text{null}} = 1.22\lambda/d \tag{9.36}$$

In this chapter we consider Fresnel zone plates, particularly as they are used as diffractive image forming lenses for high resolution soft x-ray microscopy. We begin with a relatively simple approach based on our general experience with interference phenomena. From this we obtain a physical appreciation for zone plate performance, and derive most of the useful formulae summarized on this page. We also describe the complementary features of various zone plate microscopes. We next consider formal diffraction theory to better understand the limits of spatial resolution. Pinholes are also considered, as they play an essential role in generating the spatially coherent radiation required for scanning microscopy and other applications involving spatially coherent short wavelength radiation. Finally, we conclude with applications of soft x-ray microscopy to the physical and life sciences, and a short section on the fabrication of zone plates.

9.1 INTRODUCTION

In previous chapters we have discussed the various ways in which radiation can be redirected for image formation, spectroscopic, and other applications. In Chapter 1, Figure 1.13, we summarized the basic processes of scattering, diffraction, refraction, and reflection. In Chapter 3 we studied refraction, the bending of radiation paths at the interface between materials of differing refractive index $n = 1 - \delta + i\beta$. For EUV and soft x-ray wavelengths, we observed that for all materials the ratio β/δ is sufficiently close to unity that significant refraction cannot be obtained within an absorption length. As a consequence the formation of real images by refraction of EUV or soft x-ray radiation is impractical. Glancing incidence total external reflection with curved optics provides a successful path to image formation, particularly at EUV, soft x-ray, and x-ray wavelengths where there are few competing techniques; but the image resolution is significantly compromised by aberrations. Multilayer coatings extend the use of reflective optics, as discussed in Chapter 4, particularly at EUV wavelengths longer than 5 nm, where normal incidence coatings achieve high reflectivity. With high quality curved substrates, multilayer coated mirrors permit near-diffraction-limited imaging in the EUV region, i.e., limited only by the wavelength and numerical aperture of the system.

At shorter wavelengths, particularly in the soft x-ray region extending from perhaps 0.3 nm to 5 nm, diffractive techniques using Fresnel zone plate lenses of various forms are of great interest[1–5] because of their ability to form images at very high spatial resolution, approaching the diffraction limit. Diffraction is the process by which radiation is redirected near sharp edges. As it propagates away from these sharp edges or obstacles, it interferes with nearby undiffracted radiation, producing bright and dark bands known as interference patterns. Because the diffracted radiation propagates in a new direction, the dark and bright interference patterns appear to move laterally with distance away from the obstruction. For small diffracting structures such as disks, pinholes, and gratings (repetitive lines and spaces) it is found that these diffraction patterns, and the energy they represent, propagate away from the structure at angles of order $\theta \sim \lambda/d$, where d is a characteristic dimension. With repetitive structures, such as transmission gratings, consisting of many parallel lines and spaces, the positive interference in certain directions can lead to a very strong redirection of energy. This is also possible in circular geometries, with proper placement of the radial zones, so that positive interference of the diffracted radiation occurs at a well-defined downstream position. This downstream distance is known as the focal length, and the appropriate structure that leads to this focusing of energy is known as a Fresnel zone plate lens. Capable of spatial resolution measured in tens of nanometers, these diffractive lenses are especially valuable for the study of microscopic objects of limited lateral dimensions.

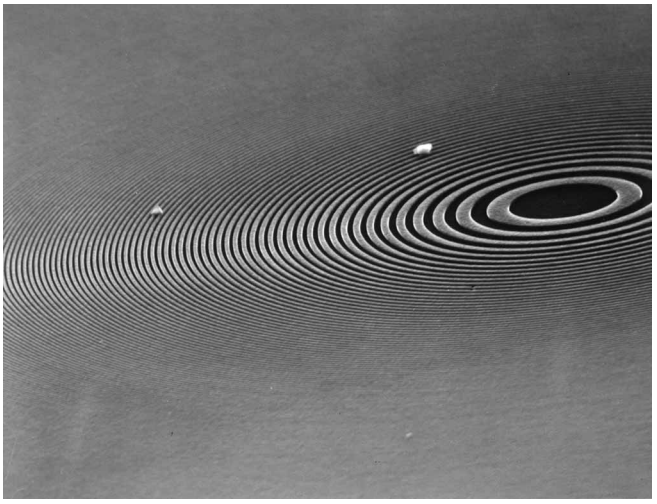

FIGURE 9.1. A Fresnel zone plate lens used for x-ray microscopy. (Courtesy of E. Anderson, LBNL.)

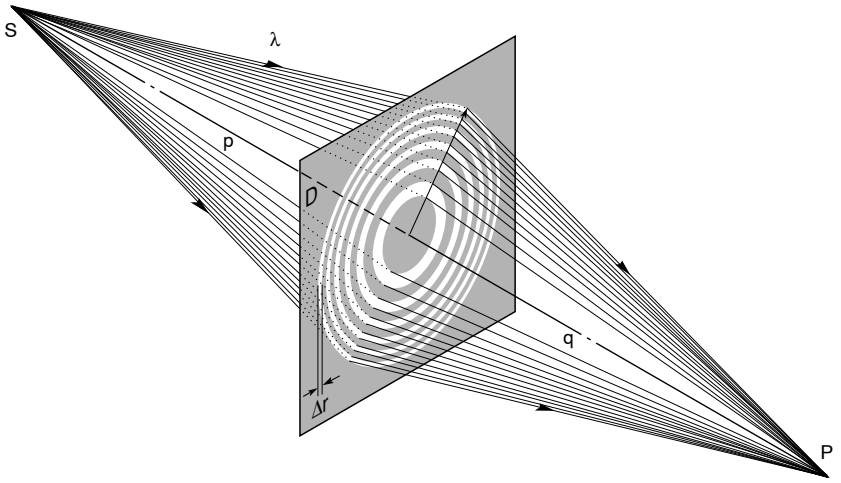

FIGURE 9.2. A Fresnel zone plate used as a diffractive lens to form an x-ray or EUV image of a source point S in the image plane at P. The lens is shown as having a diameter D and outer zone width Δr. The object and image distances are p and q, respectively.

Figure 9.1 shows a zone plate lens used in soft x-ray microscopy. Figure 9.2 illustrates the general technique for point to point imaging with a Fresnel zone plate lens. In its simplest form the zone plate consists of alternating opaque and transparent zones, essentially a circular grating, with radial zones located such that the increased path lengths through sequential transparent zones differ by one wavelength each and thus add in phase at the image point.[6–13] In this manner, on a point by point basis, the image of a full two-dimensional object can be formed in the image plane, using essentially incoherent radiation. As we understand from the previous chapter, the smallest possible spot size that can be formed at P is obtained with

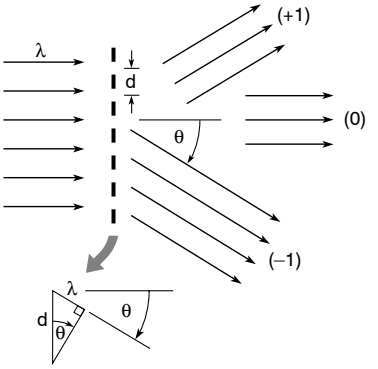

FIGURE 9.3. Diffraction from a transmission grating showing only the 0th and ±1st orders. Higher orders are omitted for clarity. Constructive interference of the diffracted radiation occurs at angles where the path length increases by λ for each additional period d of the grating, such that $\sin\theta = \lambda/d$ in first order.

spatially coherent illumination of the zone plate, a subject of interest for the formation of scanning spot microscopes, which we discuss in the following paragraphs. Of interest here as well is the practical case of partially coherent radiation and the potential advantage this has for image formation and resolution.

We begin our analysis with a simple transmission grating, as illustrated in Figure 9.3. Constructive interference occurs, in first order, at angles where the path length is increased by one wavelength, such that

$$\sin\theta = \frac{\lambda}{d} \tag{9.1}$$

This occurs for both positive and negative angles, giving rise to the ±1st orders of the grating, in addition to the 0th order in the forward direction. Higher orders will be generated at angles θ_m, corresponding to increased path lengths $m\lambda$, such that

$$\boxed{\sin\theta_m = \frac{m\lambda}{d}} \tag{9.2}$$

where $m = 0,\ \pm1,\ \pm2,\ \pm3, \ldots$. For radiation incident on the grating at an angle θ_i, measured from the normal, one readily shows that the condition for constructive interference is

$$\boxed{\sin\theta - \sin\theta_i = \frac{m\lambda}{d}} \tag{9.3}$$

where again $m = 0,\ \pm1,\ \pm2,\ \pm3, \ldots$. Equation (9.3) is known as the *grating equation*, and Eq. (9.2) is clearly a special case of it for normal incidence.

The fraction of incident energy diffracted into the various orders depends on the nature of the periodic structure, i.e., the sharpness of profile, the bar to space ratio (line width as a fraction of grating period), and the complex refractive index, which affects the absorption and phase shift in the grating. For a transmission grating of opaque lines of width equal to half the grating period, as illustrated in Figure 9.4, one can represent the transmission function in

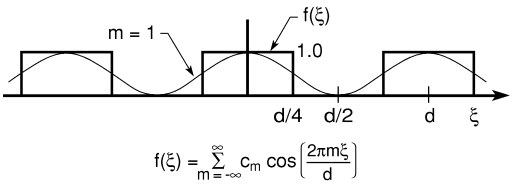

FIGURE 9.4. Representation of a transmission grating of unit absorption in terms of Fourier components. Each component m of the expansion represents an equivalent thin grating, where the coefficient c_m is related to the amount of energy diffracted to a given order m, and where the period d/m is related to the angle of diffraction for that order. Only the first term ($m = 1$) in the expansion is shown. The first coefficients are $c_0 = \frac{1}{2}$, $c_1 = 1/\pi$, $c_2 = 0$, $c_3 = 1/3\pi$, etc., as derived in the text.

a Fourier series expansion, taking even (cosine) terms only for the coordinate choice taken:

$$f(\xi) = \sum_{m=-\infty}^{\infty} c_m \cos\left(\frac{2\pi m\xi}{d}\right) \tag{9.4}$$

with coefficients

$$c_m = \frac{1}{d}\int_{-d/2}^{d/2} f(\xi)e^{-2\pi i m\xi/d}\, d\xi$$

where $f(\xi) = 1$ in the interval $|\xi| \leq d/4$, and $= 0$ in the interval $d/4 < \xi \leq d/2$. Substituting for $f(\xi)$, noting that $e^{-i\theta} = \cos\theta - i\sin\theta$ (Appendix D) and that the sine term does not contribute in this even interval, the integral for the coefficient becomes

$$c_m = \frac{2}{d}\int_0^{d/4} \cos\left(\frac{2\pi m\xi}{d}\right) d\xi$$

$$c_m = \frac{\sin(m\pi/2)}{m\pi} \tag{9.5}$$

By L'Hospital's rule, $c_0 = \frac{1}{2}$. The even order coefficients are all zero, due to the symmetry of the problem with this choice of coordinate origin. The odd order coefficients are $c_m = 1/\pi,\ -1/3\pi,\ 1/5\pi, \ldots$, for $m = \pm 1,\ \pm 3,\ \pm 5, \ldots$, respectively.

We can now represent the single rectangular grating of unit absorption by a superposition of thin cosine gratings of increasing spatial frequency $k_m = 2\pi m/d$ and transmission c_m. Each such grating corresponds to one term in the expansion, leading to radiation of the various diffractive orders m, at angles θ_m described earlier in Eq. (9.2), and associated electric fields $E_m = c_m E_0$, where E_0 is the incident electric field at the grating. From Chapter 3, Eqs. (3.18–3.20), it follows that the intensities of the various diffractive orders are given by

$$I_m = \sqrt{\epsilon_0/\mu_0}|E_m|^2 = |c_m|^2 I_0 \tag{9.6}$$

so that the efficiencies $\eta_m = I_m/I_0$ for diffraction to the various orders are proportional to $|c_m|^2$, and thus from Eq. (9.5)

$$\eta_m = \begin{cases} 0.25 & m = 0 \\ 1/m^2\pi^2 & m \text{ odd} \\ 0 & m \text{ even} \end{cases} \tag{9.7}$$

For an opaque transmission grating of equally wide lines and spaces, 25% of the incident energy is in the 0th order, approximately 10% is diffracted to each of the ±1st orders, and so forth, while the grating itself absorbs 50% of the incident energy.[14, 15]

In phase gratings the opaque lines are replaced by partially transmitting materials to reduce absorptive losses. For materials and wavelengths for which β/δ is minimal, and for thicknesses that permit a relative propagation phase shift approaching π, this can lead to a significant enhancement of diffraction efficiency.

The coefficients in Eq. (9.7) correspond to a symmetric grating of equal line and space widths, permitting a representation [Eq. (9.4)] involving only even cosine functions. For an asymmetric grating involving unequal line and space widths, odd sine functions would also be required. An example would be a grating with line widths equal to $\frac{1}{3}$ the grating period and open spaces of width equal to $\frac{2}{3}$ of the grating period. In such cases the asymmetry (sine terms) leads to non-zero even orders, i.e., finite values of $|c_m|^2$ for $m = \pm 2,\ \pm 4$, etc. This is very much analogous to the discussion of even multilayer diffraction orders for asymmetric coatings of $\Gamma \neq 0.5$, as discussed in Chapter 4, Section 4.2 and Figure 4.4 therein. This subject is relevant here, as we shall shortly consider the diffraction efficiency of zone plate lenses.

For symmetric structures of equal area in successive zones (opaque and transmissive) we will again find only odd orders, $m = \pm 1$, etc. The even orders ($m = \pm 2$) will cancel at the focal point. However, for asymmetric zones of unequal successive areas, even orders do appear. An example of this would be a zone plate where the alternate open zones are narrower than prescribed due to imperfections in the fabrication process. Depending on the degree of asymmetry, even orders of various intensities would appear.

An extensive literature exists on the subject of diffraction from transmission and reflection gratings. In particular see Born and Wolf[14] for an extensive introduction, Hecht[13] for a tutorial on blazed reflection gratings, Morrison[15] for a description of phase gratings at short wavelengths, and Michette[12] for a general description of diffraction gratings at soft x-ray wavelengths. Variable line space gratings are discussed by Hettrick and Underwood and their colleagues.[16–17] The topic of EUV/soft x-ray gratings continues to be one of active research, with applications in many fields, including synchrotron radiation, astrophysics, plasma physics, and fusion. Several recent books specifically addressing this spectral region add to the wealth of valuable literature on the subject of reflection and transmission gratings.[18–20]

In the next section we discuss Fresnel zone plates as circular diffraction gratings that also generate many orders, some of which are diffracted radially inward toward the optic axis and can form a real image (the positive orders), and some of which are diffracted radially outward, forming a virtual image (the negative orders).

9.2 THE FRESNEL ZONE PLATE LENS

The focusing properties of a Fresnel zone plate lens can be understood by considering the first order diffraction from a circular grating with the zonal periods adjusted so that at increasing radius from the optic axis the periods become shorter, and thus by Eq. (9.1) the diffraction angle becomes larger, thus permitting a real first order focus, as illustrated in Figure 9.5. If one draws a right triangle with the focal length f as one side, the radius of any zone r_n as a second side, and the hypotenuse of length $f + n\lambda/2$, then by the Pythagorean theorem the zonal radii are given by

$$f^2 + r_n^2 = \left(f + \frac{n\lambda}{2}\right)^2 \tag{9.8}$$

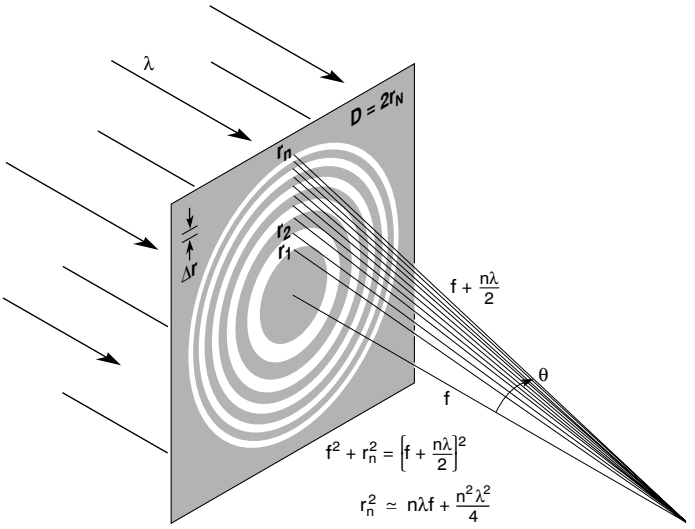

FIGURE 9.5. A Fresnel zone plate lens with plane wave illumination, showing only the convergent (+1st) order of diffraction. Sequential zones of radius r_n are specified such that the incremental path length to the focal point is $n\lambda/2$. Alternate zones are opaque in the simple transmission zone plate. With a total number of zones N the zone plate lens is fully specified. Lens characteristics such as the focal length (f), diameter (D), and numerical aperture (NA) are described in the text in terms of λ, N, and Δr, the outer zone width.

which upon expansion and consolidation of like terms becomes

$$r_n^2 = n\lambda f + \frac{n^2\lambda^2}{4} \tag{9.9}$$

The term $n^2\lambda^2/4$, which represents spherical aberration, can be ignored for $f \gg n\lambda/2$, which we will see shortly corresponds to a lens of small numerical aperture $\mathrm{NA} = \sin\theta = \lambda/(2\,\Delta r) \ll 1$, as is often the case at x-ray wavelengths. Where this is not the case, perhaps with a larger NA optic at an EUV wavelength, the term should be retained. For the low NA case Eq. (9.9) simplifies to

$$r_n \simeq \sqrt{n\lambda f} \tag{9.10}$$

showing that a real first order focus is achieved when successive zones increase in radius by $\sqrt{n}$, providing the desired prescription by which the radial grating period must decrease in order to provide a common focus. The earliest known record regarding the demonstration of focusing light with alternately opaque Fresnel zones is that of Lord Rayleigh in 1871.[6]

We can now obtain expressions for the lens diameter D, focal length f, numerical aperture $\mathrm{NA} = \sin\theta$, spatial resolution, and depth of focus. We choose to do this in terms of the wavelength λ, the total number N of zones, and the outer zone width Δr. We do this from an experimental point of view. In designing an experiment the wavelength is often a first priority, driven by the elemental composition of the material or sample under study and their characteristic absorption and emission lines. In microscopy the next priority is the spatial

resolution required to see features of interest. For zone plate lenses the spatial resolution limit is set by the outer zone width Δr, as we will see shortly. As our third choice we take N, the total number of zones. As we will see in the following paragraphs, zone plate lenses are highly chromatic, that is, the focal length of the lens varies strongly with wavelength. Thus for precise imaging it is necessary to restrict the illumination spectral bandwidth, $\Delta\lambda/\lambda$. We will see shortly that there is an inverse relationship between $\Delta\lambda/\lambda$ and N, the total number of zones. Thus the total number of zones N will be restricted by the relative spectral bandwidth. With this motivation we proceed in the following paragraphs to develop relationships for f, D, NA, resolution, and depth of focus in terms of λ, Δr, and N.

We begin by defining the outer zone width for $n \to N$,

$$\Delta r \equiv r_N - r_{N-1} \tag{9.11}$$

where N is the total number of zones, i.e., the sum of both opaque and transparent zones (twice the number of radial periods). The outer zone width Δr provides a very convenient parameter, and is useful in expressions for other lens parameters.

Now we write Eq. (9.10) twice, once for r_N and once for r_{N-1}, and subtract as follows:*

$$r_N^2 - r_{N-1}^2 = N\lambda f - (N-1)\lambda f = \lambda f$$

Using the definition of Δr given in Eq. (9.11), one also has for the left side of the above equation

$$r_N^2 - (r_N - \Delta r)^2 = 2r_N\,\Delta r - (\Delta r)^2 \simeq 2r_N\,\Delta r$$

since $\Delta r \ll r_N$ for large N. Combining the above two equations, one obtains

$$2r_N\,\Delta r \simeq \lambda f$$

or

$$D\,\Delta r \simeq \lambda f \tag{9.12}$$

From Eq. (9.10) we note that $\lambda f \simeq r_N^2/N$, so that from Eq. (9.12) one has

$$D\,\Delta r \simeq \frac{r_N^2}{N} = \frac{D^2}{4N}$$

or

$$\boxed{D \simeq 4N\,\Delta r} \tag{9.13}$$

The focal length can then be obtained from Eq. (9.12) as

$$f \simeq \frac{D\,\Delta r}{\lambda}$$

*Note that the area of successive zones, $\pi(r_n^2 - r_{n-1}^2) = \pi\lambda f$, is a constant, at least within the long focal length, small NA approximation leading from Eq. (9.9) to Eq. (9.10). Thus the areas of all zones are equal and contribute equally to the intensity of focus.

or in combination with Eq. (9.13)

$$f \simeq \frac{4N(\Delta r)^2}{\lambda} \tag{9.14}$$

This is a very important relationship for the design of zone plate microscope lenses in that it shows that the focal length scales directly with the number of zones, with the square of the outer zone width (which essentially sets the resolution), and inversely with the wavelength, thus introducing a strong chromatic effect.

The numerical aperture (NA) of a lens is defined as

$$\text{NA} \equiv \sin\theta$$

where θ is the half angle measured from the optic axis at focus back to the lens, as illustrated here in Figure 9.5. Thus the numerical aperture of a zone plate lens is given by $\text{NA} = r_N/f = D/2f$, or from Eq. (9.12)

$$\text{NA} \simeq \frac{\lambda}{2\,\Delta r} \tag{9.15}$$

which is a particularly simple form that will be convenient when considering spatial resolution. A related quantity is the lens *F-number*, which we will abbreviate as $\text{F}^{\#}$, defined as

$$\text{F}^{\#} \equiv \frac{f}{D}$$

or again using Eq. (9.12)

$$\text{F}^{\#} \simeq \frac{\Delta r}{\lambda} \tag{9.16}$$

We will return to these parameters in the following section on spatial resolution, depth of focus, and chromatic aberration.

In the preceding paragraphs we have considered the focusing conditions for a zone plate lens with plane wave illumination, as illustrated in Figure 9.5. Next we consider the point by point imaging of an object at a finite distance q from the zone plate, to an image plane at a distance p, as illustrated in Figure 9.6.

Again the successive zones, alternately transmissive and opaque, are constructed so as to add $\lambda/2$ to successive path lengths, so that

$$q_n + p_n = q + p + \frac{n\lambda}{2}$$

where for modest numerical aperture lenses

$$q_n = \left(q^2 + r_n^2\right)^{1/2} \simeq q + \frac{r_n^2}{2q}$$

$$p_n = \left(p^2 + r_n^2\right)^{1/2} \simeq p + \frac{r_n^2}{2p}$$

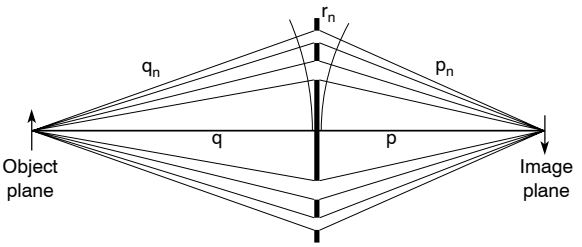

FIGURE 9.6. Point by point imaging with a Fresnel zone plate lens is illustrated. Successive propagation paths are increased by $\lambda/2$.

so that

$$q + \frac{r_n^2}{2q} + p + \frac{r_n^2}{2p} \simeq q + p + \frac{n\lambda}{2}$$

$$\frac{r_n^2}{2q} + \frac{r_n^2}{2p} \simeq \frac{n\lambda}{2}$$

$$\boxed{\frac{1}{q} + \frac{1}{p} \simeq \frac{1}{f}} \tag{9.17}$$

where from Eq. (9.10), $f = r_n^2/n\lambda$. Equation (9.17) relates the image and object distances to the focal length as for an ordinary visible light refractive lens. Similarly, one can show that the transverse magnification is

$$\boxed{M = \frac{p}{q}} \tag{9.18}$$

We now have a basic understanding of how a Fresnel zone plate can be used both to focus radiation and to form a real image of an extended object using first order diffraction.

Recall, however, that a transmission grating generates many orders, thus complicating the use of a zone plate lens and leaving only a fraction of the available photons for the primary purposes of a given experiment. The procedure, suggested in Figure 9.5, of adding a path length of $n\lambda/2$ for constructive interference of sequential zones in first order can be extended to the higher orders ($m = 2,\ 3,\ \ldots$) by adding path lengths $mn\lambda/2$. Following the same procedures used in the preceding paragraphs for the first order ($m = 1$), one finds that the radial zones correspond to phase advances for the higher order diffracted waves given by

$$r_n^2 \simeq mn\lambda f_m \tag{9.19}$$

for zones $n = 0, 1, 2, \ldots$ and diffractive orders $m = 0,\ \pm 1,\ \pm 2, \ldots$, and with corresponding

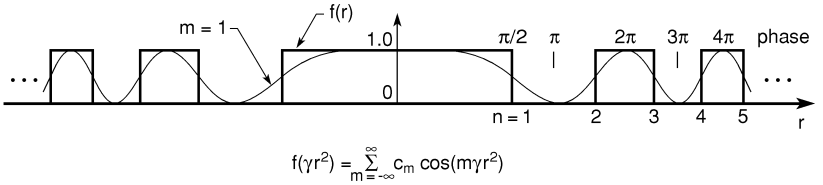

FIGURE 9.7. Representation of a Fresnel zone plate as a transmission grating in terms of the radius squared. Only the first term ($m = 1$) is shown.

focal lengths given by

$$f_m = \frac{f}{m} \tag{9.20}$$

where we note that the negative orders give rise to virtual foci of negative focal length. The diffraction efficiencies of the various orders can be analyzed much like the transmission grating efficiencies of the previous section [see Eqs. (9.4) and (9.5)]. In the case of the transmission zone plate of unity absorption in the opaque zones, one can represent the transmission function in a Fourier series expansion in terms of r^2, as suggested by Eq. (9.19).

The sketch in Figure 9.7 is useful for visualizing the Fourier decomposition and identifying the periodicity in r^2. Following Goodman,[21] we expand the transmission function in terms of γr^2, taking only odd (cosine) terms for the chosen coordinates, so that

$$f(\gamma r^2) = \sum_{m=-\infty}^{\infty} c_m \cos(m\gamma r^2) \tag{9.21}$$

where from Figure 9.7 we see[†] that $\gamma = \pi/\lambda f$. This can be written as

$$f(u) = \sum_{m=-\infty}^{\infty} c_m \cos(mu)$$

where $u = \gamma r^2 = \pi r^2/\lambda f$, and where the Fourier coefficients are given by

$$c_m = \frac{1}{2\pi} \int_{-\pi}^{\pi} f(u) \cos(mu)\, du \tag{9.22}$$

For the alternately opaque and transmissive zones of interest here the transmission function $f(u) = 1$ for $0 \le u \le \pi/2$, and $f(u) = 0$ for $\pi/2 < u \le \pi$ (see Figure 9.7), so that

$$c_m = \frac{1}{\pi} \int_0^{\pi/2} \cos mu\, du$$

[†]A radial phase shift of 2π corresponds to a difference $\Delta n = 2$ in the zone plate (one opaque, one transmissive). From Eq. (9.19), for $m = 1$, this gives an argument in the expansion parameter $\gamma(r_n^2 - r_{n-2}) = 2\lambda f\gamma = 2\pi$, or $\gamma = \pi/\lambda f$. Check this in Figure 9.7, where the phase shift between $n = 2$ and $n = 4$ corresponds to $7\pi/2 - 3\pi/2 = 2\pi$.

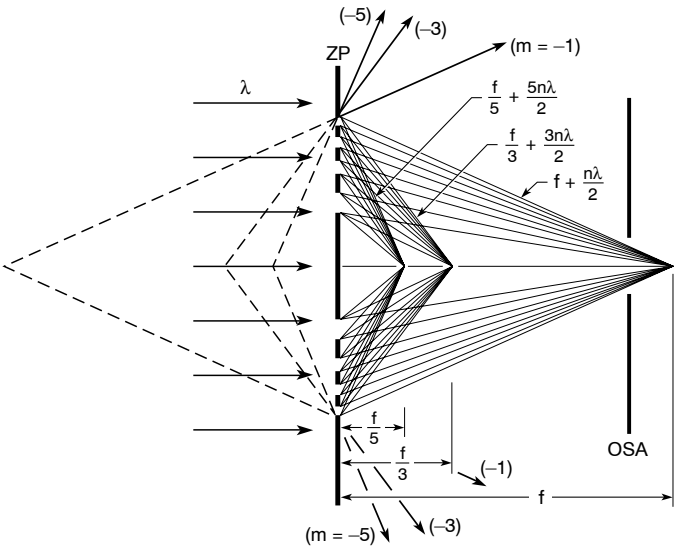

FIGURE 9.8. Zone plate diffractive focusing is illustrated for the first three positive orders. An order sorting aperture (OSA), of the type that would be used to block all but the first order, is also shown. Negative orders ($m = -1,\ -3,\ -5$) are shown as solid lines diverging from the optical axis, and projected backward to virtual foci (behind the lens) by dashed lines.

or

$$c_m = \frac{\sin(m\pi/2)}{m\pi} \tag{9.23}$$

where $m = 0,\ \pm 1,\ \pm 2,\ \pm 3, \ldots$. This is identical to the result obtained earlier for the linear transmission grating. As we observed in that case, the diffraction efficiencies to the various orders are given by [Eq. (9.16)]

$$I_m = |c_m|^2 I_0$$

so that for a Fresnel zone plate of alternately opaque and transmissive zones the diffraction efficiencies are given by

$$\eta_m = \begin{cases} \frac{1}{4} & m = 0 \\ 1/m^2\pi^2 & m \text{ odd} \\ 0 & m \text{ even} \end{cases} \tag{9.24}$$

where half the incident energy is absorbed by the opaque zones. The efficiency to the first order focus is thus about 10%, another 10% goes to the divergent $m = -1$ order, approximately 1% goes to the divergent third order ($m = 3$, virtual focus), etc., while 50% of the incident radiation is absorbed and 25% is transmitted in the forward direction ($m = 0$). As in the case of the transmission grating considered in Section 9.1, the even orders do not contribute in the symmetric case where successive zone areas are equal. The various orders are illustrated in Figure 9.8.

The decreasing efficiency with increasing order m has an interesting explanation. Within a given transmissive zone n, the even orders of m cancel at the focus, so that only odd

orders ($m = \pm 1,\ \pm 3,\ \pm 5, \ldots$) need be considered. For the odd orders of $|m| > 1$, the diffraction efficiency will be decreased by factors of $1/m^2$ relative to $m = 1$ because of canceled contributions within each transparent zone. For instance, the third order focus will receive field contributions from three sub-regions within each zone, two of which will cancel, leaving only a $\frac{1}{3}$ contribution to the electric field at the third order focus ($1/m$). As the intensity is proportional to E^2, the intensity will be diminished by $\frac{1}{9}$, i.e., by $1/m^2$. Likewise, for the fifth order focus, four of the five sub-zone contributions will cancel (in pairs), leaving only a $\frac{1}{5}$ contribution to the field, or a $\frac{1}{25}$ contribution to the intensity.

It is possible to increase the efficiency of zone plates by replacing the opaque zones with phase reversal zones by which the goal is to achieve a $\lambda/2$ phase shift relative to the open zones, with minimal absorption, as first suggested by Lord Rayleigh.[6, 8] In this manner the electric fields at focus can be increased by up to a factor of two, and thus the intensities (and efficiencies) by up to a factor of four. The required thickness Δt for obtaining a phase shift of π for a given material and wavelength is given by [see Chapter 3, Eq. (3.29)]

$$\Delta t = \frac{\lambda}{2\delta} \tag{9.25}$$

Of course, for x-rays and EUV radiation, where the refractive index $n = 1 - \delta + i\beta$, and where β/δ is non-negligible, this factor of four cannot be realized. Nonetheless significant improvements are possible. Kirz[11] has calculated the optimum zone plate thickness as a function of the parameter β/δ. He finds, for example, that the optimum thickness decreases to about 0.9 of that given in Eq. (9.25) for $\beta/\delta = 0.2$, and about 0.8 at $\beta/\delta = 0.5$. Enhanced diffraction efficiencies of zone plate lenses to first order, based on partial phase contributions in the material zones, have been reported in the literature.[22–25] The relative electric field after propagating through a finite thickness Δt is given by [Chapter 3, Eq. (3.17)]

$$\frac{E}{E_0} = e^{-\pi\beta/\delta} \tag{9.26}$$

From this the efficiencies to various orders can be calculated.[26] Note that values of δ and β, given as a function of photon energy,[27] are reproduced here in Appendix C for several common materials. Further possibilities for improved efficiency, using theoretically optimized phase profiles, are discussed in the literature.[28]

The analyses above are all based on *thin* zone plate theory in that they do not take account of finite ($\lambda/\Delta t$) wavelength effects within the zone plate. More realistic calculation for finite thickness zone plates are also discussed in the literature.[29–33]

9.3 DIFFRACTION OF RADIATION BY PINHOLE APERTURES AND ZONE PLATES

To understand the limiting spatial resolution of a lens, set by the wavelength of radiation and the numerical aperture (NA), it is necessary to have knowledge of the focal plane intensity distribution due to a point source. One can then consider two such point sources, bring them close to each other, and set some criterion for the separation distance that renders the two just resolvable. This brings us to the subject of *diffractive optics*, that is, the study of lenses, mirrors, gratings, etc., where there are features comparable in size to the irradiating wavelength that cause radiation to propagate in directions different from those given by geometrical considerations. Of particular interest here is the diffraction of short wavelength radiation by pinholes and zone plates, which are much used in this region of the spectrum. Of course,

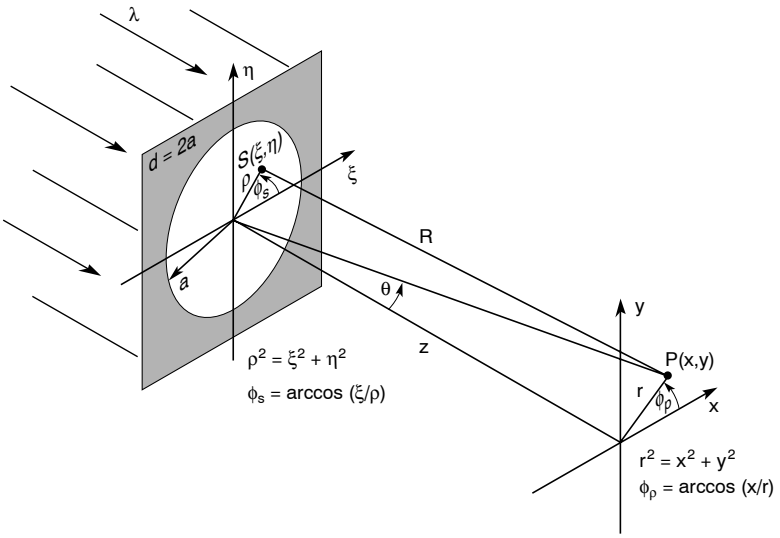

FIGURE 9.9. Geometry for the description of diffraction of radiation from an aperture plane (ξ, η) to an observation point (x, y). R is the distance from a source point $S(\xi, \eta)$ in the aperture plane to an observation point P(x, y). The two planes are parallel, separated by a distance z. The aperture illustrated here is a circle of diameter $d = 2a$. The angle θ is measured from the origin of the ξ, η-plane to the observation point P.

diffraction is a basic electromagnetic phenomenon, well known at lower wavelengths. For instance, when a common refractive lens is used to focus visible laser light, the limited lens aperture causes some angular spread of the radiation that appears to emanate from the sharp boundary, resulting in a finite width of the focal spot and some nearby ringing due to the interfering fields in the focal plane. In this section we will discuss analogous diffractive limitations that occur with zone plate lenses, and closely related diffraction from small pinholes.

There is a long history of mathematical development on the theory of diffraction that successfully predicts physical observations. Most notable is the scalar theory of diffraction developed by Kirchhoff in 1882, extending the earlier work of Huygens (1690) and Fresnel (1818), and leading to what is now known as the *Fresnel–Kirchhoff diffraction formula*,[34–39] which for small angle scattering in the near-forward direction ($\theta \simeq \lambda/d \ll 1$, where d is a characteristic dimension), can be written as[35]

$$E(x, y) = \frac{-i}{\lambda} \iint \frac{E(\xi, \eta) e^{ikR}}{R} \, d\xi \, d\eta \tag{9.27}$$

where $k = 2\pi/\lambda$, $E(x, y)$ is the electric field observed at a distant point P(x, y), $E(\xi, \eta)$ is the incident field as a function of position in the aperture plane ($z = 0$), and R is the distance from each source point $S(\xi, \eta)$ to the observation point P(x, y), as illustrated in Figure 9.9. Basically this states that the field detected in a distant plane is obtained by summing the contributions from every point in the aperture plane, allowing for its propagation distance R and phase e^{ikR}, as if each point were a secondary source of radiation. As we will see shortly, the finite aperture introduces unbalanced contributions near boundaries, leading to interference effects specific to the geometry and clearly dependent on the wavelength.

From the geometry of Figure 9.9 we see that

$$R = \sqrt{z^2 + (x-\xi)^2 + (y-\eta)^2}$$

For the case where $z \gg x,\ y$ and $z \gg \xi,\ \eta$, this becomes

$$R \simeq z + \frac{x^2}{2z} + \frac{y^2}{2z} + \frac{\xi^2}{2z} + \frac{\eta^2}{2z} - \frac{\xi x}{z} - \frac{\eta y}{z} \tag{9.28}$$

so that

$$E(x,y) = \frac{-ie^{ikz}e^{ik(x^2+y^2)/2z}}{\lambda z} \iint E(\xi,\eta) e^{ik(\xi^2+\eta^2)/2z} e^{-ik(\xi\theta_x+\eta\theta_y)}\, d\xi\, d\eta \tag{9.29}$$

where $\theta_x = x/z = r\cos\phi_p/z = \theta\cos\phi_p$ and $\theta_y = y/z = r\sin\phi_p/z = \theta\sin\phi_p$.

To proceed further we need to consider specific problems. Two problems of particular interest are those of (1) a small pinhole and (2) a Fresnel zone plate lens. The analysis of each follows.

9.3.1 Pinhole Aperture

For a small pinhole of radius a, such that $ka^2/2z \ll 1$,[‡] assuming uniform plane wave illumination such that $E(\xi,\eta) = E_0$, and that the exponent term $k(\xi^2+\eta^2)/2z$ can be neglected as second order compared to the $\xi\theta_x$ and $\eta\theta_y$ terms, Eq. (9.29) simplifies to

$$E(x,y) = \frac{-iE_0 e^{ikz}e^{ik(x^2+y^2)/2z}}{\lambda z} \iint e^{-ik(\xi\theta_x+\eta\theta_y)}\, d\xi\, d\eta \tag{9.30}$$

Converting to polar coordinates as shown in Figure 9.9 for this axisymmetric problem, where $(\xi,\eta) \to (\rho,\phi_s)$ and $(x,y) \to (r,\phi_p)$, the integral reduces to

$$E(r,\theta) = \frac{-2\pi i E_0 e^{ikz}\, e^{ikr^2/2z}}{\lambda z} \int_0^a J_0(k\rho\theta)\rho\, d\rho \tag{9.31}$$

where we have replaced r by θ, using $r = \theta z$ for final z, and where[¶] the ϕ_s-integral has led to the identification[40–43]

$$J_0(k\rho\theta) = \frac{1}{2\pi}\int_0^{2\pi} e^{ik\rho\theta\cos(\phi_s-\phi_p)}\, d\phi_s \tag{9.32}$$

where $J_0(\nu)$ is a Bessel function of the first kind, of zero order. The integral in Eq. (9.31) is of the standard form[44]

$$\int_0^1 xJ_0(\nu x)\, dx = \frac{J_1(\nu)}{\nu} \tag{9.33}$$

where we have made the substitutes $\rho = ax$ and $k\rho\theta = \nu x$, so that $\nu = ka\theta$. The field diffracted by a small pinhole, in the small angle (θ) approximation, is therefore obtained from Eqs. (9.31)

[‡]This is the *far-field* approximation, valid for $z \gg \pi d^2/4\lambda$, where $d = 2a$ is the pinhole diameter.

[¶]Note that this is mathematically identical to the treatment of partial coherence integrals in Chapter 8, leading to Eqs. (8.19) and (8.20).

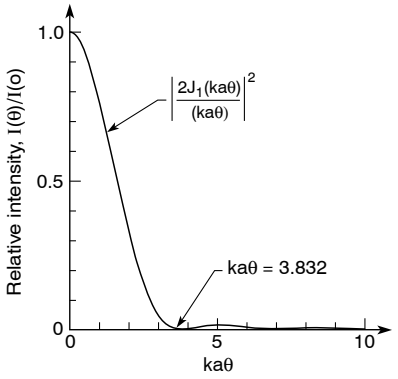

FIGURE 9.10. The far-field diffraction pattern of a circular pinhole illuminated by a uniform plane wave. $I(\theta)$ is the angular distribution of intensity in a distant (z) plane, $I(0)$ is the axial intensity at a distance z from the pinhole, a is the pinhole radius, $k = 2\pi/\lambda$ is the wavenumber, θ is measured from the axis of symmetry, and $J_1(\nu)$ is a Bessel function of the first kind, order one.

and (9.33) to be

$$E(\theta) = \frac{-2\pi i a^2 E_0 e^{ikz}\, e^{ikz\theta^2/2}}{\lambda z} \cdot \frac{J_1(ka\theta)}{ka\theta} \tag{9.34}$$

with a corresponding intensity distribution in the far field of the pinhole given by

$$\boxed{\frac{I(\theta)}{I_0} = \left(\frac{ka^2}{2z}\right)^2 \left|\frac{2J_1(ka\theta)}{ka\theta}\right|^2} \tag{9.35}$$

where $I_0 = \sqrt{\epsilon_0/\mu_0}|E_0|^2$ is the illumination intensity at the pinhole. Note that Eq. (9.35) can be written in terms of the radial coordinate in the observation plane (x, y) through the substitution $\theta = r/z$, for fixed z. Equation (9.35) gives the functional dependence of the far-field diffraction pattern of a coherently illuminated (monochromatic plane wave) pinhole, illustrated in Figure 9.10.

The angular dependence is dominated by the quantity $|2J_1(ka\theta)/ka\theta|^2$, often referred to as an Airy pattern[34, 37] after George Airy, who first described this functional dependence in 1835. The function $|2J_1(\nu)/\nu|^2$ is unity for $\nu = 0$, declines to zero at $\nu = 3.832$ (Refs. 43 and 45), and then oscillates with successively smaller maxima and minima for increasing values of ν. The central lobe of this angular diffraction pattern, sometimes called the Airy disk, is bounded by the first Airy null at

$$ka\theta = 3.832$$

which corresponds to a first null diffraction half angle

$$\boxed{\theta_{\text{null}} = \frac{0.610\lambda}{a} = \frac{1.22\lambda}{d}} \tag{9.36}$$

where $d = 2a$ is the pinhole diameter. Recall that this result is valid in the far field where $z \gg \pi a^2/\lambda$, so that the radius r of this null, given by $r = z\theta$, is much greater than the pinhole radius a, i.e., $r = z\theta \gg 2a$. Thus the far-field Airy pattern is propagating outward from the

pinhole with a half angle proportional to λ/a as in Eq. (9.36), with an Airy null of ever larger radius $r = 0.610\lambda z/a$.

Furthermore, we observe from Eq. (9.35) that the on-axis intensity in the far field of the pinhole decreases in proportion to $I(0) = I_0(ka^2/2z)^2$, or

$$I(0) = \pi \mathcal{E}_0 \left(\frac{a}{\lambda}\right)^2 \left(\frac{1}{z}\right)^2 \tag{9.37}$$

where we recall that I_0 is the incident plane wave intensity at the pinhole, where we define $\mathcal{E}_0 = \pi a^2 I_0$ as the total energy passing through the pinhole, and where $2J_1(0)/(0)$ is unity on-axis, as can be shown with use of L'Hospital's rule. Thus the on-axis intensity of the far-field diffraction pattern decreases with the inverse square of the distance z as we would expect, with a proportionality $(a/\lambda)^2$ as we also would expect on a solid angle basis with a divergence half angle given by Eq. (9.36). Approximately 84% of the incident energy $\mathcal{E}_0$ lies within the first Airy null.[34] The interesting subject of finite pinhole thickness and the effect of non-circular geometry are discussed in the literature.[46, 47]

The mathematical developments here and in Section 8.6 are similar and deserve comment. Both developments involve applications of incident radiation on a pinhole, and thus through the axial symmetry, with radius a and wavelength λ, naturally involve Bessel functions of argument $ka\theta$, where $k = 2\pi/\lambda$. The problems are quite different, however, as is the interpretation of the results. In Chapter 8 we were concerned with the subject of partial coherence, and considered the problem of *incoherent illumination* of a pinhole, finding that the *mutual coherence function* in the far field has a $J_1(v)/v$ dependence, although the radiation pattern itself may be much broader. Here we have considered *coherent illumination* of a pinhole, and have determined the resulting far-field *intensity distribution* to be proportional to $|J_1(v)/v|^2$, as shown here in Figure 9.10. Thus in the first case there may be a very broad radiation pattern within which there exist well-correlated fields near the axis $[J_1(v)/v]$, while in the second case all the radiation appears in a $|J_1(v)/v|^2$ intensity pattern.

9.3.2 Zone Plate

When a Fresnel zone plate is placed within the aperture of Figure 9.9, a large number of diffracted orders are generated. As is illustrated in Figure 9.8, the various orders are expected to come to focus (real and virtual) on axis at focal distances [see Eq. (9.19)]

$$f_m = \frac{r_1^2}{m\lambda} \tag{9.38}$$

with diffraction efficiencies given by Eq. (9.24). It is possible then to evaluate the Fresnel–Kirchhoff integral for this case by replacing the zone plate with an infinite series of thin lenses, one for each order.[21] The stepwise radial phase advance (or retardation), $mn\lambda/2$, of the wavefront associated with each zone and each order is then, as seen in Figure 9.11, given by

$$\Delta\phi_{m,n}(\rho) = k\left(\frac{mn\lambda}{2}\right)$$

which by Eq. (9.19) can be written in terms of the radius ρ_n as

$$\Delta\phi_{m,n} = \frac{k\rho_n^2}{2f_m} \tag{9.39}$$

where $f_m = f/m$, and where f is the first order ($m = +1$) focal length.

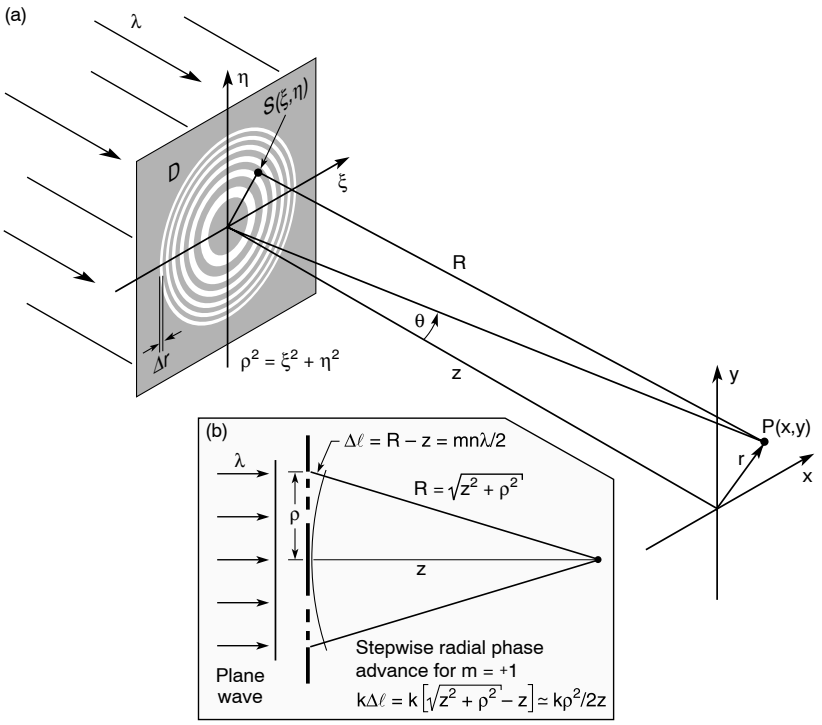

FIGURE 9.11. (a) Geometry for the description of diffraction of radiation from a Fresnel zone plate. The geometry and nomenclature is similar to that of Figure 9.9. The zones are described as a function of the radius ρ in the $\xi,\ \eta$-plane; however, for consistency with the zone plate formulae developed in Section 9.2, we take the outermost open zone to have a width Δr, and take D as the zone plate diameter. The inset (b) illustrates the wavefront curvature (phase advance) of the $m = +1$ diffracted order, which is brought to focus a distance z from the zone plate.

For a zone plate of many zones, for instance[48] $N > 100$, the first order wavefront can be approximated by a continuous radial phase advance

$$\phi(\rho) = \frac{k\rho^2}{2f} \tag{9.40}$$

where by Eq. (9.38) $f = r_1^2/\lambda$, or equivalently in terms of the outer zone width Δr and number of zones N [see Eq. (9.14)], $f \simeq 4N(\Delta r)^2/\lambda$. Thus the electric field in the aperture, as it appears in Eq. (9.27), can be written as

$$E(\xi,\ \eta) = \sum_m \frac{E_0}{|m\pi|}\, e^{-ik\rho^2/2f_m} \tag{9.41}$$

where the coefficients $|1/m\pi|$ correspond to the diffractive efficiencies of the non-zero orders, as given in Eq. (9.24), and again $f_m = f/m$.

The Fresnel–Kirchhoff diffraction formula can then be approximated for the various orders as

$$E_m(x,\ y) = \frac{-iE_0}{m\pi\lambda} \iint \frac{e^{-ik(\xi^2+\eta^2)/2f_m}\, e^{ikR}}{R}\, d\xi\, d\eta \tag{9.42}$$

where for the first order focus at $z = f$,

$$R \simeq f + \frac{x^2}{2f} + \frac{\xi^2}{2f} - \frac{\xi x}{f} + \frac{y^2}{2f} + \frac{\eta^2}{2f} - \frac{\eta y}{f} \tag{9.43}$$

as illustrated in Figure 9.11. With this expansion of R the integral for the first order field becomes

$$E_1(x, y) = \frac{-iE_0}{\pi\lambda f} e^{ikf}\, e^{ik(x^2+y^2)/2f} \iint e^{-ik(\xi x+\eta y)/f}\, d\xi\, d\eta$$

where the $-ik(\xi^2 + \eta^2)/2f$ term due to the zone plate phase advance in the first order has exactly canceled the $+ik(\xi^2 + \eta^2)2z$ term from the expansion of R at $z = f$. Following the now familiar conversion to polar coordinates for the axisymmetric geometry [see Eqs. (9.31) to (9.33)] relevant to a zone plate, the diffraction formula for the first order field becomes

$$E_1(r) = \frac{-2iE_0}{\lambda f} e^{ikf}\, e^{ikr^2/2f} \int_0^a J_0(k\rho\theta)\rho\, d\rho$$

where $\theta = r/f$, where $a = D/2$ is the outer radius of the zone plate, and where J_0 is the Bessel function of the first kind, order zero. Performing the integration, as was done in the steps leading to Eq. (9.34), one obtains for the first order field in the focal plane at $z = f$

$$E_1(\theta) = \frac{-2ia^2E_0}{\lambda f} e^{ikf}\, e^{ik\theta^2 f/2} \frac{J_1(ka\theta)}{ka\theta} \tag{9.44}$$

where $J_1(\nu)$ is the Bessel function of the first kind, order one, and where the above can be written in terms of the focal plane radius by substituting $r = f\theta$ for fixed focal length f.

The corresponding focal plane intensity, for the first order $m = +1$, is obtained by forming $I_1(\theta) = \sqrt{\epsilon_0/\mu_0}|E_1(\theta)|^2$, with the result that the focal plane intensity of the zone plate is given by

$$\boxed{\frac{I_1(\theta)}{I_0} = N^2 \left| \frac{2J_1(ka\theta)}{ka\theta} \right|^2} \tag{9.45}$$

where $I_0 = \sqrt{\epsilon_0/\mu_0}|E_0|^2$, is the illumination intensity of the aperture, N is the total number of zones in the zone plate, $D^2 = 4a^2$, and by Eq. (9.10), written for $n \to N$, we have $D^2 = 4N\lambda f$. The function $|2J_1(\nu)/\nu|^2$, the so-called Airy function that was seen earlier in Figure 9.10, is unity on axis, has its first null at $ka\theta = 3.832$, and oscillates beyond that with ever decreasing amplitude. Thus according to Eq. (9.45), the first order focus of the zone plate lens has an on-axis intensity N^2 greater than the incident intensity. The radial focal plane intensity pattern (Airy pattern) is shown in Figure 9.12.

Note that the first null occurs for

$$kD\theta/2 = 3.832$$

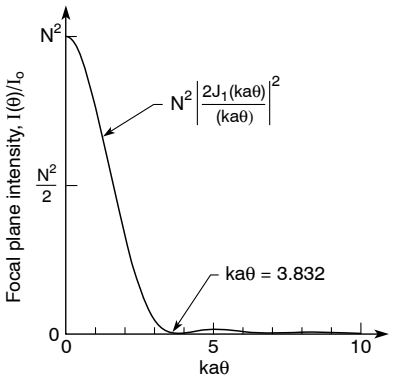

FIGURE 9.12. The Airy pattern of focal plane intensity for a zone plate lens at its first order focus. I_0 is the illumination intensity at the zone plate, N is the total number of zones, $a = D/2$ is the lens radius $k = 2\pi/\lambda$, $\theta = r/f$ is measured from the center of the lens away from the optic axis, r is the focal plane radius, and f is the focal length.

so that with focal plane radius $r = f\theta$ in Figure 9.11, the radius of the first null occurs at

$$r_{\text{null}} = \frac{0.610\lambda}{NA} \tag{9.46}$$

where in the small angle approximation ($\rho, r \ll z$) we have taken $\text{NA} = \sin\theta \simeq \theta$. This is a very well-known result that plays a significant role in determining the resolution of an ideal lens, limited only by the wavelength λ and the numerical aperture. In this ideal case the lens performance is described as *diffraction limited*. In the following sections we consider the Rayleigh criterion for determining resolution in this limit, as well as practical limitations due to various effects. We also describe how such lenses are fabricated, various microscopes in which they are used, and some examples of applications in the physical and life sciences. We note that at EUV and soft x-ray wavelengths numerical apertures approaching 0.1 are available in several laboratories, and thus Eq. (9.46) indicates the possibility of focusing such radiation to focal spots of tens of wavelengths in diameter.

An important consideration not addressed here is that of finite lens thickness. The foregoing analysis assumed opaque zones of essentially zero thickness. In practice the zones are very thick compared to the wavelength, and permit finite transmittance due to finite values of β/δ. Maser, Schneider, and Schmahl at Göttingen have approached this mathematically using a coupled-wave analysis in which incident radiation couples to many modes within the waveguide-like structure. Numerical solutions point toward enhanced resolution using higher orders of improved efficiency.[31–33]

The Moscow X-Ray Optics Group of Popov, Kopylov, and Vinogradov[29] takes a different approach. They note that at these very short wavelengths the refractive index is very close to unity, so that in calculating diffracted fields it is possible to factor out the rapidly varying z-dependence, e^{ikz} in Eq. (9.29), leaving a complex field amplitude with a relatively slow dependence on the spatial coordinates. The resultant field satisfies a parabolic wave equation similar to that encountered in quantum mechanics for a complex potential. For refractive index near unity, solutions involve a slow transverse propagation of energy and permit relatively straightforward numerically efficient solutions for arbitrary diffractive structures. With this approach it is not only possible to consider optimized zone structures, but also to efficiently calculate off-axis imaging properties, including aberrations, in thick structures. An example of a calculation by Kopylov et al.[29] is shown in Figure 9.13 for a relatively thick nickel zone

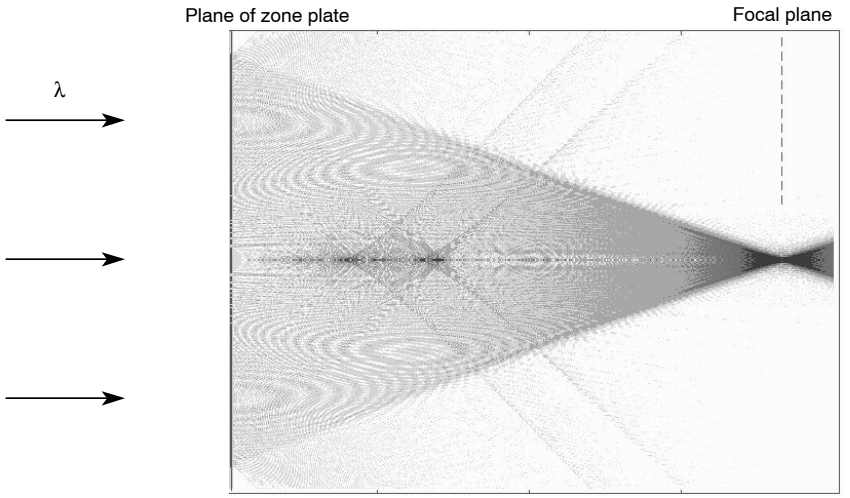

FIGURE 9.13 (see Colorplate XIII). Diffraction from a thick nickel zone plate lens calculated in the parabolic wave approximation. The zone plate thickness is 300 nm, the wavelength is 2.4 nm, the outer zone width is 30 nm, and the zone plate has 300 zones, an outer diameter of 36 μm, and a focal length of 450 μm in first order. (Courtesy of Yu.V. Kopylov and A.V. Popov,[29] Moscow Optics Group.)

plate with $\Delta t = 300$ nm, illuminated with wavelength $\lambda = 2.4$ nm, so that $\Delta t/\lambda$ is of order 100. The lens has 300 zones, an outer zone width of 30 nm, and thus a diameter of 36 μm. The calculation indicates a diffraction efficiency to first order of 26%. It also shows increased diffraction efficiency to higher orders, compared to a reference thin zone plate, including a relatively strong (2%) second order ($m = 2$), as can be seen in the illustration.

Finally, we note that although the pinhole and zone plate diffraction formulae are quite similar in form, both involving the Airy pattern $|2J_1(\nu)/\nu|^2$, the effects are quite different. In the case of the pinhole the Airy pattern is expanding radially in the far field to characteristic dimensions much larger than the original pinhole size, while in the case of the zone plate lens the Airy pattern is formed in the focal plane with characteristic lateral dimensions (focal spot size) much smaller than the zone plate diameter.

9.4 SPATIAL RESOLUTION OF A ZONE PLATE LENS

One measure of the resolution of a lens is the minimum discernible separation of two mutually incoherent point sources. This in turn depends on the so-called *point spread function* of the lens, that is, the image plane intensity distribution due to a distant point source. For an ideal lens, including an ideal zone plate of many zones, the point spread function is an Airy pattern [Eq. (9.45), Figure 9.12], whose lateral extent (spread) depends on both wavelength and lens numerical aperture. The famous Rayleigh resolution, which we discuss in the following paragraph, involves two such point sources, each producing independent Airy patterns. The Rayleigh resolution criterion corresponds to the two being brought sufficiently close that the first null of one pattern is just aligned with the peak intensity of the other, resulting is a small but discernible dip in the summed intensity distribution. More generally, one finds that the resolution depends on illumination and can, of course, be limited by lens imperfections, mounting errors, noise, and other factors. For a Fresnel zone plate lens two well-known

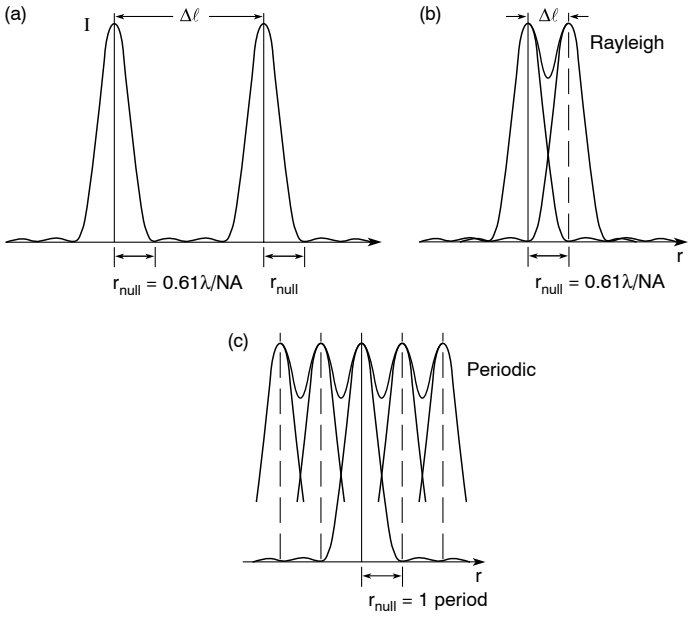

FIGURE 9.14. Airy intensity patterns due to mutually incoherent, quasi-monochromatic point sources at the image plane of a lens of numerical aperture NA. In (a) the two are well separated and easily resolved. In (b) the two are just resolved by the Rayleigh criterion. In (c) several form a periodic intensity pattern.

limitations are the inverse focal length dependence on wavelength (chromatic aberration) and zone placement errors. Other common aberrations[13] such as astigmatism and coma can also limit resolution and image fidelity. We discuss these further in the paragraphs that follow.

We begin the study of spatial resolution by considering two point sources of quasi-monochromatic radiation, each producing an Airy intensity pattern in the image plane of the lens, as illustrated in Figure 9.14(a). In each case the radius to the first null is given by Eq. (9.46). Two physical situations that would approximate this mathematically ideal limit are those of (1) a sub-resolution point of emission in the object plane of a microscope, perhaps created by a backlighted pinhole of very small dimension, and (2) a distant star of angular extent well below resolvable limits. In each case an image plane intensity distribution approximating that in Figure 9.14(a) would be obtained in near-perfect experimental conditions.

One could then imagine two such point sources of equal intensity in a noise free background. If the two were sufficiently separated, by a large distance Δl, as shown in Figure 9.14(a), the image would contain two distinct Airy patterns and we would conclude that the two sources of emission were well resolved. Next, one could imagine the two sources of emission being closer to each other, so that the Airy patterns overlapped. In the consideration here the two are assumed mutually incoherent, so that the fields do not form a time averaged interference pattern; rather, the intensities add. As the two Airy patterns are brought closer to each other, the intensity between the two peaks rises so that it becomes more difficult to discern the two. By Rayleigh's criterion the two are said to be just resolved when the first null of one overlaps the peak of the other, so that $\Delta l = r_{\text{null}}$, as illustrated in Figure 9.14(b). In this case the central Rayleigh dip in intensity is 26.5%. The corresponding *Rayleigh resolution* limit, for Δl just equal to r_{null} in Figure 9.14(b), is

$$\Delta r_{\text{Rayl.}} = \frac{0.610\lambda}{\text{NA}} \tag{9.47}$$

or equivalently, in terms of the lens $F^{\#}$ [see Eqs. (9.15) and (9.16)], where $F^{\#} \simeq 1/(2\,\text{NA}) = \Delta r/\lambda$ for small NA,

$$\Delta r_{\text{Rayl.}} = 1.22 F^{\#} \lambda = 1.22\,\Delta r \tag{9.48}$$

where Δr is the outermost zone width of the zone plate lens. If the objects are brought any closer, the intensity dip rapidly diminishes, and the two are considered unresolved. Although other criteria exist, the Rayleigh criterion is a well-known benchmark, and one that is difficult to achieve in practice, much more so to exceed, at soft x-ray and EUV wavelengths.

There is, however, an advantage that accrues with variation of the angular illumination, that is, partially coherent illumination. We discuss this in the following paragraphs.

As periodic patterns are also commonly used in tests of resolution, we also show in Figure 9.14(c) the intensity pattern that would result for a series of mutually incoherent point sources laid side by side with the respective Airy peaks and nulls overlapped in the Rayleigh manner. Here we see that the period of the resulting intensity pattern is just equal to what we have taken as the Rayleigh criterion separation, i.e.,

$$1 \text{ period} \simeq \Delta r_{\text{Rayl.}} = \frac{0.610\lambda}{\text{NA}} \tag{9.49}$$

where the intensity dip, or modulation in this case, is not greatly different than that for the just-resolved points.

Equation (9.49) is interesting for the insight it provides with regard to resolution tests involving periodic patterns. For instance, gratings of equally wide bars and spaces are frequently used for such tests, essentially to measure how the peak to valley intensity modulation varies as a function of decreasing period. Although one must be careful here to properly account for partial coherence of the illumination, Eq. (9.49) clearly suggests that the Rayleigh criterion corresponds to a full period of the intensity pattern, so that the identification of individual line or space widths, corresponding to a half period, should be numerically equal to half the Rayleigh resolution, and should be understood as such. As an example, Figure 9.15 shows an x-ray zone plate image of a radial test pattern consisting of approximately equal gold bars and spaces. The image was obtained at 2.4 nm wavelength with a zone plate of outer zone width (Δr) equal to 30 nm, corresponding to a numerical aperture [see Eq. (9.13)] NA $\simeq \lambda/(2\,\Delta r)$ of 0.04 at 2.4 nm wavelength, and a Rayleigh resolution [Eq. (9.47)] for an ideal lens of $1.22\,\Delta r = 37$ nm. The image shows 30 nm gold features, corresponding to a period of 60 nm, just resolved. The resolution is thus about 1.6 times the Rayleigh value. Further discussion of spatial resolution and its measurement is deferred, as these are affected by the illumination (partial coherence) pattern of the optical system.

Another common test of resolution is the knife-edge test. This is a particularly attractive test because of its ease of implementation, but requires a well-defined edge on the scale of EUV and soft x-ray wavelengths, which can be quite challenging. Nonetheless it is widely used and often valuable. In Figure 9.16 an effort is made to correlate the knife-edge test with the

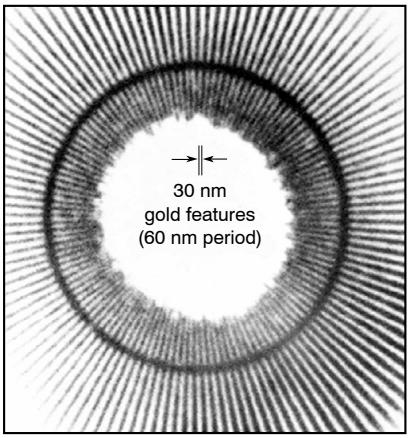

FIGURE 9.15. X-ray image at 2.4 nm wavelength of a radial gold test pattern showing 30 nm gold features (60 nm period). The soft x-ray image was obtained with a CXRO/IBM zone plate lens having a 30 nm outer zone width, and the University of Göttingen soft x-ray microscope at the BESSY synchrotron radiation facility in Berlin (see Refs. 22 and 23).

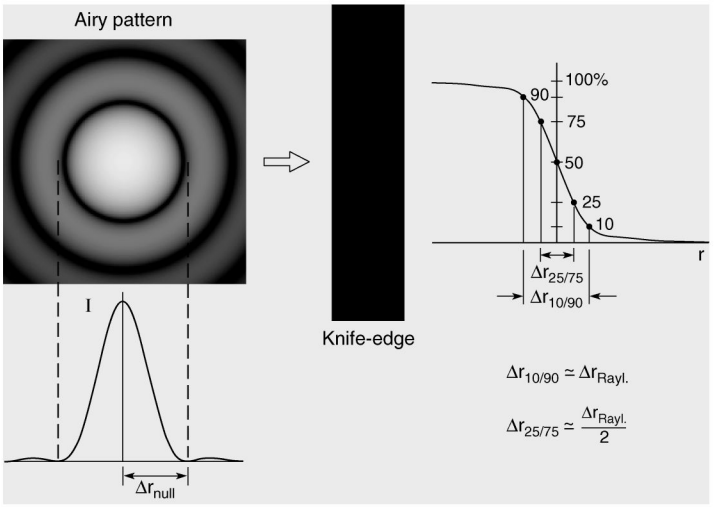

FIGURE 9.16. Simulation of a knife-edge test with an Airy image plane intensity distribution. The laterally integrated intensity is shown as a function of position as a calculated Airy pattern is scanned across a mathematically sharp knife edge. The radial position shift producing an intensity variation from 10% to 90% is approximately equal to the Rayleigh resolution, or first Airy null.

Rayleigh criterion for the case of a point source illumination. A focal plane Airy distribution is numerically scanned across a mathematically perfect knife-edge. The resultant intensity profile is shown to the right. Upon comparison, it is observed that the Rayleigh criterion corresponds to a 10% to 90% intensity variation. The 25% to 75% intensity variation overstates the spatial resolution, relative to the Rayleigh criterion, by a factor of two. Nonetheless, the 25% to 75% criterion is sometimes used because it is readily identified even with noisy data.

Figure 9.17 shows an example of knife-edge data obtained with a zone plate of 35 nm outer zone width and a wavelength of 2.4 nm. The effect of partially coherent illumination on knife-edge intensity in the image plane is illustrated in Chapter 10, Figure 10.3. The data was taken with the knife-edge in the image plane of a soft x-ray microscope at the Advanced

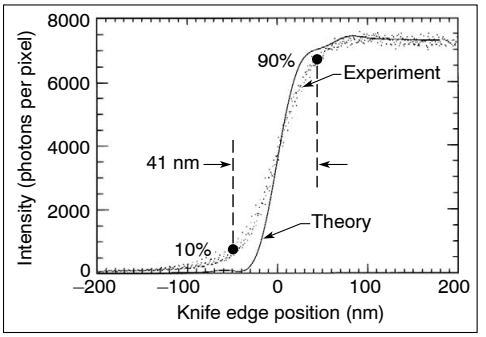

FIGURE 9.17. Image plane intensity as a function of position for a knife edge in the object plane of a full field soft x-ray microscope employing a zone plate lens of 35 nm outer zone width. The wavelength is 2.4 nm. The experimental data (dotted band) indicates a 10% to 90% resolution of 41 nm. The theoretical limit, including partially coherent microscope illumination (see text), is 29 nm. Thus the microscope achieves about 1.4 times diffraction limited resolution. (Following W. Meyer-Ilse and his colleagues,[49–51] LBNL.)

Light Source in Berkeley, and recorded with a back-thinned soft x-ray CCD. The measured 10–90% intensity separation is 41 nm, corresponding to $0.59\lambda/\text{NA}$, slightly better than the Rayleigh limit. This, however, is somewhat misleading, as the Rayleigh limit is not quite appropriate here, due to illumination effects that we discuss in a following section. In fact, these measurements, when proper account is taken of the angular illumination profile, indicate a spatial resolution of about 1.4 times the diffraction limit.[49–51]

9.5 DEPTH OF FOCUS AND SPECTRAL BANDWIDTH

The depth of focus of a lens or imaging system is the permitted displacement, away from the focal or image plane, for which the intensity on axis is diminished by some permissible small amount, or image resolution is only slightly degraded. For the focal plane of a perfect circular lens, with plane wave illumination, it can be shown[52] that the on-axis intensity decreases by only 20% when the observation plane is displaced from the ideal focal plane (smallest focal spot, thus highest axial intensity, $z = f$ in Figure 9.11) by an amount

$$\Delta z = \pm \frac{1}{2} \frac{\lambda}{(\text{NA})^2} \tag{9.50}$$

or

$$\Delta z = \pm 2\text{F}^{\#2}\lambda = \pm 2(\Delta r)^2/\lambda \tag{9.51}$$

where for the zone plate lens $\text{F}^{\#} = \Delta r/\lambda$, where Δr is the outer zone width, and $\text{NA} \simeq 1/2\text{F}^{\#}$. We observe that the depth of focus is inversely proportional to the square of the

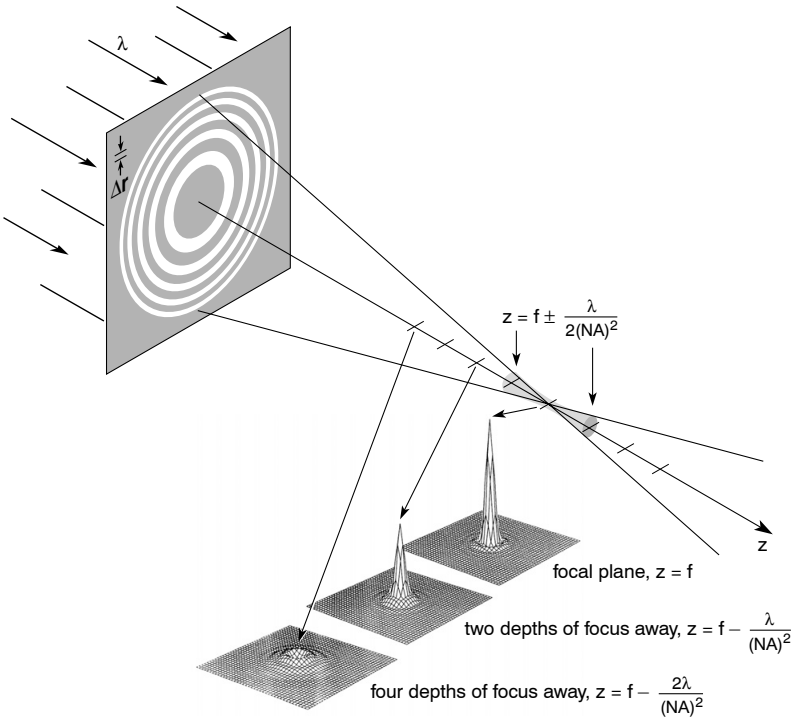

FIGURE 9.18. An illustration of intensity distribution and depth of focus for a zone plate lens with monochromatic plane wave illumination. At the focal plane the radiation is described by an Airy pattern, as given in Eq. (9.45). Within a nearby region of displacement $\Delta z = \pm\lambda/2(\text{NA})^2$, referred to as the depth of focus, the on-axis intensity decreases by only 20%. Further departures from the focal plane, such as the planes at twice and four times this amount, show significantly decreasing peak intensity. The simulated zone plate has $\Delta r = 30$ nm, $N = 300$, and $\lambda = 2.4$ nm. (Numerical simulations courtesy of N. Iskander and E. Anderson,[53] LBNL)

numerical aperture. Thus for lenses of large NA, which potentially achieve the smallest focal spot according to Eq. (9.46) or best spatial resolution according to Eq. (9.47), the depth of focus is very short, leaving little latitude for error. In microscopes and other imaging systems, this also limits the region of a thick sample that is in focus. As an example, for a zone plate lens with an outer zone width of 30 nm, the depth of focus at $\lambda = 2.4$ nm is $\Delta z = \pm 0.75$ μm. Thus the focal region in which the axial intensity is not diminished by more that 20% is restricted to 1.5 μm. Similarly, in an imaging microscope, as will be discussed in a later section, an extended three-dimensional object would have only a section 1.5 μm thick in focus; material outside that region would be seen with diminished resolution. An illustration of depth of focus is presented in Figure 9.18, including isometric views of the intensity distribution at best focus, the Airy pattern, and in places 2 and 4 depths of focus away.[53]

We observed earlier in Eq. (9.14) that the zone plate focal length has a strong wavelength dependence

$$f \simeq \frac{4N(\Delta r)^2}{\lambda}$$

Thus we can imagine that a source of spectral bandwidth $\Delta\lambda$ might have a sufficient focal

length variation to exceed the depth of focus due to diffraction. We consider now the bandwidth necessary to avoid this situation. With the focal length given by Eq. (9.14), the derivative of f with respect to wavelength is

$$df \simeq \frac{-4N(\Delta r)^2}{\lambda^2}\, d\lambda$$

Expressed in terms of the focal length [Eq. (9.14)] and the bandwidth $\Delta\lambda$, this becomes

$$\Delta f = -f \cdot \frac{\Delta\lambda}{\lambda}$$

that is, the focal length is now spread by and amount Δf due to the finite spectral bandwidth $\Delta\lambda$. This focal shift is symmetric, $\pm\Delta f/2$ about the monochromatic focal plane at f, with longer wavelengths coming to focus closer to the lens and shorter wavelengths farther away. Equating this chromatic focal shift to the diffractive depth of focus given in Eq. (9.51), one has

$$\pm\frac{2(\Delta r)^2}{\lambda} = \pm\frac{f}{2} \cdot \frac{\Delta\lambda}{\lambda}$$

or, using Eq. (9.14),

$$\frac{2(\Delta r)^2}{\lambda} = \frac{2N(\Delta r)^2}{\lambda} \cdot \frac{\Delta\lambda}{\lambda}$$

yielding the condition of maximum spectral bandwidth,

$$\boxed{\frac{\Delta\lambda}{\lambda} \leq \frac{1}{N}} \tag{9.52}$$

where $\Delta\lambda$ is the spectral bandwidth and N is the total number of zones (opaque and transmissive) in the zone plate.

Thus to avoid chromatic aberration, so that the focal plane intensity is not diminished within the depth of focus, we require that the relative spectral bandwidth $\Delta\lambda/\lambda$ be less than or equal to one over the number of zones, i.e., less than $1/N$. For a typical zone plate lens with several hundred zones this requires a relative spectral bandwidth much less than 1%. To obtain near-diffraction-limited performance, limited only by wavelength and numerical aperture as given in Eq. (9.47), a polychromatic source of broader spectral bandwidth must be monochromaticized to the extent indicated by Eq. (9.52).

9.6 SPATIAL RESOLUTION BEYOND THE RAYLEIGH LIMIT: THE EFFECTIVE ANGULAR ILLUMINATION PROFILE

In Section 9.4 we considered the ability to discern two mutually incoherent point sources, each producing an independent Airy intensity pattern in the image plane of the lens. Following Rayleigh, the criterion for just resolving these two points is that their separation should be such that the first intensity nulls of each overlap the other's central intensity peak. By extension, this corresponds to normally incident radiation illuminating a periodic structure in the object plane of a lens, as illustrated in Figures 9.19(a) and 9.20(a), such that the diffracted radiation

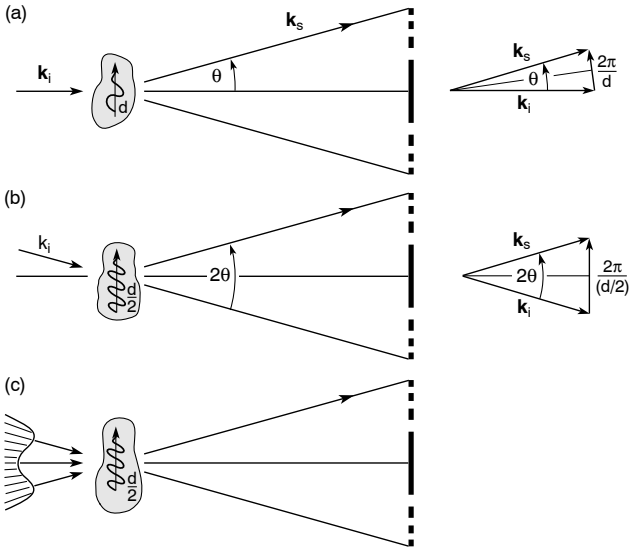

FIGURE 9.19. The effect of illumination on achievable resolution is suggested through the use of scattering diagrams. In (a) normal incidence plane wave illumination, scattered through an angle θ and collected by the lens of $\mathrm{NA} = \sin\theta$, permits one to "see" features of characteristic dimension (period) d. In (b) the illumination is oblique, entering the sample at an angle θ, allowing radiation scattered through an angle 2θ to be collected, and thus permitting one to "see" smaller features of characteristic dimension $d/2$, effectively gaining a factor of two in resolution. In practice the gains in resolution are more modest. For the gain of 2 a narrow angular cone of illumination would be required, thus sacrificing available photon flux and compromising the contrast of lower spatial frequency features. In (c) tailoring the angular distribution of the illuminating radiation is suggested as a method to control the spatial frequency response of the imaging system. A qualitative analysis of possible improvements in resolution, as described by Hopkins, is summarized in Ref. 14.

at an angle $\theta \simeq \lambda/d$ is just captured by the lens and thus contributes to image formation in the image plane (not shown). This situation can be improved, however, by bringing the incident radiation in at an oblique angle, as suggested in Figures 9.19(b) and 9.20(c).

Figures 9.19 and 9.20 approach this problem from the perspective of general scattering diagrams, as discussed in Chapter 2, and diffraction from simple gratings, respectively. In each case it is clear that in the limit of extreme illumination and acceptance, it is possible to improve resolution by a factor approaching two. Thus, for example, one might imagine a zone plate microscope[§] employing a condenser that provides an annulus of incident radiation of large numerical aperture, combined with a zone plate objective lens with the innermost zones blocked, so that only a narrow annulus of radiation is collected, corresponding to diffraction of the highest spatial frequencies in the object or sample. While not very efficient, this would permit one, in principle, to achieve a spatial resolution exceeding the incoherent Rayleigh limit by a factor approaching two. Thus in Figure 9.20(c), with oblique incident radiation, it is possible to "see" a grating of period $d = \Delta r$, rather than $d = 2\,\Delta r$ as in the case (a) of normal incidence. Here Δr is the outer zone width of the lens, which by the Rayleigh criterion would just resolve a structure of period $2\,\Delta r$ (see Figure 9.14).

[§]Or, for that matter, a visible light microscope with a high NA refractive objective lens.

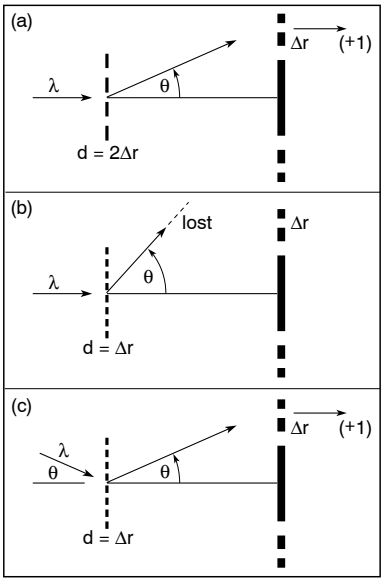

FIGURE 9.20. The effect of illumination is further demonstrated for the specific case of a zone plate lens (outer zone width Δr) collecting radiation diffracted from a transmission grating. In (a) the grating period is $d = 2\,\Delta r$, causing normal incidence radiation at wavelength λ to be partially captured by the lens. In (b) the grating period is reduced by a factor of two, causing diffraction at twice the angle and resulting in loss of the radiation, i.e., some radiation not captured by the lens and thus not contributing to an image of the grating. In (c) the illumination is oblique, at an incidence angle θ, so that diffraction from the shorter period grating is again captured by the lens. Thus, as in Figure 9.19, we see that controlling the angular distribution of incident radiation can provide improved resolution ($d = \Delta r$ vs. $d = 2\,\Delta r$) up to a factor two. Details depend on the illumination (condenser) and collection (lens) numerical apertures, the detailed angular distributions therein, the system throughput (photon flux), and the desired contrast as a function of feature size in the object.

The control of angular illumination as a method of enhancing the spatial resolution of microscopes and other imaging or printing (lithographic) optics is discussed in the literature.[49] The application to x-ray microscopes, including both the ratio of condenser to objective lens numerical aperture and the effect of objective lens central obstruction, is considered by Jochum and Meyer-Ilse.[50] It is these effects that explain how the knife-edge experimental results presented in Figure 9.17 could achieve a resolution that appears to exceed, if just slightly, the Rayleigh limit.[51]

9.7 HIGH RESOLUTION SOFT X-RAY MICROSCOPY

In this section we consider the application of zone plate lenses to high spatial resolution soft x-ray microscopy. With short wavelengths (nominally 0.4 nm to 4.4 nm) and reasonable numerical aperture lenses of high quality, these microscopes are capable of achieving spatial resolutions of several tens of nanometers, about ten times better than that of a visible light microscope. The corresponding photon energies (0.3 keV to 3 keV) span the primary (K-shell) and secondary (L-shell) resonances of half the elements in the periodic chart, providing natural contrast mechanisms for elemental (Z) and even chemical bond mapping. In their

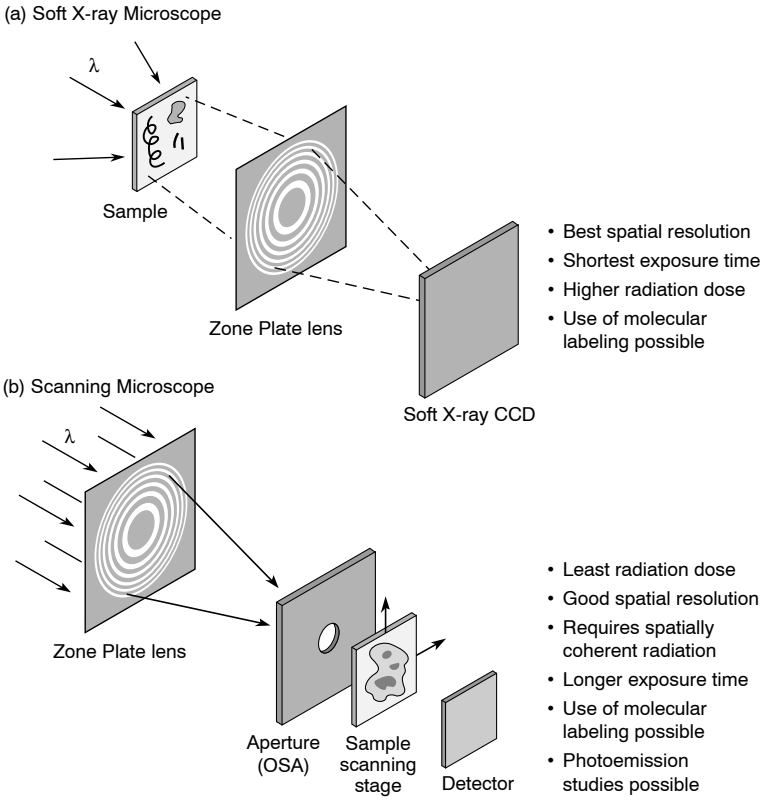

FIGURE 9.21. The two most common zone plate microscopes: (a) a soft x-ray microscope in which a complete image is formed at the CCD and (b) a scanning microscope in which the sample is scanned past a focused spot and the image is constructed electronically, pixel by pixel.

most common usage to date, these microscopes are used for the formation of images based on (1) differential absorption and phase shift of transmitted radiation from relatively thick (to 10 μm) samples, and (2) the detection of photoemitted electrons of well-defined energy (incident photon energy minus binding energy) near an accessible surface. At somewhat higher photon energies the detection of characteristic fluorescent emission also becomes possible, but with compromises in zone plate resolution.‖ Here we consider two basic microscope geometries, as illustrated in Figure 9.21.

9.7.1 The Soft X-Ray Microscope

The soft x-ray microscope is shown in Figure 9.21(a). Development of this microscope** has been pioneered by Schmahl, Rudolph, Niemann, and their colleagues[10, 54–57] at George-August University in Göttingen, at first using bending magnet radiation at LURE in France, and later at the BESSY synchrotron facility in Berlin. In this microscope the zone plate lens forms a complete image at the detector, in the manner described earlier in Figure 9.6, on a

‖Because the higher energy photons are more penetrating, the zones must be thicker. However, fabrication limits with respect to achievable aspect ratios $\Delta t/\Delta r$ then impose larger outer zone widths Δr.
**Sometimes called a transmission x-ray microscope (TXM).

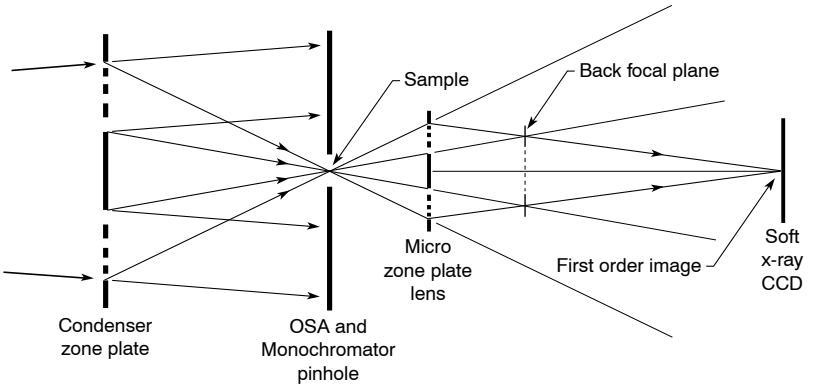

FIGURE 9.22. The soft x-ray microscope utilizes a condenser zone plate with a central stop and a sample plane order sorting aperture, or stop, to illuminate the sample with first order radiation. A *micro* zone plate with high numerical aperture collects transmitted and diffracted radiation, forming a high resolution, high magnification ($M \sim 400$ to 1000) image at the CCD. The back focal plane of the micro zone plate is available for use of an annular phase plate. (Following Schmahl, Rudolph, Niemann, and colleagues,[54–56] George-August University, Göttingen.)

parallel point by point basis, much as with the common visible light (refraction) microscope found in every biology laboratory. The achievable spatial resolution is set largely by the lens outer zone width Δr, but can be improved somewhat through optimized illumination, as discussed in Section 9.6. The illuminating radiation must be of relatively narrow spectral bandwidth, $\Delta\lambda/\lambda$ less or equal to $1/N$, where N is the number of zones, as described by Eq. (9.52).

As shown in Figure 9.21(a), the incident x-rays pass through the sample, where they are partially absorbed with a spatial variation dependent on the atoms present, their distribution, and the wavelength. The emerging radiation is then diffracted by the lens to form a first order image. Examples of images obtained are shown in the next section. The zeroth and other zone plate orders are controlled by both illumination and detection geometry, as illustrated in Figure 9.22. Phase contrast microscopy[58] at soft x-ray wavelengths[59] has been demonstrated using a back focal plane annular phase plate, whose position is indicated in Figure 9.22.

The primary advantage of the soft x-ray microscope is its simplicity and ability to form the highest spatial resolution images. Because it does not require spatially coherent radiation, it generally forms images with bending magnet radiation involving exposure times of a few seconds. Due to the relatively modest zone plate efficiency, typically 10–20% even with phase effects, the radiation dose to the sample is larger than desired. For radiation sensitive biological materials this is largely obviated through the use of cryogenic sample holders,[60–62] which maintain structural integrity even at high radiation dose. Indeed, it appears possible to conduct high resolution tomographic (three dimensional) imaging studies of biological materials through the use of multiple exposures at angularly separated views.[63]

9.7.2 The Scanning Soft X-Ray Microscope

The scanning soft x-ray microscope is illustrated in Figure 9.21(b). Development of the scanning soft x-ray microscope[††] has been pioneered by Kirz, Rarback, Jacobsen, and

[††]Often referred to as a scanning transmission x-ray microscope (STXM).

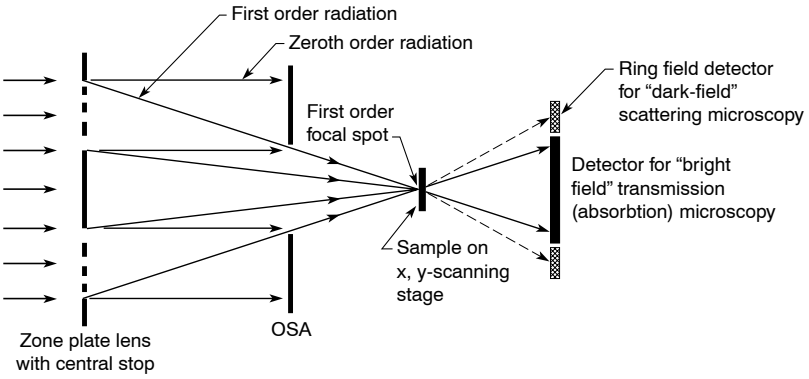

FIGURE 9.23. The scanning soft x-ray microscope utilizes a central zone plate stop and an order sorting aperture (OSA) to block all but the first order from reaching the sample. (Following J. Kirz, H. Rarback, C. Jacobsen, and colleagues,[64, 65] SUNY Stony Brook.)

colleagues[24, 25, 64–66] at SUNY Stony Brook and Brookhaven National Laboratory, at first using bending magnet radiation and later undulator radiation at Brookhaven's National Synchrotron Light Source (NSLS). In this microscope spatially coherent soft x-rays illuminate a zone plate lens, which forms a first order focal spot at the sample plane. If properly illuminated and mounted, the zone plate provides an Airy pattern focal spot intensity distribution, with resolution set by the outer zone width according to Eqs. (9.47) and (9.48). The zeroth and other orders are prevented from reaching the sample[64] by a combination of a zone plate central stop and an order sorting aperture (OSA), as shown in Figure 9.23. Thus radiation dose to the sample is minimized.

The spatially coherent illumination is generally obtained by spatially filtering undulator radiation, as was described previously in Chapter 8, Section 8.4, Figures 8.9 and 8.11. The radiation transmitted through the sample is then detected by a fast x-ray detector as the sample is raster scanned past the focal spot. An image (array of pixels) of arbitrary size is then constructed by correlating sample position with electronic signal. The scanning microscope is very flexible in that it can be used in several modes of operation. In the transmission mode, as described above, it can be used to record sample absorption versus position, repeated at various wavelengths for elemental and chemical analyses at spectral resolution set by the upstream monochromator. It can also be used in a fluorescence or luminescence mode in which incident radiation excites or indirectly causes the emission of radiation that reveals the chemical nature of the sample, or the presence of special molecular tags, again as a function of scanned position. A third mode of operation is that of detecting photoelectron emission as a function of position. Combining the latter with photoelectron spectroscopy, at each scanned position, provides a powerful tool for the study of surface composition and chemistry.

Exposure times are relatively long with the scanning microscope, despite the use of an undulator, because of the significant loss of flux incurred through spatial filtering. Typical exposure times are several minutes for a 400 by 400 pixel array. The scanning system also introduces the possibility of reduced spatial resolution through the inability to maintain nanometer placement accuracy at high scanning speed.

Soft x-ray micrographs obtained with both imaging and scanning microscopes are shown in the following sections.

TABLE 9.1. The elements important to living cells. The first four (H, C, N, O) constitute approximately 96% by weight of the human body. The following seven (Na, Mg, P, S, Cl, K, and Ca) make up most of the remaining 4%. Also important, but in trace amounts, are an additional 14 elements, a few of which are indicated.[68, 71] The K and L absorption edges are largely from Appendix B. Those in parentheses are greatly affected by bonding to neighboring atoms.

Element	Atomic no.	% by weight	K_{abs} (eV)	L_{abs} (eV)
Hydrogen (H)	1	9.5	(13.6)	
Carbon (C)	6	18.5	284	
Nitrogen (N)	7	3.3	410	(37)
Oxygen (O)	8	65.0	543	(42)
Sodium (Na)	11	0.2	1,071	(31)
Magnesium (Mg)	12	0.1	1,303	(49)
Phosphorus (P)	15	0.2	2,149	135
Sulfur (S)	16	0.3	2,472	163
Chlorine (Cl)	17	0.2	2,833	200
Potassium (K)	19	0.4	3,608	295
Calcium (Ca)	20	1.5	4,039	346
Iron (Fe)	26	<0.01	7,112	707
Copper (Cu)	29	<0.01	8,979	933
Zinc (Zn)	30	<0.01	9,659	1022
Iodine (I)	53	<0.01	33,169	4557

9.8 APPLICATIONS TO THE LIFE SCIENCES

The study of biological structures[67–71] provides unique opportunities for the use of short wavelength radiation, both because of the potential to form high spatial resolution images, by various means, and the ability to identify particular atomic elements by exploiting the coincidence between photon energy and atomic resonances of the primary constituents of organic material. For instance, living cells are known to consist largely of the four elements hydrogen, carbon, oxygen, and nitrogen, with additionally significant amounts of seven other elements, as indicated in Table 9.1, and several important trace elements (<0.01% by weight) that are critical to particular cell functions. As we saw in Chapter 1, these elements, except for hydrogen, have their primary absorption edges in the soft x-ray and x-ray spectral regions, thus providing a variety of spectroscopic tools, often in conjunction with imaging and diffraction, to probe their presence and the local environment in which they reside.

It is also of interest to consider the spatial scales of cellular and sub-cellular structures for which these short wavelength techniques are likely to be most useful. An animal cell is typically 10–30 μm across, with a nucleus 3–10 μm in diameter. Ribosomes, the two-component structures in which proteins are synthesized, are 20–30 nm across. Various macromolecules (proteins, carbohydrates, lipids, nucleic acids) have dimensions of one to several nanometers. Proteins, for instance, are typically 3–10 nm across. Glucose ($C_6H_{12}O_6$), a common sugar, is just under 1 nm long. DNA, the molecule that stores the genetic code for all living cells, consists of a double helix only 2 nm in diameter, but several centimeters long for humans, coiled into fibers and loops to form very compact structures, which open and close during

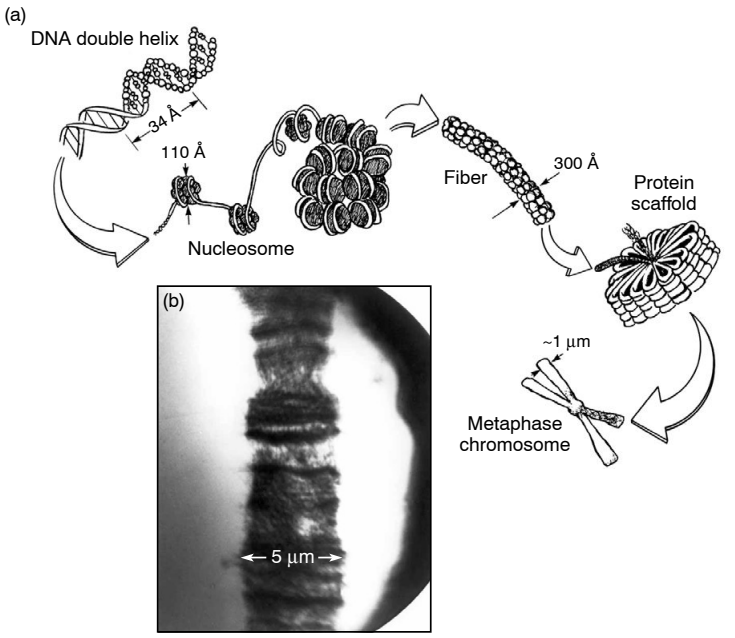

FIGURE 9.24. The packaging of a chromosome (DNA and its associated proteins) is believed to involve a sequence of ever larger beads, fibers, and loops that open at appropriate times in the cell cycle to permit transcription (reading) of particular sections of the DNA (genes) that encode the molecular sequence (instructions) for the synthesis of a specific protein. Shown in (a) is a current model for wrapping a several centimeter long, 2 nm diameter DNA molecule of 3.4 nm helical groove period, into 11 nm "beads on a string," coiled into a 30 nm diameter chromatin fiber, then looped into a protein scaffold, finally appearing as the very compact cross-shaped chromosome seen by visible light microscopy at metaphase in the cell cycle. At other times in the cycle of cell division, the structure opens for transcription (reading) of selective regions of the DNA molecule, leading to the synthesis of proteins coded by that specific region (a gene). The spatial resolution of soft x-ray microscopy provides a potential path for observing some portions of these structures for the first time in a near-native wet state. (b) A soft x-ray image of a wet but fixed giant polytene (many fiber) chromosome from a larvae of *Chironomus thumi*, obtained at 2.4 nm wavelength with the Göttingen (imaging) x-ray microscope at the BESSY synchrotron facility in Berlin. The image shows banding structure familiar from visible light microscopy,[67] as well as 60 nm fibers that could not be seen with visible light. (Courtesy of G. Schmahl, Göttingen, and M. Robert-Nicoud, University Joseph Fourier, Grenoble.)

the cell cycle to permit duplication and gene expression. Figure 9.24 illustrates a current model of DNA packaging, including the 30 nm diameter chromatin fiber (DNA and structural proteins), and the familiar cross-shaped chromosome seen at metaphase in the cell cycle. Also shown in this figure is a soft x-ray image of a polytene (large multifiber) chromosome of *Chironomus thummi*, obtained at 2.4-nm wavelength by the Göttingen group using their imaging x-ray microscope at the BESSY synchrotron facility in Berlin,[57] which shows clearly resolved features that could not be seen with visible light microscopy.

The smaller structures mentioned in the preceding text, and many of the atomic details of molecular structure that are critical to biochemical function, are comparable to x-ray wavelengths and are presently beyond the capabilities for direct image formation. The wealth of information we know about such structures (see Refs. 67–71) is obtained through techniques such as electron microscopy[72] and x-ray crystallography.[73–75] For a concise review of these

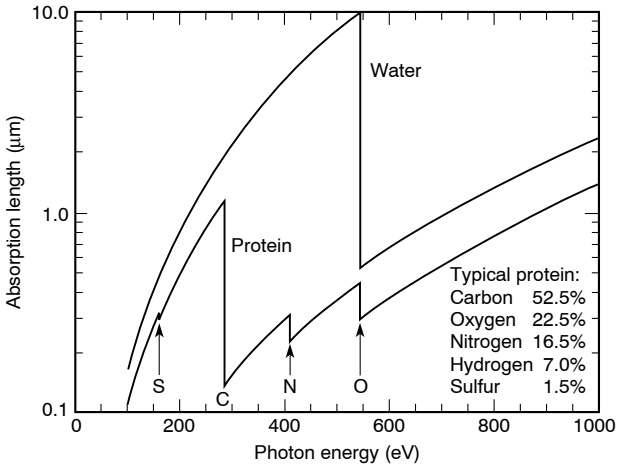

FIGURE 9.25. The absorption length for soft x-rays in water and a Generic protein as a function of photon energy. Natural contrast is obtained in the water window, between the carbon and oxygen absorption edges, where the high carbon content protein is absorbing but where water is relatively transparent (see Ref. 76).

tools, including visible light microscopy and techniques for extending resolution through fluorescence tagging, see the text by Darnell, Lodish, and Baltimore.[69]

The opportunity, however, to form direct images of thick hydrated biological material in a near-native environment, at a spatial resolution well beyond that achievable with visible light microscopy, lies in the soft x-ray spectral region.[55, 66] Natural contrast is available at soft x-ray energies due to the presence of absorption edges for all the major constituents (C, O, N) as illustrated in Table 9.1. The relative transparency of water between the carbon and oxygen absorption edges makes this a particularly attractive region for soft x-ray microscopy, as the human body, for instance, is 70% water by weight. This *water window*[76] is illustrated in Figure 9.25. It shows, for instance, that in the 400–500 eV region (2.5–3.1 nm wavelength) carbon-rich protein has a far shorter absorption length [see Chapter 3, Eq. (3.22)] than water, thus providing natural contrast for biological material in 10 μm of water, the thickness of a typical cell.[‡‡] For the biological community this natural contrast at high spatial resolution is indeed very attractive. However, there are two particular concerns, each of which is partially addressed by current research. One is that of radiation-induced damage. The other is the development of fluorescent tagging techniques to enhance the visibility of specific proteins within larger three-dimensional structures.

With regard to radiation damage, photons in this spectral region have sufficient energy to break chemical bonds and ionize constituent atoms. This can cause chemical and structural damage, potentially affecting critical function. Indeed, the energy deposited per unit mass (dose) can cause microscopically (micron scale) observable changes in structure. Several routes are available to partially mitigate these effects. For one, there is substantial variability in sensitivity to radiation dose among biological materials, so that choice of subject may be an option. Another countermeasure, widely used in electron microscopy, is chemical fixation (plasticizing). Most importantly, rapid cryofixation (quick freezing) provides a mechanism for maintaining atomic and molecular position, albeit with a loss of functionality. Nonetheless,

[‡‡]Water again becomes transparent at several keV, offering further opportunities there.

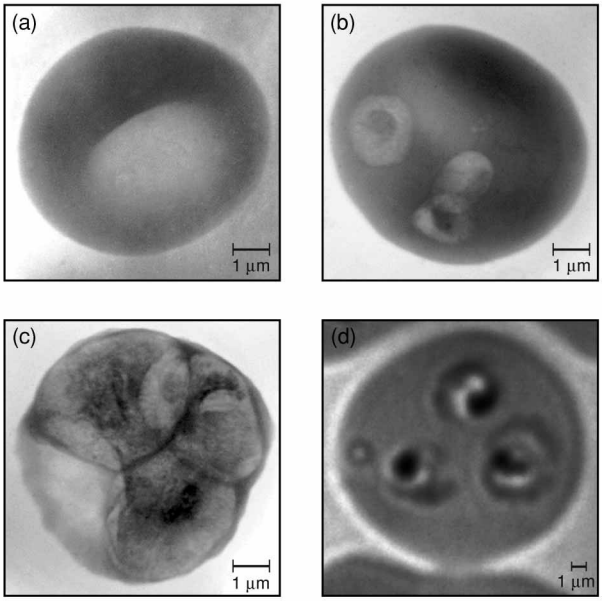

FIGURE 9.26 (see Colorplate XIV). Images of malaria infected red blood cells obtained at 2.4 nm wavelength with the high resolution soft x-ray microscope XM-1 at the Advanced Light Source in Berkeley. Image (a) shows an uninfected cell, (b) shows a newly infected cell, and (c) shows a cell 36 h after infection. All are chemically fixed. Image (d), obtained with visible light microscopy, is shown for comparison. (Courtesy of C. Magowan, W. Meyer-Ilse, and J. Brown,[80] Lawrence Berkeley National Laboratory).

radiation damage is an important constraint, and thus these countermeasures are scientifically important and actively pursued in the research community.[5]

Of great interest to the life sciences community is the structure and function of specific proteins. In general the determination of structure requires atomic resolution, obtainable only with considerably shorter x-ray wavelengths, using the techniques of protein crystallography.[73–75] Equally important is the location of proteins within the cell. Toward this end much work is done at the cellular, or more specifically subcellular, level, as evidenced by the extensive use of visible light microscopy, often in conjunction with site specific fluorescent markers (molecular labels) that help to identify the location and role of specific proteins.[77] The extension of molecular labeling techniques to soft x-ray microscopy, first pointed out by Jacobsen[90], offer substantial new opportunities for resolution of biological questions at the subcellular level. Several examples demonstrating the use of molecular labels in soft x-ray microscopy are discussed in the following sections. Recent advances in cryofixation,[61, 78] and the possibility of tomographic imaging[63] that this permits, may further enhance the potential use of soft x-ray microscopy in the life sciences.

9.8.1 Biological Applications of the Soft X-Ray Microscope

Images are shown in Figures 9.26–9.32 that illustrate the quality of structural and chemical information that can be obtained using soft x-ray microscopes and various sample preparations. All were obtained using bending magnet radiation, some at BESSY[56] in Berlin and some at the Advanced Light Source in Berkeley.[79]

The images of malaria infected red blood cells in Figure 9.26 were obtained using the soft x-ray microscope XM-1 at the Advanced Light Source in Berkeley.[79] They are part of

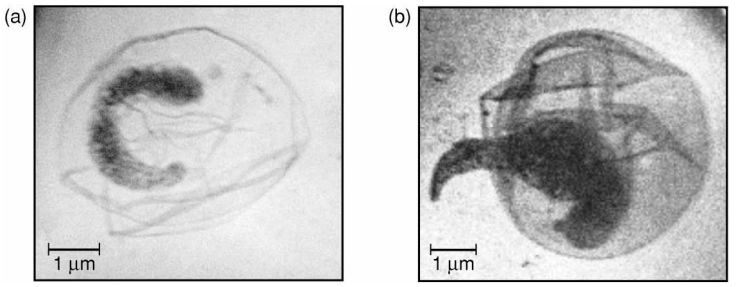

FIGURE 9.27 (see Colorplate XV). Soft x-ray images of *Cryptosporidium,* a common parasite found in lakes and rivers, and occasionally in municipal water supplies. Outbreaks of the disease caused by this sporozoite have caused loss of life in the U.S. Image (a) shows the last of four sporozoites still in its protective oocyst. Image (b) shows a sporozoite emerging from the oocyst. Images are at 2.4 nm wavelength. (Courtesy of C. Peerson, UCSF, and W. Meyer-Ilse, LBNL)

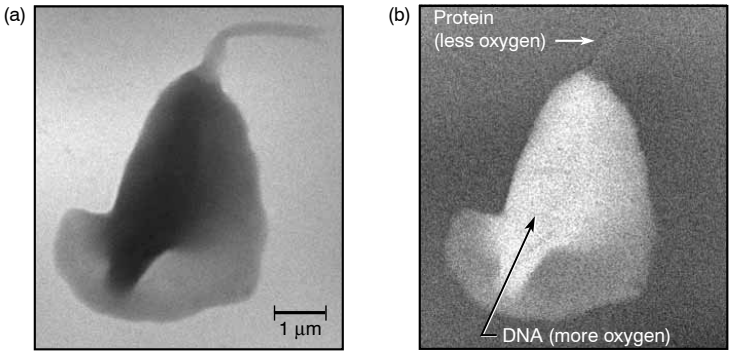

FIGURE 9.28. Soft x-ray images of transgenic sperm. Image (a) is at 539 eV (2.30 nm), where absorption by oxygen peaks. Image (b) is a differential image formed by logarithmic subtraction of images at 539 eV and 533 eV, just above and below the oxygen edge, so as to emphasize the presence of oxygen. Note that the tail is barely visible in (b). The images are not fixed. The dose for each image is 9 MGy. (Courtesy of R. Balhorn et al.,[85] LLNL, and W. Meyer-Ilse et al.,[79] LBNL.)

an extensive study[80] of the progression of the disease, involving thousands of high resolution (nominally 40 nm) soft x-rays images. The series was obtained by allowing the cells to grow in culture, interrupting that growth for selected cells at various times in the 48 h malaria life cycle, followed by chemical fixation and x-ray imaging. Because the material is fixed, longer exposure times of 20–60 s were used to obtain higher counts per pixel, thus reducing noise and improving image quality. In some studies medical countermeasures (protease inhibitors), thought to be useful in the treatment of this disease (which kills approximately 2.7 million people yearly[81]), were introduced so as to observe the effect on development of the parasite. Figure 9.26(a) shows an uninfected erythrocyte (red blood cell), (b) shows a newly infected cell, (c) shows a cell 36 h after infection, and (d) shows a visible light microscope image for comparison. The x-ray microscope image sizes in Figure 9.26 are $7\,\mu\text{m} \times 7\,\mu\text{m}$ and were obtained at $2400\times$ magnification.

Images of *Cryptosporidium,* a common parasite found in lakes, in rivers, and occasionally in public water supplies, are shown in Figure 9.27, also obtained with XM-1 in Berkeley.

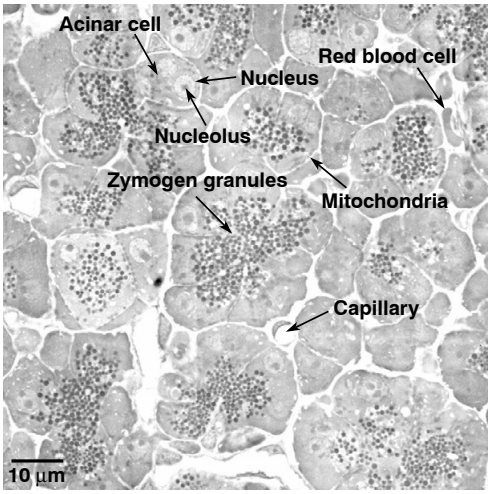

FIGURE 9.29. A composite soft x-ray image of a section of pancreatic tissue, showing several acinar cells each containing many zymogen granules, small vesicles thought to play a major role in the intracellular transport of digestive enzymes. (From B. Loo, and S. Rothman,[86] UCSF, and W. Meyer-Ilse, LBNL.)

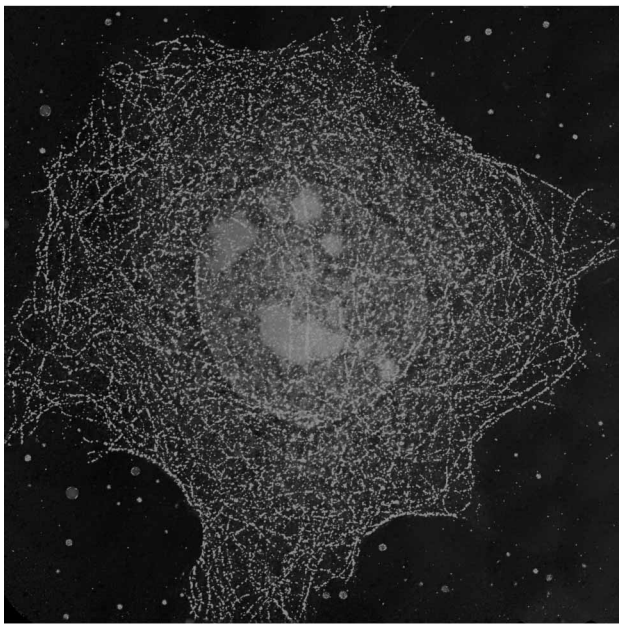

FIGURE 9.30 (see Colorplate XVI). A soft x-ray micrograph at 520 eV (2.4 nm wavelength) of a whole hydrated mouse epithelial cell (EPH4) as seen in a color coded intensity map. The image is 32 μm by 32 μm. The microtubule network, made evident by high absorption due to silver enhanced gold labels, is color coded blue in the image. The cell nucleus and nucleoli, characterized by moderately dense and absorbing proteins, are coded orange. The less absorbing more aqueous regions of the cell are color coded black. The silver enhanced gold is part of a molecular double label, discussed in the text, that permits cross correlation with visible light fluorescence in a confocal microscope. (Courtesy of C. Larabell, W. Meyer-Ilse, and colleagues,[87] Lawerence Berkeley National Laboratory.)

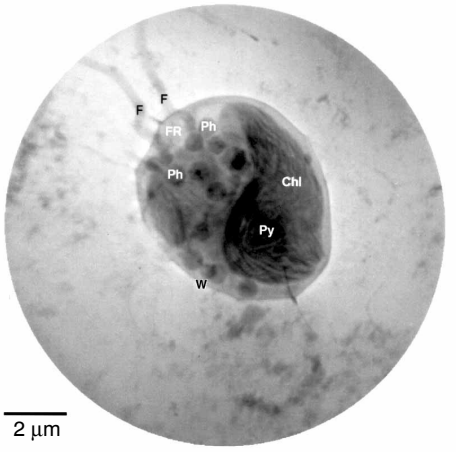

FIGURE 9.31. An image of an alga *Chlamydomonas rheinardtii*, taken at 2.4 nm wavelength with the fast cryo-preparation stage employed in the Göttingen soft x-ray microscope at BESSY in Berlin. The exposure time is 5 s. (Courtesy of G. Schneider and B. Niemann,[61] Göttingen.)

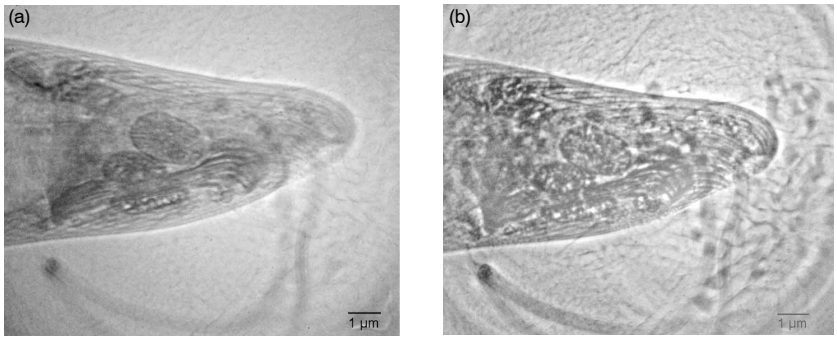

FIGURE 9.32. Amplitude and phase contrast images of the alga *Euglena gracilis* taken at 2.4 nm wavelength with the Göttingen soft x-ray microscope at BESSY. The sample was quick frozen to cryogenic temperature before the exposures. The image in (a) is a conventional transmission image in which contrast is due to absorption in the sample. The exposure time was 3 s, and the accumulated dose was 3 MGy. The image in (b) employs phase contrast to enhance the contrast of fine features. Due to illumination constraints in (b), the exposure time is somewhat longer, 15 s; however, the accumulated dose is unchanged at 3 MGy. (Courtesy of G. Schneider, G. Schmahl, T. Schliebe, M. Peuker, and P. Guttmann,[62] George-August University, Göttingen.)

Associated with animal wastes, this parasite is resistant to chlorination treatment and filtering while encapsulated in its 4–6 μm protective shell (oocyst). Long lived (typically six months), the parasites enter the human digestive tract and open in the intestine, where they feed and reproduce. Only a small number are required to induce symptoms. Recent large scale outbreaks have occurred in several U.S. cities. An outbreak in Milwaukee, Wisconsin (1993) infected about 400,000 people, resulting in 104 deaths, and an outbreak in Las Vegas, Nevada (1994) resulted in 19 deaths.[82, 83] Figure 9.27(a) shows the last of four sporozoites (parasites) still in its protective oocyst.[84] Figure 9.27(b) shows a sporozoite emerging from the oocyst. These samples were also chemically fixed.

Figure 9.28 shows images of transgenic sperm, part of a study of chromatin (the proteins that package DNA) organization[85] in mammalian sperm. Sperm are particularly radiation

hardy (relatively insensitive), permitting several images without fixation. The unfixed samples in Figure 9.28 received a dose of approximately 9 MGy per image. The image in Figure 9.28(a) was taken at 539 eV (2.30 nm wavelength), where absorption by oxygen peaks. The head and tail are seen. Figure 9.28(b) shows a differential image, formed by logarithmic subtraction of electronic images on a pixel by pixel basis [see Chapter 2, Eq. (2.24)], in this case images above and below the oxygen absorption edge, at 539 eV and 533 eV, respectively. The differential image highlights oxygen content, which in this case is larger in the head than in the tail, which is barely visible. The DNA in the sperm head is known to contain more oxygen that the protein in the tail.

Figure 9.29 shows a composite image of a section of pancreatic tissue,[86] obtained by stitching together many sub-images, in this case achieving a field of view of approximately 120 μm on a side, far larger than would normally be possible with a high resolution imaging x-ray microscope. In this example the field contains approximately 3000 by 3000 pixels, each 40 nm square. The image shows several pancreatic acinar cells, each containing many zymogen granules (small vesicles thought to play an important role in the intra-cellular transport of digestive enzymes). The vesicles are seen here as small circular dots of varying diameter and opacity. The purpose of the study is to evaluate alternative theories on the release of protein content. Also seen in several cells are the nucleus and nucleolus. In this investigation, with automated data acquisition and stitching, hundreds of images have been obtained in a single day.

As described toward the end of the previous section, an important goal for biologists is not only to determine a protein's structure but also to understand its function. Toward this end it is essential to know where the protein is within the cell, and how this might vary with time in the cell cycle and with various stimuli. A very important tool that permits spatial localization with visible light microscopy is the use of protein specific labels (molecular tags) that attach to the protein of interest and fluoresce at defined wavelengths. Figure 9.30 shows a 520 eV (2.4 nm wavelength) soft x-ray microscope image of a mouse epithelial cell[87] (EPH4), with the microtubule[¶¶] network visualized through an extension of this labeling technique. In this case a double-labeling technique involving fluoroscein and Nanogold[§§] is employed. The fluoroscein has a visible fluorescence that permits visualization of the microtubule network in a visible light confocal microscope. The same molecular tag includes a 1.4 nm gold particle, small enough to penetrate the cell membrane during the labeling process. The gold is then silver enhanced to an approximately 45 nm diameter for visualization by absorption in the soft x-ray microscope. The high absorption coefficient of the silver enhanced gold particles allows them to be easily isolated in the image. Using a color coded intensity mapping, Figure 9.30 shows these high absorption regions in blue, revealing the extensive microtubule network. At this photon energy (520 eV) regions of low protein content, largely aqueous environment, show little absorption and as a consequence appear as a black background in the figure. The moderately absorbing (unlabeled) nucleoli within the cell's nucleus appear orange. The image is actually a montage of individual soft x-ray micrographs, utilizing the overlay techniques shown earlier in Figure 9.29. This and other images in the same study show a close relationship to the visible light images, but at higher spatial resolution. Furthermore, the soft x-ray images reveal additional features of the cell, such as the nucleus and nucleoli revealed in Figure 9.30.

[¶¶] Microtubles are nominal 25 nm diameter structural filaments of great adaptability. They can provide polarity to the cell, regulate cell shape, and provide a network of fibers to guide the movement of vesicles and organelles. The microtubules consist of molecular tubulin proteins.

[§§] Nanogold and FluoroNanogold are products of Nanoprobes, Inc., Stony Brook, New York. Web site www.nanoprobes.com

As noted in an earlier section, a major concern in the study of biological samples is their sensitivity to radiation dose. A large part of the solution to this problem is the use of cryogenic techniques that maintain structural integrity of fine features to very high dose levels. This follows similar solutions to the dose problem taken in the transmission electron microscopy (TEM) community. The most active soft x-ray microscopy groups are presently implementing cryo capabilities into their microscopes. Figure 9.31 shows an image of the alga *Chlamydomonas rheinardtii*, obtained at 2.4 nm wavelength in the new cryo stage of the Göttingen soft x-ray microscope at BESSY.[61] The frozen hydrated sample is prepared by shock freezing in liquid ethane. The image shows two flagellae (F) of 300 nm diameter, their roots (FR), the chloroplast (Chl) with the pyreniod (Py), and several dense phospholipid vesicles (Ph). The exposure time was 5 s, with an accumulated dose of 4 MGy. The sample is whole, unfixed, and unstained. Further development plans include a capability for tomographic (three dimensional) images, made possible by the high dose tolerance of cryo-prepared samples.

Phase contrast soft x-ray microscopy has been developed by the Göttingen group[59, 60–62] using the geometry shown in Figure 9.22. To obtain phase contrast, radiation from the condenser is limited to a narrow annular cone that is matched by an annular phase plate in the back focal plane of the objective lens (the micro zone plate). The phase plate thickness is designed to produce a negative $3\pi/2$ phase shift of the unscattered radiation at 2.4 nm wavelength, with considerable attenuation. The incident annular cone is diffracted into first order by the micro zone plate, forming a phase shifted reference wave. The scattered radiation from within the object itself undergoes a positive $\pi/2$ phase shift, so that the two interfere with maximum (π) phase contrast. Figure 9.32 shows a side by side comparison of soft x-ray microscope images obtained by absorption (amplitude) contrast (without the phase plate) and phase contrast with the Göttingen microscope at BESSY. The images are of a frozen hydrated alga *Euglena gracilis*,[62] taken at 2.4 nm wavelength, with exposure times of 3 s (amplitude contrast) and 15 s (phase contrast). The samples are whole and unstained. The accumulated dose in each is 3 MGy. The phase contrast image shows significant contrast enhancement of fine features.

9.8.2 Biological Applications of the Scanning Soft X-Ray Microscope

The great advantages of the scanning soft x-ray microscope are the flexible modes of operation and the relatively low radiation dose delivered to the samples, as was discussed in Section 9.7.2. The lower dose[66] is accomplished in the scanning microscope by permitting only the first order (focused) radiation to reach the sample, blocking all other orders (which typically account for 90% of the energy) with an order sorting aperture, as illustrated in Figures 9.21(b) and 9.23. Sample images obtained with the scanning soft x-ray microscope at Brookhaven's National Synchrotron Light Source (NSLS) are shown in Figures 9.33–9.36.

Figure 9.33 shows three images of a bull sperm head obtained at slightly different photon energies.[88] The photon energies are selected to reveal the presence of protein and DNA through differences in their x-ray absorption near edge structure (XANES). The reference image in Figure 9.33(a) was obtained at a photon energy of 290.5 eV (4.268 nm), just above the carbon absorption edge. The images in Figure 9.33(b) and (c) were obtained at slightly longer wavelengths where chemical bonding (C=C, C=N, and C=O) leads to spectral resonances that permit enhancement of protein and DNA contributions to the absorption.[88] These studies demonstrate how chemical mapping can be used to form detailed compositional maps, from protein to DNA in this case.

An example of an image obtained using cryofixation and scanning soft x-ray microscopy[78] is shown in Figure 9.34. The image is that of a frozen hydrated 3T3 fibroblast imaged at 110 K.

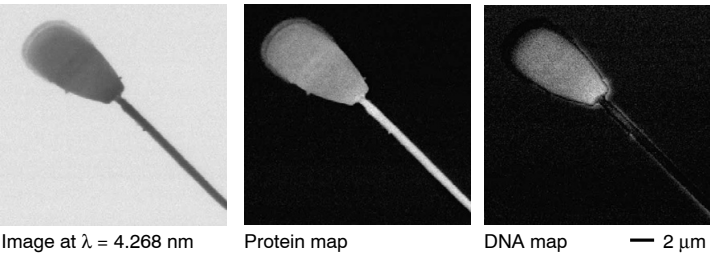

FIGURE 9.33. Image of air-dried bull sperm, showing how chemical mapping (carbon–carbon, carbon–nitrogen, and carbon–oxygen bonds) can be used to add contrast to protein and DNA content. (Courtesy of X. Zhang, R. Balhorn, LLNL, and J. Mazrimas, and J. Kirz,[85, 88] SUNY Stony Brook.)

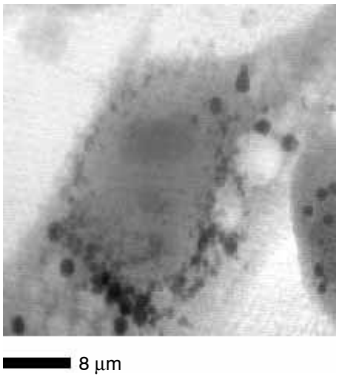

FIGURE 9.34. Image of a frozen hydrated 3T3 fibroblast at 110 K, obtained with the Stony Brook scanning soft x-ray microscope at NSLS. (Courtesy of J. Maser, C. Jacobsen, J. Kirz, and colleagues,[78] SUNY Stony Book.)

FIGURE 9.35. A stereo image pair of a human spermatozoon obtained with 20° angular separation between exposures. (Courtesy of B. Loo and S. Rothman,[89] UC San Fransisco.)

The cultured cell was grown on a Formvar coated gold grid and plunge frozen from the culture medium into liquid ethane. The cryofixation in this case makes use of techniques developed for use with high vacuum transmission electron microscopes (TEMs). Figure 9.35 shows the first stereo image pair obtained with soft x-ray microscopy. The images show a human spermatozoon, rotated 20° between images obtained with the Stony Brook–NSLS scanning microscope.[86] With cryofixation it may be possible in the near future to extend these results to full tomographic imaging.[63]

As discussed in an earlier section, the usefulness of soft x-ray microscopy can be substantially advanced by the development of site specific tags or markers, including x-ray to visible light fluorescent markers,[90] as well as dark field scattering techniques.[91–94] Techniques

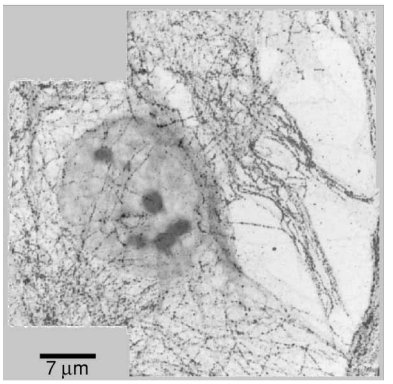

FIGURE 9.36 (see Colorplate XVII). Dark field soft x-ray scanning microscopy is demonstrated in this image of a human fibroblast, a collagen rich cell that plays an important role in the formation of extracellular matricies of connective tissue. The image, obtained at 2.50 nm wavelength with the Stony Brook scanning microscope at Brookhaven National Laboratory, consists of an overlay of the two signals: a transmission signal in gray indicative largely of absorption of x-rays by carbon, and a signal in red due to scattering of x-rays by silver enhanced gold labels attached to microtubules (cytoskeleton fibers of the cell not found in the nucleus). (Courtesy of H. Chapman, LLNL; J. Fu and C. Jacobsen, SUNY Stony Brook; and K. Hedberg, University of Oregon.[92])

employing x-ray to visible light fluorescence offer the advantage of better spatial resolution through a smaller scanning spot size, as they are combined with protein specific labeling techniques already in wide use with visible light microscopes. Preliminary images using this technique have been obtained.[90, 95, 96] Dark field imaging has been obtained with the scanning microscope by blocking the transmitted photons with a central stop just before the transmission detector (see Figure 9.22), and instead collecting the relatively weak signal due to x-rays scattered into a surrounding annular or ring-field detector.

An example of such dark field x-ray microscopy, obtained with the Stony Brook scanning microscope at 2.50 nm wavelength, is shown in Figure 9.36. The figure shows an overlay of two images of the same human fibroblast in which the microtubules (25 nm filaments that are part of the cell cytoskeleton but are not present in the nucleus) were labeled with silver enhanced gold colloids. The gray image is due to the bright field absorption signal, primarily indicating the presence of carbon. The red overlay is due to the collection of scattered x-rays into the annular ring, showing the location of gold–silver labels and thus the position of microtubules. It is clear that the scanning microscope offers many applications for studying biological material at a spatial resolution well beyond that of visible light microscopy.

9.9 APPLICATIONS TO THE PHYSICAL SCIENCES: ANALYTIC TOOLS FOR MATERIALS AND SURFACE SCIENCE AT SPATIAL RESOLUTIONS BELOW 100 NANOMETERS

Modern materials science involves ever smaller structures, for which the properties of surfaces and thin films become more important than bulk or volumetric properties. In part this

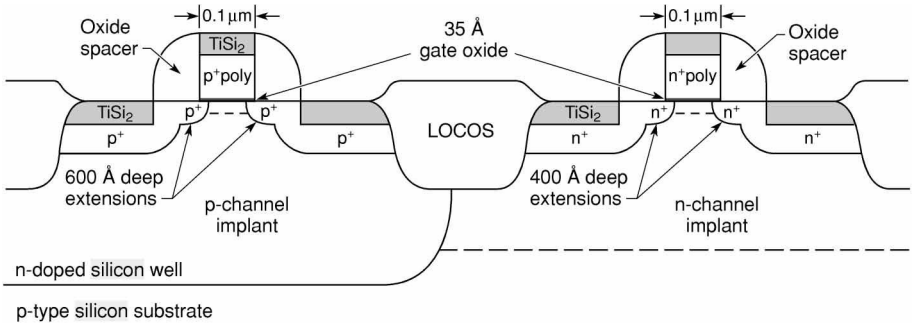

FIGURE 9.37 (see Colorplate XVIII). Cross-sectional view of a 0.1 μm complementary metal oxide semiconductor (CMOS) field effect transistor (FET) with dual n^+–p^+ doped polysilicon gates. The thin gate oxide is 0.1 μm wide and 35 Å deep. The titanium silicide provides a low resistivity interconnect. The oxide spacers and LOCOS (Localized Oxidation of Silicon) are insulator regions. Note the presence of silicon in several chemical forms (crystalline, Si substrate with various dopings, polycrystalline Si, SiO_2, and $TiSi_2$). Concentrations of dopants and impurities in the vicinity of the gate region are critical to the performance of such devices and thus may require diagnostic methods, including soft x-ray microscopy, that are element sensitive with high spatial resolution and reasonable penetration depth. (Following Y. Taur et al.[99], IBM.)

is due to simple scaling. The ratio of volume to area decreases linearly with smaller size. In some cases properties are different near surfaces, and in the limit quantum mechanical effects become important. Some applications that drive this trend toward smaller dimensions include semiconductor manufacturing, which currently fabricates devices with 250 nm critical dimensions[97][|||] and requires analytic tools for materials processing with a spatial resolution 5 to 10 times smaller (25–50 nm), and magnetic recording materials with characteristic magnetic domain sizes of 10–20 nm.[98] Relevant to this chapter is the possibility of providing an analytic capability for surfaces and thin structures with a (transverse) spatial resolution of 10–20 nm. For instance, such tools might be used to determine the chemical state of constituent atoms (such as Si, SiO_2, $TiSi_2$, etc.), or the quantitative measurement of dopant or impurity concentrations that might be present in the vicinity of critical structures. Figure 9.37 illustrates the materials and dimensions typical of what one might anticipate in a future electronic device.[99] Note that the concentrations of dopants and impurities in the vicinity of the gate region are critical to the performance of the device, and thus will require analytic techniques with both element sensitivity and high spatial resolution with reasonable penetration depth, attributes that may be unique to soft x-ray microscopy.

A very powerful and versatile tool for such studies is that of x-ray photoelectron spectroscopy[100–104] in which an incident photon transfers its energy ($\hbar\omega$) to a bound electron near the surface, resulting in a transition to a free state in the continuum above the vacuum level. As indicated in Figure 9.38, by conservation of energy the free electron has a kinetic energy E given by

$$E = \hbar\omega - E_B \tag{9.53}$$

[|||]The industry road map for major manufacturing capabilities follows a time line whereby the spatial scales decrease a factor of $\sqrt{2}$ every two or three years, thus reaching a minimum feature size of approximately 100 nm in the year 2005, requiring analytic tools of 10–20 nm spatial resolution. See Chapter 10, Section 10.1 for further discussion.

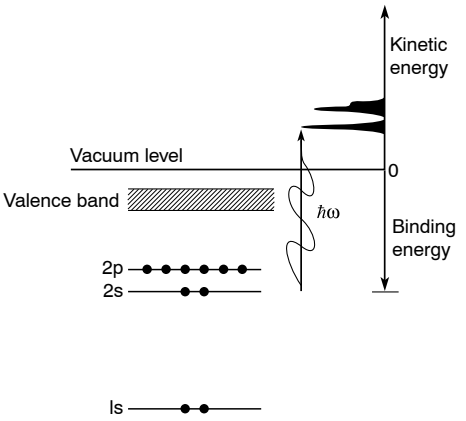

FIGURE 9.38. The process of photoemission, in which an absorbed photon transfers its energy to a bound electron near the material–vacuum interface, resulting in a transition to a free electron state in the continuum with kinetic energy equal to that of the incident photon minus the binding energy.

where E_B is the binding energy of the electron in its initial state. Photoelectron spectroscopy*** then refers to the experimental procedure for measuring the energy spectrum of the emitted electrons. From this one can determine both the elements present (C, N, . . . , Si, . . .) and the nature of their chemical bonding to neighboring atoms. For instance, the appearance of sharp features at known binding energies for various states (1s, 2s, 2p, . . .) indicates the elements present, while shifts of the binding energies provide information regarding the chemical environment, e.g., bonding with neighboring atoms [Si(111), SiO_2, etc.]. The technique is primarily a tool for the study of surfaces and thin films, due to the limited range (escape depth) of electrons in solids, typically only a few angstroms at 20–100 eV kinetic energy. The observed emission spectrum generally includes a low kinetic energy continuum ($<$10 eV) of secondary electrons,[105, 106] resulting from collisions or scattering between an emitted photoelectron (the *primary* electron) and perhaps a low binding energy conduction (*secondary*) electron.

Figure 9.39 shows a typical photoemission spectrum that in this case clearly reveals both the elements present and information regarding their chemical environment.[107] In this example the bonding of CaF_2 to a crystalline Si(111) substrate is studied as a model for insulator–semiconductor epitaxial systems because of their nearly identical lattice matching. The three spectra shown in Figure 9.39(c) correspond to approximately a monolayer (a single molecule thick on average across the surface) of CaF_2 on Si(III), to a thin film about 1 . 1 nm thick corresponding to a few monolayers of CaF_2, and to a relatively thick film ($\simeq$ 5nm) for which the photoemission signature is characteristic of bulk CaF_2. Incident photon energies of typically 135 eV were used in these studies, which were performed at the Stanford Synchrotron Radiation Laboratory (SSRL). Electron energies [see Eq. (9.53)] are given in electron volts below the silicon valence band.

For the monolayer in (a) the fluorine 2p and calcium 3p peaks, at approximately 8.3 eV and 25.6 eV, respectively, are relatively narrow atom-like features, associated in the case of calcium with bonding to the surface. In (b) there is a transition as the fluorine 2p feature broadens toward a CaF_2 bulk dominated valence band, and the Ca 3p develops a double-peaked structure reflecting both the surface dominated and bulk valence band of CaF features, at 25.6 eV and 27.9 eV, respectively. Thus there is a 2.3 eV difference in Ca 3p binding

***X-ray photoelectron spectroscopy (XPS) is also referred to as electron spectroscopy for chemical analysis (ESCA). In general both XPS and ESCA include the use of EUV, soft x-ray, and x-ray radiation.

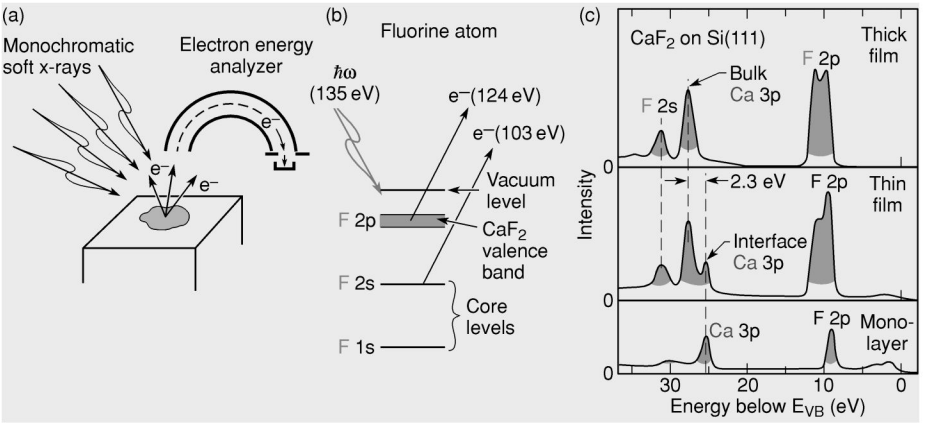

FIGURE 9.39 (see Colorplate XIX). Photoelectron spectroscopy is used to study calcium fluoride bonding to a silicon(111) substrate. The measured electron energy spectrum is shown for a monolayer of CaF_2 on Si(111), for a thin film of about 1.1 nm thickness, and for a relatively thick film of about 5 nm. (Courtesy of M. Olmsted,[107] U. Washington.)

energy for the surface and bulk dominated environments. A core level fluorine 2s feature is also clearly seen. In (c) both the fluorine 2p and calcium 3p features reflect a fully developed bulk CaF_2 signature, despite a thickness of only about 5 nm.

The shift for Ca 3p binding reflects the difference between Ca–Si bonding in the monolayer case and the fluorine dominated 3p orbitals in bulk CaF_2. In the latter, the Ca atom, which normally has two electrons in the $4s^2$ orbital, is surrounded by eight strongly electronegative fluorine atoms that draw away the two outer electrons, thus increasing the binding energy of the remaining 3p electrons. In the interface dominated case (a), the role of fluorine is diminished in favor of Ca–Si bonding, in which the calcium retains a larger fraction of the shared electrons than in the bulk, resulting in the lower binding energies observed.[107]

From these and further studies[108–110] the authors have used photoelectron spectroscopy to learn a great deal about interface formation and thin film growth in this model system. For our purposes in this chapter it demonstrates the utility of photoemission as a tool for the identification of elemental constituents and their chemical bonding under differing circumstances. Our interest now shifts to the extension of these techniques to photoemission microscopy, or *spectromicroscopy*, using zone plate optics to focus the incident radiation to sub-100-nm spot sizes.

The first use of zone plate focusing for spatially resolved photoemission was that of Ade, using the Stony Brook scanning microscopy beamline at Brookhaven.[111, 112] As illustrated in Figure 9.40, the sample consisted of aluminum and silicon dioxide strips on a Si substrate. For the data shown, a 690 eV undulator radiation was focused to a sub-micron spot size with an elliptically shaped zone plate that compensated for astigmatism in the beamline. Photoelectrons were collected and energy resolved with a cylindrical mirror analyzer (CMA) as the sample was raster scanned past the focal spot. In experiments in which the electron spectrometer was optimized for detection of selected characteristic energies, two-dimensional images, as shown in Figure 9.40, were obtained. Bright images (high photoelectron current) were obtained for Al 2p (575 eV kinetic energy), Si 2p (546 eV kinetic energy), and oxide shifted Si 2p (542 eV kinetic energy) photoelectrons. These kinetic energies are somewhat different than the values predicted by Eq. (9.53), due to issues involving localized work functions and surface preparation. The strong photoelectron signals (yellow regions in Figure 9.40) correlate with the respective regions of the sample, demonstrating spatially resolved elemental (Al, Si)

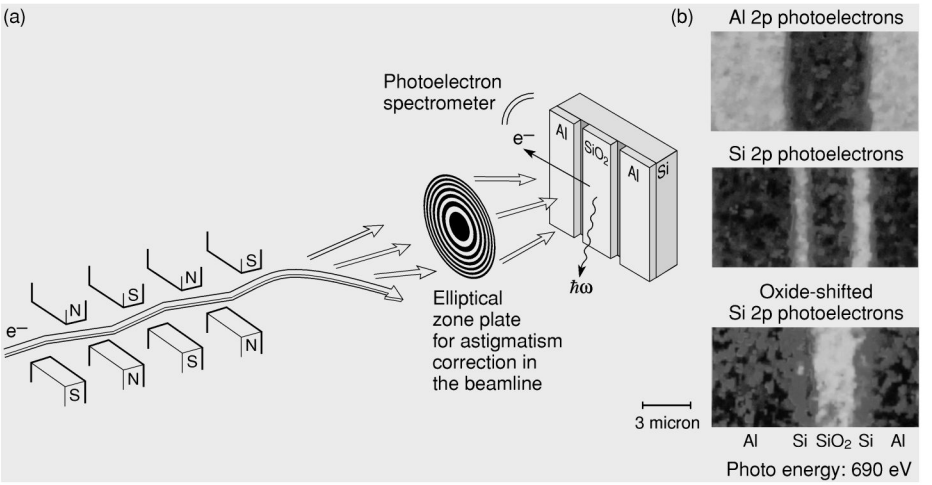

FIGURE 9.40 (see Colorplate XX). Spatially resolved photoemission from a composite Al–Si–SiO_2 sample illuminated with zone plate focused undulator radiation at Brookhaven National Laboratory. The incident photon energy is 690 eV, and the electron spectrometer passband is set for kinetic energies appropriate to the various binding energies of interest. (Courtesy of H. Ade et al.,[111, 112] SUNY Stony Brook and North Carolina State University.)

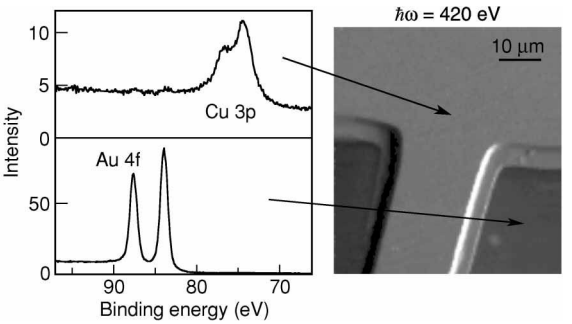

FIGURE 9.41 (see Colorplate XXI). Spatially resolved scanning photoemission image of a 100 mesh Cu grid on a gold foil, with localized spectra from Cu and gold regions. The incident photon energy is 420 eV. The image contrast is primarily due to the Cu 3p core-level intensity, but the shadows and enhancements are due to topographic effects of imaging with a small (~0.2 μm) beam spot. (From T. Warwick, J. Denlinger, E. Rotenberg, and colleagues,[113, 114] Lawrence Berkeley National Laboratory.)

and chemical (Si, SiO_2) analysis. The spatial resolution in these pioneering studies was about 0.3 to 0.5 μm.

A further example of spatially resolved photoemission, showing spectrally well-resolved gold 4f and Cu 3p electron energy spectra, obtained with a hemispherical electron analyzer and the zone plate Scanning Photoemmission Microscope (SPEM) at the ALS, is shown in Figure 9.41 for a copper grid on a gold foil.[113, 114] In the gold region well-defined Au 4f features are identified, while in the copper region a well-identified Cu 3p spectral signal is observed. The image shown in Figure 9.41 was obtained at 420 eV photon energy, with the photoelectron analyzer passband set to a 12 eV window around the Au 4g peaks, giving the gold region a bright appearance (high current) in the scanned image. The spatial and relative spectral resolutions for this particular image are approximately 0.2 μm and 8×10^3, respectively.

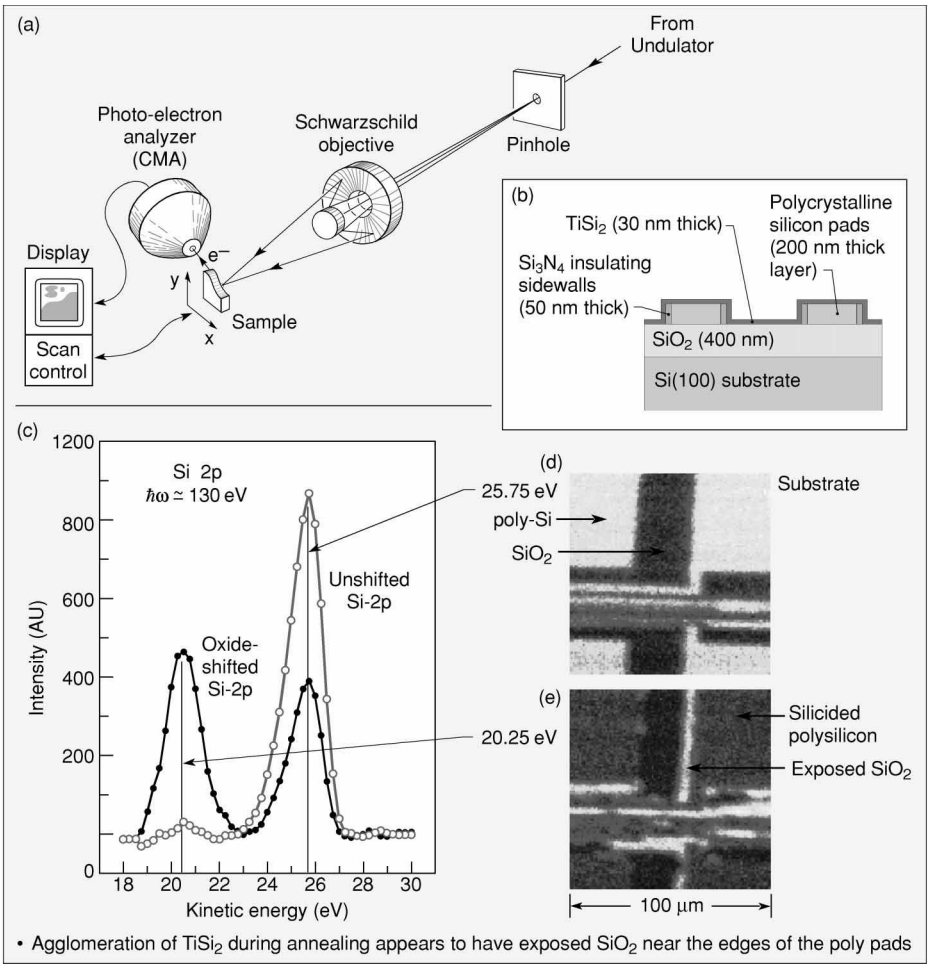

FIGURE 9.42 (see Colorplate XXII). Photoemission spectromicroscopy with multilayer coated Schwarzschild optics is illustrated in (a) and applied to a structure shown in (b). Photoelectron spectra are illustrated in (c) for two regions of an SRAM chip, one region where the silicon substrate is bare, and one region of silicon dioxide. In both cases Si 2p photoelectrons are detected during irradiation by 130 eV photons. The images in (d) and (e) are obtained at fixed electron energies corresponding to the unshifted (d) and oxide shifted (e) 2p states. The bright region (high photoelectron current) in (e) indicates an exposed region of SiO_2, initially covered with titanium silicide ($TiSi_2$). It appears that during the annealing process titanium silicide, initially covering a polysilicon pad, has agglomerated, leaving a region of SiO_2 exposed. (Courtesy of S. Singh and F. Cerrina, University of Wisconsin–Madison.[118])

Although somewhat out of place in this chapter, photoemission microscopy with multilayer coated optics, previously described in Chapter 4, provides vary similar capabilities to those with zone plates as described in the previous paragraph. The primary differences are that the multilayer coated optics are coated for specific photon energies, and thus not easily tuned. Furthermore, they are limited to photon energies below about 200 eV, where reasonably high mirror reflectivities are presently available (see Chapter 4). However, the multilayer based Schwarzschild photoelectron microscope, shown in Figure 9.42(a), offers a considerably larger working distance, which can be useful in photoemission studies.

An example of electron spectra obtained with the MAXIMUM photoemission microscope, work of Cerrina and his colleagues at the University of Wisconsin–Madison,[115–119] is also shown in Figure 9.42. For those experiments at 130 eV photon energy, the Schwarzschild optics were coated with a Ru–B_4C multilayer. The purpose of these particular experiments was to study the technologically important application of titanium silicide ($TiSi_2$), a low resistivity interconnect material used in semiconductor integrated circuits. Use of the $TiSi_2$ involves an annealing process, to form a stable low resistivity state. There is evidence that during annealing, migration and agglomeration of the titanium silicide occurs. The data in Figure 9.39 demonstrates the value of spectromicroscopy for the study of heterostructure surface chemistry on a 100 nm spatial scale.

9.10 ZONE PLATE FABRICATION

The fabrication of high resolution zone plates is an outgrowth of techniques developed for the semiconductor industry, which has for decades been involved in the manufacture of integrated circuit (IC) electronic devices based on complex material structures with micron and sub-micron features.[120–123] For zone plates, the fabrication involves writing a desired pattern in some recording medium, typically PMMA,[†††] with an electron beam,[124–126] typically of 50 keV to 100 keV electron energy, perhaps 50 nm to 10 nm in diameter, as indicated in Figure 9.43. The electron beam (e-beam) writing path is recorded by broken molecular bonds in the recording material (*resist*). The beam path is defined by deflection electrodes controlled by an electronic pattern generator, with beam blanking as necessary to move from one part of the desired pattern to another. The regions of broken bonds are then removed by a chemical *development* process, leaving a clean *mold* pattern as illustrated in Figure 9.44(b). This pattern is then transferred to some other, more appropriate material, such as gold, nickel, or germanium, which has the desired EUV/soft x-ray absorption and phase shift properties at the intended wavelength of use.

The procedure begins with a multilevel structure such as shown in Figure 9.44(a). Here a silicon wafer, with a back-etched window, has been coated with a thin film of approximately 100 nm of silicon nitride (stoichiometrically Si_3N_4) that will eventually serve as the zone plate lens's support membrane. A gold plating base about 5 nm thick, and a chromium ($\simeq$5 nm) adhesion layer, are evaporated onto the silicon nitride. An appropriate thickness of PMMA is then spun across this to form the recording medium for electron beam writing. The PMMA might typically be 100 nm or more thick, depending on the desired zone plate thickness and limitations of the pattern transfer process with regard to achievable aspect ratio of thickness to outer zone width ($\Delta t/\Delta r$). Fabrication of the desired zone plate is then accomplished by electron beam writing of the desired pattern in the top layer PMMA. After removal of resist in the e-beam-exposed areas, the thin gold plating base is exposed, and cleaned further as necessary. Gold, nickel, or some other material is then electroplated onto the base within the PMMA mold. The remaining PMMA is then removed with acetone, leaving the desired gold zone plate pattern on a thin but rather strong silicon nitride membrane, across the open window of the supporting silicon wafer. In some cases the remaining gold plating base (in the "open" zones) is removed by reactive ion etching (RIE) to improve the photon transmission and thus optical efficiency of the resultant zone plate lens. Indeed, zone plates have been made free-standing by including radial support struts written into the original pattern.[121]

[†††]The chemical name is polymethyl methacrylate.

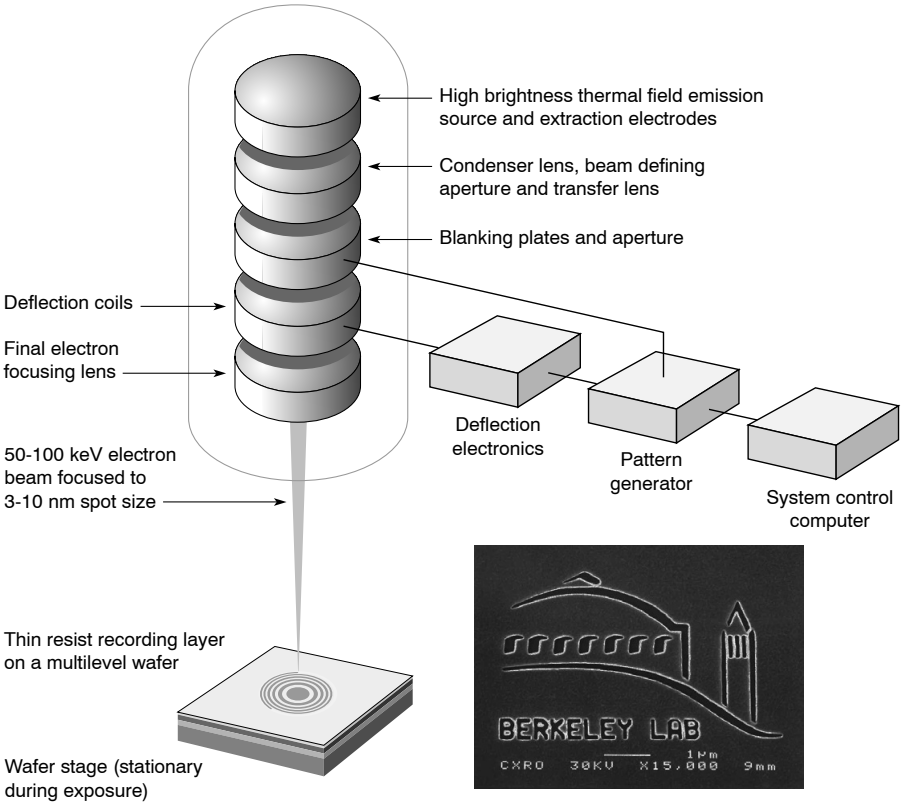

FIGURE 9.43. Electron beam patterning by writing with a small high energy beam in a molecular resist recording material. Deflection electrodes are used to steer the beam across the recording material, shown as PMMA here, as directed by an electronic pattern generator. Beam blanking permits movement without writing from zone to zone. The inset is the Lawrence Berkeley National Laboratory logo, showing the Advanced Light Source (ALS) "on the Hill" above the University of California at Berkeley campus, represented by the Campanile. The lines used to form the letters in "BERKELEY LAB" are each 90 nm wide. (Courtesy of E. Anderson, LBNL.)

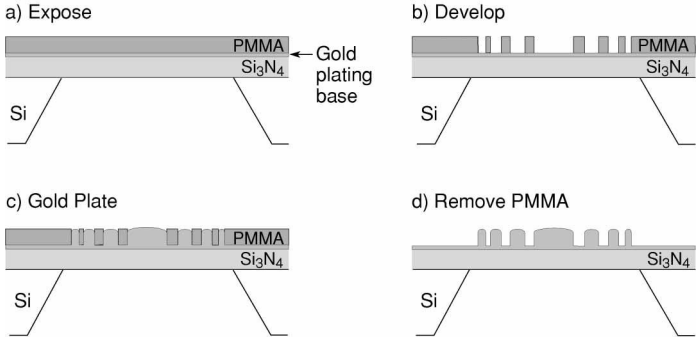

FIGURE 9.44 (see Colorplate XXIII). Nanofabrication of a gold zone plate involves a multilevel structure for recording a pattern in PMMA through (a) spatially patterned electron beam exposure, (b) development into a PMMA mold, (c) gold plating into the mold, and (d) removal of the remaining PMMA to leave a gold zone plate lens on a thin silicon nitride membrane, over an etched window in the silicon wafer substrate.

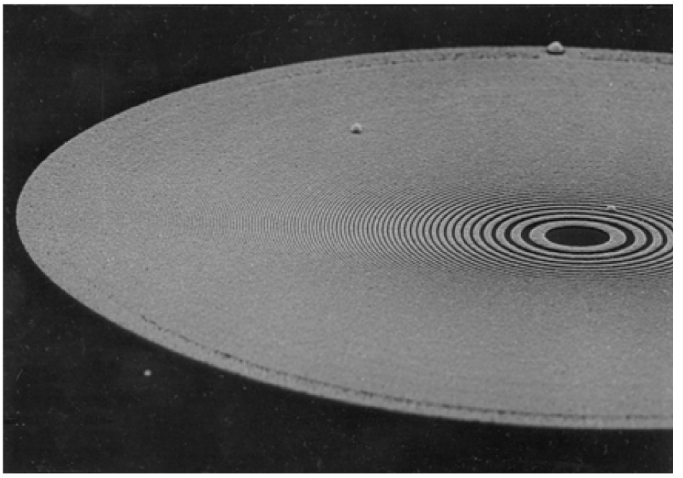

FIGURE 9.45. An SEM micrograph of a 100 nm thick gold zone plate with a 30 nm outer zone width and 300 zones. This zone plate was used to form the image in Figure 9.15. (Courtesy of E. Anderson, LBNL, and D. Kern,[126] IBM.)

For state of the art zone plates with minimal outer zone widths (Δr) of 20–40 nm, the aspect ratio ($\Delta t/\Delta r$) in the outer region is typically limited to 3 : 1 or 4 : 1. With less challenging outer zone widths the final structures can have higher aspect ratios. Figure 9.45 shows a 100 nm thick gold zone plate[126] with 30 nm outer zone width and $N = 300$ zones, intended to be relatively opaque for photon energies of 500 eV or less (2.4 nm wavelength or longer). At a wavelength of 2.4 nm this lens has a focal length of 0.45 mm, a diameter of 36 μm, and a numerical aperture of 0.04 [see Eqs. (9.13–9.15)]. A radial test pattern imaged with this zone plate in the Göttingen microscope at BESSY was shown previously in Figure 9.15. Features as small as 30 nm (half a period; recall Figure 9.13) are evident at the lower limit of contrast.

A nickel zone plate of 50 nm outer zone width, fabricated by the same procedures,[126] was shown earlier in Figure 9.1. It offers a higher efficiency at photon energies just below the L-absorption edge at 853 eV. For these zone plate lenses to achieve high spatial resolution and high efficiency, it is necessary that the zone pattern be written and transferred with high fidelity, of order $\Delta r/4$, to achieve the desired interference effects. Thus there is a substantial need for nanometer electron beam placement accuracy in the writing process, which translates to demanding diagnostic techniques and to feedback within the writing instrument, particularly in the vicinity of the beam–resist interaction region. For the Nanowriter[125] facility in Berkeley this includes transmitted, backscattered, and secondary electrons. The Nanowriter specification is centered on a 100 kV, 3 nm to 5 nm electron beam size, with 3 nm beam placement accuracy over a 65 μm wide field, and field stretching to 20 nm over a 1 cm field with the aid of $\lambda/1024$ visible light translation stage interferometry. Advances in nanofabrication, including the ability to successfully transfer ever smaller outer zone width patterns, with acceptable thickness (aspect ratio) and materials choice, will continue to pace progress in the fabrication of improved zone plates.[125–129] The eventual achievement of efficiency improving the zonal substructure (e.g., three steps per period) will further improve their utility.

Topics not discussed here but which may be of interest to the reader are the fabrication of so-called "jelly roll," or sputtered–sliced, zone plates[130] and of Bragg–Fresnel zone

plates.[131, 132] The sputtered zone plates are made using multilayer fabrication techniques, in this case coating a rotating wire with alternate materials. The idea here is to achieve very narrow outer zones with high aspect ratio. The Bragg–Fresnel zone plates combine diffraction of hard x-rays by a crystal with an overlaid zone plate pattern and thus are primarily designed for use with multi-keV x-rays. It is also possible to use a multilayer coated mirror with an overlaid zone plate pattern at somewhat lower photon energy. Both are described in the literature.[131, 132]

REFERENCES

1. G. Schmahl and D. Rudolph, Editors, *X-Ray Microscopy* (Springer-Verlag, Berlin, 1984).
2. S. Sayre, M. Howells, J. Kirz, and H. Rarback, Editors, *X-Ray Microscopy II* (Springer-Verlag, Berlin, 1988).
3. A.G. Michette, G.R. Morrison, and C.J. Buckley, Editors, *X-Ray Microscopy III* (Springer-Verlag, Berlin, 1992).
4. V.V. Aristov and A.I. Erko, Editors, *X-Ray Microscopy IV* (Bogorodskii Press, Chernogolovka, Russia, 1994).
5. J. Thieme, G. Schmahl, D. Rudolph, and E. Umbach, Editors, *X-Ray Microscopy and Spectromicroscopy* (Springer-Varlag, Heidelberg, 1998).
6. Lord Rayleigh, "Wave Theory," p. 429 in *Encylopaedia Brittanica*, Ninth Edition, Vol. 24, (1988); Rayleigh's first entry in his notebook, describing the first successful demonstration, is dated 11 April 1871.
7. J.L. Soret, "Concerning Diffraction by Circular Gratings," *Ann. Phys. Chem. 156*, 99 (1875).
8. R.W. Woods, *Physical Optics* (Macmillian, New York, 1911; Opt. Soc. Amer., Washington, DC, 1988). See comments regarding phase zone plates on pp. 37–39.
9. A.V. Baez, "A Study in Diffraction Microscopy with Special Reference to X-Rays," *J. Opt. Soc. Amer. 42*, 756 (1952).
10. G. Schmahl and D. Rudolph, "High Power Zone Plates as Image Forming Systems for Soft X-Rays" (in German), *Optik 29*, 577 (1969); B. Nieman, D. Rudolph, and G. Schmahl, "Soft X-Ray Imaging Zone Plates with Large Zone Numbers for Microscopic and Spectroscopic Applications," *Opt. Commun. 12*, 160 (1974).
11. J. Kirz, "Phase Zone Plates for X-Rays and the Extreme UV," *J. Opt. Soc. Amer. 64*, 301 (1974).
12. A.G. Michette, *Optical Systems for Soft X-Rays* (Plenum, London, 1986),
13. E. Hecht, *Optics* (Addison-Wesley, Reading, MA, 1998), Third Edition. Zone plates are discussed in Section 10.3; Section 6.3, p. 487, considers geometrical aberrations.
14. M. Born and E. Wolf, *Principles of Optics* (Cambridge Univ. Press, New York, 1999), Seventh Edition. Diffraction is discussed in Chapter 8. See p. 453 for the diffraction efficiencies of a transmission grating of arbitrary line to width ratio.
15. G.R. Morrison, "Diffractive X-Ray Optics," Chapter 8 in *X-Ray Science and Technology* (Inst. Phys., Bristol, 1993). Grating efficiencies are discussed in Section 8.2.2, p. 313.
16. M. Hettrick, J. Underwood, P. Batson, and M. Eckart, "Resolving Power of 35,000 in the Extreme Ultraviolet Employing a Grazing Incidence Spectrometer," *Appl. Opt. 27*, 200 (15 January 1988), and references therein.
17. J. Underwood, E. Gullikson, M. Koike, P. Batson, P. Denham, K. Franck, R. Tackaberry, and W. Steele, "Calibration and Standards Beamline 6.3.2 at the Advanced Light Source," *Rev. Sci. Instrum. 67* (9), 1, September 1996. Available on CD-ROM.
18. W.B. Peatman, *Gratings, Mirrors and Slits: Beamline Design for Synchrotron Radiation Sources* (Gordon and Breach, Amsterdam, 1997).
19. J.A.R. Samson and D.L. Ederer, Editors, *Methods of Vacuum Ultraviolet Spectroscopy*, Vol. I, II (Academic Press, San Diego, CA, 1998). In particular see the chapter "Diffraction Gratings" by T.

Namioka; the chapter on "Normal Incidence Monochromators and Spectrometers" by M. Koike; the chapter on "Grazing-Incidence Monochromators for Third Generation Synchrotron Radiation Sources" by H.A Padmore, M.R. Howells, and W.R. McKinney; and the chapter on "Spectrographs and Monochromators Using Varied Line Spacing Grating" by J.H. Underwood.
20. E.G. Loewen and E. Popov, *Diffraction Gratings and Applications* (Marcel Dekker, New York, 1997).
21. J.W. Goodman, *Introduction to Fourier Optics* (McGraw-Hill, New York, 1996), Second Edition, p. 124.
22. E. Anderson and D. Kern, "Nanofabrication of Zone Plates for X-Ray Microscopy," p. 75 in Ref. 3.
23. W. Meyer-Ilse, P. Guttmann, J. Thieme, D. Rudolph, G. Schmahl, E. Anderson, P. Batson, D. Attwood, N. Iskander, and D. Kern, "Experimental Characterization of Zone Plates for High Resolution X-Ray Microscopy," p. 284 in Ref. 3.
24. C. Jacobsen, S. Williams, E. Anderson, M.T. Browne, C.J. Buckley, D. Kern, J. Kirz, M. Rivers, and X. Zhang, "Diffraction-Limited Imaging in a Scanning Transmission X-Ray Microscope," *Opt. Commun. 86*, 351 (1991).
25. C. Jacobsen, J. Kirz, and S. Williams, "Resolution in Soft X-Ray Microscopes," *Ultramicroscopy 47*, 55 (1992).
26. G.R. Morrison, Ref. 15. A general discussion of x-ray zone plate efficiencies is given in Section 8.6.3, p. 338.
27. B.L. Henke, E.M. Gullikson, and J.C. Davis, *Atomic and Nucl. Data Tables 54*, 181–342 (1993).
28. R. Tatchyn, "Optimum Zone Plate Theory and Design," p. 40 in Ref. 1.
29. Y.V. Kopylov, A.V. Popov, and A.V. Vinogradov, "Application of the Parabolic Wave Equation to X-Ray Diffraction Optics," *Opt. Commun. 118*, 619 (1995).
30. V.E. Levashov and A.V. Vinogradov, "Analytical Theory of Zone Plate Efficiency," *Phys. Rev. E 49*, 5797 (1994).
31. J. Maser and G. Schmahl, "Coupled Wave Description of the Diffraction by Zone Plates with High Aspect Ratios," *Opt. Commun. 89*, 355 (1992).
32. G. Schneider, "Zone Plates with High Efficiency in High Orders of Diffraction Described by Dynamical Theory," *Appl. Phys. Lett. 71*, 2242 (1997).
33. G. Schneider and J. Maser, "Zone Plates as Imaging Optics in High Diffraction Orders Described by Coupled Wave Theory," p. IV-71 in Ref. 5.
34. M. Born and E. Wolf, Ref. 14. The classical treatise on the subject of diffraction. In particular see Chapter 8 and the historical reference therein.
35. J.W. Goodman, Ref. 21. See Chapter 3 for a clear and concise development from Maxwell's equations to the mathematical expressions of Kirchhoff and Sommerfield. Note in particular the development of Eq. (41) and comparison of the Kirchhoff and Rayleigh–Sommerfield theories in Sections 3.6 and 3.7.
36. J.D. Jackson, *Classical Electrodynamics* (Wiley, New York, 1998), Third Edition. Chapter 10 describes the extension to a vectorial diffraction theory.
37. E. Hecht, Ref. 13. An intermediate level text with many helpful illustrations and clear text. See Chapter 10 on diffraction.
38. G. Fowles, *Introduction to Modern Optics* (Dover, New York, 1975), Second Edition. Available in paperback. A compact book with good diagrams and good explanation. See Chapter 5 regarding diffraction.
39. A. Sommerfield, *Optics* (Academic Press, New York, 1964), of Lectures on Theoretical Physics, Vol. IV. See Chapter V on the theory of diffraction, particularly Sections 37 and 38 regarding the rigorous solutions to the problem of diffraction by a straightedge.
40. G.N. Watson, *A Treatise on the Theory of Bessel Functions* (Cambridge Univ. Press, 1944), p. 20.
41. I.S. Gradshteyn and I.M. Ryzhik, *Table of Integrals, Series and Products* (Academic Press, New York, 1994), Fifth Edition, Section 8.411, No. 1, p. 961.

42. F.W. Oliver, "Bessel Functions on Integral Order," p. 360, No. 9.1.21, in *Handbook of Mathematical Functions* (Dover, NY, 1972), M. Abramowitz and I. Stegun, Editors.
43. E. Kreyszig, *Advanced Engineering Mathematics* (Wiley, New York, 1992), Seventh Edition, p. 834. This book has a very readable section on Bessel functions and their applications.
44. I.S. Gradshteyn and I.M. Ryzhik, Ref. 41, p. 707, Section 6.561, No. 5.
45. S. Wolfram, *Mathematica* (Addison-Wesley, Redwood City, CA, 1991), Second Edition. This describes the commercial software program Mathematica, available through Wolfram Research, Inc.
46. K. Goldberg, E. Tejnil, and J. Bokor, "A 3-D Numerical Study of Pinhole Diffraction to Predict the Accuracy of EUV Point Diffraction Interferometry," p. 137 in *Extreme Ultraviolet Lithography* (Opt. Soc. Amer., Washington, DC, 1996), G. Kubiak and D. Kania, Editors.
47. C. Cerjan, "Scalar Wave Diffraction from a Circular Aperture," p. 142 in *Extreme Ultraviolet Lithography* (Opt. Soc. Amer., Washington, DC, 1994), F. Zernike and D. Attwood, Editors.
48. A.G. Michette, Ref. 12, p. 175.
49. M. Born and E. Wolf, Ref. 14, Sections 10.5.2 and 8.6.2.
50. L. Jochum and W. Meyer-Ilse, "Partially Coherent Image Formation with X-Ray Microscopes," *Appl. Opt. 34*, 4944 (1995).
51. J. Heck, W. Meyer-Ilse, and D. Attwood, "Resolution Determination in X-Ray Microscopy," *J. X-Ray Sci. Technol. 8*, 95 (1998); J. Heck, "Resolution Determination in X-Ray Microscopy: An Analysis of the Effects of Partial Coherence and Illumination Spectrum," M.S. thesis, Graduate Group in Applied Science and Technology, University of California, Berkeley (1997).
52. M. Born and E. Wolf, Ref. 14, p. 441, Section 8.8.2.
53. N. Iskander (unpublished), using the computer code ZCALC written by E. Anderson.
54. B. Niemann, D. Rudolph, and G. Schmahl, "X-Ray Microscopy with Synchrotron Radiation," *Appl. Opt. 15*, 1883 (1976).
55. G. Schmahl, D. Rudolph, B. Niemann, and O. Christ, "Zone Plate X-Ray Microscopy," *Q. Rev. Biophys. 13*, 297 (1980).
56. D. Rudolph, B. Niemann, G. Schmahl, and O. Christ, "The Göttingen X-Ray Microscope and X-Ray Microscopy Experiments at the BESSY Storage Ring," p. 192 in Ref. 1.
57. G. Schmahl, D. Rudolph, B. Niemann, P. Guttmann, M. Robert-Nicoud, J. Thieme, G. Schneider, C. David, M. Diehl, and T. Wilhein, "Natural Imaging of Biological Specimens with X-Ray Microscopes," p. 538 in *Synchrotron Radiation in the Biosciences* (Oxford Univ. Press, 1994), B. Chance, J. Deisenhofer, T. Sasaki, et al., Editors.
58. F. Zernike, "How I Discovered Phase Contrast," Nobel Lecture, Stockholm, December 1953, in *Science 121*, 345 (1955); also "Phase Contrast, A New Method for the Microscopic Observation of Transparent Objects, Part I," *Physica 9*, 686 (1942).
59. G. Schmahl, P. Guttmann, G. Schneider, B. Niemann, C. David, T. Wilhein, J. Thieme, and D. Rudolph, "Phase Contrast Studies of Hydrated Specimens with the X-Ray Microscope at BESSY," p. 196 in Ref. 4.
60. G. Schneider, B. Niemann, P. Guttmann, D. Rudolph, and G. Schmahl, "Cryo X-Ray Microscopy," *Synchr. Rad. News 8*, 19 (1995).
61. G. Schneider and B. Niemann, "Cryo X-Ray Microscopy Experiments with the X-Ray Microscope at BESSY," p. I-25 in Ref. 5.
62. G. Schneider, G. Schmahl, T. Schliebe, M. Peuker, and P. Guttmann, "Cryo X-Ray Microscopy in Amplitude and Phase Contrast," p. I-111 in Ref. 5.
63. B. McEwen, K. Downing, and R. Glaeser, "The Relevance of Dose Fractionation in Tomography of Radiation Sensitive Specimens," *Ultramicroscopy 60*, 357 (1995); W.S. Haddad, I. McNulty, J.E. Trebes, E.H. Anderson, R.A. Levesque, and L. Yang, "Ultrahigh Resolution X-ray Tomography," Science *266*, 1213 (1994); Y. Wang, C. Jacobsen, J. Maser, and A. Osanna, "Soft X-ray Microscopy with a Cryo STXM:II. Tomography," J. Microscopy (to be published); J. Lehr, "3D X-ray Microscopy: Tomographic Imaging of Mineral Sheaths of Bacteria with the Göttingen X-ray Microscope at BESSY" Optik *104*, 166 (1997).
64. H. Rarback, D. Shu, S.C. Feng, H. Ade, J. Kirz, I. McNulty, D.P. Kern, T.H.P. Chang, Y.

Vladimirsky, N. Iskander, D. Attwood, K. McQuaid, and S. Rothman, "Scanning X-Ray Microscope with 75-nm Resolution," *Rev. Sci. Instrum. 59*, 52 (1988).

65. J. Kirz, C. Jacobsen, S. Lindaas, S. Williams, X. Zhang, E. Anderson, and M. Howells, "Soft X-Ray Microscopy at the National Synchrotron Light Source," p. 563 in *Synchrotron Radiation in the Biosciences* (Oxford Univ. Press, 1994), B. Chance, J. Deisenhofer, T. Sasaki, et al., Editors.
66. J. Kirz, C. Jacobsen, and M. Howells, "Soft X-Ray Microscopes and Their Biological Applications," *Q. Rev. Biophys. 28*, 1 (1995).
67. B. Alberts, D. Bray, J. Lewis. M. Raaf, K. Roberts, and J. Watson, *Molecular Biology of the Cell* (Garland, New York, 1989), Second Edition.
68. N. Cambell, *Biology* (Benjamin/Cummings, Redwood City, CA, 1990), Second Edition.
69. J. Darnell, H. Lodish, and D. Baltimore, *Molecular Cell Biology* (Scientific American/Freeman, New York, 1990), Second Edition.
70. L. Stryer, *Biochemistry* (Freeman, New York, 1981), Second Edition.
71. W. Purves, G. Orians, and H.C. Heller, *Life: The Science of Biology* (Freeman, New York, 1992), Third Edition.
72. An examination of the illustrations in Refs. 67–71 shows clearly the impact of scanning electron microscopes (SEMs) on the understanding of sub-cellular structures.
73. J. Helliwell, *Macromolecular Crystallography with Synchrotron Radiation* (Cambridge Univ. Press, Cambridge, 1992); C. Carter and R. Sweet, editors, *Methods in Enzymology* (Academic Press, New York, 1997), p. 276.
74. Structural details of complex biochemical molecules, obtained using x-ray diffraction techniques, are presented in most issues of the magazines *Science, Nature,* and *Nature Structural Biology*. As specific examples see P.D. Kwong, R. Wyatt, J. Robinson, R.W. Sweet, J. Sodorski, and W.A. Hendrickson, "Structure of an HIV gp 120 Envolope Glycoprotein in Complex with the CD4 Receptor and a Neutralizing Human Antibody," *Nature 393*, 648 (18 June 1998); D. Xia, C.-A. Yu, H. Kim, J.-Z. Xia, A.M. Kachurin, L. Zhang, L. Yu, and J. Deisenhofer, "Crystal Structure of the Cytochrome bc_1 Complex from Bovine Heart Mitochondria," *Science 227*, 60 (1997); B.L. Golden, A.R. Goodling, E.R. Podell, and T.R. Cech, "A Preorganized Active Site in the Crystal Structure of the Tetrahymena Ribozyme," *Science 282*, 259 (9 October 1998).
75. See articles in Section 4 of *Synchrotron Radiation in the Biosciences* (Oxford University Press, 1994), B. Chance, J. Deisenhofer, T. Sasaki, et al., Editors; also see future meetings of the International Conference on Biology and Synchrotron Radiation, next to be held in Sao Paulo, Brazil, in the year 2001.
76. D. Sayre, J. Kirz, R. Feder, D.M. Kim, and E. Spiller, "Potential Operating Region for Ultrasoft X-Ray Microscopy of Biological Specimens," *Science 196*, 1339 (1977), and "Transmission Microscopy of Unmodified Biological Materials: Comparative Radiation Dosages with Electrons and Ultrasoft Photons," *Ultramicroscopy 2*, 337 (1977).
77. J. Gray. D. Pinkel, and J. Brown, "Fluorescence In Situ Hybridization in Cancer and Radiation Biology," *Rad. Res. 137*, 275 (1994); H. Weier, M. Wang, J. Mullikin, Y. Zhu, J.-F. Cheng, K. Greulich, A. Bensimon, and J. Gray, "Quantitative DNA Fiber Mapping," *Human Molec. Genet. 4*, 1903 (1995); S. Maiti, J. Shear. R. Williams, W. Zipfel, and W. Webb, "Measuring Serotonin Distribution in Live Cells with Three-Photon Excitation," *Science 275*, 530 (24 January 1997).
78. J. Maser, C. Jacobsen, J. Kirz, A. Osanna, S. Spector, S. Wang, and J. Warnking, "Development of a Cryo Scanning Transmission X-Ray Microscope at the NSLS, p. I-35 in Ref. 5.
79. W. Meyer-Ilse, H. Medecki, J.T. Brown, J.M. Heck, E.H. Anderson, A. Stead, T. Ford, R. Balhorn, C. Peterson, C. Magowan, and D.T. Attwood, "X-Ray Microscopy in Berkeley," p. I-1 in Ref. 5.
80. C. Magowan, J.T. Brown, J. Liang, J. Heck, R. Coppel, N. Mohandas, and W. Meyer-Ilse, "Intracellular Structures of Normal and Aberrant Plasmodium Falciparum Malaria Parasites Imaged by Soft X-Ray Microscopy," *Proc. Nat. Acad. Sci. U.S.A. 94*, 6222 (1997).
81. N.D. Kristof, "Malaria Makes a Comeback, and Is More Deadly Than Ever," *New York Times CXLVI* (January 8, 1997); "Two Cheers for the Multilateral Malaria Initiative," Editorial, *Nature*

388, 211 (17 July 1997); D. Butler, "Malaria Meeting Charts Rocky Path Ahead," *Nature 388*, 219 (17 July 1997); "The Mosquito at Your Door: Mankind is Losing the War on Malaria," *The Economist*, 23 August 1997, p. 12.

82. W. Koch, "Germs Flow from Water," *San Francisco Examiner*, 1 December 1996, p. 12.
83. D. Cuff, "Tiny Parasite Has Water Districts, Cattle Ranchers Worried," *San Ramon Valley Times* (CA), 6 January 1997, p. 1.
84. C. Peterson, C. Magowan, J. Brown, and W. Meyer-Ilse (unpublished). Images obtained with the High Resolution Soft X-Ray Microscope XM-1 at the ALS, as described in Ref. 65.
85. R. Balhorn, R.E. Braun, B. Breed, J.T. Brown, E. Evenson, J.M. Heck, J. Kirz, I. McNulty, W. Meyer-Ilse, and X. Zhang "Applications of X-Ray Microscopy to the Analysis of Sperm Chromatin," p. II-29 in Ref. 5; R. Balhorn, M. Corzett, M. Allen, C. Lee, T. Barbee, J. Koch, B. MacGowen, D. Mathews, S. Mrowka, J. Trebes, I. McNulty, L. Da Silva, J. Gray. E. Anderson, D. Kern, and D. Attwood, "Application of X-rays to the Analysis of DNA Packing in Mammalian Sperm, p. 374 in *Soft X-Ray Microscopy* (SPIE, Bellingham, WA, 1992), C. Jacobsen and J. Trebes, Editors.
86. B.W. Loo, W. Meyer-Ilse, and S.S. Rothman, "Automatic Acquisition and Assembly of Arbitrarily Large-Field, High Resolution Image. Montages in a Digital X-ray Microscope (submitted for publication).
87. W. Meyer-Ilse, D. Hamamoto, S. Lelièvre, A. Nair, and C. Larabell, "High Resolution Antigen Localization using Soft X-Ray Microscopy," (submitted for publication).
88. X. Zhang, R. Balhorn, J. Mazrimas, and J. Kirz, "Mapping and Measuring DNA to Protein Ratios in Mammalian Sperm Head by XANES Imaging," *J. Struct. Biol. 116*, 335 (1996); X. Zhang, R. Balhorn, C. Jacobsen, J. Kirz, and S. Williams, "Mapping DNA and Protein in Biological Samples Using the Scanning Transmission X-Ray Microscope," in *Proceedings of the 52nd* Annual Meeting of the Microscopy Society of America (San Francisco Press, CA, 1984), G. Bailey and A. Garratt-Reed, Editors.
89. B. Loo, S. Williams, S. Meizel, and S. Rothman, "X-Ray Stereomicroscopy: High Resolution 3-D Imaging of Human Spermatozoa in Aqueous Suspension with Natural Contrast," *J. Microscopy* (Blackwell Sci. Ltd.) *166*, RP5 (1992).
90. C. Jacobsen, S. Lindaas, S. Williams, and X. Zhang, "Scanning Luminescence X-Ray Microscopy: Imaging Fluorescence Dyes at Sub-optical Resolution," *J. Microscopy 172*, 121 (1993).
91. G.R. Morrison and M.T. Browne, "Dark-Field Imaging with the Scanning Transmission X-Ray Microscope," *Rev. Sci. Instrum. 63*, 611 (1992).
92. H.N. Chapman, J. Fu, C. Jacobsen, and S. Williams, "Dark-Field X-Ray Microscopy of Immunogold-Labeled Cells," *J. Microscopy Soc. Amer. 2*, 53 (1996).
93. H.N. Chapman, J. Jacobsen, and S. Williams, "A Characterization of Dark-Field Imaging of Colloidal Gold Labels in a Scanning Transmission Microscope," *Ultramicroscopy 62*, 191 (1996).
94. H.N. Chapman, "Phase-Retrieval X-Ray Microscopy by Wigner-Distribution Deconvolution," *Ultramicroscopy 66*, 153 (1996).
95. A. Irtel von Brenndorff, M. Moronne, C. Larabell, P. Selvin, and W. Meyer-Ilse, "Soft X-Ray Stimulated High Resolution Luminescence Microscopy," p. 338 in Ref. 4.
96. M. Moronne, C. Larabell, P. Selvin, and A. Irtel von Brenndorff, "Development of Fluorescent Probes for X-Ray Microscopy," p. 48 in *Proceedings of the 52nd Annual Meeting of the Microscopy Society of America* (San Francisco Press, CA, 1994), G. Bailey and A. Garratt-Reed, Editors.
97. "National Technology Roadmap for Semiconductors," Semiconductor Industry Association (San Jose, CA, 1997). See Chapter 10 of this book for further discussion.
98. J. Stöhr, Y. Wu, B. Hermsmeier, M. Samant, G. Harp, S. Koranda, D. Dunham, and B. Tonner, "Element-Specific Magnetic Microscopy with Circularly Polarized X-Rays," *Science 259*, 658 (4 July 1993).
99. Y. Taur, Y.-J. Mii, D. Frank, H.-S. Wong, D. Buchanan, S. Wird, S. Rishton, G. Sai-Halaszand, and E. Nowak, "CMOS Scaling into the 21st Century: 0.1 μm and Beyond," *IBM J. Res. Develop. 39*, 245 (1995).
100. D. Eastman and F. Himpsel, "Ultraviolet Radiation – An Incisive and Versatile Tool," *Phys. Today 64*, 64 (May 1981).

101. C.S. Fadley, "Basic Concepts of X-Ray Photoelectron Spectroscopy," pp. 1–157 in *Electron Spectroscopy Theory, Techniques and Applications, Vol. II* (Pergamon, New York, 1978), C.R. Brundle and A.D. Baker, Editors; C.S. Fadley et al., "Surface, Interface, and Nanostructure Characterization with Photoelectron Diffraction and Photoelectron and X-Ray Holography," *J. Surface Anal. 3*, 334–364 (1997); C.S. Fadley and P.M. Len, "Holography with X-Rays," *Nature 380*, 27 (7 March 1996); M. Tegze and G. Faigel, "X-ray Holography with Atomic Resolution" *Nature 380*, 49 (7 March 1996); G. Faigel and M. Tegze, "X-ray Holography," Rep. Prog. Phys. (London) *62*, 355–393 (1999).
102. W. Eberhardt, Editor, *Applications of Synchrotron Radiation: High Resolution Studies of Molecules and Molecular Adsorbates on Surfaces* (Springer-Verlag, Berlin, 1995).
103. S. Hüfner, *Photoelectron Spectroscopy* (Springer-Verlag, Berlin, 1996), Second Edition.
104. G. Magaritondo, "100 Years of Photoemission," *Phys. Today 41*, 66 (1988); *Introduction to Synchrotron Radiation* (Oxford Univ. Press, New York, 1988).
105. M. Seah and W. Dench, "Quantitative Electron Spectroscopy of Surfaces: A Standard Data Base for Electron Inelastic Mean Free Paths in Solids," *Surface and Interface Anal. 1*, 2 (1979).
106. D. Penn, "Electron Mean-Free-Path Calculation Using a Model Dialectric Function," *Phys. Rev B 35*, 482 (1987).
107. M. Olmstead, R. Uhrberg, R. Bringans, and R. Bachrach, "Photoemission Study of Bonding at the CaF_2-on-Si(111) Interface," *Phys. Rev. B 35*, 7526 (15 May 1987).
108. E. Rotenberg, J. Denlinger, M. Leskovar, U. Hessinger, and M. Olmstead, "Layer by Layer Resolved Core Level Shifts in CaF_2 and SrF_2 on Si(111): Theory and Experiment," *Phys. Rev. B 50*, 11052 (1994).
109. J. Denlinger, E. Rotenberg, U. Hessinger, M. Leskovar, and M. Olmstead, "Growth Kinetics of CaF_2/Si(111) Heteroepitaxy: An X-Ray Photoelectron Diffraction Study," *Phys. Rev. B 51*, 5352 (1995).
110. E. Rotenberg, J. Denlinger, and M. Olmstead, "Altered Photoemission Satellites at CaF_2- and SrF_2-on-Si(111) Interfaces," *Phys. Rev. B 53*, 1584 (1996).
111. H. Ade, "Development of a Scanning Photoemission Microscope," Ph.D. thesis, Physics Department, SUNY, Stony Brook (1990).
112. H. Ade, C.-H. Ko, E. Johnson, and E. Anderson, "Improved Images with the Scanning Photoemission Microscope at the National Synchrotron Light Source," *Surface and Interface Anal. 19*, 17 (1992); H. Ade et al., "Images of a Microelectronic Device with the X-1 SPEM, a First Generation Scanning Photoemission Microscope at the NSLS," *J. Vac. Sci. Techn. A9*, 1902 (1991).
113. J. Denlinger, E. Rotenberg, T. Warwick, G. Visser, J. Nordgren, G.-H. Guo, P. Skytt, S. Kevan, K. McCutcheon, D. Shuh, J. Bucher, N. Edelstein, J. Tobin, and B. Tonner, "First Results from the Spectromicroscopy Beamline at the Advanced Light Source," *Rev. Sci. Instrum. 66*, 1342 (1995).
114. T. Warwick, H. Ade, S. Cerasari, J. Denlinger, K. Franck, A. Garcia, S. Hayakawa, A. Hitchcock, J. Kikuma, S. Klingler, J. Kortright, G. Morrison, M. Morrone, E. Rightor, E. Rotenberg, S. Seal, H.-J. Shin, W.F. Steele, and B.P. Tonner, "Development of Scanning X-Ray Microscopes for Materials Science Spectromicroscopy at the Advanced Light Source," *J. Synchr. Rad. 5*, 1090 (1998); J. Rothe, E.M. Kneedler, K. Pecher, B.P. Tonner, K.H. Nealson, T. Grundl, W. Meyer-Ilse, and T. Warwick, "Spectromicroscopy of Mn Distributions in Micronodules Produced by Biomineralization," *J. Synchr. Rad. S6*, 359 (1999).
115. C. Capasso, W. Ng, A.K. Ray-Chaudhuri, S.H. Liang, R. Cole, Z.Y. Guo, J. Wallace, F. Cerrina, J. Underwood, R. Perera, J. Kortright, G. Da Stasio, and G. Margaritondo, "Scanning Photoemission Spectromicroscopy on MAXIMUM Reaches 0.1 Micron Resolution," *Surface Sci. 287/88*, 1046 (1993); W. Ng et al., "High Resolution Spectromicroscopy Reaches the 1000 Å Scale," *Nucl. Instr. Meth. A347*, 422 (1994).
116. A.K. Ray-Chaudhuri, "Development of a Scanning Photoemission Microscope Based on Multilayer Optics and its Initial Application to GaAs (110) Surface Studies," Ph.D. thesis, Electrical and Computer Engineering Department, University of Wisconsin–Madison (1993).
117. W. Ng, "Development of a Photoemission Microscope: MAXIMUM and its Application to Semiconductor Interfaces," Materials Science Program, University of Wisconsin–Madison (1994).
118. S. Singh, "X-Ray Photoemission Spectromicroscopy and its Application to the Study of Patterned

Titanium Silicide," Ph.D. thesis, Physics Department, University of Wisconsin–Madison (1996); S. Singh, H. Solak, N. Krasnoperov, F. Cerrina, A. Cossy, J. Diaz, J. Stöhr, and M. Samant," An X-Ray Spectromicroscopic Study of the Local Structure of Patterned Titanium Silicide," *Appl. Phys. Lett. 71*, 55 (1997); H.H. Solak, G.F. Lorusso, S. Singh-Gasson, and F. Cerrina, "In Situ X-Ray Spectromicroscopic Study of Electromigration in Patterned Al–Cu Lines," *Appl. Phys. Lett. 74*, 22 (1999).

119. G.-F. Lorusso, H. Solak, F. Cerrina, J.H. Underwood, P.J. Batson, Y. Kim, Y. Cho, C. Kisielowski, J. Krueger, and R.E. Weber, "X-Ray Photoemission Spectromicroscopy of GaN and AlGaN," *MRS Proc. 512*, 393 (1998).
120. D. Shaver, D. Flanders, N. Ceglio, and H. Smith, "X-Ray Zone Plates Fabricated Using Electron-Beam and X-Ray Lithography," *J. Vac. Sci. Techn. 16*, 1626 (1979).
121. N. Ceglio, "The Impact of Microfabrication Technology on X-Ray Optics," p. 210 in *Low Energy X-Ray Diagnostics* (Amer. Inst. Phys, New York, 1981), D. Attwood and B. Henke, Editors.
122. M.A. McCord and M.J. Rooks, "Electron Beam Lithography," Chapter 2, pp. 139–249, in *Handbook of Microlithography, Micromachining, and Microfabrication, Vol. 1: Microlithography* (SPIE, Bellingham, WA, 1997), P. Rai-Choudhury, Editor.
123. G. Owen and J.R. Sheats, "Electron Beam Lithography Systems," pp. 367–401 in *Micro-Lithography: Science and Technology* (Marcel Dekker, New York, 1998), J.R. Sheats and B.W. Smith, Editors.
124. D. Kern, P. Coane, R. Acosta, T.H.P. Chang, R. Fader, P. Houzego, W. Malzen, J. Powers, A. Speth, and R. Viswanathan, "Electron Beam Fabrication and Characterization of Fresnel Zone Plates for Soft X-Ray Microscopy," *Proc. SPIE 447*, 204 (1984).
125. E. Anderson, V. Boegli, and L. Muray, "Electron Beam Lithography Digital Pattern Generator and Electronics for Generalized Curvilinear Structures," *J. Vac. Sci. Technol. B 13*, 2529 (1995).
126. E. Anderson and D. Kern, "Nanofabrication of Zone Plates for X-Ray Microscopy," p. 75 in *X-Ray Microscopy III* (Springer-Varlag, Berlin, 1992), A.G. Michette, G.R. Morrison, and C.J. Buckley, Editors.
127. S.J. Spector, C.J. Jacobsen, and D.M. Tennant, "Process Optimization for Production of Sub-20 nm Soft X-Ray Zone Plates," *J. Vac. Sci. Techn. B 15*, 2872 (1997).
128. G. Schneider, T. Schliebe, and H. Aschoff, "Cross-Linked Polymers for Nanofabrication of High-Resolution Zone Plates in Nickel and Germanium," *J. Vac. Sci. Techn. B 13*, 2809 (1995).
129. D. Weiss, M. Peuker, and G. Schneider, "Radiation-Enhanced Network Formation in Copolymer Galvanoforms for Diffractive Nickel X-Ray Optics with High Aspect Ratios," *Appl. Phys. Lett. 72*, 1805 (1998).
130. N. Kamijo, S. Tamura, Y. Suzuki, K. Handa, A. Takeuchi, S. Yamamoto, M. Ando, K. Ohsumi, and H. Kihara, "Fabrication of Hard X-Ray Sputtered-Sliced Fresnel Phase Zone Plate," p. IV-65 in Ref. 5., A. Duevel et al., "Fabrication of Thick Zone Plates for Multi-kilovolt X-rays," X-ray Microscopy '99 (Berkeley, to be published).
131. A.I. Erko, V.V. Aristov and B. Vidal, *Diffraction X-Ray Optics* (Inst. Optics, Bristol, 1996).
132. I. Snigireva, A. Souvorov, and A. Snigirev, "Bragg–Fresnel Optics for High-Energy X-Ray Microscopy Techniques at the ESRF," p. IV-35 in Ref. 5.

HOMEWORK PROBLEMS

Homework problems for each chapter will be found at the website:
http://www.coe.berkeley.edu/AST/sxreuv

Chapter 10

EXTREME ULTRAVIOLET AND X-RAY LITHOGRAPHY

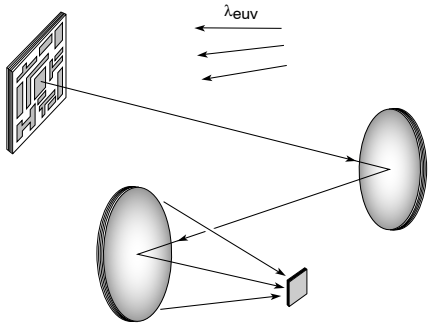

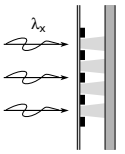

$$L_{\mathrm{w}} = k_1 \frac{\lambda}{\mathrm{NA}} \tag{10.1}$$

$$\mathrm{DOF} = \pm k_2 \frac{\lambda}{(\mathrm{NA})^2} \tag{10.2}$$

$$\sigma = \frac{\mathrm{NA}_{\mathrm{cond}}}{\mathrm{NA}_{\mathrm{obj}}} \tag{10.3}$$

$$L_{\mathrm{w}} = \alpha\sqrt{g\lambda} \tag{10.4}$$

Historically, lithography is the printing process in which an image is transferred from a flat surface, initially a smooth stone and later a metal plate, through the selective use of ink-receptive and ink-repellent treatments. Today a major application of lithography is the repetitive copying of highly detailed sub-micron spatial patterns, which after processing will form single layers of an interconnected multilevel semiconductor electronic structure commonly known as a microchip.[1] These chips are the basic building blocks of modern electronic instruments, computers, and telecommunications equipment. In this chapter we describe current state of the art lithographic equipment: deep ultraviolet (DUV) steppers that use mercury arc lamps and excimer lasers, with largely refractive optics, to print patterns with sub-quarter-micron features. The SIA Technology Road Map for Semiconductors,[2] which provides a 15-year, six-generation projection of integrated circuit (IC) characteristics, is described, with selected technical parameters for microprocessors and dynamic random access memory (DRAM) chips through the year 2012. This is followed by sections describing two candidate technologies, each of which has the potential to provide the engineering and economic solution to these

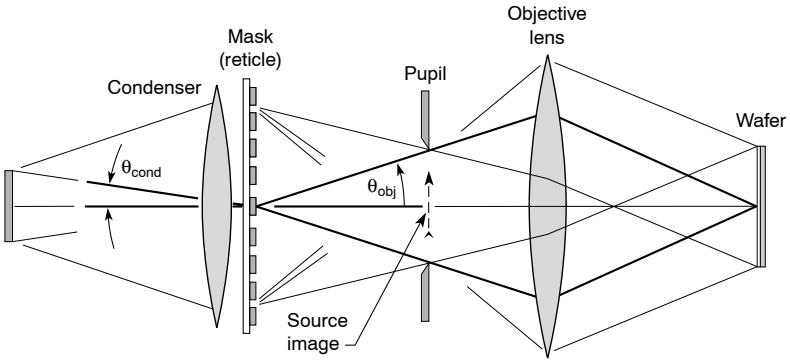

FIGURE 10.1. Optical projection lithography in which a mask pattern on a thin transmissive reticle is imaged to the wafer plane by an objective lens, typically at 4 : 1 demagnification. For deep ultraviolet (DUV) lithography the source can be a mercury arc lamp (248 nm wavelength), a KrF laser (248 nm), or an ArF laser (193 nm). The condenser optics, shown here as a single lens, illuminates the mask with numerical aperture $NA_{cond} = \sin\theta_{cond}$. The reduction optics, shown here as a single objective lens, collects light through a numerical aperture $NA_{obj} = \sin\theta_{obj}$. The illustration shows use of *Köhler illumination*, in which the condenser projects an image of the source in the pupil plane. In practice the condenser optics may have a variable numerical aperture and may employ soft apodized or hard apertures to control the angular distribution of light illuminating the mask. The degree to which phase effects (interference) can be used to enhance certain spatial frequencies is set by the partial coherence parameter $\sigma = \sin\theta_{cond}/\sin\theta_{obj}$. For low σ illumination the mask may employ phase shifting elements to enhance image contrast.

challenges in high volume manufacturing: extreme ultraviolet (EUV) lithography and soft x-ray proximity lithography, known succinctly as x-ray lithography.

10.1 DEEP ULTRAVIOLET (DUV) LITHOGRAPHY AND BEYOND

Current state of the art manufacturing of microelectronic semiconductor devices[3, 4] is accomplished using optical reduction cameras (*steppers*), such as that outlined schematically in Figure 10.1. The stepper involves a radiation source, an illumination system represented here by a single condenser lens, the mask pattern that is to be replicated, a demagnifying optical system represented here by a single objective lens, and a photoresist coated wafer to record the demagnified image of the mask pattern.[5–7]

Earlier generations of chip technology used the g-line (436 nm wavelength) and i-line (365 nm) of a mercury (Hg) arc lamp as the source. Today there is an evolution underway from the Hg arc emission band at 248 nm to krypton fluoride (KrF) and argon fluoride (ArF) excimer lasers at wavelengths of 248 nm and 193 nm, respectively. The laser sources have considerably narrower line widths[8] than the Hg emission band at 248 nm, which is of value in controlling chromatic aberrations in the largely refractive optics. Shorter laser wavelengths enable the continued march toward smaller feature sizes.

For steppers operating at 248 nm the refractive optics are fused silica, one of the few highly transmissive materials in this wavelength region. The optical systems generally include several reflective optics as well.

The condenser-optics–mask illumination system is generally quite complex, permitting variation of the illumination numerical aperture $NA_{cond} = \sin\theta_{cond}$, and masking of the angular

illumination pattern, each of which can be used to affect the sharpness of particular patterns and spatial frequencies in the image transfer process. In Figure 10.1, Köhler illumination is employed, in which the condenser optics forms an image of the source far beyond the mask, in the entrance pupil of the objective lens. This has the advantage of providing more uniform illumination of the mask, which now receives radiation from every point on the source. Generally the mask consists of an absorber pattern on a transmissive reticle. The mask pattern is generated using electron beam lithography,[9, 10] with techniques similar to those described in Chapter 9, Section 9.10. Phase shifting structures are sometimes used within the mask to enhance the sharpness (contrast) of selective features.[5, 7, 11]

The reduction imaging system is of relatively high numerical aperture $\mathrm{NA}_{\mathrm{obj}} = \sin\theta_{\mathrm{obj}}$, typically 0.5 or 0.6, which permits the printing of patterns with feature sizes approximately equal to the wavelength. The reduction optics are highly corrected so as to print near-diffraction-limited* patterns over square centimeter dimensions at the wafer.

The wafer is coated with a photosensitive polymer, known as photoresist or simply *resist*, that records the projected pattern.[12] Both positive and negative resists are used. The positive resists are rendered soluble by exposure to radiation, allowing exposed areas to be dissolved away, followed by further steps in the fabrication of desired microelectronic structures. The negative resist is rendered insoluble by radiation, so that exposed areas remain after unexposed resist is removed by a subsequent development, again followed by pattern transfer to the desired structure. High contrast resists are used, for which a process window is determined experimentally. The process window gives the allowable variations in focus and exposure for which the dimensions of the smallest printed patterns stay within narrowly confined tolerances. The process is designed to enhance the effective pattern transfer capabilities of the optical stepper. That is, the photoresist, its exposure, and its controlled development are used to extend and enhance the resolving capabilities of the imaging system.

The combination of what is called *wavefront engineering* (partially coherent mask illumination and use of phase structures),[5, 7, 11] high contrast photoresist with stringent processing controls, the use of ever shorter wavelengths to the limits of transmissive materials, and increasing numerical aperture has permitted optical projection lithography to be extended far beyond earlier perceived limitations. Indeed, the limits of this optical extension, which are influenced both by technical and by economic factors, are yet to be determined. In the following paragraphs we explore somewhat further the status of DUV lithography, followed by separate sections on two potential candidates for lithography further in the future, EUV lithography and soft x-ray proximity lithography.

For the projection printing of nanoelectronic patterns near the diffraction limits of optical systems, equations regarding minimum achievable feature sizes, optical depth of focus, and degree of partial coherence are of great interest. The achievable minimum line width L_w with lithographic systems is written as

$$L_w = k_1 \frac{\lambda}{\mathrm{NA}} \tag{10.1}$$

where λ is the wavelength, NA is the numerical aperture seen at the wafer, and k_1 is a constant that is largely dominated by the optical system, but for lithographic applications is also dependent on photoresist recording and processing. This is similar to the Rayleigh expression[13] for the minimum resolvable separation of phase-incoherent point sources by a

*"Diffraction limited" refers to ideal imaging systems limited only by the finite wavelength λ and the collection numerical aperture $\mathrm{NA} = n \sin\theta_{\mathrm{obj}}$, where n is the refractive index of the medium, typically 1 for lithographic applications.

perfect optical system, for which $k_1 = 0.61$, as we saw in Chapter 9, Section 9.4. However, the use of such a resolution criterion is inappropriate for applications of lithography where the purpose is not to achieve a faithful representation of the original object, but rather to print a pattern that (after processing) will yield an electronic structure with the desired features.[14] With high contrast resists and use of wavefront engineering as described in the previous paragraph, values of $k_1 = 0.5$ are achieved in high volume manufacturing of current computer chips. For example, quarter-micron generation chips are fabricated with 0.5 NA projection optics and a 248 nm Hg arc source, with minimum line widths just below 250 nm. Further extensions using shorter wavelengths and higher NA are discussed in the following paragraphs.

The optical depth of focus (DOF), written as

$$\mathrm{DOF} = \pm k_2 \frac{\lambda}{(\mathrm{NA})^2} \tag{10.2}$$

gives a longitudinal measure of the distance over which the image is in proper focus.[13] Quantitative measures of depths of focus are described in Chapter 9, Section 9.5 for a diffractive Fresnel zone plate lens. The expressions there are applicable to refractive optics as well. Typically $k_2 = 0.5$, so that the total ($\pm$) DOF is about $\lambda/(\mathrm{NA})^2$, or about 1 μm for the 248 nm, NA = 0.5 example considered below Eq. (10.1). This is a significant constraint on optical stepper systems, and requires constant monitoring and adjustment of the final lens-to-wafer separation distance in order to maintain highest resolution. Note also that the DOF decreases as $(\mathrm{NA})^2$, more rapidly than the improvement in resolution.

The ability to print fine, high contrast features is significantly affected by the degree of coherence within the optical system. If there exists a high degree of spatial coherence, diffraction from adjacent mask features will interfere in the image plane, significantly modifying the recorded patterns. With electric fields adding, in the coherent limit, ringing will be observed near sharp features and the contrast will vary dramatically for spatial structures that contribute to constructive or destructive interference. The parameter used to characterize the degree of partial coherence[13] is

$$\sigma = \frac{\mathrm{NA}_{\mathrm{cond}}}{\mathrm{NA}_{\mathrm{obj}}} \tag{10.3}$$

where $\mathrm{NA}_{\mathrm{cond}}$ is the illumination numerical aperture as seen from the mask, and $\mathrm{NA}_{\mathrm{obj}}$ is the collection numerical aperture of the reduction optics, also as seen from the mask. Both are shown in Figure 10.1. The coherent limit corresponds to $\sigma = 0$, as occurs for instance with a uniform plane wave illumination of $\mathrm{NA}_{\mathrm{cond}} = 0$. The incoherent limit, $\sigma = \infty$, corresponds to an illumination cone larger than the collection NA of the imaging optic; in practice $\sigma > 1$ means the illumination is effectively incoherent.

It is difficult to compare the general transfer properties of an optical system for coherent and incoherent illumination. In the incoherent limit, diffraction from various features is imaged independently at the wafer plane, and the process is accurately described by a linear modulation transfer function (MTF). In the coherent limit, electric fields interfere and the transfer function is non-linear, depending on detailed aspects of the object (mask pattern) to be imaged. Nonetheless, there is value in presenting an *apparent transfer function*,[15] as in Figure 10.2, that attempts to describe the resultant contrast achievable with patterns of various spatial frequencies, as a function of the partial coherence factor σ, understanding that the curves are object dependent.[5, 11]

In the coherent limit ($\sigma = 0$), the transfer function is flat out to a very sharp cutoff at a spatial frequency of $\mathrm{NA}_{\mathrm{obj}}/\lambda$; incident and diffracted wavefronts are both well defined, and the

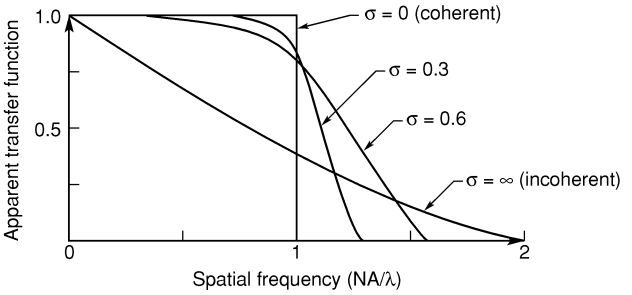

FIGURE 10.2. The apparent optical transfer properties of a perfect lens with varying degrees of partially coherent illumination. For coherent and low σ illumination, interference between diffracted radiation from nearby objects causes the transfer function to be object dependent. Spatial frequency refers to an inverse period, where one period corresponds to a line pair of one bar and one space.

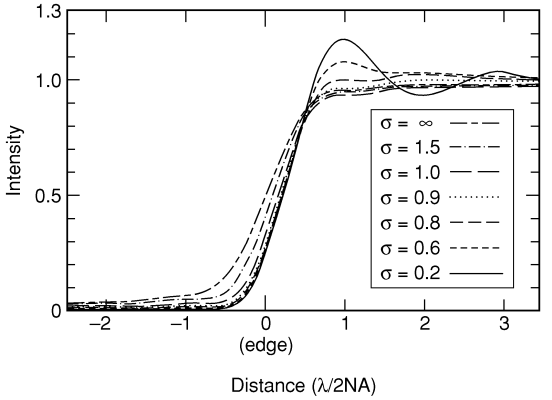

FIGURE 10.3. Intensity versus distance, in units of $\lambda/(2\,\mathrm{NA})$, across the image of a sharp edge (knife-edge) pattern as a function of partial coherence σ. (Courtesy of M. O'Toole and A. Neureuther,[16] University of California, Berkeley.)

wave is either fully captured by the lens or not at all. In the incoherent limit ($\sigma > 2$), there is a wide variety of incident wave vectors, which when diffracted are captured to varying degrees, out to twice the spatial frequency of the coherent case. Transfer of modulation out to higher spatial frequencies in the incoherent case is due to the large angle of incidence, θ_{cond}, which permits radiation to be collected after vector scattering through twice the angle available in the coherent limit. Diagrams illustrating these points with diffraction gratings were discussed in Chapter 9, Section 9.6 with regard to resolution beyond the Rayleigh limit in soft x-ray microscopes. Apparent transfer functions are shown in Figure 10.2 for partial coherence values of $\sigma = 0.3$ and 0.6, values that are often utilized in DUV lithographic systems. Figure 10.3 shows a numerical simulation of the image across a sharp edge for varying degrees of partial coherence, as calculated by O'Toole and Neureuther.[16] Notice the substantial interference effects (ringing) for the cases with a high degree of spatial coherence (low σ), and the rather smoother, but somewhat broader profiles for $\sigma \geq 1$.

An example of an optical system used today in semiconductor manufacturing is shown in Figure 10.4. It shows the projection optics layout for the DUV stepper, the Micrascan III manufactured by SVG Lithography.[17–19] The system employs 13 fused silica refractive lenses, two mirrors (one of which is an asphere), a polarizing beamsplitter, and two quarter-

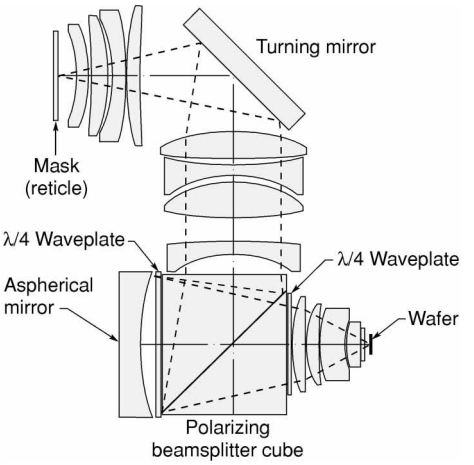

FIGURE 10.4. A commercial projection optical system for sub-250-nm generation lithography, employed in the Micrascan III, a DUV stepper with NA = 0.6, an excimer laser source, and variable illumination allowing the partial coherence factor σ to be varied from 0.3 to 0.8. (Courtesy of D. Williamson and J. Shamaly, SVG Lithography, Wilton, CT.[17–19])

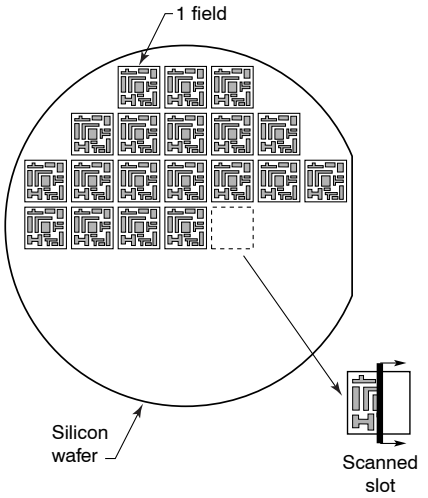

FIGURE 10.5. Step and scan lithography. With synchronous movement of the mask and wafer, at a magnification corrected sweep speed, a rectangular illumination slot is scanned across the field of what eventually will become one layer of a single computer chip. The wafer is then stepped to the next position and the mask is scanned again, repeating the process until all available fields have been printed.

wave plates.[19] The optical system has a numerical aperture $NA_{obj} = 0.6$, has a demagnification of 4, and operates with a coherence factor σ variable between 0.3 and 0.8. It uses a 15 W, 1 kHz repetition rate KrF laser at 248 nm, with a spectral bandwidth ($\Delta\lambda$) between 100 pm and 300 pm ($\lambda/\Delta\lambda > 1000$). The large number of refracting elements, in groups of four or five, work in combination to provide most of the optical power (NA) and correct variations of spherical aberration, coma, astigmatism, and distortion across the field. The aspheric mirror contributes most of the optical power (NA), and also corrects high order aberration.

This stepper is designed to print sub-250-nm generation chips in high volume manufacturing. It employs a step and scan system of synchronous mask and wafer motion in which the optical system illuminates only a narrow rectangular slot, which is scanned across the mask. The wafer is synchronously scanned at one-fourth the speed (to match the optical demagnification) until a full field is printed, as illustrated in Figure 10.5. The wafer is then stepped to the next field, and the process is repeated until all available fields on the wafer have been scanned.

Advantages of the step and scan system are that it can print over a larger dimension in the scan direction, and that aberrations of the optical system need be controlled only within the

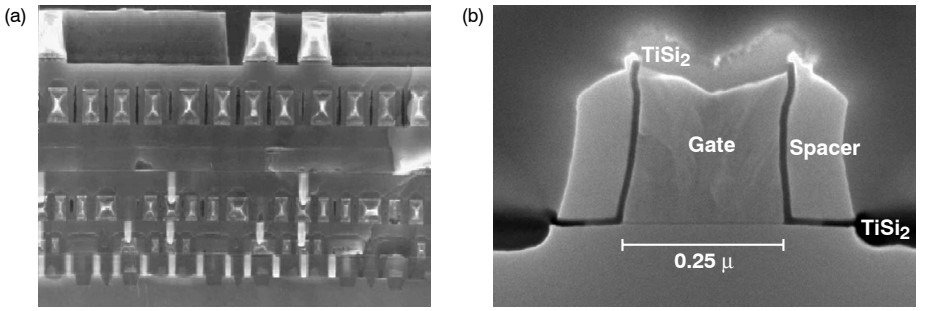

FIGURE 10.6. (a) Layout showing general topography of a Pentium II 400 MHz microprocessor chip, as seen at visible light resolution. (b) Scanning electron microscope (SEM) image of the 0.25 μm (250 nm) gate region of a single transistor on the same chip. (Courtesy of G. Neubauer and B. Triplett, Intel Corporation, Santa Clara, CA.)

smaller area of the rectangular slot. In some cases the mask contains several replicates of the same pattern. These sub-fields are called dies.

Figure 10.6 shows two images of a quarter-micron generation Pentium II microprocessor chip,[20] which has a clock speed of 400 MHz. Figure 10.6(a) is a cross-sectional view of the Pentium II, showing five levels of metallization. Each of these layers requires a separate lithographic step. The metal layers are separated by insulating oxide (SiO_2) layers, which in some areas show tungsten interconnects, known as vias, to the metal layers above and below. Figure 10.6(b) shows a scanning electron microscope (SEM) close-up view of the 0.25 μm wide gate region of a single transistor, with titanium silicide electrodes, and silicon nitride insulating spacers. For comparison, see the side view of a CMOS field effect transistor (FET) shown in Chapter 9, Figure 9.34. The quarter-micron device in Figure 10.6 was printed with an earlier Micrascan II stepper,[18] which has a 0.5 numerical aperture and uses a 2.4 kW Hg arc lamp with 248 nm central wavelength and a spectral bandwidth of 7 nm FWHM ($\lambda/\Delta\lambda \simeq 35$).

The Semiconductor Industry Association (SIA) prepares a technology roadmap for semiconductors,[2] updated every three years, that provides a 15-year six-generation projection of anticipated integrated circuit (IC) characteristics. The roadmap attempts to project into the future historic growth trends in the microelectronics industry first reported in 1965 by Gordon Moore of Intel.[21] He observed that feature sizes in the most complex circuits were decreasing by a $\sqrt{2}$ factor every two years, thus increasing the number of functional units (transistors or memory devices) per unit area by a factor of two every two years. Combined with a simultaneous factor of two growth in chip area during the same time interval, this led to an exponential growth in which functional capability quadrupled every two years, i.e., doubled every year. It was also observed that this led to an exponential decrease in cost per component. Moore points out in a more recent article[21] that this exponential growth has continued now for 35 years, albeit with variations of exponentiation time.

Table 10.1 shows an anticipated future trend in which minimum feature size is reduced on average by $\sqrt{2}$ every two to three years, increasing the number of transistors per unit area by a factor of two. With an increase in area of about 20% per year, this predicts a doubling of functionality (transistors per field) approximately every two years, about half the earlier rate. Moore points out that this exponentiation cannot continue indefinitely. Because of physical constraints the growth must slow, and eventually saturate. He describes the territory beyond the 180 nm generation as *terra incognita*.

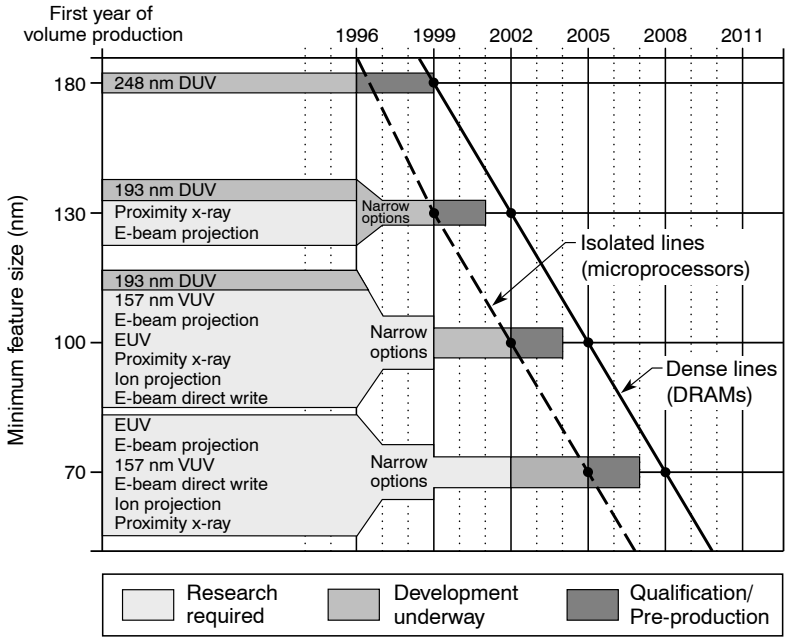

FIGURE 10.7. The National Technology Roadmap for Semiconductors is a 15-year projection of the integrated circuit (IC) technology characteristics required to maintain the historical rate of performance improvements. First year of IC volume production is shown for six generations of lithography, denoted by minimum printed feature size for isolated microprocessor lines and half-period DRAM lines. The historical trend is a $\sqrt{2}$ reduction in minimum feature size every two years. Future projections correspond to similar reductions every two to three years. The technology roadmap is a guide in that it identifies technological targets, but does not identify technical solutions. Rather it identifies potential solutions – a constantly moving target. (Courtesy of the Semiconductor Industry Association, San Jose, CA.[2])

A graphic version of the roadmap, with emphasis on candidate lithographic technologies to meet these challenges, is shown in Figure 10.7. Plotted is the first year of volume production for microprocessors (computer logic) and dynamic random access memory (DRAM) chips versus technology generation on the vertical scale, expressed in terms of minimum feature size.† Thus the 180 nm minimum feature size technology will use 248 nm DUV steppers. The next technology generation at 130 nm feature sizes is expected to use ArF steppers,[22, 23] at 193 nm wavelength, entering the market between 1999 and 2002. In practice there is likely to be an evolution from 248 nm (KrF) to 193 nm (ArF), and perhaps next to the fluorine laser (F_2) at 157 nm, with continuous upgrades due not only to wavelength and numerical aperture, but to the use of (1) so-called optical enhancements, wavefront engineering advances involving illumination control, phase masks, geometrical layout, and design rule limits, (2) tighter optical tolerances (closer to the elusive diffraction

†A *technology generation* is defined in terms of the half period (half pitch) of repetitive lines and spaces, as in a DRAM. Isolated lines generally achieve somewhat narrower line widths, as indicated in Table 10.1 for microprocessor gate widths.

TABLE 10.1. The National Technology Roadmap for Semiconductors in tabular form, showing anticipated technological characteristics for selected parameters of microprocessors and DRAM chips. The projections cover seven generations of technology, denoted by minimum feature sizes. (Courtesy of the Semiconductor Industry Association, San Jose, CA[2]; dates of entry updated April 1999.)

Year of first shipment	1997	1999	2002	2005	2008	2011
Technology Generation (nm): (Dense lines, in resist)	250	180	130	100	70	50
Isolated lines, (microprocessor gates)	200	140	100	70	50	35
DRAM Memory (bits)	256 M	1 G	4 G	16 G	64 G	256 G
Logic[a] (transistors/cm^2)	4 M	6 M	18 M	39 M	84 M	180M
Chip frequency[a] (GHz)	0.4	0.6	0.8	1.1	1.4	1.8
Gate CD control:						
3σ at post-etch (nm)	20	14	7	5	4	3
Overlay: mean + 3σ (nm)	85	65	45	35	25	20
Field size (mm × mm)	22 × 22	25 × 32	25 × 36	25 × 40	25 × 44	25 × 52
Wafer diameter (mm)	200	200	300	300	450	450

[a] High volume microprocessor.

limit[24]), and (3) ever tighter controls on photoresist contrast and processing. These lead to intermediate technology steps, and enhancements across the product lines, known as lithography *shrinks*.

To meet roadmap projections at the 100 nm entry point and beyond, the roadmap in Figure 10.7 shows several competing technologies, including 193 nm (ArF), 157 nm (F_2), proximity x-ray, electron beam projection, electron beam direct write, EUV lithography, and ion projection lithography. EUV and x-ray proximity lithography are discussed in the following sections of this chapter. The three particle beam technologies are not discussed here, but information is available to the reader elsewhere.[25] Briefly, e-beam direct write[9, 10] is very similar to the technology described in Chapter 9, Section 9.10. It offers the advantage of being able to write very detailed small-feature patterns and is usually used for the fabrication of the most advanced test structures, but is a relatively slow sequential writing tool, economically uncompetitive for high volume production in its present form. E-beam projection[26] attempts to overcome this by writing larger areas using electron scattering plate masks and broader field electron optics. This may be economically more attractive if challenges involving stability of the reticle[‡] can be met. Ion beam projection lithography has similar reticle issues and would be a rather substantial change in technology. All of the above are in a competition among technologies to meet future challenges. The winning solution, however, will not only include a technical demonstration of working devices, but also an economic advantage involving existing investments in capital and human resources (training and expertise), as well as projected profit margins.

Further details of the technology roadmap are presented in Table 10.1, which shows a selection of projected parameters[2] for microprocessors and DRAMs. Extending to the year 2011, the table shows technology generations extending from 250 nm (quarter micron technology) to 50 nm, with isolated microprocessor gate widths extending from 200 nm to 35 nm, and DRAM memory extending from 256 Mb to 256 Gb in 2011. According to these projections,

[‡]The reticle is made of a thin membrane with a patterned absorber.

the industry is targeting the 100 nm generation in the year 2005, with 70 nm processor gates, and 39 million transistors per centimeter squared, on a chip of dimensions 2.5 cm by 4.0 cm, having a chip clock rate of 1.1 GHz. A significant challenge for this same generation is the indicated 5 nm critical dimension control on gate width. This is a challenge for the lithographic technology as well as for the materials processing and metrology, as discussed for instance in Chapter 9, Section 9.9, dealing with the need for analytic tools that have elemental and chemical sensitivity on this spatial scale.

10.2 EXTREME ULTRAVIOLET (EUV) LITHOGRAPHY

One candidate technology for high volume manufacturing beyond the use of 193 nm wavelength ArF lasers is extreme ultraviolet lithography (EUVL). Based on multilayer coated reflective optics, it makes a dramatic jump in wavelength to the 11–13 nm region while maintaining the evolution of optical techniques[27–36] and the industry's investment therein. The shorter wavelength offers a continued path to smaller feature sizes, with modest NA, over several successive generations, with a substantial gain in depth of focus. Because multilayer reflectivities are limited to about 70% in this spectral region[37] (see Chapter 4), the number of mirrors used is limited by throughput considerations.

In order to correct for aberrations across the relatively large field, being limited to a few optical surfaces, one must turn to aspheric optics, that is, optics that are designed to have surfaces that depart from spherical.[38] This is significant, as the optics must also meet tight specifications[39] on polish to control scattering of radiation within and outside the printed field. Optical polishing techniques are more advanced for spherical surfaces than for aspheres; thus there is a technical challenge involved in achieving new levels of surface figure and finish (polish) to the specifications required for EUV lithography at the entry points (nodes) at 100 nm and beyond.

A simplified diagram illustrating the basic concept of EUV lithography is shown in Figure 10.8. EUV radiation at 13 nm wavelength is shown illuminating a multilayer coated reflective mask, which has an absorber pattern across its surface. An aspheric optical system reimages the pattern at 4 : 1 demagnification to the photoresist-coated wafer. Only two mirrors are shown for simplicity. The inset shows a TEM side view of a molybdenum–silicon multilayer coating. The coating has a 6.7 nm period for peak reflectivity at about 13.4 nm wavelength. This wavelength corresponds to a photon energy of 92.5 eV, just below the silicon L-absorption edge at 99 eV. Thus, the silicon acts as a low absorption spacer material, permitting the achievement of high reflectivity, again about 70%. There are other candidate material combinations,[37, 40, 41] for instance Mo/Be, which operates at wavelengths down to 11.2 nm, just below the beryllium K-absorption edge at 112 eV.

Reflectivities[42] for both Mo/Si and Mo/Be are shown in Figure 10.9, along with a graph showing the radial uniformity[37, 43] of a Mo/Si coating across a 50 mm radius mirror. Note that both Mo/Si and Mo/Be achieve reflectivities of about 70%, Mo/Si with a somewhat broader passband. For this coating the radial uniformity achieves an rms d-space variation, $\Delta d/d$, of 3×10^{-4} rms. This results in a surface height variation at the top of the multilayer stack (40.5 layer pairs) of 0.05 nm rms, or $\lambda_{\text{euv}}/250$. The systematic variation observed in Figure 10.9(b) suggests that further improvements can be expected as multilayer engineering proceeds. Furthermore, part of this systematic variation in surface height variation can be compensated in subsequent optical focusing.

An early EUVL testbed, utilizing 10 : 1 reduction Schwarzchild optics, is shown schematically in Figure 10.10(a), with an example of a printed pattern in Figure 10.10(b). The

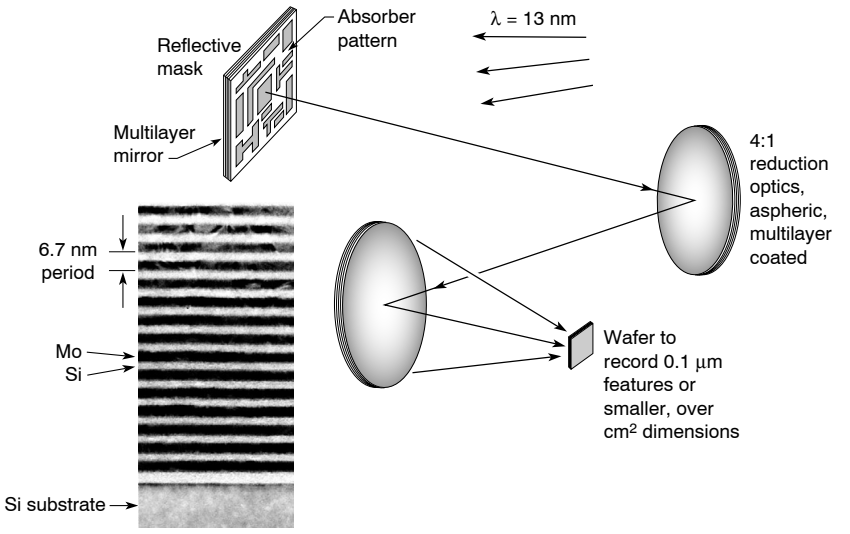

FIGURE 10.8. The basic concept of EUV lithography showing multilayer coated aspherical optics (only two for simplicity) forming a reduced image, at the photoresist covered wafer, of an absorber pattern on a multilayer coated reflective mask. The enabling technology is the availability of high reflectivity ($\simeq$ 70%) multilayer coatings in the 11–13 nm wavelength range. Shown in the inset is a TEM side view of a molybdenum–silicon multilayer mirror seen previously in Chapter 1, Figure 10.1.

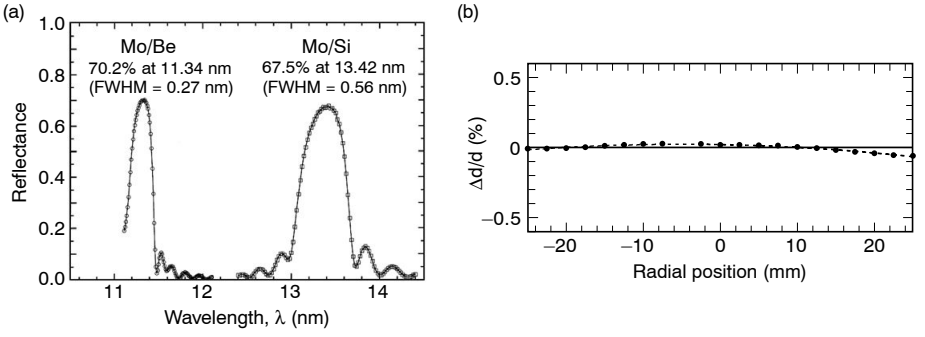

FIGURE 10.9. (a) Reflectivity of a Mo/Si multilayer mirror near its peak at 13.4 nm wavelength and of Mo/Be near its peak at 11.3 nm. (b) Multilayer uniformity expressed in terms of d-space variation across a 50 mm aperture projection optic coated with Mo/Si for use at 13.4 nm wavelength. The d-space variation in this ungraded direction departs from specifications by only 0.02% rms, corresponding to a surface height variation of 0.05 nm rms, or $\lambda_{euv}/250$. The coating is purposely tapered in the orthogonal direction, to accommodate larger variations of incidence angle, but achieves similar uniformity. (Courtesy of C. Montcalm, E. Spiller, S. Bajt, and J. Folta[37], LLNL[43]; J. Underwood and E. Gullikson, LBNL.[42])

Schwarzchild optics are spherical, have up to NA = 0.088, and are Mo/Si coated for pattern transfer experiments at 13.4 nm. The Microstepper,[44] as it is called, employs a laser-produced plasma cluster jet source, discussed earlier in Chapter 6, Section 6.7.3. The present system employs a 40 W average power, 1.06 μm wavelength Nd:YAG laser delivering 5 nsec duration pulses at a 100 Hz repetition rate. Using a xenon cluster jet, the conversion efficiency is

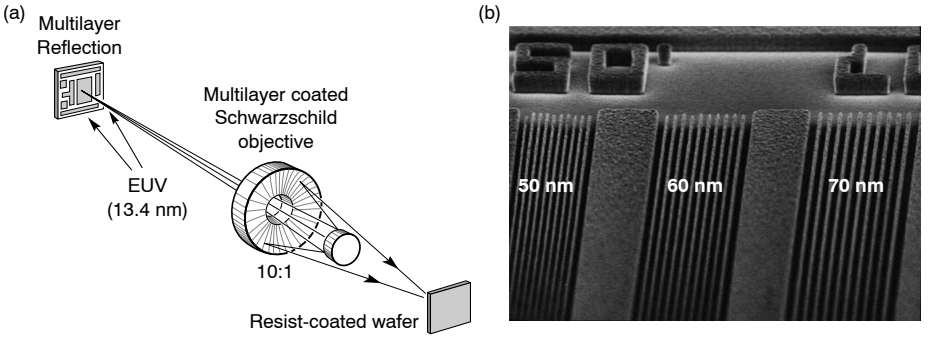

FIGURE 10.10. (a) An early EUV lithography testbed utilizing 10 : 1 reduction Schwarzschild optics. The optics are spherical with a numerical aperture of 0.07, and are coated with Mo/Si multilayers for exposures at 13.4 nm. The radiation source is a laser-produced gas jet of Xe clusters. (b) SEM image of 50 nm, 60 nm, and 70 nm wide lines printed as lines and spaces having a 1 : 2 duty cycle with the 10× microstepper shown in (a). Such patterns are used for optical alignment, resist development, and process control protocol development. (Courtesy of Sandia, Lawrence Livermore, and Lawrence Berkeley National Laboratories, and of Intel, Motorola, and Advanced Micro Devices.[44, 46])

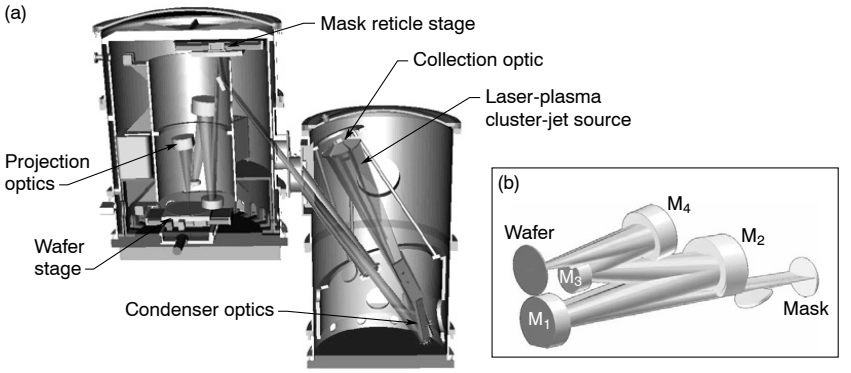

FIGURE 10.11. (a) Cut-away engineering computer aided design (CAD) drawing of a pre-manufacturing (α-like) EUV stepper. The 4 : 1 reduction optics are shown in (b). The imaging optical systems consist of four multilayer coated mirrors, three of which are aspheres. The numerical aperture is 0.1, for printing 100 nm features at $k_1 = 0.77$, with a partial coherence factor of $\sigma = 0.7$. It is a ring field, step and scan system with a 1.5 mm by 26 mm chord at the wafer, with a ± 0.5 μm depth of focus. (Courtesy of D. Tichenor and R. Stulen, Sandia National Laboratories, and D. Sweeney, Lawrence Livermore National Laboratory.[36, 38])

about 1% of the incident laser light into an EUV band of 2.5% relative spectral bandwidth at 13.4 nm, and a solid angle of 2π sr.[45] The conversion efficiency is about four times greater at 11.2 nm, where the Mo-Be reflectivity peaks. Shown in Figure 10.10(b) are 50 nm, 60 nm, and 70 nm wide lines printed as a line and space pattern with 1 : 2 duty cycle.[44, 46] The images were printed with the 0.088 NA Microstepper at 13.4 nm.

A pre-manufacturing (α-like) EUV stepper, known as the Engineering Test Stand (ETS), has been designed and is under construction. It provides a better insight into the general direction EUV lithography is going. A cut-away engineering CAD drawing is shown in Figure 10.11(a). Following the laser plasma source is a series of collection–illumination

optics, some multilayer coated and some glancing incidence, which in six parallel channels collect one-third of a hemisphere of EUV radiation for mask illumination. With a planned 1.5 kW average power laser, this will provide about 5 W of in-band (2.5% spectral width) EUV radiation at 13 nm within the collection solid angle of 2 sr.[45]

The four-element, 4 : 1 reduction optical system[38] is shown in Figure 10.11(b). It is designed for a numerical aperture of $NA_{obj} = 0.1$, printing of 100 nm critical dimension (70 nm isolated features) at $k_1 = 0.77$, and a coherence factor σ of 0.7. It is a step and scan system whose field has the shape of an arc (a *ring* field) rather than a narrow rectangle. The arc is 1.5 mm wide and has a chord of 26 mm at the wafer. The design depth of focus is $\pm 0.5\ \mu$m. Three of the mirrors are aspheric (M_1, M_2, and M_4); mirror M_3 is spherical. The maximum departure from sphericity is about 10 μm. The mirrors are typically 10 cm in diameter, cut from larger substrates. The system is telecentric at the wafer.¶ Specifications[39] for the surface figures are 0.25 nm rms ($\lambda_{EUV}/50$), 0.20 nm rms for mid-spatial frequencies (1 μm to 1 mm period surface roughness), and 0.10 nm rms for high spatial roughness. The mid-spatial frequency specification is chosen to control scattering (flare) within the camera's field of view, which affects the image contrast. The high spatial frequency specification is required to maintain high multilayer mirror reflectivity,[37, 43] which affects the system throughput. Follow-on β-tool and manufacturing steppers would require somewhat tighter specifications.

Fabrication of early EUV metal oxide semiconductor (MOS) electronic devices is described by K. Nguyen, G. Cardinale, and their colleagues.[47] Similar efforts are underway in Japan involving an EUV laboratory exposure tool based on a three aspherical mirror system and use of synchrotron radiation.[48] Led by H. Kinoshita, that effort is a collaboration among the Himeji Institute of Technology, Hitachi, and Nikon.

Development of the requisite coatings,[49, 50] optics, masks, and photoresist requires a variety of specialized diagnostic or metrology tools,[51] some of which are uniquely required due to the resonant nature of the multilayer EUV coatings. For example, a new visible light interferometer, based on the use of single mode optical fibers, has been developed[52] to a wavefront accuracy of $\lambda_{vis}/2000$, or about 0.25 nm rms, for in-shop use in the fabrication of aspherical substrates. In addition a tunable, at-wavelength interferometer has also been developed for testing the assembled optical systems.[53,54] This is important, as the multilayer coatings are resonant phase structures and it is possible that phase front variations could be introduced within the coatings. This phase shifting point diffraction interferometer has demonstrated a wavefront accuracy of $\lambda_{euv}/330$ at 13.4 nm wavelength, or 0.041 nm rms. It was described in Chapter 8, Section 8.7. Optimization of multilayer coatings has required a specialized facility[42] for measuring reflectivity to very tight specifications. To obtain the data in Figure 10.9(a) and (b) required that wavelength be measured to an accuracy of 10^{-4} and reflectivity to 10^{-3}, with a spatial resolution of order 100 μm on the coated optical surface. Measurement of EUV scattering from mid- and high-spatial-frequency roughness on multilayer coated optics has required the development of a capability covering nine orders of magnitude.[55] Defect inspection of masks and multilayer coated mask blanks requires a variety of new tools, some of which must be actinic (at-wavelength) again, due to possible phase effects within the multilayer that would not be seen by non-actinic techniques. Early work using actinic methods has been reported,[56, 57] to be followed by correlation studies with more accessible non-actinic tools.

¶Telecentric means that the chief rays at each point on the wafer are parallel. This ensures that the image size at the wafer is not sensitive to defocus, and thus demagnification is constant across the wafer.

Early results indicate that EUV lithography is making substantial progress toward demonstrating its viability in the competition for a multi-generation lithography solution for feature sizes[35,58] below 100 nm. Most notable is progress in the figure and finish of aspherical optics, development of uniform high reflectivity multilayer coatings, a host of specialized metrologies, and integration of these into a successful demonstration testbed. Additional work is underway in the areas of photoresist development, mask fabrication and inspection tools, and further options for the development of a commercial EUV source.

10.3 X-RAY PROXIMITY LITHOGRAPHY

Proximity soft x-ray lithography, known more succinctly as x-ray lithography, utilizes nominal 0.7 nm to 1.2 nm wavelength radiation (1.0 keV to 1.8 keV photon energy) in an essentially shadow casting technique just at the limits where diffraction becomes important. The technique[59] was first suggested by Spears and Smith of MIT in 1972. This was followed by an intensive development effort at IBM.[60–63] In its general manifestation it uses relatively broadband bending magnet synchrotron radiation with relatively simple beamline optics, as outlined in Figure 10.12.

The mask and wafer are maintained in close proximity, at a separation distance g, as illustrated in Figure 10.12(a). The resolution, or more precisely the minimum printable line width L_w, is dominated, to first order, by diffractive blurring at the finite wavelength λ and gap g. The general scaling of minimum line width with wavelength and gap can be understood in terms of a simple mask consisting of an absorption grating of period d, at a gap distance g from the wafer. For wavelength $\lambda \ll d$, the grating will generate first orders (± 1) at angles $\pm\lambda/d$. For a gap distance g this will cause a lateral spread of the pattern by an amount $\Delta d \simeq 2g\lambda/d$. An acceptance criterion must be set relating Δd to some fraction of d. This of course is done with full cognizance that resist contrast and processing will be used to full advantage to print sharp features as desired. For instance, if the spread Δd is limited to some fraction ϵ of d, such that $\Delta d = \epsilon d$, then $\epsilon d^2 = 2g\lambda$, or $d = \sqrt{2/\epsilon}\sqrt{g\lambda}$. If we take the minimum line width as $L_w = d/2$, then we obtain the general scaling relation

$$L_w = \alpha\sqrt{g\lambda} \tag{10.4}$$

where $\alpha = 1/\sqrt{2\epsilon}$ is a process dependent parameter of order unity. To accurately determine the proportionality constant α, one must analyze the problem more thoroughly, allowing for full diffractive effects, finite spectral bandwidth, finite mask pattern thickness, geometrical blurring of the pattern due to the finite source size, and image spread within the recording material due to photoelectron and Auger electron ranges as part of the energy absorption process.[§] Several groups have analyzed proximity lithography in more detail.[64–73]

Accurate diffraction calculations have been performed that exhibit interference effects due to sharp edges, even with finite spectral bandwidth. The inclusion of a small amount of

[§]Recall from Chapter 1, Section 1.2, that absorption of radiation leads to emission of a photoelectron, followed by a secondary readjustment of the atom whereby the core vacancy caused by photoemission is filled by an outer level electron dropping in. For low Z atoms, such as carbon in photoresist, the secondary process generally leads to the emission of a characteristic Auger electron. For a carbon atom (284 eV K-electron binding energy) absorbing a 1 keV photon, this would lead to a 716 eV photoelectron, followed by a 270 eV KLL Auger electron, both of which typically have a range measured in nanometers.

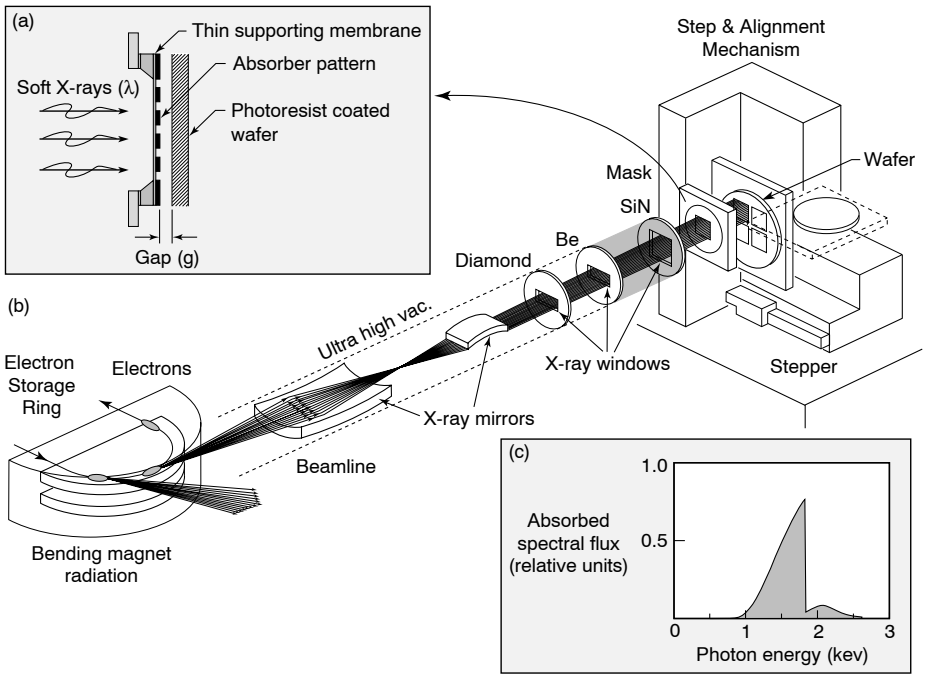

FIGURE 10.12. (a) Close-up view of the proximity mask, showing the absorber pattern on a thin supporting membrane and a resist coated wafer, separated by a small gap g. (b) A typical x-ray lithography station utilizing bending magnet radiation from an electron storage ring, a beamline to transport the radiation to the mask, and a stepper to place and align the wafer for each exposure, and to step the wafer to successive positions until all available fields have been exposed (Courtesy of S. Ishihara, NTT[73]). (c) Typical spectral distribution of bending magnet radiation absorbed by the photoresist after two mirror reflections and passage through two beryllium windows and a silicon carbide mask substrate. In this embodiment (b) the final x-ray mirror rocks to scan the mask pattern. Other x-ray steppers illuminate the full field, or vertically displace the final mirror.

geometrical blur (spatial coherence due to finite source size), perhaps $\frac{1}{3}$ of the desired feature size, is found to be beneficial in that it smooths the high spatial frequency ringing due to diffraction.[66, 67] Calculations and process control experiments for two-dimensional patterns are presented by S. Hector, V. Pol, F. Cerrina, and colleagues.[68] Allowing as well for electron range[69–71] and optimized resist processing, effective values of α below 1 are possible. For a value $\alpha = 0.7$, a mean wavelength of 1 nm, and a gap of 15 μm, Eq. (10.4) indicates that line widths as small as 90 nm can be printed. Figure 10.13 shows graphs of achievable line width verses photon energy for various values of the mask to wafer gap, as calculated by F. Cerrina and his colleagues at Wisconsin.[71] The calculations include the blurring effect of photoelectron and secondary electron range.

A series of lines and spaces is shown in Figure 10.14, obtained by soft x-ray proximity printing by J. Silverman[74] and colleagues at IBM's Advanced Lithography Facility in East Fishkill, NY. The printed patterns show well-defined lines and spaces down to 100 nm. The facility uses an Oxford Instruments compact (superconducting magnets) 0.7 GeV electron storage ring.[75] The beamline[76] employs two mirrors, One is a stationary collimating mirror that defines a horizontal stripe of radiation 50 mm wide by 3.6 mm (1σ) high. A horizontal beam uniformity of better than $\pm 2\%$ is achieved. The second mirror is a planar deflector, used

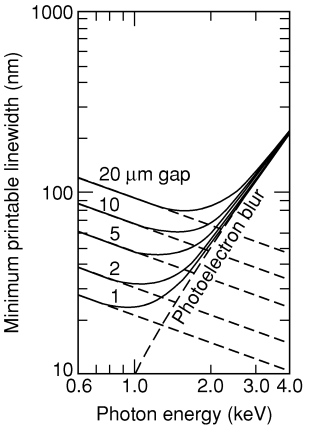

FIGURE 10.13. Minimum printable linewidth as a function of photon energy and mask to wafer gap. The effect of photoelectron and Auger electron range is included (from F. Cerrina,[14,66] University of Wisconsin, Madison.)

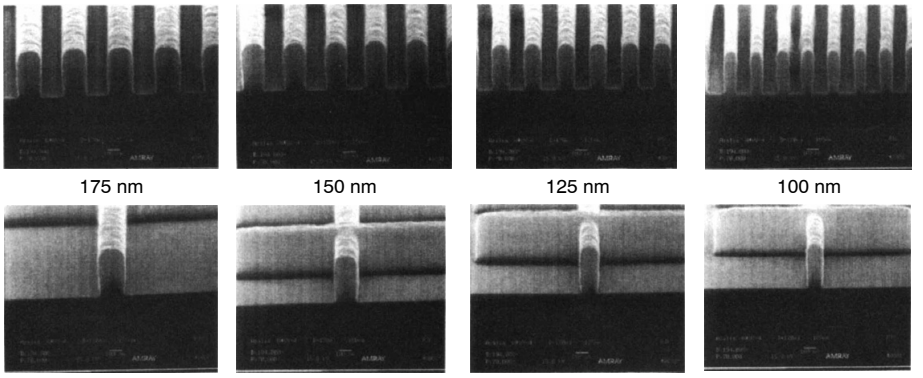

FIGURE 10.14. Lines and spaces and cross patterns printed with a 15 μm gap and 0.7 nm to 1.0 nm wavelength radiation, and recorded with UV-4 photoresist. (Courtesy of J. Silverman, IBM.[74])

to vertically scan the beam across the mask. Two beryllium windows are used for vacuum isolation. The structure was obtained by over-etching a 70 nm photoresist image.[74] This facility achieves an uptime (available for exposures)[74] greater than 98% of scheduled time, with a beam lifetime of 30 h at 300 mA beam current, and a typical exposure time of 2 s. For the results shown in Figure 10.14, a gold absorber pattern was used on a 2 μm thick silicon carbide (SiC) membrane. For several reasons there is a movement toward tantalum compounds for the absorber material, and possibly thin diamond films for the membrane. Figure 10.15 shows a complex resist pattern printed with the NTT x-ray stepper in Atsugi-shi, Japan.[77, 78]

The simplicity of x-ray lithography, which accrues through the absence of reduction optics, is offset by complexity in the mask. For DUV and EUV lithographies the mask pattern is reduced optically, typically by a factor of four, and is deposited on a substantial substrate. For x-ray lithography the mask is 1 : 1 with the wafer, and consists of an absorber pattern on a thin membrane. Both applications place a greater burden on mask fabrication. Radiation damage is also potentially greater due to the increased dose per unit area (1 : 1 vs. 4 : 1). Typical mask absorber materials include high Z elements such as gold, tantalum, and tungsten, and compounds thereof.[71, 72] Silicon carbide (SiC) is a preferred thin membrane material that combines high x-ray transmission just below the silicon K-edge at 1.84 keV (0.67 nm

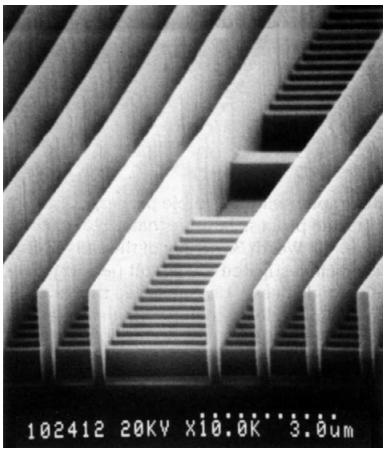

FIGURE 10.15. Resist pattern printed with x-ray lithography showing 200 nm wide by 2 μm thick lines above a base pattern of 0.5 μm lines and spaces. (Courtesy of K. Deguchi, NTT/Atsugi-shi, Japan.[77, 78])

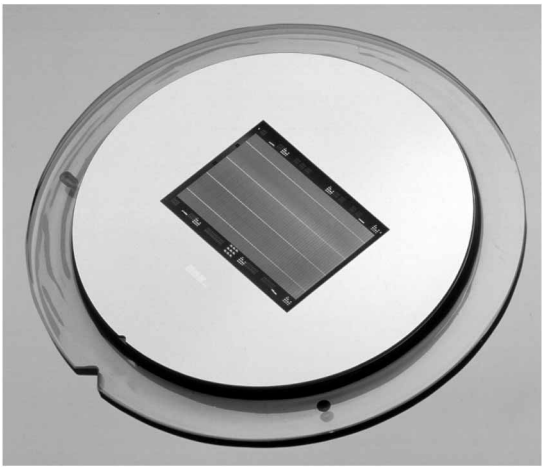

FIGURE 10.16. A 0.13 μm, 1 Gbit dynamic random access memory (DRAM) x-ray test site mask that combines the ground rules and complexity of a 1 Gbit SRAM and a 4 Gbit DRAM. The chip area is 44 $\times$ 26 mm. The mask pattern is fabricated on a silicon carbide membrane. (Courtesy of L. Brouchard, IBM Microlithographic Mask Development Center, Essex Junction, VT.)

wavelength) with high strength and stiffness. An example of a SiC supported x-ray mask for use at the 0.13 μm node is shown in Figure 10.16. Stiffness is an important property of the supporting membrane, as it helps to minimize potential distortion that might introduce changes during application of the absorber pattern, by localized heating during exposure, or by radiation induced stress. Thin diamond membranes are also of potential interest. Typical mask dimensions are 20 mm by 20 mm, or even 20 mm by 50 mm, on a 2 μm thick membrane. A thin protective cover is used to limit potential contact damage to the mask and to prevent contamination.

X-ray lithography is a relatively mature technology, well advanced on many fronts, with a substantial industrial infrastructure. Accomplishments[72, 74, 79–81] in recent years include (1) fabrication by IBM of nearly functional 64 Mb DRAM devices (with one unrepairable defect) using x-ray lithography at the gate level (1995), (2) fabrication by Mitsubishi (see

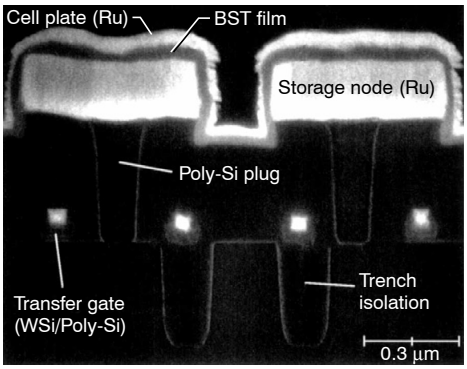

FIGURE 10.17. An SEM cross-sectional image of a 1 Gbit DRAM with 0.14 μm minimum feature size fabricated with x-ray lithography. The memory cell employs a Ru–BST–Ru stacked capacitor. (Courtesy of T. Kitayama, Mitsubishi Electric Corporation.[72])

Figure 10.17) of a 1 Gb DRAM test site with 140 nm gates (1995), (3) fabrication of a 4 Gb DRAM test site with 240 nm pitch and four x-ray levels by a joint Toshiba/NTT team (1996), (4) fabrication by IBM of a fully functional 64 kb static RAM (SRAM) with 200 nm features (1994), (5) fabrication by NTT of CMOS logic devices with 12 kb SRAMs and 200 nm features (1995), (6) fabrication by Motorola of a fully functional 0.375 μm, 1 Mb SRAM with three levels by x-ray lithography (1996), and (7) fabrication by IBM of 100 nm CMOS test circuits, including ring oscillators with 16 psec delay times (1995), and (8) fabrication by IBM of a fully functional 400 MHz PowerPC microprocessor with six million transistors, each having 180 nm (post-etch) critical dimension.[82] While poised for entry into manufacturing with a technique that could span several generations, the entrance point has continued to slip as improvements in UV optics and extensions to DUV, enhanced by clever optical and processing techniques, have postponed the need for a post-optical advanced lithography. Thus x-ray lithography continues to prepare for potential entry at a future node, perhaps at 130 nm or 100 nm.

REFERENCES

1. R. White, *How Computers Work* (Ziff-Davis, Emeryville, CA, 1997).
2. *National Technology Roadmap for Semiconductors* (Semiconductor Industry Association, San Jose, CA 95110), 1997 edition; the years of entry in Figure 10.7 and Table 10.1 reflect an April 1999 update. For future updates consult the web site http://www.sematech.org.
3. P. Rai-Choudhury, Editor, *Handbook of Microlithography, Micromachining and Microfabrication, Volume 1: Microlithography* (SPIE, Bellingham, WA, 1997).
4. J.R. Sheats and B.W. Smith, Editors, *Microlithography: Science and Technology* (Marcel Dekker, New York, 1998).
5. H.J. Levinson and W.H. Arnold, "Optical Lithography," pp. 11–138 in Ref. 3.
6. M.S. Hibbs, "System Overview of Optical Steppers and Scanners," pp. 1–107 in Ref. 4.
7. B.W. Smith, "Optics for Photolithography," pp. 171–270 in Ref. 4.
8. P. Das and U. Sengupta, "Krypton Fluoride Excimer Laser for Advanced Microlithography," pp. 271–315 in Ref. 4.
9. M.A. McCord and M.J. Rooks, "Electron Beam Lithography," pp. 139–249 in Ref. 3.
10. G. Owen and J.R. Sheats, "Electron Beam Lithography Systems", pp. 367–401 in Ref. 4.
11. A.R. Neureuther and C.A. Mack, "Optical Lithography Modeling," pp. 597–679 in Ref. 3.
12. T. Ueno, "Chemistry of Photoresist Materials," pp. 429–514; B.W. Smith, "Resist Processing," pp. 515–565; B.W. Smith and M. Hanratty, "Multilayer Resist Technology," pp. 567–614; and R.R. Kunz, "Dry Etching of Photoresists," pp. 615–644; all in Ref. 4.
13. M. Born and E. Wolf, *Principles of Optics* (Cambridge Univ. Press, 1999), Seventh Ed., Sec. 10.5.2.

14. Paraphrased from F. Cerrina, "X-Ray Lithography,"Chapter 3, p. 266 in Ref. 3.
15. J.W. Goodman, *Statistical Optics* (Wiley, New York, 1985), Chapter 7, Section 7.3.2.
16. M.M. O'Toole and A.R. Neureuther, "The Influence of Partial Coherence on Projection Printing," *Proc. SPIE 174*, 22 (1979).
17. *SVG Lithography: Micrascan Family*, company product brochure (Silicon Valley Group, Inc., Lithography Division, Wilton, CT 1998); also S.M. Reis, "The Business Behind Optical Lithography," *Opt. and Photon. News 30* (June 1998).
18. D.M. Williamson, "Catadioptic Microlithographic Reduction Lenses," p. 428 in *Proc. Int. Opt. Design Conf. 22* (OSA, Washington, DC, 1994), G.W. Forbes, Editor.
19. D. Williamson, J. McClay, K. Andresen, G. Gallatin, M. Himel, J. Ivaldi, C. Mason, A. McCullough, C. Otis, J. Shamaly, and C. Tomczyk, "Micrascan III, 0.25 μm Resolution Step and Scan System," *Proc. SPIE 2726*, 780 (1996); U.S. Patent No. 5,537,260 (16 July 1996).
20. Courtesy of G. Neubauer and B. Triplett, Intel Corporation, Santa Clara, CA.
21. G.E. Moore, "Lithography and the Future of Moore's Law," in *Electron-Beam, X-Ray, EUV, and Ion-Beam Submicrometer Lithographies for Manufacturing V* (SPIE, Bellinghom, WA, 1995), J. Warlaumont, Editor, *Proc. SPIE 2437*, 2 (1995); G.E. Moore, "Cramming More Components onto Integrated Circuits," *Electr. Mag.*, 114 (19 April 1965); G.E. Moore, in *Proc. IEEE Int. Electr. Dev. Meeting* (1975).
22. M. Rothschild, M.W. Horn, C.L. Keast, R.R. Kunz, V. Liberman, S.C. Palmateer, S.P. Doran, A.R. Forte, R.B. Goodman, J.H.C. Sedlacek, R.S. Uttaro, D. Corliss, and A. Grenville "Photolithography at 193 nm," *Lincoln Lab. J. 10*, 19 (1997); M. Rothschild et al. "How Practical is 193 nm Lithography?" *J. Vac. Sci. Technol. B 14*, 4157 (1996).
23. M. Chan, R.R. Kunz, S.P. Doran, and M. Rothschild, "Photolithography at 0.10 and 0.13 μm Using ArF Excimer Lithography in Combination with Resolution Enhancement Techniques," *J. Vac. Sci. Technol. B 15*, 2404 (1997); T.M. Bloomstein, M.W. Horn, M. Rothschild, R.R. Kunz, S.T. Palmacci, and R.B. Goodman, "Lithography with 157 nm Lasers," *J. Vac. Sci. Technol. B 15*, 2112 (1997).
24. D.M. Williamson, "The Elusive Diffraction Limit," p. 68 in *EUV Lithography* (OSA, Washington DC, 1995), F. Zernike and D. Attwood, Editors.
25. See the Sematech web site: www.sematech.org
26. L.R. Harriott, "Scattering with Angular Limitation Projection Electron Beam Lithography for Sub-Optical Lithography," *J. Vac. Sci. Technol. B 15*, 2130 (1997); H.C. Pfeiffer et al., "PREVAIL – A Next Generation Lithography," *J. Vac. Sci. Technol. B17* (1999).
27. A.M. Hawryluk, N.M. Ceglio, and D.P. Gaines,"Reflection Mask Technology for X-Ray Projection Lithography," *J. Vac. Sci. Technol. B 7*, 1702 (1989).
28. H. Kinoshita, K. Kurihara, Y. Ishii, and Y. Torii, "Soft X-Ray Reduction Lithography Using Multilayer Mirrors," *J. Vac. Sci. Technol. B 7*, 1648 (1989); also see H. Kinoshita, "SR Lithography for Manufacturing Integrated Circuit Beyond 100 nm," *J. Jpn. Soc. Synchr. Rad. Res. 11*, 51 (1998).
29. J.E. Bjorkholm, J. Bokor, R. Eichner, R.R. Freeman, J. Gregus, T.E. Jewell, W.M. Mansfield, A.A. MacDowell, E.L. Rabb, W.T. Silfvast, L.H. Szeto, D.M. Tennant, W.K. Waskiewicz, D.L. White, D.L. Windt, O.R. Wood III, and J.H. Bruning, "Reduction Imaging at 14 nm Using Multilayer Coated Optics: Printing of Features Smaller than 0.1 μm," *J. Vac. Sci. Technol. B 8*, 1509 (1990).
30. J. Bokor, Editor, *Soft X-ray Projection Lithography*, OSA Proc., Vol. 12 (OSA, Washington, DC, 1991).
31. A.M. Hawryluk and R.H. Stulen, Editors, *Soft X-Ray Projection Lithography*, OSA Proc., Vol. 18 (OSA, Washington, DC, 1993).
32. F. Zernike and D.T. Attwood, Editors, *Extreme Ultraviolet Lithography*, OSA Proc., Vol. 23 (OSA, Washington, DC, 1995).
33. G.D. Kubiak and D.R. Kania, Editors, *Extreme Ultraviolet Lithography*, OSA Trends in Optics and Photonics, Vol. 4 (OSA, Washington DC, 1996).
34. Y.Vladimirsky, Editor, *Emerging Lithographic Technologies II*, *Proc. SPIE 3331* (SPIE, Bellingham, WA, 1998).
35. C.W. Gwyn, R.H. Stulen, D.W. Sweeney, and D.T. Attwood, "Extreme Ultraviolet Lithography," *J. Vac. Sci. Techn. B 16* (1998); also see R. Stulen, D. Sweeney, C. Gwyn, and D. Attwood, "Progress in the Development of Extreme Ultraviolet Lithography," *Proc. SPIE 3676* (1999);

S. Okazaki, "The EUV Program in Japan," *Proc. SPIE 3676* (1999); J.P.H. Benschop, W. Kaiser, and D.C. Ockwell, "EUCLIDES, the European EUVL Program" SPIE 3676 (1999).

36. R.H. Stulen and D.W. Sweeney, "EUV Lithography," *IEEE J. Quant. Electr.* (1999); also S. Stulen et al., *Proc. SPIE 3676* (1999); H. Kinoshita, "SR Lithography for Manufacturing Integrated Circuit beyond 100 nm" (in Japanese), *J. Jpn. Soc. Synchr. Rad. Res. 11*, 51 (1998).
37. C. Montcalm, E. Spiller, M. Wedowski, E. M. Gullikson, and J. A. Folta, "Multilayer Coatings of 10× Projection Optics for Extreme Ultraviolet Lithography," Proc. SPIE *3676* (1999); C. Montcalm, S. Bajt, P.B. Mirkarimi, E. Spiller, F.J. Weber, and J.A. Folta, "Multilayer Reflective Coatings for Extreme Ultraviolet Lithography," p. 42 in Ref. 34.
38. D.W. Sweeney, R. Hudyma, H.N. Chapman, and D. Shafer, "EUV Optical Design for a 100 nm CD Imaging System," p. 2 in Ref. 34,
39. J.S. Taylor, G.E. Sommargren, D.W. Sweeney, and R.M. Hudyma, "The Fabrication and Testing of Optics for EUV Projection Lithography," p. 580 in Ref. 34.
40. K.M. Skulina, C.S. Alford, R.M. Bionta, D.M. Makowicki, E.M. Gullikson, R. Sonfli, J.B. Kortright, and J.H. Underwood, "Molybdenum–Silicon Multilayer Mirrors for the Extreme Ultraviolet," *Appl. Opt. 34*, 3727 (1996).
41. T.D. Nguyen and T.W. Barbee, "Residual Stress in Mo/Si and Mo_2C/Si Multilayers," *Proc. SPIE 3444*, 543 (1998).
42. J.H. Underwood and E.M. Gullikson, "Beamline for Measurement and Characterization of Multilayer Optics for EUV Lithography," p. 52 in Ref. 34.
43. C. Montcalm, E. Spiller, J.A. Folta, and M. Wedowski, "Multilayer Coating of 10× Projection Optics for Extreme Ultraviolet Lithography," *Proc. SPIE 3676* (1999); J.A. Folta, S. Bajt, T.W. Barbee, F.R. Grabner, P.B. Mirkarimi, C. Montcalm, T. Nguyen, M.A. Schmidt, E. Spiller, C.C. Walton, and M. Wedowski, "Advances in Multilayer Reflective Coatings for Extreme Ultraviolet Lithography," *Proc. SPIE 3676* (1999); also see E. Spiller, F.J. Weber, C. Montcalm, S.L. Baker, E.M. Gullikson, and J.H. Underwood, "Multilayer Coating and Tests of a 10× Extreme Ultraviolet Lithographic Camera," p. 62 in Ref. 34.
44. J.E. Goldsmith, J.E.M. Goldsmith, K.W. Berger, D.R. Bozman, G.F. Cardinale, D.R. Folk, C.C. Henderson, D.J. O'Connell, A.K. Ray-Chaudhuri, K.D. Stewart, D.A. Tichenor, H.N. Chapman, R.J. Gaughan, R.M. Hudyma, C. Montcalm, E.A. Spiller, J.S. Taylor, J.D. Williams, K.A. Goldberg, E.M. Gullikson, P. Naulleau, and J.L. Cobb, "Sub-100 nm Imaging with the EUV 10× Microstepper," *Proc. SPIE 3676* (1999).
45. G.D. Kubiak, L.J. Bernardez, and K. Krenz, "High-Power Extreme Ultraviolet Source Based on Gas Jets," p. 81 in Ref. 34 also see W. Silfvast, N. Fornaciari, and G. Kubiak, "A High Power Discharge-Pumped Source at 13.5 nm and 11.4 nm for EUVL," *Proc. SPIE 3676* (1999).
46. C.C. Henderson, D. Wheeler, T. Pollagi, D. O'Connell, J. Goldsmith, A. Fisher, G.F. Cardinale, J. Hutchinson, and V. Rao, "Top Surface Imaging Resists for EUV Lithography," p. 32 in Ref. 34; C.C. Henderson, J.L. Cobb, V. Rao, U. Okoroanyanwu, R.L. Brainard, and J.M. Calbert, "Ultrathin Photoresist for Extreme Ultraviolet Lithography," *Proc. SPIE 3676* (1999); G.F. Cardinale, C.C. Henderson, J.E.M. Goldsmith, P.J.S. Mangat, J. Cobb, and S.D. Hector, "Demonstration of Pattern Transfer into Sub-100 nm Polysilicon Line/Space Features Patterned with Extreme Ultraviolet Lithography," *J. Vac. Sci. Technol. B 17*, (1999).
47. K.B. Nguyen, G.F. Cardinale, D.A. Tichenor, G.D. Kubiak, K. Berger, A.K. Ray-Chaudhuri, Y. Perras, S.J. Haney, R. Nissen, K. Krentz, R.H. Stulen, H. Fujioka, C. Hu, J. Borker, D.M. Tennant, and L.A. Fetter, "Fabrication of MOS Devices with Extreme Ultraviolet Lithography," *J. Vac. Sci. Technol. B 14*, 4188 (1996).
48. H. Kinoshita, T. Watanabe, M. Niibe, M. Ito, H. Oizumi, H. Yamanashi, K. Murakami, T. Oshino, Y. Platinov, and N. Grupido, "Three-Aspherical-Mirror System for EUV Lithography," p. 20 in Ref. 34; also see T. Watanabe, K. Mashima, M. Niibe, and H. Kinoshita, "A Novel Design of Three-Aspherical-Mirror Imaging Optics for Extreme Ultra-Violet Lithography," *Jpn. J. Appl. Phys. 36*, 7597 (1997).
49. D.L. Windt and W.K. Waskiewicz, "Multilayer Facilities Required for Extreme Ultraviolet Lithography," *J. Vac. Sci. Technol. B 12*, 3826 (1994).

50. J.H. Underwood, "Reflective Multilayer Coatings for EUV Projection Lithography," p. 162 in Ref. 33.
51. D. Attwood, E. Anderson, P. Batson, R. Beguiristain, J. Bokor, K. Goldberg, E. Gullikson, K. Jackson, K. Nguyen, M. Koike, H. Medecki, S. Mrowka, R. Tackaberry, E. Tejnil, and J. Underwood, "At-Wavelength Metrologies for Extreme Ultraviolet Lithography" (in Japanese), *J. Future Electr. Devices 8*, 17 (1997).
52. G.E. Sommargren, "Phase Shifting Diffraction Interferometry for Measuring Extreme Ultraviolet Optics," p. 108 in Ref. 33.
53. H. Medecki, E. Tejnil, K. Goldberg, and J. Bokor, "A Phase-Shifting Point Diffraction Interferometer," *Opt. Lett. 21* 1526 (1 October 1996); H. Medecki, U.S. Patent 5,835,217 (10 Nov. 1998).
54. P. Naulleau, K. Goldberg, S. Lee, C. Chang, C. Bresloff, P. Batson, D. Attwood, and J. Bokor, "Characterization of the Accuracy of EUV Phase-Shifting Point Diffraction Interferometry," p. 114 in Ref. 34; K.A. Goldberg, P. Naulleau, S. Lee, C. Bresloff, C. Henderson, D. Attwood, and J. Bokor, "High-Accuracy Interferometry of EUV Lithographic Optical Systems," *J. Vac. Sci. Technol. B 16, 3435* (1988); K.A. Goldberg, P. Naulleau, H.N. Chapman, R.J. Gaughan, and J. Bokor, "Direct Comparison of EUV and Visible Light Interferometries," *Proc. SPIE 3676* (1999).
55. E.M. Gullikson, "Scattering from Normal Incidence EUV Optics," p. 72 in Ref. 34.
56. K. Nguyen, T. Mizota, T. Haga, H. Kinoshita, and D. Attwood, "Imaging of Extreme Ultraviolet Lithographic Masks with Programmed Substrate Defects," *J. Vac. Sci. Technol. B 12*, 3833 (1994); K. Nguyen, Ph.D. thesis, Department of Electrical Engineering and Computer Science, University of California, Berkeley (1994).
57. S. Jeong, L.E. Johnson, Y. Lin, S. Rekawa, P.Y. Yan, J.H. Underwood, and J. Bokor, "Actinic EUVL Mask Defect Inspection Systems," *Proc. SPIE 3676* (1999); S. Jeong, M. Ider, L. Johnson, Y. Lin, P. Batson, L. Levesque, P. Kearney, P.-Y. Yan, E. Gullikson, J.H. Underwood, and J. Bokor, "Actinic Detection of EUVL Mask Blank Defects," *Proc. SPIE 3546*, 524 (1998).
58. J.S. Taylor, H.N. Chapman, R.M. Hudyma, and G.E. Sommargren, "An EUVL Projection System for Sub-80 nm Imaging," *Proc. SPIE 3676* (1999); D.W. Sweeney, R. Stulen, D. Attwood, and C. Gwyn, "Progress on the Development of an EUV Lithography System," *J. Vac. Sci. Technol. B 17* (1999).
59. E. Spears and H.I. Smith, "High Resolution Pattern Replication Using Soft X-Rays," *Electr. Lett. 8*, 102 (1972); E. Spears and H.I. Smith, "X-Ray Lithography – A High Resolution Replica Process," *Solid State Technol. 15*, 21 (1972).
60. E. Spilller, D.E. Eastman, R. Feder, W.D. Grobman, W. Gudat, and J. Topalian, "Application of Synchrotron Radiation to X-Ray Lithography," *J. Appl. Phys. 47*, 5450 (1976).
61. B. Fay, J. Trotel, Y. Petroff, R. Pinchaux, and P. Thiry, "X-Ray Replication of Masks Using the Synchrotron Radiation Produced by the ACO Storage Ring," *Appl. Phys. Lett. 29*, 370 (1976).
62. H. Aritome, T. Nishimura, H. Kotani, S. Matsui, O. Nakagawa, and S. Namba, "X-Ray Lithography by Synchrotron Radiation of INS-ES," *J. Vac. Sci. Technol. 15*, 992 (1978).
63. R.D. Haelbich, J.P. Silverman, and J.M. Warlaumont, "Synchrotron Radiation X-Ray Lithography," *Nucl. Instrum. Meth. 222*, 291 (1984).
64. N. Atoda, H. Kawakatsu, H. Tanino, S. Ichimure, M. Hirata, and K. Koh, "Diffraction Effects on Pattern Replication with Synchrotron Radiation," *J. Vac. Sci. Technol. B 1*, 1267 (1983).
65. M. Suzuki, T. Kaneko, and Y. Saitoh, "Replicated Resist Pattern Resolution with Synchrotron Orbital Radiation," *J. Vac. Sci. Technol. B 7*, 47 (1989).
66. F. Cerrina, "Recent Advances in X-Ray Lithography," *Jpn. J. Appl. Phys. 31*, 4178 (1992); J.Z.Y. Guo and F. Cerrina, "Modeling X-Ray Proximity Lithography," *IBM J. Res. Dev. 37*, 331 (1993).
67. S.D. Hector, M.L. Schattenburg, E.H. Anderson, W. Chu, V.W. Wong, and H.I. Smith, "Modeling and Experimental Verification of Illumination and Diffraction Effects on Image Quality in X-Ray Lithography," *J. Vac. Sci. Technol. B 10*, 3164 (1992); S.D. Hector, H.I. Smith, and M.L. Schattenburg, "Simultaneous Optimization of Spectrum, Spatial Coherence, Gap, Feature Bias, and Absorber Thickness in Synchrotron-Based X-Ray Lithography," *J. Vac. Sci. Technol. B* 11, 2981 (1993).
68. S. Hector, V. Pol, M. Khan, S. Bollepalli, and F. Cerrina, "Investigation of Mask Pattern Proximity Correction to Reduce Image Shortening in X-Ray Lithography," *Microelectr. Engrg. 41/42*, 271 (1998); S. Hector, V. Pol, A. Krasnoperova, J. Maldonado, A. Flamholz, D. Heald, C. Stahlhammer,

D. Galburt, R. Amodero, T. Donohue, S. Wind, J. Buchigniano, R. Viswanathan, M. Kahn, S. Bollepalli, and F. Cerrina, "X-Ray Lithography for $\leq$ 100 nm Ground Rules in Complex Patterns," *J. Vac. Sci. Technol. B 15*, 2517 (1997).

69. K. Early, M.L. Schattenburg, and H.I. Smith, "Absence of Resolution Degradation in X-Ray Lithography for λ from 4.5 nm to 0.83 nm," *Microelectron. Engrg. 11*, 317 (1990).
70. L.E. Ocola and F. Cerrina, "Parametric Modeling of Photoelectron Effects in X-Ray Lithography," *J. Vac. Sci. Technol. B 11*, 2839 (1993).
71. F. Cerrina, "X-Ray Lithography," Chapter 3, pp. 251–319, in *Handbook of Microlithography, Micromachining and Microfabrication, Volume 1: Microlithography* (SPIE, Bellingham, WA, 1997).
72. Y. Nishioka, K. Shiozawa, T. Oishi, K. Kanamoto, Y. Tokuda, H. Sumitani, S. Aya, H. Yabe, K. Itoga, T. Hilfumi, K. Marumoto, T. Kuroiwa, T. Kawahara, T. Nishikawa, T. Oomori, T. Fujino, S. Yamamoto, S. Uzawa, M. Kimata, M. Nunoshita, and H. Abe, "Giga-bit Scale DRAM Cell with New Simple Ru/(Ba,Sr)Ti03/Ru Stacked Capacitors Using X-Ray Lithography," p. 903 in *Int. Electron. Dev. Meet. Tech. Dig.* (IEEE, New York, 1995); also see S. Aya, H. Yabe, K. Kise, K. Kitamura, S. Ami, K. Sasaki, H. Sumitani, and K. Marumoto, "X-Ray Mask Fabrication by Ultra-Low Stress Film Deposition and High Acceleration Voltage Electron Beam Writing Technologies, *J. Vac. Sci. Technol. B* (to be published).
73. S. Ishihara, "The Development of SOR Lithography Technology," *NTT Rev. 7*, 18 (1995).
74. J.P. Silverman, "X-Ray Lithography: Status, Challenges, and Outlook for 0.13 μm," *J. Vac. Sci. Technol. B 15*, 2117 (1997).
75. D.E. Andrews, M.L. Wilson, A.I. Smith, V.C. Kempson, A.L. Purvis, R.J. Anderson, A.S. Bhutta, and A.R. Jorden, "Helios: A Compact Superconducting X-Ray Source for Production Lithography," *Proc. SPIE 1263*, 124 (1990); C.N. Archie, "Performance of the IBM Synchrotron X-Ray Source for Lithography," *IBM J. Res. Dev. 37*, 373 (1993).
76. J.P. Silverman, C.N. Archie, J.M. Oberschmidt, and R.P. Rippstein, "Performance of a Wide-Field Flux Delivering System for Synchrotron X-Ray Lithography," *J. Vac. Sci. Technol. B 11*, 2976 (1993).
77. K. Deguchi, K. Miyoshi, T. Ishii, and T. Marsuda, "Patterning Characteristics of a Chemically-Amplified Negative Resist in Synchrotron Radiation Lithography," *Jpn. J. Appl. Phys. 31*, 2954 (1992); K. Deguchi, K. Miyoshi, H. Ban, H. Kyuragi, S. Konaka, and T. Matsuda, "Application of X-Ray Lithography with a Single-Layer Resist Process to Sub-Quarter Micron Large Scale Integrated Circuit Fabrication," *J. Vac. Sci. Technol. B 10*, 3145 (1992).
78. K. Deguchi, K. Miyoshi, M. Oda, T. Matsuda, A. Ozawa, and T. Yoshihara, "Extendibility of Synchrotron Radiation Lithography to the Sub-100 nm Region," *J. Vac. Sci. Technol. B 14*, 4294 (1996).
79. S. Hector, "Status and Future of X-Ray Lithography," *Microelectr. Engrg. 41/42*, 25 (1998).
80. R. Viswanathan, R.E. Acosta, D. Seeger, H. Voelker, A. Wilson, I. Babich, J. Maldonado, J. Warlaumont, O. Vladimirsky, and F. Hohn, "Fully Scaled 0.5 μm Metal-Oxide-Semiconductor Circuits by Synchrotron X-Ray Lithography: Mask Fabrication and Characterization," *J. Vac. Sci. Technol. B 6*, 2196 (1988).
81. R. Viswanathan et al., "Fabrication of High Performance 512K Static Random Access Memories on 0.25 μm Complimentary Metal-Oxide Semiconductor Technology Using X-Ray Lithography, *J. Vac. Sci. Technol. B 11*, 2910 (1993).
82. J.S. Silverman, presented at Next Generation Lithography Workshop (December 1998); also see R. De Jule, "Next Generation Lithography Tools: The Choices Narrow," Semiconductor International *22*, 48 (March 1999).

HOMEWORK PROBLEMS

Homework problems for each chapter will be found at the website:
http://www.coe.berkeley.edu/AST/sxreuv

Appendix A

UNITS AND PHYSICAL CONSTANTS

A.1 THE INTERNATIONAL SYSTEM OF UNITS (SI)

TABLE A.1. SI base units.[1, 2]

Quantity	Name of unit	Unit symbol
Length	meter	m
Mass	kilogram	kg
Time	second	s
Electric current	ampere	A
Thermodynamic temperature	kelvin	K
Amount of substance	mole	mol
Luminous intensity	candela	cd

TABLE A.2. SI prefixes.

Factor	Prefix	Symbol	Factor	Prefix	Symbol
10^{24}	yotta	Y	10^{-1}	deci	d
10^{21}	zetta	Z	10^{-2}	centi	c
10^{18}	exa	E	10^{-3}	milli	m
10^{15}	peta	P	10^{-6}	micro	μ
10^{12}	tera	T	10^{-9}	nano	n
10^{9}	giga	G	10^{-12}	pico	p
10^{6}	mega	M	10^{-15}	femto	f
10^{3}	kilo	k	10^{-18}	atto	a
10^{2}	hecto	h	10^{-21}	zepto	z
10^{1}	deka	da	10^{-24}	yocto	y

TABLE A.3. Examples of derived units.

Quantity (symbol)	Name of unit	Unit symbol	Equivalent
Plane angle (θ)	radian	rad	$\mathrm{m/m} = 1$
Solid angle (Ω)	steradian	sr	$\mathrm{m^2/m^2} = 1$
Velocity (v)			m/s
Acceleration (a)			$\mathrm{m/s^2}$
Frequency (f)	hertz	Hz	$\mathrm{s^{-1}}$
Force (F)	newton	N	$\mathrm{kg \cdot m/s^2}$
Pressure (P)	pascal	Pa	$\mathrm{N/m^2}$
Energy ($\mathcal{E}$)	joule	J	$\mathrm{N \cdot m}$, $\mathrm{kg \cdot m^2/s^2}$
Momentum (p)			$\mathrm{N \cdot s}$, $\mathrm{kg \cdot m/s}$
Power (P)	watt	W	J/s
Electric charge (q)	coulomb	C	$\mathrm{A \cdot s}$
Electric potential (V)	volt	V	J/C, W/A
Resistance (R)	ohm	Ω	V/A
Capacitance (C)	farad	F	C/V
Magnetic flux (ϕ)	weber	Wb	$\mathrm{V \cdot s}$
Inductance (L)	henry	H	Wb/A
Electric field strength (E)			V/m, N/C
Electric displacement (D)			$\mathrm{C/m^2}$
Magnetic flux density (B)	tesla	T	$\mathrm{Wb/m^2}$, $\mathrm{N/(A \cdot m)}$
Magnetic field strength (H)			A/m
Temperature (T)	degree Celsius	$^\circ$C	$\mathrm{K} - 273.15$
Intensity (I)			$\mathrm{J \cdot s^{-1} \cdot m^{-2}}$
Brightness (B)			$\mathrm{J \cdot s^{-1} \cdot m^{-2} \cdot rad^{-2}}$

TABLE A.4. Conversion factors.

Length	angstrom	$1\ \text{Å} = 10^{-10}$ m
Area	barn	$1\ \text{barn} = 10^{-28}\ \mathrm{m^2}$
Volume	liter	$1\ \mathrm{L} = 10^{-3}\ \mathrm{m^3} = 1000\ \mathrm{cm^3}$
Plane angle	degree	$1^\circ = (\pi/180)$ rad $\simeq 17.45$ mrad
	arcminute	$1' = 1/60^\circ = (\pi/10{,}800)$ rad $\simeq 290.9\ \mu$rad
	arcsecond	$1'' = 1/60' = (\pi/648{,}000)$ rad $\simeq 4.848\ \mu$rad
Mass	atomic mass unit	$m_u = 1.660{,}540{,}2(10) \times 10^{-27}$ kg
		1 dalton = 1 amu
Time	minute	1 min = 60 s
	hour	1 h = 60 min = 3600 s
	day	1 d = 24 h = 86,400 s
Pressure	standard atmosphere	1 atm = 101, 325 Pa
		1 atm = 760 mmHg = 760 torr
	bar	$1\ \text{bar} = 10^5$ Pa
Acceleration	gravitational accel. at earth's surface	$g = 9.806\ 65\ \mathrm{m/s^2}$
Energy	electron volt	$1\ \mathrm{eV} = 1.602{,}177{,}33(49) \times 10^{-19}$ J
	calorie	1 cal = 4.1868 J
Absorbed energy	gray	1 Gy = 100 rad = 1 J/kg
Magnetic flux density	gauss	$1\ \mathrm{G} = 10^{-4}\ \mathrm{T} = 10^{-4}\ \mathrm{Wb/m^2}$
Wavelength in vacuum	photon energy	$\lambda \cdot \hbar\omega = hc = 1239.842\ \mathrm{eV} \cdot$ nm
Molar definition	atomic mass unit	$m_\mathrm{u} \cdot N_A = 1\ \mathrm{g} = 10^{-3}$ kg (exactly)

A.2 PHYSICAL CONSTANTS[3, 4]

TABLE A.5.

Quantity	Symbol	Value[a]	Units
Speed of light in vacuum	c	299,792,458 (exactly)	$\mathrm{m \cdot s^{-1}}$
Permeability of vacuum	μ_0	$4\pi \times 10^{-7}$ (exactly)	$\mathrm{N \cdot A^{-2}}$
Permittivity of vacuum	ϵ_0	$1/(\mu_0 c^2) = 8.854\ 187\ 817...$	$10^{-12}\ \mathrm{F \cdot m^{-1}}$
Planck's constant	h	4.135,669,2(12)	$10^{-15}\ \mathrm{eV \cdot s}$
Planck's constant/2π	$\hbar$	6.582,122,0(20)	$10^{-16}\ \mathrm{eV \cdot s}$
Electron charge	e	1.602,177,33(49)	$10^{-19}\ \mathrm{C}$
Electron mass	m	9.109,389,7(54)	$10^{-31}\ \mathrm{kg}$
Electron rest energy	mc^2	0.510,999,06(15)	MeV
Proton mass	m_p	1.672,623,1(10)	$10^{-27}\ \mathrm{kg}$
Neutron mass	m_n	1.674,928,6(10)	$10^{-27}\ \mathrm{kg}$
Atomic mass unit $[m(^{12}\mathrm{C})/12]$	m_u	1.660,540,2(10)	$10^{-27}\ \mathrm{kg}$
Rydberg constant $(me^4/32\pi^2\epsilon_0^2\,\hbar^2)$	$R_\infty hc$	13.605,698,1(40)	eV
Bohr radius $(4\pi\epsilon_0^2\,\hbar^2/me^2)$	a_0	0.529,177,249(24)	$10^{-10}\ \mathrm{m}$
Classical electron radius$(e^2/4\pi\epsilon_0 mc^2)$	r_e	2.817,940,92(38)	$10^{-15}\ \mathrm{m}$
Thomson cross section $(8\pi r_e^2/3)$	σ_e	0.665,246,16(18)	$10^{-28}\ \mathrm{m^2}$
Fine-structure constant $(e^2/4\pi\epsilon_0\,\hbar c)$	α	7.297,353,08(33)	10^{-3}
Compton wavelength (h/mc)	λ_C	2.426, 310,58(22)	$10^{-12}\ \mathrm{m}$
Bohr magneton $(e\hbar/2m)$	μ_B	5.788,382,63(52)	$10^{-5}\ \mathrm{eV \cdot T^{-1}}$
Nuclear magneton $(e\,\hbar/2m_p)$	μ_N	3.152,451,66(28)	$10^{-8}\ \mathrm{eV \cdot T^{-1}}$
Avogadro's number	N_A	6.022,136,7(36)	$10^{23}\ \mathrm{mol^{-1}}$
Boltzmann constant (R/N_A)	κ	8.617,385(73)	$10^{-5}\ \mathrm{eV \cdot K^{-1}}$
Stefan–Boltzmann constant $[(\pi^2/60)\kappa^4/\hbar^3c^2]$	σ	5.670,51(19)	$10^{-8}\ \mathrm{W \cdot m^{-2} \cdot K^{-4}}$
Universal (molar) gas constant	R	8.314,510(70)	$\mathrm{J \cdot\ mol^{-1} \cdot K^{-1}}$
Molar volume (ideal gas) (RT/P) (at 273.15 K, 101,325 Pa)	V_m	22,414.10(19)	$\mathrm{cm^3 \cdot mol^{-1}}$
Loschmidt's number (N_A/V_m)	n_L	2.686,763(23)	$10^{25}\ \mathrm{m^{-3}}$
Photon energy–wavelength product	hc	1239.8424(04)	$\mathrm{eV \cdot nm}$

[a] The numbers in parentheses indicate the uncertainties in the last digits. For example, $h = 4.1356692(12)$ is equivalent to $h = 4.1356692 \pm 0.0000012$.

REFERENCES

1. R.A. Nelson, "Guide for Metric Practice," *Phys. Today BG 15* (August 1995).
2. Inst. Electr. Electron. Eng., "American National Standard for Metric Practice," ANSI/IEEE Std. 268–1992 (IEEE, New York, 1992).
3. E.R. Cohen and B.N. Taylor, "The Fundamental Physical Constants," *Phys. Today*, p. BG9 (August 1995).
4. http://physics.nist.gov/PhysRefData/contents-constants.html

Appendix B

ELECTRON BINDING ENERGIES, PRINCIPAL K- AND L-SHELL EMISSION LINES, AND AUGER ELECTRON ENERGIES

TABLE B.1. Electron binding energies in electron volts for the elements in their natural forms.[a]

Element	K 1s	L_1 2s	L_2 $2p_{1/2}$	L_3 $2p_{3/2}$	M_1 3s	M_2 $3p_{1/2}$	M_3 $3p_{3/2}$	M_4 $3d_{3/2}$	M_5 $3d_{5/2}$	N_1 4s	N_2 $4p_{1/2}$	N_3 $4p_{3/2}$
1 H	13.6											
2 He	24.6[b]											
3 Li	54.7[b]											
4 Be	111.5[b]											
5 B	188[b]											
6 C	284.2[b]											
7 N	409.9[b]	37.3[b]										
8 O	543.1[b]	41.6[b]										
9 F	696.7[b]											
10 Ne	870.2[b]	48.5[b]	21.7[b]	21.6[b]								
11 Na	1070.8[c]	63.5[c]	30.4[c]	30.5[b]								
12 Mg	1303.0[c]	88.6[b]	49.6[c]	49.2[c]								
13 Al	1559.6	117.8[b]	72.9[b]	72.5[b]								
14 Si	1838.9	149.7[b]	99.8[b]	99.2[b]								
15 P	2145.5	189[b]	136[b]	135[b]								
16 S	2472	230.9[b]	163.6[b]	162.5[b]								
17 Cl	2822.4	270.2[b]	202[b]	200[b]								
18 Ar	3205.9[b]	326.3[b]	250.6[b]	248.4[b]	29.3[b]	15.9[b]	15.7[b]					
19 K	3608.4[b]	378.6[b]	297.3[b]	294.6[b]	34.8[b]	18.3[b]	18.3[b]					
20 Ca	4038.5[b]	438.4[c]	349.7[c]	346.2[c]	44.3[c]	25.4[c]	25.4[c]					
21 Sc	4492.8	498.0[b]	403.6[b]	398.7[b]	51.1[b]	28.3[b]	28.3[b]					
22 Ti	4966.4	560.9[c]	461.2[c]	453.8[c]	58.7[c]	32.6[c]	32.6[c]					
23 V	5465.1	626.7[c]	519.8[c]	512.1[c]	66.3[c]	37.2[c]	37.2[c]					
24 Cr	5989.2	695.7[c]	583.8[c]	574.1[c]	74.1[c]	42.2[c]	42.2[c]					
25 Mn	6539.0	769.1[c]	649.9[c]	638.7[c]	82.3[c]	47.2[c]	47.2[c]					
26 Fe	7112.0	844.6[c]	719.9[c]	706.8[c]	91.3[c]	52.7[c]	52.7[c]					
27 Co	7708.9	925.1[c]	793.3[c]	778.1[c]	101.0[c]	58.9[c]	58.9[c]					
28 Ni	8332.8	1008.6[c]	870.0[c]	852.7[c]	110.8[c]	68.0[c]	66.2[c]					
29 Cu	8978.9	1096.7[c]	952.3[c]	932.5[c]	122.5[c]	77.3[c]	75.1[c]					
30 Zn	9658.6	1196.2[b]	1044.9[b]	1021.8[b]	139.8[b]	91.4[b]	88.6[b]	10.2[b]	10.1[b]			

(*Continued*)

TABLE B.1. (*Continued*)

Element	K 1s	$L_1$2s	L_2 2$p_{1/2}$	L_3 2$p_{3/2}$	$M_1$3s	M_2 3$p_{1/2}$	M_3 3$p_{3/2}$	M_4 3$d_{3/2}$	M_5 3$d_{5/2}$	$N_1$4s	N_2 4$p_{1/2}$	N_3 4$p_{3/2}$
31 Ga	10367.1	1299.0[b]	1143.2[c]	1116.4[c]	159.5[c]	103.5[c]	103.5[c]	18.7[c]	18.7[c]			
32 Ge	11103.1	1414.6[b]	1248.1[b]	1217.0[b]	180.1[b]	124.9[b]	120.8[b]	29.0[b]	29.0[b]			
33 As	11866.7	1527.0[b]	1359.1[b]	1323.6[b]	204.7[b]	146.2[b]	141.2[b]	41.7[b]	41.7[b]			
34 Se	12657.8	1652.0[b]	1474.3[b]	1433.9[b]	229.6[b]	166.5[b]	160.7[b]	55.5[b]	54.6[b]			
35 Br	13473.7	1782.0[b]	1596.0[b]	1549.9[b]	257[b]	189[b]	182[b]	70[b]	69[b]			
36 Kr	14325.6	1921.0	1730.9[b]	1678.4[b]	292.8[b]	222.2[b]	214.4	95.0[b]	93.8[b]	27.5[b]	14.1[b]	14.1[b]
37 Rb	15199.7	2065.1	1863.9	1804.4	326.7[b]	248.7[b]	239.1[b]	113.0[b]	112[b]	30.5[b]	16.3[b]	15.3[b]
38 Sr	16104.6	2216.3	2006.8	1939.6	358.7[c]	280.3[c]	270.0[c]	136.0[c]	134.2[c]	38.9[c]	20.3[c]	20.3[c]
39 Y	17038.4	2372.5	2155.5	2080.0	392.0[b]	310.6[b]	298.8[b]	157.7[c]	155.8[c]	43.8[b]	24.4[b]	23.1[b]
40 Zr	17997.6	2531.6	2306.7	2222.3	430.3[c]	343.5[c]	329.8[c]	181.1[c]	178.8[c]	50.6[c]	28.5[c]	27.7[c]
41 Nb	18985.6	2697.7	2464.7	2370.5	466.6[c]	376.1[c]	360.6[c]	205.0[c]	202.3[c]	56.4[c]	32.6[c]	30.8[c]
42 Mo	19999.5	2865.5	2625.1	2520.2	506.3[c]	411.6[c]	394.0[c]	231.1[c]	227.9[c]	63.2[c]	37.6[c]	35.5[c]
43 Tc	21044.0	3042.5	2793.2	2676.9	544[b]	445[b]	425[b]	257[b]	253[b]	68[b]	39[c]	39[b]
44 Ru	22117.2	3224.0	2966.9	2837.9	586.2[c]	483.5[c]	461.4[c]	284.2[c]	280.0[c]	75.0[c]	46.5[c]	43.2[c]
45 Rh	23219.9	3411.9	3146.1	3003.8	628.1[c]	521.3[c]	496.5[c]	311.9[c]	307.2[c]	81.4[b]	50.5[c]	47.3[c]
46 Pd	24350.3	3604.3	3330.3	3173.3	671.6[c]	559.9[c]	532.3[c]	340.5[c]	335.2[c]	87.6[b]	55.7[c]	50.9[c]
47 Ag	25514.0	3805.8	3523.7	3351.1	719.0[c]	603.8[c]	573.0[c]	374.0[c]	368.0[c]	97.0[c]	63.7[c]	58.3[c]
48 Cd	26711.2	4018.0	3727.0	3537.5	772.0[c]	652.6[c]	618.4[c]	411.9[c]	405.2[c]	109.8[c]	63.9[c]	63.9[c]
49 In	27939.9	4237.5	3938.0	3730.1	827.2[c]	703.2[c]	665.3[c]	451.4[c]	443.9[c]	122.7[c]	73.5[c]	73.5[c]
50 Sn	29200.1	4464.7	4156.1	3928.8	884.7[c]	756.5[c]	714.6[c]	493.2[c]	484.9[c]	137.1[c]	83.6[c]	83.6[c]
51 Sb	30491.2	4698.3	4380.4	4132.2	946[c]	812.7[c]	766.4[c]	537.5[c]	528.2[c]	153.2[c]	95.6[c]	95.6[c]
52 Te	31813.8	4939.2	4612.0	4341.4	1006[c]	870.8[c]	820.8[c]	583.4[c]	573.0[c]	169.4[c]	103.3[c]	103.3[c]
53 I	33169.4	5188.1	4852.1	4557.1	1072[b]	931[b]	875[b]	631[b]	620[b]	186[b]	123[b]	123[b]
54 Xe	34561.4	5452.8	5103.7	4782.2	1148.7[b]	1002.1[b]	940.6[b]	689.0[b]	676.4[b]	213.2[b]	146.7	145.5[b]
55 Cs	35984.6	5714.3	5359.4	5011.9	1211[b]	1071[b]	1003[b]	740.5[b]	726.6[b]	232.3[b]	172.4[b]	161.3[b]
56 Ba	37440.6	5988.8	5623.6	5247.0	1293[b]	1137[b]	1063[b]	795.7[b]	780.5[b]	253.5[c]	192178	.6[c]
57 La	38924.6	6266.3	5890.6	5482.7	1362[b]	1209[b]	1128[b]	853[b]	836[b]	247.7[b]	205.8	196.0[b]
58 Ce	40443.0	6548.8	6164.2	5723.4	1436[b]	1274[b]	1187[b]	902.4[b]	883.8[b]	291.0[b]	223.2	206.5[b]
59 Pr	41990.6	6834.8	6440.4	5964.3	1511.0	1337.4	1242.2	948.3[b]	928.8[b]	304.5	236.3	217.6
60 Nd	43568.9	7126.0	6721.5	6207.9	1575.3	1402.8	1297.4	1003.3[b]	980.4[b]	319.2[b]	243.3	224.6
61 Pm	45184.0	7427.9	7012.8	6459.3	—	1471.4	1356.9	1051.5	1026.9	—	242	242
62 Sm	46834.2	7736.8	7311.8	6716.2	1722.8	1540.7	1419.8	1110.9[b]	1083.4[b]	347.2[b]	265.6	247.4
63 Eu	48519.0	8052.0	7617.1	6976.9	1800.0	1613.9	1480.6	1158.6[b]	1127.5[b]	360	284	257
64 Gd	50239.1	8375.6	7930.3	7242.8	1880.8	1688.3	1544.0	1221.9[b]	1189.6[b]	378.6[b]	286	270.9
65 Tb	51995.7	8708.0	8251.6	7514.0	1967.5	1767.7	1611.3	1276.9[b]	1241.1[b]	396.0[b]	322.4[b]	284.1[b]
66 Dy	53788.5	9045.8	8580.6	7790.1	2046.8	1841.8	1675.6	1332.5	1292.6[b]	414.2[b]	333.5[b]	293.2[b]
67 Ho	55617.7	9394.2	8917.8	8071.1	2128.3	1922.8	1741.2	1391.5	1351.4	432.4[b]	343.5	308.2[b]
68 Er	57485.5	9751.3	9264.3	8357.9	2206.5	2005.8	1811.8	1453.3	1409.3	449.8[b]	366.2	320.2[b]
69 Tm	59398.6	10115.7	9616.9	8648.0	2306.8	2089.8	1884.5	1514.6	1467.7	470.9[b]	385.9[b]	332.6[b]
70 Yb	61332.3	10486.4	9978.2	8943.6	2398.1	2173.0	1949.8	1576.3	1527.8	480.5[b]	388.7[b]	339.7[b]

(*Continued*)

TABLE B.1. (*Continued*)

Element	K 1s	L_1 2s	L_2 $2p_{1/2}$	L_3 $2p_{3/2}$	M_1 3s	M_2 $3p_{1/2}$	M_3 $3p_{3/2}$	M_4 $3d_{3/2}$	M_5 $3d_{5/2}$	N_1 4s	N_2 $4p_{1/2}$	N_3 $4p_{3/2}$
71 Lu	63313.8	10870.4	10348.6	9244.1	2491.2	2263.5	2023.6	1639.4	1588.5	506.8[b]	412.4[b]	359.2[b]
72 Hf	65350.8	11270.7	10739.4	9560.7	2600.9	2365.4	2107.6	1716.4	1661.7	538[b]	438.2[c]	380.7[c]
73 Ta	67416.4	11681.5	11136.1	9881.1	2708.0	2468.7	2194.0	1793.2	1735.1	563.4[c]	463.4[c]	400.9[c]
74 W	69525.0	12099.8	11544.0	10206.8	2819.6	2574.9	2281.0	1871.6	1809.2	594.1[c]	490.4[c]	423.6[c]
75 Re	71676.4	12526.7	11958.7	10535.3	2931.7	2681.6	2367.3	1948.9	1882.9	625.4	518.7[c]	446.8[c]
76 0s	73870.8	12968.0	12385.0	10870.9	3048.5	2792.2	2457.2	2030.8	1960.1	658.2[c]	549.1[c]	470.7[c]
77 Ir	76111.0	13418.5	12824.1	11215.2	3173.7	2908.7	2550.7	2116.1	2040.4	691.1[c]	577.8[c]	495.8[c]
78 Pt	78394.8	13879.9	13272.6	11563.7	3296.0	3026.5	2645.4	2201.9	2121.6	725.4[c]	609.1[c]	519.4[c]
79 Au	80724.9	14352.8	13733.6	11918.7	3424.9	3147.8	2743.0	2291.1	2205.7	762.1[c]	642.7[c]	546.3[c]
80 Hg	83102.3	14839.3	14208.7	12283.9	3561.6	3278.5	2847.1	2384.9	2294.9	802.2[c]	680.2[c]	576.6[c]
81 Tl	85530.4	15346.7	14697.9	12657.5	3704.1	3415.7	2956.6	2485.1	2389.3	846.2[c]	720.5[c]	609.5[c]
82 Pb	88004.5	15860.8	15200.0	13035.2	3850.7	3554.2	3066.4	2585.6	2484.0	891.8[c]	761.9[c]	643.5[c]
83 Bi	90525.9	16387.5	15711.1	13418.6	3999.1	3696.3	3176.9	2687.6	2579.6	939[c]	805.2[c]	678.8[c]
84 Po	93105.0	16939.3	16244.3	13813.8	4149.4	3854.1	3301.9	2798.0	2683.0	995[b]	851[b]	705[b]
85 At	95729.9	17493	16784.7	14213.5	4317	4008	3426	2908.7	2786.7	1042[b]	886[b]	740[b]
86 Rn	98404	18049	17337.1	14619.4	4482	4159	3538	3021.5	2892.4	1097[b]	929[b]	768[b]
87 Fr	101137	18639	17906.5	15031.2	4652	4327	3663	3136.2	2999.9	1153[b]	980[b]	810[b]
88 Ra	103921.9	19236.7	18484.3	15444.4	4822.0	4489.5	3791.8	3248.4	3104.9	1208[b]	1057.6[b]	879.1[b]
89 Ac	106755.3	19840.	19083.2	15871.0	5002	4656	3909	3370.2	3219.0	1269[b]	1080[b]	890[b]
90 Th	109650.9	20472.1	19693.2	16300.3	5182.3	4830.4	4046.1	3490.8	3332.0	1330[b]	1168[b]	966.4[c]
91 Pa	112601.4	21104.6	20313.7	16733.1	5366.9	5000.9	4173.8	3611.2	3441.8	1387[b]	1224[b]	1007[b]
92 U	115606.1	21757.4	20947.6	17166.3	5548.0	5182.2	4303.4	3727.6	3551.7	1439[b]	1271[b]	1043.0[c]

Element	N_4 $4d_{3/2}$	N_5 $4d_{5/2}$	N_6 $4f_{5/2}$	N_7 $4f_{7/2}$	O_1 5s	O_2 $5p_{1/2}$	O_3 $5p_{3/2}$	O_4 $5d_{3/2}$	O_5 $5d_{5/2}$	P_1 6s	P_2 $6p_{1/2}$	P_3 $6p_{3/2}$
48 Cd	11.7[c]	l0.7[c]										
49 In	17.7[c]	16.9[c]										
50 Sn	24.9[c]	23.9[c]										
51 Sb	33.3[c]	32.1[c]										
52 Te	41.9[c]	40.4[c]										
53 I	50[b]	50[b]										
54 Xe	69.5[b]	67.5[b]	—	—	23.3[b]	13.4[b]	12.1[b]					
55 Cs	79.8[b]	77.5[b]	—	—	22.7	14.2[b]	12.1[b]					
56 Ba	92.6[c]	89.9[c]	—	—	30.3[c]	17.0[c]	14.8[c]					
57 La	105.3[b]	102.5[b]	—	—	34.3[b]	19.3[b]	16.8[b]					
58 Ce	109[b]	—	—	—	37.8	19.8[b]	17.0[b]					
59 Pr	115.1[b]	115.1[b]	—	—	37.4	22.3	22.3					
60 Nd	120.5[b]	120.5[b]	—	—	37.5	21.1	21.1					
61 Pm	120	120	—	—	—	—	—					
62 Sm	129	129	—	—	37.4	21.3	21.3					
63 Eu	133	127.7[b]	—	—	31.8	22.0	22.0					
64 Gd	140.5	142.6[b]	—	—	43.5[b]	20	20					
65 Tb	150.5[b]	150.5[b]	—	—	45.6[b]	28.7[b]	22.6[b]					

(*Continued*)

TABLE B.1. (*Continued*)

Element	$N_4 4d_{3/2}$	$N_5 4d_{5/2}$	$N_6 4f_{5/2}$	$N_7 4f_{7/2}$	$O_1 5s$	$O_2 5p_{1/2}$	$O_3 5p_{3/2}$	$O_4 5d_{3/2}$	$O_5 5d_{5/2}$	$P_1 6s$	$P_2 6p_{1/2}$	$P_3 6p_{3/2}$
66 Dy	153.6[b]	153.6[b]	—	—	49.9[b]	29.5	23.1					
67 Ho	160[b]	160[b]	—	—	49.3[b]	30.8[b]	24.1[b]					
68 Er	167.6[b]	167.6[b]	—	—	50.6[b]	31.4[b]	24.7[b]					
69 Tm	175.5[b]	175.5[b]	—	—	54.7[b]	31.8[b]	25.0[b]					
70 Yb	191.2[b]	182.4[b]	—	—	52.0[b]	30.3[b]	24.1[b]					
71 Lu	206.1[b]	196.3[c]	8.9[b]	7.5[b]	57.3[b]	33.6[b]	26.7[b]					
72 Hf	220.0[c]	211.5[c]	15.9[c]	14.2[c]	64.2[c]	38[b]	29.9[b]					
73 Ta	237.9[c]	226.4[c]	23.5[c]	21.6[c]	69.7[c]	42.2[b]	32.7[b]					
74 W	255.9[c]	243.5[c]	33.6[b]	31.4[c]	75.6[c]	45.3[b]	36.8[b]					
75 Re	273.9[c]	260.5[c]	42.9[b]	40.5[c]	83[c]	45.6[b]	34.6[b]					
76 0s	293.1[c]	278.5[c]	53.4[c]	50.7[c]	84[c]	58[b]	44.5[c]					
77 Ir	311.9[c]	296.3[c]	63.8[c]	60.8[c]	95.2[b]	63.0[b]	48.0[c]					
78 Pt	331.6[c]	314.6[c]	74.5[c]	71.2[c]	101[c]	65.3[b]	51.7[c]					
79 Au	353.2[c]	335.1[c]	87.6[c]	83.9[c]	107.2[b]	74.2[c]	57.2[c]					
80 Hg	378.2[c]	358.8[c]	104.0[c]	99.9[c]	127[c]	83.1[c]	64.5[c]	9.6[c]	7.8[c]			
81 Ti	405.7[c]	385.0[c]	122.2[c]	117.8[c]	136.[b]	94.6[c]	73.5[c]	14.7[c]	12.5[c]			
82 Pb	434.3[c]	412.2[c]	141.7[c]	136.9[c]	147[b]	106.4[c]	83.3[c]	20.7[c]	18.1[c]			
83 Bi	464.0[c]	440.1[c]	162.3[c]	157.0[c]	159.3[b]	119.0[c]	92.6[c]	26.9[c]	23.8[c]			
84 Po	500[b]	473[b]	184[b]	184[b]	177[b]	132[b]	104[b]	31[b]	31[b]			
85 At	533[b]	507[b]	210[b]	210[b]	195[b]	148[b]	115[b]	40[b]	40[b]			
86 Rn	567[b]	541[b]	238[b]	238[b]	214[b]	164[b]	127[b]	48[b]	48[b]	26		
87 Fr	603[b]	577[b]	268[b]	268[b]	234[b]	182[b]	140[b]	58[b]	58[b]	34	15	15
88 Ra	635.9[b]	602.7[b]	299[b]	299[b]	254[b]	200[b]	153[b]	68[b]	68[b]	44	19	19
89 Ac	675[b]	639[b]	319[b]	319[b]	272[b]	215[b]	167[b]	80[b]	80[b]	—	—	—
90 Th	712.1[c]	675.2[c]	342.4[c]	333.1[c]	290[b]	229[b]	182[b]	92.5[c]	85.4[c]	41.4[c]	24.5[c]	16.6[c]
91 Pa	743[b]	708[b]	371[b]	360[b]	310[b]	232[b]	232[b]	94[b]	94[b]	—	—	—
92 U	778.3[c]	736.2[c]	388.2[b]	377.4[c]	321[b]	257[b]	192[b]	102.8[c]	94.2[c]	43.9[c]	26.8[c]	16.8[c]

[a] Electron binding energies for the elements in their natural forms, as compiled by G.P. Williams, Brookhaven National Laboratory, in Ref. 1, Chapter 1. The energies are given in electron volts relative to the vacuum level for the rare gases and for H_2, N_2, O_2, F_2, and Cl_2; relative to the Fermi level for the metals; and relative to the top of the valence bands for semiconductors. Values are based largely on those given by J.A. Bearden and A.F. Barr, "Reevaluation of X-Ray Atomic Energy Levels," *Rev. Mod. Phys. 39*, 125 (1967); corrected in 1998 by E. Gullikson (LBNL, unpublished). For further updates consult the Web site http://www-cxro.lbl.gov

[b] From M. Cardona and L. Lay, Editors, *Photoemission in Solids I: General Principles* (Springer-Verlag, Berlin, 1978).

[c] From J.C. Fuggle and N. Mårtensson, "Core-Level Binding Energies in Metals," *J. Electron. Spectrosc. Relat. Phenom. 21*, 275 (1980).

TABLE B.2. Photon energies, in electron volts, of principal K and L shell emission lines.[a]

Element	$K\alpha_1$	$K\alpha_2$	$K\beta_1$	$L\alpha_1$	$L\alpha_2$	$L\beta_1$	$L\beta_2$	$L\gamma_1$
3 Li	54.3							
4 Be	108.5							
5 B	183.3							
6 C	277							
7 N	392.4							
8 O	524.9							
9 F	676.8							
10 Ne	848.6	848.6						
11 Na	1,040.98	1,040.98	1,071.1					
12 Mg	1,253.60	1,253.60	1,302.2					
13 Al	1,486.70	1,486.27	1,557.45					
14 Si	1,739.98	1,739.38	1,835.94					
15 P	2,013.7	2,012.7	2,139.1					
16 S	2,307.84	2,306.64	2,464.04					
17 Cl	2,622.39	2,620.78	2,815.6					
18 Ar	2,957.70	2,955.63	3,190.5					
19 K	3,313.8	3,311.1	3,589.6					
20 Ca	3,691.68	3,688.09	4,012.7	341.3	341.3	344.9		
21 Sc	4,090.6	4,086.1	4,460.5	395.4	395.4	399.6		
22 Ti	4,510.84	4,504.86	4,931.81	452.2	452.2	458.4		
23 V	4,952.20	4,944.64	5,427.29	511.3	511.3	519.2		
24 Cr	5,414.72	5,405.509	5,946.71	572.8	572.8	582.8		
25 Mn	5,898.75	5,887.65	6,490.45	637.4	637.4	648.8		
26 Fe	6,403.84	6,390.84	7,057.98	705.0	705.0	718.5		
27 Co	6,930.32	6,915.30	7,649.43	776.2	776.2	791.4		
28 Ni	7,478.15	7,460.89	8,264.66	851.5	851.5	868.8		
29 Cu	8,047.78	8,027.83	8,905.29	929.7	929.7	949.8		
30 Zn	8,638.86	8,615.78	9,572.0	1,011.7	1,011.7	1,034.7		
31 Ga	9,251.74	9,224.82	10,264.2	1,097.92	1,097.92	1,124.8		
32 Ge	9,886.42	9,855.32	10,982.1	1,188.00	1,188.00	1,218.5		
33 As	10,543.72	10,507.99	11,726.2	1,282.0	1,282.0	1,317.0		
34 Se	11,222.4	11,181.4	12,495.9	1,379.10	1,379.10	1,419.23		
35 Br	11,924.2	11,877.6	13,291.4	1,480.43	1,480.43	1,525.90		
36 Kr	12,649	12,598	14,112	1,586.0	1,586.0	1,636.6		
37 Rb	13,395.3	13,335.8	14,961.3	1,694.13	1,692.56	1,752.17		
38 Sr	14,165	14,097.9	15,835.7	1,806.56	1,804.74	1,871.72		
39 Y	14,958.4	14,882.9	16,737.8	1,922.56	1,920.47	1,995.84		
40 Zr	15,775.1	15,690.9	17,667.8	2,042.36	2,039.9	2,124.4	2,219.4	2,302.7
41 Nb	16,615.1	16,521.0	18,622.5	2,165.89	2,163.0	2,257.4	2,367.0	2,461.8
42 Mo	17,479.34	17,374.3	19,608.3	2,293.16	2,289.85	2,394.81	2,518.3	2,623.5
43 Tc	18,367.1	18,250.8	20,619	2,424.0	—	2,536.8	—	—
44 Ru	19,279.2	19,150.4	21,656.8	2,558.55	2,554.31	2,683.23	2,836.0	2,964.5
45 Rh	20,216.1	20,073.7	22,723.6	2,696.74	2,692.05	2,834.41	3,001.3	3,143.8
46 Pd	21,177.1	21,020.1	23,818.7	2,838.61	2,833.29	2,990.22	3,171.79	3,328.7
47Ag	22,162.92	21,990.3	24,942.4	2,984.31	2,978.21	3,150.94	3,347.81	3,519.59
48 Cd	23,173.6	22,984.1	26,095.5	3,133.73	3,126.91	3,316.57	3,528.12	3,716.86
49 In	24,209.7	24,002.0	27,275.9	3,286.94	3,279.29	3,487.21	3,713.81	3,920.81
50 Sn	25,271.3	25,044.0	28,486.0	3,443.98	3,435.42	3,662.80	3,904.86	4,131.12

(*Continued*)

TABLE B.2. (*Continued*)

Element	$K\alpha_1$	$K\alpha_2$	$K\beta_1$	$L\alpha_1$	$L\alpha_2$	$L\beta_1$	$L\beta_2$	$L\gamma_1$
51 Sb	26,359.1	26,110.8	29,725.6	3,604.72	3,595.32	3,843.57	4,100.78	4,347.79
52 Te	27,472.3	27,201.7	30,995.7	3,769.33	3,758.8	4,029.58	4,301.7	4,570.9
53 I	28,612.0	28,317.2	32,294.7	3,937.65	3,926.04	4,220.72	4,507.5	4,800.9
54 Xe	29,779	29,458	33,624	4,109.9	—	—	—	—
55 Cs	30,972.8	30,625.1	34,986.9	4,286.5	4,272.2	4,619.8	4,935.9	5,280.4
56 Ba	32,193.6	31,817.1	36,378.2	4,466.26	4,450.90	4,827.53	5,156.5	5,531.1
57 La	33,441.8	33,034.1	37,801.0	4,650.97	4,634.23	5,042.1	5,383.5	5,788.5
58 Ce	34,719.7	34,278.9	39,257.3	4,840.2	4,823.0	5,262.2	5,613.4	6,052
59 Pr	36,026.3	35,550.2	40,748.2	5,033.7	5,013.5	5,488.9	5,850	6,322.1
60 Nd	37,361.0	36,847.4	42,271.3	5,230.4	5,207.7	5,721.6	6,089.4	6,602.1
61 Pm	38,724.7	38,171.2	43,826	5,432.5	5,407.8	5,961	6,339	6,892
62 Sm	40,118.1	39,522.4	45,413	5,636.1	5,609.0	6,205.1	6,586	7,178
63 Eu	41,542.2	40,901.9	47,037.9	5,845.7	5,816.6	6,456.4	6,843.2	7,480.3
64 Gd	42,996.2	42,308.9	48,697	6,057.2	6,025.0	6,713.2	7,102.8	7,785.8
65 Tb	44,481.6	43,744.1	50,382	6,272.8	6,238.0	6,978	7,366.7	8,102
66 Dy	45,998.4	45,207.8	52,119	6,495.2	6,457.7	7,247.7	7,635.7	8,418.8
67 Ho	47,546.7	46,699.7	53,877	6,719.8	6,679.5	7,525.3	7,911	8,747
68 Er	49,127.7	48,221.1	55,681	6,948.7	6,905.0	7,810.9	8,189.0	9,089
69 Tm	50,741.6	49,772.6	57,517	7,179.9	7,133.1	8,101	8,468	9,426
70 Yb	52,388.9	51,354.0	5,937	7,415.6	7,367.3	8,401.8	8,758.8	9,780.1
71 Lu	54,069.8	52,965.0	61,283	7,655.5	7,604.9	8,709.0	9,048.9	10,143.4
72 Hf	55,790.2	54,611.4	63,234	7,899.0	7,844.6	9,022.7	9,347.3	10,515.8
73 Ta	57,532	56,277	65,223	8,146.1	8,087.9	9,343.1	9,651.8	10,895.2
74W	59,318.24	57,981.7	67,2443	8,397.6	8,335.2	9,672.35	9,961.5	11,285.9
75 Re	61,140.3	59,717.9	69,310	8,652.5	8,586.2	10,010.0	10,275.2	11,685.4
76 Os	63,000.5	61,486.7	71,413	8,911.7	8,841.0	10,355.3	10,598.5	12,095.3
77 Ir	64,895.6	63,286.7	73,560.8	9,175.1	9,099.5	10,708.3	10,920.3	12,512.6
78 Pt	66,832	65,112	75,748	9,442.3	9,361.8	11,070.7	11,250.5	12,942.0
79 Au	68,803.7	66,989.5	77,984	9,713.3	9,628.0	11,442.3	11,584.7	13,381.7
80 Hg	70,819	68,895	80,253	9,988.8	9,897.6	11,822.6	11,924.1	13,830.1
81 Tl	72,871.5	70,831.9	82,576	10,268.5	10,172.8	12,213.3	12,271.5	14,291.5
82 Pb	74,969.4	72,804.2	84,936	10,551.5	10,449.5	12,613.7	12,622.6	14,764.4
83 Bi	77,107.9	74,814.8	87,343	10,838.8	10,730.91	13,023.5	12,979.9	15,247.7
84 Po	79,290	76,862	8,980	11,130.8	11,015.8	13,447	13,340.4	15,744
85 At	8,152	7,895	9,230	11,426.8	11,304.8	13,876	—	16,251
86 Rn	8,378	8,107	9,487	11,727.0	11,597.9	14,316	—	16,770
87 Fr	8,610	8,323	9,747	12,031.3	11,895.0	14,770	1,445	17,303
88 Ra	8,847	8,543	10,013	12,339.7	12,196.2	15,235.8	14,841.4	17,849
89 Ac	90,884	8,767	10,285	12,652.0	12,500.8	15,713	—	18,408
90 Th	93,350	89,953	105,609	12,968.7	12,809.6	16,202.2	15,623.7	18,982.5
91 Pa	95,868	92,287	108,427	13,290.7	13,122.2	16,702	16,024	19,568
92 U	98,439	94,665	111,300	13,614.7	13,438.8	17,220.0	16,428.3	20,167.1
93 Np	—	—	—	13,944.1	13,759.7	17,750.2	16,840.0	20,784.8
94 Pu	—	—	—	14,278.6	14,084.2	18,293.7	17,255.3	21,417.3
95 Am	—	—	—	14,617.2	14,411.9	18,852.0	17,676.5	22,065.2

[a] Photon energies in electron volts of some characteristic emission lines of the elements of atomic number $3 \leq Z \leq 95$, as compiled by J. Kortright, "Characteristic X-Ray Energies," in *X-Ray Data Booklet* (Lawrence Berkeley National Laboratory Pub-490 Rev. 2, 1999). Values are largely based on those given by J.A. Bearden, "X-Ray Wavelengths," *Rev. Mod. Phys. 39*, 78 (1967), which should be consulted for a more complete listing. Updates may also be noted at the Web site http:/www-cxro.lbl.gov/data-booklet/

TABLE B.3. Curves showing Auger energies, in electron volts, for elements of atomic number $3 \leq Z \leq 92$. Only dominant energies are given, and only for principal Auger peaks. The literature should be consulted for detailed tabulations, and for shifted values in various common compounds.[1–3] (Courtesy of Physical Electronics, Inc.[1])

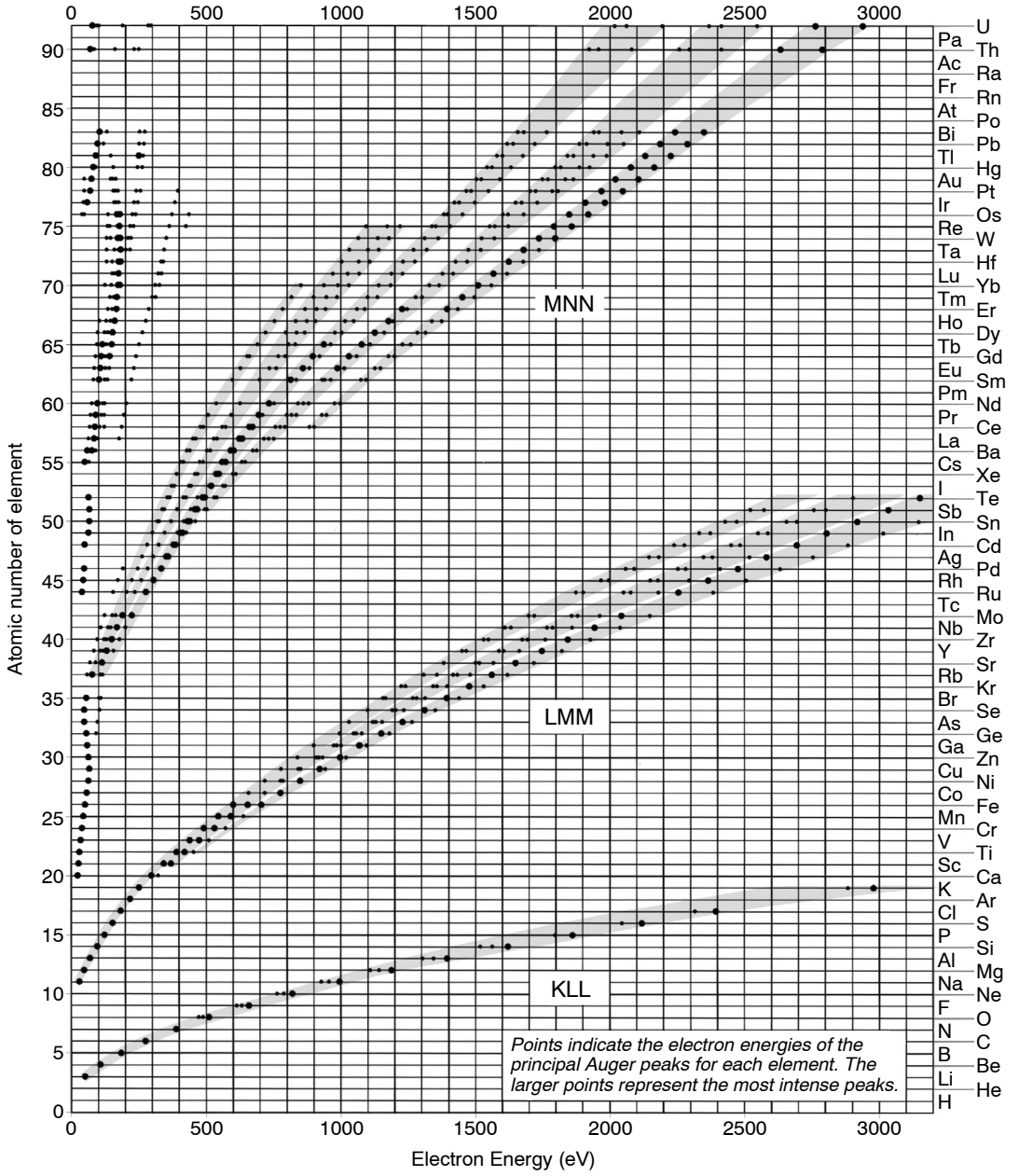

REFERENCES

1. K.D. Childs, B.A. Carlson, L.A. Vanier, J.F. Moulder, D.F. Paul, W.F. Stickle, and D.G. Watson, *Handbook of Auger Electron Spectroscopy* (Physical Electronics, Eden Prairie, MN, 1995), C.L. Hedberg, Editor.
2. J.F. Moulder, W.F. Stickle, P.E. Sobol, and K.D. Bomben, *Handbook of X-Ray Photoelectron Spectroscopy* (Physical Electronics, Eden Prairie, MN, 1995).
3. D. Briggs, *Handbook of X-Ray and Ultraviolet Photoelectron Spectroscopy* (Heyden, London, 1977).

Appendix C

ATOMIC SCATTERING FACTORS, ATOMIC ABSORPTION COEFFICIENTS, AND SUBSHELL PHOTOIONIZATION CROSS-SECTIONS

TABLE C.1. Atomic scattering factors f_1^0 and f_2^0 for several common elements in their natural form, in the approximation $\Delta\mathbf{k} \cdot \Delta\mathbf{r_s} \rightarrow \mathbf{0}$. As described in Chapter 2, Section 2.7, this approximation is satisfied for forward scattering or for long wavelengths (greater than the Bohr radius), and denoted here by the superscript zero. Also given are values for the absorption coefficient μ in cm^2/g, as described in Chapter 3, Section 3.2. Values are from Henke, Gullikson, and Davis.[1] Their procedure is to obtain μ as a function of energy by making a fit to the best available experimental data, for each element as it is commonly found in nature. Values of $f_2^0(\omega)$ are then obtained using a relationship equivalent to Eq. (3.26) as given here in Chapter 3, Section 3.2. Values for $f_1^0(\omega)$ are then calculated using Kramers–Kronig relations, equivalent to that given as Eq. (3.85a) in Chapter 3, Section 3.8.

σ_a(barns/atom) = μ(cm^2/g) × 1.67
E(keV)μ(cm^2/g) = f_2^0 × 41746.8

Hydrogen (H)
Z = 1
Atomic weight = 1.008

Energy (eV)	f_1^0	f_2^0	μ (cm^2/g)
30	1.075	3.035E–01	4.224E+05
70	1.052	5.768E–02	3.440E+04
100	1.033	2.759E–02	1.152E+04
300	1.006	2.570E–03	3.576E+02
700	1.001	3.720E–04	2.219E+01
1000	1.001	1.624E–04	6.778E+00
3000	1.000	1.202E–05	1.673E–01
7000	1.000	1.553E–06	9.262E–03
10000	1.000	6.580E–07	2.747E–03
30000	1.000	4.405E–08	6.130E–05

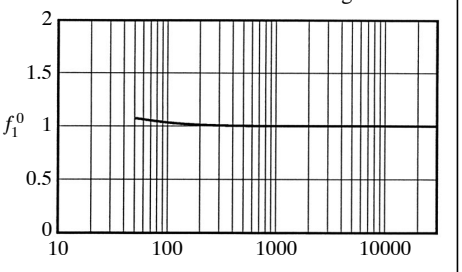

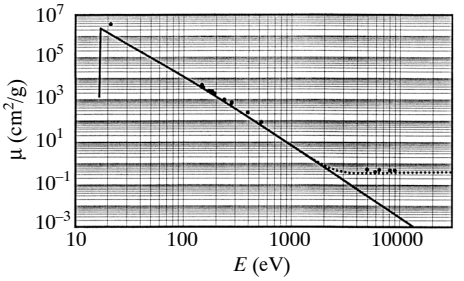

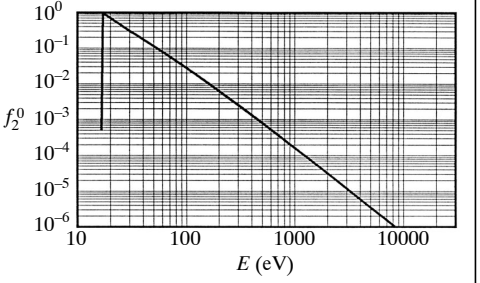

Edge Energies: K 13.6 eV

(*Continued*)

TABLE C.1. (*Continued*)

σ_a(barns/atom) = μ(cm^2/g) × 14.97
E(keV)μ(cm^2/g) = f_2^0 × 4669.04

Beryllium (Be)
Z = 4
Atomic weight = 9.012

Energy (eV)	f_1^0	f_2^0	μ (cm^2/g)
30	1.787	4.396E–01	6.841E+04
70	1.669	2.497E–01	1.666E+04
100	0.647	1.591E–01	7.431E+03
300	4.333	1.150E+00	1.790E+04
700	4.217	2.571E–01	1.715E+03
1000	4.140	1.282E–01	5.986E+02
3000	4.026	1.360E–02	2.117E+01
7000	4.005	2.106E–03	1.405E+00
10000	4.003	9.384E–04	4.381E–01
30000	4.000	7.379E–05	1.148E–02

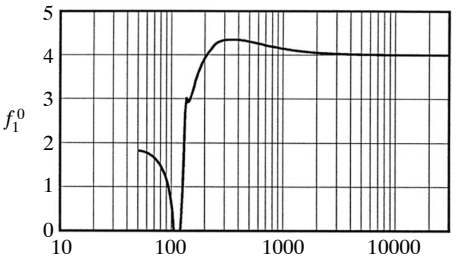

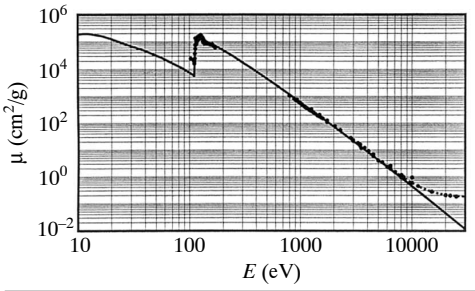

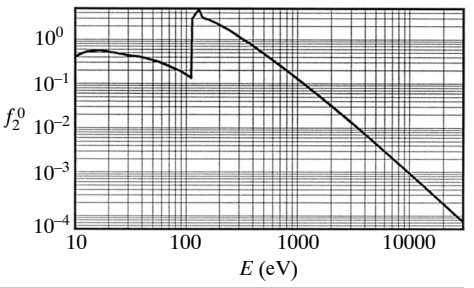

Edge Energies: K 111.5 eV

σ_a(barns/atom) = (cm^2/g) × 19.95
E(keV)(cm^2/g) = f_2^0 × 3503.31

Carbon (C)
Z = 6
Atomic weight = 12.011

Energy (eV)	f_1^0	f_2^0	(cm^2/g)
30	3.692	2.664E+00	3.111E+05
70	4.249	1.039E+00	5.201E+04
100	4.253	6.960E-01	2.438E+04
300	2.703	3.923E+00	4.581E+04
700	6.316	1.174E+00	5.878E+03
1000	6.332	6.328E–01	2.217E+03
3000	6.097	7.745E–02	9.044E+01
7000	6.025	1.306E–02	6.536E+00
10000	6.013	5.892E–03	2.064E+00
30000	6.000	4.425E–04	5.168E–02

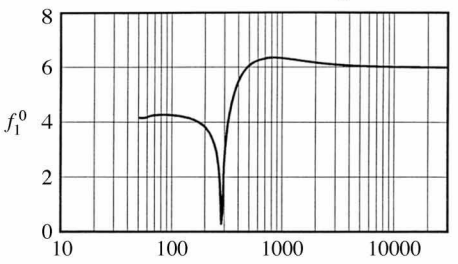

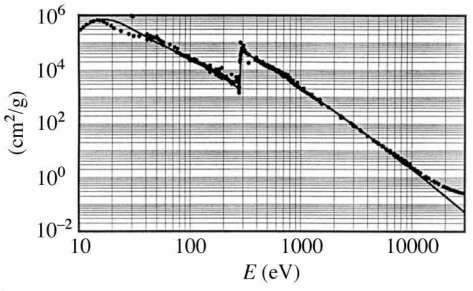

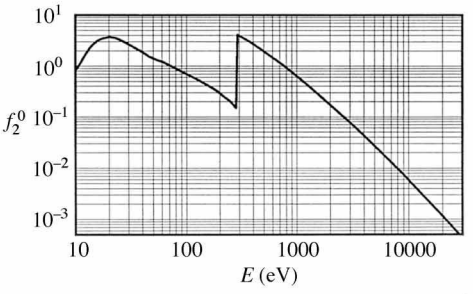

Edge Energies: K 284.2 eV

(*Continued*)

TABLE C.1. (*Continued*)

σ_a(barns/atom) = (cm^2/g) × 23.26
E(keV)(cm^2/g) = f_2^0 × 3004.14

Nitrogen (N)
Z = 7
Atomic weight = 14.007

Energy (eV)	f_1^0	f_2^0	(cm^2/g)
30	3.225	4.373E+00	4.379E+05
70	5.158	2.123E+00	9.110E+04
100	5.421	1.449E+00	4.354E+04
300	4.887	3.056E–01	3.060E+03
700	7.088	1.971E+00	8.459E+03
1000	7.353	1.100E+00	3.306E+03
3000	7.152	1.434E–01	1.436E+02
7000	7.041	2.481E–02	1.065E+01
10000	7.022	1.140E–02	3.424E+00
30000	7.001	9.389E–04	9.402E–02

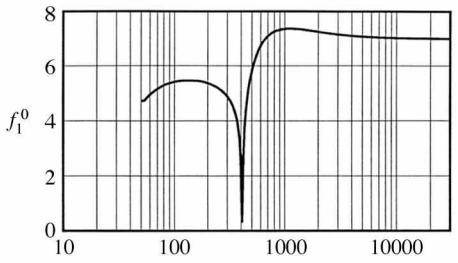

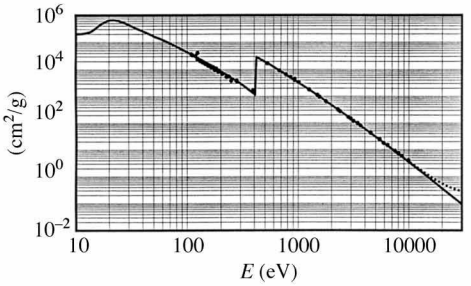

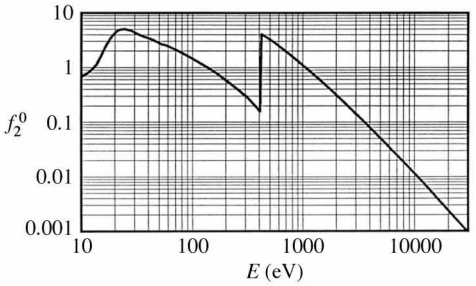

Edge Energies: K 409.9 eV L_1 37.3 eV

σ_a(barns/atom) = (cm^2/g) × 26.57
E(keV)(cm^2/g) = f_2^0 × 2629.99

Oxygen (O)
Z = 8
Atomic weight = 15.999

Energy (eV)	f_1^0	f_2^0	(cm^2/g)
30	1.415	4.661E+00	4.086E+05
70	5.433	3.381E+00	1.270E+05
100	6.158	2.582E+00	6.791E+04
300	6.312	5.645E–01	4.948E+03
700	7.246	3.054E+00	1.148E+03
1000	8.226	1.755E+00	4.615E+03
3000	8.216	2.516E–01	2.205E+02
7000	8.066	4.533E–02	1.703E+01
10000	8.036	2.110E–02	5.548E+00
30000	8.002	1.808E–03	1.585E–01

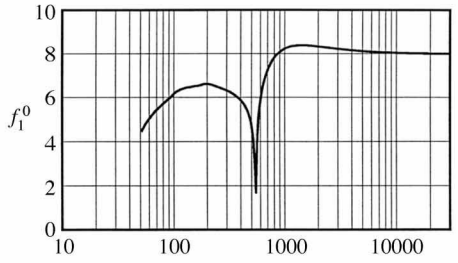

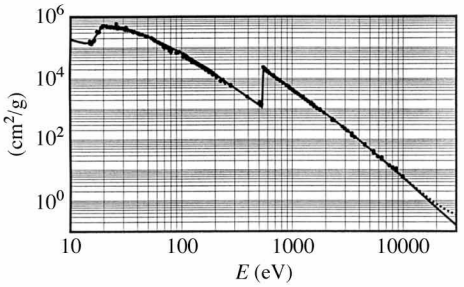

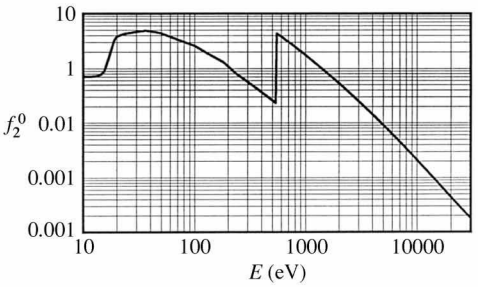

Edge Energies: K 543.1 eV L_1 41.6 eV

(*Continued*)

TABLE C.1. (*Continued*)

σ_a(barns/atom) = (cm^2/g) × 44.80
E(keV)(cm^2/g) = f_2^0 × 1559.52

Aluminum (Al)
Z = 13
Atomic weight = 26.982

Energy (eV)	f_1^0	f_2^0	(cm^2/g)
30	2.320	1.737E–01	9.030E+03
70	–1.449	2.495E–01	5.559E+03
100	0.059	6.908E+00	1.077E+05
300	12.01	5.017E+00	2.608E+04
700	12.10	1.406E+00	3.133E+03
1000	11.65	7.626E–01	1.189E+03
3000	13.36	1.501E+00	7.805E+02
7000	13.25	3.161E–01	7.041E+01
10000	13.16	1.581E–01	2.466E+01
30000	13.02	1.649E–02	8.570E–01

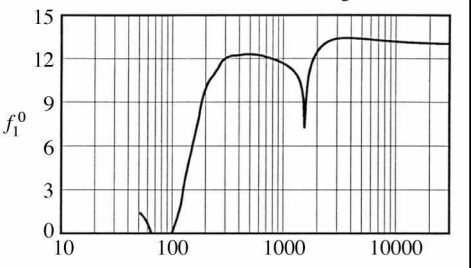

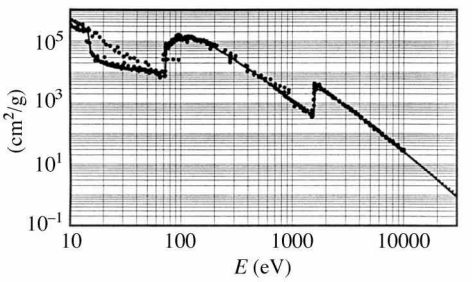

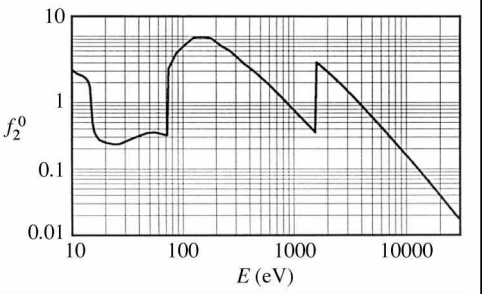

Edge Energies: K 1559.6 eV L_1 117.8 eV
L_2 72.9 eV
L_3 72.5 eV

σ_a(barns/atom) = (cm^2/g) × 46.64
E(keV)(cm^2/g) = f_2^0 × 1498.22

Silicon (Si)
Z = 14
Atomic weight = 28.086

Energy (eV)	f_1^0	f_2^0	(cm^2/g)
30	3.799	3.734E–01	1.865E+04
70	2.448	5.701E–01	1.220E+04
100	–5.657	4.580E+00	6.862E+04
300	12.00	6.439E+00	3.216E+04
700	13.31	1.951E+00	4.175E+03
1000	13.00	1.070E+00	1.602E+03
3000	14.23	1.961E+00	9.792E+02
7000	14.33	4.240E–01	9.075E+01
10000	14.28	2.135E–01	3.199E+01
30000	14.02	2.285E–02	1.141E+00

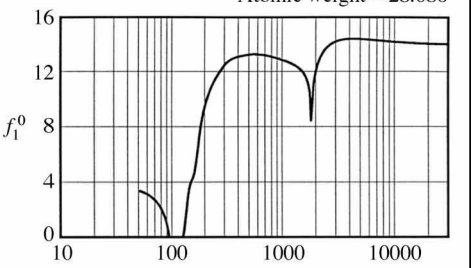

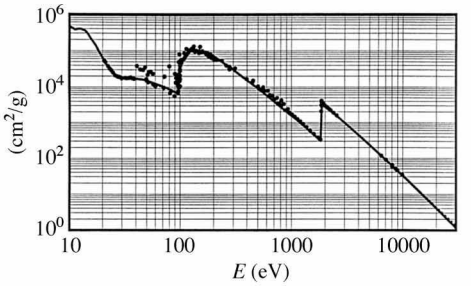

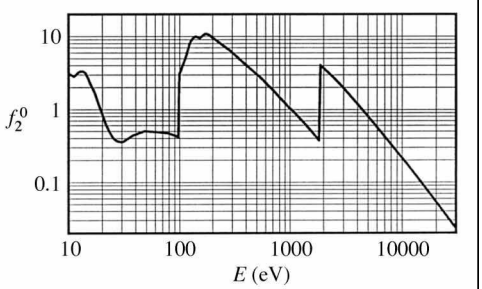

Edge Energies: K 1838.9 eV L_1 149.7 eV
L_2 99.8 eV
L_3 99.2 eV

(*Continued*)

TABLE C.1. (*Continued*)

σ_a(barns/atom) = (cm^2/g) × 58.87
E(keV)(cm^2/g) = f_2^0 × 1186.88

Chlorine (Cl)
Z = 17
Atomic weight = 35.453

Energy (eV)	f_1^0	f_2^0	(cm^2/g)
30	10.00	4.697E+00	1.858E+05
70	5.637	1.299E+00	2.203E+04
100	5.632	1.489E+00	1.768E+04
300	10.42	1.118E+01	4.421E+04
700	16.53	4.118E+00	6.982E+03
1000	16.50	2.374E+00	2.818E+03
3000	14.71	3.764E+00	1.489E+03
7000	17.40	9.014E–01	1.528E+02
10000	17.31	4.663E–01	5.535E+01
30000	17.06	5.358E–02	2.120E+00

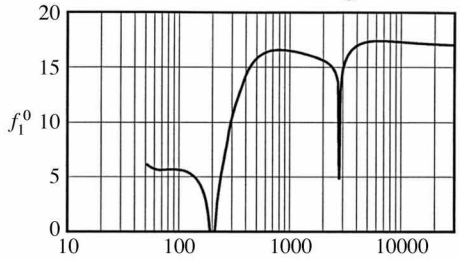

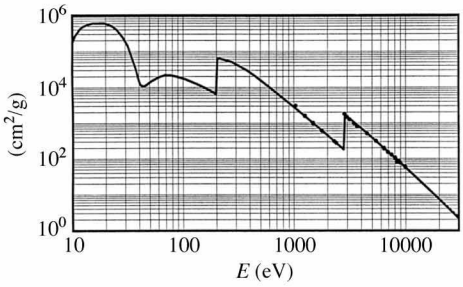

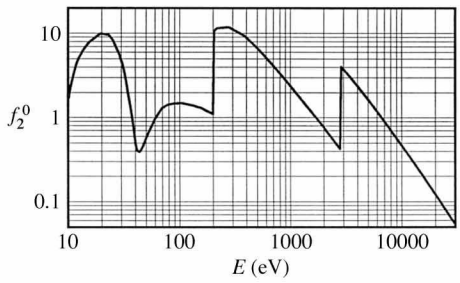

Edge Energies: K 2822.4 eV L$_1$ 270.2 eV
L$_2$ 201.6 eV
L$_3$ 200.0 eV

σ_a(barns/atom) = (cm^2/g) × 92.74
E(keV)(cm^2/g) = f_2^0 × 753.46

Iron (Fe)
Z = 26
Atomic weight = 55.847

Energy (eV)	f_1^0	f_2^0	(cm^2/g)
30	4.610	3.219E+00	8.085E+04
70	7.664	7.727E+00	8.317E+04
100	9.043	7.668E+00	5.777E+04
300	15.98	5.584E+00	1.402E+04
700	1.152	2.024E+00	2.178E+03
1000	22.27	1.196E+01	9.014E+03
3000	25.74	2.159E+00	5.422E+02
7000	22.00	4.952E–01	5.330E+01
10000	25.98	2.267E+00	1.708E+02
30000	26.20	3.038E–01	7.631E+00

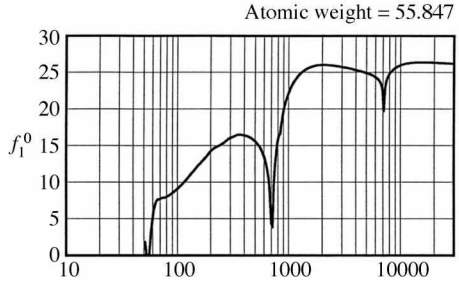

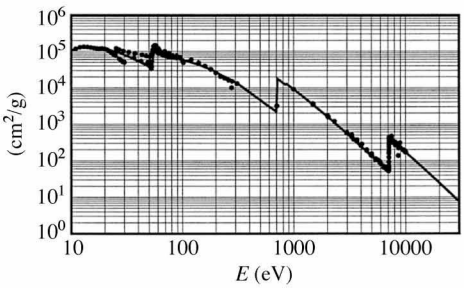

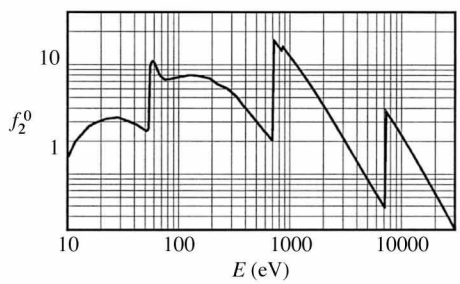

Edge Energies: K 7112.0 eV L$_1$ 844.6 eV M$_1$ 91.3 eV
L$_2$ 719.9 eV M$_2$ 52.7 eV
L$_3$ 706.8 eV M$_3$ 52.7 eV

(*Continued*)

TABLE C.1. (*Continued*)

σ_a(barns/atom) = (cm^2/g) × 97.46
E(keV)(cm^2/g) = f_2^0 × 716.92

Nickel (Ni)
Z = 28
Atomic weight = 58.693

Energy (eV)	f_1^0	f_2^0	(cm^2/g)
30	4.136	3.658E+00	8.742E+04
70	1.899	8.582E+00	8.789E+04
100	7.746	9.790E+00	7.018E+04
300	17.75	7.698E+00	1.840E+04
700	16.38	2.810E+00	2.878E+03
1000	18.14	1.456E+01	1.044E+04
3000	27.92	2.890E+00	6.907E+02
7000	26.40	6.775E–01	6.939E+01
10000	27.33	2.911E+00	2.087E+02
30000	28.23	4.090E–01	9.774E+00

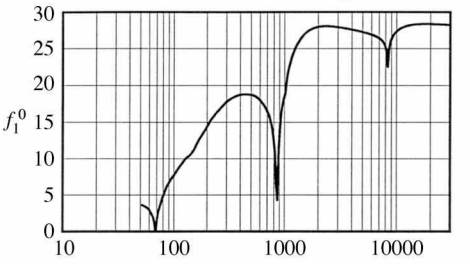

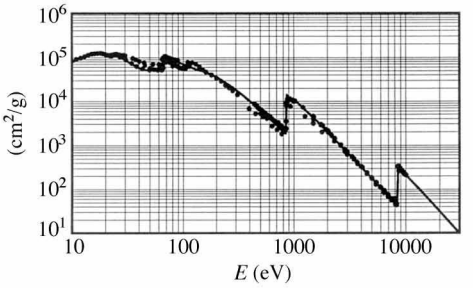

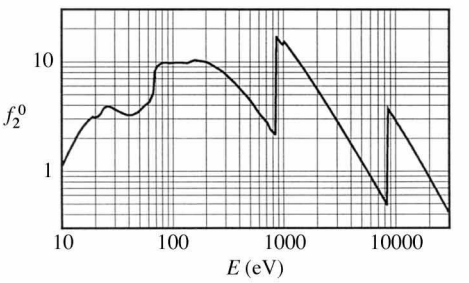

Edge Energies: K 8332.8 eV L_1 1008.6 eV M_1 110.8 eV
L_2 870.0 eV M_2 68.0 eV
L_3 852.7 eV M_3 66.2 eV

σ_a(barns/atom) = (cm^2/g) × 105.52
E(keV)(cm^2/g) = f_2^0 × 662.17

Copper (Cu)
Z = 29
Atomic weight = 63.546

Energy (eV)	f_1^0	f_2^0	(cm^2/g)
30	1.701	4.838E+00	1.068E+05
70	4.223	7.469E+00	7.066E+04
100	5.891	9.478E+00	6.276E+04
300	18.21	8.434E+00	1.862E+04
700	18.37	3.439E+00	3.253E+03
1000	16.61	1.620E+01	1.073E+04
3000	29.03	3.356E+00	7.408E+02
7000	27.68	7.828E–01	7.405E+01
10000	27.71	3.281E+00	2.173E+02
30000	29.26	4.727E–01	1.043E+01

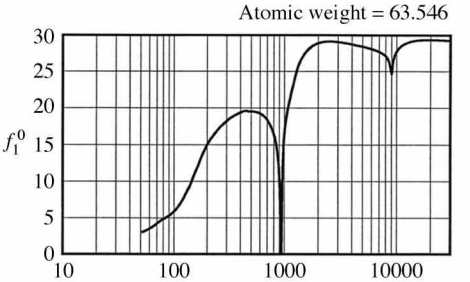

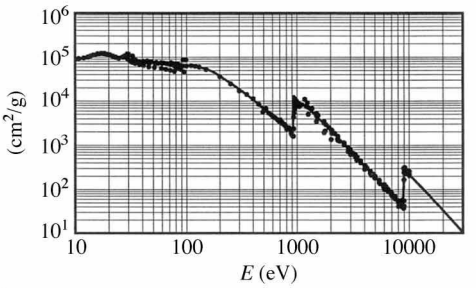

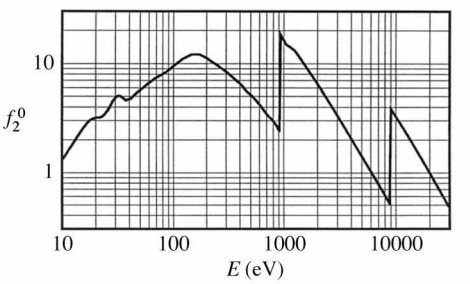

Edge Energies: K 8978.9 eV L_1 1096.7 eV M_1 122.5 eV
L_2 952.3 eV M_2 77.3 eV
L_3 932.5 eV M_3 75.1 eV

(*Continued*)

TABLE C.1. (*Continued*)

σ_a(barns/atom) = (cm^2/g) × 159.31
E(keV)(cm^2/g) = f_2^0 × 438.59

Molybdenum (Mo)
Z = 42
Atomic weight = 95.940

Energy (eV)	f_1^0	f_2^0	(cm^2/g)
30	1.071	5.292E+00	7.736E+04
70	19.38	4.732E+00	2.965E+04
100	14.02	1.124E+00	4.931E+03
300	4.609	1.568E+01	2.292E+04
700	31.41	1.819E+01	1.140E+04
1000	35.15	1.188E+01	5.210E+03
3000	35.88	1.366E+01	1.997E+03
7000	42.11	3.493E+00	2.189E+02
10000	41.67	1.881E+00	8.248E+01
30000	42.04	1.894E+00	2.769E+01

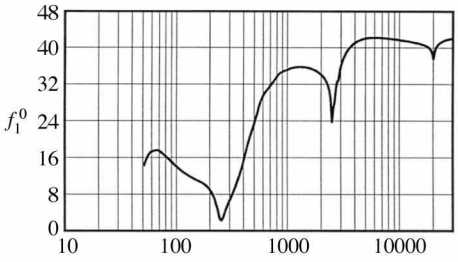

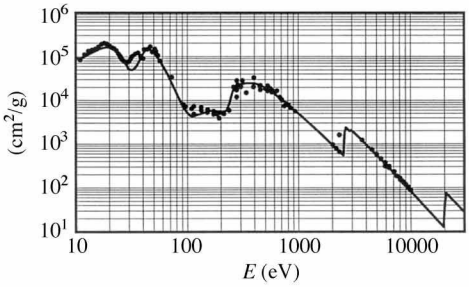

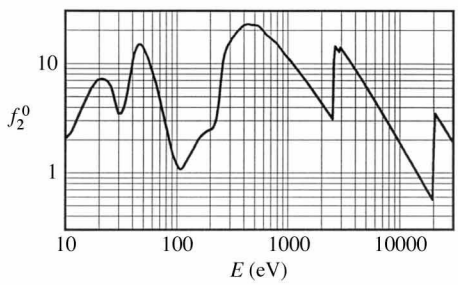

Edge Energies: K 19999.5 eV
L_1 2865.5 eV
L_2 2625.1 eV
L_3 2520.2 eV
M_1 506.3 eV
M_2 411.6 eV
M_3 394.0 eV
M_4 231.1 eV
M_5 227.9 eV
N_1 63.2 eV
N_2 37.6 eV
N_3 35.5 eV

σ_a(barns/atom) = (cm^2/g) × 167.83
E(keV)(cm^2/g) = f_2^0 × 416.33

Ruthenium (Ru)
Z = 44
Atomic weight = 101.070

Energy (eV)	f_1^0	f_2^0	(cm^2/g)
30	8.613	6.852E+00	9.509E+04
70	19.46	1.048E+01	6.230E+04
100	17.43	2.078E+00	8.650E+03
300	3.531	6.472E+00	8.981E+03
700	31.77	2.049E+01	1.219E+04
1000	36.94	1.381E+01	5.747E+03
3000	31.15	1.380E+01	1.915E+03
7000	44.15	4.147E+00	2.466E+02
10000	43.82	2.235E+00	9.306E+01
30000	43.82	2.200E+00	3.053E+01

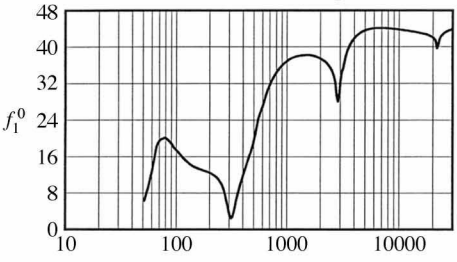

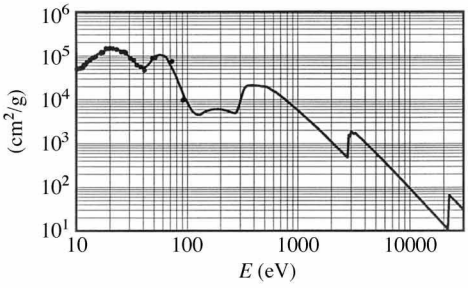

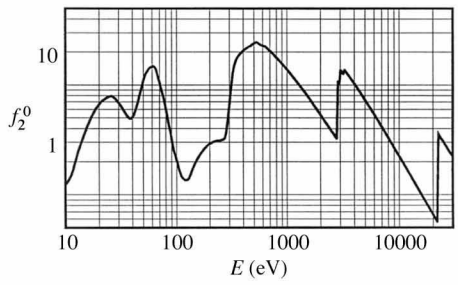

Edge Energies: K 22117.2 eV
L_1 3224.0 eV
L_2 2966.9 eV
L_3 2837.9 eV
M_1 586.2 eV
M_2 483.5 eV
M_3 461.4 eV
M_4 284.2 eV
M_5 280.0 eV
N_1 75.0 eV
N_2 46.5 eV
N_3 43.2 eV

(*Continued*)

TABLE C.1. (*Continued*)

σ_a(barns/atom) = (cm^2/g) × 179.12
E(keV)(cm^2/g) = f_2^0 × 390.09

Silver (Ag)
Z = 47
Atomic weight = 107.868

Energy (eV)	f_1^0	f_2^0	(cm^2/g)
30	−1.680	1.051E+01	1.366E+05
70	11.74	1.929E+01	1.075E+05
100	26.63	1.109E+01	4.326E+04
300	13.18	4.821E+00	6.269E+03
700	29.04	2.594E+01	1.446E+04
1000	38.90	1.821E+01	7.103E+03
3000	38.15	3.900E+00	5.072E+02
7000	47.12	5.407E+00	3.013E+02
10000	47.02	2.928E+00	1.142E+02
30000	46.19	2.752E+00	3.579E+01

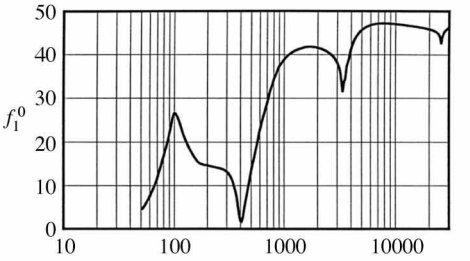

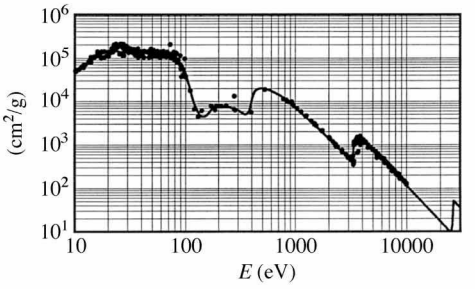

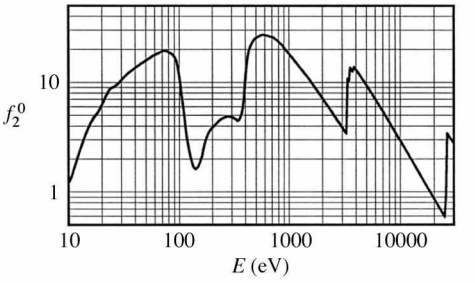

Edge Energies: K 25514.0 eV
L_1 3805.8 eV
L_2 3523.7 eV
L_3 3351.1 eV
M_1 719.0 eV
M_2 603.8 eV
M_3 573.0 eV
M_4 374.0 eV
M_3 368.0 eV
N_1 97.0 eV
N_2 63.7 eV
N_3 58.3 eV

σ_a(barns/atom) = (cm^2/g) × 305.29
E(keV)(cm^2/g) = f_2^0 × 228.87

Tungsten (W)
Z = 74
Atomic weight = 183.850

Energy (eV)	f_1^0	f_2^0	(cm^2/g)
30	4.668	4.227E+00	3.225E+04
70	15.03	1.090E+01	3.564E+04
100	12.64	8.017E+00	1.835E+04
300	21.17	2.282E+01	1.741E+04
700	41.46	2.303E+01	7.531E+03
1000	46.38	1.727E+01	3.953E+03
3000	65.29	2.549E+01	1.944E+03
7000	69.85	7.186E+00	2.350E+02
10000	64.09	4.074E+00	9.325E+01
30000	73.51	2.714E+00	2.070E+01

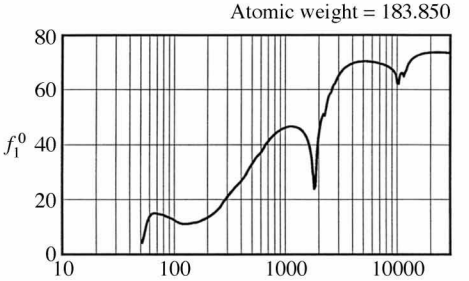

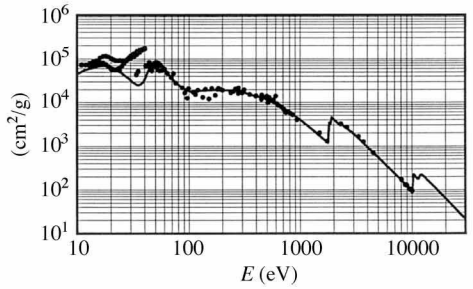

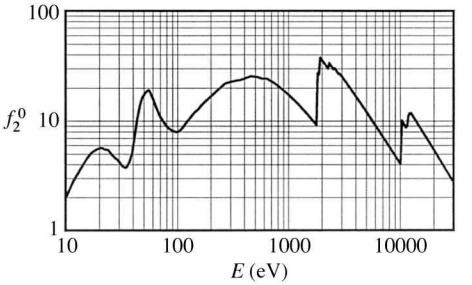

Edge Energies: L_1 12099.8 eV
L_2 11544.0 eV
L_3 10206.8 eV
M_1 2819.6 eV
M_2 2574.9 eV
M_3 2281.0 eV
M_4 1871.6 eV
M_5 1809.2 eV
N_1 594.1 eV
N_2 490.4 eV
N_3 423.6 eV
N_4 255.9 eV
N_5 243.5 eV
N_6 33.6 eV
N_7 31.4 eV
O_1 75.6 eV
O_2 45.3 eV
O_3 36.8 eV

(*Continued*)

TABLE C.1. (*Continued*)

σ_a(barns/atom) = (cm^2/g) × 327.08
E(keV)(cm^2/g) = f_2^0 × 213.63

Gold (Au)
Z = 79
Atomic weight = 196.967

Energy (eV)	f_1^0	f_2^0	(cm^2/g)
30	3.399	1.215E+01	8.650E+04
70	16.58	1.341E+01	4.093E+04
100	21.00	8.642E+00	1.846E+04
300	14.89	2.155E+01	1.534E+04
700	40.71	2.980E+01	9.093E+03
1000	51.72	2.531E+01	5.406E+03
3000	61.30	2.978E+01	2.121E+03
7000	75.42	9.680E+00	2.954E+02
10000	73.45	5.420E+00	1.158E+02
30000	78.58	3.626E+00	2.582E+01

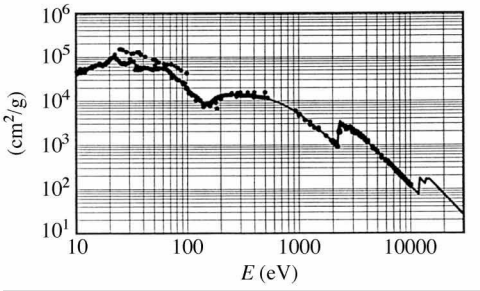

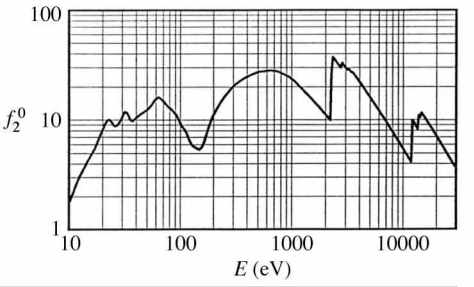

Edge Energies:

L_1	14352.8 eV	M_1	3424.9 eV	N_1	762.1 eV	N_6	87.6 eV	O_1	107.2 eV
L_2	13733.6 eV	M_2	3147.8 eV	N_2	642.7 eV	N_7	83.9 eV	O_2	74.2 eV
L_3	11918.7 eV	M_3	2743.0 eV	N_3	546.3 eV			O_3	57.2 eV
		M_4	2291.1 eV	N_4	353.2 eV				
		M_5	2205.7 eV	N_5	335.1 eV				

TABLE C.2. Atomic subshell photoemission cross-sections, calculated for isolated atoms by Yeh and Lindau.[2]

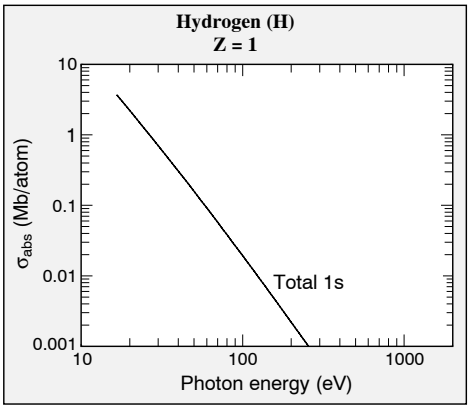

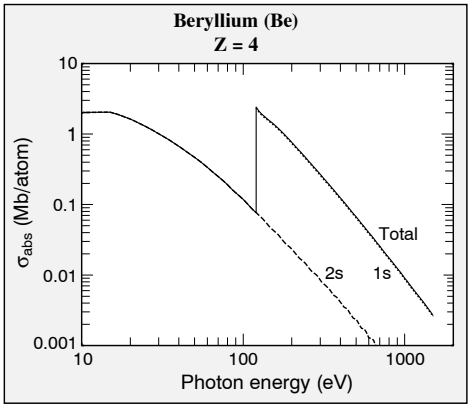

(*Continued*)

TABLE C.2. (*Continued*)

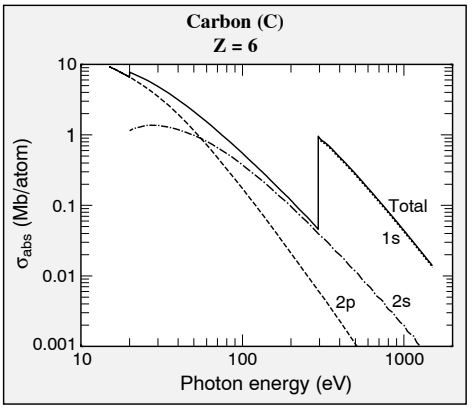

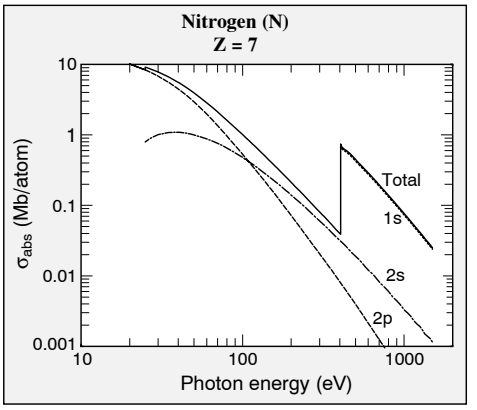

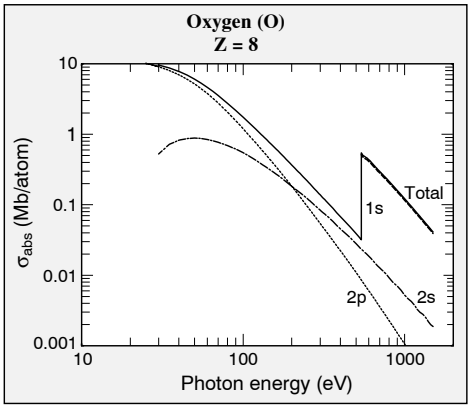

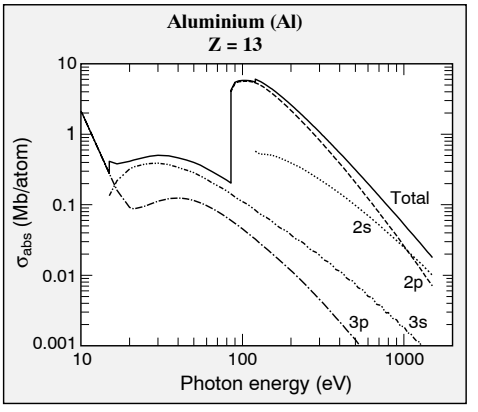

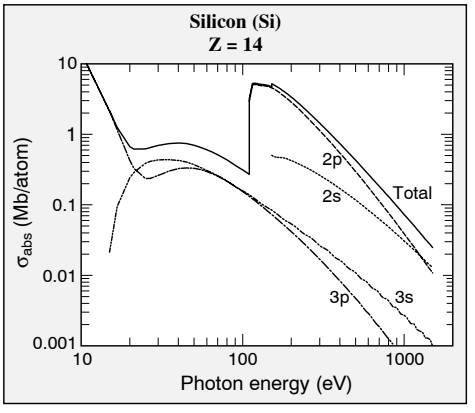

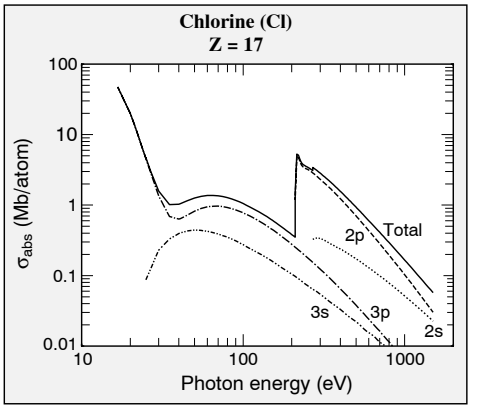

(*Continued*)

TABLE C.2. (*Continued*)

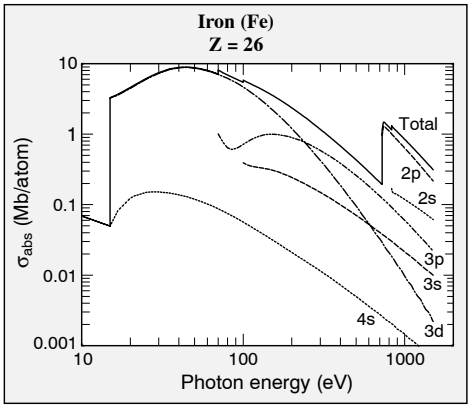

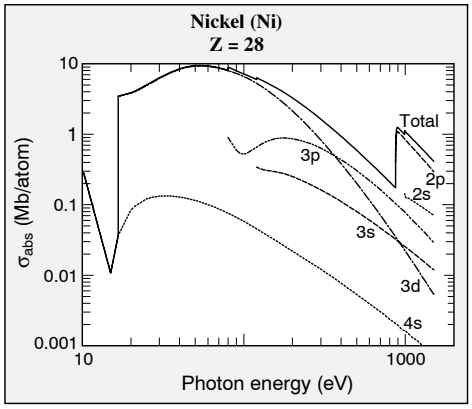

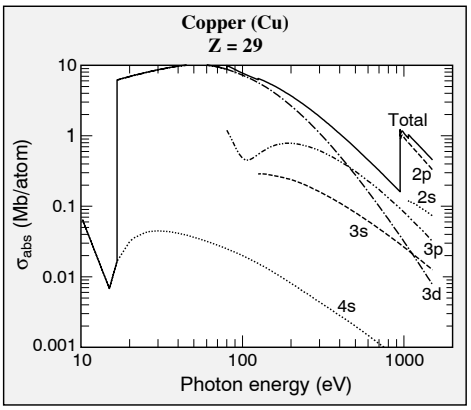

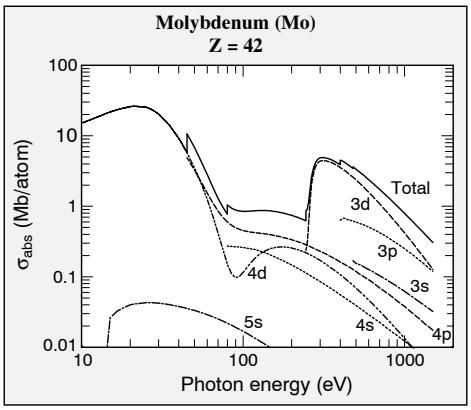

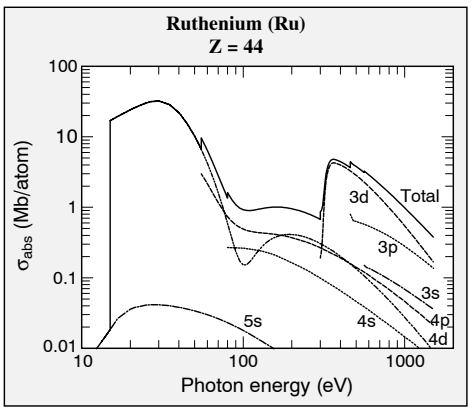

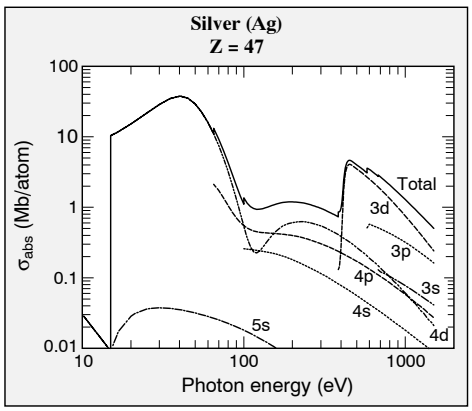

(*Continued*)

TABLE C.2. (*Continued*)

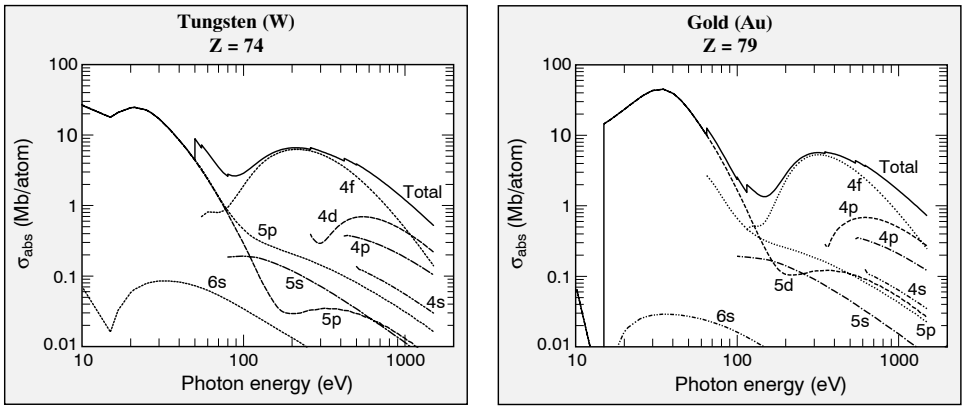

REFERENCES

1. B.L. Henke, E.M. Gullikson, and J.C. Davis, "X-Ray Interactions: Photoabsorption, Scattering, Transmission, and Reflection at $E = 50$–$30{,}000$ eV, $Z = 1$–92," *Atomic Data and Nucl. Data Tables 54*, 181 (1993). Current updates are maintained by E.M. Gullikson at http://www-cxro.lbl.gov/
2. J.-J. Yeh and I. Lindau, "Atomic Subshell Photoionization Cross Sections and Asymmetry Parameters: $1 \leq Z \leq 103$," *Atomic Data and Nucl. Data Tables 32*, 1–155 (1985); J.-J. Yeh, *Atomic Calculation of Photoionization Cross-Sections and Asymmetry Parameters* (Gordon and Breach, Langhorne, PA, 1993); I. Lindau, "Photoemission Cross Sections," Chapter 1, p. 3, in *Synchrotron Radiation Research: Advances in Surface and Interface Science*, Vol. 2 (Plenum, New York, 1992), R.Z. Bachrach, Editor; J.-J. Yeh, "Metal/Silicon Interfaces and their Oxidation Behavior – A Photoemission Spectroscopy Analysis," Ph.D. Thesis in Applied Physics, Stanford University (1987).

Appendix D

MATHEMATICAL AND VECTOR RELATIONSHIPS

CONTENTS

D.1 VECTOR AND TENSOR FORMULAS

$$\mathbf{A}\cdot(\mathbf{B}\times\mathbf{C})=\mathbf{B}\cdot(\mathbf{C}\times\mathbf{A})=\mathbf{C}\cdot(\mathbf{A}\times\mathbf{B}) \tag{D.1}$$

$$\mathbf{A}\times(\mathbf{B}\times\mathbf{C})=(\mathbf{A}\cdot\mathbf{C})\mathbf{B}-(\mathbf{A}\cdot\mathbf{B})\mathbf{C} \tag{D.2}$$

$$\nabla\cdot(f\mathbf{A})=f\nabla\cdot\mathbf{A}+\mathbf{A}\cdot\nabla f \tag{D.3}$$

$$\nabla\times(f\mathbf{A})=f\nabla\times\mathbf{A}+\nabla f\times\mathbf{A} \tag{D.4}$$

$$\nabla\cdot(\mathbf{A}\times\mathbf{B})=\mathbf{B}\cdot(\nabla\times\mathbf{A})-\mathbf{A}\cdot(\nabla\times\mathbf{B}) \tag{D.5}$$

$$\nabla\times(\mathbf{A}\times\mathbf{B})=\mathbf{A}(\nabla\cdot\mathbf{B})-\mathbf{B}(\nabla\cdot\mathbf{A})+(\mathbf{B}\cdot\nabla)\mathbf{A}-(\mathbf{A}\cdot\nabla)\mathbf{B} \tag{D.6}$$

$$\nabla\times(\nabla\times\mathbf{A})=\nabla(\nabla\cdot\mathbf{A})-\nabla^2\mathbf{A} \tag{D.7}$$

$$\nabla\times\nabla f=0 \tag{D.8}$$

$$\nabla\cdot(\nabla\times\mathbf{A})=0 \tag{D.9}$$

$$\nabla\cdot(\mathbf{AB})=\mathbf{B}(\nabla\cdot\mathbf{A})+(\mathbf{A}\cdot\nabla)\mathbf{B} \tag{D.10}$$

Integral relations for a vector field **B** over a volume V, an area A with (normal) vector differential component $d\mathbf{A}$, and line contour element s of local vector component $d\mathbf{s}$. A circle indicates an integral over a closed contour or over a closed surface:

$$\iiint_V \nabla \cdot \mathbf{B}\, dV = \oiint_A \mathbf{B} \cdot d\mathbf{A} \tag{D.11}$$

(Gauss's divergence theorem)

$$\iint_A (\nabla \times \mathbf{B}) \cdot d\mathbf{A} = \oint_s \mathbf{B} \cdot d\mathbf{s} \tag{D.12}$$

(Stokes's theorem)

D.2 SERIES EXPANSIONS

Assuming $x \ll 1$ and m real, except where stated otherwise,

$$f(x) = f(s) + f'(s)(x-s) + \frac{f''(s)}{2!}(x-s)^2 + \cdots$$

$$+ \frac{f^n(s)(x-s)^n}{n!} \qquad (x-s) \ll 1$$

$$f(x) = f(0) + xf'(0) + \frac{x^2}{2!}f''(0) + \cdots$$

$$\sin x = x - \frac{x^3}{3!} + \frac{x^5}{5!} - \cdots$$

$$\cos x = 1 - \frac{x^2}{2!} + \frac{x^4}{4!} - \cdots$$

$$\tan x = x + \frac{x^3}{3} + \frac{2x^5}{15} + \cdots \qquad \left(x^2 < \frac{\pi^2}{4}\right)$$

$$\sqrt{1-x} = 1 - \frac{x}{2} - \frac{1}{2^2 2!}x^2 - \frac{1\cdot 3}{2^3 3!}x^3 + \cdots$$

$$(1-x^2)^{-1/2} = 1 + \frac{x^2}{2} + \frac{1\cdot 3}{2^2 2!}x^4 + \cdots$$

$$(1+x)^m = 1 + \frac{m}{1!}x + \frac{m(m-1)}{2!}x^2 + \frac{m(m-1)(m-2)}{3!}x^3 + \cdots$$

$$e^x = 1 + x + \frac{x^2}{2!} + \frac{x^3}{3!} + \cdots + \frac{x^n}{n!}$$

$$\frac{1}{1-x} = 1 + x + x^2 + x^3 + \cdots$$

$$e^{\sin x} = 1 + x + \frac{x^2}{2!} - \frac{3x^4}{4!} - \frac{8x^5}{5!} - \cdots \qquad x^2 < \frac{\pi^2}{4}$$

$$e^{\cos x} = e\left(1 - \frac{x^2}{2!} + \frac{4x^4}{4!} - \frac{31x^6}{6!} + \cdots\right) \qquad x^2 < \frac{\pi^2}{4}$$

$$\sinh x = x + \frac{x^3}{3!} + \frac{x^5}{5!} + \cdots$$

$$\cosh x = 1 + \frac{x^2}{2!} + \frac{x^4}{4!} + \cdots$$

$$\tanh x = x - \frac{x^3}{3} + \frac{2x^5}{15} - \cdots$$

$$J_0(x) = 1 - \frac{x^2}{2^2(1!)^2} + \frac{x^4}{2^4(2!)^2} - \frac{x^6}{2^6(3!)^2} + \cdots$$

$$J_1(x) = \frac{x}{2} - \frac{x^3}{2^3 1!\,2!} + \frac{x^5}{2^5 2!\,3!} - \frac{x^7}{2^7 3!\,4!} + \cdots$$

For complex $z = x + iy$:

$$\sin z = z - \frac{z^3}{3!} + \cdots$$

$$\cos z = 1 - \frac{z^2}{2!} + \cdots$$

$$\sinh z = z + \frac{z^3}{3!} + \frac{z^5}{5!} + \cdots$$

$$\cosh z = 1 + \frac{z^2}{2!} + \frac{z^4}{4!} + \cdots$$

$$\tanh z = z - \frac{z^3}{3} + \frac{2z^5}{15} - \cdots$$

$$e^z = 1 + z + \frac{z^2}{2!} + \cdots$$

D.3 TRIGONOMETRIC RELATIONSHIPS

$$e^{\pm i\theta} = \cos\theta \pm i\sin\theta, \quad \theta \text{ real}$$

$$\sin(\alpha \pm \beta) = \sin\alpha\cos\beta \pm \cos\alpha\sin\beta$$

$$\cos(\alpha \pm \beta) = \cos\alpha\cos\beta \mp \sin\alpha\sin\beta$$

$$\tan(\alpha \pm \beta) = \frac{\tan\alpha \pm \tan\beta}{1 \mp \tan\alpha\tan\beta}, \quad \tan\left(\frac{\pi}{4} + \beta\right) = \frac{1 + \tan\beta}{1 - \tan\beta}$$

$$\sin 2\alpha = 2\sin\alpha\cos\alpha$$

$$\cos 2\alpha = \begin{cases} \cos^2\alpha - \sin^2\alpha \\ 2\cos^2\alpha - 1 \\ 1 - 2\sin^2\alpha \end{cases}$$

$$\cos\frac{\alpha}{2} = \sqrt{\frac{1}{2}(1+\cos\alpha)}$$

$$\sin\frac{\alpha}{2} = \sqrt{\frac{1}{2}(1-\cos\alpha)}$$

$$2\sin\alpha\cos\beta = \sin(\alpha+\beta) + \sin(\alpha-\beta)$$

$$2\cos\alpha\cos\beta = \cos(\alpha+\beta) + \cos(\alpha-\beta)$$

$$2\sin\alpha\sin\beta = \cos(\alpha-\beta) - \cos(\alpha+\beta)$$

$$\sin\alpha + \sin\beta = 2\sin\tfrac{1}{2}(\alpha+\beta)\cos\tfrac{1}{2}(\alpha-\beta)$$

$$\sin 3\alpha = 3\sin\alpha - 4\sin^3\alpha$$

$$\cos 3\alpha = 4\cos^3\alpha - 3\cos\alpha$$

$$\frac{a}{\sin\alpha} = \frac{b}{\sin\beta} = \frac{c}{\sin\gamma}$$

$$a^2 = b^2 + c^2 - 2bc\cos\alpha$$

$$\tan^2\theta + 1 = \sec^2\theta, \quad 1 + \cot^2\theta = \csc^2\theta$$

$$\sinh x = \frac{e^x - e^{-x}}{2}, \quad \sinh(-x) = -\sinh x$$

$$\cosh x = \frac{e^x + e^{-x}}{2}, \quad \cosh(-x) = \cosh x$$

$$\tanh x = \sinh x / \cosh x$$

$$\cosh^2 x - \sinh^2 x = 1$$

In spherical coordinates the angle between two vectors is given by

$$\cos\Theta = \cos\theta_1\cos\theta_2 + \sin\theta_1\sin\theta_2\cos(\phi_2 - \phi_1)$$

where $(\theta_1,\ \phi_1)$ and $(\theta_2,\ \phi_2)$ are the respective polar and azimuthal angular pairs.

D.4 DEFINITE INTEGRALS

Assuming x real, $a > 0$:

$$\int_0^\infty e^{-ax}\,dx = \frac{1}{a}$$

$$\int_c^d xe^{-ax}dx = -\frac{e^{-ax}}{a^2}(ax+1)\Big|_c^d$$

$$\frac{1}{\sqrt{2\pi}\sigma}\int_{-\infty}^{\infty} e^{-x^2/2\sigma^2}\,dx = 1$$

$$\int_0^{\infty} (\cos bx)e^{-a^2x^2}dx = \frac{\sqrt{\pi}}{2a}e^{-b^2/4a^2}$$

$$\int_0^{\infty} xe^{-x^2}dx = \frac{1}{2}$$

$$\int_0^{\infty} x^2e^{-x^2}dx = \frac{\sqrt{\pi}}{4}$$

$$\int_0^{\infty} e^{-ax}\left\{\begin{matrix}\cos mx\\ \sin mx\end{matrix}\right\}dx = \frac{\left\{\begin{matrix}a\\ m\end{matrix}\right\}}{a^2+m^2}$$

$$\int_0^{\infty} \frac{\sin x}{x}\,dx = \frac{\pi}{2}$$

$$\int_0^{\infty} \frac{\cos x}{x}\,dx = \infty$$

$$\int_0^{\infty} \frac{\tan x}{x}\,dx = \frac{\pi}{2}$$

$$\int_0^{\pi} \sin^2 mx\,dx = \int_0^{\pi} \cos^2 mx\,dx = \frac{\pi}{2}$$

$$\int_0^{\infty} \frac{\sin^2 x\,dx}{x^2} = \frac{\pi}{2}$$

$$\int_{-\pi}^{\pi} \cos nx \cos mx\,dx = \begin{cases}0 & n \neq m\\ \pi & n = m\end{cases}$$

$$\int_{-\pi}^{\pi} \sin nx \cos mx\,dx = 0$$

D.5 FUNCTIONS OF A COMPLEX VARIABLE

$$z = x + iy = r(\cos\theta + i\sin\theta) = re^{i\theta}$$

$$e^z = e^x(\cos y + i\sin y)$$

$$e^{iz} = \cos z + i\sin z$$

$$\sqrt{i} = \pm\frac{\sqrt{2}}{2}(1+i)$$

$$\sin z = \frac{e^{iz} - e^{-iz}}{2i}, \quad \sin(-z) = -\sin z$$

$$\cos z = \frac{e^{iz} + e^{-iz}}{2}, \quad \cos(-z) = \cos z$$

$$\sinh z = \frac{e^{z} - e^{-z}}{2} = -i\sin(iz)$$

$$\cosh z = \frac{e^{z} + e^{-z}}{2} = \cos(iz)$$

$$\tanh z = \frac{\sinh z}{\cosh z}$$

$$\cos^2 z + \sin^2 z = 1$$

$$\cosh^2 z - \sinh^2 z = 1$$

$$\sin 2z = 2\sin z \cos z$$

$$\sin z = \sin x \cosh y + i \cos x \sinh y$$

$$= \sin x \cos iy + \cos x \sin iy$$

$$\cos z = \cos x \cosh y - i \sin x \sinh y$$

$$= \cos x \cos iy - \sin x \sin iy$$

$$\sinh z = \sinh x \cos y + i \cosh x \sin y$$

$$\cosh z = \cosh x \cos y + i \sinh x \sin y$$

$$\cos iy = \cosh y$$

$$\sin iy = i \sinh y$$

$$\frac{d}{dz}e^{z} = e^{z}$$

$$\frac{d}{dz}\sin z = \cos z$$

$$\frac{d}{dz}\cos z = -\sin z$$

$$\frac{d}{dz}\cosh z = \sinh z$$

$$\frac{d}{dz}\sinh z = \cosh z$$

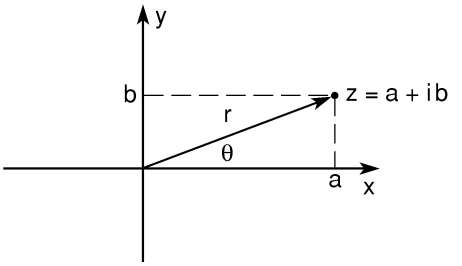

$$r = \sqrt{a^2 + b^2}$$

$$\cos\theta = \frac{a}{r} = \frac{a}{\sqrt{a^2 + b^2}}$$

$$\sin\theta = \frac{b}{r} = \frac{b}{\sqrt{a^2 + b^2}}$$

$$\sqrt{z} = \sqrt{a + ib} = r^{1/2}e^{i\theta/2} = r^{1/2}\left(\cos\frac{\theta}{2} + i\sin\frac{\theta}{2}\right)$$

$$\sqrt{a + ib} = (a^2 + b^2)^{1/4}\left[\sqrt{\tfrac{1}{2}(1 + \cos\theta)} + i\sqrt{\tfrac{1}{2}(1 - \cos\theta)}\right]$$

$$\sqrt{a + ib} = (a^2 + b^2)^{1/4}\left[\sqrt{\frac{1}{2}\left(1 + \frac{a}{\sqrt{a^2 + b^2}}\right)}\right.$$

$$\left. + i\sqrt{\frac{1}{2}\left(1 - \frac{a}{\sqrt{a^2 + b^2}}\right)}\right]$$

$$\sqrt{a + ib} = \frac{1}{\sqrt{2}}\left[\sqrt{\sqrt{a^2 + b^2} + a} + i\sqrt{\sqrt{a^2 + b^2} - a}\right]$$

similarly

$$\sqrt{a - ib} = \frac{1}{\sqrt{2}}\left[\sqrt{\sqrt{a^2 + b^2} + a} - i\sqrt{\sqrt{a^2 + b^2} - a}\right]$$

Cauchy Integral Formula

$$\oint \frac{f(z)}{z - z_0}\,dz = 2\pi i f(z_0)$$

D.6 FOURIER TRANSFORM[11–13]

$$F(\mathbf{k}) = \iiint f(\mathbf{r}) e^{-i\mathbf{k}\cdot\mathbf{r}} d\mathbf{r}$$

$$f(\mathbf{r}) = \frac{1}{(2\pi)^3} \iiint F(\mathbf{k}) e^{i\mathbf{k}\cdot\mathbf{r}} d\mathbf{k}$$

D.7 THE DIRAC DELTA FUNCTION

The Dirac delta function $\delta(x)$ has the properties that it is zero for all x except $x = 0$, where it is infinite:

$$\delta(x) = \begin{cases} 0 & x \neq 0 \\ \infty & x = 0 \end{cases}$$

with the normalization condition

$$\int_{\text{all } x} \delta(x)\, dx = 1$$

With a displaced origin the function is

$$\delta(x - a) = \begin{cases} 0 & x \neq a \\ \infty & x = a \end{cases}$$

which has the *sifting property*

$$\int_{\text{all } x} f(x)\delta(x - a)\, dx = f(a)$$

Integrating by parts, one can show that the derivative function $\delta'(x - a)$ has the property

$$\int_{\text{all } x} f(x)\delta'(x - a)\, dx = -f'(a)$$

A shorthand notation for the delta function in three dimensions is, in Cartesian coordinates,

$$\delta(\mathbf{r}) \equiv \delta(x)\,\delta(y)\,\delta(z)$$

D.8 THE CAUCHY PRINCIPAL VALUE THEOREM

The Cauchy principal value of an integral is defined as the integral over a restricted range that avoids a contribution from an isolated singularity. Thus, for example, if a function $f(x)$ has a singularity at $x = a$, in the interval $0 < a < \infty$, the principal value of the integral would be written as

$$\mathcal{P} \int_0^\infty f(x)\, dx = \lim_{\delta \to 0} \left[\int_0^{a-\delta} f(x)\, dx + \int_{a+\delta}^\infty f(x)\, dx \right]$$

As a specific example, we consider the function $f(x) = 1/x$, where x represents a physical quantity with a small imaginary component ϵ. Forming real and imaginary components

$$\frac{1}{x \mp i\epsilon} = \frac{x}{x^2 + \epsilon^2} \pm i\frac{\epsilon}{x^2 + \epsilon^2}$$

the first term is to behave like $1/x$ everywhere except at $x = 0$, in the limit that ϵ goes to zero. Exactly at $x = 0$ this first term is zero, for arbitrarily small but finite ϵ. Thus this first term represents the Cauchy principal portion of the function $1/x$. The second imaginary term behaves like a Dirac delta function in the limit that ϵ goes to zero. It can be integrated using a standard trigonometric substitution. Performing this integration, one obtains the relationship

$$\lim_{\epsilon \to 0} \frac{1}{x \mp i\epsilon} = \mathcal{P}\left(\frac{1}{x}\right) \pm i\pi\delta(x)$$

where $\mathcal{P}(1/x)$ behaves like the function $1/x$ everywhere except at $x = 0$, where it is zero.

REFERENCES

1. J. Stratten, *Electromagnetic Theory* (McGraw-Hill, New York, 1941).
2. J.D. Jackson, *Classical Electrodynamics* (Wiley, New York, 1998), Third Edition.
3. D.R. Nicholson, *Introduction to Plasma Theory* (Wiley, New York, 1983).
4. S. Solimeno, B. Crosignani, and P.Di Porto, *Guiding, Diffraction and Confinement of Optical Radiation* (Academic, New York, 1986).
5. I.S. Gradshteyn and I.M. Ryzhik, *Tables of Series and Products* (Academic, New York, 1994), Fifth Edition.
6. P.M. Morse and H. Feshbach, *Methods of Theoretical Physics* (McGraw-Hill, New York, 1953).
7. H.B. Dwight, *Tables of Integrals and Other Mathematical Data* (MacMillan, New York, 1961), Fourth Edition.
8. G. Arfken, *Mathematical Methods for Physicists* (Academic, New York, 1985), Third Edition.
9. E. Kreyszig, *Advanced Engineering Mathematics* (Wiley, New York, 1993), Seventh Edition.
10. M. Abramowitz and I.A. Stegun, *Handbook of Mathematical Functions* (Dover, New York, 1972).
11. D.C. Champeney, *Fourier Transforms and their Physical Applications* (Academic Press, NY, 1973).
12. R.N. Bracewell, *The Fourier Transform and Its Applications* (McGraw-Hill, NY, 1986), Second Edition.
13. I.N. Sneddon, *Fourier Transforms* (Dover, New York, 1995).

Appendix E

SOME INTEGRATIONS IN k, ω-SPACE

In Chapter 2 the electric field radiated by an accelerated charge is calculated using Fourier–Laplace transform techniques that involve a four dimensional integration in $\mathbf{k}$, ω-space, essentially a summation of responses at all frequencies ω and all wavenumbers $k = 2\pi/\lambda$ in all directions (i.e., the wave vector $\mathbf{k}$). The radiated electric field at a position $\mathbf{r}$ and at a time t is expressed in Chapter 2, Eq. (2.22) in integral form, as

$$\mathbf{E}(\mathbf{r}, t) = \frac{ie}{\epsilon_o} \int_{\mathbf{k}} \int_{\omega} \frac{\omega \mathbf{v}_T(\omega) e^{-i(\omega t - \mathbf{k}\cdot\mathbf{r})}}{\omega^2 - k^2 c^2} \frac{d\omega\, d\mathbf{k}}{(2\pi)^4} \tag{2.22}$$

To aid us in the k-space integration we utilize the vector coordinates shown in Figure E.1, which is identical to Figure 2.3, with the addition that it shows explicitly the vector electric field $\mathbf{E}_i$ associated with the incident wave that is to be scattered by a single free electron. For a modest electric field, such that we can ignore the $\mathbf{v} \times \mathbf{B}$ term in the Lorentz force, the acceleration of the electron is given by $m\mathbf{a} = -e\mathbf{E}_i$, and in this harmonic analysis where $\mathbf{a} = d\mathbf{v}/dt = -i\omega\mathbf{v}$, the induced electron velocity is given by $\mathbf{v} = -ie\mathbf{E}/m\omega$, so that $\mathbf{E}_i$, $\mathbf{a}$, and $\mathbf{v}$ all have the same vector direction. To perform the k-space integration in Eq. [2.22] we note that the transverse component of velocity is given by $\mathbf{v}_T = -\mathbf{k}_0 \times (\mathbf{k}_0 \times \mathbf{v})$, with scalar magnitude $\mathrm{v}_T = |\mathbf{v}_T| = |\mathbf{v}| \sin\Theta$, where Θ is measured from the direction of acceleration to the direction of observation $\mathbf{k}_0$. The k-space integration in Eq. [2.22] is thus performed with Θ treated as a fixed quantity. In essence it represents the observation direction $\mathbf{r}$ in $\mathbf{E}(\mathbf{r}, t)$, while the integration is performed over the k-space coordinates. For fixed polarization direction $\mathbf{E}_i$ and fixed observation direction $\mathbf{k}_0$, the angle Θ is constant and thus $\mathbf{v}_T$ passes through the k-space integrals. The integral expression for $\mathbf{E}(\mathbf{r}, t)$ is then

$$\mathbf{E}(\mathbf{r}, t) = \frac{ie}{\epsilon_0} \int_{\omega} \omega \mathbf{v}_T(\omega) e^{-i\omega t} \underbrace{\int_k \left[\frac{e^{i\mathbf{k}\cdot\mathbf{r}}}{(\omega + kc)(\omega - kc)} \frac{d\mathbf{k}}{(2\pi)^3} \right]}_{\text{a function } G(\omega;\, \mathbf{r})} \frac{d\omega}{2\pi}$$

where we have introduced an arbitarily named function $G(\omega; \mathbf{r})$ to represent the requisite k-space integration in what follows. To perform the integration we use polar coordinates

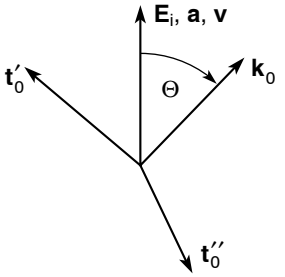

FIGURE E.1. Vector coordinates for scattering calculations involving a point-source electron caused to oscillate with an acceleration **a** and a velocity **v** by an incident electric field of polarization $\mathbf{E}_i$. The radiation is calculated for an observation direction $\mathbf{k}_0$. The angle Θ is measured from the direction of acceleration **a** to the direction of observed scattering $\mathbf{k}_0$. The unit vectors are defined by $\mathbf{k}_0 \times \mathbf{t}'_0 = \mathbf{t}''_0$. Polar coordinates $(k,\ \theta,\ \phi)$ are oriented around $\mathbf{k}_0$.

oriented around $\mathbf{k}_0$, as introduced* in Chapter 2:

$$d\mathbf{k} = k^2 \underbrace{\sin\theta\, d\theta\, d\phi}_{d\Omega}\, dk \tag{2.23a}$$

where

$$0 \le k \le \infty \tag{2.23b}$$

$$0 \le \theta \le \pi \tag{2.23c}$$

$$0 \le \phi \le 2\pi \tag{2.23d}$$

so that for a vector **r**, at polar angle θ to **k**, the phase term that occurs in Eq. (2.22) becomes

$$\mathbf{k} \cdot \mathbf{r} = kr\cos\theta \tag{2.23e}$$

The first integral, $G(\omega; \mathbf{r})$, can then be evaluated as

$$G(\omega;\mathbf{r}) = \int_0^\infty \int_0^{2\pi} \int_0^\pi \frac{e^{i\mathbf{k}\cdot\mathbf{r}}}{(\omega + kc)(\omega - kc)} \frac{k^2 \sin\theta\, d\theta\, d\phi\, dk}{(2\pi)^3}$$

which upon integration over ϕ becomes

$$G(\omega;\mathbf{r}) = \frac{-1}{(2\pi c)^2} \int_o^\infty \frac{1}{\left(k + \frac{\omega}{c}\right)\left(k - \frac{\omega}{c}\right)} \left[\int_0^\pi \frac{e^{ikr\cos\theta} ikr \sin\theta\, d\theta}{ikr}\right] k^2\, dk$$

$$G(\omega;\mathbf{r}) = \frac{-1}{(2\pi c)^2} \int_0^\infty \frac{1}{\left(k + \frac{\omega}{c}\right)\left(k - \frac{\omega}{c}\right)} \left[\int_0^\pi \frac{e^{ikr\cos\theta} d(ikr\cos\theta)}{-ikr}\right] k^2\, dk$$

*Recall that $d\mathbf{k}$ is not a vector, but rather shorthand notation for a volume element in differential space. For instance, in rectangular coordinates $d\mathbf{k} = dk_x\, dk_y\, dk_z$.

Then using $\int_a^b e^u du = e^u|_a^b$,

$$G(\omega;\mathbf{r}) = \frac{-1}{(2\pi c)^2}\int_0^\infty \frac{1}{\left(k+\frac{\omega}{c}\right)\left(k-\frac{\omega}{c}\right)} \underbrace{\left[\frac{e^{ikr\cos\theta}|_o^\pi}{-ikr}\right]}_{\frac{e^{-ikr}-e^{ikr}}{-ikr}} k^2 dk$$

$$G(\omega;\mathbf{r}) = \frac{-i}{(2\pi c)^2 r}\int_0^\infty \frac{(e^{-ikr}-e^{ikr})}{\left(k+\frac{\omega}{c}\right)\left(k-\frac{\omega}{c}\right)} k\,dk$$

$$G(\omega;\mathbf{r}) = \frac{i}{(2\pi c)^2 r}\left\{\left[\int_0^\infty \frac{e^{ikr}k\,dk}{\left(k+\frac{\omega}{c}\right)\left(k-\frac{\omega}{c}\right)}\right] - \left[\int_0^\infty \frac{e^{-ikr}k\,dk}{\left(k+\frac{\omega}{c}\right)\left(k-\frac{\omega}{c}\right)}\right]\right\}$$

To perform these integrations using the *Cauchy integral formula* (see Appendix D, Ref. 9)

$$\oint \frac{f(z)}{z-z_o}\,dz = 2\pi i f(z_o)$$

we need to extend the k-integration from $-\infty$ to $+\infty$. To achieve this we change variables in the second integral above, replacing k by $-k'$, so that

$$G(\omega;\mathbf{r}) = \frac{i}{(2\pi c)^2 r}\left\{\left[\int_0^\infty \frac{e^{ikr}k\,dk}{\left(k+\frac{\omega}{c}\right)\left(k-\frac{\omega}{c}\right)}\right] - \left[\int_0^{-\infty} \underbrace{\frac{e^{ik'r}k'dk'}{\left(-k'+\frac{\omega}{c}\right)\left(-k'-\frac{\omega}{c}\right)}}_{\left(k'-\frac{\omega}{c}\right)\left(k'+\frac{\omega}{c}\right)}\right]\right\}$$

We note that the integration $-\int_0^{-\infty}$ can be replaced by $+\int_{-\infty}^0$, so that the k-integration can now be written compactly as

$$G(\omega;\mathbf{r}) = \frac{i}{(2\pi c)^2 r}\left[\int_{-\infty}^{+\infty} \frac{e^{ikr}k\,dk}{\left(k+\frac{\omega}{c}\right)\left(k-\frac{\omega}{c}\right)}\right]$$

which can now be evaluated by closing the contour integral and using the Cauchy integral formula. Thus we identify $f(k) = ke^{ikr}/(k+\omega/c)$ and close the integration contour with a very large semicircle in the upper half of the complex k-plane, such that the integrand goes to zero along the added semicircular path. Note that in the complex k-plane we have $k = k_r + ik_i$, so that $e^{ikr} = e^{ik_r r}e^{-k_i r}$. For radiated fields at large distances r, the factor $e^{-k_i r}$ goes to zero for $k_i > 0$. Thus we close the contour in the upper half plane where this added semicircular path closes the contour but adds nothing to the integral.

Note that in Figure E.2 the poles at $k = \omega/c$ and $-\omega/c$ are shown shifted slightly off axis to indicate wave decay (rather than growth) as the waves propagate in their respective directions. This is justified by noting that there is always some absorption or scattering loss in real physical systems.

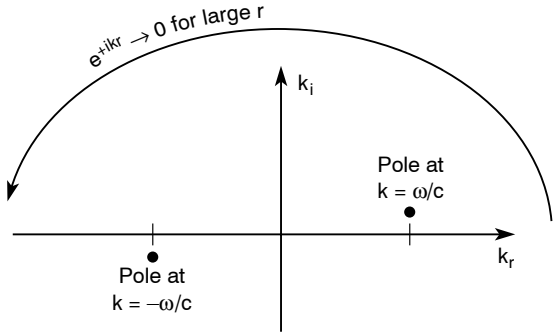

FIGURE E.2. Integration in the complex k-plane.

The integration of $G(\omega;\mathbf{r})$ then becomes

$$G(\omega;\mathbf{r}) = \frac{i}{(2\pi c)^2 r} \underbrace{\oint \frac{f(k)\,dk}{k - \frac{\omega}{c}}}_{2\pi i f\left(\frac{\omega}{c}\right)}$$

Recalling that we defined $f(k) = ke^{ikr}/(k + \frac{\omega}{c})$, we have

$$G(\omega;\mathbf{r}) = \frac{i}{(2\pi c)^2 r}\left[2\pi i \frac{(\frac{\omega}{c})e^{i\omega r/c}}{\frac{\omega}{c} + \frac{\omega}{c}}\right]$$

$$G(\omega;\mathbf{r}) = \frac{-e^{i\omega r/c}}{4\pi c^2 r}$$

Having completed the k-integrations involved in our function $G(\omega;\mathbf{r})$, we return to Eq. (2.22), where the expression for $\mathbf{E}(\mathbf{r},t)$ now involves only a frequency integration

$$\mathbf{E}(\mathbf{r},t) = \frac{ie}{\epsilon_0}\int_{-\infty}^{\infty} \omega \mathbf{v}_T(\omega) e^{-i\omega t}\left[\frac{-e^{i\omega r/c}}{4\pi c^2 r}\right]\frac{d\omega}{2\pi}$$

or

$$\mathbf{E}(\mathbf{r},t) = \frac{e}{4\pi\epsilon_o c^2 r}\int_{-\infty}^{\infty} \underbrace{(-i\omega)\mathbf{v}_T(\omega)e^{-i\omega(t-r/c)}}_{\frac{d}{dt}\left[\mathbf{v}_T(\omega)e^{-i\omega(t-r/c)}\right]}\frac{d\omega}{2\pi} \tag{2.24}$$

$$\mathbf{E}(\mathbf{r},t) = \frac{e}{4\pi\epsilon_o c^2 r}\frac{d}{dt}\underbrace{\int_{-\infty}^{\infty} \mathbf{v}_T(\omega)e^{-i\omega(t-r/c)}\frac{d\omega}{2\pi}}_{\mathbf{v}_T\left(t-\frac{r}{c}\right)}$$

where the last notation recognizes the transform of $\mathbf{v}_T(\omega)$ in the variable $t' = t - r/c$.

Identifying the acceleration as

$$\mathbf{a}_T\left(t-\frac{r}{c}\right)=\frac{d}{dt}\mathbf{v}_T\left(t-\frac{r}{c}\right)$$

the electric field associated with the radiated wave can be written as

$$\boxed{\mathbf{E}(\mathbf{r},t)=\frac{e\mathbf{a}_T\left(t-\frac{r}{c}\right)}{4\pi\epsilon_0 c^2 r}} \tag{2.25}$$

which is the form given in Chapter 2 as Eq. (2.25). The physical interpretation of this expression is described in the text of Chaper 2, following Eq. (2.25).

Appendix F

LORENTZ SPACE–TIME TRANSFORMATIONS

In our studies of radiation from charged particles moving at velocities approaching that of light, a number of interesting phenomena are observed, such as the searchlight effect wherein radiation from the charged particle is constrained to a very narrow forward radiation cone. Furthermore, the calculation of detailed angular radiation patterns, in the frame of reference moving with the charged particle, and wavelength distributions are readily accomplished.[1] The results can then be transformed back to the laboratory, or observer, frame of reference. For instance, the calculation of undulator radiation reduces to use of the well-known formula for so-called *dipole radiation* from a simple oscillating electron. With this approach we need solve Maxwell's equations for only the simplest radiating system, a small amplitude oscillating electron. This approach is not only simple to follow, but gives valuable physical insights to the radiation process and the parameters that characterize it.

In order to relate calculations in one frame of reference to those in another frame of reference when the relative speed between the two approaches that of light, we must make use of the Lorentz space-time transformations, which provide relationships between spatial and temporal scales in the two frames of reference, and are consistent both with Einstein's postulates of special relativity and with all known experiments (see Ref. 2 for a discussion of the Lorentz transformations and their reduction to Galilean transformations as $v/c \to 0$).

The *Lorentz space-time transformations* between coordinates (x, y, z, t) in frame of reference S and coordinates (x', y', z', t') in frame of reference S', which moves at velocity v with respect to S in the z, z' direction (see Figure F.1), are as follows:

$$z = \gamma(z' + \beta ct') \tag{F.1a}$$

$$t = \gamma\left(t' + \frac{\beta z'}{c}\right) \tag{F.1b}$$

$$y = y' \quad \text{and} \quad x = x' \tag{F.1c}$$

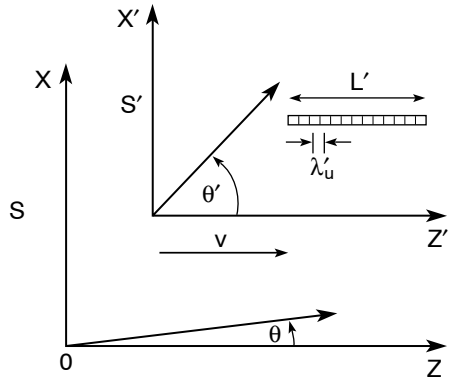

FIGURE F.1. Two frames of reference S and S' with relative velocity v, which approaches the speed of light in vacuum, c.

and

$$z' = \gamma(z - \beta ct) \tag{F.2a}$$

$$t' = \gamma\left(t - \frac{\beta z}{c}\right) \tag{F.2b}$$

$$y' = y \quad \text{and} \quad x' = x \tag{F.2c}$$

where c is the velocity of light in vacuum,

$$\beta \equiv \frac{v}{c} \tag{F.3}$$

and

$$\gamma \equiv \frac{1}{\sqrt{1 - \beta^2}} \tag{F.4}$$

Note that $\beta < 1$, and that for β approaching zero, γ approaches unity, and thus the Galilean transformations are obtained, i.e., $t = t'$ and $z = z' + vt'$.

We use these relationships to transform charged particle trajectories and radiation characteristics between natural frames of reference. We find it convenient to have at hand angular relationships that follow from Eqs (E.1–E.4), angle dependent Doppler shifts that follow therefrom, and expressions for the well-known time dilation and (Lorentz) length contraction characteristics of observations made between relativistically related coordinate systems.

F.1 FREQUENCY AND WAVENUMBER RELATIONS

To develop relationships between frequency and wavelength as observed in the two coordinate systems S and S', we consider a propagating wave observed from both systems. For such a wave the amplitude varies according to a phase factor

$$e^{i\phi} = e^{i(\omega t - \mathbf{k}\cdot\mathbf{r})}$$

where the wavenumber $|\mathbf{k}| = 2\pi/\lambda$ and where $\omega = 2\pi f$. In our coordinate systems S and S', the phase can be written as

$$\phi = \omega t - k_z z - k_x x - k_y y \tag{F.5a}$$

$$\phi' = \omega' t' - k'_z z' - k'_x x' - k'_y y' \tag{F.5b}$$

Since the phase has a particular value at some given space-time point (it might be at the crest of wave amplitude), it must be the same in both coordinate systems, and thus we can set Eq. (F.5a) equal to Eq. (F.5b), viz.,

$$\omega t - k_z z - k_x x - k_y y = \omega' t' - k'_z z' - k'_x x' - k'_y y'$$

The desired frequency and wavenumber (wavelength) relationships can be obtained by substituting the Lorentz relationships [Eq. (F.2)] into the identical phase relationship above. Making appropriate substitutions for t', z', x', and y' in the phase relationship, we have

$$\omega t - k_z x - k_x x - k_y y = \omega' \left[\gamma\left(t - \frac{\beta z}{c}\right)\right] - k'_z[\gamma(z - \beta ct)] - k'_x x - k'_y y$$

or by rearranging terms

$$\omega t - k_z z - k_x x - k_y y = [\omega'\gamma + \gamma\beta c k'_z]t - \left[\gamma k'_z + \gamma\omega'\frac{\beta}{c}\right] z - k'_x x - k'_y y$$

As this relationship must hold for arbitrary space-time position, we can match coefficients term by term in the above equation. Doing so, we obtain

$$\omega = \gamma(\omega' + \beta c k'_z) \tag{F.6a}$$

$$k_z = \gamma\left(k'_z + \frac{\beta\omega'}{c}\right) \tag{F.6b}$$

$$k_x = k'_x \quad \text{and} \quad k_y = k'_y \tag{F.6c}$$

and the inverse transformations

$$\omega' = \gamma(\omega - \beta c k_z) \tag{F.7a}$$

$$k'_z = \gamma\left(k_z - \frac{\beta\omega}{c}\right) \tag{F.7b}$$

$$k'_x = k_x \quad \text{and} \quad k'_y = k_y \tag{F.7c}$$

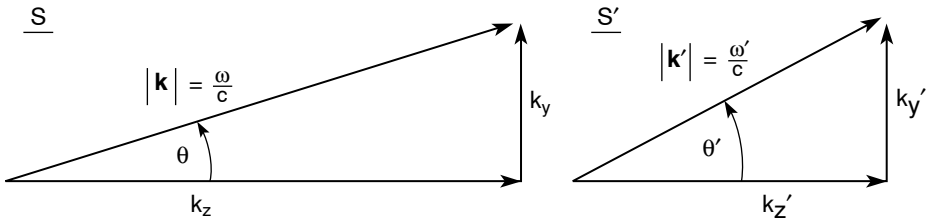

FIGURE F.2. The wave vector **k** for a wave propagating at an angle θ to the z-axis in the S frame of reference, and the same wave as observed in the S' frame of reference, with wave vector $\mathbf{k}'$ at an angle θ' to the (common) z-axis.

which relate wave propagation characteristics of frequency and wavenumber in two frames of reference moving at relativistic speed with respect to each other. They are commonly referred to as the *energy–momentum relations* because for a photon $E = \hbar\omega$ and $\mathbf{p} = \hbar\mathbf{k}$. Note that the relationships between ω and ω' are dependent on the angle of observation in that what appears in Eqs. (F.6) and (F.7) is the axial component of the wave vector (**k**), i.e., k_z.

The relationships take on quite a simple form if we decompose the wave vector in both reference frames, and introduce the angles θ and θ', representing the propagation direction measured from the common z, z' axis. This is illustrated in Figure F.2.

Utilizing the vector identifications evident in Figure F.2, the expression relating ω and ω' [Eq. (F.6a)] becomes

$$\omega = \gamma(\omega' + \beta c k_z') = \gamma\left(\omega' + \beta c \frac{\omega'}{c}\cos\theta'\right)$$

$$\boxed{\omega = \omega'\gamma(1 + \beta\cos\theta')} \tag{F.8a}$$

and from Eq. (F.7)

$$\omega' = \gamma(\omega - \beta c k_z) = \gamma\left(\omega - \beta c \frac{\omega}{c}\cos\theta\right)$$

or

$$\boxed{\omega' = \omega\gamma(1 - \beta\cos\theta)} \tag{F.8b}$$

Equations (F.8a) and (F.8b) describe the relativistically correct form for the Doppler shift (Refs. 3 and 4) of frequency when there is motion between the source and receiver (observer) that approaches the velocity of light.

A familiar form of Eq. (F.8a) is that for a source $\omega' = \omega_s$ moving toward the observer directly along the z-axis, where θ' is zero and $\cos\theta'$ is unity. Identifying the frequency $\omega = \omega_R$ as that received in the observer's frame of reference, one has

$$\omega = \omega'\gamma(1 + \beta)$$

Noting that

$$\gamma = \frac{1}{\sqrt{1-\beta^2}} = \frac{1}{\sqrt{1-\beta}\sqrt{1+\beta}}$$

one obtains the familiar form (Ref. 2)

$$\omega_R = \omega_S \sqrt{\frac{1+\beta}{1-\beta}} \quad \text{(forward, } \theta = 0\text{)}$$

or equivalently

$$f_R = f_S \sqrt{\frac{1+\beta}{1-\beta}}$$

as is sometimes seen.

F.2 ANGULAR TRANSFORMATIONS

Angular transformations between the two frames of reference (Ref. 3) can be obtained from the energy–momentum transformations, Eqs. (F.6) and (F.7). Again using the propagating wave depicted in Figure F.2, we can write

$$\cos\theta = \frac{k_z}{k} = \frac{k_z c}{\omega} = \frac{\gamma\left(k'_z + \frac{\beta\omega'}{c}\right)c}{\gamma(\omega' + \beta c k'_z)}$$

$$\cos\theta = \frac{\gamma\left[\frac{\omega'\cos\theta'}{c} + \frac{\beta\omega'}{c}\right]c}{\gamma\left[\omega' + \beta c \cdot \frac{\omega'}{c}\cos\theta'\right]}$$

or

$$\boxed{\cos\theta = \frac{\cos\theta' + \beta}{1 + \beta\cos\theta'}} \tag{F.9a}$$

Similarly

$$\cos\theta' = \frac{k'_z}{k'} = \frac{k'_z c}{\omega'} = \frac{\gamma\left(k_z - \frac{\beta\omega}{c}\right)c}{\gamma(\omega - \beta c k_z)}$$

$$\cos\theta' = \frac{\gamma\left[\frac{\omega\cos\theta}{c} - \frac{\beta\omega}{c}\right]c}{\gamma\left[\omega - \beta c\frac{\omega\cos\theta}{c}\right]}$$

or

$$\boxed{\cos\theta' = \frac{\cos\theta - \beta}{1 - \beta\cos\theta}} \tag{F.9b}$$

which gives us equations relating θ and θ' as a function of $\beta = v/c$. In similar fashion we can define $\sin\theta' = k'_y/k'$ to obtain

$$\sin\theta' = \frac{k'_y c}{\omega'} = \frac{k_y c}{\gamma(\omega - \beta c k_z)}$$

$$\sin\theta' = \frac{(k\sin\theta)c}{\gamma(\omega - \beta c k\cos\theta)}$$

or

$$\boxed{\sin\theta' = \frac{\sin\theta}{\gamma(1 - \beta\cos\theta)}} \tag{F.10a}$$

Then defining $\sin\theta = k_y/k = k_y c/\omega$ and using Eq. (F.6), one finds in similar fashion that

$$\boxed{\sin\theta = \frac{\sin\theta'}{\gamma(1 + \beta\cos\theta')}} \tag{F.10b}$$

Noting that $\tan\theta = \sin\theta/\cos\theta$ and that $\tan\theta' = \sin\theta'/\cos\theta'$, one finds that

$$\boxed{\tan\theta = \frac{\sin\theta'}{\gamma(\cos\theta' + \beta)}} \tag{F.11a}$$

$$\boxed{\tan\theta' = \frac{\sin\theta}{\gamma(\cos\theta - \beta)}} \tag{F.11b}$$

which could also be obtained by starting with $\tan\theta = k_y/k_z$, etc.

The $\tan\theta$ relation is convenient for illustrating the searchlight effect characteristic of synchrotron radiation from relativistic electrons for which $\gamma \gg 1$. For highly relativistic electrons experiencing significant acceleration, even if the radiation pattern is rather broad – for instance, $0 < \theta' < \pi/4$ in the electron (S') frame of reference – Eq. (F.11a) indicates that all this will be folded into a very narrow forward radiation cone, with half angle of order $1/2\gamma$.

F.3 THE LORENTZ CONTRACTION OF LENGTH

The Lorentz transformations contain information regarding differences of apparent length of the same object seen from two frames of reference, moving relative to each other at a relativistic speed. This applies not only to the traditional meter stick, but, more relevant to our studies, to periodic magnet structures. Figure F.1 includes such an object with length L' in S', and substructure of periodicity λ_u'.

To understand the apparent differences in length, as seen in S and S' at a given instant of time, consider an object at rest in frame S with endpoints (z_1', t') and (z_2', t') in S', and (z_1, t), (z_2, t) in S. According to the Lorentz transformations, Eq. (F.1), the positions are related by

$$z_1 = \gamma(z_1' + \beta ct')$$

and

$$z_2 = \gamma(z_2' + \beta ct')$$

Subtracting, we have

$$z_1 - z_2 = \gamma[z_1' - z_2' + \beta ct' - \beta ct']$$

and thus

$$z_1 - z_2 = \gamma(z_1' - z_2')$$

Defining $L = z_1 - z_2$ and $L' = z_1' - z_2'$, we have

$$L = \gamma L'$$

or

$$\boxed{L' = L/\gamma} \tag{F.12}$$

which succinctly describes the Lorentz contraction of length. An object of length L as seen in frame of reference S appears significantly shorter (L/γ) in the frame of reference S' that is moving at a relative velocity approaching that of light. Similarly, a structure of periodicity λ_u in S will be observed as one of periodicity λ_u/γ in S'. Note that $\beta = v/c$ and $\gamma = 1/\sqrt{1-\beta^2}$, so that for β approaching unity (v approaching c), γ is very large and the contraction factor can be orders of magnitude. On the other hand, for non-relativistic velocities β approaches zero, γ approaches unity, and there is little or no contraction.

F.4 TIME DILATION

We next ask, what is the relationship between time intervals as observed from a given position? The position of observation is described as z in S, and as z' in S'. Referring to the beginning of the time interval as t_1', and the end as t_2' in S', and as t_1 and t_2 respectively in S, we can write from Eq. (F.1) that

$$t_1 = \gamma\left(t_1' + \frac{\beta z'}{c}\right)$$

and

$$t_2 = \gamma\left(t_2' + \frac{\beta z'}{c}\right)$$

Subtracting, and referring to the time intervals as $\Delta t = t_2 - t_1$ and $\Delta t' = t_2' - t_1'$, one has

$$\Delta t = \gamma\,\Delta t'$$

or

$$\boxed{\Delta t' = \Delta t/\gamma} \tag{F.13}$$

expressing algebraically what is known as *time dilation*. Equation (F.13) leads to the statement that "(relativistically) moving clocks run slow." In the famous *twin paradox*, although a time interval might be $\Delta t = 1$ second on earth, about the time of a heartbeat, the moving twin on a relativistic rocketship sees the elapsed time as much shorter, of order 1 second/γ, far too short for a heartbeat. Thus the relativistically moving twin ages more slowly.

F.5 TRANSFORMING $dP'/d\Omega'$ TO $dP/d\Omega$

In the sections dealing with the transformation of radiated power per unit solid angle from S' to S, there are several places where the algebra becomes tedious and distractive. Here, we have treated several of these items separately.

(1) **The $\sin^2\Theta'$ Factor:** Dipole radiation involves a $\sin^2\Theta'$ dependence in the S' frame. For the fundamental with oscillation in the x'-direction, this is written in θ', ϕ' as

$$\sin^2\Theta' = 1 - \sin^2\theta'\cos^2\phi'$$

From our section on the Lorentz transformations, Eq. (F.10a), in terms of time averaged values γ^* and β^* (see Chapter 5, Sections 5.4 and 5.5),

$$\sin\theta' = \frac{\sin\theta}{\gamma^*(1 - \beta^*\cos\theta)}$$

Noting the γ-relations developed earlier [Eqs. (5.26) and (5.67)], we have

$$\beta^* \simeq 1 - \frac{1}{2\gamma^{*2}}$$

The denominator of Eq. (F.10a) takes the form for small θ of order $1/\gamma$:

$$1 - \beta^*\cos\theta \simeq 1 - \beta^*\left(1 - \frac{\theta^2}{2} + \cdots\right)$$

$$1 - \beta^*\cos\theta \simeq 1 - \left(1 - \frac{1}{2\gamma^{*2}}\right)\left(1 - \frac{\theta^2}{2}\right)$$

$$1 - \beta^* \cos\theta \simeq \frac{1}{2\gamma^{*2}} + \frac{\theta^2}{2}$$

$$1 - \beta^* \cos\theta \simeq \frac{1}{2\gamma^{*2}}(1 + \gamma^{*2}\theta^2)$$

Substitution into Eq. (F.10a) gives

$$\sin\theta' \simeq \frac{\theta}{\gamma^* \left(\frac{1}{2\gamma^{*2}}(1 + \gamma^{*2}\theta^2)\right)}$$

or

$$\sin\theta' \simeq \frac{2\gamma^*\theta}{1 + \gamma^{*2}\theta^2} \tag{F.14}$$

Then Eq. (5.36) becomes

$$\sin^2\Theta' = 1 - \sin^2\theta' \cos^2\phi'$$

$$\sin^2\Theta' \simeq 1 - \frac{(2\gamma^*\theta)^2}{(1 + \gamma^{*2}\theta^2)^2}\cos^2\phi$$

$$\sin^2\Theta' \simeq \frac{(1 + \gamma^{*2}\theta^2)^2 - 4\gamma^{*2}\theta^2\cos^2\phi}{(1 + \gamma^{*2}\theta^2)^2}$$

$$\sin^2\Theta' \simeq \frac{1 + 2\gamma^{*2}\theta^2(1 - 2\cos^2\phi) + \gamma^{*4}\theta^4}{(1 + \gamma^{*2}\theta^2)^2} \tag{F.15}$$

as was used in Eq. (5.44).

(2) **Transformation from $d\Omega'$ to $d\Omega$:** As a next step, we wish to Lorentz-transform the solid angle

$$d\Omega' = \sin\theta' d\theta' d\phi'$$

to a θ, ϕ-coordinate system. Since ϕ and ϕ' are in planes perpendicular to the relativistic motion between the S and S' frames, the simple relationship $\phi' = \phi$ is true. Hence,

$$d\phi' = d\phi$$

By Eq. (F.14) we have a relation between θ and θ'. Now, all that is needed is a relationship between $d\theta'$ and $d\theta$. Toward this end, we can again use Eq. (F.14). This time, we take a derivative on both sides:

$$\cos\theta' d\theta' \simeq \frac{(1 + \gamma^{*2}\theta^2)(2\gamma^* d\theta) - 2\gamma^*\theta(2\gamma^{*2}\theta\, d\theta)}{(1 + \gamma^{*2}\theta^2)^2}$$

$$\cos\theta' d\theta' \simeq \frac{2\gamma^*(1 - \gamma^{*2}\theta^2)}{(1 + \gamma^{*2}\theta^2)^2} d\theta$$

To eliminate $\cos\theta'$, we note that

$$\cos^2\theta' = 1 - \sin^2\theta' \simeq 1 - \frac{(2\gamma^*\theta)^2}{(1 + \gamma^{*2}\theta^2)^2}$$

When written with a common denominator, expanded, and like terms collected, this gives

$$\cos\theta' \simeq \frac{1-\gamma^{*2}\theta^2}{1+\gamma^{*2}\theta^2}$$

Combining equations involving $\cos\theta'$ above, one has

$$\frac{1-\gamma^{*2}\theta^2}{1+\gamma^{*2}\theta^2}\,d\theta' \simeq \frac{2\gamma^*(1-\gamma^{*2}\theta^2)}{(1+\gamma^{*2}\theta^2)^2}\,d\theta$$

or

$$d\theta' \simeq \frac{2\gamma^*}{1+\gamma^{*2}\theta^2}\,d\theta \tag{F.16}$$

The equation for solid angle then becomes

$$d\Omega' \simeq \sin\theta' d\theta' d\phi \simeq \frac{4\gamma^{*2}}{(1+\gamma^{*2}\theta^2)^2}\cdot\theta\,d\theta\,d\phi \tag{F.17}$$

as was used in Eq. (5.45).

(3) **The $d\Omega$ Integrals:** In calculating the power radiated, it is necessary to integrate $dP/d\Omega$ [Chapter 5, Eq. (5.47)] over all solid angles. Because integration over ϕ contributes 2π to the integral [see paragraph before Eq. (5.50a)], the integration reduces to

$$\int_0^\pi\int_0^{2\pi}\frac{1+\gamma^{*4}\theta^4}{(1+\gamma^{*2}\theta^2)^5}\theta\,d\theta\,d\phi = \frac{2\pi}{\gamma^{*2}}\int_0^\pi\frac{(1+\gamma^{*4}\theta^4)(\gamma^*\theta)\,d(\gamma^*\theta)}{(1+\gamma^{*2}\theta^2)^5}$$

Substituting

$$u = \gamma^*\theta$$

$$x = 1+u^2$$

$$dx = 2u\,du$$

the integrand becomes $1+u^4 = 1+(u^2)^2 = 1+(x-1)^2 = x^2-2x+2$. Hence,

$$\int_0^\pi\int_0^{2\pi}\frac{1+\gamma^{*4}\theta^4}{(1+\gamma^{*2}\theta^2)^5}\theta\,d\theta\,d\phi = \frac{2\pi}{\gamma^{*2}}\cdot\frac{1}{2}\int_1^{(1+\pi^2\gamma^{*2})}\frac{(x^2-2x+2)\,dx}{x^5}$$

$$\int_0^\pi\int_0^{2\pi}\frac{1+\gamma^{*4}\theta^4}{(1+\gamma^{*2}\theta^2)^5}\theta\,d\theta\,d\phi = \frac{\pi}{\gamma^{*2}}\int_1^\infty\left(\frac{1}{x^3}-\frac{2}{x^4}+\frac{2}{x^5}\right)dx$$

$$\int_0^\pi\int_0^{2\pi}\frac{1+\gamma^{*4}\theta^4}{(1+\gamma^{*2}\theta^2)^5}\theta\,d\theta\,d\phi = \frac{\pi}{\gamma^{*2}}\left[\frac{1}{(-2x^2)}+\frac{2}{(3x^3)}+\frac{2}{(-4x^4)}\right]_1^\infty$$

Therefore the integral taking us from Eq. (5.47) to Eq. (5.50) becomes

$$\int_0^{\pi}\int_0^{2\pi} \frac{1+\gamma^{*4}\theta^4}{(1+\gamma^{*2}\theta^2)^5}\theta\, d\theta\, d\phi = \frac{\pi}{3\gamma^{*2}} \tag{F.18}$$

REFERENCES

1. J.D. Jackson, "The Impact of Special Relativity on Theoretical Physics," *Physics Today 40*, 34 (May 1987).
2. P.A. Tipler, *Modern Physics* (Worth, New York, 1978), pp. 21–23.
3. G. Joos, *Theoretical Physics*, (Hafner, New York, 1934), pp. 233–235.
4. L. Landau and E. Lifshitz, *The Classical Theory of Fields* (Addison-Wesley, Reading, MA, 1951), p. 121.

Index

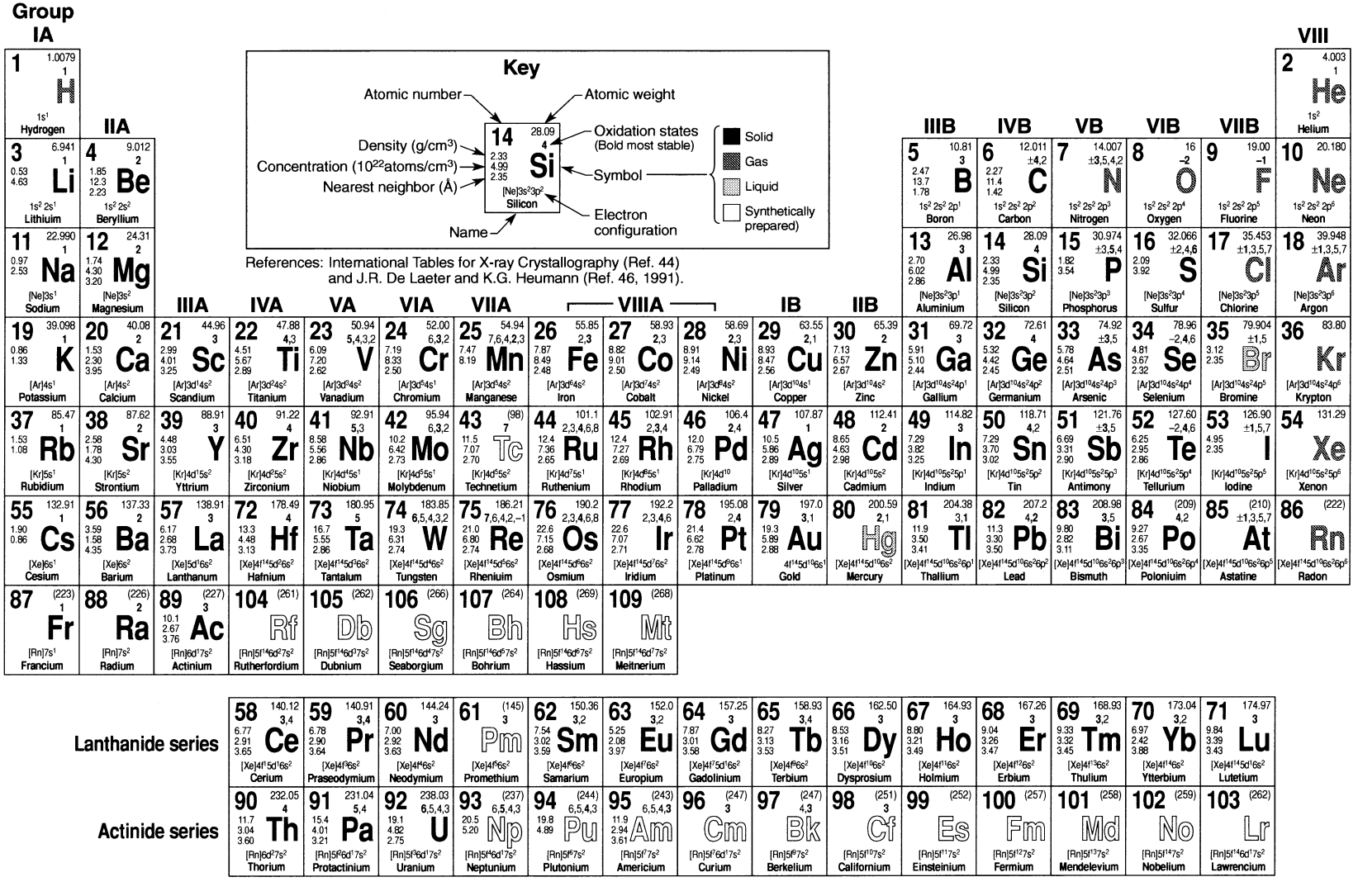
Group IA
VIII
IIA
IIIA
IVA
VA
VIA
VIIA
VIIIA
IB
IIB
IIIB
IVB
VB
VIB
VIIB
Key
Atomic number
Atomic weight
Density (g/cm3)
Concentration (10^22atoms/cm3)
Nearest neighbor (Å)
Oxidation states (Bold most stable)
Symbol
Name
Electron configuration
Solid
Gas
Liquid
Synthetically prepared)
14 28.09 4 2.33 4.99 2.35 Si [Ne]3s23p2 Silicon
References: International Tables for X-ray Crystallography (Ref. 44) and J.R. De Laeter and K.G. Heumann (Ref. 46, 1991).
1 1.0079 1 H 1s1 Hydrogen
2 4.003 1 He 1s2 Helium
3 6.941 1 0.53 4.63 Li 1s2 2s1 Lithium
4 9.012 2 1.85 12.3 2.23 Be 1s2 2s2 Beryllium
5 10.81 3 2.47 13.7 1.78 B 1s2 2s2 2p1 Boron
6 12.011 ±4,2 2.27 11.4 1.42 C 1s2 2s2 2p2 Carbon
7 14.007 ±3,5,4,2 N 1s2 2s2 2p3 Nitrogen
8 16 −2 O 1s2 2s2 2p4 Oxygen
9 19.00 −1 F 1s2 2s2 2p5 Fluorine
10 20.180 Ne 1s2 2s2 2p6 Neon
11 22.990 1 0.97 2.53 Na [Ne]3s1 Sodium
12 24.31 2 1.74 4.30 3.20 Mg [Ne]3s2 Magnesium
13 26.98 3 2.70 6.02 2.86 Al [Ne]3s23p1 Aluminium
14 28.09 4 2.33 4.99 2.35 Si [Ne]3s23p2 Silicon
15 30.974 ±3,5,4 1.82 3.54 P [Ne]3s23p3 Phosphorus
16 32.066 ±2,4,6 2.09 3.92 S [Ne]3s23p4 Sulfur
17 35.453 ±1,3,5,7 Cl [Ne]3s23p5 Chlorine
18 39.948 ±1,3,5,7 Ar [Ne]3s23p6 Argon
19 39.098 1 0.86 1.33 K [Ar]4s1 Potassium
20 40.08 2 1.53 2.30 3.95 Ca [Ar]4s2 Calcium
21 44.96 3 2.99 4.01 3.25 Sc [Ar]3d14s2 Scandium
22 47.88 4,3 4.51 5.67 2.89 Ti [Ar]3d24s2 Titanium
23 50.94 5,4,3,2 6.09 7.20 2.62 V [Ar]3d34s2 Vanadium
24 52.00 6,3,2 7.19 8.33 2.50 Cr [Ar]3d54s1 Chromium
25 54.94 7,6,4,2,3 7.47 8.19 Mn [Ar]3d54s2 Manganese
26 55.85 2,3 7.87 8.49 2.48 Fe [Ar]3d64s2 Iron
27 58.93 2,3 8.82 9.01 2.50 Co [Ar]3d74s2 Cobalt
28 58.69 2,3 8.91 9.14 2.49 Ni [Ar]3d84s2 Nickel
29 63.55 2,1 8.93 8.47 2.56 Cu [Ar]3d104s1 Copper
30 65.39 2 7.13 6.57 2.67 Zn [Ar]3d104s2 Zinc
31 69.72 3 5.91 5.10 2.44 Ga [Ar]3d104s24p1 Gallium
32 72.61 4 5.32 4.42 2.45 Ge [Ar]3d104s24p2 Germanium
33 74.92 ±3,5 5.78 4.64 2.51 As [Ar]3d104s24p3 Arsenic
34 78.96 −2,4,6 4.81 3.67 2.32 Se [Ar]3d104s24p4 Selenium
35 79.904 ±1,5 3.12 2.35 Br [Ar]3d104s24p5 Bromine
36 83.80 Kr [Ar]3d104s24p6 Krypton
37 85.47 1 1.53 1.08 Rb [Kr]5s1 Rubidium
38 87.62 2 2.58 1.78 4.30 Sr [Kr]5s2 Strontium
39 88.91 3 4.48 3.03 3.55 Y [Kr]4d15s2 Yttrium
40 91.22 4 6.51 4.30 3.18 Zr [Kr]4d25s2 Zirconium
41 92.91 5,3 8.58 5.56 2.86 Nb [Kr]4d45s1 Niobium
42 95.94 6,3,2 10.2 6.42 2.73 Mo [Kr]4d55s1 Molybdenum
43 (98) 7 11.5 7.07 2.70 Tc [Kr]4d55s2 Technetium
44 101.1 2,3,4,6,8 12.4 7.36 2.65 Ru [Kr]4d75s1 Ruthenium
45 102.91 2,3,4 12.4 7.27 2.69 Rh [Kr]4d85s1 Rhodium
46 106.4 2,4 12.0 6.79 2.75 Pd [Kr]4d10 Palladium
47 107.87 1 10.5 5.86 2.89 Ag [Kr]4d105s1 Silver
48 112.41 2 8.65 4.63 2.98 Cd [Kr]4d105s2 Cadmium
49 114.82 3 7.29 3.82 3.25 In [Kr]4d105s25p1 Indium
50 118.71 4,2 7.29 3.70 3.02 Sn [Kr]4d105s25p2 Tin
51 121.76 ±3,5 6.69 3.31 2.90 Sb [Kr]4d105s25p3 Antimony
52 127.60 −2,4,6 6.25 2.95 2.86 Te [Kr]4d105s25p4 Tellurium
53 126.90 ±1,5,7 4.95 2.35 I [Kr]4d105s25p5 Iodine
54 131.29 Xe [Kr]4d105s25p6 Xenon
55 132.91 1 1.90 0.86 Cs [Xe]6s1 Cesium
56 137.33 2 3.59 1.58 4.35 Ba [Xe]6s2 Barium
57 138.91 3 6.17 2.68 3.73 La [Xe]5d16s2 Lanthanum
72 178.49 4 13.3 4.48 3.13 Hf [Xe]4f145d26s2 Hafnium
73 180.95 5 16.7 5.55 2.86 Ta [Xe]4f145d36s2 Tantalum
74 183.85 6,5,4,3,2 19.3 6.31 2.74 W [Xe]4f145d46s2 Tungsten
75 186.21 7,6,4,2,−1 21.0 6.80 2.74 Re [Xe]4f145d56s2 Rheniuim
76 190.2 2,3,4,6,8 22.6 7.15 2.68 Os [Xe]4f145d66s2 Osmium
77 192.2 2,3,4,6 22.6 7.07 2.71 Ir [Xe]4f145d76s2 Iridium
78 195.08 2,4 21.4 6.62 2.78 Pt [Xe]4f145d96s1 Platinum
79 197.0 3,1 19.3 5.89 2.88 Au 4f145d106s1 Gold
80 200.59 2,1 Hg [Xe]4f145d106s2 Mercury
81 204.38 3,1 11.9 3.50 3.41 Tl [Xe]4f145d106s26p1 Thallium
82 207.2 4,2 11.3 3.30 3.50 Pb [Xe]4f145d106s26p2 Lead
83 208.98 3,5 9.80 2.82 3.11 Bi [Xe]4f145d106s26p3 Bismuth
84 (209) 4,2 9.27 2.67 3.35 Po [Xe]4f145d106s26p4 Poloniuim
85 (210) ±1,3,5,7 At [Xe]4f145d106s26p5 Astatine
86 (222) Rn [Xe]4f145d106s26p6 Radon
87 (223) 1 Fr [Rn]7s1 Francium
88 (226) 2 Ra [Rn]7s2 Radium
89 (227) 3 10.1 2.67 3.76 Ac [Rn]6d17s2 Actinium
104 (261) Rf [Rn]5f146d27s2 Rutherfordium
105 (262) Db [Rn]5f146d37s2 Dubnium
106 (266) Sg [Rn]5f146d47s2 Seaborgium
107 (264) Bh [Rn]5f146d57s2 Bohrium
108 (269) Hs [Rn]5f146d67s2 Hassium
109 (268) Mt [Rn]5f146d77s2 Meitnerium
Lanthanide series
58 140.12 3,4 6.77 2.91 3.65 Ce [Xe]4f15d16s2 Cerium
59 140.91 3,4 6.78 2.90 3.64 Pr [Xe]4f36s2 Praseodymium
60 144.24 3 7.00 2.92 3.63 Nd [Xe]4f46s2 Neodymium
61 (145) 3 Pm [Xe]4f56s2 Promethium
62 150.36 3,2 7.54 3.02 3.59 Sm [Xe]4f66s2 Samarium
63 152.0 3,2 5.25 2.08 3.97 Eu [Xe]4f76s2 Europium
64 157.25 3 7.87 3.01 3.58 Gd [Xe]4f75d16s2 Gadolinium
65 158.93 3,4 8.27 3.13 3.53 Tb [Xe]4f96s2 Terbium
66 162.50 3 8.53 3.16 3.51 Dy [Xe]4f106s2 Dysprosium
67 164.93 3 8.80 3.21 3.49 Ho [Xe]4f116s2 Holmium
68 167.26 3 9.04 3.26 3.47 Er [Xe]4f126s2 Erbium
69 168.93 3,2 9.33 3.32 3.45 Tm [Xe]4f136s2 Thulium
70 173.04 3,2 6.97 2.42 3.88 Yb [Xe]4f146s2 Ytterbium
71 174.97 3 9.84 3.39 3.43 Lu [Xe]4f145d16s2 Lutetium
Actinide series
90 232.05 4 11.7 3.04 3.60 Th [Rn]6d27s2 Thorium
91 231.04 5,4 15.4 4.01 3.21 Pa [Rn]5f26d17s2 Protactinium
92 238.03 6,5,4,3 19.1 4.82 2.75 U [Rn]5f36d17s2 Uranium
93 (237) 6,5,4,3 20.5 5.20 Np [Rn]5f46d17s2 Neptunium
94 (244) 6,5,4,3 19.8 4.89 Pu [Rn]5f67s2 Plutonium
95 (243) 6,5,4,3 11.9 2.94 3.61 Am [Rn]5f77s2 Americium
96 (247) 3 Cm [Rn]5f76d17s2 Curium
97 (247) 4,3 Bk [Rn]5f97s2 Berkelium
98 (251) 3 Cf [Rn]5f107s2 Californium
99 (252) Es [Rn]5f117s2 Einsteinium
100 (257) Fm [Rn]5f127s2 Fermium
101 (258) Md [Rn]5f137s2 Mendelevium
102 (259) No [Rn]5f147s2 Nobelium
103 (262) Lr [Rn]5f146d17s2 Lawrencium

The colour figures in the following plate section have been replaced with black and white images for this digital reprinting. At the time of going to press the original images were available in colour for download from http://www.cambridge.org/9780521029971

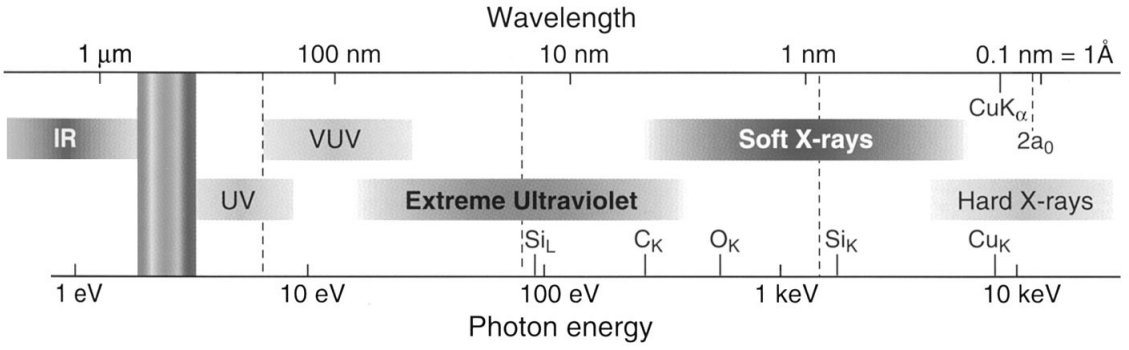

COLORPLATE I. The electromagnetic spectrum as it extends from the infrared (IR) to the x-ray regions. Visible light is shown with red (650 nm), green (530 nm), and blue (470 nm) wavelengths. At shorter wavelengths are ultraviolet (UV) radiation, extreme ultraviolet radiation (EUV), soft x-rays (SXR), and hard x-rays. Shown for reference are the silicon L-absorption edge at 99.2 eV (12.5 nm wavelength), the carbon K-absorption edge at 284 eV (4.37 nm), the oxygen K-absorption edge at 543 eV (2.28 nm), the silicon K-absorption edge at 1.84 keV (0.674 nm), the copper K-absorption edge at 8.98 keV (0.138 nm), the copper K_α-emission line at 0.154 nm or 1.54 Å (8.05 keV), and twice the Bohr radius at $2a_0 = 1.06$ Å, the diameter of the $n = 1$ orbit in Bohr's model of the hydrogen atom, but more generally a dimension within which resides most of the charge for all atoms. Vertical dashed lines correspond to the transmission limits of common window materials used to isolate vacuum. Shown are approximate transmission limits for common thicknesses of fused silica (pure SiO_2) at 200 nm, a thin film of silicon nitride (~100 nm thick Si_3N_4) at 15 nm, and an 8-μm thick beryllium foil at a wavelength of about 1 nm. See text, p. 2.

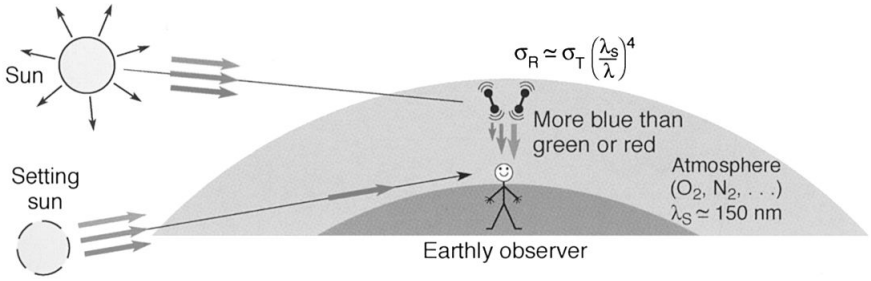

COLORPLATE II. Looking upward, the earthly observer at night sees only blackness or the occasional star. However during daylight, indirect light is scattered toward the observer when looking overhead. This scattering is caused by non-uniformities in the atmospheric density of O_2 and N_2, and appears blue because of the strong wavelength dependence of light scattering by bound electrons. Upon direct viewing of the sun, particularly at sunset, the light path is long and passes through the most dense portion of the atmosphere. As much of the residual light reaching the observer at sunset is greatly depleted in blue and green, the sun appears red, as do any clouds off which this reddish light might reflect. Very fine atmospheric dust, such as volcanic ash, causes a similar effect. See text, p. 44.

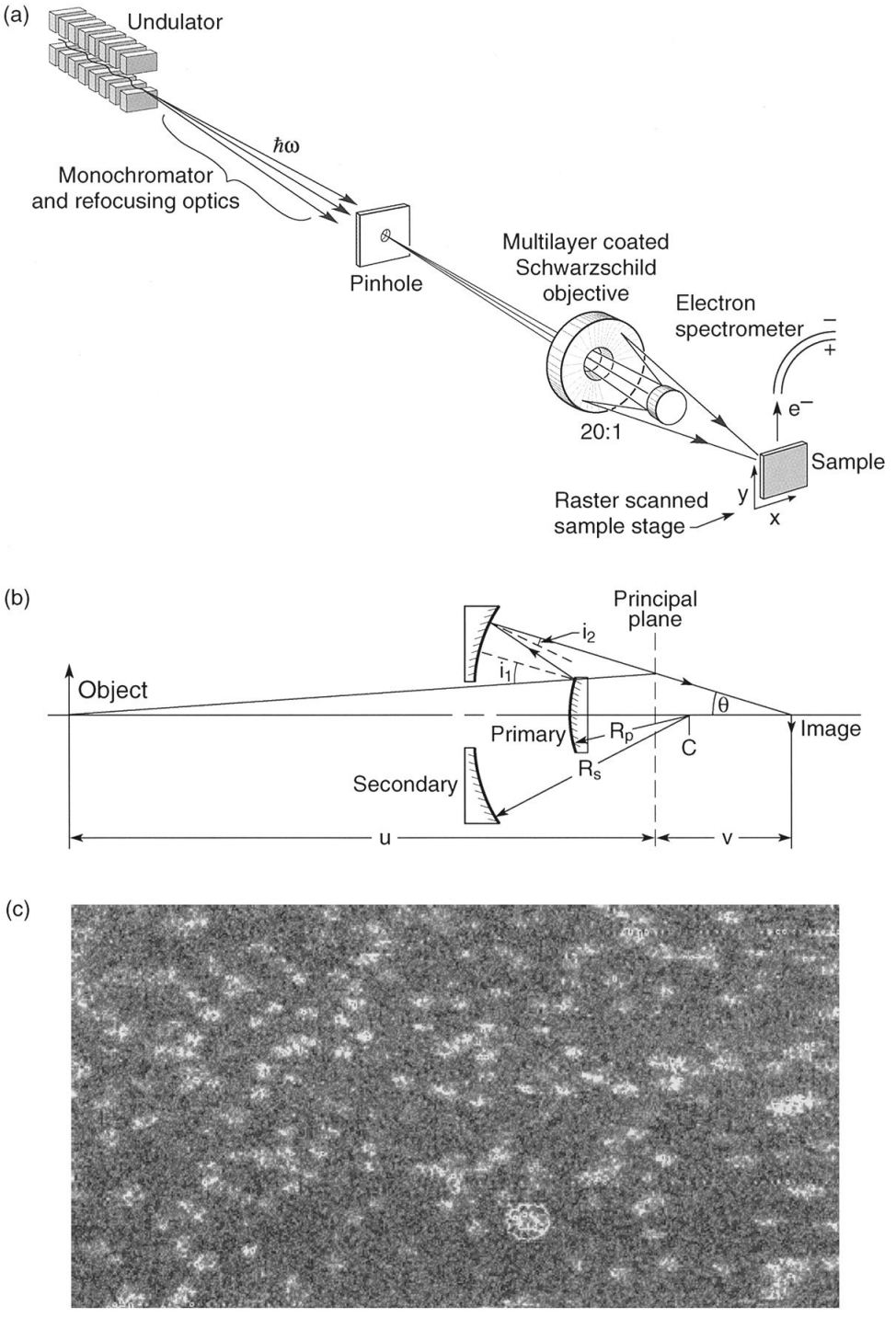

COLORPLATE III. (a) The photoemission microscope of Cerrina, Underwood, and colleagues, employing a multilayer coated Schwarzschild objective to focus monochromatic undulator radiation to a nominal 100 nm spot size. Photoelectron energy distributions are measured as a function of position as the sample position (x, y) is raster scanned. (b) Details of the Schwarzschild optics are shown. The object is a pinhole demagnified $(u/v = 20)$ to a reduced focal spot size. (c) A secondary electron photoemission micrograph of an AlGaN thin film. The incident photon energy is 126 eV, and the collected secondary electrons have a kinetic energy of 5 eV. Lateral inhomogeneities show a mean grain size of about 2 μm in this 30 μm $\times$ 60 μm image. (Courtesy of J.F. Lorusso and F. Cerrina, University of Wisconsin, Madison.) See text, p. 109.

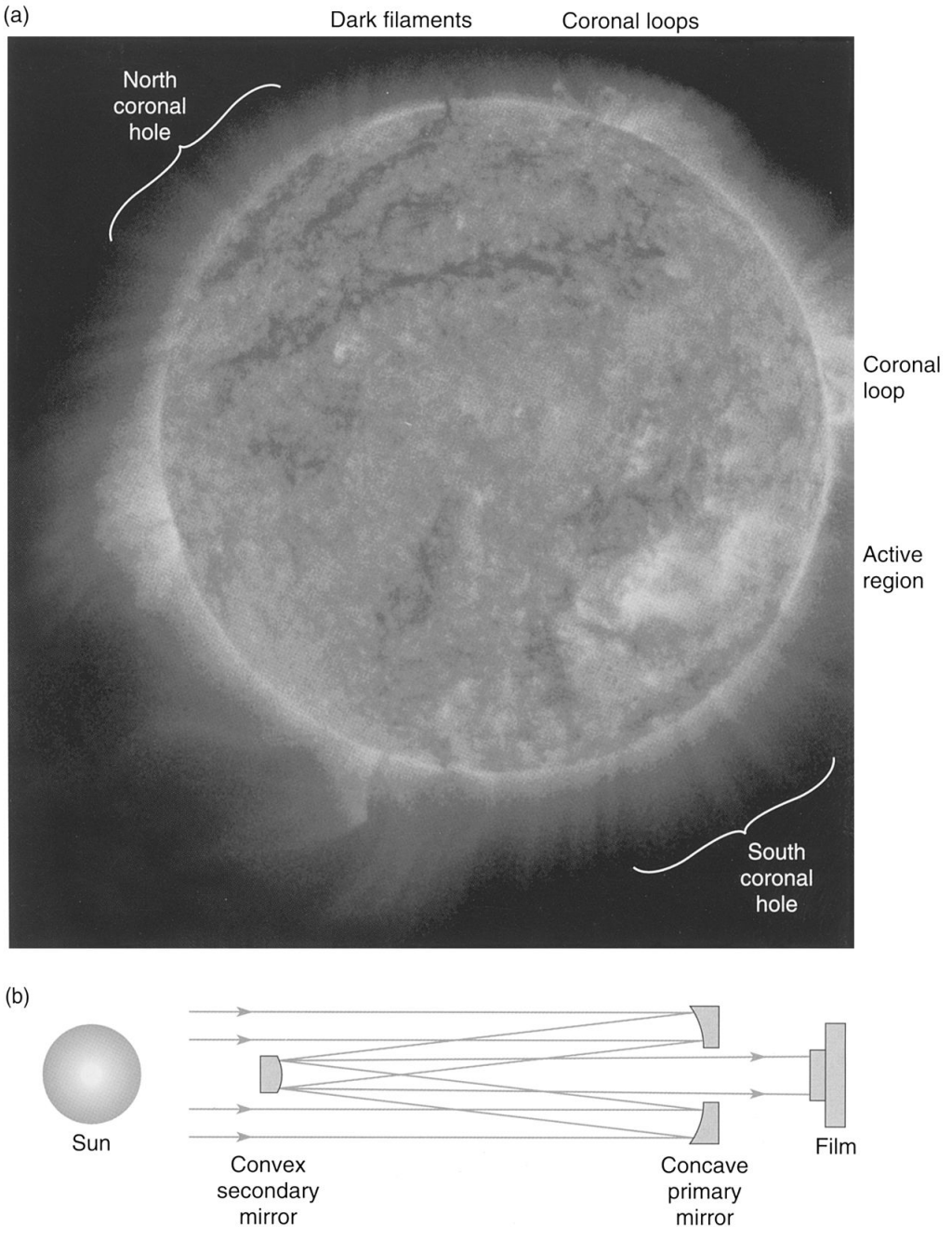

COLORPLATE IV. (a) EUV image of the sun obtained with a rocket launched Cassegrain telescope employing multilayer coated normal incidence optics. (b) The telescope employs Mo/Si-coated spherical optics that, in combination with an aluminum L-edge filter, provide a 17.1 nm to 17.5 nm spectral bandpass. It achieves an angular resolution of about 1.2 arcsec (5.8 μrad). (Courtesy of A.B.C. Walker, T.W. Barbee, R.B. Hoover, and J.F. Lindblom; Stanford University, LLNL, and NASA.) See text, p. 111.

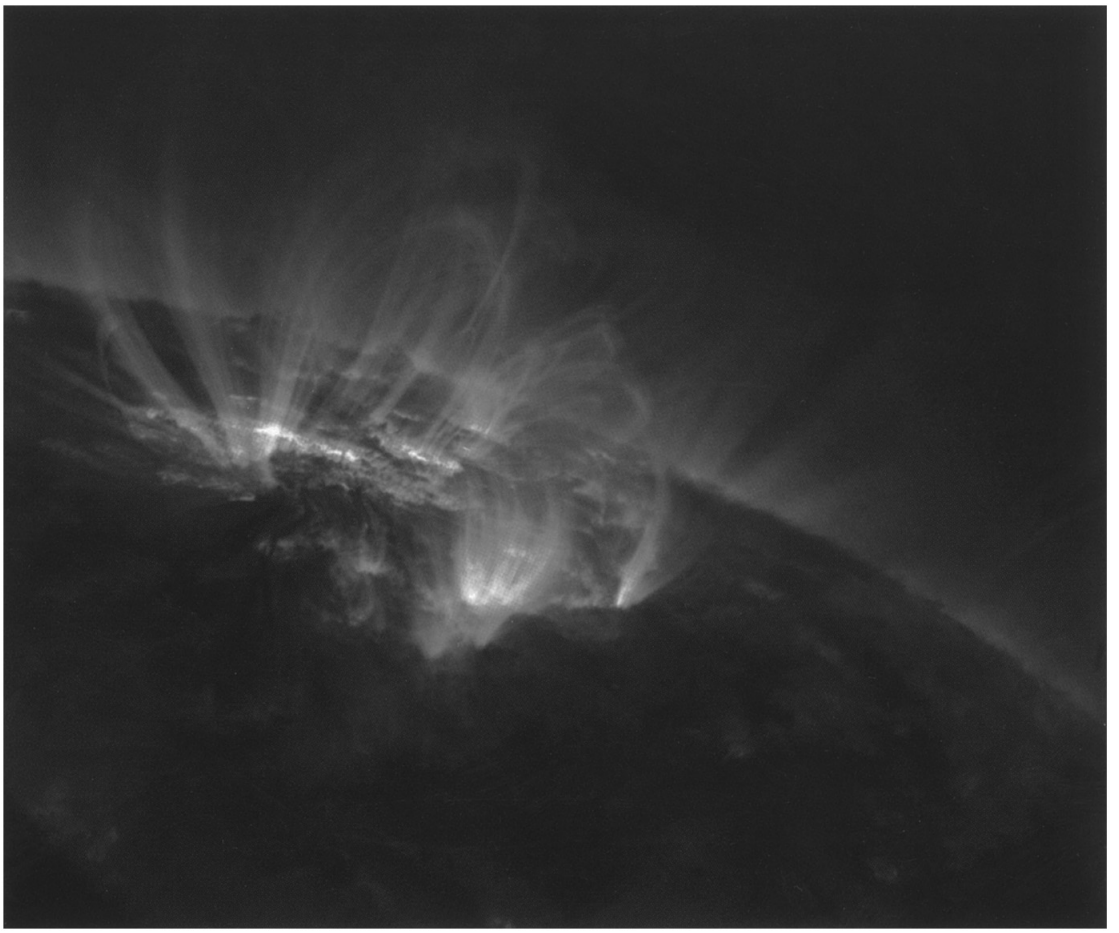

COLORPLATE V. An EUV image of the solar corona showing arcsecond details of loops near the solar limb. (Courtesy of L. Golub, A. Title, C. Wolfson, B. Handy, T.W. Barbee; Smithsonian Astrophysical Laboratory, Lockheed Martin, LLNL, and NASA.) See text, p. 112.

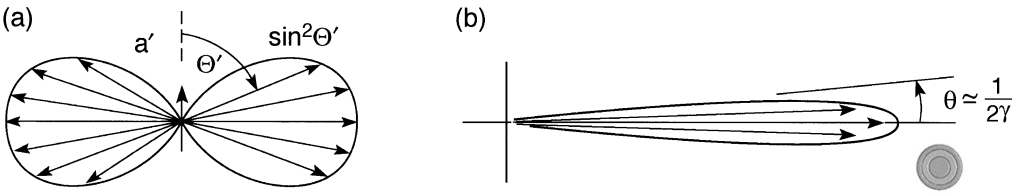

COLORPLATE VI. (a) Illustration of the radiation pattern of an oscillating electron in the frame of reference moving with the average electron speed. (b) Illustration of the radiation pattern of a highly relativistic electron as observed in the laboratory frame of reference. The shortest wavelengths are observed on axis. (Following Hofmann.) See text, p. 138.

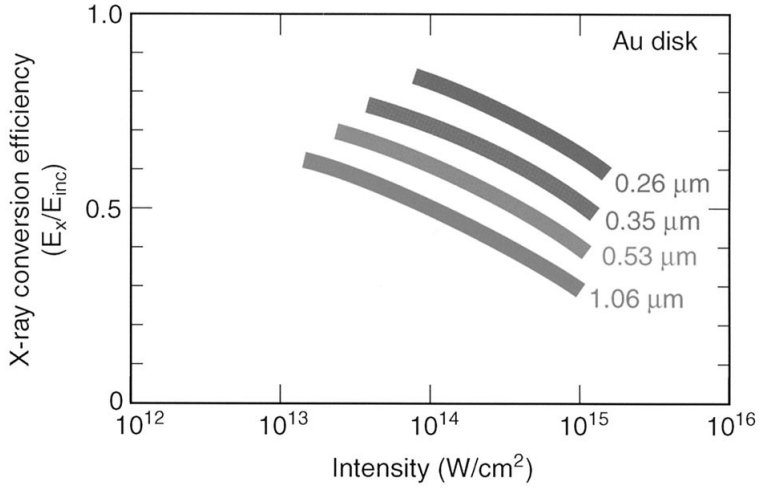

COLORPLATE VII. Curves showing the trend of x-ray conversion energy within the broad 0.1 keV to 1.5 keV spectral window, divided by the incident laser energy, assuming a Lambertian ($\cos\theta$) angular distribution in the emission hemisphere. Efficiency is shown as a function of intensity for Nd laser light at 1.06 μm (red) and its harmonics at 0.53 μm (green), 0.35 μm (blue), and 0.26 μm (ultraviolet) for nanosecond duration pulses. The target is a gold disk. The curves are derived largely from the data of R. Kauffman, H. Kornblum, G. Tirsell, P. Lee, R. Turner, and colleagues, Lawrence Livermore National Laboratory. See text, p. 258.

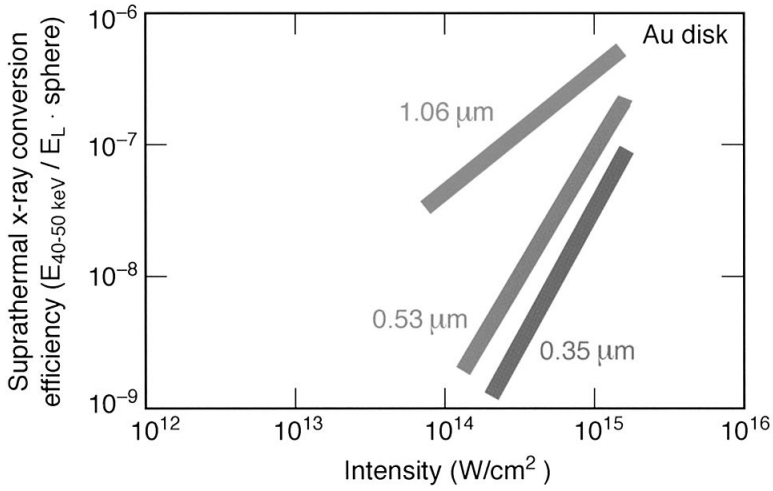

COLORPLATE VIII. Curves showing the general trend of suprathermal x-ray generation vs. laser intensity and wavelength. The specific data here shows radiated energy in a 40–50 keV spectral window, as a function of incident laser intensity for three wavelengths: 1.06 μm (red), 0.53 μm (green), and 0.35 μm (blue). The curves are derived from the data of E.M. Campbell, B. Pruett, R. Turner, F. Ze, and W. Mead, LLNL. See text, p. 259.

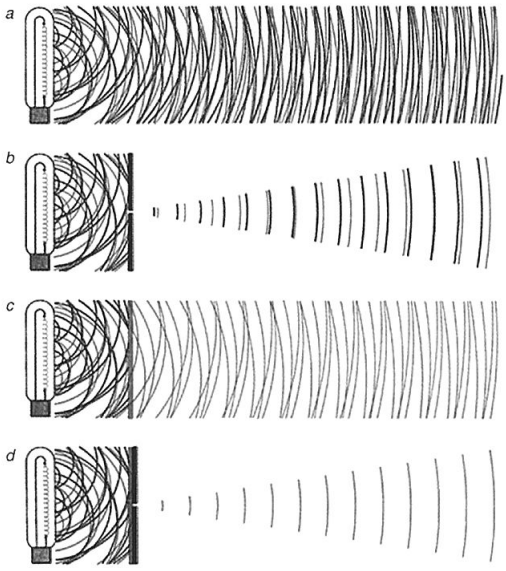

COLORPLATE IX. Spatial and spectral filtering is illustrated as a procedure to produce coherent radiation, albeit at greatly diminished power, from an ordinary thermal source of visible light. In the nomenclature used here, d would be the diameter of the pinhole shown in part (d), and θ would be the divergence half angle in part (d), set either by the radiation emission characteristics, by a downstream acceptance aperture, or by a lens. (Courtesy of A. Schawlow, Stanford.) See text, p. 309.

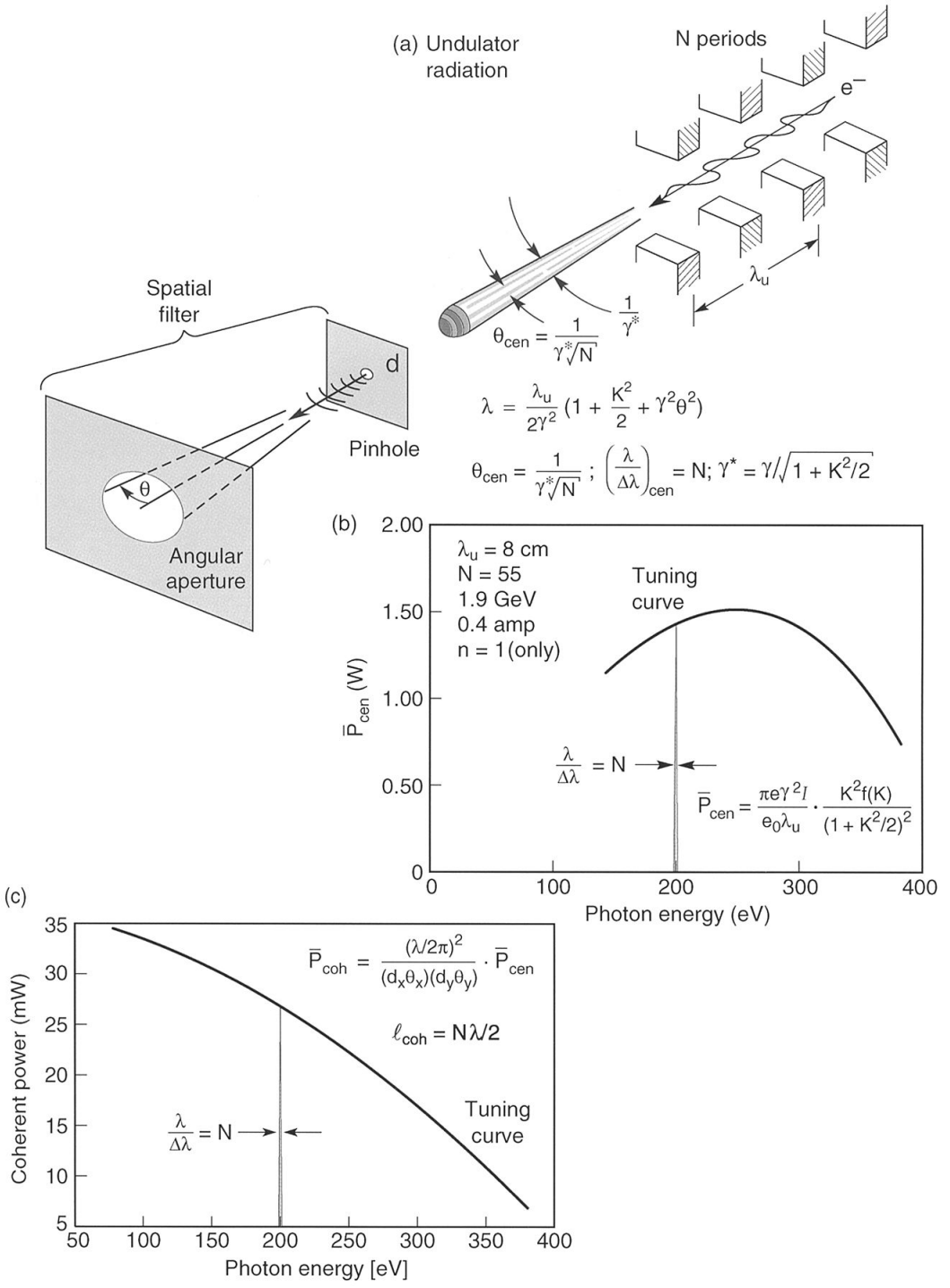

COLORPLATE X. (a) Undulator radiation with a pinhole spatial filter. (b) Power in the central radiation cone (θ_{cen}, $1/N$ relative spectral bandwidth) for an 8 cm period undulator at the Advanced Light Source (ALS) at Lawrence Berkeley National Laboratory. (c) Time-averaged coherent power after spatial filtering ($d \cdot \theta = \lambda/2\pi$). See text, p. 311.

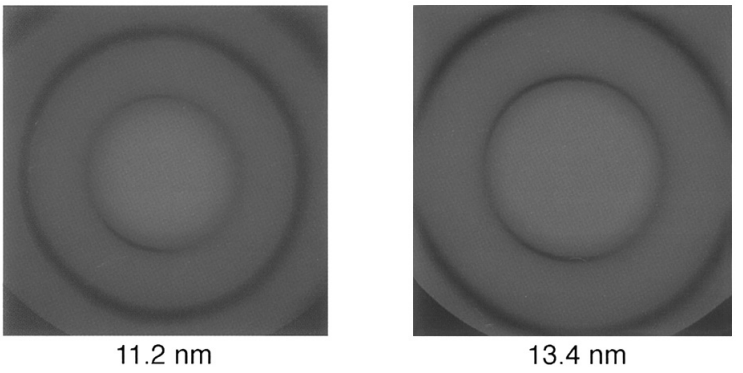

COLORPLATE XI. Far-field images (Airy patterns) of spatially filtered undulator radiation at wavelengths of 11.2 nm and 13.4 nm. Wavelength tuning is accomplished through variation of the magnetic field, and thus K, for an 8 cm period undulator at the Advanced Light Source. The beamline and pinhole spatial filter are illustrated in Colorplate X and discussed in the text. A 1.1 μm diameter pinhole was used, and the monochromator was set for a relative spectral bandwidth of 1/1100. The measured power in the central Airy disk is 11 μW at 13.4 nm wavelength. Radiation within the central Airy disk is used for spatially coherent experimentation. (Courtesy of P. Naulleau and colleagues, LBNL.) See text, p. 318.

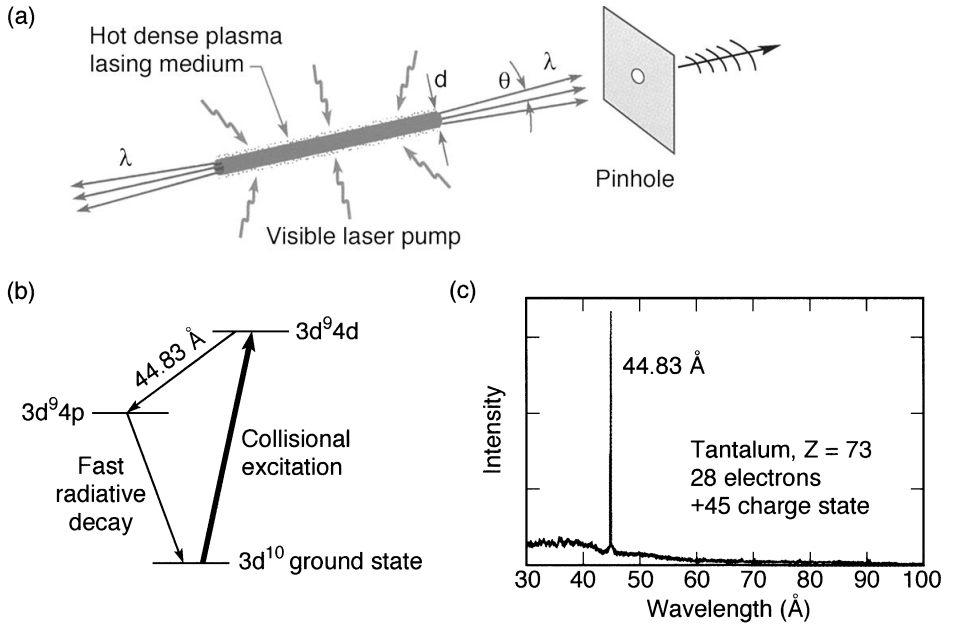

COLORPLATE XII. Soft x-ray lasing is demonstrated on a 4d to 4p ($J = 0$ to 1) transition at 4.483 nm wavelength (276.6 eV) in nickel-like tantalum atoms ($Z = 73$, 28 electrons, +45 charge state). The highly stripped atoms are created and collisionally pumped in a hot dense laser plasma created by a high power 250 psec pulse duration terawatt laser pulse. A multimode 100 kW pulse is produced in both directions at 4.483 nm wavelength. Spatial filtering to a single transverse mode would yield a 20 mW pulse of spatially coherent radiation with a 25-μm longitudinal coherence length. (Courtesy of B. MacGowan and colleagues, LLNL.) See text, p. 320.

The colour figures in the following plate section have been replaced with black and white images for this digital reprinting. At the time of going to press the original images were available in colour for download from http://www.cambridge.org/9780521029971

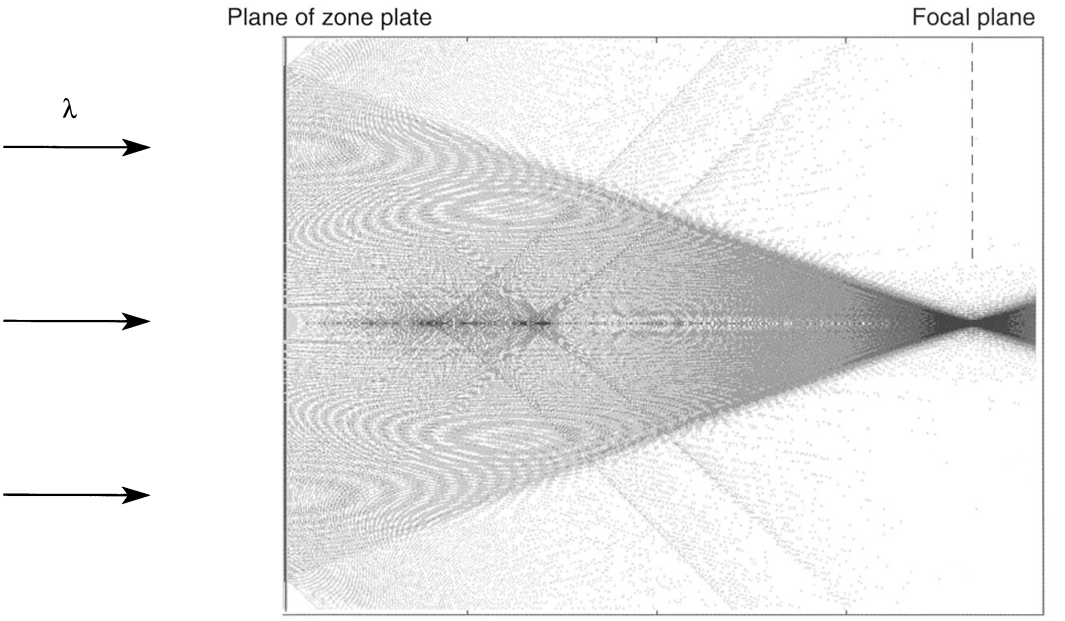

COLORPLATE XIII. Diffraction from a thick nickel zone plate lens calculated in the parabolic wave approximation. The zone plate thickness is 300 nm, the wavelength is 2.4 nm, the outer zone width is 30 nm, and the zone plate has 300 zones, an outer diameter of 36 μm, and a focal length of 450 μm in first order. (Courtesy of Yu.V. Kopylov and A.V. Popov, Moscow Optics Group.) See text, p. 357.

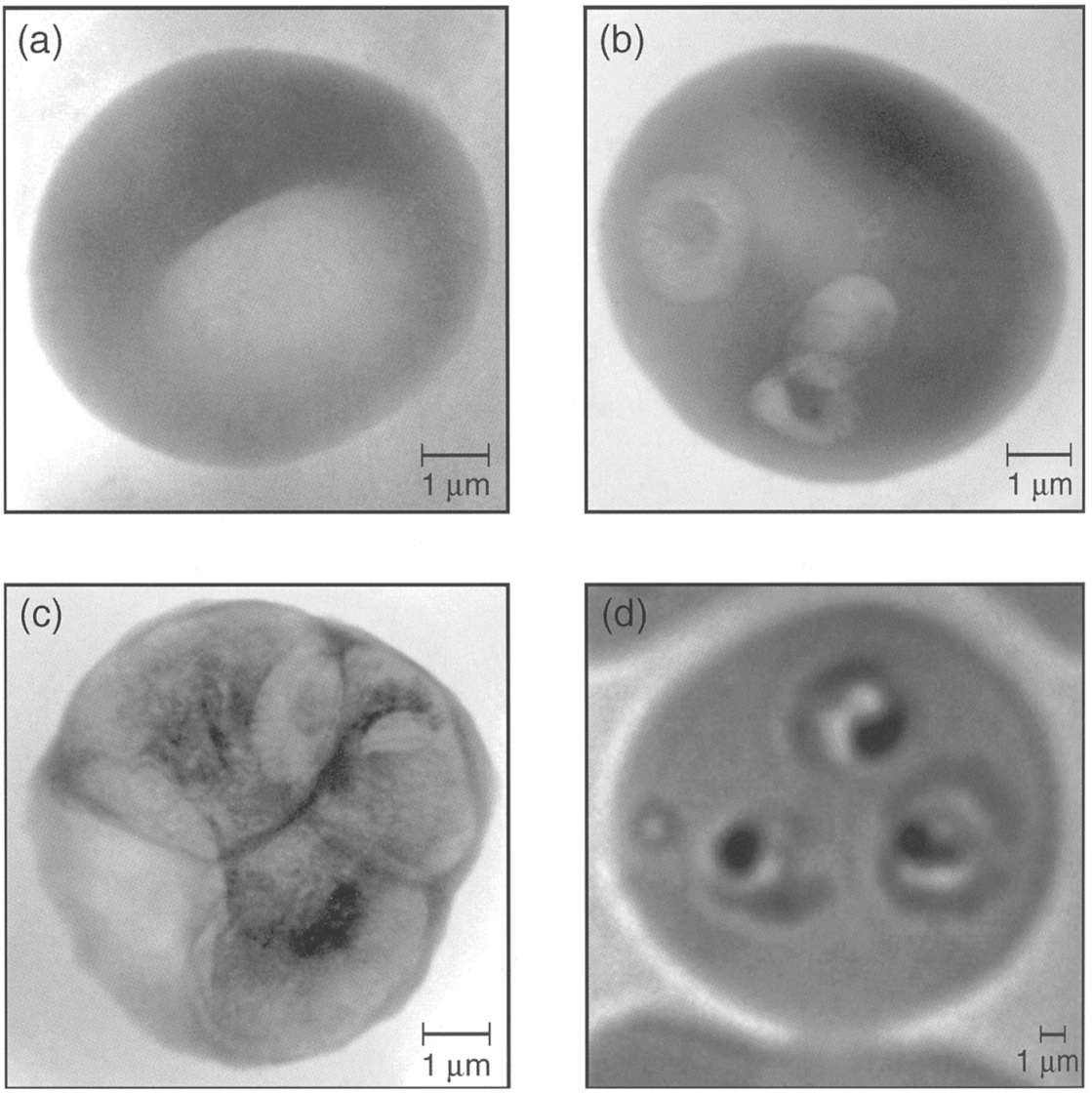

COLORPLATE XIV. Images of malaria infected red blood cells obtained at 2.4 nm wavelength with the high resolution soft x-ray microscope XM-1 at the Advanced Light Source in Berkeley. Image (a) shows an uninfected cell, (b) shows a newly infected cell, and (c) shows a cell 36 h after infection. All are chemically fixed. From C. Magowan, W. Meyer-Ilse, and J. Brown, LBNL. Image (d), obtained with visible light microscopy, is shown for comparison. See text, p. 372.

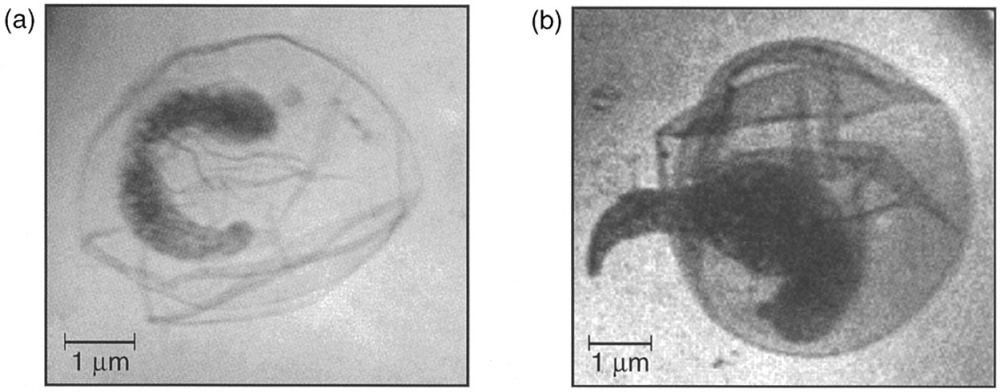

COLORPLATE XV. Soft x-ray images of *Cryptosporidium*, a common parasite found in lakes and rivers, and occasionally in municipal water supplies. Outbreaks of the disease caused by this sporozoite have caused loss of life in the U.S. Image (a) shows the last of four sporozoites still in its protective oocyst. Image (b) shows a sporozoite emerging from the oocyst. Images are at 2.4 nm wavelength. (Courtesy of C. Peterson, UCSF, and W. Meyer-Ilse, LBNL.) See text, p. 373.

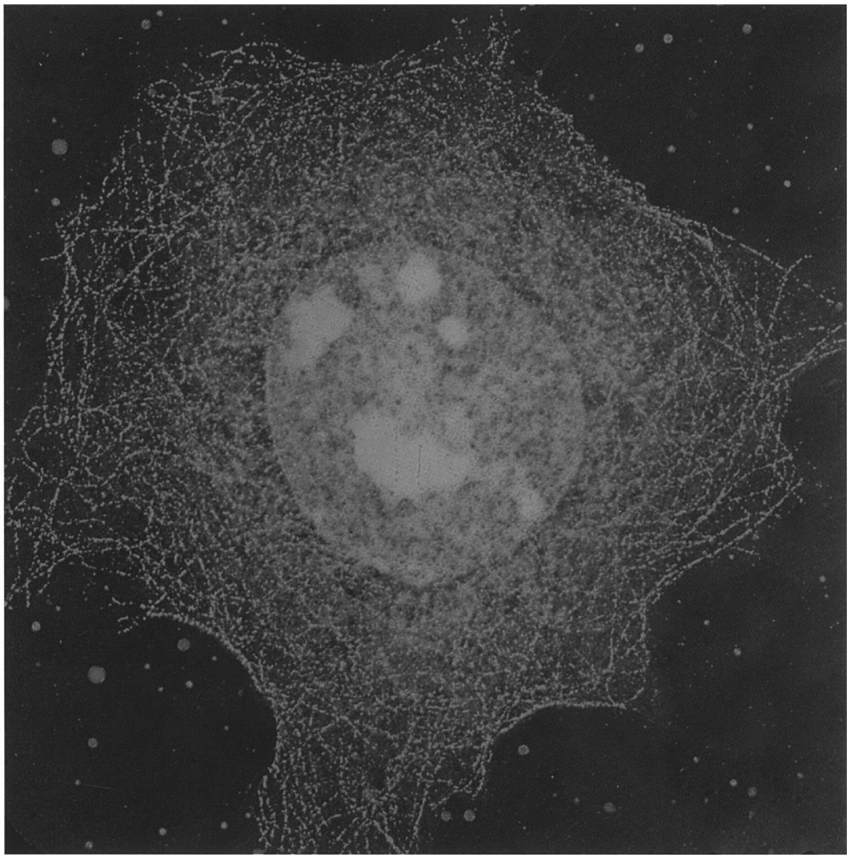

COLORPLATE XVI. A soft x-ray micrograph at 520 eV (2.4 nm wavelength) of a whole hydrated mouse epithelial cell (EPH4). The image is 32 μm by 32 μm. The microtubule network, made evident by high absorption due to silver enhanced gold labels, is color coded blue in the image. The cell nucleus and nucleoli, characterized by moderately absorbing proteins, are coded orange. The less absorbing more aqueous regions of the cell are color coded black. The silver enhanced gold is part of a molecular double label, discussed in the text, that permits cross correlation with visible light fluorescence in a confocal microscope. (Courtesy of C. Larabell, W. Meyer-Ilse, and colleagues, Lawrence Berkeley National Laboratory.) See text, p. 374.

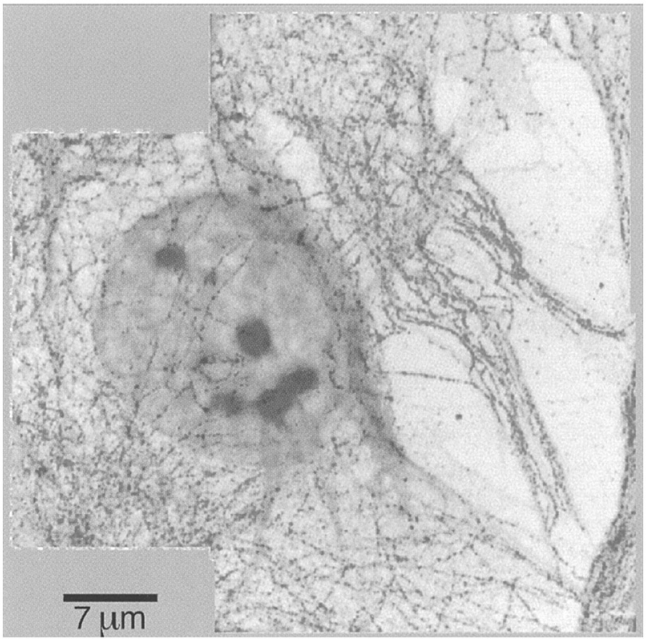

COLORPLATE XVII. Dark field soft x-ray scanning microscopy is demonstrated in this image of a human fibroblast, a collagen rich cell that plays an important role in the formation of extracellular matricies of connective tissue. The image obtained at 2.50 nm wavelength with the Stony Brook scanning microscope at Brookhaven National Laboratory, consists of an overlay of the two signals: a transmission signal in gray indicative largely of absorption of x-rays by carbon, and a signal in red due to scattering of x-rays by silver enhanced gold labels attached to microtubules (cytoskeleton fibers of the cell not found in the nucleus). (Courtesy of H. Chapman; LLNL, J Fu and C. Jacobsen, SUNY Stony Brook; and K. Hedberg, University of Oregon.) See text, p. 379.

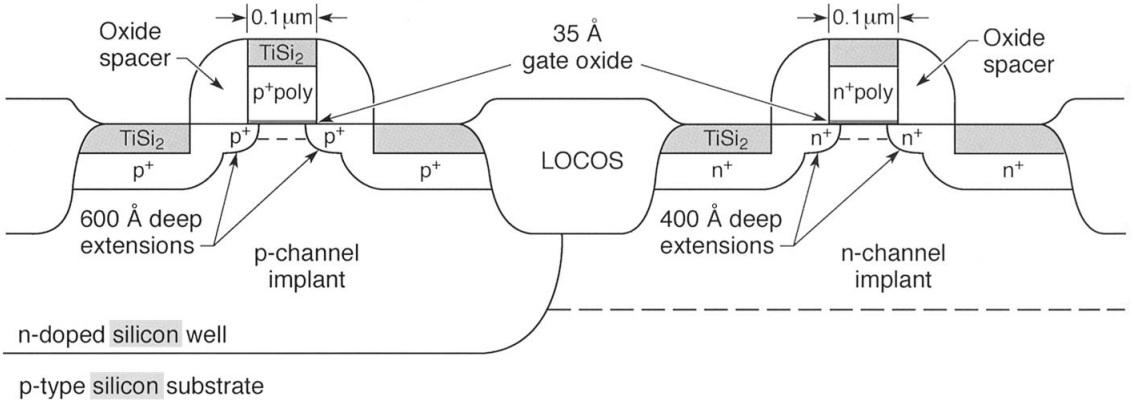

COLORPLATE XVIII. Cross-sectional view of a 0.1 μm complementary metal oxide semiconductor (CMOS) field effect transistor (FET) with dual n^+–p^+ doped polysilicon gates. The thin gate oxide is 0.1 μm wide and 35 Å deep. The titanium silicide provides a low resistivity interconnect. The oxide spacers and LOCOS are insulator regions. Note the presence of silicon in several chemical forms (crystalline, Si substrate with various dopings, polycrystalline Si, SiO_2, and $TiSi_2$). Concentrations of dopants and impurities in the vicinity of the gate region are critical to the performance of such devices and thus may require diagnostic methods, including soft x-ray microscopy, that are element sensitive with high spatial resolution and reasonable penetration depth. (Following Y. Taur et al., IBM.) See text, p. 380.

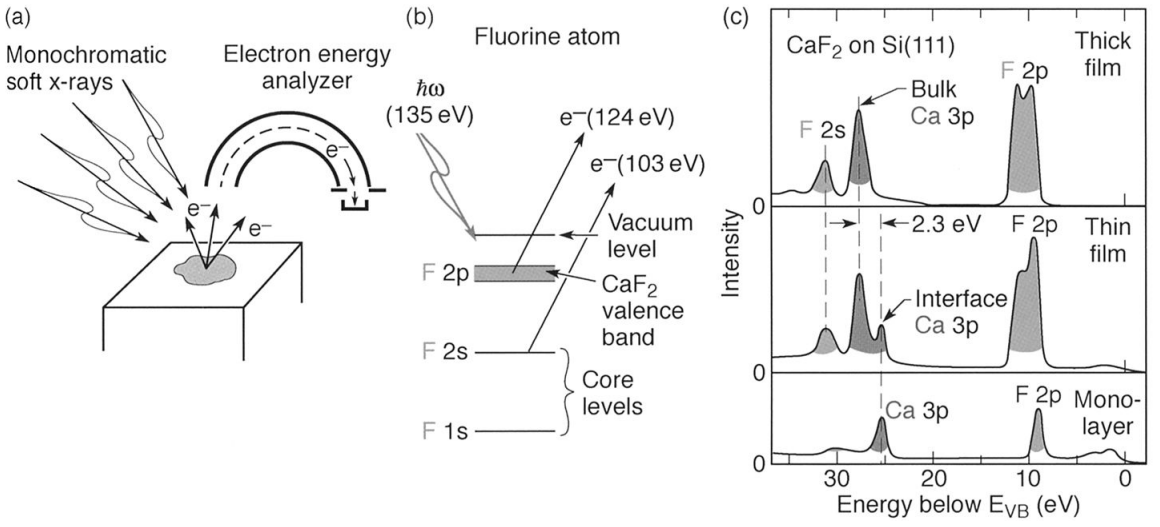

COLORPLATE XIX. Photoelectron spectroscopy is used to study calcium fluoride bonding to a silicon(111) substrate. The measured electron energy spectrum is shown for a monolayer of CaF_2 on Si(111), for a thin film of about 1.1 nm thickness, and for a relatively thick film of about 5 nm. (Courtesy of M. Olmsted, U. Washington.) See text, p. 382.

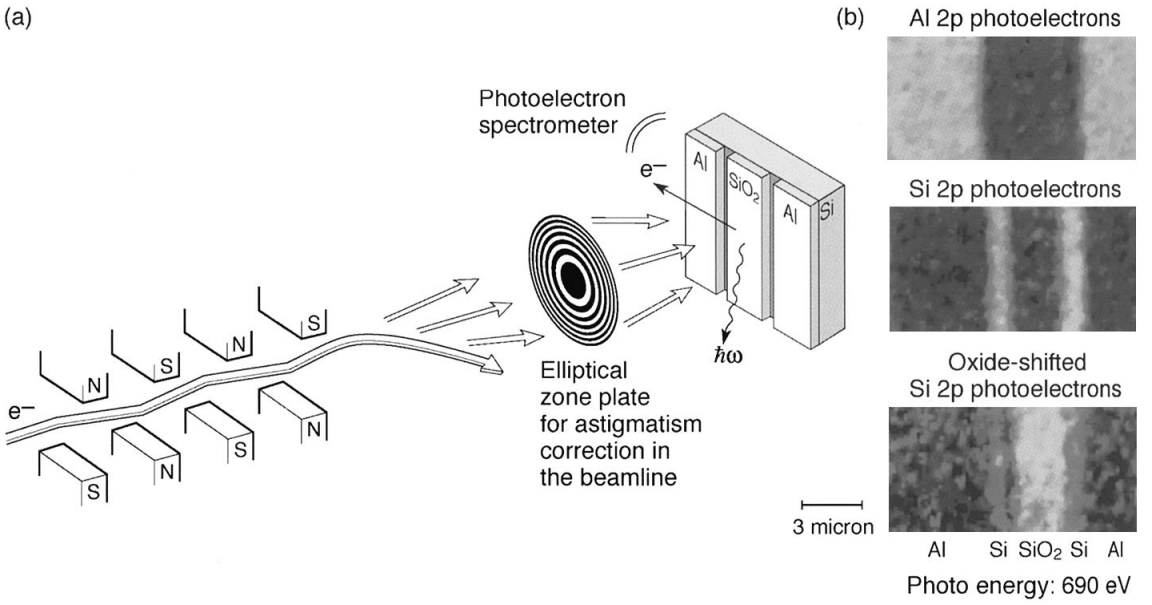

COLORPLATE XX. Spatially resolved photoemission from a composite Al–Si–SiO_2 sample illuminated with zone plate focused undulator radiation at Brookhaven National Laboratory. The incident photon energy is 690 eV, and the electron spectrometer pass-band is set for kinetic energies appropriate to the various binding energies of interest. (Courtesy of H. Ade et al., SUNY Stony Brook and North Carolina State University.) See text, p. 383.

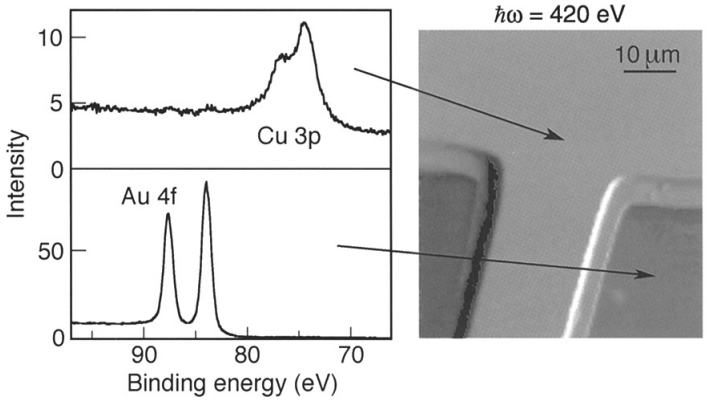

COLORPLATE XXI. Spatially resolved scanning photoemission image of a 100 mesh Cu grid on a gold foil, with localized spectra from Cu and gold regions. The incident photon energy is 420 eV. The image contrast is primarily due to the Cu 3p core-level intensity, but the shadows and enhancements are due to topographic effects of imaging with a small (~0.2 μm) beam spot. (From T. Warwick, J. Denlinger, E. Rotenberg, and colleagues, Lawrence Berkeley National Laboratory.) See text, p. 383.

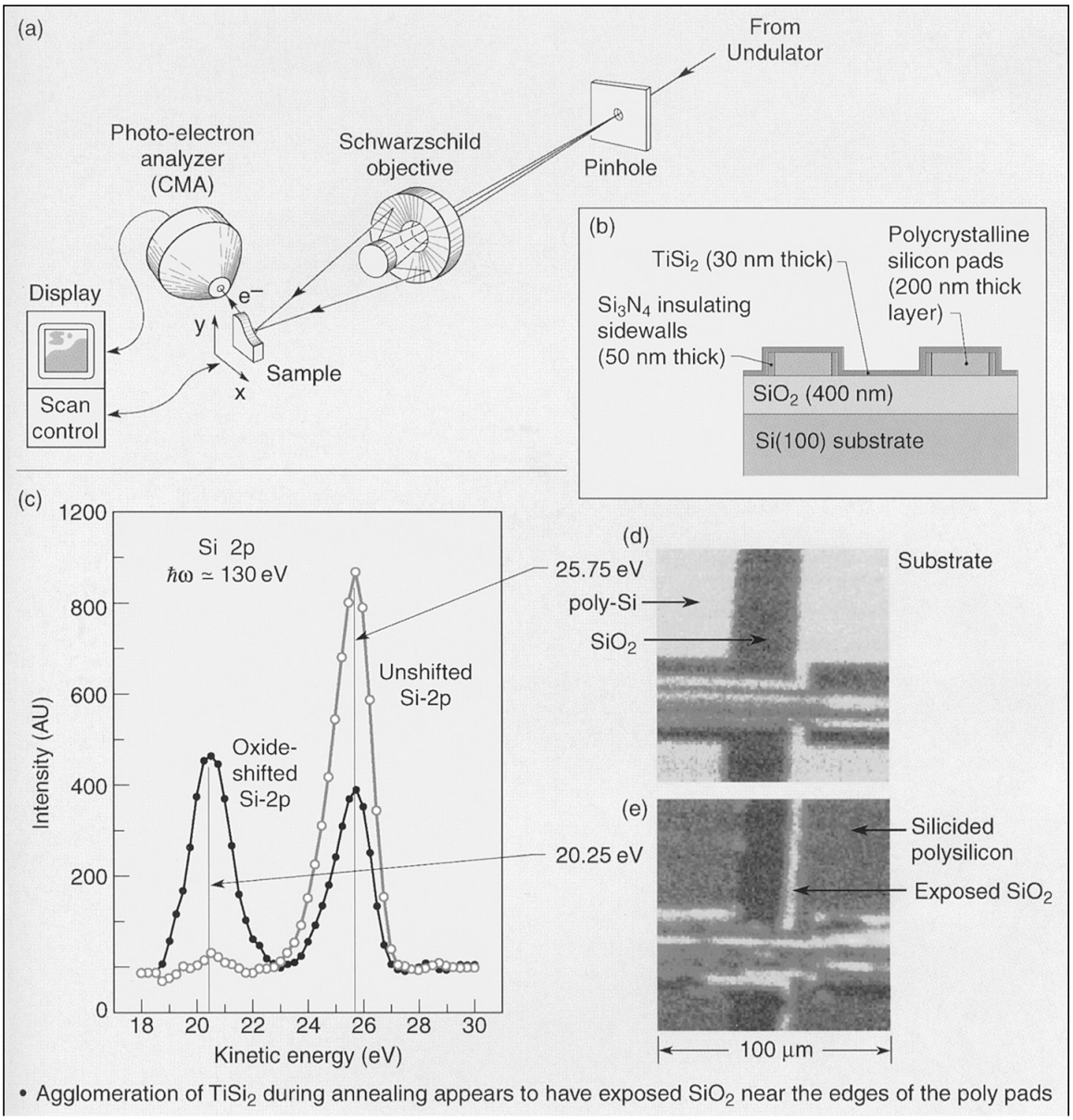

COLORPLATE XXII. Photoemission spectromicroscopy with multilayer coated Schwarzschild optics is illustrated in (a) and applied to a structure shown in (b). Photoelectron spectra are illustrated in (c) for two regions of an SRAM chip, one region where the silicon substrate is bare, and one region of silicon dioxide. In both cases Si 2p photoelectrons are detected during irradiation by 130 eV photons. The images in (d) and (e) are obtained at fixed electron energies corresponding to the unshifted (d) and oxide shifted (e) 2p states. The bright region (high photoelectron current) in (e) indicates an exposed region of SiO_2, initially covered with titanium silicide ($TiSi_2$). It appears that during the annealing process titanium silicide, initially covering a polysilicon pad, has agglomerated, leaving a region of SiO_2 exposed. (Courtesy of S. Singh and F. Cerrina, University of Wisconsin-Madison.) See text, p. 384.

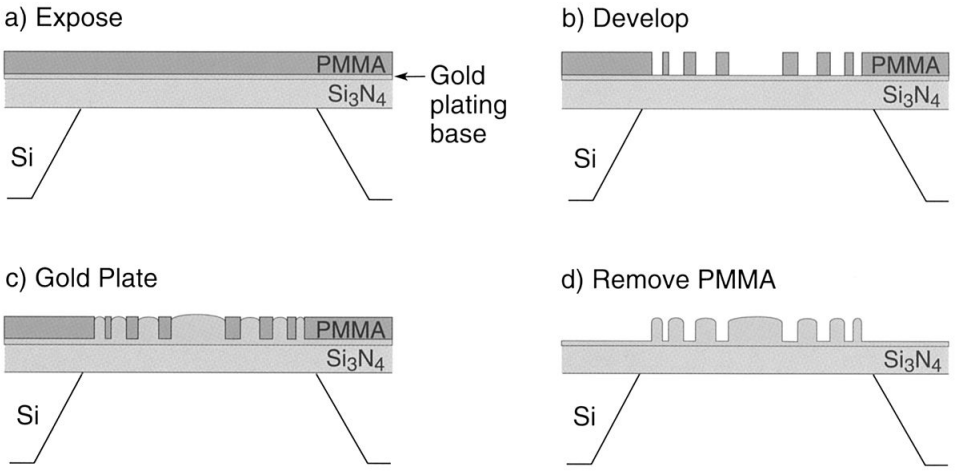

COLORPLATE XXIII. Nanofabrication of a gold zone plate involves a multilevel structure for recording a pattern in PMMA through (a) spatially patterned electron beam exposure, (b) development into a PMMA mold, (c) gold plating into the mold, and (d) removal of the remaining PMMA to leave a gold zone plate lens on a thin silicon nitride membrane, over an etched window in the silicon wafer substrate. (Courtesy of Erik Anderson, LBNL.) See text, p. 386.